Summer 2020

# Exploratory Molten Flux Crystal Growth of Complex Uranium Oxides

Christian A. Juillerat

Exploratory Molten Flux Crystal Growth of Complex Uranium Oxides

by

Christian A. Juillerat

Bachelor of Arts
Lake Forest College, 2016

---

Submitted in Partial Fulfillment of the Requirements

For the Degree of Doctor of Philosophy in

Chemistry

College of Arts and Sciences

University of South Carolina

2020

Accepted by:

Hans-Conrad zur Loye, Major Professor

Richard Adams, Committee Member

Dmitry Peryshkov, Committee Member

Sophya Garashchuk, Committee Member

Jochen Lauterbach, Committee Member

Cheryl L. Addy, Vice Provost and Dean of the Graduate School

## Dedication

For the numerous friends, family, teachers, and mentors that helped me along the way, but especially to my husband, Jacob, who has been there every step of the way.

## Acknowledgements

Over the many years that it took to get to this point, I have received tremendous help, support, and encouragement from many people. First, I'd like to thank my advisor, Dr. zur Loye, for giving me the opportunity and freedom to work in his lab. I'd also like to thank Dr. zur Loye, Dr. Taylor-Perry, and Dr. Lovelace for helping me to pursue and explore my teaching interests. Additionally, I'd like to my committee members for always being very flexible and being genuinely interested in my graduate research. I'd like to specifically thank Dr. Jason Cody for introducing me to crystal growth and characterization and giving me my first taste of research, as well as planting the idea of pursuing a Ph.D.

Next I need to thank all of the members of the zur Loye group, both past and present, for their abundance of help and encouragement. I'd like to especially thank Dr. Gregory Morrison for teaching me essentially all of my lab skills and always making time to listen and provide second opinions.

I'd like to thank my family, especially my husband. Jacob, I am so grateful that we are journeying through life together and glad you've been able to go through this experience with me—I know having you by my side has made this pursuit easier.

Finally, I thank God for the gifts and talents that have enabled me to pursue my degree—without Him I am nothing. He continues to surprise me as He orchestrates my life and things come together in ways I could never have imagined.

*Thank you to the DOE for financially supporting the research presented here and the NSF for the IGERT fellowship that supported my studies.*

## Abstract

While the use of nuclear technology has proven useful for energy generation and for military use, the proper disposal and storage of the resulting nuclear waste requires serious attention to ensure radioactive species are indefinitely sequestered to protect the biosphere. There are several classifications of nuclear waste such as spent nuclear fuel (from industrial power plants), low level waste (slightly contaminated trash), and high level waste (HLW) which is in the form of a sludge, precipitated salt, or liquid. Each of these requires a different approach to processing and storage. Of these, HLW requires the most attention because it is the most expensive, highest risk, and will take longest to process and store. While the current method of incorporating the HLW into a glass is very successful, it is inefficient for a few of the species found in this waste such as Cs, I, and Tc.

The lack of a universal waste storage material not only calls us to further characterize known materials that are good candidates for waste sequestration, but also to discover new materials with potentially better properties than those of existing materials. Crystal growth, in general, is well suited for material discovery as it facilitates the preparation of new complex compositions in the absence of a fully established crystal chemistry and crystals can be efficiently characterized by single crystal X-ray diffraction. This work explores the exploratory flux crystal growth of uranium oxide framework structures and characterizes their structures as well as thermal and ion exchange properties which are useful for preliminary screening of potential wasteforms and discovering structure-property relationships.

Table of Contents

Dedication ..... iii

Acknowledgements ..... iv

Abstract ..... v

List of Tables ..... viii

List of Figures ..... xi

List of Abbreviations ..... xvii

List of Compounds ..... xviii

Introduction to Nuclear Waste Forms, Crystal Growth, and Uranium Oxides ..... 1

Chapter 1: Versatile Uranyl Germanate Framework Hosting Twelve Different Alkali Halide 1D Salt Inclusions ..... 23

Chapter 2: A Family of Layered Phosphates Crystallizing in a Rare Geometrical Isomer of the Phosphuranylite Topology: Synthesis, Characterization, and Computational Modeling of $A_4[(UO_2)_3O_2(PO_4)_2]$ (A = alkali metals) Exhibiting Intra-layer Ion Exchange ..... 60

Chapter 3: Crystal Growth and Structure Characterization of Three Layered Uranyl Phosphates and Their Relation to the Phosphuranylite Family ..... 100

Chapter 4: Observation of an Unusual Uranyl Cation-Cation Interaction in the Strongly Fluorescent Layered Uranyl Phosphates $Rb_6[(UO_2)_7O_4(PO_4)_4]$ and $Cs_6[(UO_2)_7O_4(PO_4)_4$ ..... 123

Chapter 5: Observation of the Same New Sheet Topology in Both the Layered Uranyl Oxide-Phosphate $Cs_{11}[(UO_2)_{12}(PO_4)_3O_{13}]$ and the Layered Uranyl Oxyfluoride-Phosphate $Rb_{11}[UO_2)_{12}(PO_4)_3O_{12}F_2]$ Prepared by Flux Crystal Growth ..... 140

Chapter 6: Overstepping Löwenstein's Rule – a Route to Unique Aluminophosphate Frameworks with 3D Salt-Inclusion and Ion Exchange Properties ..... 171

Chapter 7: $Cs_2(UO_2)Al_2O_5$: An Unprecedented Uranium Aluminate Discovered Serendipitously by Molten Flux Methods .....214

Chapter 8: Targeted Crystal Growth of Uranium Gallophosphates Via the Systematic Exploration of the $UF_4$-$GaPO_4$-ACl (A = Cs, Rb) Phase Space .....231

Chapter 9: Structure and Stability of Alkali Gallates Structurally Reminiscent of Hollandite .....266

Chapter 10: Flux Crystal Growth of Uranium(V) Containing Oxyfluoride Perovskites.....292

Chapter 11: Fluorination and reduction of $CaCrO_3$ by topochemical methods.....326

Chapter 12: Conclusions and future directions .....349

Appendix A: Understanding the Stability of Salt-Inclusion Phases for Nuclear Waste-forms through Volume-based Thermodynamic .....356

Appendix B: Understanding the polymorphism of $A_4[(UO_2)_3(PO_4)_2O_2]$ (A=alkali metals) uranyl phosphate framework structure .....379

Appendix C: Permission to Reproduce Published Materials .....411

# List of Tables

Table I.1: Selected fluxes and eutectis and their melting points ..... 11

Table 1.1: Reactant ratios for synthesized uranium germanate SIMs (mmol) ..... 29

Table 1.2: Crystallographic Data for Compounds 1.1-1.13 ..... 38

Table 1.3: Pore Volumes, Salt-Inclusion Volumes, Pore Diameters for 1.1-1.12..... 51

Table 2.1: Reactant amounts in mmols for compounds 1.1-1.6 ..... 65

Table 2.2: Crystallographic data and information for 2.1-2.8 ..... 67

Table 2.3: Auxiliary thermodynamic data ..... 72

Table 2.4: Bond valence sums and bond distances for $Cs_{1.4}K_{2.6}[(UO_2)_3O_2(PO_4)_2]$ ..... 77

Table 2.5: Bond valence sums and bond distances for $Cs_{0.7}K_{3.3}[(UO_2)_3O_2(PO_4)_2]$ ..... 77

Table 2.6: Bond valence sums and bond distances for $Rb_{1.4}K_{2.6}[(UO_2)_3O_2(PO_4)_2]$ ..... 78

Table 2.7: Bond valence sums and bond distances for $K_4[(UO_2)_3O_2(PO_4)_2]$ ..... 78

Table 2.8: Bond valence sums for $K_{2.1}Na_{0.7}Rb_{1.2}[(UO_2)_3O_2(PO_4)_2]$ ..... 78

Table 2.9: Bond valence sums for $K_{2.9}Na_{0.9}Rb_{0.2}[(UO_2)_3O_2(PO_4)_2]$ ..... 79

Table 2.10: Enthalpies of formation from VBT and DFT for 2.1-2.6 ..... 86

Table 2.11: Molar volumes from XRD, entropy, and lattice potentials of 2.1-2.6 ..... 87

Table 2.12: DFT calculated enthalpy of formation, in kJ/mol, of ion exchange products ... 91

Table 2.13: DFT calculated total energies of isolated alkali ions, in kJ/mol ..... 91

Table 2.14: Ion exchange energies of possible compositions from Table 12..... 91

Table 2.15: Molar volumes and lattice potential energy of ion exchange compositions ..... 93

Table 2.16: Ion exchange energies of possible compositions from Table 15.....94

Table 3.1: Full crystallographic data for 3.1-3.3 .....107

Table 3.2: Bond valence sums and bond distances for $CsNa_3[(UO_2)_3O_2(PO_4)_2]$ .....108

Table 3.3: Bond valence sums and bond distances for $Cs_2Na_4[(UO_2)_5O_5(PO_4)_2]$ .....108

Table 3.4: Bond valence sums and bond distances for $Rb_6[(UO_2)_5O_5(PO_4)_2]$ .....109

Table 4.1: Full crystallographic data for 4.1 and 4.2 .....127

Table 4.2: Bond valence sums and bond distances for $Cs_6[(UO_2)_7O_4(PO_4)_4]$ .....130

Table 4.3: Bond valence sums and bond distances for $Rb_6[(UO_2)_7O_4(PO_4)_4]$ .....130

Table 4.4: Results from Volume Based Thermodynamic Approach.....136

Table 5.1: Crystallographic details of structures 5.1-5.4.....146

Table 5.2: Bond valence sums and bond distances for $Cs_{11}[(UO_2)_{12}(PO_4)_3O_{13}]$ .....156

Table 5.3: Bond valence sums and bond distances for $Rb_{11}[UO_2)_{12}(PO_4)_3O_{12}F_2]$ .....157

Table 5.4: BVSs and bond distances for $Cs_{4.4}K_{0.6}[(UO_2)_6O_4F(PO_4)_4(UO_2)]$ .....157

Table 5.5: BVSs and bond distances for $Rb_{4.4}K_{0.6}[(UO_2)_6O_4F(PO_4)_4(UO_2)]$ .....158

Table 5.6. Reaction enthalpies ($\Delta_r H$) and $\Delta\Delta_r H$ of 5.1, 5.2, and related phases .....161

Table 6.1: Crystallographic information for structures 6.1-6.8.....185

Table 7.1: Full crystallographic data for $Cs_2UO_2Al_2O_5$ .....220

Table 7.2. Bond valence sums and bond distances for $Cs_2UO_2Al_2O_5$.....220

Table 7.3. Chemical potential, in eV, of the ions, in vacuum and in water.....223

Table 7.4. Crystallographic data from DFT+*U* relaxed structures.....223

Table 8.1: Crystallographic data for compounds 8.1-8.6 .....238

Table 8.2: Phase space summary of $UF_4$-$GaPO_4$-RbCl in 5mL fused silica crucibles....246

Table 8.3: Phase space summary of $UF_4$-$GaPO_4$-RbCl in 5mL Pt crucibles .....247

Table 8.4: Phase space summary of $UF_4$-$GaPO_4$-CsCl in 5mL Pt crucibles ..... 248

Table 8.5: BVS and bond distances for $Cs_2UO_2Ga_2O_5$ (8.2) ..... 250

Table 8.6: BVS and bond distances for $[Rb_{5.93}Cl_{0.93}][(UO_2)_5(PO_4)_5]$(8.3) ..... 252

Table 8.7: BVS and bond distances for $Rb_{11}[(UO_2)_8(PO_4)_9]$ (8.4) ..... 254

Table 8.8: BVS and bond distances for $Rb_{7.6}[(UO_2)_8O_{8.6}F_{0.4}(PO_4)_2]$(8.5) ..... 256

Table 8.9: BVS and bond distances for $Rb_6[(UO_2)_5O_2(PO_4)_4$ (8.6) ..... 258

Table 8.10: Total information content of structures 8.2-8.6 ..... 259

Table 9.1: Full crystallographic data for structures 9.1-9.3 ..... 270

Table 9.2: Measured pH of solutions before and after leach testing of 9.1 ..... 274

Table 9.3: M-O bond distances in structures 9.1-9.3 ..... 280

Table 10.1: Crystallographic information for structures 10.1-10.3 ..... 300

Table 10.2: The % ratio of U oxidation states recorded by XPS for 10.1-10.3 ..... 310

Table 10.3: Surface atomic ratios determined by XPS before and after sputtering ..... 310

Table 11.1: Crystallographic parameters of fluorinated $CaCrO_3$ ..... 335

Table 11.2: Crystallographic parameters of $CaCrO_3$ ..... 335

Table 11.3: Crystallographic parameters of $CaCrO_{2.5}$ ..... 335

Table 11.4. Bond Valence Sums for different anion ordering models ..... 336

Table A.1: Collection of auxiliary data for use in Born-Haber-Fajans cycle ..... 361

Table A.2: List of SIMs treated using VBT, along with the crystallographic data to calculate the formula unit volume ($V_m$) ..... 362

Table A.3: Thermochemical cycles for SIMs framework components ..... 365

Table A.4: Enthalpies of formation, Gibbs energies of formation, and standard entropies of SIMs from VBT compared with DFT and Experiment ..... 368

Table B.1: Full crystallographic data for $Cs_4[(UO_2)_3(PO_4)_2O_2]$ ..... 388

# List of Figures

Figure I.1: Visual summary of fluxes and approximate operating temperatures ..... 8

Figure I.2: Reaction vessels for flux reactions ..... 10

Figure I.3: A simplistic representation of the crystallization process ..... 11

Figure I.4: Uranium VI coordination ..... 16

Figure I.5: Autunite and phosphuranylite topologies ..... 17

Figure 1.1: Photographs of product crystals of 1.1, 1.3, 1.6, 1.7, 1.13 ..... 28

Figure 1.2: PXRD patterns of 1.6 and 1.12 ..... 42

Figure 1.3: Structures of 1.2 and 1.7 ..... 45

Figure 1.4: Comparison of the Cs2 and K3 sites 1.2 and 1.7 ..... 48

Figure 1.5: The salt inclusions of 1.1, 1.5, and 1.6 ..... 48

Figure 1.6: Pore Volume vs. Salt Inclusion Volume ..... 50

Figure 1.7: The structure of 1.13 ..... 53

Figure 1.8: UV-vis of 1.6 and 1.12 ..... 54

Figure 1.9: Fluorescence of 1.6 and 1.12 ..... 55

Figure 2.1. Geometrical isomers of the phosphuranylite topology ..... 63

Figure 2.2: Reaction Vessel for 2.1-2.8 ..... 65

Figure 2.3: Crystal pictures of 2.1 2.2, 2.4, 2.7, 2.6 ..... 65

Figure 2.4: VBT method flow chart ..... 71

Figure 2.5: Thermochemical cycle for ion exchange of 2.4 ..... 73

Figure 2.6: Structure of 2.1-2.4 ..... 79

Figure 2.7: Structures of 2.5 and 2.6 ..... 79

Figure 2.8: PXRD patterans of 2.2, 2.3, 2.4, and ion exchange products ..... 81

Figure 2.9: Structure of 2.7 ..... 83

Figure 2.10: Fluorescence spectra of 2.2-2.4 ..... 84

Figure 2.11: UV-vis spectra of 2.2-2.4 ..... 84

Figure 2.12: Born-Haber cycle used to calculate the formation enthalpy of 2.2 ..... 87

Figure 2.13: Graph thermodynamic values for 2.1-2.6 as a function of molar volume .... 88

Figure 2.14: Graph of the content during ion exchange reactions ..... 90

Figure 3.1: The phosphuranylite and extended phosphuranylite topologies ..... 104

Figure 3.2: Optical images of crystals 3.1 and 3.3 ..... 105

Figure 3.3: The known geometric isomers of the phosphuranylite topology ..... 113

Figure 3.4: The structures of 3.1 and 3.2 ..... 114

Figure 3.5: The structure of $Rb_6[(UO_2)_5O_5(PO_4)_2]$ (3.3) ..... 115

Figure 3.6: The known geometric isomers of the extended phosphuranylite topology .. 117

Figure 4.1: Orange plate crystals of 4.1 and 4.2 ..... 125

Figure 4.2: PXRD patterns of 4.1 and 4.2 ..... 126

Figure 4.3: The construction of $A_6[(UO_2)_7O_4(PO_4)_4]$ from phosphuranylite (PU) units and dimers ..... 129

Figure 4.4: The CCI observed in $A_6[(UO_2)_7O_4(PO_4)_4]$ ..... 129

Figure 4.5: UV-vis spectra for 4.1 and 4.2 ..... 131

Figure 4.6: Emission and excitation spectra for 4.1 and 4.2 ..... 132

Figure 4.7: Optical pictures of powders of 4.1 and 4.2 ..... 132

Figure 4.8: Born-Haber cycle used to calculate formation enthalpy of **4.1** and **4.2** ..... 134

Figure 4.9: PXRD patterns of ion exchange products ..... 135

Figure 5.1: Optical images of single crystals of 5.1 and 5.2 ..... 145

Figure 5.2: Sheet topology of 5.1 and 5.2 ..... 154

Figure 5.3: Sheets in 5.1 and 5.2 ..... 155

Figure 5.4: Structure of 5.3 and 5.4 ..... 160

Figure 5.5: Quasi-Gibbs reaction energies ($\Delta_r g$) of 5.1, 5.2, and related phases ..... 162

Figure 5.6: PXRD of 5.1 and the resulting powder ion exchange products ..... 163

Figure 5.7: PXRD of 5.2 and the resulting powder ion exchange product ..... 164

Figure 5.8: The UV-vis optical absorption spectra of 5.1 and 5.2 ..... 165

Figure 5.9: The fluorescence spectra of 5.1 and 5.2 ..... 165

Figure 5.10: Density of states and atom resolved projected DOS of 5.1 and 5.2 ..... 166

Figure 6.1: The $[Al_2O(PO_4)_6]^{14-}$ building block ..... 175

Figure 6.2: PXRD pattern of 6.3 obtained by a solid state reaction ..... 178

Figure 6.3: TGA of powder samples of 6.6 before and after NaCl ion exchange ..... 191

Figure 6.4: PXRD pattern of the bulk ion exchange product of 6.6 soaked in NaCl ..... 192

Figure 6.5: PXRD pattern of 6.6 ..... 192

Figure 6.6: Structure of 6.1 ..... 195

Figure 6.7: Structure of 6.2 ..... 196

Figure 6.8: The framework structure of 6.3 ..... 198

Figure 6.9:Topologies of the framework and salt inclusion of 6.3 ..... 199

Figure 6.10: Structure of 6.4-6.6 ..... 201

Figure 6.11: Comparison of the alkali metal sites in 6.5 and 6.7 ..... 201

Figure 6.12: Comparison of 6.6 and ion exchange product 6.8 ..... 203

Figure 6.13: Construction of 6.3-6.5 from the aluminophosphate building block ..... 204

Figure 6.14: Structural evolution of 6.1-6.8 ..... 206

Figure 6.15: UV-vis spectra of compounds 1-6 ..... 207

Figure 6.16: Emission fluorescence spectra of 6.1–6.6 ..... 208

Figure 7.1: Single crystals of $Cs_2(UO_2)Al_2O_5$ ..... 217

Figure 7.2: PXRD pattern of $Cs_2(UO_2)Al_2O_5$ ..... 219

Figure 7.3: Structure of $Cs_2(UO_2)Al_2O_5$ ..... 218

Figure 7.4: Diffuse scattering of 7.1 ..... 221

Figure 7.5: PXRD pattern of the K ion exchange product ..... 224

Figure 7.6: Total and partial density of states (DOS) of $Cs_2UO_2Al_2O_5$ ..... 226

Figure 7.7: Normalized UV-vis fluorescence spectra of $Cs_2(UO_2)Al_2O_5$ ..... 226

Figure 8.1: Optical images of single crystals of 8.2-8.6 ..... 235

Figure 8.2: Powder diffraction data of 8.1 ..... 249

Figure 8.3: The layered structure of 8.1 ..... 249

Figure 8.4: The structure of 8.2 ..... 251

Figure 8.5: The structure of 8.3 ..... 251

Figure 8.6: The structure of 8.4 ..... 254

Figure 8.7: The structure of 8.5 ..... 256

Figure 8.8: The layered structure of 8.6 ..... 257

Figure 8.9: The fluorescence emission spectra of structure 8.1-8.6 ..... 259

Figure 9.1: The hollandite structure type, $A_xM_8O_{16}$ ..... 268

Figure 9.2: Structure of 9.1 and 9.2, $AGa_7O_{11}$ (A = Rb, Cs) ..... 278

Figure 9.3: Frameworks and underlying nets of 9.1 and hollandite ..... 279

Figure 9.4: Tunnel dimensions of 9.1-9.3 and hollandite ..... 279

Figure 9.5: Selected metal coordination environments in 9.1 and 9.3 ..... 280

Figure 9.6: Structure of 9.3 ..... 281

Figure 9.7: Visual summary of ion exchange reactions of 9.1 and 9.3 ..... 283

Figure 9.8: PXRD patterns of $CsGa_7O_{11}$ ion exchange reactions ..... 284

Figure 9.9: PXRD patterns of $RbGa_4In_5O_{14}$ ion exchange reactions ..... 285

Figure 9.10: PXRD patterns of $CsGa_7O_{11}$ before and after leach experiments ..... 286

Figure 9.11: The calculated fractional release of Cs in leach tests of 9.1 ..... 288

Figure 10.1: Single of crystals of a) 10.2 and b) 10.1 ..... 298

Figure 10.2: Structure of 10.1 and its relation to the perovskite family ..... 307

Figure 10.3: XANES spectra of 10.1-10.3 ..... 308

Figure 10.4: XPS spectra of 10.1-10.3 measured after synthesis with no further treatment ..... 309

Figure 10.5: XPS spectra of 10.1-10.3 after 30 seconds of Ar sputtering ..... 311

Figure 10.6: PXRD of 10.1-10.3 ..... 313

Figure 10.7: $\chi$ vs T plot of three different samples of 10.2 ..... 314

Figure 10.8. Density of states (DOS) of 10.1-10.3 ..... 315

Figure 10.9: Effect of F atoms as FNN in projected density of states (pDOS) ..... 316

Figure 10.10: UV-vis spectra of 10.1-10.1.1 ..... 317

Figure 11.1: Structures of $ACrO_2$ (A = Ca, Sr) ..... 329

Figure 11.2: SXRD patterns of the products of $CaCrO_3$ and PVDF or g-$C_3N_4$ ..... 332

Figure 11.3: Rietveld refinement against PXRD data of fluorinated $CaCrO_3$ ..... 333

Figure 11.4: Rietveld refinement against PXRD data of $CaCrO_3$ ..... 334

Figure 11.5: Rietveld refinement against PXRD data of $CaCrO_{2.5}$ ..... 334

Figure 11.6: Cr 2*p* core level XPS spectra of $CaCrO_3$ and its fluorinated phase ..... 337

Figure 11.7: Wide scan XPS spectra of $CaCrO_3$ and its fluorinated phase ..... 337

Figure 11.8: Structures of $CaCrO_3$, $CaCrO_{2.5}$, $CaCrO_{2.67}$, and $CaCrO_{3-x}F_x$ ..... 338

Figure 11.9: Chromium coordination environments in $CaCrO_3$ and $CaCrO_{3-x}F_x$ ..... 340

Figure 11.10: $\chi$ (*T*) plot of $CaCrO_3$, $CaCrO_{2.5}$, and $CaCrO_{2.5}F_{0.5}$ ..... 344

Figure 11.11: *H/M* (*T*) plot of $CaCrO_3$, $CaCrO_{2.5}$, and $CaCrO_{2.5}F_{0.5}$ ..... 344

Figure A.1: Schematic for calculating thermodynamic values from VBT methods ..... 360

Figure A.2: Thermochemical cycle for a uranyl silicate salt inclusion ..... 364

Figure A.3: Lattice potential energy ($U_{pot}$) as a function of $V_m$ for SIMs ..... 366

Figure A.4: VBT computed formation enthalpies using experimental and DFT Calculated $V_m$ ..... 367

Figure A.5: Gibbs energy of formation as a function of $V_m$ for silicate and germanate SIMs ..... 367

Figure B.1: Structures of the two polymorphs of $A_4[(UO_2)_3(PO_4)_2O_2]$ ..... 389

Figure B.2: Volume and bond distances of the layered and 3D polymorphs ..... 391

Figure B.3: Calculated total energy difference, between the 3D and layered polymorphs ..... 393

Figure B.4: Comparison of DFT- and VBT-derived $\Delta E$ ..... 395

Figure B.5: Band gaps of a) layered, and b) 3D polymorphs ..... 396

Figure B.6: Density of states (DOS) of a) layered polymorphs and b) 3D polymorphs ..... 397

Figure B.7: Projected DOS (PDOS) of K containing polymorphs ..... 399

Figure B.8: ICOHP per 1NN bonds in the a) layered and b) 3D polymorphs ..... 402

Figure B.9: Absorption indexes for: a) layered and b) 3D polymorphs ..... 405

## List of Abbreviations

BVS ..... Bond Valence Sum

CCI ..... Cation-Cation Interaction

cif ..... Crystallographic Information File

DFT ..... Density Functional Theory

DOS ..... Density of States

EDS ..... Energy Dispersive Spectroscopy

HLW ..... High Level Waste

PXRD ..... Powder X-ray Diffraction

SEM ..... Scanning Electron Microscopy

SIM ..... Salt Inclusion Material

S.G. ..... Space Group

SXRD ..... Single Crystal X-ray diffraction

TGA ..... Thermogravimetric Analysis

UV-Vis ..... Ultraviolet-Visible Spectroscopy

VBT ..... Volume Based Thermodynamics

XANES ..... X-ray Absorption Near Edge Spectroscopy

XPS ..... X-ray Photoelectron Spectroscopy

# List of Compounds by Chapter


1.1 $[Cs_2Cs_5F][(UO_2)_3(Ge_2O_7)_2]$ ..... 1

1.2 $[Cs_6Ag_2Cl_2][(UO_2)_3(Ge_2O_7)_2]$ ..... 1

1.3 $[Cs_6Ag_{0.3}Na_{1.7}Cl_2][(UO_2)_3(Ge_2O_7)_2]$ ..... 1

1.4 $[Cs_6Ag_{0.4}Na_{1.6}Cl_2][(UO_2)_3(Ge_2O_7)_2]$ ..... 1

1.5 $[Cs_6K_2Cl_2][(UO_2)_3(Ge_2O_7)_2]$ ..... 1

1.6 $[Cs_6K_{1.9}Ag_{0.1}Cl_2][(UO_2)_3(Ge_2O_7)_2]$ ..... 1

1.7 $[KK_6Cl][(UO_2)_3(Ge_2O_7)_2]$ ..... 1

1.8 $[KK_6Br_{0.6}F_{0.4}][(UO_2)_3(Ge_2O_7)_2]$ ..... 1

1.9 $[Na_{0.9}Rb_{6.1}F][(UO_2)_3(Ge_2O_7)_2]$ ..... 1

1.10 $[K_{0.6}Na_{0.4}K_5CsCl_{0.5}F_{0.5}][(UO_2)_3(Ge_2O_7)_2]$ ..... 1

1.11 $[K_{0.8}Na_{0.2}K_{4.8}Cs_{1.2}Cl_{0.5}F_{0.5}][(UO_2)_3(Ge_2O_7)_2]$ ..... 1

1.12 $[KK_{1.8}Cs_{4.2}F][(UO_2)_3(Ge_2O_7)_2]$ ..... 1

1.13 $[Cs_6Cs_{0.71}Cl_{0.71}][(UO_2)_3O_3(Ge_2O_7)]$ ..... 1

2.1 $Cs_{1.4}K_{2.6}(PO_4)_2[(UO_2)_3O_2]$ ..... 2

2.2 $Cs_{0.7}K_{3.3}[(UO_2)_3O_2(PO_4)_2]$ ..... 2

2.3 $Rb_{1.4}K_{2.6}[(UO_2)_3O_2(PO_4)_2]$ ..... 2

2.4 $K_4[(UO_2)_3O_2(PO_4)_2]$ ..... 2

2.5 $K_{2.9}Na_{0.9}Rb_{0.2}[(UO_2)_3O_2(PO_4)_2]$ ..... 2

2.6 $K_{2.1}Na_{0.7}Rb_{1.2}[(UO_2)_3O_2(PO_4)_2]$ ..... 2

2.7 $Cs_{1.7}K_{4.3}[(UO_2)_5O_5(PO_4)_2]$ ..... 2

2.8 $Rb_{1.6}K_{4.4}[(UO_2)_5O_5(PO_4)_2]$ ..... 2

3.1 $CsNa_3[(UO_2)_3O_2(PO_4)_2]$ ..... 3

3.2 $Cs_2Na_4[(UO_2)_5O_5(PO_4)_2]$ ..... 3

3.3 $Rb_6[(UO_2)_5O_5(PO_4)_2]$ ..... 3

4.1 $Rb_6[(UO_2)_7O_4(PO_4)_4]$ ..... 4

4.2 $Cs_6[(UO_2)_7O_4(PO_4)_4]$ ..... 4

5.1 $Cs_{11}[(UO_2)_{12}(PO_4)_3O_{13}]$ ..... 5

5.2 $Rb_{11}[UO_2)_{12}(PO_4)_3O_{12}F_2]$ ..... 5

5.3 $Cs_{4.4}K_{0.6}[(UO_2)_6O_4F(PO_4)_4(UO_2)]$ ..... 5

5.4 $Rb_{4.4}K_{0.6}[(UO_2)_6O_4F(PO_4)_4(UO_2)]$ ..... 5

6.1 $[Cs_4Cs_4Cl][(UO_2)_4(PO_4)_5]$ ..... 6

6.2 $Cs_4[UO_2Al_2(PO_4)_4]$ ..... 6

6.3 $[Cs_{13}Cl_5][(UO_2)_3Al_2O(PO_4)_6]$ ..... 6

6.4 $Rb_7[Al_2O(PO_4)_3][(UO_2)_6O_4(PO_4)_2]$ ..... 6

6.5 $Cs_3[Al_2O(PO_4)_3][(UO_2)_3O_2]$ ..... 6

6.6 $Rb_3[Al_2O(PO_4)_3][(UO_2)_3O_2]$ ..... 6

7.1 $Cs_2(UO_2)Al_2O_5$ ..... 7

8.1 $Cs_4[UO_2Ga_2(PO_4)_4]$ ..... 8

8.2 $CsUO_2Ga_2O_5$ ..... 8

8.3 $[Rb_{5.93}Cl_{0.93}][(UO_2)_5(PO_4)_5]$ ..... 8

8.4 $Rb_{11}[(UO_2)_8(PO_4)_9]$ ..... 8

8.5 $Rb_{7.6}[(UO_2)_8O_{8.6}F_{0.4}(PO_4)_2]$ ..... 8

8.6 $Rb_6[(UO_2)_5O_2(PO_4)_4]$ ..... 8

9.1 $CsGa_7O_{11}$ ..... 9

9.2 $RbGa_7O_{11}$ ..... 9

9.3 $RbGa_4In_5O_{14}$ ..... 9

10.1 $Rb_4NaU_3O_{12-x}F_x$ ..... 10

10.2 $K_4NaU_3O_{12-x}F_x$ ..... 10

10.3 $Rb_{2.1}K_{1.9}KU_3O_{12-x}F_x$ ..... 10

B.1 $Cs_4[(UO_2)_3(PO_4)_2O_2]$ ..... B

# Introduction to Nuclear Waste Forms, Crystal Growth, and Uranium Oxides[1]

[1]Reproduced in part from Juillerat, C. A.; Klepov, V. V.; Morrison, G.; Pace, K. A.; zur Loye, H.-C., Flux Crystal Growth: A Versatile Technique to Reveal the Crystal Chemistry of Complex Uranium Oxides, *Dalton Trans.* **2019**, *48*, 3162-3181 and Klepov, Vladislav V.; Juillerat, Christian A.; Pace, Kristen A.; Morrison, Gregory; zur Loye, H.-C., 'Soft' Alkali Bromide and Iodide Fluxes for Crystal Growth, *Frontiers in Chemistry*, **2020**, DOI: 10.3389/fchem.2020.00518.

**Waste form motivation and history**

Research and production of nuclear materials in the US largely began during the Manhattan Project in World War II and continued on into the Cold War. While the use and development of nuclear weapons has been significantly diminished over the past several decades, nuclear energy is continuing to garner attention both in the military and private sectors and the continued use and development of these technologies depends on our ability to safely sequester radionuclides for hundreds of thousands of years and prevent the migration of radionuclides in the environment. A variety of different classes of wastes have been generated ranging from slightly contaminated trash to highly chemically and radioactive toxic liquids, the latter of which is called High Level Waste (HLW) and is in the form of a sludge, precipitated salt, or liquid and is stored in tanks at the Savannah River and Hanford Sites. While all radioactive waste needs to be stored safely and securely, the HLW has the highest priority since the HLW cleanup is the most expensive, highest risk, will take the longest to process and store, and is arguably the most difficult waste storage challenge.[1]

Nuclear waste forms should entirely contain the radioactive chemical species and function as the first barrier to the release of any radionuclides, followed by the container the waste form is stored in, and then the location (i.e. geological sound national repository). Ideal, imagined waste forms should have a large capacity for immobilizing radionuclides, be chemically and physically resistant to alteration, have a high tolerance to radiation effects, be chemically flexible to accommodate a mixture of constituents, be compatible with the disposal environment, and be easily fabricated and processed.[1]

The development of nuclear waste forms started soon after World War II, and extensive research and development programs on nuclear waste were undertaken in the late 70s and early 80s that identified crystalline and glassy materials as good waste form candidates. However, upon the 1981 decision to immobilize HLW in the US using a borosilicate glass, the research activity, especially on crystalline waste forms, greatly decreased. This borosilicate glass waste form, also referred to as a vitreous waste form, is an amorphous glass waste form that is produced by incorporating the waste stream with the borosilicate glass melt at ~1200 °C and by cooling the glass to the solid state without crystallization.[1] Vitreous waste forms meet many of the criteria for an ideal waste form, such as flexible processing, scalability, chemical flexibility, and durability. The vitreous waste form is not free from limitations, and one major one is the limited waste loading that is constrained by the crystallization and melt characteristics of the glass, since partial crystallization is known to diminish the leach resistance and long-term performance of glass waste forms. Species that are glass-immiscible, such as sulphates, chlorides, and molybdates, are particularly challenging for glass waste forms. Glass waste forms also do not efficiently incorporate volatile species like Cs, I, and Tc, due to the high melt temperature of the glass, and off-gas from the melt must be recaptured. These problematic species would benefit from new waste forms that cater to these species, and this will be the primary motivation for this dissertation.[2]

Crystalline (also called ceramic) waste forms are a potential alternative for these volatile and problematic isotopes because these radionuclides can be incorporated onto specific crystallographic sites within the crystal structure, thus immobilizing the radionuclide.[3] Crystalline waste forms are particularly advantageous because of the

numerous characterization methods that can be used to characterize the structure of these materials, which is much more challenging for amorphous materials. If the crystalline materials contain multiple cation and anion sites capable of accommodating a variety of radionuclides, the resulting waste load has the potential to be much greater than what can be accommodated by glass waste forms. Additionally, crystalline materials are potentially attractive for containing α-emitting radioisotopes that are long lived (such as plutonium and neptunium), and among the most promising, because crystalline materials that sustain damage due to large self-irradiation doses given off by actinides can remain chemically durable.[4] For these reasons, this dissertation will aim to expand the knowledge base of crystalline waste forms.[1]

**The role of exploratory crystal growth**

The absence of a universal storage material, and the lack of an appointed waste form for Cs orphan waste streams, not only calls us to further characterize known materials that are good candidates for waste sequestration, but also to discover new materials with potentially better properties than those of existing materials. On the way to finding new materials with improved properties for waste storage, we can also learn a great deal about actinide coordination chemistry and the chemistry of other radioisotopes that will aid in the discovery, development, and design of future waste forms. The preparation of a new material is not trivial as the targeted synthesis of an unknown compound is inherently challenging. In some relatively simple systems, there exists extensive literature that one can use to make targeted predictions of new compositions and the expected structural variants. For example, in the case of perovskite oxides, a simple set of rules exists to predict new compounds that will crystallize in the perovskite or related

structure types. Unfortunately, this prediction becomes prohibitively difficult for more complex compositions and structures, especially when the crystal chemistry is not well-understood and, even more so, when the structure type is unknown. This is where exploratory crystal growth is inherently useful, as it facilitates the preparation of new complex compositions in the absence of a fully established crystal chemistry; and, since the new compositions are isolated as single crystals, the structures of which can readily be determined. There are several extensively used crystal growth methods, but this dissertation will focus on utilizing flux crystal growth as the method for discovering new complex crystalline uranium oxide materials, including germanates, phosphates, aluminophosphates, aluminates, and gallates.

**Flux crystal growth**

The flux, typically an inorganic solid at room temperature, functions as the solvent at the high temperatures at which crystals are obtained via a *conceptually* well understood sequence of events, beginning with nucleation and finishing with growth.[5, 6] Our understanding of the steps leading to the nucleation of *specific phases*, however, is still in its infancy, although we do understand, in general, the underlying factors for nucleation to take place. In order for the nucleus, once formed, to grow and not re-dissolve, it must reach a critical size that is a function of the degree of supersaturation. In general, the higher the degree of supersaturation, the smaller the critical nucleus size can be. For that reason, it is preferred to use a flux that is able to dissolve a large quantity of the reagents and that exhibits a significant change in solubility with temperature to achieve this supersaturation. The nucleation process has a temperature dependence and requires a minimum temperature for nucleation to occur and, furthermore, has an optimum temperature range in which the

nucleation is at its maximum. Finding these optimum conditions, which tend to be unique for each system and change for even minor compositional adjustments, is largely a matter of trial and error. Starting with a set of conditions that are known to yield crystals of a related composition or structure is a good first approach and adjustments in temperature, concentration, time, reagent identity, etc., are made as needed.

*Designing Flux Reactions.* In general, the flux growth of new materials involves, first, the determination of conditions that are suitable for crystal growth within a specific system, including reactant starting materials, a flux component, a reaction vessel, and a temperature profile. The starting reagents are most commonly considered first since they largely control the composition of the target product. Next, a flux must be then chosen to dissolve the chosen reactants, a reaction vessel must be chosen that will successfully contain the flux, and lastly a temperature profile must be picked that supports all three of the previous choices. Once these conditions are determined, reaction conditions, especially reactant concentrations and dwell temperature, can be varied with the goal of avoiding known phases and targeting new compounds.

*Starting Materials.* There are several common approaches to choosing starting materials that include recrystallization of a polycrystalline precursor and r, the reaction of the elements or binary reagents, although starting material selection is oftentimes a matter of reagent availability. Often, a polycrystalline sample of the desired product (precursor) can be obtained easily by other methods, typically by solid state methods, and then recrystallized in a flux to obtain a single crystalline product.[7] In this approach, the choice of flux is essential, as the flux should dissolve the starting material in order to aid in the crystallization; however, the flux must not form stable compounds with the components of

the precursor, which is often difficult to achieve since the solvent must break the covalent bonds of the precursor. It is hard to predict which flux will be suitable for this role, especially for alkali halide fluxes, as they contain alkali metal cations that readily incorporate into the final products. More often, different fluxes are tested for suitability with a given system, similar to what is done in the selection of an organic solvent for organic reactions.

Other approaches use fluxes both as a reactant and a crystallization medium at the same time. One such approach involves the use of elements as starting materials and has proved useful for the precise control over the reaction composition in a closed system. The downside of using some of the elements is their volatility and difficulties with handling hazardous substances. For example, the use of chlorine or bromine is rather limited in closed systems, such as evacuated fused silica tubes, while chloride/bromide fluxes can offer a safe and convenient source of chloride/bromide.[8–11] The use of binaries is especially efficient for exploratory crystal growth as it enables fast screening of phase space and identification of stable compositions. The downside of using the binary compounds is the occasional difficulty of obtaining binary phases that are not commercially available or binary starting reagents that contain unexpected impurities that alter the outcome of the reaction, with product formation depending on the reagent's lot. [12] For example, rare earth sulfides are not currently commercially available, except for lanthanum sulfide, and require additional experiments to prepare the pure starting materials.[13]

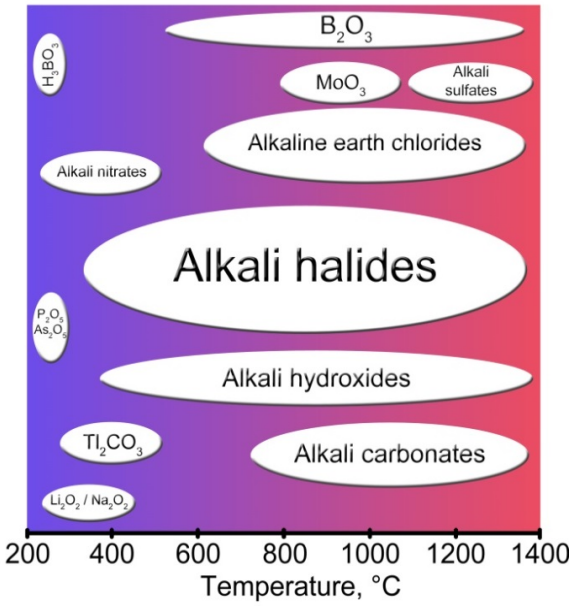


**Figure I.1:** Visual summary of fluxes and their approximate operating temperature ranges.

*Choosing a Flux.* The flux is the high temperature solution that functions as the solvent for crystallization and, more often than not, consists of a single, simple inorganic compound, such as $B_2O_3$, KCl, KOH, PbO, $Bi_2O_3$, or $Na_2CO_3$, which melt at conveniently low temperatures (Figure I.1). The combination of different solids to form eutectic compositions is one effective way to obtain an even lower melting flux. A "good" flux has certain attributes including the ability to dissolve a significant quantity of the reagents, a large change in the solubility with temperature, a low melting point, low volatility, low cost and finally, easy removal post-crystal growth via dissolution in a common solvent. Unlike a solid state reaction, which offers the final product in, ideally, pure form at the end of a reaction, flux crystal growth involves one crucial step after the reaction is completed – separation of residual flux from the products. For alkali halide fluxes, those used in the following chapters, most of the common polar solvents serve this purpose well. Although water is the preferred choice to dissolve an alkali halide flux, air- or moisture-sensitive

products require the use of anhydrous organic solvents, such as methanol, ethanol, or DMF. These solvents offer a relatively fast, within hours, removal of a residual flux, with little damage to moisture sensitive crystals. There is no "universal flux" although many fluxes can be used interchangeably and most crystals can be grown out of more than one solvent system, although there are some advantages and disadvantages to all of them.

There are several chemical factors that influence the ability of a flux to dissolve the reagents and to promote crystal growth. For example, materials that are good fluxes include those that form a compound with the solute at lower temperatures or in different concentration ranges. The optimal concentration for flux crystal growth is unique to each system, although 1:10 molar ratio of reagents to flux is typically a good starting point. In addition, the presence of an anion or cation common to the flux and the reagent can have a positive impact on the solution chemistry and solubility as does matching the polarizability of the solvent and the solute. One important advantage of choosing the flux by matching the physical and chemical properties is the formation of high quality crystals. A detailed introduction to fluxes is given in the review by Bugaris and zur Loye.[5]

*Reaction Vessel.* The reaction vessel used for crystal growth also is an important consideration, as many fluxes are highly reactive and will dissolve and/or chemically react with various containers. Therefore, one has to take into consideration the compatibility of the reaction vessel and the flux. "Inert" containers include platinum and gold, which however, are quite expensive and, in the case of gold, limit the crystal growth temperature to lie below 1064°C. Alumina crucibles are often used as a less expensive alternative and are considered chemically resistant towards halide but not fluoride melts. In addition, they can be attacked by hydroxide fluxes, leading to the incorporation of aluminum into the

crystal product. Fluoride based fluxes cannot be used with alumina, as they readily react/dissolve alumina crucibles. Silver is a better alternative for both hydroxide and fluoride fluxes as silver is substantially inert towards them (Figure I.2). Fused silica is a good choice for crystal growth experiments requiring a sealed reaction environment, for example to grow crystals containing elements in reduced oxidation states, as long as a silica compatible flux is chosen. Numerous other refractories and metal containers have been used, as appropriate for the flux used, and there is no universal container that is ideal for all flux growth experiments.

**Figure I.2:** Reaction vessels for flux reactions. Platinum crucible (left), alumina crucible (middle), silver tube (right).

*Temperature Profiles.* For crystal growth to occur, a solution must be sufficiently supersaturated to facilitate nucleation. In molten solutions, it is important to select a flux that is capable of dissolving the reactants and that has a substantial change in solubility over the temperature range of interest, otherwise, the nucleated crystals will be re-dissolved and no single crystals will form. The optimal rate of nucleation occurs over a given temperature range that is specific to each system, thus exploratory crystal growth largely focuses on this determination (Figure I.3).[5, 14]

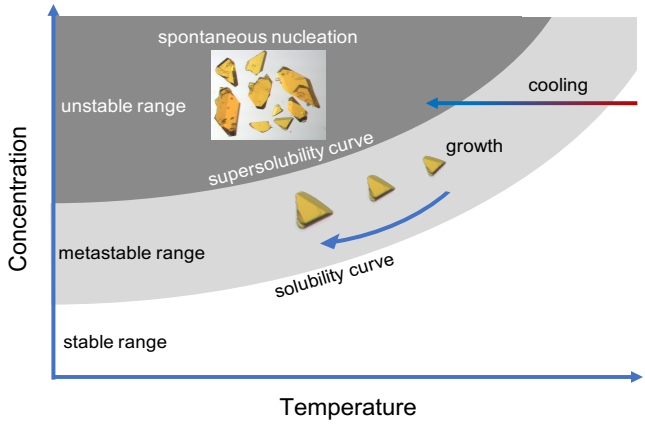


**Figure I.3:** A simplistic representation of the crystallization process.

**Table I.1:** Selected fluxes and eutectics and their melting points.

| Salt | m. p. °C | Salt | m. p. °C | Eutectics (molar ratio) | m. p. °C |
|---|---|---|---|---|---|
| NaCl | 801 | NaF | 993 | NaF/NaCl (0.34, 0.6) | 679 |
| KCl | 770 | KF | 858 | KF/KCl (0.45,0.55) | 600 |
| RbCl | 718 | RbF | 795 | RbF/RbCl (0.47, 0.53) | 544 |
| CsCl | 645 | CsF | 682 | CsF/CsCl (0.50,0.50) | 432 |

Indeed, selecting an appropriate reaction temperature is among the most critical considerations to make when conducting crystal growth experiments. Alkali halide fluxes offer a great deal of versatility when it comes to accessible temperature ranges, and have generally been used over a wide temperature range from approximately 400-1000°C. The melting points of the alkali halide fluxes and some selected eutectics are listed in Table I.1. An extremely helpful tool in flux selection is the FactSage thermochemical database, which offers a large number of binary salt phase diagrams with the compositions and melting points of eutectic mixtures[15–17] For alkali halide fluxes, most reported syntheses use reaction temperatures 50-200°C higher than the melting point of the flux. There are many examples that indicate a significant influence of the reaction temperature on the resulting

crystal morphology; for example, lower temperatures may produce irregularly-shaped crystals while increasing temperature may favor more defined morphologies.

Among reported flux syntheses a wide range of dwell times are used from none at all to up to 6 months. There is not much correlation between the flux used and selected dwell times, although many report increasing dwell times results in larger crystals. The dwell time also may have a significant impact on the product obtained, if under shorter dwell times a kinetic product is obtained, and over longer dwell times the thermodynamically stable product is obtained. The reported cooling rates and temperatures are also highly varied with cooling rates generally between 1-20 °C per hour over a range of 200-500 °C below the dwell temperature (usually, always below the melting point of the flux by 50-100 °C).

**Salt Inclusion Materials**

One of the relatively new classes of crystalline materials proposed for radionuclide storage are salt inclusion materials (SIMs) due to their versatility in storing radionuclides in both the framework and the salt inclusion, which is advantageous for reducing the volume of processed waste.[2] Salt-inclusion materials are hierarchical structures that have a wide compositional flexibility and structural variability arising from the covalent metal oxide framework composed of oxyanions ($SiO_4$, $PO_4$, etc.) and metal oxide units (in our case, $UO_x$ polyhedra) that create voids filled by a complex ionic salt lattice. The salt inclusions, the complex salt lattices, can either be 0-D, 1-D, 2-D, or 3D, where the simplest example is a single halide anion surround by alkali or alkaline earth cations. Uranium salt inclusion materials can generally be described by the formula $[A_mB_nX][(UO_2)_p(M_qO_r)_t]$,

where the first bracket lists the non salt-inclusion cations, $A_m$, and the salt inclusion, $B_nX$, and the second bracket details the uranium and oxyanion building units.

We are particularly interested in three dimensional porous SIMs that are prospective new hosts for the safe, long-term storage of the most abundant radioisotopes found in nuclear waste such as $^{137}Cs$, $^{90}Sr$, $^{129}I$, Pu, and U, which pose significant environmental threats due to their mobility. Salt inclusion materials have the potential to sequester multiple radionuclides due to the presence of both a metal oxyanion framework that can incorporate actinide species, and the salt inclusion that can contain ionic radionuclides.[2] Such porous frameworks also offer additional flexibility by being good candidates for ion exchange, post synthesis, where a non-radioactive salt component is exchanged for a radioisotope, further increasing the SIM's usefulness for waste sequestration.

Morrison et al. demonstrated the versatility of SIMs to store multiple radionuclides by synthesizing uranyl silicate salt inclusion materials that contain uranium in the framework and other radionuclides of interest, such as Cs, in the salt inclusion; in addition he reported on a large variety of structurally characterized uranium silicate SIMs.[18–20] Morrison et al. worked specifically to identify the flux conditions that result in salt inclusion materials, rather than less complex uranium containing oxides, and concluded that small surface area to volume ratios of the reaction vessel, using $UF_4$ over other uranium oxides as the uranium source, and the use of alkali halide fluxes provided ideal conditions for targeting this class of materials. Due to the success of his method, these experimental conditions are widely used in this dissertation, as we are striving to expand the library of known uranium SIMs by replacing the silicate building blocks with other oxyanions such

as phosphate, borate, aluminate, vanadate, molybdate, and germanate. The primary goal of this dissertation is the exploratory flux crystal growth of uranium oxides, followed by the secondary goal of targeting specifically new salt inclusion materials.

Due to the large library of known uranium silicate SIMs, targeting uranium germanate SIMs is a natural direction for this dissertation considering the similarity in chemistry of these two elements. Prior to this dissertation there had been no reports of germanium containing SIMs, although uranium germanate frameworks with large pores have been produced under hydrothermal conditions, for example $Cs_2[(UO_2)(Ge_2O_6)](H_2O)$, $Ag[(UO_2)_2(HGe_2O_7)](H_2O)$, $Ag_2[(UO_2)_3(GeO_4)_2](H_2O_2)_2$,[21] $(UO_2)_2(GeO_4)(H_2O)_2$,[22] $Cu(H_2O)_4(UO_2)_2(HGeO_4)_2(H_2O)_2$,[23] $Cs_6[(UO_2)_3(Ge_2O_7)_2](H_2O)_4$,[24] $A_3(U_2O_4)(Ge_2O_7)$ (A = Rb, Cs), [25] and $Rb_3(U_3O_6)(Ge_2O_7)$.[25] In addition to germanates, this dissertation also discusses uranium phosphate salt inclusion materials, as a significant number of transition metal phosphate SIMs have been reported and uranium phosphates are among the most abundant uranium minerals.[26–31]

**Introduction to Uranium Chemistry**

Before diving into the new uranium oxide structures reported in this dissertation, it is beneficial to be well acquainted with a general knowledge of uranium chemistry, and to some extent uranium mineralogy, which is well summarized in many works of Peter C. Burns.[29, 30, 32, 33] Uranium is a natural occurring radioactive element that has been used in nuclear energy and nuclear weapons related research. There are three naturally occurring isotopes of uranium, U-238, U-235, and U-234, and U-238 is among the easiest of the actinides to handle as it has a long half-life and releases α particles that are easily blocked by human skin requiring minimal personal protective equipment (PPE), such as gloves, lab

coat, and safety glasses, along with an awareness that ingestion or inhalation is harmful to the human body.

Uranium in solid state oxides is found in the 4+, 5+, or 6+ oxidation state, where the 4+ oxidation state is most abundant in the earth's crust, 6+ is the most easily accessible synthetically, and 5+ is rare in either case. Uranium 6+ chemistry is the focus of this thesis as it is easily obtained under the desired experimental conditions as heating in an oxygen atmosphere readily oxidizes $U^{4+}$ or $U^{5+}$ to the 6+ oxidation state. To target the synthesis of $U^{4+}$, evacuated and sealed reaction vessels and/or reducing conditions must be used to prevent the formation of oxidized species. $U^{6+}$ almost always forms double bonds (using valence bond theory, and formally a bond order of three if approaching from molecular orbital theory)[34] with two axial oxygens creating the nearly liner $UO_2^{2+}$, uranyl, ion. The number of non-uranyl $U^{6+}$ compounds is very small compared to those containing the uranyl ion. Among several review papers only 13 non-uranyl compounds are reported and at least 727 uranyl compounds are reported, highlighting the ubiquity of the uranyl ion.[33, 35] The stability of the uranyl ion, and thus its ubiquity, arises from the relativistic quantum effects on the energy of the electrons. The relativistic quantum effects arise from the high atomic number of uranium and cause the non-valence 6*p* electrons to interact with 5*f* orbitals to create hybrid orbitals that can form strong, linear bonding interactions with small atoms like oxygen or nitrogen.[36 37]

The $UO_2^{2+}$ ion is characterized by two short axially bonded oxygen atoms with bond lengths averaging 1.80 Å, as compared to bond lengths ranging between 2.1 and 2.7 Å for equatorially bonded oxygens. In oxide extended structures, the uranyl ion can be found coordinated to 4, 5, or 6 equatorial oxygens resulting in square-, pentagonal-, or

hexagonal-bipyramids (Figure I.4). Due to the strength of the axial oxygen bonds, these oxygens have a nearly satisfied bond valence requirement, and are thus usually inert. (In the case that the axial oxygens are coordinated to another atom, usually to another uranium center, they are referred to as cation-cation interactions (CCIs) that occur in less than 2% of known U compounds and are further discussed in chapter IV).[33] The inertness of the uranyl oxygens results in the tendency of uranium polyhedra to coordinate to additional building units via the equatorial oxygens, whether other uranium polyhedra or oxyanions, to create 2D sheet structures. In fact, 59.4% of the 727 structures reported in a recent and expansive review of $U^{6+}$ structures are comprised of 2D sheets. Overcoming the tendency to form two dimensionality of uranium oxide materials was one of the biggest challenges of the research described in this thesis, which specifically targeted 3D materials.

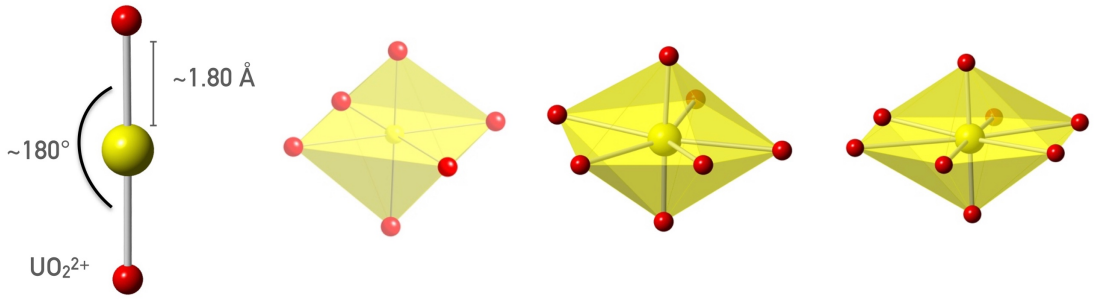


**Figure I.4:** Uranium VI coordination. From left to right: uranyl ion, square-, pentagonal-, and hexagonal-bipyramid.

In the previous section, phosphates were identified among the desired oxyanions to replace silicates in the known library of uranium SIMs. Thus, it is beneficial to discuss briefly the trends in uranium phosphate mineralogy, especially since several structural motifs commonly belonging to uranium phosphate minerals are present in multiple structures discussed in this dissertation. Uranium phosphates make up a significant portion

of all uranium minerals, about 25%, and are important for understanding the mobility of uranium in the environment. There are 45 known uranyl phosphate minerals; however, the complete structure solutions are known for only 15 of them.[38] All of the 45 known uranyl phosphate mineral structures are based on 2D sheets of corner and edge sharing uranyl polyhedra and phosphate tetrahedra. The most common topologies among the phosphate minerals are autunite, meta-autunite, and phosphuranylite topologies (Figure I.5).[39,38] The autunite and meta-autunite topologies are based upon corner sharing uranyl square bipyramids and phosphate tetrahedra; whereas, the phosphuranylite-type sheets contain pentagonal and hexagonal uranyl bipyramids that edge share to form chains that are crossed linked by corner sharing phosphate tetrahedra.[38] The autunite and phosphuranylite have 1:1 and 3:2 ratios of uranium to phosphorous, respectively.[40] The phosphuranylite topology will appear several times throughout this dissertation.

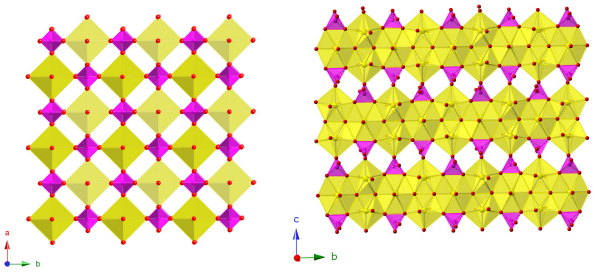

**Figure I.5:** Autunite (left) and phosphuranylite topologies (right).

**Chapter Descriptions**

The primary goal of this dissertation was to synthesis new uranium oxides, particularly 3D salt inclusion materials containing new varieties of oxyanions. Since our group was already successful in synthesizing uranium silicate SIMs, this dissertation starts with a discussion of uranium germanate SIMs in chapter 1 before moving on to other

oxyanions. In chapters 2 through 5 several families of layered phosphates are discussed, and chapter 6 reports on the first uranium phosphate and uranium aluminophosphate SIMs. Chapter 7 reports the first alkali uranium aluminate and chapter 8 reports on gallate analogs to aluminum containing structures discussed in chapters 6 and 7. Chapter 9 reports on a family of alkali gallates, structurally related to the hollandite family, and discusses their relevance to the field of nuclear waste storage.

The topics covered in chapters 10 and 11 are further removed from the goal of obtaining uranium SIMs; however, summarize significant work. Chapter 10 reports $U^{5+}$ containing perovskites, which were discovered while targeting uranium phosphate materials and were further explored and characterized due to the rarity of $U^{5+}$ containing phases. The research reported in Chapter 11 was performed at the National Institute for Materials Science (NIMs) in Tsukuba, Japan, as a part of the Integrative Graduate Education and Research Trainee fellowship. Chapter 11 summarizes the synthesis and characterization of a perovskite, $CaCrO_3$, obtained by high pressure methods and the fluorinated and reduced phases obtained via post-synthetic treatment.

While Appendices A and B are not primary works of mine, they are significant to the overall goal of this dissertation and contain significant contributions of mine. Appendix A summarizes the computational work on the germanates discussed in chapter 1 and was performed by our collaborators in the Besmann group. Appendix B is a computational study, by the Besmann group, on two polymorphs of $A_4[(UO_2)_3(PO_4)_2O_2]$, one of which is reported in chapter 2 while the other the other is reported in Appendix B for the first time. Lastly, Appendix C contains all the relevant copyright information for the chapters that have been already published in various scientific journals.

**References:**


(1) Council, N. R. *Waste Forms Technology and Performance: Final Report.* National Academies Press: Washington, DC, 2011;

(2) zur Loye, H.-C.; Besmann, T.; Amoroso, J.; Brinkman, K.; Grandjean, A.; Henager, C. H.; Hu, S.; Misture, S. T.; Phillpot, S.; Shustova, N. B.; Wang, H.; Koch, R. J.; Gregory Morrison; Dolgopolova, E., Hierarchical Materials as Tailored Nuclear Waste Forms: A Perspective, *Chem. Mater.* **2018**, *30*, 4475-4488.

(3) Utlak, S. A.; Besmann, T. M.; Brinkman, K. S.; Amoroso, J. W., Thermodynamic assessment of the hollandite high-level radioactive waste form, *J. Am. Ceram. Soc.* **2019**, *102*, 6284-6297.

(4) Burakov, B. E.; Lee, W. E.; Ojovan, M. I. *Crystalline Materials for Actinide Immobilisation.* 1; Imperial College Press: London, UK, 2011;

(5) Bugaris, D. E.; zur Loye, H.-C., Materials discovery by flux crystal growth: Quartenary and higher oxides, *Angew. Chem. Int. Ed.* **2012**, *51*, 3780-3811.

(6) Elwell, D.; Scheel, H. J. *Crystal Growth from High-Temperature Solutions.* Academic Press: New York, 1975;

(7) Zeng, H. Y.; Zheng, F. K.; Guo, G. C.; Huang, J. S., Syntheses and single-crystal structures of $La_3AgSnS_7$, $Ln_3M_xMS_7$ (Ln= La, Ho, Er; M= Ge, Sn; $1/4 \leq x \leq 1/2$), *J. Alloys Compd.* **2008**, *458*, 123-129.

(8) Cortese, A. J.; Wilkins, B.; Smith, M. D.; Morrison, G.; zur Loye, H.-C., Single crystal growth and characterization of the first reduced lanthanum molybdenum oxychloride, $La_{20}Mo_{12}O_{63}Cl_4$, with an unusual trigonal prismatic $MoO_6$ unit, *Solid State Sciences* **2015**, *48*, 133-140.

(9) Read, C. M.; Smith, M. D.; zur Loye, H.-C., Synthesis, Crystal Structure, and Optical Properties of a New Complex Uranium Oxychloride, $KUO_3Cl$, *J. Chem. Cryst.* **2015**, *45*, 440-444.

(10) Ruck, M.; Schmidt, P., Synthesen und Kristallstrukturen der homöotypen Selenitbromide $Bi_8(SeO_3)_9Br_6$ und $CsSm_{21}(SeO_3)_{24}Br_{16}$, *Z. Anorg. Allg. Chem.* **2003**, *629*, 2133-2143.

(11) Yahia, H. B.; Rodewalk, U. C.; Pöttgen, R., Crystal Structure of $La_3OBr[AsO_3]_2$, *Z. Naturforsch.* **2010**, *65b*, 1289-1292.

(12) Wells, D. M.; Chan, G. H.; Ellis, D. E.; Ibers, J. A., $UTa_2O(S_2)_3Cl_6$: A ribbon structure containing a heterobimetallic 5d-5f $M_3$ cluster, *J. Solid State Chem.* **2010**, *183*, 285-290.

(13) Klepov, V. V.; Breton, L. S.; Pace, K. A.; Kocevski, V.; Besmann, T. M.; zur Loye, H.-C., Size-Driven Stability of Lanthanide Thiophosphates Grown from an Iodide Flux, *Inorg. Chem.* **2019**, *58*, 6565-6573.

(14) Juillerat, C. A.; Klepov, V. V.; Morrison, G.; Pace, K. A.; zur Loye, H.-C., Flux Crystal Growth: A Versatile Technique to Reveal the Crystal Chemistry of Complex Uranium Oxides, *Dalton Trans.* **2019**, *48*, 3162-3181.

(15) Bale, C. W.; Chartrand, P.; Degterov, S. A.; Eriksson, G.; Hack, K.; Mahfoud, R. B.; Melançon, J.; Pelton, A. D.; Petersen, S., FactSafe thermochemical software and databases, *Calphad* **2002**, *26*, 189-228.

(16) Bale, C. W.; Bélisle, E.; Chartrand, P.; Decterov, S. A.; Eriksson, G.; Hack, K.; Jung, I.-H.; Kang, Y.-B.; Melançon, J.; Pelton, A. D.; Robelin, C.; Petersen, S., FactSage thermochemical software and databases — recent developments, *Calphad* **2009**, *33*, 295-311.

(17) Bale, C. W.; Bélisle, E.; Chartrand, P.; Decterov, S. A.; Eriksson, G.; Gheribi, A. E.; Hack, K.; Jung, I.-H.; Kang, Y.-B.; Melançon, J.; Pelton, A. D.; Petersen, S.; Robelin, C.; Sangster, J.; Spencer, P.; Van Ende, M.-A., FactSage thermochemical software and databases, 2010–2016, *Calphad* **2016**, *54*, 35-53.

(18) Morrison, G.; zur Loye, H.-C., Flux Growth of $[NaK_6F][(UO_2)_3(Si_2O_7)_2]$ and $[KK_6Cl][(UO_2)_3(Si_2O_7)_2]$: The Effect of Surface Area to Volume Ratios on Reaction Products, *Cryst. Growth Des.* **2016**, *16*, 1294-1299.

(19) Morrison, G.; Smith, M. D.; zur Loye, H.-C., Understanding the Formation of Salt-Inclusion Phases: An Enhanced Flux Growth Method for the Targeted Synthesis of Salt-Inclusion Cesium Halide Uranyl Silicates, *J. Am. Chem. Soc.* **2016**, *138*, 7121-7129.

(20) Lee, C. S.; Wang, S. L.; Chen, Y. H.; Lii, K. H., Flux synthesis of salt-inclusion uranyl silicates:$[K_3Cs_4F][(UO_2)_3(Si_2O_7)_2]$ and $[NaRb_6F][(UO_2)_3(Si_2O_7)_2]$, *Inorg. Chem.* **2009**, *48*, 8357-8361.

(21) Ling, J.; Morrison, J. M.; Ward, M.; Poinsatte-Jones, K.; Burns, P. C., Syntheses, Structures, and Characterization of Open-Framework Uranyl Germanates, *Inorg. Chem.* **2010**, *49*, 7123-7128.

(22) Legros, J. P.; Jeannin, Y., Coordination de l'uranium par l'ion germanate. II. Structure du germanate d'uranyle dihydrat'e $(UO_2)_2GeO_4(H_2O)_2$, *Acta Crystallographica Section* **1975**, *B31*, 1140-1143.

(23) Legros, J. P.; Jeannin, Y., Coordination de l'uranium par l'ion germanate. I. Structure d'un uranyl germanate de cuivre $[Cu(H_2O)_4](UO_2HGeO_4)_2.2H_2O$, *Acta Cryst.* **1975**, *B31*, 1133-1139.

(24) Lin, C. H.; Chiang, R. K.; Lii, K. H., Synthesis of Thermally Stable Extra-Large Pore Crystalline Materials: A Uranyl Germanate with 12-Ring Channels, *J. Am. Chem. Soc.* **2009**, *131*, 2068-2069.

(25) Lin, C.-H.; Chen, C.-S.; Shiryaev, A. A.; Zubavichus, Y. V.; Lii, K.-H., $K_3(U_3O_6)(Si_2O_7)$ and $Rb_3(U_3O_6)(Ge_2O_7)$: A Pentavalent-Uranium Silicate and Germanate, *Inorg. Chem.* **2008**, *47*, 4445-4447.

(26) Etheredge, K. M. S.; Hwu, S.-J., A Novel Honeycomb-like Copper(II) Phosphate Framework, [BaCl][CuPO4], *Inorg. Chem.* **1995**, *34*, 3123-3125.

(27) Hwu, S. J. *A New Class of Hybrid Materials via Salt-inclusion Synthesis.* John Wiley & Sons: 2006;

(28) Gao, J.; Li, J.; Sulejmanovic, D.; Hwu, S.-J., $M_3(P_2O_7)^{22-}$-Type Open Frameworks Featuring $[M_2O_8]$ and $[M_3O_{12}]$ Multinuclear Transition-Metal Oxide Units. Serendipitous Synthesis of Six Polymorphic Salt-Inclusion Magnetic Solids: $Na_2M_3(P_2O_7)_2{\cdot}ACl$ (M = Mn, Fe; A = Rb, Cs) and $K_2M_3(P_2O_7)_2{\cdot}CsCl$ (M = Fe, Mn), *Inorg. Chem.* **2015**, *54*, 1136-1144.

(29) Burns, P. C.; Ewing, R. C.; Hawthorne, F. C., The crystal chemistry of hexavalent uranium: polyhedron geometries, bond-valence parameters, and polymerization of polyhedra, *Can. Mineral.* **1997**, *35*, 1551-1570.

(30) Burns, P. C.; Finch, R. *Uranium: Mineralogy, Geochemistry & the Environment (Reviews in Mineralogy & Geochemistry).* Mineralogical Society of America: 1999-10;

(31) Locock, A. J., Crystal chemistry of actinide phosphates and arsenates, **2007**, *Structural Chemistry of Inorganic Actinide Compounds*, 217-278.

(32) Burns, P. C., $U^{6+}$ minerals and inorganic compounds: insights into an expanded structural hierarchy of crystal structures, *Can. Mineral.* **2005**, *43*, 1839-1894.

(33) Lussier, A. J.; Lopez, R. A. K.; Burns, P. C., A revised and expanded structure hierarchy of natural and synthetic hexavalent uranium compounds, *Can. Mineral.* **2016**, *54*, 177-283.

(34) Pyykkö, P.; Li, J.; Runeberg, N., Quasirelativistic pseudopotential study of species isoelectronic to uranyl and the equatorial coordination of uranyl, *The Journal of Physical Chemistry* **1994**, *98*, 4809-4813.

(35) Krivovichev,; Plášil, J., Chapter 3: Mineralogy and crystallography of uranium, **2013**, *Uranium: From Cradle to Grave*, 15-119.

(36) Denning, R. G., Electronic Structure and Bonding in Actinyl Ions and their Analogs, *The Journal of Physical Chemistry A* **2007**, *111*, 4125-4143.

(37) Boncella, J. M., Uranium gets a reaction, *Nature* **2008**, *451*, 250-252.

(38) Burns, P. C., A new uranyl phosphate chain in the structure of parsonsite, *Am. Mineral.* **2000**, *85*, 801-805.

(39) Alekseev, E. V.; Krivovichev, S. V.; Depmeier, W.; Knorr, K., Complex topology of uranyl polyphosphate frameworks: crystal structures of α-, β-$K[(UO_2)(P_3O_9)]$ and $K[(UO_2)_2(P_3O_{10})]$, *Z. Anorg. Allg. Chem.* **2008**, *634*, 1527-1532.

(40) Renard, C.; Obbade, S.; Abraham, F., Channels occupancy and distortion in new lithium uranyl phosphates with three-dimensional open-frameworks, *J. Solid State Chem.* **2009**, *182*, 1377-1386.

# Chapter 1

# Versatile Uranyl Germanate Framework Hosting Twelve Different Alkali Halide 1D Salt Inclusions[1]

[1]Reproduced with permission from Juillerat, C. A.; Moore, E. E.; Morrison, G.; Smith, M. D.; Besmann, T. M.; zur Loye, H.-C., *Inorg. Chem.* **2018**, *57*, 11606-11615. © 2018 American Chemical Society

**Abstract:** Single crystals of thirteen new uranyl germanate salt inclusion materials were grown from alkali halide fluxes: $[Cs_2Cs_5F][(UO_2)_3(Ge_2O_7)_2]$ (**1.1**), $[Cs_6Ag_2Cl_2][(UO_2)_3(Ge_2O_7)_2]$ (**1.2**), $[Cs_6Ag_{0.3}Na_{1.7}Cl_2][(UO_2)_3(Ge_2O_7)_2]$ (**1.3**), $[Cs_6Ag_{0.4}Na_{1.6}Cl_2][(UO_2)_3(Ge_2O_7)_2]$ (**1.4**), $[Cs_6K_2Cl_2][(UO_2)_3(Ge_2O_7)_2]$ (**1.5**), $[Cs_6K_{1.9}Ag_{0.1}Cl_2][(UO_2)_3(Ge_2O_7)_2]$ (**1.6**), $[KK_6Cl][(UO_2)_3(Ge_2O_7)_2]$ (**1.7**), $[KK_6Br_{0.6}F_{0.4}][(UO_2)_3(Ge_2O_7)_2]$ (**1.8**), $[Na_{0.9}Rb_{6.1}F][(UO_2)_3(Ge_2O_7)_2]$ (**1.9**), $[K_{0.6}Na_{0.4}K_5CsCl_{0.5}F_{0.5}][(UO_2)_3(Ge_2O_7)_2]$ (**1.10**), $[K_{0.8}Na_{0.2}K_{4.8}Cs_{1.2}Cl_{0.5}F_{0.5}][(UO_2)_3(Ge_2O_7)_2]$ (**1.11**), $[KK_{1.8}Cs_{4.2}F][(UO_2)_3(Ge_2O_7)_2]$ (**1.12**), and $[Cs_6Cs_{0.71}Cl_{0.71}][(UO_2)_3O_3(Ge_2O_7)]$ (**1.13**). Structures **1.1-1.12** contain the same $[(UO_2)_3(Ge_2O_7)_2]^{6-}$ framework whose pores are filled with varied salt species selected by the choice of the specific alkali halide flux used for crystal growth. The size and identity of the salt species also influences whether the $[(UO_2)_3(Ge_2O_7)_2]^{6-}$ framework adopts a monoclinic or orthorhombic symmetry. The 13$^{th}$ composition, $[Cs_6Cs_{0.71}Cl_{0.71}][(UO_2)_3O_3(Ge_2O_7)]$ (**1.13**), crystallizes in a new structure type in the hexagonal crystal system and contains large channels. Optical characterization was performed on $[Cs_6K_{1.9}Ag_{0.1}Cl_2][(UO_2)_3(Ge_2O_7)_2]$ (**1.6**) and $[KK_{1.8}Cs_{4.2}F][(UO_2)_3(Ge_2O_7)_2]$ (**1.12**) and both exhibit UV-vis absorption and luminescence typical of the uranyl group. The fluorine containing composition luminesces ten times as intensely as does the chlorine containing composition.

**Introduction.** Salt inclusion materials (SIMs) are being investigated as potential nuclear waste storage materials because of their versatility in storing radionuclides in both the framework and the salt inclusion, which is advantageous for reducing the volume of processed waste.[1] In addition, it is possible to ion exchange, post synthesis, a non-radioactive salt component for a radioisotope, further increasing the SIM's usefulness for

waste sequestration. SIMs contain covalent metal oxide frameworks with void spaces that are filled by ionic salt lattices. The SIMs discussed in this paper are described by the general formula $[A_mB_nX][(UO_2)_3(Ge_2O_7)_t]$, where the first bracket contains the salt inclusion ($B_nX$), composed of alkali metal cations and halide anions, and non-salt inclusion cations ($A_m$); the second set of brackets describes the framework composition, $[(UO_2)_3(Ge_2O_7)_t]$.

Morrison et al. demonstrated the versatility of SIMs to store multiple radionuclides by synthesizing uranyl silicate salt inclusion materials that contain uranium in the framework and other radionuclides of interest, such as Cs, in the salt inclusion.[2, 3] A large variety of uranium silicate salt inclusion materials are known and include $[K_3Cs_4F][(UO_2)_3(Si_2O_7)_2]$, $[NaRb_6F][(UO_2)_3(Si_2O_7)_2]$, $[NaK_6F][(UO_2)_3(Si_2O_7)_2]$, $[KK_6Cl][(UO_2)_3(Si_2O_7)_2]$, $[Cs_2Cs_5F][(UO_2)_3(Si_2O_7)_2]$, $[Cs_3F][(UO_2)(Si_4O_{10})]$, $[Cs_2Cs_5F][(UO_2)_2(Si_6O_{17})]$, and $[Cs_9Cs_6Cl][(UO_2)_7(Si_6O_{17})_2(Si_4O_{12})]$.[2–4] These Si SIMs were all synthesized by molten flux methods and U is present as the U(VI) uranyl ion, $UO_2^{2+}$, and is found in a six coordinate square bipyramidal coordination environment. $U^{6+}$ typically appears as the uranyl ion, $UO_2^{2+}$, which features ~180° O-U-O bonds with short bond distances of ~1.80 Å. These cations can equatorially coordinate with other oxygens (and sometimes halides) with bond lengths typically ranging between 2.2 and 2.7 Å.[5] In the uranyl silicate SIMs, the silicate units have tetrahedral coordination environments and link with the uranyl polyhedra to form a 3D framework containing large open channels that house the salt inclusion. Additionally, the mixed-valence uranium(V,VI) silicate SIM, $[Na_9F_2][(U^VO_2)(U^{VI}O_2)_2(Si_2O_7)_2]$, was synthesized under high pressure, high temperature

hydrothermal conditions; its structure is also composed of $UO_6$ polyhedra and silicate tetrahedra.[6]

We are striving to expand the library of known uranium containing SIMs by replacing silicate tetrahedral units with different framework building blocks, such as phosphate, borate, aluminate, vanadate, molybdate, and germanate oxyanions. While numerous non-uranium containing phosphate and silicate SIMs have been reported in the literature, to date there have been no reports of germanium containing SIMs, although uranium germanate frameworks with large pores exist, for example $Cs_2[(UO_2)(Ge_2O_6)](H_2O)$, $Ag[(UO_2)_2(HGe_2O_7)](H_2O)$, $Ag_2[(UO_2)_3(GeO_4)_2](H_2O_2)_2$,[7] $(UO_2)_2(GeO_4)(H_2O)_2$,[8] $Cu(H_2O)_4(UO_2)_2(HGeO_4)_2(H_2O)_2$,[9] $Cs_6[(UO_2)_3(Ge_2O_7)_2](H_2O)_4$,[10] $A_3(U_2O_4)(Ge_2O_7)$ (A = Rb, Cs),[11] and $Rb_3(U_3O_6)(Ge_2O_7)$.[12] All of these frameworks have been produced under hydrothermal conditions, unlike the uranium germanate SIMs in this paper that were synthesized using the molten flux method in order to favor the incorporation of salt species. Twelve of the 13 reported structures, $[Cs_2Cs_5F][(UO_2)_3(Ge_2O_7)_2]$ (**1.1**), $[Cs_6Ag_2Cl_2][(UO_2)_3(Ge_2O_7)_2]$ (**1.2**), $[Cs_6Ag_{0.3}Na_{1.7}Cl_2][(UO_2)_3(Ge_2O_7)_2]$ (**1.3**), $[Cs_6Ag_{0.4}Na_{1.6}Cl_2][(UO_2)_3(Ge_2O_7)_2]$ (**1.4**), $[Cs_6K_2Cl_2][(UO_2)_3(Ge_2O_7)_2]$ (**1.5**), $[Cs_6K_{1.9}Ag_{0.1}Cl_2][(UO_2)_3(Ge_2O_7)_2]$ (**1.6**), $[KK_6Cl][(UO_2)_3(Ge_2O_7)_2]$ (**1.7**), $[KK_6Br_{0.6}F_{0.4}][(UO_2)_3(Ge_2O_7)_2]$ (**1.8**), $[Na_{0.9}Rb_{6.1}F][(UO_2)_3(Ge_2O_7)_2]$ (**1.9**), $[K_{0.6}Na_{0.4}K_5CsCl_{0.5}F_{0.5}][(UO_2)_3(Ge_2O_7)_2]$ (**1.10**), $[K_{0.8}Na_{0.2}K_{4.8}Cs_{1.2}Cl_{0.5}F_{0.5}][(UO_2)_3(Ge_2O_7)_2]$ (**1.11**), and $[KK_{1.8}Cs_{4.2}F][(UO_2)_3(Ge_2O_7)_2]$ (**1.12**), contain the same framework first reported for $Cs_6[(UO_2)_3(Ge_2O_7)_2](H_2O)_4$,[10] however, in the cases of **1.1-1.12**, the pores are filled with a variety of salt inclusions rather than simply cesium cations and water. These 12 Ge based SIMs have known silicate SIMs

with analogous frameworks, including $[K_3Cs_4F][(UO_2)_3(Si_2O_7)_2]$, $[NaRb_6F][(UO_2)_3(Si_2O_7)_2]$,[4] $[NaK_6F][(UO_2)_3(Si_2O_7)_2]$, $[KK_6Cl][(UO_2)_3(Si_2O_7)_2]$,[2] and $[Cs_2Cs_5F][(UO_2)_3(Si_2O_7)_2]$.[3] In addition, we are reporting the synthesis and structure of $[Cs_6Cs_{0.71}Cl_{0.71}][(UO_2)_3O_3(Ge_2O_7)]$ (**1.13**), which contains a previously unreported hexagonal uranium germanate framework. The discussion in this paper focuses on the synthesis, crystal structures, and optical properties of these 13 new uranium germanate SIMs.

**Experimental:**

**Synthesis.** The uranyl germanate SIMs were prepared using molten flux methods developed by Morrison et al.[2, 3, 13] $UF_4$ (International Bio-Analytical Industries, powder, ACS grade), $GeO_2$ (Alfa Aesar, powder, 99.999%), CsF (Alfa Aesar, powder, 99%), CsCl (Alfa Aesar, powder, 99%), CsI (Alfa Aesar, 99.9%), RbF (Alfa Aesar, powder, 99.1%), KF (Alfa Aesar, powder, 99%), KCl (Mallinckrodt Chemicals, powder, 99.6%), KBr (Mallinckrodt Chemicals, powder), NaF (Alfa Aesar, powder, 99%), NaCl (Fisher Chemical, powder, 99%), and NaBr (Alfa Aesar, powder, 99%) were used as received. ***Caution!*** *Although the uranium precursor used contained depleted uranium, standard safety measures for handling radioactive substances must be followed.* Generally, unless otherwise stated, 0.5 mmol $UF_4$, 0.667 mmol $GeO_2$, and 20 mmols of desired alkali halide flux (see Table 1.1) were loaded into silver tubes that measured 5.7 cm high and 1.2 cm in diameter. These silver tubes were covered with loose-fitting silver caps and heated in air in a box furnace to 875 °C in 1.5 h, held for 12 h, and slow cooled to 400 °C at 6 °C/h. After heating, the tubes were cut down to the level of the flux and sonicated in water to dissolve the flux. All of the products were yellow needles of various sizes (Figure 1.1), and reactions

run in chloride, bromide, or iodide containing fluxes produced the corresponding non-water-soluble silver halides as a byproduct from reaction of the flux with the walls of the silver tube. The presence of these silver halide byproducts made obtaining high yields and pure phases of structures that formed as small needles difficult (Figure 1.1a, d, e). Fortunately, for some compositions larger crystals could be grown and manually separated to result in calculated yields > 70% based on uranium. Structures **1.2-1.4,** and **1.6** have $Ag^{+}$ ions that originated from the silver tube and have been incorporated into the salt inclusion. Table 1.1 lists the ratios of reactants used for the synthesis of each reported compound. Crystals of **1.6** and **1.12**, structurally representative of the monoclinic and orthorhombic SIMs, were hand-picked to obtain pure samples for optical characterization. The purity of the samples was confirmed by powder X-ray diffraction.

Red needles of the hexagonal phase $[Cs_6Cs_{0.71}Cl_{0.71}][(UO_2)_3O_3(Ge_2O_7)]$ **(1.13)** were obtained by increasing the ratio of U:Ge to 0.5 mmol of $UF_4$ to 0.33 mmol of $GeO_2$, using 20 mmol of CsCl as the flux, and the same heating profile as discussed previously. This phase grows in tandem with $[Cs_6Ag_2Cl_2][(UO_2)_3(Ge_2O_7)_2]$ (**1.2**) and is difficult to manually separate, even though $[Cs_6Cs_{0.71}Cl_{0.71}][(UO_2)_3O_3(Ge_2O_7)]$ (**1.13**) crystallizes as

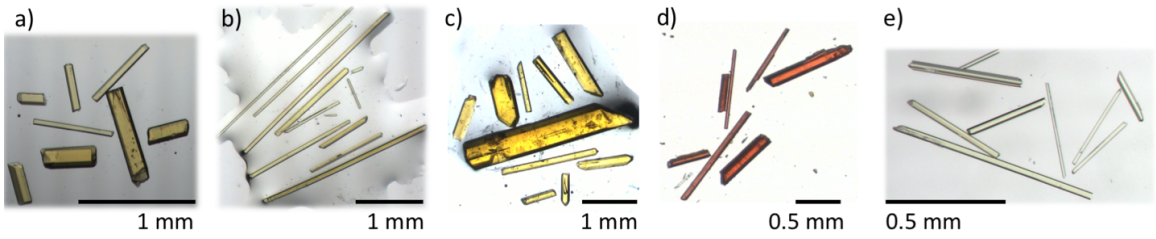


**Figure 1.1:** Photographs of product crystals of 1.1, 1.3, 1.6, 1.7, 1.13. a) $[Cs_2Cs_5F][(UO_2)_3(Ge_2O_7)_2]$ (**1**), b) $[Cs_6K_{1.9}Ag_{0.1}Cl_2][(UO_2)_3(Ge_2O_7)_2]$ (**6**) c) $[Cs_6Ag_{0.3}Na_{1.7}Cl_2][(UO_2)_3(Ge_2O_7)_2]$ (**3**), d) $[Cs_6Cs_{0.71}Cl_{0.71}][(UO_2)_3O_3(Ge_2O_7)]$ (**13**) e) $[KK_6Cl][(UO_2)_3(Ge_2O_7)_2]$ (**7**).

**Table 1.1:** Reactant ratios for synthesized uranium germanate SIMs (mmol)

| Framework SI | $[Cs_2Cs_5F]$ **1.1** | $[Cs_6Ag_2Cl_2]$ **1.2** | $[Cs_6Ag_{0.3}Na_{1.7}Cl_2]$ **1.3** | $[(UO_2)_3(Ge_2O_7)_2]^{6-}$ $[Cs_6Ag_{0.4}Na_{1.6}Cl_2]$ **1.4** | $[Cs_6K_2Cl_2]$ **1.5** | $[Cs_6K_{1.9}Ag_{0.1}Cl_2]$ **1.6** | $[KK_6Cl]$ **1.7** |
|---|---|---|---|---|---|---|---|
| $UF_4$ | 0.5 | 0.5 | 0.5 | 0.5 | 0.5 | 0.5 | 0.5 |
| $GeO_2$ | 0.667 | 0.667 | 0.667 | 0.667 | 0.667 | 0.334 | |
| CsF | 20 | -- | -- | 9 | 9 | 9 | |
| CsCl | — | 10 | 10 | 11 | 11 | 11 | |
| CsI | — | -- | 10 | — | — | — | |
| KF | | | | | | | 9 |
| KCl | — | -- | — | — | 3 | 3 | 11 |
| NaCl | — | -- | — | 3 | — | — | |
| NaI | — | -- | 3 | — | — | — | |



**Table 1.1 cont.**

| Framework SI | $[KK_6Br_{0.6}F_{0.4}]$ **1.8** | $[Na_{0.9}Rb_{6.1}F]$ **1.9** | $[(UO_2)_3(Ge_2O_7)_2]^{6-}$ $[K_{0.6}Na_{0.4}K_5CsCl_{0.5}F_{0.5}]$ **1.10** | $[K_{0.8}Na_{0.2}K_{4.8}Cs_{1.2}Cl_{0.5}F_{0.5}]$ **1.11** | $[KK_{1.8}Cs_{4.2}F]$ **1.12** |
|---|---|---|---|---|---|
| $UF_4$ | 0.5 | 0.5 | 0.5 | 0.5 | 0.5 |
| $GeO_2$ | 0.667 | 0.667 | 0.667 | 0.667 | 0.667 |
| CsF | — | — | — | — | 12 |
| CsCl | — | — | 1 | 1 | — |
| RbF | — | 14 | — | — | — |
| KF | 8 | — | 13 | 13 | 8 |
| KBr | 12 | — | — | — | — |
| NaF | — | 6 | 7 | 7 | — |

red needles and $[Cs_2Cs_5Cl][(UO_2)_3(Ge_2O_7)_2]$ crystallizes as yellow needles, because of their small size and tendency to grow together. So far, variations in temperature profile and amounts of $GeO_2$ have not proved successful in solely growing the red phase.

**Structures.** The structure of each of the 13 compounds was determined using single crystal X-ray diffraction (SXRD) data collected on a Bruker D8 QUEST diffractometer with an APEX II CCD detector and a microfocus source (Mo K$\alpha$ radiation, $\lambda$ = 0.71073 Å) or a Bruker D8 QUEST diffractometer equipped with a PHOTON 100 CMOS area detector and a microfocus source (Mo K$\alpha$ radiation, $\lambda$ = 0.71073 Å). The raw data were reduced and corrected for absorption effects using SAINT+ and SADABS programs within APEX 3.[14] The SHELXT solution program employing intrinsic phasing was used to obtain an initial structure that was refined using the SHELXL refinement program.[15] Both SHELXT and SHELXL were used within the Olex 2 GUI.[16, 17] The addsym and twinrotmap programs within PLATON were used to verify the space group and check for the prescence of twinning.[18] Full crystallographic details are provided in Table 1.2.

Structures **1.1**-**1.6** crystallize in the monoclinic space group $P2_1/n$. The uranyl germanate framework, $[(UO_2)_3(Ge_2O_7)]^{6-}$, in each of these structures is identical with no detectable disorder. There are two U sites, two Ge sites, and ten O sites in the asymmetric unit. U1 lies on the special position 0 ½ 0 with Wyckoff site symbol 2*c* and -1 symmetry, while all other atoms lie on general positions. While the solution of the metal oxide framework is straightforward in each of these structures, all atoms of the salt inclusion component of each structure are disordered on general positions.

The sites for the salt inclusion area of the structure were allowed to freely refine and the presence of all potential chemically reasonable elements identified by EDS was

considered in the structure solution process in order to assure assigning to the appropriate elements. In several structures, one or more of the sites could not be freely refined for a unique element and these cases were modeled as a mixture of two elements that best matched the magnitude of the electron density of that site. Anion site disorder was also observed. The structure solution for each, including disorder and split sites, are thoroughly discussed for each structure below.

For **1.1**, a two-component twinned specimen with volume fractions of 0.6027(10) and 0.3973(1) was used and data were collected at a crystal-to-detector distance of 10 cm to increase spot separation and decrease the number of overlaps. For **1.2**, data was collected at a standard distance of 40 mm and a twin law was found using the TwinRotMap functionality in PLATON. The data was refined as a 2-component twin using the twin law (-1 0 0 0 -1 0 0.189 0 1) with a small volume fraction of 0.0208(5). A similar procedure was used for **1.6**, which was refined using the twin law (-1 0 -0.007 0 -1 0 0 0 1) with a volume fraction of 0.0817(12). The remaining structures were also checked for twinning using the TwinRotMap functionality in PLATON, however, no twinning was found.

The salt inclusion in **1.1** can be described as disordered corner-sharing $FCs_6$ octahedra. In **1.1** there are two primary sites within the channels, one is a cation site and the other an anion site. The cation site refines well as two partially occupied Cs sites, which are each further disordered about an inversion center for a total of four Cs sites. These refine well with occupancies of 0.33(8) 0.33(8), 0.17(8), and 0.17(8). The anion site, the fluorine site, models reasonably well with one unique site that is 50% occupied and disordered over an inversion center to create two total sites after symmetry that add up to a fully occupied fluorine site.

In structure **1.2** the channels contained a total of five sites, where four of them are cation sites and occupy the edge of the channel, while one anion site occupies the center of the channel. The anion site freely refines to an occupancy of one when labeled as chlorine. Three of the cation sites freely refine to fully occupied Cs sites, while one refines to an occupancy less than one. This site, when modeled as a Ag cation, freely refines to one, and the presence of Ag in the sample is confirmed by EDS. The residual electron density in this solution is larger than other structures, but at a value of 6.657 is acceptable considering the presence of heavy absorbers U and Cs. The largest residual electron densities are 1.4 Å away from one of the U sites and modeling split U or O sites do not make chemical sense.

The salt inclusions in structures **1.3** and **1.4** are similar to **1.2**, where the Ag1 site in **1.2** is also occupied by Na in **1.3** and **1.4**. When freely refining this site in **1.3** and **1.4**, the occupancy is too small for a Cs cation, but too large for Na. EDS indicates the presence of Ag in the structure, so the site occupancy was constrained to one and was refined as being partially occupied by both Ag and Na resulting in Ag occupancies of 0.184(3) and 0.134(2), in **1.3** and **1.4**, respectively.

Structures **1.5** and **1.6** are similar to **1.2**-**1.4** where there are four cation sites, but in the **1.5** and **1.6** the anion site is split into Cl1A and Cl1B with occupancies of 0.644(8) and 0.356(8), respectively, for **1.5** and 0.731(10) and 0.269(10) for **1.6**. In both structures there is minor disorder in some of the Cs sites, for example, in **1.5** Cs2 is split into Cs2A and Cs2B with occupancies of 0.523(4) and 0.477(4), while in **1.6** Cs3 is split into Cs3A and Cs3B with occupancies of 0.961(4) and 0.039(4). Similar to **1.3** and **1.4**, the K site in **1.6** freely refines to less than 1 and the refinement of the site as both K and Ag improves the solution and is supported by EDS results. Contrastingly, K1 freely refines to 1 in **1.5.**

Structures **1.7-1.12** are based on the same $[(UO_2)_3(Ge_2O_7)_2]^{6-}$ framework. All crystallize in the orthorhombic crystal setting in either the *Pnnm*, $P2_1nm$, or $Bb2_1m$ space groups. All contain isolated $B_6X$ octahedra (X = halide, B = alkali metal) and an additional alkali site that is nested between uranyl polyhedra and is not part of the salt inclusion. The substitution of mixed alkali species on the available alkali sites influences the symmetry and space group of the structure (vide infra).

Structures **1.7-1.10** crystallize in the *Pnnm* space group with two U sites, one Ge site, three alkali sites, one halide site, and seven oxygen sites in the asymmetric unit. In **7**, U1, K3, and Cl1 lie on special positions with 2/*m* symmetry and are assigned to Wyckoff position 2*a*, 2*b*, and 3*c*, respectively. U2, K1, O2, O4, O6, and O7 are on the 4*g* Wyckoff position with site symmetry *m,* and all other atoms lie on general positions. The K1 and K2 sites are a part of the salt inclusion, while the K3 site, not part of the salt inclusion, is nested in the framework between uranyl polyhedra. In **1.8-1.10**, the alkali cation sites are labeled analogously.

The compositions and lattice parameters of **1.10** and **1.11** are quite similar, where the salt inclusion contains K, Cs, Cl, and F, and the non salt inclusion cation site is occupied by both K and Na; however, they crystallize in different space groups. Solutions of **1.11** in the *Pnnm* space group resulted in $R_1$ and $wR_2$ values of 0.0723 and 0.1637, respectively, while when solved in the $P2_1nm$ space group, these values dropped significantly to 0.0396 and 0.0911. A non-standard setting was used for **1.11** for ease of comparison with the standard Pnnm setting of **1.10**. In the $P2_1nm$ structure for **1.11** there are three unique U sites, two Ge, 13 O, five alkali sites, and one anion site in the asymmetric unit, all of which lie on general positions. The lower space group symmetry of **1.11** can most easily be

explained by the compositional non-equivalence of the salt inclusion $B_6X$ octahedra. The equatorial alkali cations, when viewed along the *a* axis for **1.7**-**1.10**, are all symmetrically equivalent (K2), while for **1.11** there are two equatorial sites (K3, K4) that are occupied by Cs and K, but in different proportions. The Cs3/K3 site occupancies refine to 0.186(11) and 0.814(11), respectively, while the Cs4/K4 site refines to 0.393(11) and 0.607(11).

The final $[(UO_2)_3(Ge_2O_7)_2]^{6-}$ structure, **1.12**, crystallizes in the $Bb2_1m$ space group, with three unique U sites, two Ge sites, 14 O sites, five alkali sites, and one fluorine site, all of which lie on general positions. Again, a non-standard setting was used to aid in comparison between related structures. The solution was refined as a 2-component twin using the twin law (1 0 0 0 -1 0 0 0 -1) with a minor twin volume fraction of 0.436(5). The non salt inclusion cation, K3, freely refines to a fully occupied potassium cation. Within the salt inclusion, there are four unique cation sites, where K2, Cs3, and Cs4 freely refine to fully occupied K or Cs, and the K1/Cs1 site refines to occupancies of 0.822(4) and 0.178(4), respectively.

$[Cs_6Cs_{0.71}Cl_{0.71}][(UO_2)_3O_3(Ge_2O_7)]$ (**1.13**) crystallizes in the hexagonal crystal system. The presence of a $6_3$ screw axis was indicated by the pattern of systematic absences in the intensity data. A reasonable solution was obtained in space group $P6_3/m$ (No. 176). The structure consists of a $[(UO_2)_3O_3(Ge_2O_7)]^{6-}$ framework surrounding large channels containing six non-salt inclusion cesium cations that hug the channel walls and the neutral disordered $Cs_{0.71}Cl_{0.71}$ salt inclusion. The non-salt inclusion cations can be considered as part of the neutral framework, $[Cs_6(UO_2)_3O_3(Ge_2O_7)]$. Disorder exists in both the framework and in the channel part of the structure. The asymmetric unit of the $[Cs_6(UO_2)_3O_3(Ge_2O_7)]$ framework consists of one uranium atom located on an inversion

center (U1, site 6*g*), two cesium atoms located on mirror planes (Cs1, Cs2, site 6*h*), one germanium atom located on a threefold axis (Ge1, site 4*f*), and four oxygen atoms (O1-O4). O1 is located on a general position (site 12*i*) and O2 is located on a mirror plane (site 6*h*). Oxygen atoms O3 and O4, part of a $Ge_2O_7$ group, are both disordered over three positions each, suggesting multiple bent Ge-O-Ge bridges and twisted -$GeO_3$ conformations of the $Ge_2O_7$ group. The disorder in the $Ge_2O_7$ group and in the cesium chloride salt inclusion are thoroughly discussed below.

For **1.13**, $[Cs_6Cs_{0.71}Cl_{0.71}][(UO_2)_3O_3(Ge_2O_7)]$, there is disorder in both the framework and in the salt inclusion. In the $Ge_2O_7$ group, O3 is split into three general positions (O3A, O3B, O3C) each of which was refined with a fixed occupancy of 1/3. O4 is located on a mirror plane (6h) but is disordered over three symmetry-equivalent sites across a nearby -6 axis (site 2*d*). O4 was also refined with 1/3-occupancy. The neutral $[Cs_6(UO_2)_3(Ge_2O_7)_3]$ framework surrounds channels along the [001] direction in which significant electron density, primarily localized in four peaks, was observed. Based on distances and occupancy refinements, these atoms are all disordered and partially occupied. The two peaks near the center of the channel axis were assigned as cesium atoms Cs3 and Cs4, giving reasonable distances to framework atoms. The largest peak, located in the center of the channel, only refined acceptably as a heavier Cs atom, consistently giving an occupancy value near 0.5 (Cs3 occupancy = 0.495(4)). The second largest peak refined to a cesium occupancy of Cs4 = 0.036(1). The two peaks nearer to the framework atoms were modeled as chlorine atoms Cl3 and Cl4 on the basis of EDS demonstrating chlorine in the crystal. The Cl occupancies refined to Cl1 = 0.070(3) and Cl2 = 0.048(4). The channel disorder model presented herewith exactly satisfies charge balance, giving support to the

model. Clearly the disorder obscures the precise atomic distribution within the channels and should be regarded as approximate. Neither the oxygen disorder around the germanium atoms nor the channel disorder was resolved by lowering the space group symmetry from $P6_3/m$, as a similar disorder was also observed in lower space groups such as $P$-6 and $P6_3$. The crystal is a near-perfect merohedral twin, as inclusion of the twin law [0 1 0 / 1 0 0 / 0 0 -1] reduced the $R1$ value from *ca*. 7% to 2.3%. The major twin volume fraction refined to 0.498(2). All atoms were refined with anisotropic displacement parameters. The anisotropic displacement parameters of O3A-O3C and of Cs3/Cs4 were each separately held equal. Those of O4 were restrained to a spherical form using an ISOR instruction. Displacement parameters for the small chlorine fractions could not be refined freely or anisotropically and were fixed arbitrarily at 0.030 $Å^2$. The largest residual electron density peak and hole in the final difference map are +1.32 and -0.95 $e^-/Å^3$, located 0.41 Å from Cs2 and 1.62 from Cs1, respectively.

**Powder X-ray Diffraction.** Data were collected on a Bruker D2 Phaser equipped with a LYNXEYE silicon strip detector or a Rigaku Ultima IV diffractometer equipped with a DTex detector, both with Cu K$\alpha$ ($\lambda$ = 1.54056 Å) sources. PXRD patterns of **1.6** and **1.12** are shown in Figure 1.2. The PXRD was used for product identification and to confirm purity of samples selected for optical measurements.

**Energy dispersive spectroscopy.** EDS was used to verify the presence of the appropriate elements in each single crystal used for structure determination, and on bulk powders of **1.6** and **1.12**. Data were collected on a TESCAN Vega-3 SBU equipped with an EDS detector.

**Optical Properties.** UV-vis and fluorescence measurements were performed on bulk samples of $[Cs_6K_{1.9}Ag_{0.1}Cl_2][(UO_2)_3(Ge_2O_7)_2]$ (**1.6**) and $[KK_{1.8}Cs_{4.2}F][(UO_2)_3(Ge_2O_7)_2]$ (**1.12**), representative of the monoclinic and orthorhombic structures, respectively. UV-vis diffuse reflectance data were collected using a PerkinElmer Lambda 35 UV/vis scanning spectrophotometer equipped with an integrating sphere. Diffuse reflectance data were converted to absorbance using the Kubelka-Munk equation and normalized.[19] A PerkinElmer LS55 Luminescence spectrometer was used to collect fluorescence data. Excitation spectra were collected at emission wavelengths of 535 nm **6** or 534 nm **1.12** and emission spectra were collected at an excitation wavelength of 378 nm **6** or 414 nm **1.12**.

**Results and Discussion:**

**Synthesis.** The successful use of essentially any alkali halide flux in Ge-based SIM synthesis demonstrates the ability of the $[(UO_2)_3(Ge_2O_7)_2]^{6-}$ framework to readily host Cs, Rb, K, Na, Ag, Br, Cl, and F ions in the salt lattice, where the identity of the flux directly influences the salt species incorporated into the framework. The $[(UO_2)_3(Ge_2O_7)_2]^{6-}$ framework readily forms in pure fluoride and chloride fluxes, and eutectic mixtures thereof, but synthetic conditions using pure bromide or iodide fluxes did not produce the desired compositions. However, by using eutectic mixtures of CsI/CsCl and KF/KBr, the $[(UO_2)_3(Ge_2O_7)_2]^{6-}$ framework could be formed in the presence of bromide and iodide fluxes. While bromine was successfully incorporated into one of the structures, $[KK_6Br_{0.6}F_{0.4}][(UO_2)_3(Ge_2O_7)_2]$ (**1.8**), iodine was not incorporated regardless of the flux identity or the dwell temperature used. The iodide ion is large with an ionic radius of 2.20 Å,[20] and even when paired with $Na^+$, does not lead to the formation of a salt inclusion

**Table 1.2:** Crystallographic Data for Compounds 1.1-1.13

| Framework | $[(UO_2)_3(Ge_2O_7)_2]^{6-}$ | | | | | |
|---|---|---|---|---|---|---|
| Salt Inclusion | $[Cs_2Cs_5F]$ | $[Cs_6Ag_2Cl_2]$ | $[Cs_6Ag_{0.3}Na_{1.7}Cl_2]$ | $[Cs_6Ag_{0.4}Na_{1.6}Cl_2]$ | $[Cs_6K_2Cl_2]$ | $[Cs_6K_{1.9}Ag_{0.1}Cl_2]$ |
| Compound | **1.1** | **1.2** | **1.3** | **1.4** | **1.5** | **1.6** |
| S. G. | $P2_1/n$ | $P2_1/n$ | $P2_1/n$ | $P2_1/n$ | $P2_1/n$ | $P2_1/n$ |
| a, Å | 7.6779(3) | 7.6168(2) | 7.6019(3) | 7.6006(3) | 7.5452(3) | 7.5758(3) |
| b. Å | 10.0432(4) | 10.1949(3) | 10.1339(4) | 10.1291(3) | 10.1363(4) | 10.1947(4) |
| c, Å | 18.8387(8) | 18.6922(5) | 18.7573(7) | 18.7794(7) | 19.1001(7) | 19.1196(8) |
| β, ° | 92.1387(14) | 92.2126(11) | 91.502(2) | 91.654(1) | 90.5930(10) | 90.524(2) |
| V, Å$^3$ | 1451.65(10) | 1450.41(7) | 1444.51(10) | 1445.17(19) | 1460.71(10) | 1476.60(10) |
| Crystal size (mm$^3$) | 0.08 x 0.01 x 0.01 | 0.04 x 0.02 x 0.02 | 0.06 x 0.01 x 0.01 | 0.02 x 0.02 x 0.02 | 0.02 x 0.04 x 0.02 | 0.06 x 0.02 x 0.02 |
| Temperature (K) | 301(2) | 300.0 | 302.01 | 302.5 | 302.64 | 302.01 |
| Density (g cm$^{-3}$) | 5.202 | 5.515 | 5.199 | 5.215 | 5.163 | 5.127 |
| $\theta$ range (deg) | *2.164-30.538* | *2.676-36.345* | *2.866-36.345* | 2.170-32.655 | *2.893-36.346* | *2.689-36.407* |
| $\mu$ (mm$^{-1}$) | 29.481 | 29.761 | 28.767 | 28.815 | 28.535 | 28.291 |

**Table 1.2 cont.:** Crystallographic Data for Compounds 1.1-1.13

| Data Collection and Refinement | | | | | | |
|---|---|---|---|---|---|---|
| Compound | **1.1** | **1.2** | **1.3** | **1.4** | **1.5** | **1.6** |
| Collected reflections | 67200 | 54189 | 145386 | 50852 | 117213 | 146508 |
| Unique reflections | 6142 | 7069 | 7005 | 5302 | 7038 | 7165 |
| $R_{int}$ | 0.0484 | 0.0348 | 0.0521 | 0.0510 | 0.0363 | 0.0434 |
| $h$ | $-10 \le h \le 10$ | $-12 \le h \le 12$ | $-12 \le h \le 12$ | $-11 \le h \le 11$ | $-12 \le h \le 12$ | $-11 \le h \le 12$ |
| $k$ | $0 \le k \le 14$ | $-16 \le k \le 16$ | $-16 \le k \le 16$ | $-15 \le k \le 15$ | $-16 \le k \le 16$ | $-16 \le k \le 16$ |
| $l$ | $0 \le l \le 26$ | $-31 \le l \le 31$ | $-31 \le l \le 31$ | $-28 \le l \le 28$ | $-31 \le l \le 31$ | $-31 \le l \le 31$ |
| $\Delta\rho_{max}$ (e Å$^{-3}$) | 1.783 | 6.657 | 2.577 | 2.552 | 3.801 | 6.489 |
| $\Delta\rho_{min}$ (e Å$^{-3}$) | -1.660 | -3.492 | -1.426 | -2.119 | -2.382 | -3.661 |
| *GoF* | 1.171 | 1.190 | 1.084 | 1.042 | 1.231 | 1.191 |
| Extinction | 0.00051(5) | 0.00039(2) | 0.000075(10) | 0.00055(2) | 0.00245(11) | 0.00015(2) |
| $R_1(F)$ *for* $I>2\,\sigma(I)$ | 0.0369 | 0.0384 | 0.0214 | 0.0267 | 0.0310 | 0.0417 |
| $wR_2(F_0^2)^b$ | 0.0915 | 0.0935 | 0.0392 | 0.0546 | 0.0690 | 0.0870 |

[a] $R_1 = \Sigma\big||F_0| - |F_c|\big|/\Sigma|F_0|$. [b] $wR_2 = [\Sigma w\left(F_0^2 - F_c^2\right)^2/\Sigma w\left(F_0^2\right)^2]^{1/2}$; $P = (F_0^2 + 2F_c^2)/3$; $w = 1/\left[\sigma^2\left(F_0^2\right) + (0.0291P)^2 + 34.2701P\right]$ for **1.1**, $w = 1/\left[\sigma^2\left(F_0^2\right) + 60.4982P\right]$ for **1.2**, $w = 1/\left[\sigma^2\left(F_0^2\right) + (0.0076P)^2 + 6.8910P\right]$ for **1.3**, $w = 1/\left[\sigma^2\left(F_0^2\right) + (0.0155P)^2 + 14.2662P\right]$ for **1.4**, $w = 1/\left[\sigma^2\left(F_0^2\right) + (0.0049P)^2 + 22.6144P\right]$ for **1.5**, and $w = 1/\left[\sigma^2\left(F_0^2\right) + 50.3032P\right]$ for **1.6**.

**Table 1.2 cont.:** Crystallographic Data for Compounds 1.1-1.13

| Framework | $[(UO_2)_3(Ge_2O_7)_2]^{6-}$ | | | | | | $[(UO_2)_3O_3(Ge_2O_7)]^{6-}$ |
|---|---|---|---|---|---|---|---|
| Salt Inclusion | $[KK_6Cl]$ | $[KK_6Br_{0.6}F_{0.4}]$ | $[Na_{0.9}Rb_{6.1}F]$ | $[K_{0.6}Na_{0.4}K_5CsCl_{0.5}F_{0.5}]$ | $[K_{0.8}Na_{0.2}K_{4.8}Cs_{1.2}Cl_{0.5}F_{0.5}]$ | $[KK_{1.8}Cs_{4.2}F]$ | $[Cs_6Cs_{0.71}Cl_{0.71}]$ |
| Compound | **1.7** | **1.8** | **1.9** | **1.10** | **1.11** | **1.12** | **1.13** |
| S. G. | *Pnnm* | *Pnnm* | *Pnnm* | *Pnnm* | $P2_1nm$ | $Bb2_1m$ | $P6_3/m$ |
| a, Å | 11.3756(5) | 11.3912(10) | 11.3983(3) | 11.4024(3) | 11.4324(15) | 22.8824(5) | 13.1200(11) |
| b. Å | 13.7260(6) | 13.7645(13) | 13.6733(4) | 13.7707(3) | 13.8332(19) | 14.2844(3) | 13.1200(11) |
| c, Å | 8.0532(4) | 8.0588(7) | 8.0935(2) | 8.0160(2) | 7.9947(10) | 7.9924(2) | 8.6827(8) |
| V, $Å^3$ | 1257.44(10) | 1263.6(2) | 1261.39(6) | 1258.66(5) | 1264.3(3) | 2612.41(10) | 1294.4(2) |
| Crystal size ($mm^3$) | 0.05 x 0.01 x 0.01 | 0.05 x 0.01 x 0.01 | 0.06 x 0.01 x 0.01 | 0.04 x 0.02 x 0.02 | 0.09 x 0.02 x 0.02 | 0.03 x 0.01 x 0.01 | 0.10 x 0.08 x 0.04 |
| Temp. (K) | 303.12 | 303.6 | 302.5 | 300.1 | 302 | 299.99 | 300 |
| Density ($gcm^{-3}$) | 4.315 | 4.347 | 4.948 | 4.531 | 4.549 | 5.108 | 5.214 |
| $\theta$ range ° | 2.933-36.348 | 2.929-37.021 | 2.326-50.594 | 2.319-36.391 | 2.311-28.297 | 2.699-36.340 | 2.346-35.091 |

**Table 1.2 cont.:** Crystallographic Data for Compounds 1.1-1.13

| Data Collection and Refinement | | | | | | | |
|---|---|---|---|---|---|---|---|
| Compound | **1.7** | **1.8** | **1.9** | **1.10** | **1.11** | **1.12** | **1.13** |
| Collected reflections | 125095 | 52719 | 141748 | 124391 | 78040 | 31877 | 62171 |
| Unique reflections | 3229 | 3395 | 7083 | 3233 | 3376 | 6655 | 2013 |
| $R_{int}$ | 0.0616 | 0.0520 | 0.0568 | 0.0388 | 0.0396 | 0.0336 | 0.0548 |
| $h$ | $-18 \le h \le 18$ | $-19 \le h \le 19$ | $-24 \le h \le 24$ | $-19 \le h \le 19$ | $-15 \le h \le 15$ | $-25 \le h \le 38$ | $-21 \le h \le 21$ |
| $k$ | $-22 \le k \le 22$ | $-23 \le k \le 23$ | $-28 \le k \le 29$ | $-22 \le k \le 22$ | $-18 \le k \le 28$ | $-23 \le k \le 22$ | $-21 \le k \le 21$ |
| $l$ | $-13 \le l \le 13$ | $-13 \le l \le 13$ | $-17 \le l \le 17$ | $-13 \le l \le 13$ | $-10 \le l \le 10$ | $-13 \le l \le 10$ | $-14 \le l \le 14$ |
| $\Delta\rho_{max}$ (e Å$^{-3}$) | 2.497 | 1.938 | 4.312 | 4.814 | 5.880 | 1.463 | 1.324 |
| $\Delta\rho_{min}$ (e Å$^{-3}$) | -1.126 | -3.499 | -3.288 | -2.855 | -2.148 | -0.923 | -0.948 |
| *GoF* | 1.119 | 1.209 | 1.077 | 1.332 | 1.068 | 1.061 | 1.114 |
| Extinction coefficient | 0.00032(3) | 0.00028(3) | 0.00120(4) | 0.00011(4) | -- | 0.000040(9) | 0.00106(5) |
| $R_1(F)$ *for* $I>2\,\sigma(I)$ | 0.0168 | 0.0273 | 0.0220 | 0.0316 | 0.0351 | 0.0211 | 0.0230 |
| $wR_2(F_0^2)^b$ | 0.0386 | 0.0427 | 0.0420 | 0.0669 | 0.0911 | 0.0426 | 0.0513 |

[a] $R_1 = \Sigma\big||F_0| - |F_c|\big|/\Sigma|F_0|$. [b] $wR_2 = [\Sigma w(F_0^2 - F_c^2)^2/\Sigma w(F_0^2)^2]^{1/2}$; $P = (F_0^2 + 2F_c^2)/3$; $w = 1/[\sigma^2(F_0^2) + (0.0132P)^2 + 3.1506P]$ for **1.7**, $w = 1/[\sigma^2(F_0^2) + (0.0036P)^2 + 6.0562P]$ for **1.8**, $w = 1/[\sigma^2(F_0^2) + (0.0114P)^2 + 2.6617P]$ for **1.9**, $w = 1/[\sigma^2(F_0^2) + 18.4966P]$ for **1.10**, $w = 1/[\sigma^2(F_0^2) + (0.0443P)^2 + 27.6384P]$ for **1.11**, $w = 1/[\sigma^2(F_0^2) + (0.0169P)^2 + 5.1796P]$ for **1.12**, and $w = 1/[\sigma^2(F_0^2) + (0.0209P)^2 + 3.2206P]$ for **1.1**

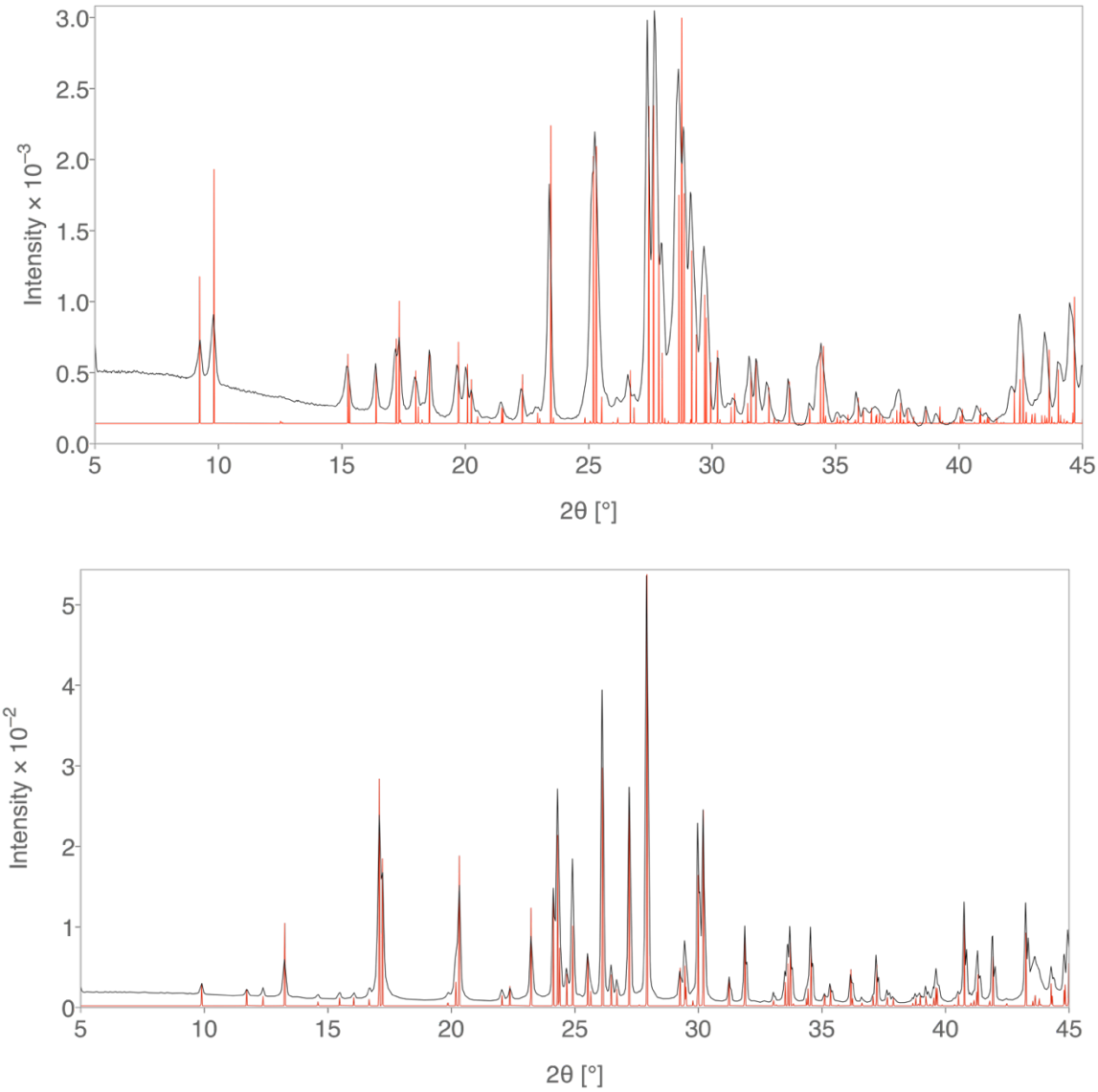


**Figure 1.2:** PXRD patterns of 1.6 and 1.12. $[Cs_6K_{1.9}Ag_{0.1}Cl_2][(UO_2)_3(Ge_2O_7)_2]$ (**6**) (top) and $[KK_{1.8}Cs_{4.2}F][(UO_2)_3(Ge_2O_7)_2]$ (**12**) (bottom). The calculated patterns from the CIFs are in red, and the experimental data is in black. The broad hump between 5 and 15 2 theta in the $[Cs_6K_{1.9}Ag_{0.1}Cl_2][(UO_2)_3(Ge_2O_7)_2]$ is caused by iron fluorescence from the steel sample holder.

phase; instead, these reactions result in non-porous three dimensional alkali uranium oxides and alkali uranium germanate phases that we will report on in the near future.

The synthesis of the uranium germanate salt inclusion materials was most successful when using a reaction temperature of 875 °C, unlike the synthesis of the uranium silicate SIMs developed by Morrison et al., that form at an optimum dwell temperature of 800 °C. Structures **1.1** and **1.3** could also be synthesized at 800 °C, but the higher temperature significantly increased crystal quality and was, therefore, used for the synthesis of all the other structures reported herein.

As summarized in Morrison et al. 2016,[2] silver tubes with dimensions of 5.7 cm tall with 1.2 cm diameter proved essential, as compared to larger silver crucibles with higher surface area to volume ratios, in favoring salt inclusions phases over less complex oxide phases. By limiting the surface area to volume ratio, we hypothesize that less atmospheric oxygen is incorporated into the flux, and by limiting the incorporation of oxygen into the reaction salt inclusion phases are formed. Attempts were made to overcome the insoluble silver halide side products by synthesizing the uranyl germanate SIMs in platinum crucibles (3.0 cm tall by 2.5 cm in diameter) and in alumina crucibles (2.6 cm tall by 1.8 cm in diameter), using only chloride containing fluxes in the alumina crucibles to avoid crucible dissolution by the fluoride flux. These reactions were unsuccessful in producing phase pure products of the germanate SIMs and instead produced predominantly oxide phases such us $Cs_2Ge_6O_{13}$, $Na_2Ge_4O_9$, $Cs_4U_5O_{17}$, and $A_2U_2O_7$ (A = Cs, K, Na), as identified by PXRD.

Structures **1.3** and **1.4**, **1.5** and **1.6**, **1.10** and **1.11**, all contain very similar compositions, and the variation in their lattice parameters and bond distances that exceeds

three times the standard deviations (ESD), confirms that they are indeed dissimilar from each other. However, it would be difficult to ascertain by PXRD, whether a sample was phase pure or whether it contained small amounts of **1.3** or **1.4**, or **1.5** or **1.6** as a second phase impurity due to the almost insignificant differences in the diffraction patterns for the alternate structures, exacerbated by the complicated nature of low symmetry, monoclinic diffraction patterns, and peak overlap. In any case, for potential nuclear waste sequestration applications, the exact composition of the waste form will not be as important as its ability to incorporate a wide variety of radioactive alkali or alkaline earth metals and halides, as has been successfully demonstrated for this class of materials.

$[Cs_6Cs_{0.71}Cl_{0.71}][(UO_2)_3O_3(Ge_2O_7)]$ was synthesized by increasing the U:Ge ratio, to favor a uranium rich framework composition. Regardless of the chloride flux used, necessary for the cesium chloride salt inclusion, the yield could not be increased, nor could the size of the single crystals. Additional compositions of this $[(UO_2)_3O_3(Ge_2O_7)]^{6-}$ framework were attempted by further increasing the ratio of U:Ge and by trying other fluxes, similar as what was done for synthesizing **1.1**-**1.12**; these trials, however, were unsuccessful.

**Structure.** The SIMs that adopt the $[(UO_2)_3(Ge_2O_7)_2]^{6-}$ framework, **1.1**-**1.12**, (Figure 1.3), have identical connectivity with slight variations in bond lengths and bond angles to accommodate the different sizes of the salt inclusions. The uranium and germanium polyhedra adopt typical coordination geometries in the framework, which consist of uranyl square bipyramids and $Ge_2O_7^{6-}$ pyrogermanate units. Uranyl square bipyramids and germanium tetrahedra alternate to form 12 membered rings that create the channels. Each uranyl square bipyramid is bonded to four germanium tetrahedra through

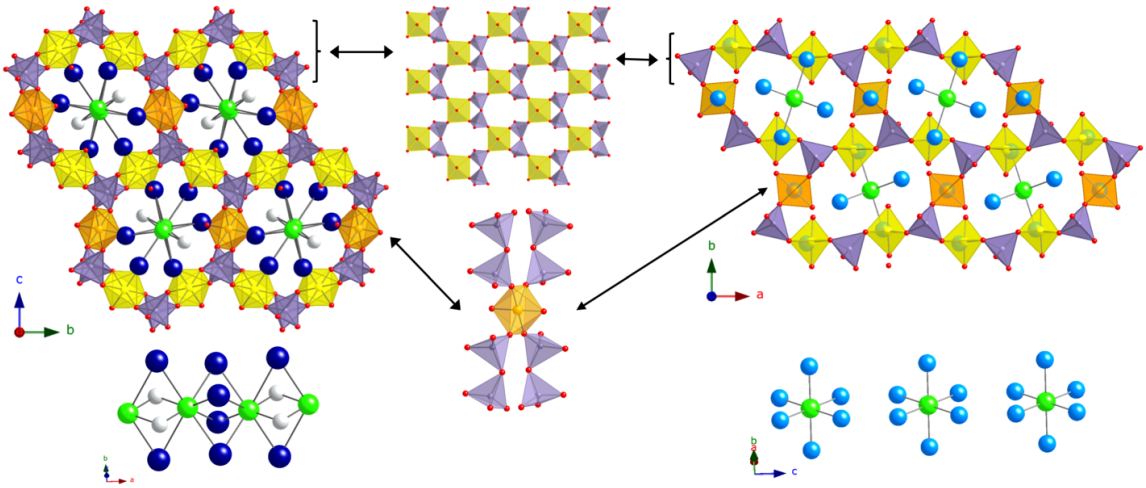

**Figure 1.3:** Structures of 1.2 and 1.7. (top left) Monoclinic structure of $[Cs_6Ag_2Cl_2][(UO_2)_3(Ge_2O_7)_2]$ down the *a* direction and (bottom left) a 90° rotated view of its salt inclusion. (top right) The orthorhombic structure of $[KK_6Cl][(UO_2)_3(Ge_2O_7)_2]$ down the *c* direction and (bottom right) a 90° rotated view of its salt inclusion. In the middle of the figure, the framework components of uranyl germanate sheets (top middle) connected by uranyl square bipyramids (lower middle) is shown. Uranium is yellow and orange, germanium is gray, oxygen red, chlorine green, silver in white, cesium dark blue, and potassium light blue.

its equatorial bonds. Each germanium tetrahedron is bonded to one other germanium tetrahedron forming a pyrogermanate dimer and is also bonded to three different uranyl square bipyramids. This framework can be deconstructed into $(UO_2)_2(Ge_2O_7)_2^{8-}$ sheets linked together by uranium square bipyramids, shown in Figure 1.3, where the top chain of alternating germanium dimers and uranyl polyhedra has been highlighted, isolated, and rotated 90° to show the uranyl germanate sheets comprised of U2. Below the sheet in Figure 1.3, the coordination environment of the uranium square bipyramid (U1) that connects the sheets is shown. This framework has been previously reported in $Cs_6[(UO_2)_3(Ge_2O_7)_2](H_2O)_4$ which was synthesized by the Lii group via high temperature hydrothermal methods in 2009.[10] Since there are only cations and water molecules in the channel, the framework is not a SIM. The Si analog of this framework has also been observed in

$[NaRb_6F][(UO_2)_3(Si_2O_7)_2]$,[4] $[NaK_6F][(UO_2)_3(Si_2O_7)_2]$, $[KK_6Cl][(UO_2)_3(Si_2O_7)_2]$,[2] $[Cs_2Cs_5F][(UO_2)_3(Si_2O_7)_2]$,[3] and $[K_3Cs_4F][(UO_2)_3(Si_2O_7)_2]$.[4] The 12 unique uranyl germanate SIMs with the $[(UO_2)_3(Ge_2O_7)_2]^{6-}$ framework crystallize in monoclinic or orthorhombic space groups. All monoclinic structures adopt the $P2_1/n$ space group, whereas there are three different orthorhombic space groups: *Pnnm*, $P2_1nm$, or $Bb2_1m$.

In the orthorhombic structures **1.7**-**1.12** the cation sites K3 in **1.7**, **1.8**, **1.10**, **1.12**, Na3/Rb3 in **1.9**, and K5 in **1.11** are nested in the framework between uranyl polyhedra and coordinate to 8 oxygen atoms creating a hexagonal bipyramid coordination environment (Figure 1.4b). These cation sites are not associated with the salt inclusion because the distances from this site to the closest anion site are greater than 5.613 Å. This is significantly different from the salt inclusion bond distances in the $B_6X$ octahedra, which range between 2.750 and 3.239 Å. All orthorhombic SIMs have a salt lattice consisting of isolated $B_6X$ units, where B is an alkali cation and X is a halogen anion (Figure 1.3). The term isolated is used to distinguish between the monoclinic SIMs **1.1**-**1.6** which contain salt inlcusion chains as opposed to the non corner-sharing $B_6X$ units in **1.7**-**1.12**. $[KK_6Cl]$ (**1.6**) and $[KK_6Br_{0.6}F_{0.4}]$ (**1.7**) are the simplest, where all alkali sites are fully occupied by K. In the $[Na_{0.9}Rb_{0.1}Rb_6F][(UO_2)_3(Ge_2O_7)_2]$ (**1.8**) structure, the Rb sites involved in the salt inclusion are fully occupied, and the non-salt inclusion A site Na3/Rb3, located between the uranyl polyhedra, is partially occupied by Na and Rb, likely due to the smaller size of Na as compared to K. In both $[K_{0.6}Na_{0.4}K_5CsCl_{0.5}F_{0.5}]$ (**1.10**) and $[K_{0.8}Na_{0.2}K_{4.8}Cs_{1.2}Cl_{0.5}F_{0.5}]$ (**1.11**) the non-salt lattice alkali site is partially occupied by both K and Na and the axial alkali sites, that are perpindicular to the *c* direction as shown in Figure 1.3, in the $B_6X$ units are fully occupied K. The equatorial sites in both are partially

occupied by both K and Cs. The most notable difference is that in **1.10** all equatorial sites are symmetrically equivalent, which is not the case in **1.11** or **1.12** and explains the reduction in space group symmetry. In $[KK_{1.8}Cs_{4.2}F]$ (**1.12**) the equatorial sites in the $B_6X$ units are fully occupied with Cs, while all other alkali sites are partially occupied by both K and Cs. While in the *Pnnm* structures **1.7**-**1.10** and $P2_1nm$ structure **1.11** each $(UO_2)_2(Ge_2O_7)_2^{8-}$ sheet is made up of one symmetrically unique U site (U2 in **1.7**-**1.10** and alternating layers of U1 and U3 in **1.11**), $Bb2_1m$ contains alternating U2 and U3 polyhedra in the *a* direction which explains the doubling in the *a* lattice parameter. The two different U polyhedra in the same layer is a result of the presence both K and Cs cations between the uranyl polyhedra.

All of the monoclinic structures contain six or more cesium cations per formula unit. Cesium is significantly larger than postassium with crystal radii of 1.88 Å and 1.65 Å for 8-coordinate sites, respectively.[20] Due to the larger size of cesium, it is too large to fit between uranyl square bipyramids, as in the case of postassium, and instead shifts to either side of the site creating U-Cs-U angles of ~120° as opposed to 180° in the orthorhombic structures (Figure 1.4a). This suggests that it is the larger size of the species in the channels that forces the framework into the monoclinic setting. $[Cs_2Cs_5F][(UO_2)_3(Ge_2O_7)_2]$ (**1**) contains $B_6X$ octahedra similar to those found in the orthorhombic structures; however, these units are edge-sharing creating 1D chains down the *a* axis instead of being isolated. The $[Cs_2Cs_5F][(UO_2)_3(Ge_2O_7)_2]$ (**1**) (Figure 1.5a) structure can be described as a salt lattice of corner sharing $Cs_6X$ units. This structure is the Ge analog of $[Cs_2Cs_5F][(UO_2)_3(Si_2O_7)_2]$[3] where the disorder in the salt inclusion is different between the two structures likely due to

the size difference between Si and Ge. The disordered F site is split across three positions and the corner shared Cs site is split across an inversion center creating four Cs positions.

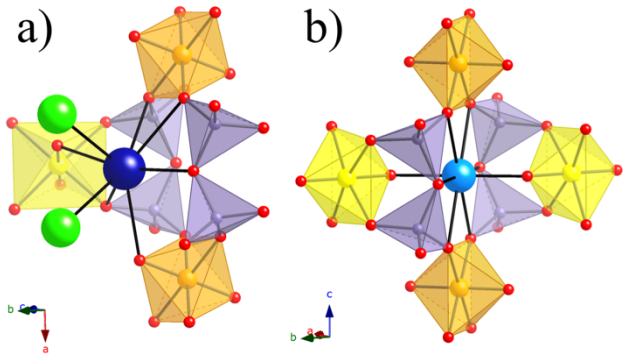


**Figure 1.4:** Comparison of the Cs2 and K3 sites 1.2 and 1.7. a) $[Cs_6Ag_2Cl_2][(UO_2)_3(Ge_2O_7)_2]$ and b) $KK_6Cl][(UO_2)_3(Ge_2O_7)_2]$ demonstrating the change in alkali coordination enviroment due to the size of the alkali cation.

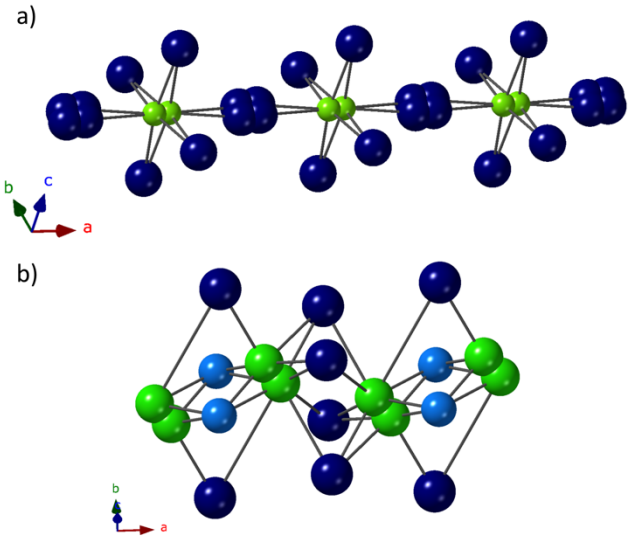


**Figure 1.5:** The salt inclusions of 1.1, 1.5, and 1.6. a) $[Cs_2Cs_5F][(UO_2)_3(Ge_2O_7)_2]$ (**1.1**) b) The salt inclusion of $[Cs_6K_2Cl_2][(UO_2)_3(Ge_2O_7)_2]$ (**1.5**), and $[Cs_6K_{1.9}Ag_{0.1}Cl_2][(UO_2)_3(Ge_2O_7)_2]$ (**1.6**). Cesium atoms are dark blue, potassium are light blue, and fluorine/chlorine are green.

The Cs1-F distances range from 5.479 to 5.942 Å, and are significantly longer than the Cs-F distances in the octahedra, which are 3.03 – 3.90 Å. This large difference in bond distances suggests that Cs1 is not part of the salt inclusion. The rest of the monoclinic structures, **1.2**-**1.6**, have Cs-Cl bond distances between 3.31-4.843 Å and all Cs cations are considered part of the salt inclusion, even though not all of the interactions can be considered fully bonded. When determining whether or not a cationic species is considered to be part of the salt inclusion, the sum of the van der Waals radii were compared to the interatomic distances. For example, for the Cs-F salt inclusion, the crystallographic van der Waals radii for Cs and F are 3.0 Å and 1.5 Å, respectively, and therefore any interatomic distance less than 4.5 Å is considered to be the result of some bonding interaction and, thus, part of the Cs-F salt inclusion.[21]

The salt inclusion in $[Cs_6Ag_2Cl_2][(UO_2)_3(Ge_2O_7)_2]$ (**1.2**) can be described as chains of face sharing 8-coordinate chlorine polyhedra, $ClAg_2Cs_6$. Two different faces are shared, one comprised of four cesium atoms, and another of two silver and two cesium atoms. The salt inclusions in **1.2**, **1.3** and **1.4** are isostructural, where the Ag site in **1.2** is partially occupied by both Ag and Na in **1.3** and **1.4**. The larger size of K as compared to Ag (ionic radii of 1.51 and 1.00 Å, respectively) causes a disordered chlorine site in **1.5** and **1.6** (Figure 1.5b), which is the primary difference between the salt inclusions found in **1.2**-**1.4** and those found in **1.5**-**1.6**.[20] Due to the disorder in the chlorine site and the size of the potassium, the chlorine is 6- and 5-coordinated for the Cl1A and Cl1B sites, respectively. It is interesting to note that the salt inclusions found in **1.2**-**1.6** are unlike any observed in the Si analogs, in contrast with structures **1.1**, **1.7**-**1.8**, **1.9**-**1.11**, and **1.12** that contain salt

inlcusions similar to those seen in $[Cs_2Cs_5F][(UO_2)_3(Si_2O_7)_2]$,[3] $[KK_6Cl][(UO_2)_3(Si_2O_7)_2]$,[2] $[NaRb_6F][(UO_2)_3(Si_2O_7)_2]$,[4] and $[K_3Cs_4F][(UO_2)_3(Si_2O_7)_2]$,[4] respectively.

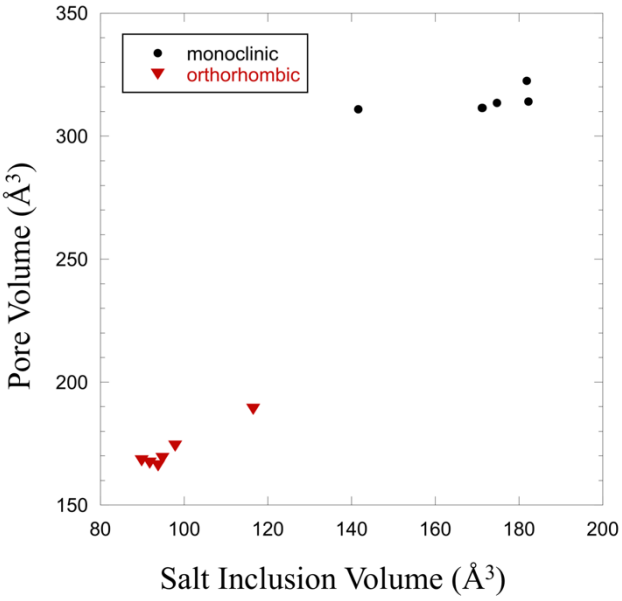


**Figure 1.6:** Pore Volume vs. Salt Inclusion Volume. The pore volume per channel per unit cell plotted against the salt inclusion volume, showing clear distinction between the

To demonstrate the impact of salt inclusion size on the framework, the pore volume per channel per unit cell of the framework has been plotted as a function of the volume of the salt inclusion (Figure 1.6). The pore volume per channel per unit cell was determined by removing the ionic species in the channels and using the Calc Solv functionality in PLATON and dividing the resulting volume by Z, the number of formula units per unit cell.[18] The salt-inclusion volumes were calculated by the summation of "thermochemical radii",[22] an adaptation of the Goldschmidt[23] ionic radii used to describe complex salts such as those in SIMs.[24] The percent-volume is derived from the thermochemical volume of the salt and the formula-unit volume obtained from XRD patterns.[25] The pore-size diameters

are calculated using the Zeo++ software, which considers the largest included sphere or void within a crystalline porous material using Voronoii decomposition methods.[26] The voids are representative of the pores created by the salt-inclusions, which are removed from the crystal structure to perform the pore-diameter calculation. The results of the pore diameter, salt-inclusion volume, and pore volume are consolidated in Table 1.3 and the pore volume vs. salt-inclusion volume is plotted in Figure 1.6 which clearly shows a distinction between the orthorhombic and monoclinic structures. As expected, the compressed pores in the orthorhombic structures have smaller pore volume and pore diameter as compared to the more open monoclinic structures, and the volume of the salt inclusion determines the pore size, and thus the symmetry of the uranyl germanate framework.

**Table 1.3:** Pore Volumes, Salt-Inclusion Volumes, Pore Diameters for 1.1-1.12

| Compound | Salt Inclusion Volume (Å$^3$) | Pore Volume per channel per unit cell (Å$^3$) | Pore Diameter (Å) |
|---|---|---|---|
| **1.1** | 141.6 | 311 | 5.654 |
| **1.2** | 174.7 | 314 | 5.157 |
| **1.3** | 171.1 | 312 | 5.244 |
| **1.4** | 171.3 | 312 | 5.272 |
| **1.5** | 182.3 | 314 | 5.434 |
| **1.6** | 181.9 | 322 | 5.422 |
| **1.7** | 93.8 | 166 | 4.981 |
| **1.8** | 89.9 | 168 | 5.009 |
| **1.9** | 97.9 | 174 | 5.083 |
| **1.10** | 91.8 | 167 | 5.041 |
| **1.11** | 94.8 | 169 | 5.065 |
| **1.12** | 116.5 | 189 | 5.403 |

$[Cs_6Cs_{0.71}Cl_{0.71}][(UO_2)_3O_3(Ge_2O_7)]$ (**1.13**) contains a new framework, $[(UO_2)_3O_3(Ge_2O_7)]^{6-}$, not yet reported in the literature. It crystallizes in the $P6_3/m$ space group with lattice parameters $a$ = 13.1200(11) Å and $c$ = 8.6867(2) Å. This framework is also built of uranyl square bipyramids and $Ge_2O_7^{6-}$ pyrogermanate dimers and forms a 12-membered ring of alternating uranium and germanium polyhedra (Figure 1.7b). Unlike the $[(UO_2)_3(Ge_2O_7)_2]^{6-}$ framework, the uranyl polyhedra corner share to make 1D chains down the $c$-axis. Similar to the $[(UO_2)_3(Ge_2O_7)_2]^{6-}$ framework, each uranyl polyhedron corner shares with four germanium tetrahedra that are a part of three separate $Ge_2O_7^{6-}$ dimers. Each $GeO_4$ tetrahedron is split across three positions, where the Ge atom roughly stays in the same position, but there are three positions for each O atom. If one considers the topology of the framework by picturing a single pore being unrolled into a flat sheet (Figure 1.7c) it matches the known topology of a uranyl vanadate, $Cs_4[(UO_2)_2(V_2O_7)O_2]$.[27] In $[Cs_6Cs_{0.71}Cl_{0.71}][(UO_2)_3O_3(Ge_2O_7)]$, all oxygen sites in the germanium tetrahedra are triply split, unlike in the vanadate topology. The pores contain Cs and Cl ions that are severely disordered, where Cs1 and Cs2 hug the edge of the channel and are fully occupied, Cs3 is in the center of the channel has an occupancy of 0.495(4), and Cs4 has an occupancy of 0.036(1). Chlorine sites Cl1 and Cl2 have occupancies of 0.070(3) and 0.048(4), respectively (Figure 1.7a). The crystallographic model detailed in the supporting information should be regarded as approximate, and it is likely that the significant disorder is in fact the result of a bent chain of alternating Cl-Cs-Cl-Cs atoms in the pores.

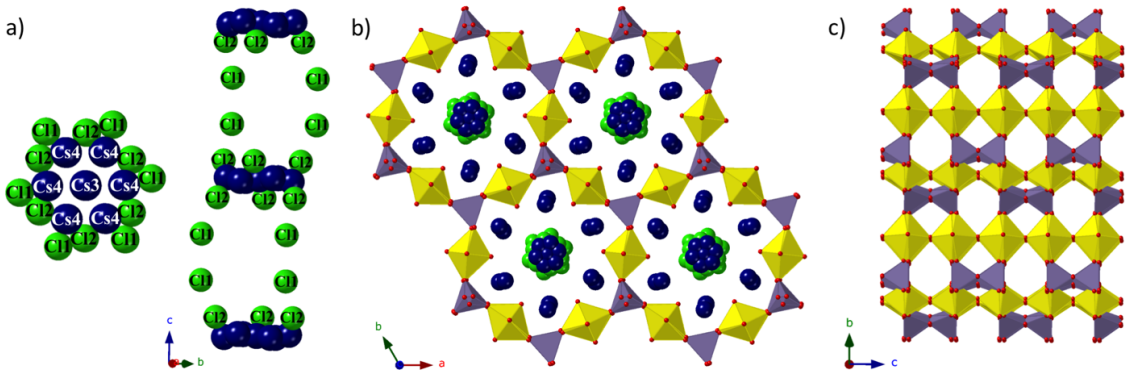


**Figure 1.7:** a) The disordered cesium chloride salt inclusion shown down the *c* axis. b) A view of $[Cs_6Cs_{0.71}Cl_{0.71}][(UO_2)_3O_3(Ge_2O_7)]$ (**13**) in the *c* direction. c) A view of the $[(UO_2)_3O_3(Ge_2O_7)]^{6-}$ framework in the *a* direction to show the sheet topology. Uranium atoms are yellow, germanium gray, oxygen red, cesium dark blue, and chlorine green.

DFT and VBT studies on uranyl salt inclusion materials were recently reported by Moore et. al, which concluded that the $[(UO_2)_3(Ge_2O_7)_2]^{6-}$ and analogous, $[(UO_2)_3(Si_2O_7)_2]^{6-}$ frameworks are thermodynamically stable.[24] VBT methods predict the average formation enthalpies of the silicates and germanates to be -14781 kJ/mol and -13972 kJ/mol, respectivley, while DFT methods predict -9365 kJ/mol and -7967 kJ/mol, respectively. The analogous uranyl silicate SIMs by DFT calculations are more negative by 16.1% when compared to the germanates , and 5.6% more negative as predicted by VBT. The discrepancies between the VBT and DFT results are partly accounted for by the fact that DFT calculations assume at 0 K in a vacuum, while VBT predicts formation enthalpies at 298 K. Despite these differences, the trends and conclusions drawn from both methods are the same, and future thermodynamic measurements will need to be performed to further refine the computational methods.

**Optical Properties.** Optical characterization was performed on $[Cs_6K_{1.9}Ag_{0.1}Cl_2][(UO_2)_3(Ge_2O_7)_2]$ (**1.6**) and $[KK_{1.8}Cs_{4.2}F][(UO_2)_3(Ge_2O_7)_2]$ (**1.12**), which

are representative of the monoclinic and orthorhombic structures, respectively. The optical properties are primarily influenced by the coordination environments of the uranium atoms, and the optical properties of the other monoclinic and orthorhombic structures are expected to be very similar. The UV-vis spectra of $[Cs_6K_{1.9}Ag_{0.1}Cl_2][(UO_2)_3(Ge_2O_7)_2]$ (**1.6**) and $[KK_{1.8}Cs_{4.2}F][(UO_2)_3(Ge_2O_7)_2]$ (**1.12**) are displayed in Figure 1.8 and show broad absorbance over 200-515 nm with estimated band gaps of 2.4 eV, indicating the two compounds are semiconductors.

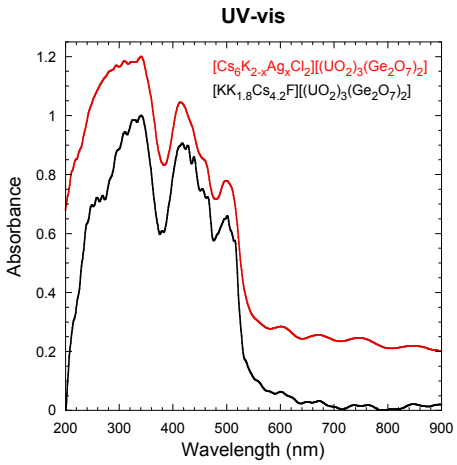


**Figure 1.8:** UV-vis of 1.6 and 1.12

The fluorescence spectra of $[Cs_6K_{1.9}Ag_{0.1}Cl_2][(UO_2)_3(Ge_2O_7)_2]$ (**1.6**) and $[KK_{1.8}Cs_{4.2}F][(UO_2)_3(Ge_2O_7)_2]$ (**1.12**) and optical pictures of ground crystals under artificial and long wave UV light ($\lambda$ = 365 nm) are shown in Figure 1.9. Both compounds exhibit typical yellow-green luminescence of uranyl-containing materials with the most intense emission peak at 534 or 535 nm resulting from the electronic emission from the lowest vibrational level of the first excited state to the lowest vibrational level of the ground

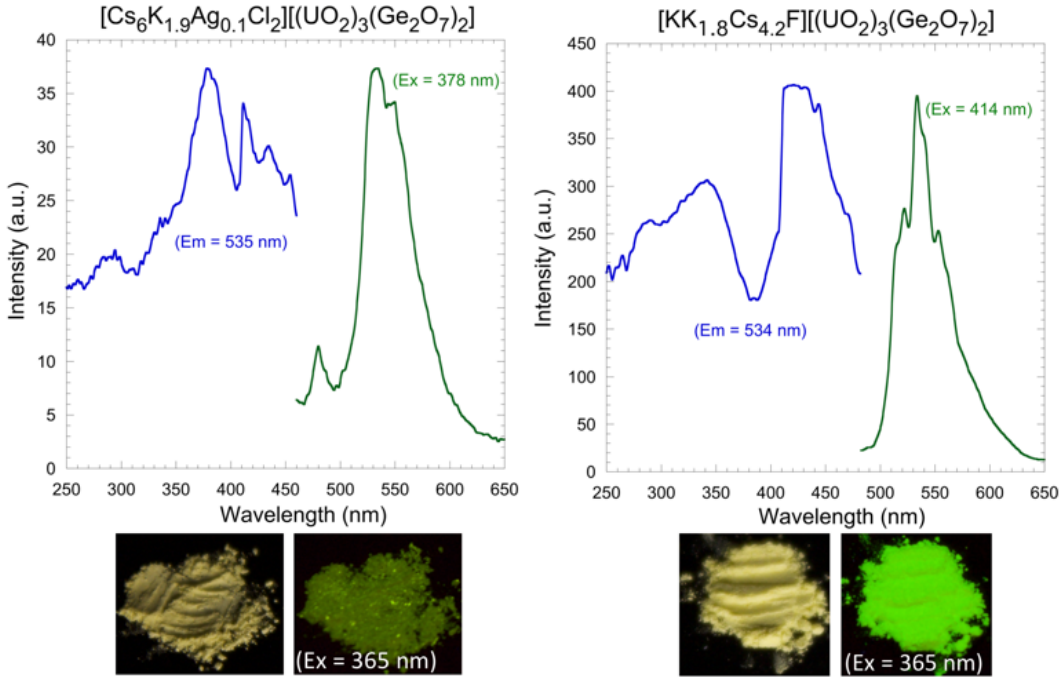


**Figure 1.8: Fluorescence of 1.6 and 1.12.** The fluorescence excitation and emission spectra of $[Cs_6K_{1.9}Ag_{0.1}Cl_2][(UO_2)_3(Ge_2O_7)_2]$ (**6**) and $[KK_{1.8}Cs_{4.2}F][(UO_2)_3(Ge_2O_7)_2]$ (**12**) along with optical pictures of ground crystals under artificial and UV light.

state. Smaller peaks around the ~535 nm emission arise from different vibrational levels of the same electronic emission. There is a significant difference in the intensity of the luminescence, both visually and spectroscopically, where $[KK_{1.8}Cs_{4.2}F][(UO_2)_3(Ge_2O_7)_2]$ is approximately ten times more intense than $[Cs_6K_{1.9}Ag_{0.1}Cl_2][(UO_2)_3(Ge_2O_7)_2]$. As also observed in the silicate SIMs, $[KK_6Cl][(UO_2)_3(Si_2O_7)_2]$ and $[NaK_6F][(UO_2)_3(Si_2O_7)_2]$, the $Cl^-$ containing SIM exhibits less intense fluorescence than the $F^-$ containing SIM, consistent with the fact that $Cl^-$ is known to quench uranyl luminescence by either donating or accepting an electron to/from the excited uranyl center. The fluorescence spectra of $[KK_{1.8}Cs_{4.2}F][(UO_2)_3(Ge_2O_7)_2]$, $[KK_6Cl][(UO_2)_3(Si_2O_7)_2]$, and $[NaK_6F][(UO_2)_3(Si_2O_7)_2]$ all contain the same basic shape with emission peaks between 533-536 nm, and excitation

peaks between 411-414 nm, while the $[Cs_6K_{1.9}Ag_{0.1}Cl_2][(UO_2)_3(Ge_2O_7)_2]$ excitation peak occurs at 378 nm. This variation may arise from the slight difference in the uranium environment, such as U-O bond distances and bond angles, as $[KK_{1.8}Cs_{4.2}F][(UO_2)_3(Ge_2O_7)_2]$, $[KK_6Cl][(UO_2)_3(Si_2O_7)_2]$, and $[NaK_6F][(UO_2)_3(Si_2O_7)_2]$ are all orthorhombic structures in the *Pnnm* space group, while $[Cs_6K_{1.9}Ag_{0.1}Cl_2][(UO_2)_3(Ge_2O_7)_2]$ is monoclinic with space group $P2_1/n$.

**Conclusions.** Thirteen new uranyl germanate salt inclusion materials were synthesized by molten flux methods using a variety of alkali halide fluxes. The identity of the flux determines the salt species that occupies the channels of the uranyl germanate framework, and the size of the salt inclusion species influences whether the framework adopts a monoclinic or orthorhombic symmetry. The reaction between the chloride flux and the silver tube resulted in the presence of AgCl impurities in the SIM product, which made isolation of phase pure products more difficult. DFT and VBT calculations reported similar formation enthalpies as the analogous uranium silicon SIMs. Optical characterization was performed on two representative samples, the monoclinic $[Cs_6K_{1.9}Ag_{0.1}Cl_2][(UO_2)_3(Ge_2O_7)_2]$ (**1.6**) and orthorhombic $[KK_{1.8}Cs_{4.2}F][(UO_2)_3(Ge_2O_7)_2]$ (**1.12**). There are no significant differences in the UV-vis spectra between the two compounds; however, the $F^-$ containing sample luminesces ten times more intensely than does the $Cl^-$ containing composition. We have successfully incorporated most alkali and halide species into this versatile uranyl germanate framework including Cs, Rb, K, Na, Br, Cl, and F. The incorporation of both Cs and U in a salt inclusion material is advantageous for nuclear waste storage, and the ability to store a variety of salt compositions is also desirable. We will continue to expand the library of salt inclusion compounds by expanding

our synthesis to target the inclusion of other important radionuclides, particularly I and Sr. Additionally, experiments exploring the ion exchange capabilities of these structures are of interest in order to effect post synthetic modifications of the structure to include target radionuclides, and to explore potential leaching of these materials.

**Acknowledgements.** This work was supported as part of the Center for Hierarchical Waste Form Materials, an Energy Frontier Research Center funded by the U.S. Department of Energy, Office of Science, Basic Energy Sciences under Award No. DE-SC0016574. C. Juillerat is additionally supported by an NSF IGERT Graduate Fellowship under grant number 1250052.

**References:**

(1) zur Loye, H.-C.; Besmann, T.; Amoroso, J.; Brinkman, K.; Grandjean, A.; Henager, C. H.; Hu, S.; Misture, S. T.; Phillpot, S.; Shustova, N. B.; Wang, H.; Koch, R. J.; Gregory Morrison; Dolgopolova, E., Hierarchical Materials as Tailored Nuclear Waste Forms: A Perspective, *Chem. Mater.* **2018**, *30*, 4475-4488.

(2) Morrison, G.; zur Loye, H.-C., Flux Growth of $[NaK_6F][(UO_2)_3(Si_2O_7)_2]$ and $[KK_6Cl][(UO_2)_3(Si_2O_7)_2]$: The Effect of Surface Area to Volume Ratios on Reaction Products, *Cryst. Growth Des.* **2016**, *16*, 1294-1299.

(3) Morrison, G.; Smith, M. D.; zur Loye, H.-C., Understanding the Formation of Salt-Inclusion Phases: An Enhanced Flux Growth Method for the Targeted Synthesis of Salt-Inclusion Cesium Halide Uranyl Silicates, *J. Am. Chem. Soc.* **2016**, *138*, 7121-7129.

(4) Lee, C. S.; Wang, S. L.; Chen, Y. H.; Lii, K. H., Flux synthesis of salt-inclusion uranyl silicates:$[K_3Cs_4F][(UO_2)_3(Si_2O_7)_2]$ and $[NaRb_6F][(UO_2)_3(Si_2O_7)_2]$, *Inorg. Chem.* **2009**, *48*, 8357-8361.

(5) Burns, P. C., $U^{6+}$ minerals and inorganic compounds: insights into an expanded structural hierarchy of crystal structures, *Can. Mineral.* **2005**, *43*, 1839-1894.

(6) Chang, Y.-C.; Chang, W.-J.; Boudin, S.; Lii, K.-H., High-Temperature, High-Pressure Hydrothermal Synthesis and Characterization of a Salt-Inclusion Mixed-

Valence Uranium(V,VI) Silicate: $[Na_9F_2][(U^VO_2)(U^{VI}O_2)_2(Si_2O_7)_2]$, *Inorg. Chem.* **2013**, *52*, 7230-7235.

(7) Ling, J.; Morrison, J. M.; Ward, M.; Poinsatte-Jones, K.; Burns, P. C., Syntheses, Structures, and Characterization of Open-Framework Uranyl Germanates, *Inorg. Chem.* **2010**, *49*, 7123-7128.

(8) Legros, J. P.; Jeannin, Y., Coordination de l'uranium par l'ion germanate. II. Structure du germanate d'uranyle dihydrat'e $(UO_2)_2GeO_4(H_2O)_2$, *Acta Crystallographica Section* **1975**, *B31*, 1140-1143.

(9) Legros, J. P.; Jeannin, Y., Coordination de l'uranium par l'ion germanate. I. Structure d'un uranyl germanate de cuivre $[Cu(H_2O)_4](UO_2HGeO_4)_2.2H_2O$, *Acta Cryst.* **1975**, *B31*, 1133-1139.

(10) Lin, C. H.; Chiang, R. K.; Lii, K. H., Synthesis of Thermally Stable Extra-Large Pore Crystalline Materials: A Uranyl Germanate with 12-Ring Channels, *J. Am. Chem. Soc.* **2009**, *131*, 2068-2069.

(11) Lin, C.; Lii, K., $A_3(U_2O_4)(Ge_2O_7)$ (A=Rb, Cs): Mixed-Valence Uranium(V,VI) Germanates, *Angew. Chem., Int. Ed.* **2008**, *47*, 8711-8713.

(12) Lin, C.-H.; Chen, C.-S.; Shiryaev, A. A.; Zubavichus, Y. V.; Lii, K.-H., $K_3(U_3O_6)(Si_2O_7)$ and $Rb_3(U_3O_6)(Ge_2O_7)$: A Pentavalent-Uranium Silicate and Germanate, *Inorg. Chem.* **2008**, *47*, 4445-4447.

(13) Bugaris, D. E.; zur Loye, H.-C., Materials discovery by flux crystal growth: Quartenary and higher oxides, *Angew. Chem. Int. Ed.* **2012**, *51*, 3780-3811.

(14) Bruker. *APEX3, SAINT+, and SADABS.* Bruker AXS Inc.: Madison, Wisconsin, USA, 2015;

(15) Sheldrick, G. M., Crystal structure refinement with SHELXL, *Acta Cryst.* **2015**, *C71*, 3-8.

(16) Sheldrick, G. M., SHELXT - Integrated space-group and crystal-structure determination, *Acta Cryst.* **2015**, *A71*, 3-8.

(17) Dolomanov, O. V.; Bourhis, L. J.; Gildea, R. J.; Howard, J. A. K.; Pushman, H., OLEX2: a complete structure solution, *J. Appl. Crystallogr.* **2009**, *42*, 339-341.

(18) Spek, A. L., Structure validation in chemical crystallography, *Acta Cryst.* **2009**, *D65*, 148-155.

(19) Kubelka, P.; Munk, F. Z., Ein Beitrag Zur Optik Der Farbanstriche, *Z. Techn. Phys.* **1931**, *12*, 593-601.

(20) Shannon, R. D., Revised effective ionic radii and systematic studies of interatomic distances in halides and chalcogenides, *Acta Cryst.* **1976**, *A32*, 751-767.

(21) Batsanov, S. S., Van der Waals Radii of Elements, *Inoraganic Materials* **2001**, *37*, 871-885.

(22) Glasser, L., Lattice Energies of Crystals with Multiple Ions: A Generalized Kapustinksii Equation, *Inorg. Chem.* **1995**, *34*, 4935-4936.

(23) Goldschmidt, V. M., Crystal Structure and Chemical Constitution, *Trans. Faraday Soc.* **1929**, *25*, 253-283.

(24) Moore, E. E.; Kocevski, V.; Juillerat, C. A.; Morrison, G.; Zhao, M.; Brinkman, K.; Loye, H.-C. Z.; Besmann, T., Understanding the Stability of Salt Inclusion Phases for Nuclear Waste-forms through Volume-based Thermodynamics, *Scientific Reports* **2018**, *8*, 15294.

(25) Glasser, L.; Jenkins, H. D. B., Predictive thermodynamics for ionic solids and liquids, *Phys. Chem. Chem. Phys.* **2016**, *18*, 21226-22140.

(26) Willems, T. F.; Rycroft, H.; Kazi, M.; Meza, J. C.; Haranczyk, M., Algorithms and tools for high-throughput geometry-based analysis of crystalline porous materials, *Microporous Mesoporous Mater.* **2012**, *149*, 134-141.

(27) Obbade, S.; Dion, C.; Saadi, M.; Abraham, F., Synthesis, crystal structure and electrical characterization of $Cs_4[(UO_2)_2(V_2O_7)O_2]$, a uranyl divanadate with chains of corner-sharing uranyl square bipyramids, *J. Solid State Chem.* **2004**, *1771*, 1567-1574.

# Chapter 2

## A Family of Layered Phosphates Crystallizing in a Rare Geometrical Isomer of the Phosphuranylite Topology: Synthesis, Characterization, and Computational Modeling of $A_4[(UO_2)_3O_2(PO_4)_2]$ (A = alkali metals) Exhibiting Intra-layer Ion Exchange[1]

[1]Reproduced with permission from Juillerat, C. A.; Moore, E. E.; Kocevski, V.; Besmann, T. M.; zur Loye, H.-C. *Inorg. Chem.* **2018**, *57*, 4726-4738. © 2018 American Chemical Society

**Abstract:** Single crystals of eight new layered uranyl phosphates, $Cs_{1.4}K_{2.6}[(UO_2)_3O_2(PO_4)_2]$, $Cs_{0.7}K_{3.3}[(UO_2)_3O_2(PO_4)_2]$, $Rb_{1.4}K_{2.6}[(UO_2)_3O_2(PO_4)_2]$, $K_4[(UO_2)_3O_2(PO_4)_2]$, $K_{2.9}Na_{0.9}Rb_{0.2}[(UO_2)_3O_2(PO_4)_2]$, $K_{2.1}Na_{0.7}Rb_{1.2}[(UO_2)_3O_2(PO_4)_2]$, $Cs_{1.7}K_{4.3}[(UO_2)_5O_5(PO_4)_2]$, and $Rb_{1.6}K_{4.4}[(UO_2)_5O_5(PO_4)_2]$ were grown from alkali chloride fluxes. All structures crystallize in the monoclinic space group, $P2_1/c$, and contain uranyl phosphate layers with alkali metals located between the layers for charge balance. Ion exchange experiments on $Cs_{0.7}K_{3.3}[(UO_2)_3O_2(PO_4)_2]$, $Rb_{1.4}K_{2.6}[(UO_2)_3O_2(PO_4)_2]$, and $K_4[(UO_2)_3O_2(PO_4)_2]$ demonstrated that Cs and Rb cations cannot be exchanged for K cations; however, K cations can be readily exchanged for Na, Rb, and Cs. Enthalpies of formation were calculated from density functional theory (DFT) and volume based thermodynamics (VBT) for all six structures. A value for the enthalpy of formation of the phosphuranylite sheet, $[(UO_2)_3O_2(PO_4)_2]^{4-}$, was derived using single ion additive methods coupled with VBT. DFT and VBT calculations were used to justify results of the ion exchange experiments. $Cs_{0.7}K_{3.3}[(UO_2)_3O_2(PO_4)_2]$, $Rb_{1.4}K_{2.6}[(UO_2)_3O_2(PO_4)_2]$, and $K_4[(UO_2)_3O_2(PO_4)_2]$ exhibit typical luminescence of the uranyl group.

**Introduction**. The need to effectively immobilize radioactive waste in wasteforms that will safely endure for hundreds to thousands of years was understood from the moment that the first nuclear waste was generated.[1] Achieving this goal may require the development of multiple new waste form approaches to address specific, problematic isotopes and to effectively and safely meet the requirements for long term storage. Particularly in the case of radioactive elements that are, or that can over time, transform into water soluble species or air volatile species, such as technetium or cesium, there is a clear need for custom waste forms that will maintain such isotopes in their inert oxidation

states and coordination environments in the millennia to come. Layered phosphates are being suggested as potential waste forms for volatile species, such as cesium, provided they can be incorporated into the structure, either during synthesis or post-synthesis via ion-exchange.

Uranium phosphates have been previously studied to investigate actinide mobility in the environment, especially in preparation for developing a long term geological repository for nuclear waste. This is due to the prevalence of phosphate minerals in the earth's crust and the low solubility of actinide phosphates.[2,3,4,5,6,7] We are exploring the synthesis and characterization of uranium phosphates to enhance our understanding of the potential ion exchange capacity for incorporating radioactive cesium into layered phosphates. Uranium (VI) phosphates are of particular interest because the hexavalent state of uranium is easily accessible in a variety of systems and tends to favor the formation of layered architectures. The uranyl ion, $UO_2^{2+}$, features strong U-O axial bonds that have short bond lengths of ~1.80 Å, and $UO_2^{2+}$ can equatorially coordinate with additional ligands to form square, pentagonal, and hexagonal bipyramids.[8] Typically the uranyl oxygens remain non-bonding while the equatorial bonds connect adjacent uranyl groups via corner and edge sharing resulting in layered topologies.

Uranyl phosphates make up ~25% of all known uranyl minerals and have two dominant topologies: phosphuranylite and autunite. The autunite topology consists only of squares and is comprised of phosphate tetrahedra and uranyl square bipyramids, while the phosphuranylite topology is more diverse and is constructed of phosphate tetrahedra and pentagonal- and hexagonal-uranyl bipyramidal units. The pentagonal and hexagonal uranyl bipyramids edge share to form chains that are connected together by edge and corner

sharing phosphate tetrahedra.[3] Within the phosphuranylite class, there are four geometric isomers that occur in minerals,[9] and a fifth that has been reported in a uranyl arsenate, $K_4[(UO_2)_3O_2(AsO_4)_2]$.[10] These geometric isomers primarily differ by the orientations of the phosphate (or other non-sheet ligands). Historically such layered phosphates have been described by looking at the chains of phosphate tetrahedra and the pair of tetrahedra that edge share with the hexagonal uranyl bipyramid. For example, in vanmeersscheite[11] (Figure 2.1), the tetrahedra point up-down up-down up-down (ududud) and each pair of tetrahedra that are attached to the hexagonal uranyl bipyramid have the same orientation (S = same) with udududS as the overall description of the isomer. The other three geometric isomers of the phosphuranylite sheet anion topology are uudduuSS, uudduuO (O = opposite), and uudduudSSO where the pairs of tetrahedra vary in a same-same-opposite sequence.[9, 12, 13] The most recent isomer reported, uuuuuuO (Figure 2.1), was first observed in $K_4[(UO_2)_3O_2(AsO_4)_2]$, and is the isomer of all six of the compounds reported herein: $Cs_{1.4}K_{2.6}(PO_4)_2[(UO_2)_3O_2]$ (**2.1**), $Cs_{0.7}K_{3.3}[(UO_2)_3O_2(PO_4)_2]$ (**2.2**), $Rb_{1.4}K_{2.6}[(UO_2)_3O_2(PO_4)_2]$ (**2.3**), $K_4[(UO_2)_3O_2(PO_4)_2]$ (**2.4**), $K_{2.9}Na_{0.9}Rb_{0.2}[(UO_2)_3O_2(PO_4)_2]$ (**2.5**) and $K_{2.1}Na_{0.7}Rb_{1.2}[(UO_2)_3O_2(PO_4)_2]$ (**2.6**) These six new layered uranyl phosphates are the first

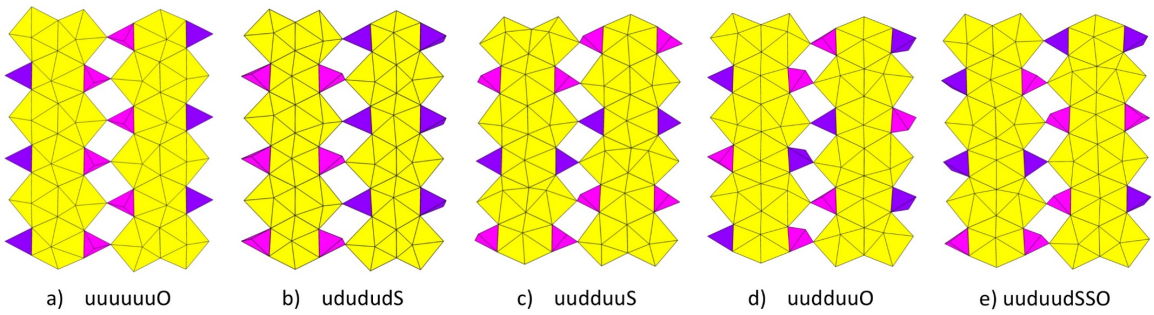


**Figure 2.1:** Geometrical isomers of the phosphuranylite topology. Uranium polyhedra are yellow, phosphate tetrahedra in the up orientation are pink, and those that are down are purple. Examples of compounds exhibiting these isomers are a) the materials in this work, b) vanmeersscheite[11], c) phosphuranylite[12], d) phurcalite[13], and e) bergenite[9].

phosphates to adopt this particular geometric isomer. In this paper we report on the synthesis, structure, physical characterization, ion exchange behavior, and modeling of these materials.

**Experimental:**

**Synthesis.** $UF_4$ (International Bio-Analytical Industries, powder, ACS grade), $AlPO_4$ (Alfa Aesar, powder, 99.99%), CsCl (Alfa Aesar, powder, 99%), NaCl (Fisher Chemical, powder, 99.0%), KCl (Mallinckrodt Chemicals, powder, 99.6%), and RbCl (Alfa Aesar, powder, 99.8%) were used as received. ***Caution!*** *Although the uranium precursor used contained depleted uranium, standard safety measures for handling radioactive substances must be followed.*

Six phases numerically labeled as follows, $Cs_{1.4}K_{2.6}[(UO_2)_3O_2(PO_4)_2]$ (**2.1**), $Cs_{0.7}K_{3.3}[(UO_2)_3O_2(PO_4)_2]$ (**2.2**), $Rb_{1.4}K_{2.6}[(UO_2)_3O_2(PO_4)_2]$ (**2.3**), $K_4[(UO_2)_3O_2(PO_4)_2]$ (**2.4**), $K_{2.9}Na_{0.9}Rb_{0.2}[(UO_2)_3O_2(PO_4)_2]$ (**2.5**) and $K_{2.1}Na_{0.7}Rb_{1.2}[(UO_2)_3O_2(PO_4)_2]$ (**2.6**), were synthesized by molten flux crystal growth methods using alkali chloride fluxes.[14, 15] For each reaction 0.5 mmol of $UF_4$, 0.33 mmol of $AlPO_4$, and 20 or 40 mmols of a single or mixed alkali chloride flux (details in Table 2.1) were loaded into 5 mL alumina crucibles measuring 2.6 mm high and 1.8 mm in diameter. The vessels were loosely covered by alumina caps or contained in a ceramic holder (Figure 2.2) with a larger inverted alumina crucible placed over the smaller crucible to eliminate flux volatility issues. The samples were heated to 875 $^oC$ over 1.5 h, held for 12 h, and then slow cooled to 400 $^oC$ at a rate of 6 $^oC$/h. The samples were sonicated in water to aid in the dissolution of the flux and 1-2 mm yellow rods and plates of the product were obtained (Figure 2.3). The yellow

crystalline product grows among an orange phase identified as $Cs_{1.7}K_{4.3}[(UO_2)_5O_5(PO_4)_2]$ (**2.7**) and $Rb_{1.6}K_{4.4}[(UO_2)_5O_5(PO_4)_2]$ (**2.8**) by single crystal X-ray diffraction.

**Table 2.1:** Reactant amounts in mmols for compounds 1.1-1.6

| $A_4$ | $A_4[(UO_2)_3O_2(PO_4)_2]$ (A = alkali metal) | | | | | |
|---|---|---|---|---|---|---|
| | $Cs_{1.4}K_{2.6}$ (**2.1**) | $Cs_{0.7}K_{3.3}$ (**2.2**) | $Rb_{1.4}K_{2.6}$ (**2.3**) | $K_4$ (**2.4**) | $K_{2.1}Na_{0.7}Rb_{1.2}$ (**2.5**) | $K_{2.9}Na_{0.9}Rb_{0.2}$ (**2.6**) |
| $UF_4$ | 0.5 | 0.5 | 0.5 | 0.5 | 0.5 | 0.5 |
| $AlPO_4$ | 2 | 0.33 | 0.33 | 0.33 | 0.33 | 0.33 |
| CsCl | 20 | 20 | — | — | — | — |
| RbCl | — | — | 20 | — | 10 | — |
| KCl | 4 | 20 | 20 | 20 | 10 | 20 |

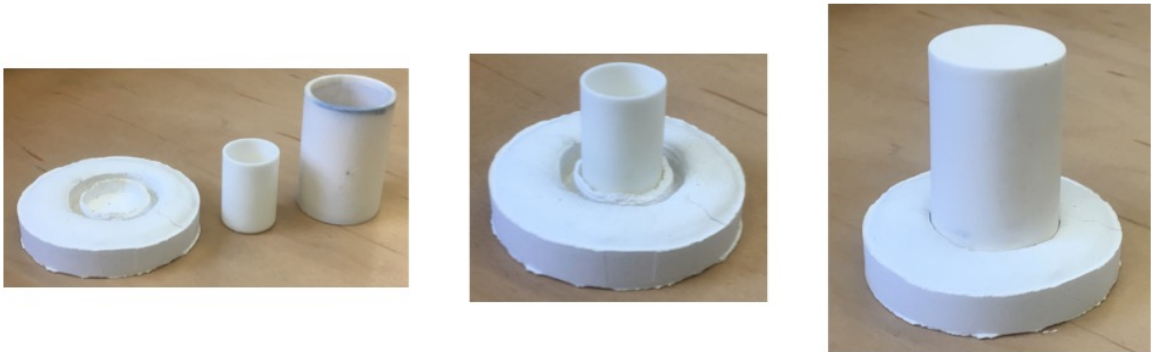

**Figure 2.2:** Reaction Vessel for 2.1-2.8. Concrete holder with a 5 mL and 20 mL alumina crucible used to contain the flux for individual reactions and prevent contamination of unintended alkali species.

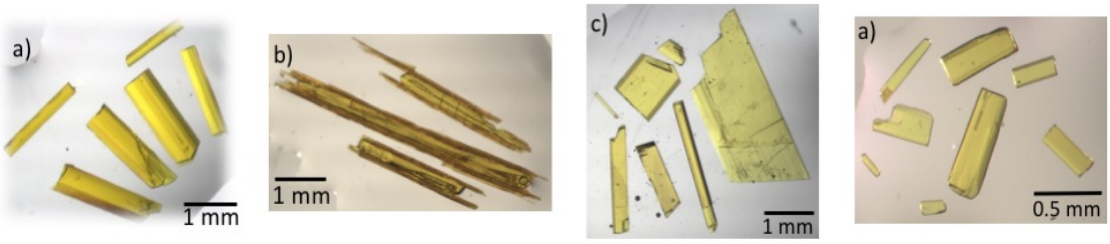


**Figure 2.3:** Crystal pictures of 2.1 2.2, 2.4, 2.7, 2.6. a) $Cs_{0.7}K_{3.3}[(UO_2)_3O_2(PO_4)_2]$, b) the intergrowth of $Cs_{1.4}K_{2.6}[(UO_2)_3O_2(PO_4)_2]$ and $Cs_{1.7}K_{4.3}[(UO_2)_5O_5(PO_4)_2]$, c) $K_4[(UO_2)_3O_2(PO_4)_2]$, and d) $K_{2.1}Na_{0.7}Rb_{1.2}[(UO_2)_3O_2(PO_4)_2]$.

**Structure.** Structure determinations for **2.1**-**2.8** were performed using a Bruker D8 Quest single crystal X-ray diffractometer (SXRD) equipped with a Mo Kα microfocus source (λ = 0.71073 Å) For products **2.1**-**2.6** small crystals cut from thin rectangular yellow plates were used, for **2.7** and **2.8** crystals used for collection were cut from orange needles. Data collection covered 99.8-100% of reciprocal space up to $2\theta_{max}$ = 36.3° with average redundancy >10, and after absorption correction $R_{int}$ = 0.0325— 0.0558. The raw data were reduced and corrected for absorption effects using SAINT+ and SADABS programs within the APEX 3 software.[16] The SHELXT solution program, an intrinsic phasing solution method, was used to obtain an initial structure that was refined using the SHELXL program.[17,18] Both SHELXT and SHELXL were used within the Olex 2 GUI.[19] Full crystallographic data can be found in Table 2.2.

For **2.1**-**2.8** all atoms were refined with anisotropic displacement parameters. Free refinements of the site occupancy factors were performed on all metal atoms, and showed no significant deviations from full occupancy for the U and P atoms; however, free refinements of the alkali metal sites indicated mixed occupancy by more than one alkali metal that was confirmed by EDS. Each alkali metal site was constrained to a full occupancy by the mixed alkali elements. In **2.4**, free refinements of the K site showed no significant deviation from full occupancy. For **2.1**-**2.6** a physically reasonable structure solution was obtained in the centrosymmetric space group, $P2_1/c$. The final structure was checked using the ADDSYM program in PLATON, which found no missed symmetry elements.[20] In the $P2_1/c$ space group structures **2.1**-**2.6** have asymmetric units containing two U sites, one P site, eight O sites (some are split into A and B), and two alkali metal sites. U(2) is at the origin with Wyckoff symbol 2*a* and symmetry $\bar{1}$, while all other sites

**Table 2.2:** Crystallographic data and information for 2.1-2.8

| | $A_4[(UO_2)_3O_2(PO_4)_2]$ (A = alkali metal) | | | | | | $A_6[(UO_2)_5O_5(PO_4)_2]$ | |
|---|---|---|---|---|---|---|---|---|
| | $Cs_{1.4}K_{2.6}$ **(2.1)** | $Cs_{0.7}K_{3.3}$ **(2.2)** | $Rb_{1.4}K_{2.6}$ **(2.3)** | $K_4$ **(2.4)** | $K_{2.1}Na_{0.7}Rb_{1.2}$ **(2.5)** | $K_{2.9}Na_{0.9}Rb_{0.2}$ **(2.6)** | $Cs_{1.7}K_{4.3}$ **(2.7)** | $Rb_{1.6}K_{4.4}$ **(2.8)** |
| S. G. | $P2_1/c$ | $P2_1/c$ | $P2_1/c$ | $P2_1/c$ | $P2_1/c$ | $P2_1/c$ | $P2_1/c$ | $P2_1/c$ |
| a, Å | 6.9655(3) | 6.8606(2) | 6.8135(2) | 6.75192(2) | 6.7192(2) | 6.6360(2) | 7.0126(3) | 6.8805(2) |
| b. Å | 16.9723(7) | 16.8937(5) | 16.8886(4) | 16.8422(5) | 16.8408(6) | 16.7983(5) | 24.4238(11) | 24.3128(8) |
| c, Å | 7.0553(3) | 7.0480(2) | 7.0489(2) | 7.0430(2) | 7.0270(2) | 7.0181(2) | 7.0677(3) | 7.0604(2) |
| β, ° | 99.458(2) | 99.3280(10) | 99.477(1) | 99.9970(10) | 99.9970(10) | 100.0900(10) | 99.157(2) | 99.3290(10) |
| V, $Å^3$ | 822.74(6) | 806.07(4) | 800.05(4) | 789.32(4) | 783.08(4) | 770.23(4) | 1192.09(9) | 1165.47(6) |
| Crystal size ($mm^3$) | 0.05 x 0.02 x 0.01 | 0.05 x 0.04 x 0.01 | 0.08 x 0.01 x 0.01 | 0.08 x 0.04 x 0.01 | 0.03 x 0.03 x 0.01 | 0.04 x 0.04 x 0.02 | 0.1 x 0.01 x 0.01 | 0.04 x 0.02 x 0.01 |
| Temp. (K) | 299.99 | 300.01 | 299.97 | 300.02 | 300.02 | 300.01 | 302.48 | 300.02 |
| Density ($gcm^{-3}$) | 5.342 | 5.169 | 5.202 | 5.000 | 5.220 | 5.099 | 5.588 | 5.493 |
| $\theta$ range (deg) | 2.400-36.332 | 2.411-36.359 | 2.412-36.349 | 3.170-36.384 | 2.419-36.385 | 3.118-36.348 | 3.036-36.341 | 3.000-36.365 |
| $\mu$ ($mm^{-1}$) | 33.512 | 32.759 | 35.461 | 32.038 | 35.401 | 33.285 | 37.248 | 38.915 |

**Table 2.2 cont.:** Crystallographic data and information for 2.1-2.8

| Data Collection and Refinement | | | | | | | | |
|---|---|---|---|---|---|---|---|---|
| | $Cs_{1.4}K_{2.6}$ (**2.1**) | $Cs_{0.7}K_{3.3}$ (**2.2**) | $Rb_{1.4}K_{2.6}$ (**2.3**) | $K_4$ (**2.4**) | $K_{2.1}Na_{0.7}Rb_{1.2}$ (**2.5**) | $K_{2.9}Na_{0.9}Rb_{0.2}$ (**2.6**) | $Cs_{1.7}K_{4.3}$ (**2.7**) | $Rb_{1.6}K_{4.4}$ (**2.8**) |
| Collected | 49879 | 75271 | 39787 | 73212 | 78627 | 76867 | 122488 | 119091 |
| Unique | 3996 | 3921 | 3878 | 3837 | 3807 | 3728 | 5799 | 5665 |
| $R_{int}$ | 0.0325 | 0.0558 | 0.0359 | 0.0392 | 0.0411 | 0.0373 | 0.0402 | 0.0561 |
| $h$ | $-11 \le h \le 11$ | $-11 \le h \le 11$ | $-11 \le h \le 11$ | $-11 \le h \le 11$ | $-11 \le h \le 11$ | $-11 \le h \le 11$ | $-11 \le h \le 11$ | $-11 \le h \le 11$ |
| $k$ | $-28 \le k \le 28$ | $-28 \le k \le 28$ | $-28 \le k \le 28$ | $-28 \le k \le 28$ | $-28 \le k \le 28$ | $-11 \le k \le 11$ | $-40 \le k \le 40$ | $-40 \le k \le 40$ |
| $l$ | $-11 \le l \le 11$ | $-11 \le l \le 11$ | $-11 \le l \le 11$ | $-11 \le l \le 11$ | $-11 \le l \le 11$ | $-11 \le l \le 11$ | $-11 \le l \le 11$ | $-11 \le l \le 11$ |
| $\Delta\rho_{max}$ (e Å$^{-3}$) | 3.146 | 3.250 | 2.674 | 1.329 | 1.900 | 0.935 | 4.415 | 4.012 |
| $\Delta\rho_{min}$ (e Å$^{-3}$) | -2.100 | -2.239 | -2.004 | -0.932 | -0.941 | -1.095 | -2.919 | -2.452 |
| *GoF* | 1.117 | 1.058 | 1.165 | 1.170 | 1.096 | 1.116 | 1.082 | 1.078 |
| Extinction coefficient | 0.00024(4) | -- | 0.00059(5) | 0.00078(6) | 0.00011(4) | 0.00065(5) | 0.00019(2) | 0.00030(3) |
| $R_1(F)$ for $F_0^2 > 2\sigma(F_0^2)$[a] | 0.0181 | 0.0232 | 0.0188 | 0.0122 | 0.0148 | 0.0117 | 0.0165 | 0.0213 |
| $R_w(F_0^2)$[b] | 0.0389 | 0.0573 | 0.0358 | 0.0275 | 0.0311 | 0.0257 | 0.0355 | 0.0505 |

[a] $R_1 = \Sigma\big||F_0| - |F_c|\big|/\Sigma|F_0|$. [b] $wR_2 = [\Sigma w(F_0^2 - F_c^2)^2/\Sigma w(F_0^2)^2]^{1/2}$; $P = (F_0^2 + 2F_c^2)/3$; $w = 1/[\sigma^2(F_0^2) + (0.0130P)^2 + 3.5983P]$ for **2.1**, $w = 1/[\sigma^2(F_0^2) + (0.0305P)^2 + 2.2262P]$ for **2.2**, $w = 1/[\sigma^2(F_0^2) + (0.0088P)^2 + 2.2169P]$ for **2.3**, $w = 1/[\sigma^2(F_0^2) + (0.0082P)^2 + 1.0361P]$ for **2.4**, $w = 1/[\sigma^2(F_0^2) + (0.0120P)^2 + 1.0409P]$ for **2.5**, $w = 1/[\sigma^2(F_0^2) + (0.0080P)^2 + 0.9326P]$ for **2.6**, $w = 1/[\sigma^2(F_0^2) + (0.0118P)^2 + 5.0618P]$ for **2.7**, and $= 1/[\sigma^2(F_0^2) + (0.0236P)^2 + 4.3252P]$ for **2.8**.

lie on general positions with Wyckoff symbol 4*e*. For structures **7** and **8** the asymmetric unit has 3 U sites, 1 P site, 12 O sites, and three alkali metal sites. U(1) lies on Wyckoff site 2a with symmetry $\bar{1}$, O11 lies on 2*c* with $\bar{1}$ symmetry, and all other sites lie on general positions.

For **5** and **6** the O6 site had large anisotropic displacement parameters resulting in prolate O sites and splitting this site into two produced oblate O sites with occupancies of 0.54(4) O6A, 0.46(4) O6B and 0.56(9) O6A, 0.44(9) O6B, for **5** and **6**, respectively. In **5** the O8 site was also prolate and had large anisotropic displacement parameters, splitting the site resulted in oblate O sites with occupancies of 0.51(8) O8A and 0.49(8) O8B.

**PXRD.** Powder X-ray diffraction (PXRD) data were obtained on each of the three phase pure samples, **2**, **3**, and **4** and on ion exchange products. For the phases, ground samples were packed into a sample well and data were collected on a Bruker D2 Phaser equipped with an LYNXEYE silicon strip detector and a Cu Kα source. For the ion exchange products, samples were placed onto a silicon zero background slide, and data were collected on a Rigaku Ultima IV diffractometer with a Cu Kα source and a D/teX detector. The PXRD patterns were used for product identification and to confirm sample purity.

**EDS.** The presence of the appropriate elements in each of the materials was confirmed by data collected on a TESCAN Vega-3 SBU equipped with an EDS detector. Qualitatively, EDS confirmed the presence of the expected elements and did not show any indication of the presence of other elements such as F, Cl, Ag, or Al.

**Optical Properties.** UV-vis diffuse reflectance data were collected using a PerkinElmer Lambda 35 UV/vis scanning spectrometer equipped with an integrating

sphere. Diffuse reflectance data were internally converted to absorbance using the Kubelka-Munk equation.[21] Fluorescence data were collected using a PerkinElmer LS55Luminescence spectrometer by first exciting at 365 nm to find the appropriate excitation peak, then using the peak from the excitation spectrum to collect another emission spectrum. Typically, the excitation wavelength was ~525 nm and the emission wavelength was ~340 nm or 412 nm.

**Ion exchange.** Ion exchange experiments were performed by soaking 30 mg of ground crystalline samples of $Cs_{0.7}K_{3.3}[(UO_2)_3O_2(PO_4)_2]$ (**2.2**), $Rb_{1.4}K_{2.6}[(UO_2)_3O_2(PO_4)_2]$ (**2.3**), and $K_4[(UO_2)_3O_2(PO_4)_2]$ (**2.4**) in ~4 mL concentrated salt solutions in a 1 dram vial. $Cs_{0.7}K_{3.3}[(UO_2)_3O_2(PO_4)_2]$ was soaked in 11 M CsCl and 4 M KCl solutions, $Rb_{1.4}K_{2.6}[(UO_2)_3O_2(PO_4)_2]$ in 4 M KCl, and $K_4[(UO_2)_3O_2(PO_4)_2]$ in 7 M RbCl and 6 m NaCl solutions. The vials were heated in a mineral oil bath, without stirring, at 90 ºC for 2 to 10 days before centrifuging, decanting, rinsing with water, and repeating the process of washing at least 4 times. The same experiments were also performed on 30 mg samples of single crystals of **2.2-2.4.** The ion exchange products were characterized by PXRD and EDS.

**VBT Calculations.** Predictive thermodynamics is a valuable technique as it can provide guidelines for understanding the stability of newly synthesized materials. Volume based thermodynamics (VBT) is a tool developed by Glasser et al**.** for estimating thermodynamic parameters of unanalyzed or even hypothetical materials for which experimental thermochemical data is thus lacking.[22,23,24] This allows for the development of a library of Gibbs energies of the new class of compounds synthesized herein and aids in understanding their relative stabilities. The method can be applied to a class of materials

such as anhydrous minerals by using simple salt approximations when individual components of the system do not have reliable auxiliary information for determining a thermodynamic cycle to obtain enthalpy or energy of formation.[25]

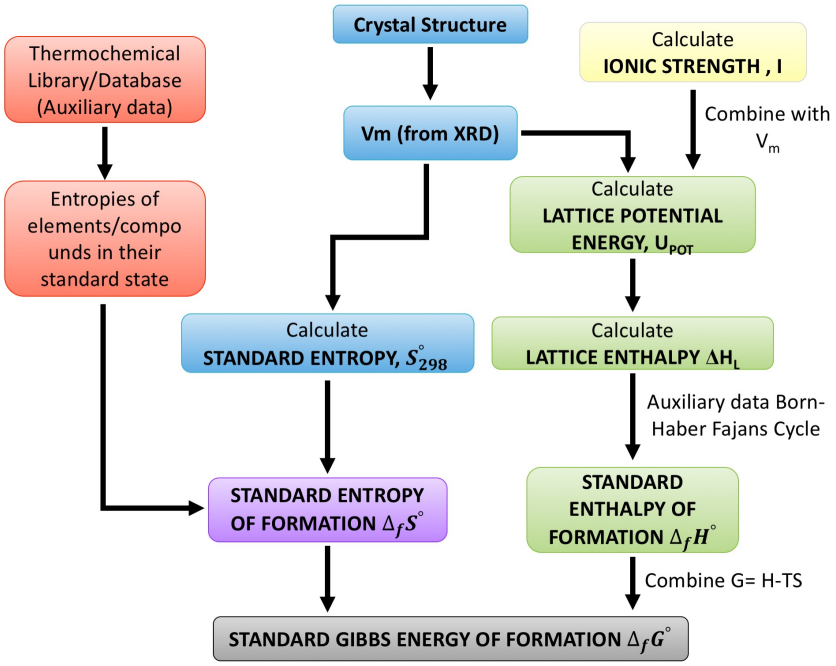


**Figure 2.4**: VBT method flow chart. Description of correlations derived from crystallographic data relating auxiliary information to calculated thermodynamic values via VBT.

The VBT correlation makes use of a well-known quantity such as the formula unit volume obtained from diffraction data in the form of cell volume divided by the number of formula units, Z. Figure 2.4 summarizes the methodology. The molar volume ($V_m$) combined with the ionic strength is used to calculate the standard entropy and lattice potential energy. VBT was used to calculate thermodynamic quantities for the synthesized and ion exchanged uranyl phosphates. The entropy is calculated from Eq. 1, where the constants ($k$ = 1262 and $c$ = 13) are derived for known mineral phases[26] and the standard entropy of formation is calculated from the auxiliary data[27,28,29,30] in Table 2.3.

$$S^{\circ}_{298.15} = k\,V_{\mathrm{m}} + c \quad (1)$$

**Table 2.3:** Auxiliary thermodynamic data. Data for Born-Haber-Fajans Cycles and Standard Entropy of Formation

| Species | $\Delta H_{sub}$ | *IE* | *IE (2nd)* | $\Delta H_{dis}$ | *EA* | *S(298)* | $\Delta H_{hyd}$ |
|---|---|---|---|---|---|---|---|
| | [kJ/mol] | | | [J/mol/K] | | [kJ/mol] | |
| $UO_2$ (s) | 622.9[a] | 591.3[b] | 1380[b] | --- | --- | 77.03[b] | --- |
| $PO_2$ (g) | --- | --- | --- | -315[d,¥] | -330.0[c] | 253.7[d] | --- |
| $O_2$ (g) | --- | --- | --- | 493.6[d] | -42.46[d] | 205.1[d] | --- |
| O (g) | --- | --- | --- | --- | -141.0[d] | 161.1[d] | --- |
| Na (s) | 107.5[d] | 495.8[d] | --- | --- | --- | 51.46[d] | -416[e] |
| K (s) | 89.9[d] | 418.8[d] | --- | --- | --- | 65.67[d] | -334[e] |
| Rb (s) | 80.9[d] | 403.0[d] | --- | --- | --- | 76.78[d] | -308[e] |
| Cs (s) | 76.5[d] | 375.7[d] | --- | --- | --- | 85.15[d] | -283[e] |

The lattice potential ($U_{pot}$) calculated using Eq. 2 from the ionic strength ($2I = 42$) of the individual components, i.e. phosphate and uranyl ions and other cations and anions that make up the structure of these layered uranyl phosphates, where $A$ is the standard electrostatic Madelung constant (121.39 kJ/mol).[22,23]

$$U_{\mathrm{pot}} = A\,I\,(2I/V_{\mathrm{m}})^{1/3} \quad (2)$$

Equation 3 converts the lattice potential to a useable enthalpic value, using the number of ion types ($s_i$) and a constant ($c_i$) related to whether the ion is monatomic or polyatomic (linear/nonlinear).

$$\Delta H_{\mathrm{L}} = U_{\mathrm{pot}} + \sum_{i=1}^{n} s_i \left(\frac{c_i}{2} - 2\right) RT \quad (3)$$

This value allows for the calculation of the standard enthalpy of formation through the Born-Haber-Fajans cycle in which the constituents of the compounds are broken down into their gaseous ionic components and the reaction energy is calculated by summation of the energy from the gas state and the lattice potential resulting in the energetics of formation

of the solid. Gaseous components from the solid phase are obtained from the auxiliary information in Table 2.3 and are sublimation ($\Delta \boldsymbol{H}_{\mathbf{sub}}$) or dissociation + ($\Delta \boldsymbol{H}_{\mathbf{dis}}$) enthalpies combined with ionization potentials (**IP**) or electron affinities (**EA**) for cationic or anionic species respectively.

$$\Delta_f \boldsymbol{H}^{\circ}_{\mathbf{298.15}} = \Delta \boldsymbol{H}_{\mathbf{sub}} + \mathbf{IP} + \Delta \boldsymbol{H}_{\mathbf{dis}} + \mathbf{EA} + \Delta \boldsymbol{H}_{\mathbf{L}} \quad \textbf{(4)}$$

Finally, the Gibbs energy of formation, $\Delta_f \boldsymbol{G}$, is calculated by combining the standard enthalpy and entropy of formation:

$$\Delta_f \boldsymbol{G}^{\circ}_{\mathbf{298.15}} = \Delta_f \boldsymbol{H}^{\circ}_{\mathbf{298.15}} + \boldsymbol{T}\, \Delta_f \boldsymbol{S}^{\circ}_{\mathbf{298.15}} \quad \textbf{(5)}$$

The mixing entropy is calculated to account for the influence of the various alkali metal layers, where the contribution due to mixing is greater for the partially occupied cation layers. The following expression for the mixing entropy is used, where $\boldsymbol{n}$ is the number of moles, $\boldsymbol{R}$ is the ideal gas constant, and $\boldsymbol{x_i}$ is the mole fraction of each constituent.

$$\boldsymbol{S_{mix}} = -\boldsymbol{nR} \sum_i \boldsymbol{x_i ln(x_i)} \quad \textbf{(6)}$$

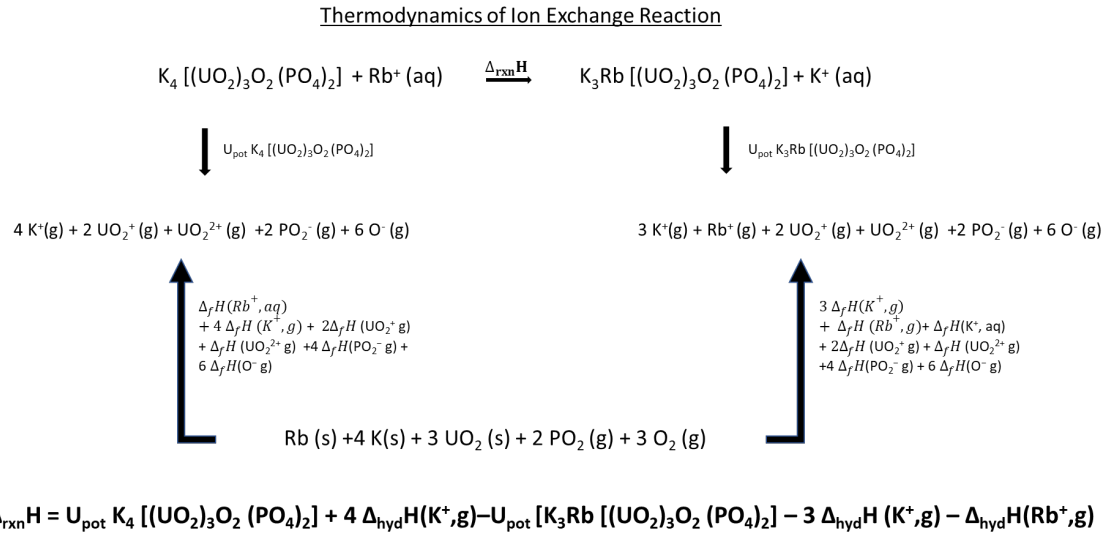


**Figure 2.5:** Thermochemical cycle for ion exchange of 2.4.

Energetics of ion exchange reactions can be similarly calculated using VBT.[31] (See Figure 2.5 for a thermochemical reaction cycle of aqueous ion exchange). In this case, the lattice potential is used along with the enthalpy difference for the aqueous alkali metals, i.e., essentially the hydration enthalpy of the elements. These reaction enthalpies are used to predict the feasibility of ion exchange for these phosphuranylite based structures.

**First-principles calculations.** We performed first-principles calculations using density functional theory (DFT) via the Vienna Ab-initio Simulation Package (VASP) pseudopotential code,[32,33] with the Perdew-Burke-Ernzerhof (PBE) generalized-gradient approximation,[34] employing the projector augmented plane wave (PAW) method.[35, 36] The energy cutoff for the plane wave basis expansion was set to 520 eV, and the convergence criteria for the total energies and the ionic forces was set to $10^{-4}$ eV and $10^{-3}$ eV/Å, respectively. We used a 6×2×6 Monkhorst-Pack k-mesh, which was shown to give converged total energies. To consider the magnetic properties of uranium and to capture the correlated nature of uranium 5*f* electrons, we performed spin-polarized calculations and used the DFT+*U* method.[37, 38] Considering that the U atoms are surrounded by O atoms, we chose *Ueff* = 4.0 eV, a *Ueff*-value that is close to that obtained from relating experimental results for $UO_2$[39,40] and has been proven to reproduce well the structural parameters and band gaps of for $UO_3$ polymorphs.[41, 42, 43] Every cell was fully relaxed, i.e., cell volume, cell shape and ionic positions.

We used the DFT calculated total energies to calculate enthalpies of formation, $\Delta_f \boldsymbol{H}$, using the equation:

$$\Delta_f \boldsymbol{H} = \boldsymbol{E}_{\mathbf{tot}} - \sum_i \boldsymbol{N}_i \boldsymbol{E}_i \qquad \textbf{(7)}$$

where $E_{tot}$ is the total energy of the system and $E_i$ is the ground state energy per atom of the element ***i***. The summation is done over every atomic species, ***i***, in the system.

**Results and Discussion:**

**Synthesis.** $Cs_{1.4}K_{2.6}[(UO_2)_3O_2(PO_4)_2]$ was synthesized using 0.5 mmol of $UF_4$, 0.33 mmol of $AlPO_4$, and 10 mmol of KCl and 10 mmol of CsCl as the flux. Under these conditions 90% yield of a mixed phase product was obtained, consisting of orange needles of $Cs_{1.7}K_{4.3}[(UO_2)_5O_5(PO_4)_2]$ and yellow plates of $Cs_{1.4}K_{2.6}[(UO_2)_3O_2(PO_4)_2]$, in an approximately 1:1 ratio. The two phases were intergrown, which made manual separation of the phases time consuming and at times incomplete (Figure 2.3). Altering the synthesis conditions by using twice as much flux, 20 mmol of KCl and 20 mmol of CsCl, resulted in a nearly quantitative yield of predominantly the yellow plate phase with only small amounts of the unknown orange phase. Interestingly, the alkali metal composition of the yellow platelets produced under these flux rich conditions, $Cs_{0.7}K_{3.3}[(UO_2)_3O_2(PO_4)_2]$, crystallized with a higher potassium to cesium ratio, 3.3:0.7 (K:Cs) vs 2.6:1.4, despite the fact that the ratio of Cs to K was kept the same. Attempts to modify the reaction conditions to favor the orange needle phase over the yellow phase were not successful, and thus no further characterization on phases **2.7** and **2.8** was performed.

Two of the phases, $K_{2.9}Na_{0.9}Rb_{0.2}[(UO_2)_3O_2(PO_4)_2]$ (**2.5**) and $K_{2.1}Na_{0.7}Rb_{1.2}[(UO_2)_3O_2(PO_4)_2]$ (**2.6**), were obtained serendipitously as they contain alkali metals that were not part of the original reaction mixture. It was determined that by only loosely covering the crucibles with alumina plates, the volatile halide fluxes were able to diffuse into neighboring reaction vessels and alter the reagent mix. To prevent this from occurring in subsequent syntheses, ceramic holders with a larger inverted alumina crucible

covering the smaller reaction vessel were used (Figure 2.2). The reaction with 20 mmol of KCl was repeated and produced the pure potassium phase, $K_4[(UO_2)_3O_2(PO_4)_2]$ with no significant impurities. Considering that all six phases possess the same uranyl phosphate sheets, it appears that by simply changing the alkali metal mixture in the flux one can obtain any number of complex alkali layered metal mixtures. However, attempts to obtain a structure in the same family with a high sodium content was not possible and reactions always resulted in $Na_2U_2O_7$ as the major product. Synthesis of these phases was attempted with only Cs or Rb, and all attempts were unsuccessful at obtaining the desired layered phases.

**Structure Description.** $Cs_{1.4}K_{2.6}[(UO_2)_3O_2(PO_4)_2]$ (**2.1**), $Cs_{0.7}K_{3.3}[(UO_2)_3O_2(PO_4)_2]$ (**2.2**), $Rb_{1.4}K_{2.6}[(UO_2)_3O_2(PO_4)_2]$ (**2.3**), $K_4[(UO_2)_3O_2(PO_4)_2]$ (**2.4**), $K_{2.9}Na_{0.9}Rb_{0.2}[(UO_2)_3O_2(PO_4)_2]$ (**2.5**), and $K_{2.1}Na_{0.7}Rb_{1.2}[(UO_2)_3O_2(PO_4)_2]$ (**2.6**), crystallize in the monoclinic space group $P2_1/c$ with lattice parameters ranging between $6.6360(2) \leq a \leq 6.9655(3)$ Å, $16.7983(5) \leq b \leq 16.9723(7)$ Å, $7.0181(2) \leq c \leq 7.0553(3)$ Å, and $99.3280(10) \leq \beta \leq 100.0900(10)$ deg. Full crystallographic data for each compound can be found in Table 2.2 and bond valence sums and bond distances are collected in Tables 2.4-2.9. In the asymmetric unit there are two U sites, one P site, eight O sites (some are split into A and B), and two alkali metal sites. All six structures have isomorphic layers based on the phosphuranylite topology and are comprised of phosphate tetrahedra and uranyl pentagonal and hexagonal bipyramids.[8] The $UO_7$ polyhedra edge-share to form $U_2O_{12}$ dimers that edge share with $UO_8$ hexagonal bipyramids to construct a chain of alternating pentagon dimers and hexagons. These chains are linked to adjacent chains by phosphate tetrahedra that corner and edge share with the

chains (Figure 2.6a). There are several geometrical isomers in the phosphuranylite group that differ only by the orientation of the phosphate tetrahedra.[8] All six phases reported here crystallize as the same isomer. Interestingly, none of the four known geometrical isomers observed in uranyl minerals match the layers in the six compounds; however, this geometrical isomer of the phosphuranylite anion-topology has been observed in a uranyl arsenate, $K_4[(UO_2)_3O_2(AsO_4)_2]$.[10] $K_4[(UO_2)_3O_2(PO_4)_2]$ (**2.4**) is isostructural with $K_4[(UO_2)_3O_2(AsO_4)_2]$ and both contain fully occupied potassium sites between the phosphuranylite based layers that stack in the *a* direction. The other compositions contain phosphuranylite based layers with unique chemical compositions which are a function of the different constituent alkali metals.

**Table 2.4:** Bond valence sums and bond distances for $Cs_{1.4}K_{2.6}[(UO_2)_3O_2(PO_4)_2]$

| Interaction | Distance | Interaction | Distance | Interaction | Distance |
|---|---|---|---|---|---|
| U1-O1 (x2) | 1.817(2) | U2-O2 | 2.389(2) | P1-O2 | 1.566(2) |
| U1-O2 (x2) | 2.570(2) | U2-O3 | 2.388(3) | P1-O3 | 1.566(2) |
| U1-O3 (x2) | 2.548(2) | U2-O4 | 2.2520(19) | P1-O6 | 1.515(3) |
| U1-O4 (x2) | 2.256(2) | U2-O4 | 2.2581(19) | P1-O8 | 1.488(3) |
| **BVS U1** | **5.990** | U2-O5 | 1.823(2) | **BVS P1** | **5.030** |
| | | U2-O6 | 2.288(2) | | |
| | | U2-O7 | 1.816(2) | | |
| | | **BVS U2** | **6.151** | | |

**Table 2.5:** Bond valence sums and bond distances for $Cs_{0.7}K_{3.3}[(UO_2)_3O_2(PO_4)_2]$

| Interaction | Distance | Interaction | Distance | Interaction | Distance |
|---|---|---|---|---|---|
| U1-O1 (x2) | 1.814(3) | U2-O2 | 2.378(3) | P1-O2 | 1.563(3) |
| U1-O2 (x2) | 2.5620(3) | U2-O3 | 2.399(3) | P1-O3 | 1.563(3) |
| U1-O3 (x2) | 2.557(3) | U2-O4 | 2.265(2) | P1-O6 | 1.517(3) |
| U1-O4 (x2) | 2.246(3) | U2-O4 | 2.254(2) | P1-O8 | 1.488(4) |
| **BVS U1** | **5.990** | U2-O5 | 1.818(3) | **BVS P1** | **5.042** |
| | | U2-O6 | 2.274(3) | | |
| | | U2-O7 | 1.819(3) | | |
| | | **BVS U2** | **6.163** | | |

**Table 2.6:** Bond valence sums and bond distances for $Rb_{1.4}K_{2.6}[(UO_2)_3O_2(PO_4)_2]$

| Interaction | Distance | Interaction | Distance | Interaction | Distance |
|---|---|---|---|---|---|
| U1-O1 (x2) | 1.819(2) | U2-O2 | 2.397(2) | P1-O2 | 1.561(2) |
| U1-O2 (x2) | 2.5690(2) | U2-O3 | 2.381(2) | P1-O3 | 1.560(2) |
| U1-O3 (x2) | 2.566(2) | U2-O4 | 2.267(2) | P1-O6 | 1.522(3) |
| U1-O4 (x2) | 2.243(2) | U2-O4 | 2.2552(19) | P1-O8 | 1.490(3) |
| **BVS U1** | **5.987** | U2-O5 | 1.818(3) | **BVS P1** | **5.030** |
| | | U2-O6 | 2.275(3) | | |
| | | U2-O7 | 1.818(3) | | |
| | | **BVS U2** | **6.160** | | |

**Table 2.7:** Bond valence sums and bond distances for $K_4[(UO_2)_3O_2(PO_4)_2]$

| Interaction | Distance | Interaction | Distance | Interaction | Distance |
|---|---|---|---|---|---|
| U1-O1 (x2) | 1.8169(15) | U2-O2 | 2.3729(14) | P1-O2 | 1.5582(15) |
| U1-O2 (x2) | 2.5578(16) | U2-O3 | 2.4089(14) | P1-O3 | 1.5594(15) |
| U1-O3 (x2) | 2.5785(15) | U2-O4 | 2.2718(13) | P1-O6 | 1.5170(17) |
| U1-O4 (x2) | 2.243(14) | U2-O4 | 2.253(13) | P1-O8 | 1.4967(18) |
| **BVS U1** | **5.999** | U2-O5 | 1.8200(15) | **BVS P1** | **5.035** |
| | | U2-O6 | 2.2772(17) | | |
| | | U2-O7 | 1.8181(16) | | |
| | | **BVS U2** | **6.144** | | |

**Table 2.8:** Bond valence sums for $K_{2.1}Na_{0.7}Rb_{1.2}[(UO_2)_3O_2(PO_4)_2]$.

| Interaction | Distance | Interaction | Distance | Interaction | Distance |
|---|---|---|---|---|---|
| U1-O1 (x2) | 1.8126(19) | U2-O2 | 2.3828(17) | P1-O2 | 1.5479(19) |
| U1-O2 (x2) | 2.5771(19) | U2-O3 | 2.3805(17) | P1-O3 | 1.5526(1() |
| U1-O3 (x2) | 2.5807(19) | U2-O4 | 2.2590(17) | P1-O6A | 1.5526(3) |
| U1-O4 (x2) | 2.2335(19) | U2-O4 | 2.2533(17) | P1-O6B | 1.522(3) |
| **BVS U1** | **6.020** | U2-O5 | 1.813(2) | P1-O8 | 1.48(3) |
| | | U2-O6A | 2.274(4) | **BVS P1** | **5.069** |
| | | U2-O6B | 2.284(9) | | |
| | | U2-O7 | 1.816(2) | | |
| | | **BVS U2** | **6.206** | | |

**Table 2.9:** Bond valence sums for $K_{2.9}Na_{0.9}Rb_{0.2}[(UO_2)_3O_2(PO_4)_2]$.

| Interaction | Distance | Interaction | Distance | Interaction | Distance |
|---|---|---|---|---|---|
| U1-O1 (x2) | 1.8099(17) | U2-O2 | 2.3838(15) | P1-O2 | 1.5461(16) |
| U1-O2 (x2) | 2.5810(16) | U2-O3 | 2.3762(15) | P1-O3 | 1.5523(16) |
| U1-O3 (x2) | 2.5764(17) | U2-O4 | 2.2509(15) | P1-O6A | 1.598(4) |
| U1-O4 (x2) | 2.2317(16) | U2-O4 | 2.2584(15) | P1-O6B | 1.450(5) |
| **BVS U1** | **6.042** | U2-O5 | 1.812(2) | P1-O8A | 1.550(4) |
| | | U2-O6A | 2.274(4) | P1-O8B | 1.477(5) |
| | | U2-O6B | 2.274(5) | **BVS P1** | **5.118** |
| | | U2-O7 | 1.816(2) | | |
| | | **BVS U2** | **6.214** | | |

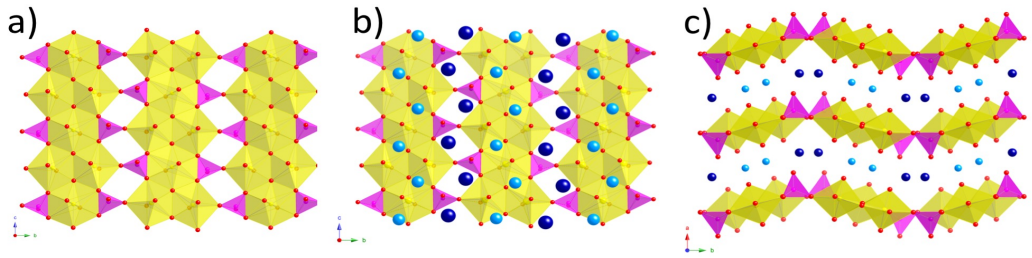


**Figure 2.6:** a) The $[(UO_2)_3O_2(PO_4)_2]^{4-}$layers, found in **2.1-2.6**. b) The $[(UO_2)_3O_2(PO_4)_2]^{4-}$ layers plus a layer of alkali cations c) Stacking of the layers in the *a* direction in **2.1-2.3**. Uranium polyhedra are yellow, phosphate tetrahedra magenta, the larger alkali site is dark blue, and the smaller is light blue.

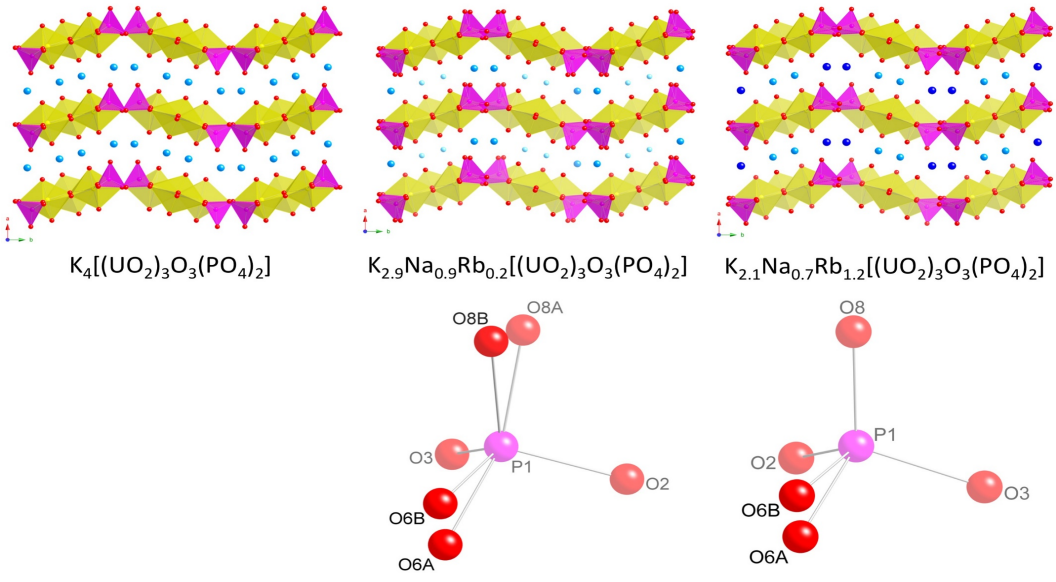


**Figure 2.7:** Structures of 2.5 and 2.6. Showing slight differences from the Figure 2.6.

Structures **2.1, 2.2,** and **2.4-2.6** all have mixed alkali sites, where the larger alkali metal is located between the phosphate tetrahedra, while the smaller alkali metal is located between the uranyl polyhedra. This is likely a space filling issue since between the layers there is more space between the phosphate tetrahedra than between the uranyl polyhedra. For example, in the Cs/K and Rb/K structures, the alkali site between the phosphate tetrahedra is occupied both by Cs and K, or Rb and K, while the smaller alkali site is fully occupied by K. In the two structures with three alkali species, K/Rb occupy the larger alkali site, and K/Na occupy the smaller site. In both of these structures, $K_{2.9}Na_{0.9}Rb_{0.2}[(UO_2)_3O_2(PO_4)_2]$ (**2.6**) and $K_{2.1}Na_{0.7}Rb_{1.2}[(UO_2)_3O_2(PO_4)_2]$ (**2.5**), there is disorder in the oxygen anions bonded to the phosphorus atom (Figure 2.7). In $K_{2.9}Na_{0.9}Rb_{0.2}[(UO_2)_3O_2(PO_4)_2]$, O6 which is shared by P1 and U2, is split into two sites, O6A and O6B. O8, the phosphate oxygen that points into the layers is also split into two sites, O8A and O8B. In $K_{2.1}Na_{0.7}Rb_{1.2}[(UO_2)_3O_2(PO_4)_2]$, only O6 is split. These split positions are likely the result of having two differently sized alkali metals occupying the same crystallographic site.

The PXRD patterns in Figure 2.8 show good agreement between calculated and experimental patterns of products **2.2**, **2.3**, and **2.4**; however, the peaks do not display the expected intensities as a consequence of extreme preferred orientation in the (1 0 0) direction of the platelet shaped crystals. To better view the details of these patterns, the tops of the peaks in the (1 0 0) direction have been cutoff. Nevertheless, the patterns confirm pure samples of products **2.2**, **2.3**, and **2.4**. The PXRD patterns of the ion exchange products are also shown in Figure 2.8. Since the ion exchange products were loaded onto zero background slides, instead of packed into sample wells, the preferred orientation is

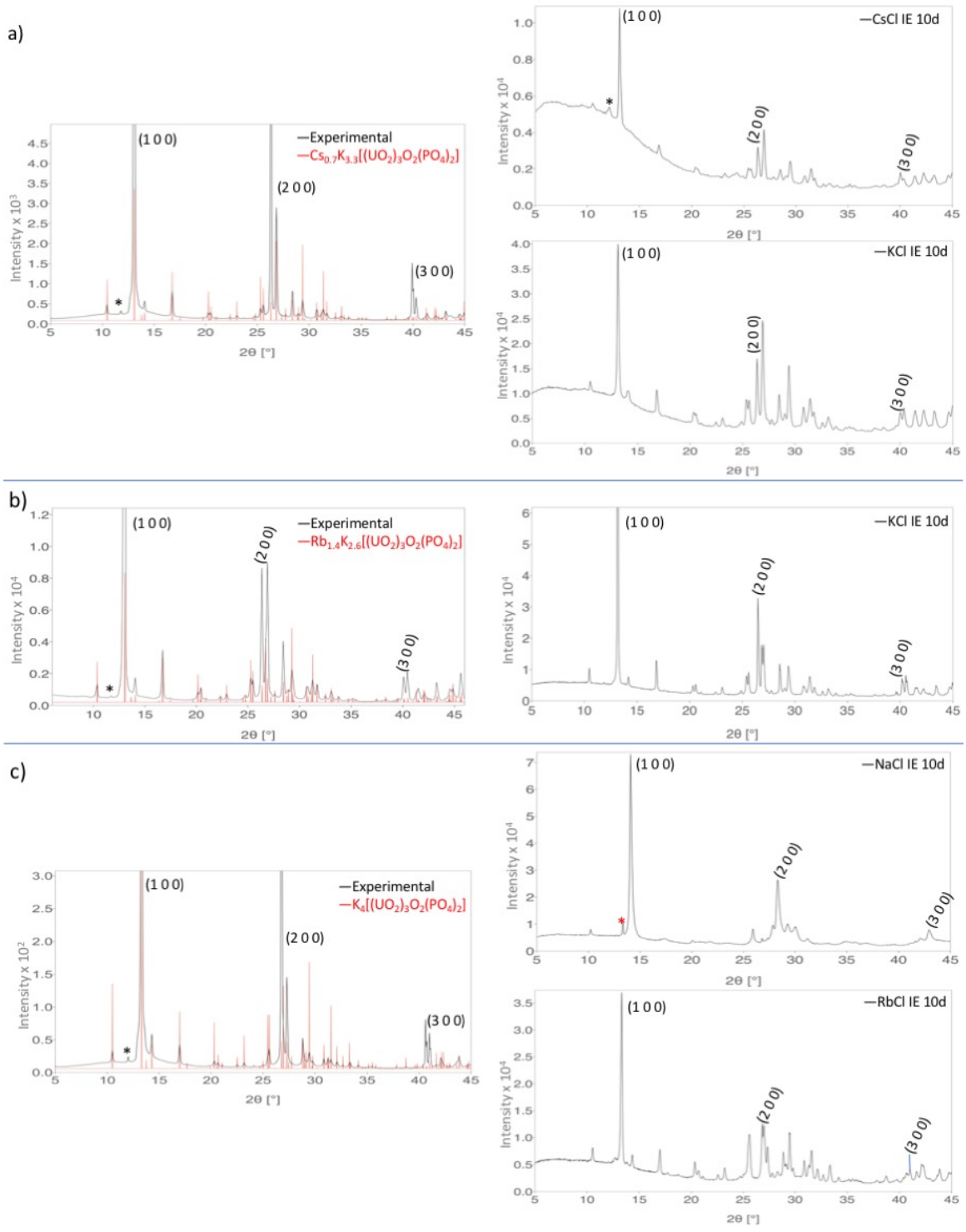


**Figure 2.8:** PXRD patterans of 2.2, 2.3, 2.4, and ion exchange products. a) PXRD of **2.2** on the left, and IE products of **2.2** soaked in CsCl and KCl on the right. b) PXRD of **2.3** of the left and IE product of **2.3** soaked in KCl on the right. c) PXRD of **2.4** on the left, and IE products of **2.4** soaked in NaCl and RbCl on the right. Black asterisks mark Kβ peaks and the red asterisk indicates a small unidentified impurity.

less severe. Also, the broad hump between 5-15° $2\theta$ is due to iron fluorescence from the sample holder. All of the ion exchanged products generate diffraction patterns similar to that of the pure starting materials, indicating that the sheet structure stays intact during the ion exchange process and the only structural change is caused by the change in the identity of the alkali metal cation. Not unexpectedly, some peak broadening is observed after the ion exchange, likely due to loss of crystallinity caused by the ion exchange process.

Structure **2.7** and **2.8** are isostructural and also crystallize in the monoclinic space group $P\,2_1/c$ with lattice with lattice parameters $a$ = 7.0126(3), $b$ = 24.4238(11), $c$ = 7.0677(3), $\beta$ = 99.157(2)°, and $a$ = 6.8805(2), $b$ = 24.3128(8), $c$ = 7.0604(2), and $\beta$ = 99.390(10), respectively. The $a$, $c$, and $\beta$ lattice paramaters are similar to structure **2.1**-**2.6** while $b$ is significantly larger to account for the added uranium and alkali metal sites. Figure 2.9 demonstrates the relationship between the $[(UO_2)_3O_2(PO_4)_2]^{4-}$ and the $[(UO_2)_5O_5(PO_4)_2]^{6-}$ layers. The uranyl phosphate sheet is constructed of mirror image chains of uranyl pentagonal bipyramids that are connected by uranyl square bipyramids. These units are connected to subsequent units by edge and corner sharing phosphate tetrahedra. This sheet topology can be described as a combination of the uranophane and $\beta$-$U_3O_8$ topologies and had been previously observed in $K_6[(UO_2)_5O_5(AsO_4)_2]$, which is isostructural with **2.7** and **2.8**.[10] As seen in structures **2.1**-**2.6**, adjacent phosphate tetrahedra point in the same direction and stack in the same direction of tetrahedra in the adjacent layers, creating a larger space between the phosphate tetrahedra compared to the uranyl polyhedra. For this reason, the alkali site directly below the phosphate tetrahedra is partially occupied by Cs/K and Rb/K accommodating the larger alkali cation, while K cations lie between uranyl polyhedra. The similarity in structure between $A_4[(UO_2)_3O_2(PO_4)_2]$ and the

$A_6[(UO_2)_5O_5(PO_4)_2]$ helps explain the aggressive intergrowth of the yellow and orange phases.

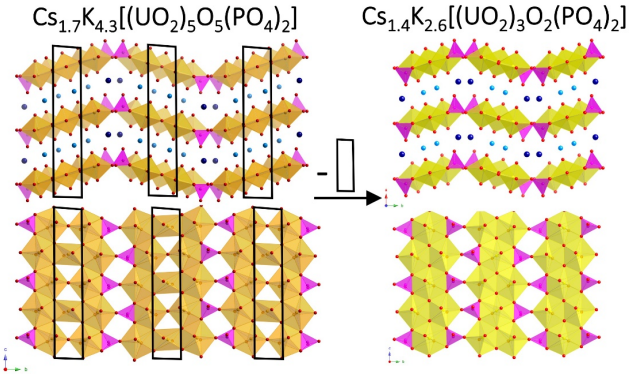


**Figure 2.9:** The relationship between the $Cs_{1.4}K_{2.6}[(UO_2)_3O_2(PO_4)_2]$ and $Cs_{1.7}K_{4.3}[(UO_2)_5O_5(PO_4)_2]$ structures is shown by the removal of two uranyl sites in the $Cs_{1.7}K_{4.3}[(UO_2)_5O_5(PO_4)_2]$ structure. Uranyl polyhedra are yellow or orange, phosphate tetrahedra in magenta, Cs/K sites in dark blue, K in light blue, and oxygen atoms in red.

**Optical Properties.** The fluorescence spectra for $Cs_{0.7}K_{3.3}[(UO_2)_3O_2(PO_4)_2]$ (**2.2**), $Rb_{1.4}K_{2.6}[(UO_2)_3O_2(PO_4)_2]$ (**2.3**), and $K_4[(UO_2)_3O_2(PO_4)_2]$ (**2.4**) are shown in Figure 2.10. All three compounds exhibit yellow-green luminescence typical of uranyl containing materials with the most intense emission peak at ~525 nm resulting from the electronic emission from the lowest vibrational level of the first excited state to the lowest vibrational level of the ground state.[44] There are several smaller peaks in the range of 450 to 600 nm which originate from different vibrational levels of the same electronic emission. The compound with the largest interlayer spacing, $Cs_{0.7}K_{3.3}[(UO_2)_3O_2(PO_4)_2]$ (**2.1**), fluoresces more intensely, although visually, the intensities are indistinguishable. The UV-vis absorbance spectra for $Cs_{0.7}K_{3.3}[(UO_2)_3O_2(PO_4)_2]$ (**2.2**), $Rb_{1.4}K_{2.6}[(UO_2)_3O_2(PO_4)_2]$ (**2.3**), and $K_4[(UO_2)_3O_2(PO_4)_2]$ (**2.4**) are shown in Figure 2.11 and display broad absorbance

between 200 and 520 nm. The band gaps are estimated to be 2.4 eV, indicating that all three materials are semiconductors.

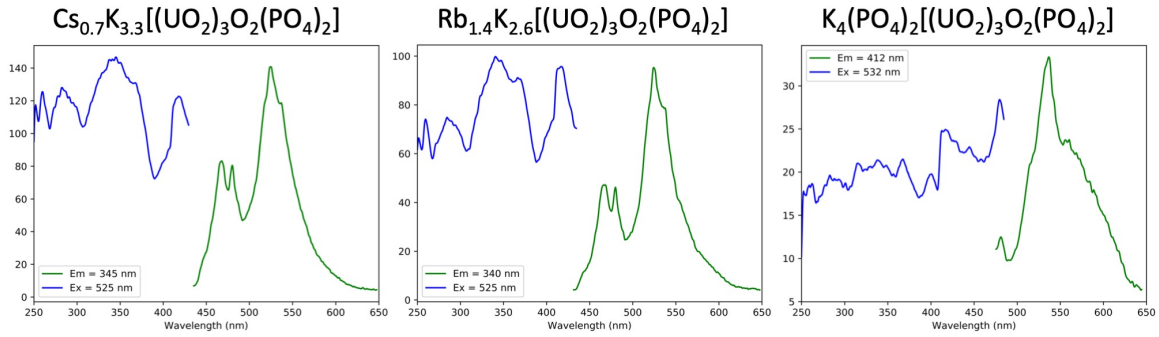


**Figure 2.10:** Fluorescence spectra of 2.2-2.4.

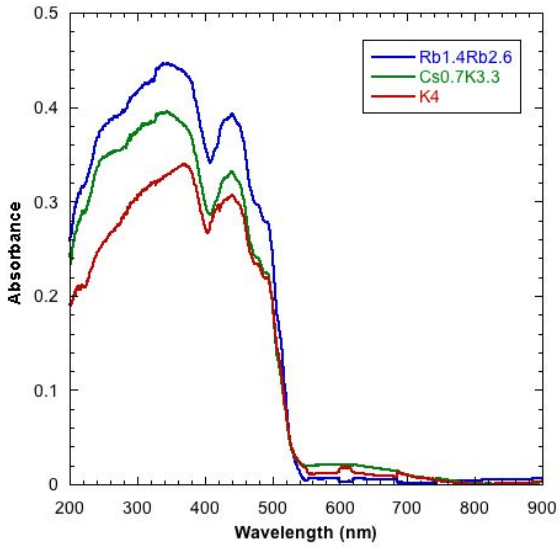


**Figure 2.11:** UV-vis spectra of 2.2-2.4.

**Modeling.** The model system used for the first-principles calculations was derived from the experimentally determined structures. However, except for the $K_4[(UO_2)_3O_2(PO_4)_2]$ system, all other systems have partial occupancies on the alkali cation site. To obtain the lowest energy structure at the specific composition requires generating a large number of supercells, where the alkali cations on the site with partial occupancy are

randomly replaced. With the $Cs_{1.4}K_{2.6}[(UO_2)_3O_2(PO_4)_2]$ system as an example, a super cell of 250 atoms (5 times larger) would be required to capture the $Cs_{1.4}K_{2.6}$ composition, with 77520 possible combinations. Performing calculations for such a big system, and large number of possible combinations is very time consuming and a computationally demanding task. For that reason, a primitive cell with only 8 cations in 2 distinct sites was used and, via adding or removing 1 cation, the concentration of the alkali cations was changed in increments of 0.5 per formula unit. The enthalpies of formation for the systems with partial occupancies were calculated as a weighted average of the formation enthalpies of the system with the closest composition to the experimentally reported one. For example, if $A_xB_y[(UO_2)_3O_2(PO_4)_2]$ is the experimentally reported concentration, and $A_{x1}B_{y1}[(UO_2)_3O_2(PO_4)_2]$ and $A_{x2}B_{y2}[(UO_2)_3O_2(PO_4)_2]$ are the closest compositions with enthalpies of formation $\Delta \boldsymbol{H}_1$ and $\Delta \boldsymbol{H}_2$, respectively, the enthalpy of formation of the system with partial occupancy, $\Delta_f \boldsymbol{H}_{\mathbf{mix}}$, is from Eq. 8:

$$\Delta_f \boldsymbol{H} = 2(\boldsymbol{x} - \boldsymbol{x}_1)\Delta \boldsymbol{H}_1 + 2(\boldsymbol{y}_2 - \boldsymbol{y})\Delta \boldsymbol{H}_2 \quad \textbf{(8)}$$

The computed $\Delta_f \boldsymbol{H}$ values are listed in Table 2.10 for the various alkali metal compositions. It should be noted, however, that calculations using DFT values are for 0 K, whereas to obtain the Gibbs energy at higher temperatures we need to determine the entropy. Unfortunately, to evaluate the necessary vibrational and configurational entropy requires the phonon density of states, and considering the large system size with low symmetry, such phonon calculations would be very computationally demanding and beyond the scope of this study.

**Table 2.10:** Enthalpies of formation from VBT and DFT for 2.1-2.6. All values are in kJ/mol/formula unit

| $A_4$ | $\Delta_f H^\circ_0$ (DFT) | $\Delta_f H^\circ_{298.15}$ (VBT) | $\Delta_f G^\circ_{298.15}$ (VBT) |
|---|---|---|---|
| $Cs_{1.4}K_{2.6}$ | -6598 | -6966 | -6601 |
| $Cs_{0.7}K_{3.3}$ | -6530 | -7009 | -6643 |
| $Rb_{1.4}K_{2.6}$ | -6607 | -7033 | -6668 |
| $K_4$ | -6600 | -7054 | -6685 |
| $K_{2.1}Na_{0.7}Rb_{1.2}$ | -6586 | -7048 | -6686 |
| $K_{2.9}Na_{0.9}Rb_{0.2}$ | -6569 | -7072 | -6710 |

For VBT the molar volumes, $V_m$, are derived from the SXRD data found in Table 2.2 by dividing the cell volume by the number of formula units per cell. Calculations of the standard entropy and lattice potential energy obtained using Eq. 1 and Eq. 2, respectively, employ the calculated $V_m$ values. These are summarized in Table 2.11 for each of the layered phosphate structures. Thermochemical cycles were constructed from the results to obtain the formation enthalpy of each of the compounds. The cycle (Born-Haber-Fajans) depends strictly on the auxiliary data available in the literature, which can be limiting. In this case, information on the gaseous phosphate anion is replaced by that of phosphorous oxide with a single negative charge as there are no thermodynamic data available for the formation of $PO_4^{3-}$ (g). Consequently, various oxidation states of the uranyl cation must be considered as well as available data for the electron affinity for the oxygen anion to charge balance the compound. We have therefore chosen to use the cycle seen in Figure 2.12 for the calculation of the formation enthalpies with the auxiliary data of Table 2.4**.**

The resulting values for the enthalpy of formation of each layered uranyl phosphate computed by VBT are compared to those from DFT in Table 2.10. The derived Gibbs energies of formation using Eq. 5, which are calculated with $S^\circ_{298.15}$ from VBT and auxiliary data to arrive at the standard entropy of formation and include the mixing entropy

**Table 2.11:** Molar volumes from XRD, entropy, and lattice potentials of 2.1-2.6.

| $A_4$ | $V_m$ ($A^3$) | $S$ (J/mol/K) | $U_{pot}$ (kJ/mol) |
|---|---|---|---|
| $Cs_{1.4}K_{2.6}$ | 411.4 | 532 | 11914 |
| $Cs_{0.7}K_{3.3}$ | 403.0 | 522 | 11996 |
| $Rb_{1.4}K_{2.6}$ | 400.0 | 518 | 12026 |
| $K_4$ | 394.7 | 511 | 12080 |
| $K_{2.1}Na_{0.7}Rb_{1.2}$ | 391.5 | 507 | 12112 |
| $K_{2.9}Na_{0.9}Rb_{0.2}$ | 385.1 | 499 | 12179 |

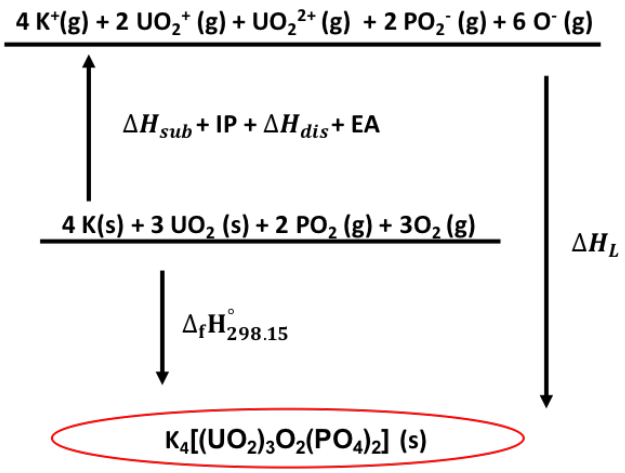


**Figure 2.12:** Born-Haber cycle used to calculate the formation enthalpy of 2.4.

due to the different cationic species, Eq. 6 are also given for reference in Table 2.10. The VBT enthalpy values are used as a benchmark comparison to DFT, although they cannot be exactly compared as, again, the latter values are calculated at 0 K, and thus caution must be taken when comparing their relative orders of magnitude, as temperature effects might be significant. The enthalpy and Gibbs energy of formation vary linearly with respect to $V_{m,}$ (Figure 2.13) where the structures with larger cations such as Cs and Rb are somewhat less stable, i.e., possess more positive $\Delta_f G$ values. Linear regression of the data allows for

the prediction of energetics with respect to molar volume, which is largely related to cation size, as $V_m$ is directly proportional to the average cation radius.

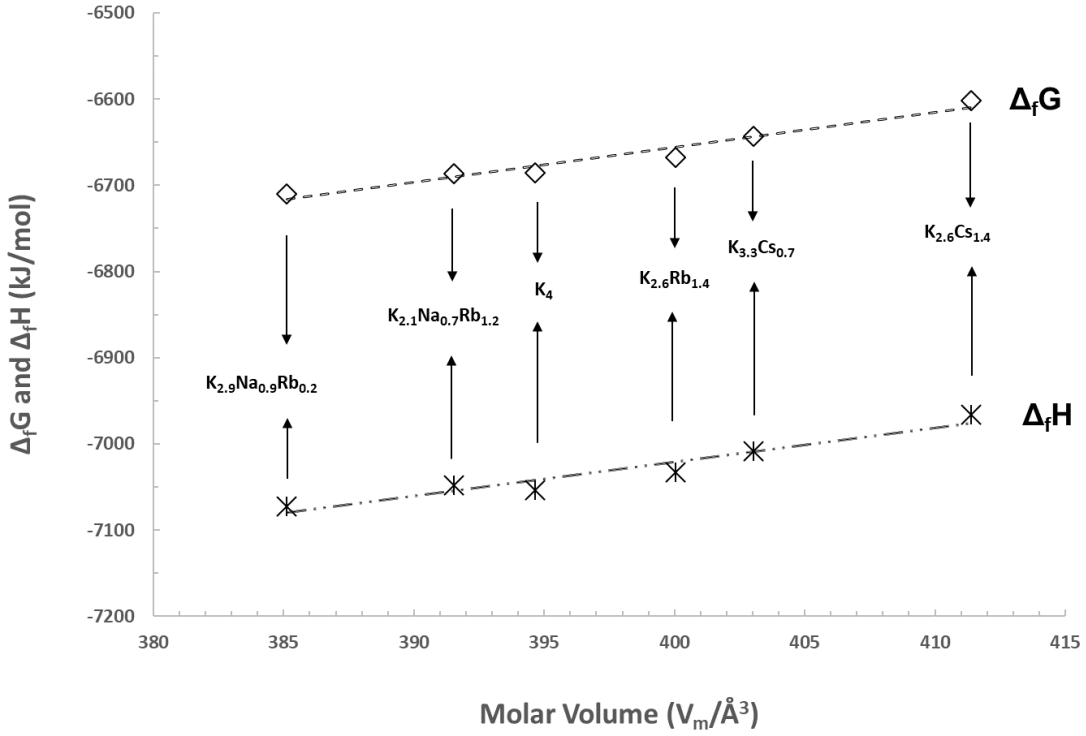


**Figure 2.13:** Graph thermodynamic values for 2.1-2.6 as a function of molar volume. The Gibbs energy values are calculated with the entropy of formation and entropy of mixing

Extrapolation to the formation enthalpy of the phosphuranylite sheet was accomplished by applying the single-ion additive method for the alkali metals derived by Glasser et al.[17] By applying the values of the enthalpy of formation for the cations, a linear relationship in composition for the $\Delta_f H$ $[(UO_2)_3O_2(PO_4)_2]^{4-}$ sheet is observed, with values differing by 2.4% depending on the cationic species. The average value derived for $\Delta_f H$ $[(UO_2)_3O_2(PO_4)_2]^{4-}$ = -5779 ± 50 kJ/mol, a value that can be compared to the enthalpy of formation of a similar compound: $(PO_4)_2(UO_2)_3$ = -5491 kJ/mol measured by solution calorimetry in concentrated $H_2SO_4$ by Cordfunke et al.[45] More recently, it has been found that phosphate compounds and minerals have proven difficult to properly fit estimated

energetics of formation.[46, 47] Holland et al. noted that the fitting formation enthalpies derived by the thermodynamic difference rule to experimental values of inorganic oxides (silicates, vanadates and borates) required the exclusion of the $P_2O_5$ phosphates to obtain an acceptable linear regression fit.[46] Similarly, Drouet et al. was unable to find a relation between cation size and formation enthalpy for apatite minerals and instead relied on other properties such as electronegativity for an acceptable fit.[47] This work is significant in that it is the first attempt to establish a value for a complex structure such as the phosphuranylite sheet, $[(UO_2)_3O_2(PO_4)_2]^{4-}$, using VBT.

**Ion exchange.** Successful partial ion exchange of the alkali species can be observed in as little as 2 days by examining the shift in the PXRD patterns (Figure 2.8) and elemental composition as determined by EDS (Figure 2.14). As a semi-quantitative method, the EDS values can reasonably be treated with approximately 10% relative uncertainty. The pure K phase was soaked in RbCl and NaCl solutions and resulted in a final composition determined by EDS of $Rb_{1.1}K_{2.9}$ and $K_{0.3}Na_{3.7}$ (Here forth we will refer to the phases by just the alkali composition). No significant change in alkali composition was detected in the experiments soaking $Cs_{0.7}K_{3.3}$ and $Rb_{1.4}K_{2.6}$ in KCl, suggesting that it is unfavorable for the larger alkali metals, Cs and Rb, to exchange with K. This is desirable for potential waste form materials, since cesium is one of the daughter products contained in nuclear waste. By soaking the $Cs_{0.7}K_{3.3}$ composition in CsCl, a final composition of $Cs_{1.9}K_{2.1}$ was obtained after 10 days, suggesting that the opposite, however, can occur with the exchange of K by Cs. The experiments run on single crystals resulted in a loss of crystallinity too severe to obtain a structure solution by SXRD, but when ground and examined as powder samples, yielded results consistent with those obtained from the powder ion exchange experiments.

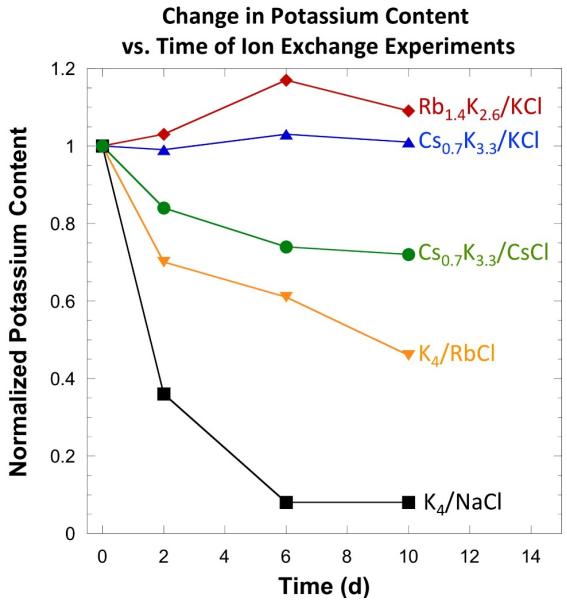


**Figure 2.14:** Graph of the K content during ion exchange reactions. The K content is normalized to the amount identified by EDS prior to ion exchange. Each experiment is identified by the initial alkali composition and the saturated salt solution used.

The enthalpies of formation calculated using DFT for compounds **2.1-2.6** detailed in Table 2.10 provide for relative stabilities. To estimate the enthalpies for ion exchange, we also calculated the enthalpies of formation for the ion exchange products ($Cs_{1.9}K_{2.1}$, $Rb_{1.1}K_{2.9}$ and $K_{0.3}Na_{3.7}$) and the total energy for isolated alkali ion;[48] the results are shown in Tables 2.12 and 2.13. Using the enthalpies of formation and the total energies of isolated ions, we calculated the ion exchange energies, $\Delta_{ie}\boldsymbol{E}$, using the equation:

$$\Delta_{ie}\boldsymbol{E} = \boldsymbol{E}^{p}_{tot} + n\boldsymbol{E}^{ex} - \boldsymbol{E}^{r}_{tot} - n\boldsymbol{E}^{in} \quad (9)$$

where $\boldsymbol{E}^{p}_{tot}$ and $\boldsymbol{E}^{r}_{tot}$ are the total energies of the ion exchange product and reactant, respectively, $\boldsymbol{E}^{ex}$ and $\boldsymbol{E}^{in}$ are the total energies of the exchanged and inserted ions, and $n$ is the number of exchanged ions. The ion exchange energies calculated from DFT are summarized in Table 2.14. Evidently, exchanging the $K^+$ ions, from $K_4$, with $Na^+$ ions to

form $K_{0.3}Na_{3.7}$ compound and exchanging $K^+$ ions, from $Cs_{0.7}K_{3.3}$, with $Cs^+$ ions to form $Cs_{1.9}K_{2.1}$ compound are favorable processes, indicated by the negative ion exchange energies. However, we obtain a positive ion exchange energy for the exchange of the $K^+$ ions from $K_4$ with $Rb^+$ ions to form $Rb_{1.1}K_{2.9}$ compound, meaning that the formation of $Rb_{1.1}K_{2.9}$ composition from $K_4$ is thermodynamically unfavorable. In general, the DFT calculations show that exchanging $K^+$ ions with larger ions, $Rb^+$ and $Cs^+$, is unfavorable process, whereas exchanging $K^+$ with $Na^+$ is favorable. The fact that in the current DFT calculations include neither the hydration enthalpy of the system and the ions nor the effect of temperature above 0 K may explain the discrepancy between the DFT and experimental results for the $Rb_{1.1}K_{2.9}$ composition and the ions exchange between $K^+$ and larger ions.

**Table 2.12:** DFT calculated enthalpy of formation, in kJ/mol, of ion exchange products.

| Alkali Metal Layer(s) | $\Delta_f H_{DFT}$ (kJ/mol) |
|---|---|
| $Cs_{1.9}K_{2.1}$ | -6642.6 |
| $Rb_{1.1}K_{2.9}$ | -6580.5 |
| $K_{0.3}Na_{3.7}$ | -6486.5 |

**Table 2.13:** DFT calculated total energies of isolated alkali ions, in kJ/mol.

| Alkali Metal Ion | $E_{ion}$ (kJ/mol) |
|---|---|
| $Na^+$ | 497.9 |
| $K^+$ | 417.1 |
| $Rb^+$ | 396.4 |
| $Cs^+$ | 371.0 |

**Table 2.14:** Ion exchange energies of possible compositions from Table 2.12

| Initial layer | Final layer | $\Delta_{ie}E$ (kJ/mol) |
|---|---|---|
| $K_4$ | $K_{0.3}Na_{3.7}$ | -571.9 |
| $K_4$ | $Rb_{1.1}K_{2.9}$ | 53.7 |
| $Cs_{0.7}K_{3.3}$ | $Cs_{1.9}K_{2.1}$ | -73.1 |
| $Cs_{0.7}K_{3.3}$ | $K_4$ | -227.9 |
| $Rb_{1.4}K_{2.6}$ | $K_4$ | -69.5 |

Unlike DFT, which gives the energies at 0 K in vacuum, the VBT method of calculating ion exchange energies makes use of the hydration energies of the cations that exchange within the layered system, as well as the lattice potential of the structure. The lattice potential of the starting material is calculated from the SXRD data as described in Table 2.3, however the lattice potential of the newly substituted (ion-exchanged) material is unknown. We can calculate this value by establishing an average molar volume of the phosphuranylite $[(UO_2)_3O_2(PO_4)_2]^{4-}$ parent ion from the known structures and substitute various alkali metals with known $V_m$ from thermochemical radii derived from the Goldschmidt ionic radii.[49] We are thus able to predict molar volumes of hypothetical layered structures for which new lattice potentials are derived and used for ion exchange as described in the supplemental information.

The ion exchange reaction of alkali metals depends on two competing factors, both of which are size dependent. The lattice potential of these systems is largely governed by the cations within the layers, as the system with larger ions have smaller lattice potentials (see Table 2.3), which plays into the stability of the compounds. The competing mechanisms however are that while the structures with larger ions between the layers might be inherently less stable, the larger ions have lower hydration energies compared to their smaller counterparts. In a given aqueous solution, smaller ions such as sodium or potassium have a higher affinity for water and would therefore rather remain in solution. The VBT calculations for simply exchanging K with Na result in positive enthalpies (see Tables 2.15 and 2.16) indicating that it is not favorable, although this might be overcome by greatly increasing the Na ion concentration in the solution, possibly resulting in a new structure that is not predicted by VBT. When exchanging K with Rb, similarly positive ion exchange

**Table 2.15:** Molar volumes and lattice potential energy of ion exchange compositions.

| Alkali layer | $V_m$ ($A^3$) | $U_{pot}$ (kJ/mol) |
|---|---|---|
| $Na_4$ | 370.5 | 12337 |
| $Rb_4$ | 410.2 | 11926 |
| $K_3Rb$ | 398.2 | 12044 |
| $K_2Rb_2$ | 402.2 | 12004 |
| $K_3Na$ | 388.3 | 12146 |
| $K_2Na_2$ | 382.4 | 12208 |
| $KNa_3$ | 376.4 | 12272 |
| $KRb_3$ | 406.2 | 11965 |
| $Cs_2K_2$ | 412.1 | 11907 |

enthalpies are computed indicating this reaction to be unfavorable, although exchanging to $RbK_3$ has a small energy barrier which could potentially be overcome by increasing the Rb concentration. Exchanging the partially substituted $Cs_{0.7}K_{3.3}$ to result in higher Cs concentration such as $Cs_2K_2$ was also calculated to have a positive enthalpy of exchange. This is due to the fact that although the hydration energy to pull the $K^+$ into solution is thermodynamically favorable, the driving force for $Cs^+$ to be included in the structure ($-\Delta H_{hyd}$) isn't large enough to overcome the more stable lattice potential of the original $Cs_{0.7}K_{3.3}$ structure. A similar argument is made for the favorable VBT exchange energy to full $K_4$; where the higher affinity for $K^+$ to stay in solution cannot compete with the increased stability in lattice potential of the pure potassium phase. The difference in enthalpies for the following two ion exchange products, $Rb_{1.1}K_{2.9}$ and $Cs_{1.9}K_{2.1}$, are relatively small (<23 kJ/mol) and could possibly become thermodynamically stable when entropic considerations at the standard state temperature of 298.15K are taken into account. VBT predicts sodium exchange to be unfavorable, and thus more detailed descriptions are necessary to support the experimental observation. Both methods use an average structure derived from the single crystal data of the 6 compounds, which are relatively close in size

since they all contain potassium between the layers. A primarily sodium containing structure was not experimentally observed and the ionic size difference could be a significant factor impacting the DFT and VBT results.

**Table 2.16:** Ion exchange energies of possible compositions from Table 2.15

| Initial layer | Final layer | $\Delta_{ie}E$ (kJ/mol) |
|---|---|---|
| $K_4$ | $K_3Rb$ | 9.6 |
| $K_4$ | $K_2Rb_2$ | 23.7 |
| $K_4$ | $KRb_3$ | 37.2 |
| $K_4$ | $Rb_4$ | 50.2 |
| $K_4$ | $K_3Na$ | 15.9 |
| $K_4$ | $K_2Na_2$ | 35.5 |
| $K_4$ | $KNa_3$ | 53.9 |
| $K_4$ | $Na_4$ | 70.9 |
| $Cs_{0.7}K_{3.3}$ | $K_4$ | -48.3 |
| $Cs_{0.7}K_{3.3}$ | $Cs_2K_2$ | 22.5 |
| $Rb_{1.4}K_{2.6}$ | $K_3Rb$ | 27.0 |
| $Rb_{1.4}K_{2.6}$ | $K_4$ | 17.4 |

**Conclusions.** Crystals of eight new uranyl phosphates were synthesized by the molten flux growth method in alkali chloride melts. The amount of flux proved important when targeting the formation of a single phase vs. a mixture of phases. Increasing the relative amount of flux to reagents lead to single phase products of **2.2**-**2.4** that could be isolated and used in the ion exchange experiments to see if larger alkali metals could be exchanged for smaller ones and vice versa. Potassium can be exchanged for Rb, Cs, and Na, while Cs and Rb cations are retained in the structure, which is ideal for nuclear waste storage applications. DFT and VBT methods were used to calculate enthalpies of formation for structures **2.1**-**2.6** and, while demonstrating good agreement, further experimentally derived thermodynamic values are needed to validate these methods. In both VBT and DFT results, the differences in enthalpies between the six phases was minor (less than 2.4%),

suggesting that a large range of alkali compositions between the phosphuranylite based layers are energetically favorable. VBT methods were used to calculate the Gibbs energy of formation of each of structures **2.1**-**2.6** by incorporating the mixing entropy of the cation layers, resulting in a linear trend with respect to $V_m$. The formation enthalpy of the phosphuranylite sheet, $[(UO_2)_3O_2(PO_4)_2]^{4-}$, was derived using VBT and single ion additive methods and found to be in relative good agreement with experimental data for a similar uranyl phosphate compound. This allows for the prediction of the formation of new compounds based on this sheet structure. DFT successfully predicted the ion exchange experiments resulting in $Na_{3.7}K_{0.3}$ and $Cs_{1.9}K_{2.1}$ products to be energetically favorable. VBT predicted these same experiments to have small, positive enthalpies that could potentially be energetically favorable once entropic terms are considered. Both DFT and VBT predicted the $Rb_{1.1}K_{2.9}$ ion exchange product to be energetically unfavorable in contrast to what has been observed.

**Acknowledgements.** This work was supported as part of the Center for Hierarchical Waste Form Materials, an Energy Frontier Research Center funded by the U.S. Department of Energy, Office of Science, Basic Energy Sciences under Award No. DE-SC0016574. C. Juillerat is additionally supported by an NSF IGERT Graduate Fellowship under grant number 1250052. V.K., E.M., and T.B. acknowledge the use of HPC clusters Bolden and Hyperion, supported by the Division of Information Technology at University of South Carolina.

**References:**


(1) Kirst, W. E. *Clinton Laboratories process manual. Section 8. Waste disposal: Wet B process*; Wilmington, DE, 1943;

(2) Ling, J.; Wu, S.; Chen, F.; Simonetti, A.; Shafer, J. T.; Albrecht-Schmitt, T. E., Does Iodate Incorporate into Layered Uranyl Phosphates Under Hydrothermal Conditions, *Inorg. Chem.* **2009**, *48*, 10995-11001.

(3) Burns, P. C., A new uranyl phosphate chain in the structure of parsonsite, *Am. Mineral.* **2000**, *85*, 801-805.

(4) Yagoubi, S.; Renard, C.; Abraham, F.; Obbade, S., Molten salt flux synthesis and crystal structure of a new open-framework uranyl phosphate $Cs_3(UO_2)_2(PO_4)O_2$: Spectroscopic characterization and cationic mobility studies, *J. Solid State Chem.* **2013**, *200*, 13-21.

(5) Villa, E. M.; Marr, C. J.; Jouffret, L. J.; Alekseev, E. V.; Depmeier, W.; Albrecht-Schmitt, T. E., Systematic evolution from uranyl(VI) phosphites to uranium(IV) phosphates., *Inorg. Chem.* **2012**, *51*, 6548-6558.

(6) Villa, E. M.; Marr, C. J.; Diwu, J.; Alekseev, E. V.; Depmeier, W.; Albrecht-Schmitt, T. E., From Order to Disorder and Back Again: In Situ Hydrothermal Redox Reactions of Uranium Phosphites and Phosphates, *Inorg. Chem.* **2013**, *52*, 965-973.

(7) Wu, S.; Kowalski, P. M.; Yu, N.; Malcherek, T.; Depmeier, W.; Bosbach, D.; Wang, S.; Suleimanov, E. V.; Albrecht-Schmitt, T. E.; Alekseev, E. V., Highly Distorted Uranyl Ion Coordination and One/Two-Dimensional Structural Relationship in the $Ba_2[UO_2(TO_4)_2]$ (T = P, As) System: An Experimental and Computational Study, *Inorg. Chem.* **2014**, *53*, 7650-7660.

(8) Burns, P. C., $U^{6+}$ minerals and inorganic compounds: insights into an expanded structural hierarchy of crystal structures, *Can. Mineral.* **2005**, *43*, 1839-1894.

(9) Locock, A. J.; Burns, P. C., The crystal structure of bergenite, a new geometrical isomer of the phosphuranylite group, *Can. Mineral.* **2003**, *41*, 91-101.

(10) Liu, H. K.; Ramachandran, E.; Chen, Y. H.; Chang, W. J.; Lii, K. H., High-Temperature, High-Pressure Hydrothermal Synthesis, Characterization, and Structural Relationships of Layered Uranyl Arsenates, *Inorg. Chem.* **2014**, *53*, 9065-9072.

(11) Piret, P.; Deliens, M., Vanmeersscheite uranium uranyl phosphate hydrate $U(UO_2)_3(PO_4)_2(OH)_6[4\ H_2O]$ and meta-vanmeersscheite $U(UO_2)_3(PO_4)_2(OH)_6[2\ H_2O]$, new minerals, *Bull. Mineral. 105*, 125-128.

(12) Demartin, F.; Diella, V.; Donzelli, S.; Gramaccioli, C. M.; Pilati, T., The importance of accurate crystal structure determination of uranium minerals. I. Phosphuranylite $KCa(H_3O)_3(UO_2)_7(PO_4)_4O_4[8H_2O]$, *Acta Cryst.* **1991**, *B47*, 439-446.

(13) Atencio, D.; Neumann, R.; Silva, A. J. G. C.; Mascarenhas, Y. P., Phurcalite from Perus, Sao Paulo, Brazil, and redetermination of its crystal structure, *Can. Mineral.* **1991**, *29*, 95-105.

(14) Bugaris, D. E.; zur Loye, H.-C., Materials discovery by flux crystal growth: Quartenary and higher oxides, *Angew. Chem. Int. Ed.* **2012**, *51*, 3780-3811.

(15) Morrison, G.; Smith, M. D.; zur Loye, H.-C., Understanding the Formation of Salt-Inclusion Phases: An Enhanced Flux Growth Method for the Targeted Synthesis of Salt-Inclusion Cesium Halide Uranyl Silicates, *J. Am. Chem. Soc.* **2016**, *138*, 7121-7129.

(16) Bruker. *APEX3, SAINT+, and SADABS*; Bruker AXS Inc.: Madison, Wisconsin, USA, 2015;

(17) Sheldrick, G. M., SHELXT - Integrated space-group and crystal-structure determination, *Acta Cryst.* **2015**, *A71*, 3-8.

(18) Sheldrick, G. M., Crystal structure refinement with SHELXL, *Acta Cryst.* **2015**, *C71*, 3-8.

(19) Dolomanov, O. V.; Bourhis, L. J.; Gildea, R. J.; Howard, J. A. K.; Pushman, H., OLEX2: a complete structure solution, *J. Appl. Crystallogr.* **2009**, *42*, 339-341.

(20) Spek, A. L., Structure validation in chemical crystallography, *Acta Cryst.* **2009**, *D65*, 148-155.

(21) Kubelka, P.; Munk, F. Z., Ein Beitrag Zur Optik Der Farbanstriche, *Z. Techn. Phys.* **1931**, *12*, 593-601.

(22) Glasser, L.; Jenkins, H. D. B., Volume-Based Thermodynamics: A prescription for its application and usage in approximating and predicting thermodynamic data, *J. Chem. Eng. Data.* **2011**, *56*, 874-880.

(23) Glasser, L.; Jenkins, H. D. B., Predictive thermodynamics for ionic solids and liquids, *Phys. Chem. Chem. Phys.* **2016**, *18*, 21226-22140.

(24) Jenkins, H. D. B.;, H. K. R.; Passmore, J.; Glasser, L., Relationships amoung Ionic Lattice Energies, Molecular (formula Unit) Volumes and Thermochemical Radii., *Inorg. Chem.* **1999**, *38*, 3609-3620.

(25) Yoder, C. H.; Flora, N. J., Geochemical applications of the simple salt approximation to the lattice energies of complex materials, *Am. Mineral.* **2005**, *90*, 488-496.

(26) Jenkins, H. D. B.; Glasser, L., Standard absolute entropy, $S^{o}_{298}$, values from volume or density, *Inorg. Chem.* **2003**, *42*, 8702-8708.

(27) Konings, R. J. M.; Benes, O.; Kovacs, A.; Manara, D.; Sedmidubsky, D.; Gorokhov, L.; Iorish, V. S.; Yungman, V.; Shenyavskaya, E.; Osina, E., The thermodynami properties of f-elements and their compounds. Part 2. The lanthanid and actinide oxides, *J. Phys. Chem. Ref. Data* **2014**, *43*, 0131101.

(28) Jr., M. W. C., NIST-JANAF thermochemical tables fourth edition part I, Al-Co, *J. Phys. Chem. Ref. Data, Monogr.* **1998**, *9*,

(29) Han, J.; Goncharov, V.; Kaledin, L. A.; Komissarov, A. V.; Heaven, M. C., Electronic spectroscopy and ionization potential of $UO_2$ in the gas phase, *J. Chem. Phys.* **2004**, *120*, 5155-5163.

(30) Xu, C.; Beer, E. D.; Neumark, D. M., Photoelectron spectroscopy of $PO_2^-$, *J. Chem. Phys.* **1996**, *104*, 2749-2751.

(31) Rosseinsky, D. R.; Glasser, L.; Jenkins, H. D. B., Thermodynamic clarification of the curious ferric/potassium ion exchange accompanying the electrochromic redox reactions of prussian ble, iron(III) hexacyanoferrate(II), *J. Am. Chem. Soc.* **2004**, *126*, 10472-10477.

(32) Kresse, G.; Furthmuller, J., Efficient iterative schemes for \sl ab-initio total-energy calculations using a plane-wave basis set, *Phys. Rev. B* **1996**, *54*, 11169-11186.

(33) Kresse, G.; Furthmuller, J., Efficiency of ab-initio total energy calculations for metals and semiconductors using a plane-wave basis set, *Comput. Mater. Sci.* **1996**, *6*, 15-50.

(34) Perdew, J. P.; Burke, K.; Ernzerhof, M., Generalized Gradient Approximation Made Simple, *Phys. Rev. Lett.* **1997**, *78*, 1396-1399.

(35) Blochl, P. E., Projector augmented-wave method, *Phys. Rev. B* **1994**, *50*, 17953-17979.

(36) Kresse, G.; Joubert, D., From ultrasoft pseudopotentials to the projector augmented-wave method, *Phys. Rev. B* **1999**, *59*, 1758-1775.

(37) Anisimov, V. I.; Solovyev, I. V.; Korotin, M. A.; Czyzyk, M. T.; Sawatzky, G. A., Density-functional theory and NiO photoemission spectra, *Phys. Rev. B* **1993**, *48*, 16929-16934.

(38) Liechtenstein, A. I.; Anisimov, V. I.; Zaanen, J., Density-functional theory and strong interactions: Orbital ordering in Mott-Hubbard insulators, *Phys. Rev. B* **1995**, *52*, R5467-R5470.

(39) Schoenes, J., Recent specroscopic studies of $UO_2$, *J. Chem. Soc., Faraday Trans. 2* **1987**, *83*, 1205-1213.

(40) Kotani, A.; Takao, Y., Systematic Analysis of Core Photoemission Spectra for Actinide Di-Oxides and Rare-Earth Sesqui-Oxides, *Prog. Theor. Phys. Suppl.* **1992**, *108*, 117-131.

(41) Brincat, N. A.; Parker, S. C.; Molinari, M.; Allen, G. C.; Storr, M. T., Ab Initio Investigation of the $UO_3$ Polymorphs: Structural Properties and Thermodynamic Stability, *Inorg. Chem.* **2014**, *53*, 12253-12264.

(42) Colmenero, F.; Bonales, L. J.; Cobos, J.; Timon, V., Density Functional Theory Study of the Thermodynamic and Rama Vibrational Properties of γ-$UO_3$ Polymorph, *J. Phys. Chem. C* **2017**, *121*, 14507-14516.

(43) Casillas-Trujillo, L.; Baldinozzi, G.; Patel, M. K.; Xu, H.; Sickafus, K. E., Comparison of bonding and charge denisty in δ-$UO_3$, γ-$UO_3$, and $La_6UO_12$, *Phys. Rev. Mat.* **2017**, *1*, 065404-065414.

(44) Wang, Z.; Zachara, J. M.; Gassman, P. L.; Liu, C.;, O. Q.; Yantasee, W.; Catalano, J. G., Fluorescence spectroscopy of U(VI)-silicates and U(VI)-contaminated Hanford sediment, *Geochim. Cosmochim. Acta* **2005**, *69*, 1391-1403.

(45) Cordfunke, E. H. P.; Ouweltjes, W., Standard enthalpies of formation of uranium compounds. XII. Anhydrous phosphates., *J. Chem. Thermodyn.* **1985**, *17*, 465-471.

(46) Holland, D.; Jenkins, H. B. D., An assessment of thermodynamic difference rule for mixed inorganic oxides and comments on the entalpies of formation of phosphates, *Thermochim. Acta* **2015**, *601*, 63-67.

(47) Drouet, C., A comprehensive guide to experimental and predicted thermodynamic properties of phosphate apatite minerals in view of applicative purposes, *J. Chem. Thermodyn.* **2015**, *81*, 143-159.

(48) For calculating the total energies of isolated alkali ions we used 20×20×20 Å cubic cell with an ion placed in the middle of the cell. We applied image-charge correction because the total energies converge faster as a function of the cell volume. The ions total energies were converged at the used cell volume.,

(49) Goldschmidt, V. M., Crystal Structure and Chemical Constitution, *Trans. Faraday Soc.* **1929**, *25*, 253-283.

# Chapter 3

## Crystal Growth and Structure Characterization of Three Layered Uranyl Phosphates and Their Relation to the Phosphuranylite Family[1]

[1]Reproduced with permission from Juillerat, C. A.; zur Loye, H.-C. *Cryst. Growth Des.* **2019**, *19*, 1183-1189. © 2019 American Chemical Society

**Abstract:** Three new materials related to the phosphuranylite family were synthesized by using alkali chloride fluxes at 875 °C: $CsNa_3[(UO_2)_3O_2(PO_4)_2]$ (**3.1**), $Cs_2Na_4[(UO_2)_5O_5(PO_4)_2]$ (**3.2**), and $Rb_6[(UO_2)_5O_5(PO_4)_2]$ (**3.3**). $CsNa_3[(UO_2)_3O_2(PO_4)_2]$ (**3.1**) crystallizes in the triclinic space group $P\bar{1}$ with the lattice parameters, $a$=6.9809(3) Å, $b$=9.3326(4) Å, $c$=12.9626(5) Å, $\alpha$=71.5620(10)°, $\beta$=78.9430(10)°, and $\gamma$=68.0840(1)°, $Cs_2Na_4[(UO_2)_5O_5(PO_4)_2]$ (**3.2**) crystallizes in the triclinic space group $P\bar{1}$ with the lattice parameters, $a$=6.9890(3) Å, $b$=12.9652(6) Å, $c$=13.2086(6) Å, $\alpha$=96.224(2)°, $\beta$=101.433(2)°, and $\gamma$=105.459(2)°, and $Rb_6(PO_4)_2[(UO_2)_5O_5]$ crystallizes in the $P2_1/m$ space group with the lattice parameters, $a$=6.9255(3) Å, $b$=24.773(1) Å, $c$=7.07647(3) Å, and $\beta$=90.741(1)°. The sheets of **3.1** are based on the phosphuranylite topology while the sheets of **3.2** and **3.3** contain sheets based on the $U_3O_8$ and uranophane topologies but differ in the orientation of the phosphate tetrahedra. The region between the sheets contain the alkali cations and are not all identical in structures **3.1** and **3.2**. The geometrical isomers found in these sheet structures and their relationship to known sheet topologies is discussed.

**Introduction.** Layered uranium (VI) phosphate materials continue to receive attention in the actinide community due to their large structural variety and low solubility, which makes them of interest to the wasteform community. Historically most investigations were focused on obtaining new uranium containing compositions and to crystallize them in novel structure types with the long term goal being to better understand uranium crystal chemistry, in general, and the local coordination chemistry, in specific. The low solubility of actinide phosphates is a valuable property for nuclear waste applications, where issues including environmental mobility, environmental remediation,

waste processing, and the development of novel nuclear waste storage materials are being investigated.[1]

The phosphuranylite sheet anion topology is one of the most dominant structure types for uranium phosphate and arsenate minerals and this sheet topology is also found in synthetic materials. To date, there are 17 synthetic compounds and 17 structurally characterized minerals belonging to the phosphuranylite class. The phosphuranylite materials are a compositionally varied class of materials composed of sheets, sometimes connected by U or Th polyhedra, separated by monovalent and/or divalent cations and water in mineral structures. The phosphuranylite sheet anion topology contains triangles, squares, pentagons, and hexagons where there are typically chains of $UO_8$ square bipyramids and dimers of $UO_7$ pentagonal bipyramids that are connected together by tetrahedral (P, As, V), trigonal pyramidal (Se, Te), or trigonal planar (C) building units.[2–7] This arrangement always leads to vacant square coordination sites and the hexagonal uranium sites can at times also be vacant, as seen in the johannite mineral, although materials that have vacant hexagons will not be considered further in this work. Also related to the family of phosphuranylite materials, are a few that are framework structures constructed of phosphuranylite-type chains and these include $A_3[Al_2O_7(PO_2)_3][(UO_2)_3O_2]$ (A = Rb, Cs),[6] the arsenate mineral nielsbohrite,[3] and $[(UO_2)_3(PO_4)O(OH)(H_2O)_2](H_2O)$, which will be included in the discussion of synthetically derived phosphuranylite materials.[8]

The phosphuranylite topology consists of chains of uranyl pentagonal and hexagonal bipyramids whose edges are decorated with tetrahedral building units that connect the chains into layers through edge and corner sharing (Figure 3.1a). Related to

this phosphuranylite topology is the sheet anion topology observed in 'extended phosphuranylite' systems, the structural relationship of which is illustrated in Figures 3.1b and 1c, which is observed in the synthetic materials $Cs_{1.7}K_{4.3}[(UO_2)_5O_5(PO_4)_2]$, $Rb_{1.6}K_{4.4}[(UO_2)_5O_5(PO_4)_2]$,[5] $K_6[(UO_2)_5O_5(PO_4)_2]$,[9] $M_6[(UO_2)_5O_5(VO_4)_2]$ (M=K, Na),[10] $K_6[UO_2)_5O_5(AsO_4)_2]$,[4] $\alpha$- and $\beta$-$Rb_6[(UO_2)_5O_5(VO_4)_2]$,[11] and $K_4[(UO_2)_5(TeO_3)_2O_5]$.[12] This topology contains mirror image chains of pentagons that are connected together through an additional uranium site not found in the regular phosphuranylite topology to create wider chains that are connected into layers through edge and corner sharing via the tetrahedral building units. This topology can be obtained if one envisions extending the phosphuranylite topology by cutting the chains of hexagons and pentagons in half and inserting additional uranium sites (Figure 3.1b). This topology will be referred to as the 'extended phosphuranylite' topology throughout this paper.

Herein, we report the flux crystal growth and structural characterization of three new materials $CsNa_3[(UO_2)_3O_2(PO_4)_2]$ (**3.1**), $Cs_2Na_4[(UO_2)_5O_5(PO_4)_2]$ (**3.2**), and (**3.3**) that crystallize in the phosphuranylite and extended phosphuranylite topologies. We will discuss the structures of these materials and their geometrical isomers of the phosphuranylite and extended phosphuranylite topologies and present a new general classification scheme for the extended phosphuranylite topologies based on the one for the phosphuranylite topologies.

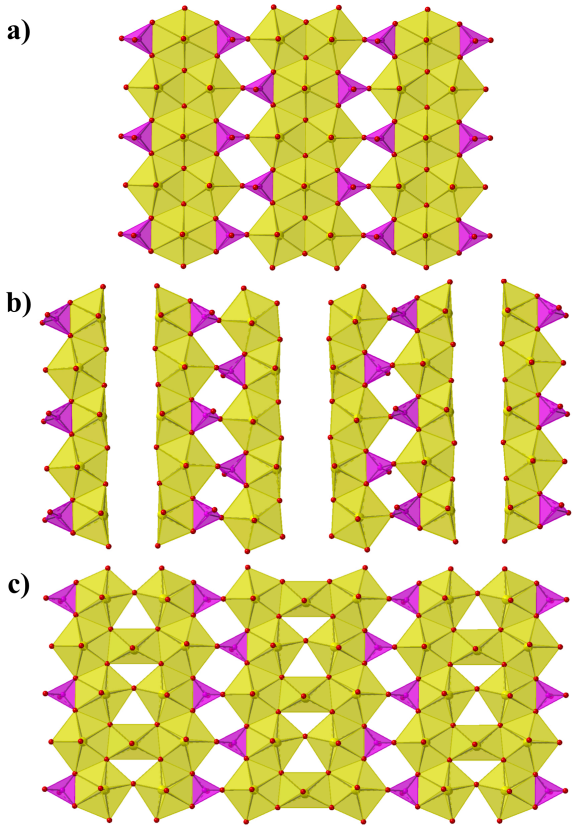


**Figure 3.1:** The phosphuranylite and extended phosphuranylite topologies. a) The phosphuranylite sheet anion topology b) The expansion of the phosphuranylite topology by cutting the chains of uranyl pentagonal and hexagonal bipyramids in half c) the insertion of additional uranium sites to obtain the extended phosphuranylite topology.

**Experimental:**

**Synthesis.** $UF_4$ (International Bio-Analytical Industries, powder, ACS grade), $UO_2(NO_3)_2 \cdot 6H_2O$, $AlPO_4$ (Alfa Aesar, powder, 99.99%), CsCl (Alfa Aesar, powder, 99%), RbCl (Alfa Aesar, powder, 99.8%), and NaCl (Fisher Chemical, powder, 99.0%) were used as received. ***Caution!*** *Although the uranium precursor used contained depleted uranium, standard safety measures for handling radioactive substances must be followed.*

Crystals of all three phases were obtained using molten alkali chloride fluxes.[13] Small orange needles of $Cs_2Na_4[(UO_2)_5O_5(PO_4)_2]$ (**3.2**) were produced in a large excess of AgCl byproduct by loading 0.5 mmol $UF_4$, 2 mmol of $AlPO_4$, 4 mmol of NaCl, and 20 mmol of CsCl into silver tubes measuring 5.7 cm tall by 1.8 cm wide. The reaction was heated to 875 °C in 1.5 h, held for 12 h, and slow cooled to 400 °C at 6 °C/h. Both $CsNa_3[(UO_2)_3O_2(PO_4)_2]$ (**3.1**) and $Rb_6[(UO_2)_5O_5(PO_4)_2]$ (**3.3**) were synthesized in alumina crucibles that were covered by larger inverted crucibles as previously described[5] and heated under the same conditions as **3.2**. To obtain the yellow single crystals of $CsNa_3[(UO_2)_3O_2(PO_4)_2]$ (**3.1**) (Figure 3.2), 0.5 mmol $UF_4$, 0.33 mmol of $AlPO_4$, 5 mmol of CsCl, and 5 mmol of NaCl were used. $Rb_6[(UO_2)_5O_5(PO_4)_2]$ (**3.3**) was synthesized using 0.5 mmol $UF_4$, 0.33 mmol of $AlPO_4$, and 20 mmol of RbCl and this reaction produced orange plates of **3.3** and yellow rods of $Rb_7[Al_2O_7(PO_2)_3][(UO_2)_6O_4(PO_4)_2$.[6]

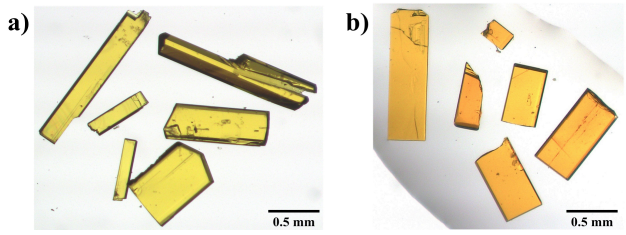


**Figure 3.2:** Optical images of crystals **3.1** and **3.3.** a) crystals of **3.1** b) crystals of **3.3.**

**Structure.** Single crystal X-ray diffraction data were collected on a Bruker D8 Quest single crystal X-ray diffractometer equipped with a Mo Kα microfocus source (λ = 0.71073 Å). The raw data were reduced and corrected using SAINT+ and SADABS within the APEX 3 software.[14] The SHELXT intrinsic phasing solution program was used to obtain an initial structure that was subsequently refined using SHELXL.[15, 16] PLATON programs ADDSYM and TwinRotMap were used to check for missing symmetry elements

and minor twin components.[17] Energy dispersive spectroscopy (EDS) preformed on a TESCAN Vega-3 SBU equipped with an EDS detector was used to obtain quantitative elemental analysis in order verify the elemental contents of the structures. All metal atoms were allowed to individually freely refine and no significant deviation from unity was observed. Full crystallographic data is reported in Table 3.1 and tables of selected bond distances and bond valence sums are included in Table 3.2-3.4.

$CsNa_3[(UO_2)_3O_2(PO_4)_2]$ (**3.1**) crystallizes in the triclinic space group $P\bar{1}$ with the lattice parameters, $a$=6.9809(3) Å, $b$=9.3326(4) Å, $c$=12.9626(5) Å, $\alpha$=71.5620(10) deg, $\beta$=78.9430(10) deg, and $\gamma$=68.0840(1) deg. Within the asymmetric unit there are three U sites, two P sites, four Na sites, and 16 O sites where all lie on general positions (Wykoff site 2i), except Na3 and Na4 that lie on Wyckoff sites 1a and 1b, respectively and have -1 symmetry.

$Cs_2Na_4[(UO_2)_5O_5(PO_4)_2]$ (**2.2**) crystallizes in the triclinic space group $P\bar{1}$ with the lattice parameters, $a$=6.9890(3) Å, $b$=12.9652(6) Å, $c$=13.2086(6) Å, $\alpha$=96.224(2) deg, $\beta$=101.433(2) deg, and $\gamma$=105.459(2) deg. The asymmetric unit contains five symmetrically unique U sites, two P sites, two Cs sites, and five Na sites, and 23 O sites. Similar to **3.1**, all atoms lie on general positions, except Na3 and Na5 that like on Wyckoff sites 1c and 1g, respectively, with -1 symmetry. After refinement a large, but an acceptable magnitude considering the heavy scatterers in the structure, electron density peak of 5.886 remains—attempts to collect on additional crystals and at lower temperatures in order to improve the structure solution were unsuccessful. The low temperature, 100 K, data collection resulted in the best refinement and is reported in Table 3.1.

**Table 3.1:** Full crystallographic data for 3.1-3.3.

| Compound | $CsNa_3[(UO_2)_3O_2(PO_4)_2]$ **3.1** | $Cs_2Na_4[(UO_2)_5O_5(PO_4)_2]$ **3.2** | $Rb_6[(UO_2)_5O_5(PO_4)_2]$ **3.3** |
|---|---|---|---|
| Space group | *P-1* | *P-1* | *P21/m* |
| $a$ (Å) | 6.9809(3) | 6.9732(3) | 6.9255(3) |
| $b$ (Å) | 9.3326(4) | 12.9576(5) | 24.7730(10) |
| $c$ (Å) | 12.9626(5) | 13.1389(10) | 7.0547(3) |
| $\alpha$ (deg) | 71.5620(10) | 96.4130(10) | 90 |
| $\beta$ (deg) | 78.9430(10) | 101.377(2) | 90.7410(10) |
| $\gamma$ (deg) | 68.0840(1) | 105.3960(10) | 90 |
| $V$ (Å$^3$) | 740.65(5) | 1105.05(8) | 1210.24(9) |
| Crystal color | yellow | orange-yellow | orange |
| Crystal size (mm$^3$) | 0.02 x 0.02 x 0.05 | 0.02 x 0.02 x 0.05 | 0.02 x 0.05 x 0.06 |
| Temperature (K) | 300 | 100 | 300 |
| Density (g cm$^{-3}$) | 5.533 | 5.944 | 5.851 |
| $\theta$ range (deg) | 2.442 — 36.330 | 2.498 — 36.332 | 2.466 — 36.364 |
| $\mu$ (mm$^{-1}$) | 35.528 | 40.087 | 45.536 |
| Collected reflections | 75239 | 113264 | 123881 |
| Unique reflections | 7198 | 10726 | 5988 |
| $R_{int}$ | 0.0450 | 0.0445 | 0.0393 |
| $h$ | -11 < h < 11 | -11 < h < 11 | -11 < h < 11 |
| $k$ | -15 < k < 15 | -21 < k < 21 | -41 < k < 41 |
| $l$ | -21 < l < 21 | -21 < l < 21 | -11 < l < 11 |
| $\Delta\rho_{max}$ (e Å$^{-3}$) | 1.909 | 5.886 | 5.278 |
| $\Delta\rho_{min}$ (e Å$^{-3}$) | -2.498 | -2.281 | -2.432 |
| *GoF* | 1.108 | 1.144 | 1.199 |
| Extinction coefficient | 0.00036(3) | 0.000112(19) | 0.00090(4) |
| $R_1(F)$ [a] | 0.0181 | 0.0272 | 0.0232 |
| $R_w(F_0^2)$[b] | 0.0353 | 0.0627 | 0.0566 |

[a] $R_1 = \Sigma||F_0| - |F_c||/\Sigma|F_0|$ for $F_0^2 > 2\sigma(F_0^2)$. [b] $wR_2 = [\Sigma w(F_0^2 - F_c^2)^2/\Sigma w(F_0^2)^2]^{1/2}$; $P = (F_0^2 + 2F_c^2)/3$; $w = 1/[\sigma^2(F_0^2) + (0.0017P)^2 + 1.7972P]$ for **3.1**, $w = 1/[\sigma^2(F_0^2) + (0.0201P)^2 + 15.1774P]$ for **3.2**, and $w = 1/[\sigma^2(F_0^2) + (0.0115P)^2 + 16.9843P]$ for **3.3**.

$Rb_6(PO_4)_2[(UO_2)_5O_5]$ crystallizes in the $P2_1/m$ space group with the lattice parameters, $a$=6.9255(3) Å, $b$=24.773(1) Å, $c$=7.07647(3) Å, and $\beta$=90.741(1) deg. The solution was refined as a two-component twin using twin law -1 0 -0.025 0 -1 0 0 0 1 with a volume fraction of 1%. The addition of the twin law with small volume fraction

**Table 3.2:** Bond valence sums and bond distances for $CsNa_3[(UO_2)_3O_2(PO_4)_2]$.

| Interaction | Distance | Interaction | Distance | Interaction | Distance |
|---|---|---|---|---|---|
| U1 – O1 | 1.823(2) | U2 – O3 | 2.355(2) | U3 – O5 | 2.248(2) |
| U1 – O2 | 1.791(2) | U2 – O4 | 2.375(2) | U3 – O6 | 2.376(2) |
| U1 – O3 | 2.603(2) | U2 – O5 | 2.242(2) | U3 – O7 | 2.350(2) |
| U1 – O4 | 2.590(2) | U2 – O8 | 2.241(2) | U3 – O8 | 2.240(2) |
| U1 – O5 | 2.216(2) | U2 – O9 | 1.832(2) | U3 – O12 | 1.827(2) |
| U1 – O6 | 2.609(2) | U2 – O10 | 1.812(2) | U3 – O13 | 1.816(2) |
| U1 – O7 | 2.583(2) | U2 – O11 | 2.339(2) | U3 – O14 | 2.330(2) |
| U1 – O8 | 2.225(2) | **BVS U2** | **6.088** | **BVS U3** | **6.098** |
| **BVS U1** | **5.927** | P1 – O3 | 1.529(2) | P2 – O6 | 1.552(2) |
| | | P1 – O4 | 1.552(2) | P2 – O7 | 1.553(2) |
| | | P1 – O14 | 1.524(2) | P2 – O11 | 1.525(2) |
| | | P1 – O15 | 1.506(2) | P2 – O16 | 1.502(2) |
| | | **BVS P1** | **5.096** | **BVS P2** | **5.028** |

**Table 3.3:** Bond valence sums and bond distances for $Cs_2Na_4[(UO_2)_5O_5(PO_4)_2]$.

| Interaction | Distance | Interaction | Distance | Interaction | Distance |
|---|---|---|---|---|---|
| U1 – O1 | 1.845(4) | U2 – O3 | 2.359(4) | U4 – O5 | 2.235(4) |
| U1 – O2 | 1.840(4) | U2 – O3 | 2.196(4) | U4 – O6 | 2.232(4) |
| U1 – O3 | 2.304(4) | U2 – O7 | 1.833(4) | U4 – O14 | 2.141(4) |
| U1 – O4 | 2.220(4) | U2 – O8 | 1.806(4) | U4 – O15 | 1.850(4) |
| U1 – O5 | 2.215(4) | U2 – O9 | 2.342(4) | U4 – O16 | 1.838(4) |
| U1 – O6 | 2.296(4) | U2 – O10 | 2.391(4) | U4 – O17 | 2.494(4) |
| **BVS U1** | **5.911** | U2 – O11 | 2.360(4) | U4 – O18 | 2.522(4) |
| P1 – O10 | 1.552(4) | **BVS U2** | **6..002** | **BVS U4** | **5.984** |
| P1 – O11 | 1.567(4) | U3 – O3 | 2.236(4) | U5 – O5 | 2.173(4) |
| P1 – O21 | 1.522(4) | U3 – O4 | 2.237(4) | U5 – O6 | 2.350(4) |
| P1 – O22 | 1.515(4) | U3 – O10 | 2.521(4) | U5 – O17 | 2.355(4) |
| **BVS P1** | **4.947** | U3 – O11 | 2.498(4) | U5 – O18 | 2.397(4) |
| P2 – O9 | 1.522(4) | U3 – O12 | 1.852(4) | U5 – O19 | 1.824(4) |
| P2 – O17 | 1.570(4) | U3 – O13 | 1.844(4) | U5 – O20 | 1.828(4) |
| P2 – O18 | 1.551(4) | U3 – O14 | 2.159(3) | U5 – O21 | 2.303(4) |
| P2 – O23 | 1.504(4) | **BVS U3** | **5.921** | **BVS U5** | **6.050** |
| **BVS P2** | **4.981** | | | | |

**Table 3.4:** Bond valence sums and bond distances for $Rb_6[(UO_2)_5O_5(PO_4)_2]$.

| Interaction | Distance | Interaction | Distance | Interaction | Distance |
|---|---|---|---|---|---|
| U1 – O1 | 1.842(4) | U2 – O3 | 1.815(3) | U3 – O5 | 1.842(5) |
| U1 – O2 | 1.840(4) | U2 – O4 | 1.809(4) | U3 – O6 | 1.829(5) |
| U1 – O7 | 2.256(3) | U2 – O7 | 2.223(3) | U3 – O7 (x2) | 2.235(3) |
| U1 – O8 | 2.134(1) | U2 – O9 | 2.375(3) | U3 – O9 (x2) | 2.284(3) |
| U1 – O9 | 2.258(3 | U2 – O10 | 2.359(3) | **BVS U3** | **5.941** |
| U1 – O12 | 2.507(3) | U2 – O12 | 2.370(3) | P1 – O10 | 1.531(3) |
| U1 – O13 | 2.491(3) | U2 – O13 | 2.464(3) | P1 – O11 | 1.486(4) |
| **BVS U1** | **5.965** | **BVS U2** | **5.896** | P1 – O12 | 1.570(3) |
| | | | | P1 – O13 | 1.566(3) |
| | | | | **BVS P1** | **4.970** |

significantly improved the $R_1$ value from 0.0272 to 0.0232 and the maximum and minimum residual density peaks from 6.3/-3.5 to 5.3/-2.4. The asymmetric unit contains 3 U sites, 1 P site, 4 Rb sites, and 13 O sites. U3, Rb1, O5, O6, O8 lie on Wyckoff site 2e with *m* symmetry and Rb4A lies on site 2a with -1 symmetry, while all other sites lie on general positions. There is disorder on the Rb4 site, which is split into Rb4A and Rb4B, where a sump command was used to constrain the sum of the occupancies of the two Rb4A, due to the inversion symmetry, and one Rb4B site to one and this constraint resulted in in occupancies of 0.288(17) and 0.356(9) for Rb4A and Rb4B, respectively.

**Results and Discussion:**

**Synthesis.** Among the 32 structures containing the phosphuranylite chains and sheets, 16 were synthetically obtained, while the rest are naturally occurring minerals. Structure **2** in this text, the six $A_4[(UO_2)_3O_2(PO_4)_2]$ compositions,[5, 18] and aluminophosphates $Rb_7[Al_2O_7(PO_2)_3][(UO_2)_6O_4(PO_4)_2$ and $A_3[Al_2O_7(PO_2)_3][(UO_2)_3O_2]$ (A = Rb, Cs) [6] were obtained by molten flux methods using alkali chloride fluxes, while $A_4[(UO_2)_3O_2(AsO_4)_2]$ (A = K, Rb),[4] $Li_2(H_2O)_6[(UO_2)_3(SeO_3)_2O_2]$,[7] $Sr[(UO_2)_3(SeO_3)_2O_2](H_2O)_4$,[8] and $[(UO_2)_3(PO_4)O(OH)(H_2O)_2](H_2O)$[8] were obtained by

various hydrothermal methods. Similarly, with the extended phosphuranylite type structures, all were synthesized using alkali halide fluxes, except for $K_6[(UO_2)_5O_5(AsO_4)_2]$[4] which was synthesized by high pressure, high temperature hydrothermal methods. These reports suggest that alkali halide flux growth methods are a good synthetic route for the synthesis of new structures of the phosphuranylite and extended phosphuranylite types.

Typically, uranium phosphates crystals have been obtained by hydrothermal, solid state, or molten flux methods. Regardless of the synthesis route, $UO_2(NO_3)_2$ is among the most widely used uranium source although the common uranium oxides $U_3O_8$, $UO_2$, $UO_3$ are also used. The phosphate sources are more widely varied where wet chemical routes tend to use solutions of $H_3PO_4$ or $H_3PO_3$,[19–24] and less commonly solutions of $Na_4P_2O_7$ and $K_4P_2O_7$,[25] where solid state and molten flux synthetic routes most often use $P_2O_5$, $(NH_4)_2HPO_4$, or $NH_4H_2PO_4$.[26–32] While $P_2O_5$ is very common in solid state and molten flux synthesis, sometimes as a flux, it is better suited for synthesis in closed systems due to the fact that $P_2O_5$ is very reactive to atmospheric water and should be handled in the glove box for accurate masses. $(NH_4)_2HPO_4$ and $NH_4H_2PO_4$, where $(NH_4)_2HPO_4$ loses $NH_3$ at 70 °C to become $NH_4H_2PO_4$, are often used instead of $P_2O_5$ due to the ease of handling the ammonium based reagents in air. $AlPO_4$ is a fairly unique phosphate source for molten flux methods and can lead to the synthesis of both phosphates and aluminophosphates and leads to the synthesis of different phosphate products as compared to the use of $(NH_4)_2HPO_4$ and $NH_4H_2PO_4$ phosphate sources. Thus far, the $AlPO_4$ starting material has led to the discovery of 15 new uranium phosphates/aluminophosphates including those described in this article. The large variety of phosphate sources available to the solid state chemist including $BPO_4$,[33] $A_4P_2O_7$ (A = Na, K),[34] $AlPO_4$, $Na_3PO_4$, $APO_3$ (A = Na, K),[35] $AH_2PO_4$

(A = Na, K), and $A_2HPO_4$ (A = Na, K), are under explored in uranium phosphate chemistry with few examples of syntheses using these reagents. The use of different phosphate sources should be studied in order to obtain new and unique structures as well as to increase our understanding of why different phosphate sources lead to different products.

In the synthesis of $Cs_2Na_4[(UO_2)_5O_5(PO_4)_2]$ (**3.2**), the large amount of AgCl produced by the chloride flux interaction with the silver reaction vessel during the synthesis made isolating the very small and brittle orange needles difficult. As in the recently reported synthesis of the $A_4[(UO_2)_3O_2(PO_4)_2]$ family, reactions with the same reactant loading and heating were carried out in alumina reaction vessels. All attempts in alumina crucibles, including conducting multiple crystal growth reactions utilizing different amount of flux, yielded only the yellow crystals of $CsNa_3[(UO_2)_3O_2(PO_4)_2]$ (**3.1**). In the synthesis of the $A_4[(UO_2)_3O_2(PO_4)_2]$ materials, it was shown that increasing the flux to 40 mmol improved the yield of the desired phase, $A_4[(UO_2)_3O_2(PO_4)_2]$, over side products of $A_6[(UO_2)_5O_5(PO_4)_2]$. In order to target $Cs_2Na_4[(UO_2)_5O_5(PO_4)_2]$ (**3.2**), the reverse was attempted. However, decreasing the flux to 5 mmol was unsuccessful and the $CsNa_3[(UO_2)_3O_2(PO_4)_2]$ (**3.1**) phase still preferentially formed.

$Rb_6[(UO_2)_5O_5(PO_4)_2]$ (**3.3**) also proved difficult to isolate over the recently published products $Rb_6[(UO_2)_7O_4(PO_4)_4]$,[36] $Rb_3[Al_2O_7(PO_2)_3][(UO_2)_3O_2]$, and $Rb_7[Al_2O_7(PO_2)_3][(UO_2)_6O_4(PO_4)_2$.[6] All form under similar conditions of 0.5 mmol $UF_4$, 0.2-0.5 mmol $AlPO_4$, 10/20 mmol of RbCl, and 775-875 °C reaction temperature. The lower temperature of 775 °C favored the formation of $Rb_3[Al_2O_7(PO_2)_3][(UO_2)_3O_2]$, while 10 mmols of RbCl flux at 875 °C primarily produced $Rb_6[(UO_2)_7O_4(PO_4)_4]$, and 20 mmols produced $Rb_7[Al_2O_7(PO_2)_3][(UO_2)_6O_4(PO_4)_2$ with small amounts of the title compound

$Rb_6[(UO_2)_5O_5(PO_4)_2]$ (**3.3**). Attempts to optimize the synthesis for $Rb_6[(UO_2)_5O_5(PO_4)_2]$ (**3.3**) by changing the amount of flux (2.5 – 40 mmol), varying the temperature, and using a non-Al containing phosphorus source, $(NH_4)_2HPO_4$, were unsuccessful. Reactions using $(NH_4)_2HPO_4$ as the phosphate source favored the synthesis of the $Rb_6[(UO_2)_7O_4(PO_4)_4]$ phase regardless of the uranium to phosphorus ratio used and **3.3** could not be obtained with this reagent.

**Structure.** $CsNa_3[(UO_2)_3O_2(PO_4)_2]$ (**3.1**), $Cs_2Na_4[(UO_2)_5O_5(PO_4)_2]$ (**3.2**), and $Rb_6[(UO_2)_5O_5(PO_4)_2]$ (**3.3**), contain the well-known phosphuranylite or extended phosphuranylite topologies discussed in the introduction and shown in Figures 3.1a and 3.1c, respectively. $CsNa_3[(UO_2)_3O_2(PO_4)_2]$ (**3.1**) adopts the phosphuranylite topology, however, is the first reported example of the uuuuuuS geometric isomer of this sheet anion topology. The geometric isomers of the phosphuranylite family have previously been identified by the pattern of the direction in which the phosphate tetrahedra (or As, V, or Se building units) point, whether that is below or above the plane of the layer. First the pattern in which all phosphate tetrahedra between two uranyl chains are identified with 'u' and 'd' to signify up and down, respectively. Second, the pattern of pairs of phosphate tetrahedra that edge share with the hexagonal uranyl bipyramids are identified where the letters 'S' and 'O' are used to describe whether the two tetrahedra point in the same or opposite directions, respectively. All documented isomers are represented in Figure 3.3. Isomers c and e-g are only found in natural minerals, while b and d have only been observed in synthetic materials of $A_4[(UO_2)_3O_2(PO_4)_2]$ and $Sr[(UO_2)_3(SeO_3)_2O_2](H_2O)_4$. $CsNa_3[(UO_2)_3O_2(PO_4)_2]$ (**3.1**) contains a new isomer as described in Figure 3.3a, where all phosphate tetrahedra within the same layer point in the same direction. Unlike other

reported phosphuranylite type layered systems, the layers within **3.1** are not all the same, the phosphate tetrahedra in subsequent layers point in opposite directions and the phosphate tetrahedra do not align vertically (Figure 3.4). As a consequence, this creates two different interlayer distances where there is a smaller distance between layers in which the phosphate tetrahedra point towards each other, and larger distances where they point away from each other. This is likely a consequence of having two significantly different sized cations-Cs and Na, and as expected solely Na cations lie between layers where $PO_4$ units point in towards each other, whereas both Cs and Na cations lie between layers in which $PO_4$ units point away from each other. In these latter layers, the larger Cs cations are located in the gap created by the outward pointing $PO_4$ units and the Na cations lie between uranyl polyhedra. This follows a similar trend as observed in the $A_{1.4}K_{2.6}[(UO_2)_3O_2(PO_4)_2]$ (A = Rb, Cs) structures,[5] where the sites between phosphate tetrahedra were occupied by a mixture of K and Cs or Rb, and the site between uranyl polyhedra were solely K.

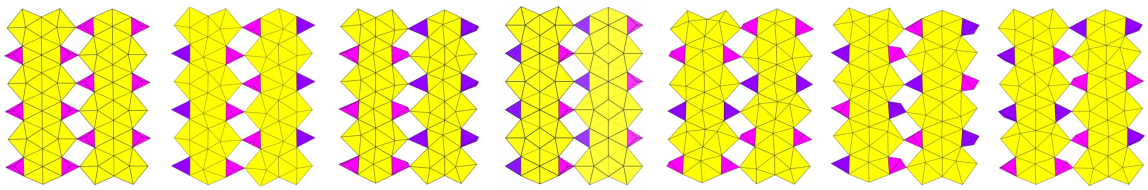


**Figure 3.3**: The known geometric isomers of the phosphuranylite topology. Uranium polyhedra are yellow, tetrahedra of trigonal pyramidal in the up orientation are pink, and those in the down orientation are purple. Examples of compounds exhibiting these isomers are a) $CsNa_3[(UO_2)_3O_2(PO_4)_2]$ (**3.1**), b) $A_{1.4}K_{2.6}[(UO_2)_3O_2(PO_4)_2]$,[5] c) vanmeersscheite,[37] d) $Sr[(UO_2)_3(SeO_3)_2O_2](H_2O)_4$,[8] e) phosphuranylite,[38] f) phurcalite,[39] and g) bergenite.[40]

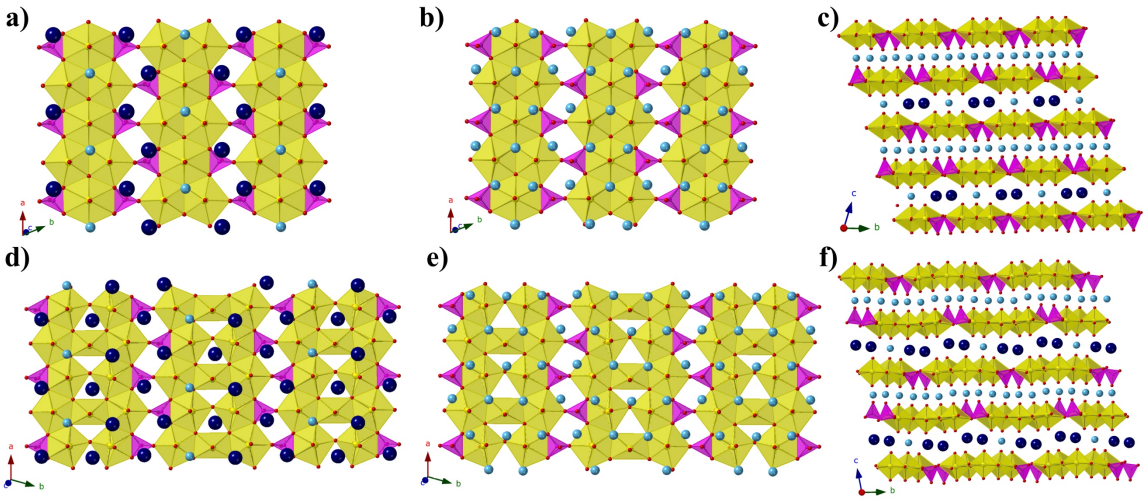


**Figure 3.4:** The structures of 3.1 and 3.2. The sheet topology and the overlaid cations of $CsNa_3[(UO_2)_3O_2(PO_4)_2]$ (**3.1**) are shown in a) and b) and the sheet stacking is shown in c). The structure of $Cs_2Na_4[(UO_2)_5O_5(PO_4)_2]$ (**2**) is depicted in analogous way in d), e), and f). Uranyl polyhedra are yellow, oxygen atoms are red, and phosphate tetrahedra are magenta.

$Cs_2Na_4[(UO_2)_5O_5(PO_4)_2]$ (**3.2**) and $Rb_6[(UO_2)_5O_5(PO_4)_2]$ (**3.3**), shown in Figure 3.4 and 5. both adopt new isomers of the 'extended phosphuranylite' sheet topology. These layered uranyl phosphates contain chains of edge-sharing uranyl pentagonal bipyramids that are connected to a mirror image uranyl pentagonal bipyramid chain through edge sharing with an additional uranyl polyhedra (referred to as the interior U), as in the $U_3O_8$ structure. These $[(UO_2)_5O_5]$ units are connected via edge-sharing and corner-sharing phosphate tetrahedra, similar to the uranophane topology. The extended phosphuranylite sheet topology can contain either $\alpha$-$U_3O_8$ or $\beta$-$U_3O_8$ units (Figure 3.6d) depending on the coordination of the interior uranyl polyhedra. The difference between the $\alpha$-$U_3O_8$ or $\beta$-$U_3O_8$ topologies stems from the 7- or 6-coordinate interior uranium polyhedra. In order to determine which best describes the structures $Cs_2Na_4[(UO_2)_5O_5(PO_4)_2]$ (**3.2**) and $Rb_6[(UO_2)_5O_5(PO_4)_2]$ (**3.3**) the U-O bond distances and bond valence sums were investigated for the uranium in question which is U1 and U3 for structures **3.2** and **3.3**,

respectively. Bond valence sums (BVS) were calculated using $R_{ij}$ and $b$ parameters by Burns specific to the coordination geometry of the uranium center.[41] For **3.2**, if one considers U1 as 6-coordinate with equatorial U-O bonds between U1 and O3, O4, O5, and O6, the bond distances fall between 2.215 and 2.296 Å and are usual for uranium coordination and yield a BVS of 5.911, in good agreement with the expected value of 6. If one includes the U1-O14 bond with length 2.815 Å, which is on the long end of the range of reported values for uranyl pentagonal bipyramid U-O distances (1.7 – 2.8Å),[42] the BVS comes out to 5.835 as result of the different $R_{ij}$ and $b$ values reported for 6- and 7-coordinate uranium. Similarly for **3.3**, considering U3 as a square bipyramid yields a BVS of 5.941, but including the 2.998 Å U3-O8 bonding interaction the sum is 5.800. Because the bond valence sums suggest the coordination environment is most accurately described as 6-coordinate, and we have represented the structures as such, but it is important to note that these long U-O distances can still be considered as interaction especially considering that the sum of the crystallographic van der Waals radii is 3.57 Å.[43]

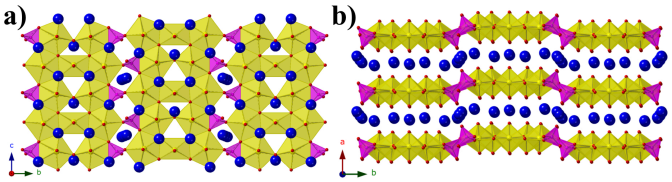


**Figure 3.5:** The structure of $Rb_6[(UO_2)_5O_5(PO_4)_2]$ **(3.3).** Views of the *cb* plane (a) and the *ab* plane (b). Uranyl polyhedra are yellow, oxygen atoms are red, and phosphate tetrahedra are magenta.

The topologies of $Cs_2Na_4[(UO_2)_5O_5(PO_4)_2]$ (**3.2**) and $Rb_6[(UO_2)_5O_5(PO_4)_2]$ (**3.3**) only differ in the orientation of the phosphate tetrahedra (Figure 3.5). In $Cs_2Na_4[(UO_2)_5O_5(PO_4)_2]$ (**3.2**), all the phosphate tetrahedra within the same sheet point in

the same direction, but adjacent layers have phosphate tetrahedra pointing in the opposite direction. When the layers are stacked the phosphate tetrahedra are staggered. This geometric isomer of the extended phosphuranylite sheet topology can be described in a similar method to the isomers of the phosphuranylite topology. By first looking at section of phosphate tetrahedra between $[(UO_2)_5O_5]$ units and labeling 'u' and 'd' as appropriate, and then looking at the pairs of phosphate tetrahedra that edge share with $U_2O_{14}$ dimers, the isomer obtained is 'uuuuuuS' as seen in the related structure, $CsNa_3[(UO_2)_3O_2(PO_4)_2]$ (**3.1**). The positions of the alkali metals are similar to those observed in $CsNa_3[(UO_2)_3O_2(PO_4)_2]$ (**3.1**), where the smaller sodium cations lie between layers in which phosphate tetrahedra in adjacent sheets point towards each other, while the mixed Cs/Na layer occurs when adjacent sheets have phosphate tetrahedra pointing away from each other. While the geometric isomers could be labeled to describe the presence of the interior square uranyl bipyramid or pentagonal bipyramid, we have decided to only use the isomer label to describe the orientation of the phosphate tetrahedra. The isomer observed in **3.3** can be labeled as 'udududS' which is analogous to the phosphuranylite based mineral vanmeersscheite.[37]

There are nine additional compounds that belong to this family: $Cs_{1.7}K_{4.3}[(UO_2)_5O_5(PO_4)_2]$, $Rb_{1.6}K_{4.4}[(UO_2)_5O_5(PO_4)_2]$,[5] $K_6[(UO_2)_5O_5(PO_4)_2]$,[9] $M_6[(UO_2)_5O_5(VO_4)_2]$ (M=K, Na),[10] $K_6[UO_2)_5O_5(AsO_4)_2]$,[4] $\beta$-$Rb_6[(UO_2)_5O_5(VO_4)_2]$, $\alpha$-$Rb_6[(UO_2)_5O_5(VO_4)_2]$ and $K_4[(UO_2)_5(TeO_3)_2O_5]$.[12] The latter two, $\alpha$-$Rb_6[(UO_2)_5O_5(VO_4)_2]$[44] and $K_4[(UO_2)_5(TeO_3)_2O_5]$[12] both adopt the udududO isomer, while the rest of the named compositions contain the uuuuuuO isomer. The trigonal pyramidal $(TeO_3)^{2-}$ units in $K_4[(UO_2)_5(TeO_3)_2O_5]$ can be described in similar manners as

$(TO_4)^{3-}$ (T = P, As, V) tetrahedra due to the lone pair on Te that causes a pyramidal rather than a planar geometry. $\alpha$-$Rb_6[(UO_2)_5O_5(VO_4)_2]$ and $K_4[(UO_2)_5(TeO_3)_2O_5]$ are also set apart by the difference in the interior U coordination. In the vanadate, the interior uranium is best considered as 7-coordinate, while in the tellurite it is a 6-coordinate square bipyramid. The ordering of the middle U pentagonal bipyramids in the udududO isomer is analogous to udududS as described for $Rb_6[(UO_2)_5O_5(PO_4)_2]$ (**3.3**). It is natural to wonder if the remaining 3 phosphuranylite isomers (Figure 3.3e-g) can be synthesized in extended phosphuranylite structures, given that there are already four common isomers between the two families.

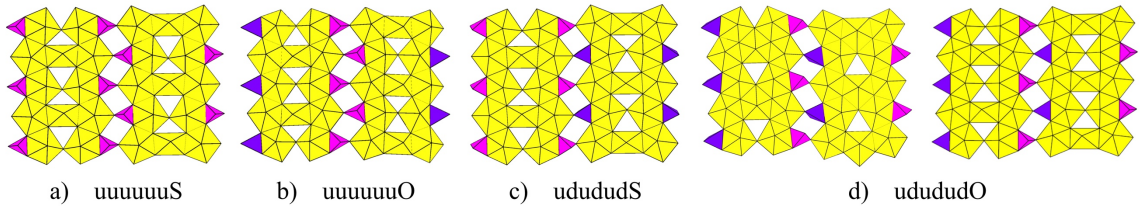


**Figure 3.6:** The known geometric isomers of the extended phosphuranylite topology. Uranium polyhedra are yellow, tetrahedra of trigonal pyramidal in the up orientation are pink, and those in the down orientation are purple. Examples of compounds exhibiting these isomers are a) $Cs_2Na_4[(UO_2)_5O_5(PO_4)_2]$ (**3.2**) b) $Cs_{1.7}K_{4.3}[(UO_2)_5O_5(PO_4)_2]$,[5] c) $Rb_6[(UO_2)_5O_5(PO_4)_2]$ (**3.3**), d) $\alpha$-$Rb_6[(UO_2)_5O_5(VO_4)_2]$,[44] and $K_4[(UO_2)_5(TeO_3)_2O_5]$.[12]

**Conclusion.** Three new crystal structures belonging to the phosphuranylite and extended phosphuranylite families have been synthesized as single crystals and structurally characterized. Each adopts a new geometrical isomer of the fairly well known topologies. The synthetic methods used to obtain the phosphuranylite and extended phosphuranylite materials were discussed and the alkali molten flux growth method has produced the majority of the reported materials including phosphates, vanadates, and tellurites, while hydrothermal methods have been used for selenites and arsenates. Future studies should

continue to explore this diverse family of materials and aim to incorporate polyhedral building blocks containing Cr, As, Al, and Se via the molten flux method.

**Acknowledgements.** Research was conducted by the Center for Hierarchical Wasteform Materials (CHWM), an Energy Frontier Research Center (EFRC). Research was supported by the U.S. Department of Energy, Office of Basic Energy Sciences, Division of Materials Sciences and Engineering under Award DE-SC0016574. C. Juillerat is additionally supported by an NSF IGERT Graduate Fellowship under grant number 1250052.

**References:**

(1) zur Loye, H.-C.; Besmann, T.; Amoroso, J.; Brinkman, K.; Grandjean, A.; Henager, C. H.; Hu, S.; Misture, S. T.; Phillpot, S.; Shustova, N. B.; Wang, H.; Koch, R. J.; Gregory Morrison; Dolgopolova, E., Hierarchical Materials as Tailored Nuclear Waste Forms: A Perspective, *Chem. Mater.* **2018**, *30*, 4475-4488.

(2) Locock, A. J., Crystal chemistry of actinide phosphates and arsenates, **2007**, *Structural Chemistry of Inorganic Actinide Compounds*, 217-278.

(3) Lussier, A. J.; Lopez, R. A. K.; Burns, P. C., A revised and expanded structure hierarchy of natural and synthetic hexavalent uranium compounds, *Can. Mineral.* **2016**, *54*, 177-283.

(4) Liu, H. K.; Ramachandran, E.; Chen, Y. H.; Chang, W. J.; Lii, K. H., High-Temperature, High-Pressure Hydrothermal Synthesis, Characterization, and Structural Relationships of Layered Uranyl Arsenates, *Inorg. Chem.* **2014**, *53*, 9065-9072.

(5) Juillerat, C. A.; Moore, E. E.; Kocevski, V.; Besmann, T. M.; zur Loye, H.-C., A Family of Layered Phosphates Crystallizing in a Rare Geometrical Isomer of the Phosphuranylite Topology: Synthesis, Characterization, and Computational Modeling of $A_4[(UO_2)_3O_2(PO_4)_2]$ (A = alkali metals) Exhibiting Intra-layer Ion Exchange, *Inorg. Chem.* **2018**, *57*, 4726-4738.

(6) Juillerat, C. A.; Klepov, V. V.; Alekseev, E. V.; zur Loye, H.-C., Overstepping Löwenstein's Rule – a Route to Unique Aluminophosphate Frameworks with 3D Salt-Inclusion and Ion Exchange Properties, *Inorg. Chem.* **2018**, *58*, 724-736.

(7) Wylie, E. M.; Burns, P. C., Crystal structures of six new uranyl selenate and selenite compounds and their relationship with uranyl mineral structures, *Can. Mineral.* **2012**, *50*, 147-157.

(8) Almond, P. M.; Albrecht-Schmitt, T. E., Hydrothermal synthesis and crystal chemistry of the new strontium uranyl selenites, $Sr[(UO_2)_3(SeO_3)_2O_2]\bullet 4H_2O$ and $Sr[UO_2(SeO_3)_2]$, *Am. Mineral.* **2004**, *89*, 976-980.

(9) Klepov, V. V., Private Communication,

(10) Dion, C.; Obbade, S.; Raekelboom, E.; Abraham, F.; Saadi, M., Synthesis, Crystal Structure, and Comparison of Two New Uranyl Vanadate Layered Compounds: $M_6(UO_2)_5(VO_4)_2O_5$ with M=Na, K, *J. Solid State Chem.* **2000**, *155*, 342-353.

(11) Obbade, S.; Dion, C.; Duvieubourg, L.; Saadi, M.; Abraham, F., Synthesis and crystal structure of α and β-$Rb_6U_5V_2O_{23}$, a new layered compound, *J. Solid State Chem.* **2003**, *173*, 1-12.

(12) Woodward, J. D.; Albrecht-Schmitt, T. E., Molten salt flux synthesis and structure of the new layered uranyl tellurite, $K_4[(UO_2)_5(TeO_3)_2O_5]$, *J. Solid State Chem.* **2005**, *178*, 2922-2926.

(13) Bugaris, D. E.; zur Loye, H.-C., Materials discovery by flux crystal growth: Quartenary and higher oxides, *Angew. Chem. Int. Ed.* **2012**, *51*, 3780-3811.

(14) Bruker. *APEX3, SAINT+, and SADABS.* Bruker AXS Inc.: Madison, Wisconsin, USA, 2015;

(15) Sheldrick, G. M., Crystal structure refinement with SHELXL, *Acta Cryst.* **2015**, *C71*, 3-8.

(16) Sheldrick, G. M., SHELXT - Integrated space-group and crystal-structure determination, *Acta Cryst.* **2015**, *A71*, 3-8.

(17) Spek, A. L., Structure validation in chemical crystallography, *Acta Cryst.* **2009**, *D65*, 148-155.

(18) Kocevski, V.; Juillerat, C. A.; Moore, E. E.; zur Loye, H.-C.; Besmann, T., Understanding the polymorphism of $A_4[(UO_2)_3(PO_4)_2O_3]$ (A=alkali metals) uranyl phosphate framework structures, *Cryst. Growth Des.* **2018**, *19,* 966-975.

(19) Villa, E. M.; Marr, C. J.; Diwu, J.; Alekseev, E. V.; Depmeier, W.; Albrecht-Schmitt, T. E., From Order to Disorder and Back Again: In Situ Hydrothermal Redox Reactions of Uranium Phosphites and Phosphates, *Inorg. Chem.* **2013**, *52*, 965-973.

(20) Villa, E. M.; Marr, C. J.; Jouffret, L. J.; Alekseev, E. V.; Depmeier, W.; Albrecht-Schmitt, T. E., Systematic evolution from uranyl(VI) phosphites to uranium(IV) phosphates., *Inorg. Chem.* **2012**, *51*, 6548-6558.

(21) Ling, J.; Wu, S.; Chen, F.; Simonetti, A.; Shafer, J. T.; Albrecht-Schmitt, T. E., Does Iodate Incorporate into Layered Uranyl Phosphates Under Hydrothermal Conditions?, *Inorg. Chem.* **2009**, *48*, 10995-11001.

(22) Kang Min Ok, J. B., Shiv Halasyamani, Dermot O'Hare., New Layered Uranium Phosphate Fluorides: Synthesis, Structures, characterizations, and ion-exchange properties of $A(UO_2)F(HPO_4)xH_2O$ ($A = Cs^+, Rb^+, K^+$; x = 0-1), *Inorg. Chem.* **2006**, *45*, 10207-10214.

(23) Shvareva, T. Y.; Albrecht-Schmitt, T. E., General route to three-dimensional framework uranyl transition metal phosphates with atypical structural motifs: the case examples of $Cs_2\{(UO_2)_4[Co(H_2O)_2]_2(HPO_4)(PO_4)_4\}$ and $Cs_{3+x}[(UO_2)_3CuH_{4-x}(PO_4)_5]\cdot H_2O$., *Inorg. Chem.* **2006**, *45*, 1900-1902.

(24) Shvareva, T. Y.; Sullens, T. A.; Shehee, T. C.; Albrecht-Schmitt, T. E., Syntheses, structures, and ion-exchange properties of the three-dimensional framework uranyl gallium phosphates, $Cs_4[(UO_2)_2(GaOH)_2(PO_4)_4]\cdot H_2O$ and $Cs[UO_2Ga(PO_4)_2]$, *Inorg. Chem.* **2005**, *44*, 300-305.

(25) Ling, J.; Qiu, J.; Sigmon, G. E.; Ward, M.; Szymanowski, J. E. S.; Burns, P. C., Uranium Pyrophosphate/Methylenediphosphonate Polyoxometalate Cage Clusters, *J. Am. Chem. Soc.* **2010**, *132*, 13395-13402.

(26) Alekseev, E. V.; Krivovichev, S. V.; Depmeier, W., Rubidium uranyl phosphates and arsenates with polymeric tetrahedral anions: Syntheses and structures of $Rb_4[(UO_2)_6(P_2O_7)_4(H_2O)]$, $Rb_2[(UO_2)_3(P_2O_7)(P_4O_{12})]$ and $Rb[(UO_2)_2(As_3O_{10})]$, *J. Solid State Chem.* **2009**, *182*, 2074-2080.

(27) Alekseev, E. V.; Krivovichev, S. V.; Depmeier, W., Crystal chemistry of anhydrous Li uranyl phosphates and arsenates. II. Tubular fragments and cation–cation interactions in the 3D framework structures of $Li_6[(UO_2)_{12}(PO_4)_8(P_4O_{13})]$, $Li_5[(UO_2)_{13}(AsO_4)_9(As_2O_7)]$, $Li[(UO_2)_4(AsO_4)_3]$ and $Li_3[(UO_2)_7(AsO_4)_5O)]$, *J. Solid State Chem.* **2009**, *182*, 2977-2984.

(28) Alekseev, E. V.; Krivovichev, S. V.; Malcherek, T.; Depmeier, W., Crystal chemistry of anhydrous Li uranyl phosphates and arsenates. I. Polymorphism and structure topology: Synthesis and crystal structures of α-$Li[(UO_2)(PO_4)]$, α-$Li[(UO_2)(AsO_4)]$,

β-Li[$(UO_2)(AsO_4)$] and $Li_2[(UO_2)_3(P_2O_7)_2]$, *J. Solid State Chem.* **2008**, *181*, 3010-3015.

(29) Alekseev, E. V.; Krivovichev, S. V.; Depmeier, W.; Knorr, K., Complex topology of uranyl polyphosphate frameworks: crystal structures of α-, β-$K[(UO_2)(P_3O_9)]$ and $K[(UO_2)_2(P_3O_{10})]$, *Z. Anorg. Allg. Chem.* **2008**, *634*, 1527-1532.

(30) Linde, S. A.; Gorbunova, Y. E.; Lavrov, A. V.; Pobedina, A. B., Synthesis and structure of crystals of uranyl pyrophosphates $M_2UO_2P_2O_7$ (M = rubidium, cesium)., *Izv. Akad. Nauk SSSR, Neorg. Mater.* **1981**, *17*, 1062-1066.

(31) Renard, C.; Obbade, S.; Abraham, F., Channels occupancy and distortion in new lithium uranyl phosphates with three-dimensional open-frameworks, *J. Solid State Chem.* **2009**, *182*, 1377-1386.

(32) Guesdon, A.; Chardon, J.; Provost, J.; Raveau, B., A copper uranyl monophosphate built up from $[CuO_2]_\infty$ Chains: $Cu_2UO_2(PO_4)_2$, *J. Solid State Chem.* **2002**, *165*, 89-93.

(33) Wu, S.; Kowalski, P. M.; Yu, N.; Malcherek, T.; Depmeier, W.; Bosbach, D.; Wang, S.; Suleimanov, E. V.; Albrecht-Schmitt, T. E.; Alekseev, E. V., Highly Distorted Uranyl Ion Coordination and One/Two-Dimensional Structural Relationship in the $Ba_2[UO_2(TO_4)_2]$ (T = P, As) System: An Experimental and Computational Study, *Inorg. Chem.* **2014**, *53*, 7650-7660.

(34) Linde, S. A.; Gorbunova, Y. E.; Lavrov, A. V., Structure of potassium uranyl phosphate ($K_4UO_2(PO_4)_2$) crystals., *Zh. Neorg. Khim.* **1980**, *25*, 1992-1994.

(35) Linde, S. A.; Gorbunova, Y. E.; Lavrov, A. V.; Pobedina, A., Synthesis and structure of sodium uranyl pyrophosphate ($Na_2UO_2P_2O_7$) crystals., *Zh. Neorg. Khim.* **1984**, *29*, 1533-1537.

(36) Juillerat, C. A.; Moore, E. E.; Besmann, T. B.; zur Loye, H.-C., Observation of an Unusual Uranyl Cation-Cation Interaction in the Strongly Fluorescent Layered Uranyl Phosphates $Rb_6[(UO_2)_7O_4(PO_4)_4]$ and $Cs_6[(UO_2)_7O_4(PO_4)_4]$, *Inorg. Chem.* **2018**, *57*, 3675-3678.

(37) Piret, P.; Deliens, M., Vanmeersscheite uranium uranyl phosphate hydrate $U(UO_2)_3(PO_4)_2(OH)_6[4•H_2O]$ and meta-vanmeersscheite $U(UO_2)_3(PO_4)_2(OH)_6[2•H_2O]$, new minerals, *Bull. Mineral.* **1982**, *105*, 125-128.

(38) Demartin, F.; Diella, V.; Donzelli, S.; Gramaccioli, C. M.; Pilati, T., The importance of accurate crystal structure determination of uranium minerals. I. Phosphuranylite $KCa(H_3O)_3(UO_2)_7(PO_4)_4O_4[8H_2O]$, *Acta Cryst.* **1991**, *B47*, 439-446.

(39) Atencio, D.; Neumann, R.; Silva, A. J. G. C.; Mascarenhas, Y. P., Phurcalite from Perus, Sao Paulo, Brazil, and redetermination of its crystal structure, *Can. Mineral.* **1991**, *29*, 95-105.

(40) Locock, A. J.; Burns, P. C., The crystal structure of bergenite, a new geometrical isomer of the phosphuranylite group, *Can. Mineral.* **2003**, *41*, 91-101.

(41) Burns, P. C.; Ewing, R. C.; Hawthorne, F. C., The crystal chemistry of hexavalent uranium: polyhedron geometries, bond-valence parameters, and polymerization of polyhedra, *Can. Mineral.* **1997**, *35*, 1551-1570.

(42) Burns, P. C., $U^{6+}$ minerals and inorganic compounds: insights into an expanded structural hierarchy of crystal structures, *Can. Mineral.* **2005**, *43*, 1839-1894.

(43) Batsanov, S. S., Van der Waals Radii of Elements, *Inorg. Mater.* **2001**, *37*, 871-885.

(44) Obbade, S.; Dion, C.; Duvieubourg, L.; Saadi, M.; Abraham, F., Synthesis and crystal structure of α and β-$Rb_6U_5V_2O_{23}$, a new layered compound, *J. Solid State Chem.* **2003**, *173*, 1-12.

# Chapter 4

## Observation of an Unusual Uranyl Cation-Cation Interaction in the Strongly Fluorescent Layered Uranyl Phosphates $Rb_6[(UO_2)_7O_4(PO_4)_4]$ and $Cs_6[(UO_2)_7O_4(PO_4)_4$[1]

[1]Reproduced with permission from Juillerat, C. A.; Moore, E. E.; Besmann, T. B.; zur Loye, H.-C. *Inorg. Chem.* **2018**, *57*, 3675-3678. © 2018 American Chemical Society

**Abstract:** Single crystals of two new uranyl phosphates, $A_6[(UO_2)_7O_4(PO_4)_4]$ (A=Cs, Rb), featuring cation-cation interactions (CCIs) rarely observed in U(VI) compounds were synthesized by molten flux methods. This structure crystallizes in the triclinic space group $P\bar{1}$ with lattice parameters, a = 9.2092(4) Å, b = 9.8405(4) Å, c = 10.1856(5) Å, α = 92.876(2)o, β = 95.675(2)o, and γ = 93.139(2)o for A = Cs and a = 9.2166(9) Å, b = 9.3771(10) Å, c = 10.1210(11) Å, α = 89.981(4)o, β = 96.136(4)o, and γ=92.790(4)o for A = Rb. The optical properties are reported for both compounds and compared to a layered uranyl phosphate, $K_4[(UO_2)_3O_2(PO_4)_2]$, having a similar phosphuranylite based structure, but no CCIs. Partial ion exchange of Cs and Rb cations into the $Rb_6[(UO_2)_7O_4(PO_4)_4]$ and $Cs_6[(UO_2)_7O_4(PO_4)_4]$ structures, respectively, was achieved.

Uranium chemistry has been studied since the mid-twentieth century for predominantly nuclear weapons and nuclear energy applications, and more recently for applications related to environmental protection and nuclear waste storage.[1, 2, 3, 4] We are interested in studying U(VI) chemistry to primarily develop the basic understanding necessary to design the next nuclear wasteforms.[5] U(VI) ubiquitously appears in the form of the UO22+, uranyl, an ion that features strong axial oxygen bonds with average distances of ~1.8 Å.[6] Because of the stronger axial U-O bond, the 'yl' oxygens are typically inert and do not participate in additional bonding. Cation-cation interactions (CCIs) are an exception where the 'yl' oxygen bonds with another U center. CCIs are known in other penta- and hexavalent actinides that form the $AnO^{2+}$ ion (An= U-Am);[7] however, they are much less frequent among uranyl materials. In a recent review, only 50 out of 2500 U(VI) compounds were found to contain CCIs;[8] noticeably, of those 50 CCI containing compounds only one was observed in a layered structure. Several layered uranyl oxychlorides have also been

reported where, unlike in the phosphates described herein, the CCIs are sterically mediated by the larger chlorine atoms.[9] The observed layered uranyl phosphate compounds feature a uranyl CCI that is, to date, unreported in the literature for uranyl systems.

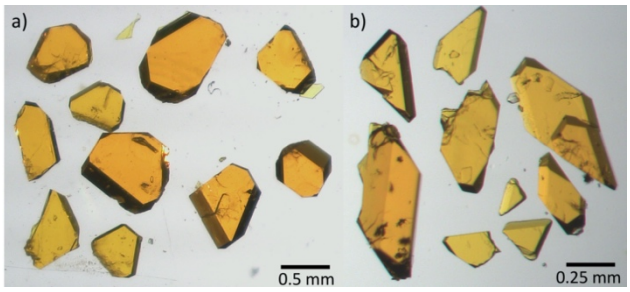


**Figure 4.1:** Orange plate crystals of 4.1 and 4.2.

The title compounds were synthesized by molten flux methods.[10] $UF_4$ (International Bio-Analytical Industries, powder, ACS grade), $AlPO_4$ (Alfa Aesar, powder, 99.99%), CsCl (Alfa Aesar, powder, 99%), and RbCl (Alfa Aesar, powder, 99.8%) were used as received. ***Caution!*** *Although the uranium precursor used contained depleted uranium, standard safety measures for handling radioactive substances must be followed.* For each reaction, 0.5 mmol $UF_4$, 0.2 mmol $AlPO_4$, and 10 mmol of RbCl or 20 mmol of CsCl were loaded into alumina crucibles with alumina caps and heated to 875 °C in 1.5 h, held for 12 h, and cooled to 450 °C at 6 °C/h. The products were then sonicated in water and isolated via vacuum filtration in good yield (~70%) (Figure 4.1). The orange plate single crystals were hand picked from other minor unidentified phases to obtain a phase pure sample and the phase purity was confirmed by grinding the crystals into a powder and collecting powder X-ray diffraction data using a Bruker D2 Phaser equipped with an LYNXEYE silicon strip detector and a Cu K$\alpha$ source (Figure 4.2). The intensities of the calculated

PXRD pattern of both compounds differs from the experimentally observed intensities due to the presence of severe preferred orientation of the plate crystals in the (0 1 -1) direction.

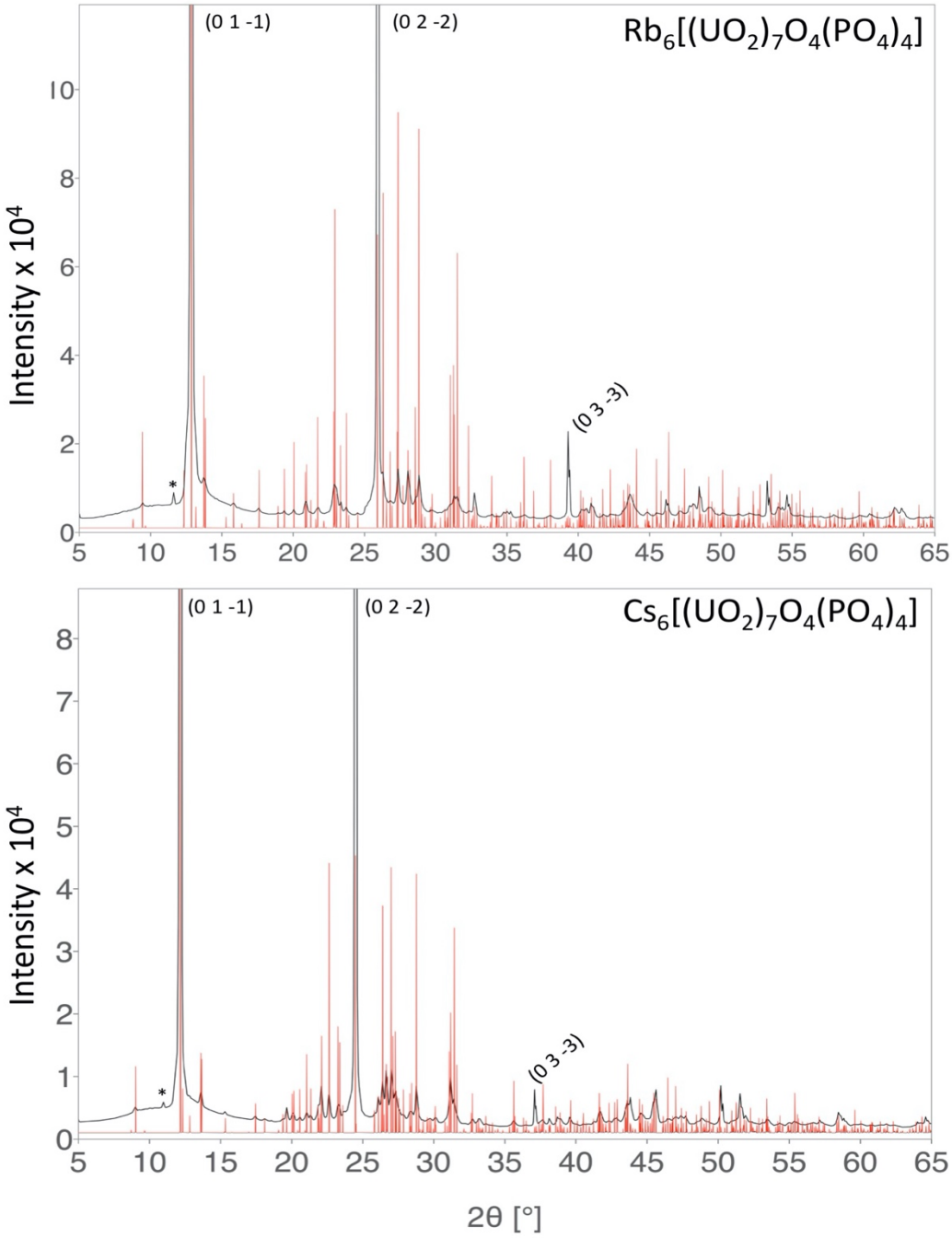


**Figure 4.2**: PXRD patterns of $Cs_6(PO_4)_4[(UO_2)_7O_4]$ and $Rb_6(PO_4)_4[(UO_2)_7O_4]$ with experimental patterns in black and calculated patterns in red. Asterisk (*) denotes a weak $K_\beta$ peak.

**Table 4.1:** Full crystallographic data for $Cs_6[(UO_2)_7O_4(PO_4)_4]$ and $Rb_6[(UO_2)_7O_4(PO_4)_4]$

| Compound<br>Space group | $Cs_6[(UO_2)_7O_4(PO_4)_4]$ (**4.1**)<br>$P\bar{1}$ | $Rb_6[(UO_2)_7O_4(PO_4)_4]$ (**4.2**)<br>$P\bar{1}$ |
|---|---|---|
| $a$ (Å) | 9.2117(8) | 9.2166(9) |
| $b$ (Å) | 9.8248(8) | 9.3771(10) |
| $c$ (Å) | 10.2174(9) | 10.1210(11) |
| $\alpha$ (deg) | 92.995(3) | 89.981(4) |
| $\beta$ (deg) | 95.683(3) | 96.136(4) |
| $\gamma$ (deg) | 93.052(3) | 92.790(4) |
| $V$ (Å$^3$) | 915.71(7) | 868.65(16) |
| Crystal size (mm$^3$) | 0.04 x 0.02 x 0.01 | 0.05 x 0.02 x 0.01 |
| Temperature (K) | 300.02 | 300.27 |
| Density (g cm$^{-3}$) | 5.669 | 5.442 |
| $\theta$ range (deg) | 2.266-30.578 | 2.844-36.317 |
| $\mu$ (mm$^{-1}$) | 36.926 | 41.149 |
| Collected reflections | 65695 | 88207 |
| Unique reflections | 5606 | 8417 |
| $R_{int}$ | 0.0347 | 0.0369 |
| $h$ | $-13 \le h \le 13$ | $-15 \le h \le 15$ |
| $k$ | $-14 \le k \le 14$ | $-15 \le k \le 15$ |
| $l$ | $-14 \le l \le 14$ | $-16 \le l \le 16$ |
| $\Delta\rho_{max}$ (e Å$^{-3}$) | 6.987 | 2.274 |
| $\Delta\rho_{min}$ (e Å$^{-3}$) | -2.579 | -2.147 |
| *GoF* | 1.065 | 1.090 |
| Extinction coefficient | -- | -- |
| $R_1(F)$ for $F_0^2>2\sigma(F_0^2)$[a] | 0.0236 | 0.0180 |
| $R_w(F_0^2)$[b] | 0.0544 | 0.0398 |

[a] $R_1 = \Sigma||F_0| - |F_c||/\Sigma|F_0|$. [b] $wR_2 = [\Sigma w(F_0^2 - F_c^2)^2/\Sigma w(F_0^2)^2]^{1/2}$; $P = (F_0^2 + 2F_c^2)/3$; $w = 1/[\sigma^2(F_0^2) + (0.0132P)^2 + 2.5306P]$ for $Rb_6[(UO_2)_7O_4(PO_4)_4]$, $w = 1/[\sigma^2(F_0^2) + (0.0221P)^2 + 10.4351P]$ for $Cs_6[(UO_2)_7O_4(PO_4)_4]$.

The structure of each material was determined by single-crystal X-ray diffraction (SCXRD) using a Bruker D8 Quest single crystal X-ray diffractometer equipped with a Mo Kα microfocus source (λ = 0.71073 Å). The absorption correction was performed using SAINT+ and SADABS programs within the APEX 3 software.[11] After reduction and absorption correction, the structure was solved by SHELXT, an intrinsic phasing solution

method, and refined using SHELXL, both of which were used within the Olex 2 GUI.[12, 13, 14] Full crystallographic data are shown in Table 1.

$Rb_6[(UO_2)_7O_4(PO_4)_4]$ and $Cs_6[(UO_2)_7O_4(PO_4)_4]$ were refined with anisotropic displacement parameters. The site occupancy factors of each metal atom were freely refined to confirm no significant deviation from full occupancy. A physically reasonable structure was obtained in the triclinic, centrosymmetric space group $P\bar{1}$, and the ADDSYM program within PLATON did not find any missed symmetry elements. The asymmetric unit contains four U sites, two P sites, 17 O sites, and three Cs sites. U(1) is at the origin with Wyckoff symbol 1*a* and site symmetry $\bar{1}$, while all other sites lie on general positions with Wyckoff symbol 2*i.* While both structures are free of disorder, the Cs solution contains a moderate q peak with residual electron density of 6.987. This q peak is 0.53 Å away from a U atom. Attempts to resolve the residual electron density by splitting the site results in unreasonable U-O bond distances. Attempts to collect on smaller crystals of higher quality also resulted in this residual electron density; however, it is less than 10% of the electron density of U and a good crystal solution is still obtained. Elemental compositions of the compounds were confirmed qualitatively by EDS using TESCAN Vega-3 SBU equipped with an EDS detector.

$A_6[(UO_2)_7O_4(PO_4)_4]$ is constructed of uranyl phosphate layers of the composition $[(UO_2)_7O_4(PO_4)_4]^{6-}$ that are charge balanced by $Cs^+$ or $Rb^+$ cations located between the layers. The layers are made up of phosphate tetrahedra, uranyl pentagonal bipyramids, and uranyl hexagonal bipyramids. The layer can be deconstructed into units of the phosphuranylite (PU) topology that are connected into chains via edge-sharing between two pentagonal bipyramids (Figure 4.3). These chains are further connected into sheets by

corner and edge-sharing through phosphate tetrahedra, similar to the PU topology, and by uranyl CCIs that are formed by the edge sharing of two pentagonal bipyramidal uranyl units.

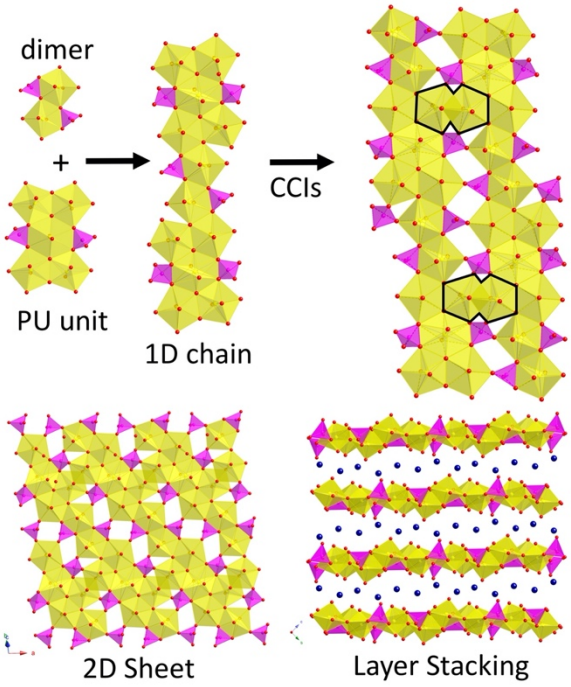


**Figure 4.3.** The construction of $A_6[(UO_2)_7O_4(PO_4)_4]$ from phosphuranylite (PU) units and dimers. The uranyl polyhedra are shown in yellow, phosphate tetrahedra in magenta, Cs atoms in dark blue, and oxygen atoms in red. CCI interactions are outlined in black.

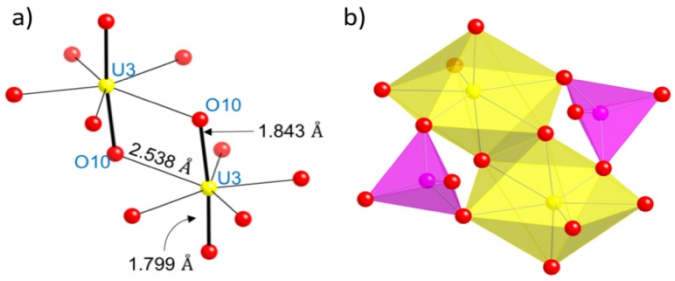


**Figure 4.4.** The CCI observed in $A_6[(UO_2)_7O_4(PO_4)_4]$. Bond distances of the Cs analog are provided. Uranyl bonds are bolded for emphasis.

**Table 4.2:** Bond valence sums and bond distances for $Cs_6[(UO_2)_7O_4(PO_4)_4]$

| Interaction | Distance | Interaction | Distance | Interaction | Distance |
|---|---|---|---|---|---|
| U1-O1 (x2) | 1.797(5) | U2-O2 | 2.283(4) | U3-O2 | 2.197(4) |
| U1-O2 (x2) | 2.220(4) | U2-O4 | 2.439(4) | U3-O3 | 2.462(4) |
| U1-O3 (x2) | 2.715(5) | U2-O5 | 1.785(5) | U3-O9 | 2.187(4) |
| U1-O4 (x2) | 2.594(4) | U2-O6 | 1.791(5) | U3-O10 | 1.843(4) |
| **BVS U1** | **5.996** | U2-O7 | 2.284(4) | U3-O10 | 2.538(4) |
| U4-O8 | 2.477(4) | U2-O8 | 2.399(4) | U3-O11 | 1.799(5) |
| U4-O9 | 2.213(4) | U2-O9 | 2.364(4) | U3-O12 | 2.318(4) |
| U4-O13 | 1.795(5) | **BVS U2** | **6.130** | **BVS U3** | **6.084** |
| U4-O14 | 1.787(5) | P1-O3 | 1.549(4) | P2-O7 | 1.531(4) |
| U4-O15 | 2.390(4) | P1-O4 | 1.545(4) | P2-O8 | 1.570(4) |
| U4-O16 | 2.331(4) | P1-O12 | 1.539(4) | P2-O16 | 1.563(4) |
| U4-O16 | 2.489(4) | P1-O15 | 1.525(4) | P2-O17 | 1.478(5) |
| **BVS U2** | **6.006** | **BVS P1** | **4.933** | **BVS P1** | **5.010** |

**Table 4.3:** Bond valence sums and bond distances for $Rb_6[(UO_2)_7O_4(PO_4)_4]$

| Interaction | Distance | Interaction | Distance | Interaction | Distance |
|---|---|---|---|---|---|
| U1-O1 (x2) | 1.800(2) | U2-O2 | 2.274(2) | U3-O2 | 2.198(2) |
| U1-O2 (x2) | 2.211(2) | U2-O4 | 2.441(2) | U3-O3 | 2.472(2) |
| U1-O3 (x2) | 2.685(2) | U2-O5 | 1.795(3) | U3-O9 | 2.186(2) |
| U1-O4 (x2) | 2.601(2) | U2-O6 | 1.790(3) | U3-O10 | 1.853(2) |
| **BVS U1** | **5.996** | U2-O7 | 2.286(2) | U3-O10 | 2.527(2) |
| U4-O8 | 2.472(2) | U2-O8 | 2.403(2) | U3-O11 | 1.796(3) |
| U4-O9 | 2.216(2) | U2-O9 | 2.354(2) | U3-O12 | 2.330(2) |
| U4-O13 | 1.798(3) | **BVS U2** | **6.115** | **BVS U3** | **6.051** |
| U4-O14 | 1.789(2) | P1-O3 | 1.547(2) | P2-O7 | 1.528(2) |
| U4-O15 | 2.392(2) | P1-O4 | 1.549(2) | P2-O8 | 1.563(2) |
| U4-O16 | 2.334(2) | P1-O12 | 1.537(2) | P2-O16 | 1.558(2) |
| U4-O16 | 2.488(2) | P1-O15 | 1.527(2) | P2-O17 | 1.485(3) |
| **BVS U2** | **5.986** | **BVS P1** | **4.923** | **BVS P1** | **5.031** |

The CCIs in the structure are created by uranyl pentagonal bipyramids that share a unique edge that includes one axial (O10) and one equatorial oxygen (O10), thereby forming two simultaneous CCIs between them (see Figure 4.4). This CCI has only been observed in a Np(V) compound, $Na_4[(NpO_2)_2C_6(COO)_6$, and is rare even among Np(V)

compounds.[7] These CCIs would be classified as Type 7 uranyl interactions, based on the recently published classification scheme by Read et al.[9] This type of CCI in U(VI) chemistry was first hypothesized in Fortier et al. but no example compounds of this type were given, and this class of CCI was not reported in the 2014 review of CCIs in U(V) by Serezhkin et. al.[8, 15] This CCI is reminiscent of edge-sharing octahedra in metal oxide materials such as pillared perovskites, $Nd_3Ti_4O_{12}$, and $La_5Mo_4O_{16}$, where the edge-sharing octahedra have exceptionally short M-M bond distances, i. e. Re-Re bonds of of 2.407 Å in $La_5Re_3MnO_{16}$ and Ti-Ti bonds of 2.760 Å in $Nd_3Ti_4O_{12}$.[16] While the U-O bond distances involved in the CCIs in this structure are longer than average, the U-U bond is shorter at 3.563 Å. Both U-O(10) bonds are longer than typical U-O bond distances, which is characteristic of CCIs. For A = Cs the U3-O10 bond length is 1.843 Å as compared to the other uranyl bond distances in the structure which are in the range 1.785 – 1.799 Å. The equatorial U3-O10 bond is 2.523 Å and is longer than other U-O bond distances in the same polyhedron. Bond distances and valence sums for the uranyl and phosphate polyhedra for both structures are listed in Tables 4.2 and 4.3.[17, 18]

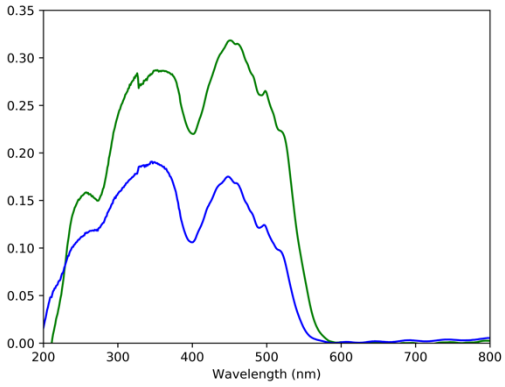


**Figure 4.5:** UV-vis spectra for **4.1** (green) and **4.2** (blue).

Optical measurements on both compounds were performed using a PerkinElmer Lambda 35 UV-vis scanning spectrometer equipped with an integrating sphere and a PerkinElmer LS55 Luminescence spectrometer. The UV-vis diffuse reflectance data were internally converted to absorbance using the Kubelka-Munk equation.[19] The UV-vis data show absorption edges of 570 nm and 550 nm with estimated band gaps of 2.2 eV and 2.3 eV for the Cs and Rb compounds, respectively (Figure 4.5). UV-vis data and fluorescence data for each compound show similar features, as expected for isostructural materials.

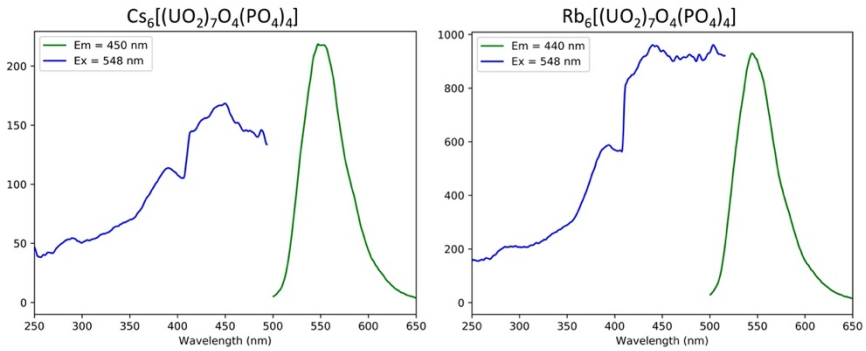


**Figure 4.6:** Emission and excitation spectra for 4.1 and 4.2

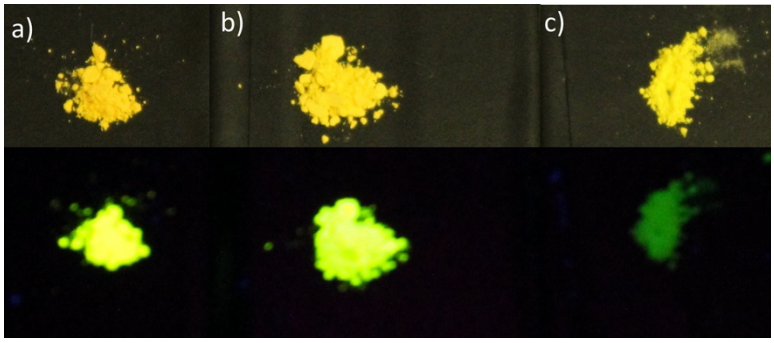


**Figure 4.7.** Optical pictures of powders of 4.1 and 4.2. Powders of $Cs_6[(UO_2)_7O_4(PO_4)_4]$ (a), $Rb_6[(UO_2)_7O_4(PO_4)_4]$ (b), and $K_4[(UO_2)_3O_2(PO_4)_2]$ (c) are shown under artificial light (top) and under long-wave (365 nm) UV light (bottom).

It is generally accepted that uranyl phases containing CCIs luminesce more intensely than those not containing CCIs. To test this phenomenon, the fluorescence spectra of the Rb and Cs analogs and that of a structurally related phosphate compound recently prepared by our group, $K_4[(UO_2)_3O_2(PO_4)_2]$,[20] were collected. For the Cs analog, a 10% attenuator was used to decrease the intensity to measurable levels. The fluorescence emission spectra feature one large peak at 548 nm (Figure 4.6). Visually, the luminescence when excited at 365 nm using a handheld UV lamp is very intense and significantly more so than that of $K_4[(UO_2)_3O_2(PO_4)_2]$ (Figure 4.7). The structure of $K_4[(UO_2)_3O_2(PO_4)_2]$ is also based upon the phosphuranylite topology, supporting that it is the presence of the CCIs between the phosphuranylite units in the title structures that results in a much more intense luminescence.

Volume based thermodynamics has recently been used to calculate the enthalpy and Gibbs energy of formation of novel phosphuranylite based structure in reference 19. The values calculated in this work are based on the same methods but differ slightly due to the structural differences in the cation-cation interaction layers of the $A_6(PO_4)_4[(UO_2)_7O_4]$ uranyl phosphate layered structures. The notable differences occur with respect to the following equations:

$$\boldsymbol{U_{pot} = A\, I\, (2I/V_m)^{1/3}} \qquad \textbf{(1)}$$

where $\boldsymbol{U_{pot}}$ is the lattice potential, $\boldsymbol{I}$ is the ionic strength factor (in this structure type, 2I=86). Similarly, the converted lattice enthalpy differs slightly due to differing structural components compared to reference 19 with $\boldsymbol{s_i}$ being the number of ion types and $\boldsymbol{c_i}$ is a constant that reflects whether the constituent is monatomic or polyatomic (linear/nonlinear).

$$\Delta H_{\mathrm{L}} = U_{\mathrm{pot}} + \sum_{i=1}^{n} s_i \left(\frac{c_i}{2} - 2\right) RT \qquad (2)$$

The enthalpy and Gibbs energy of formation (including entropy of mixing) are calculated in the same manner as before, with an updated thermochemical cycle as seen below. The auxiliary information is the same as in reference 19 and the references therein. The results including the molar volume ($V_m$), standard entropy, lattice potential energy, enthalpy and Gibbs energy of formation from VBT are tabulated below in Table 4.4.

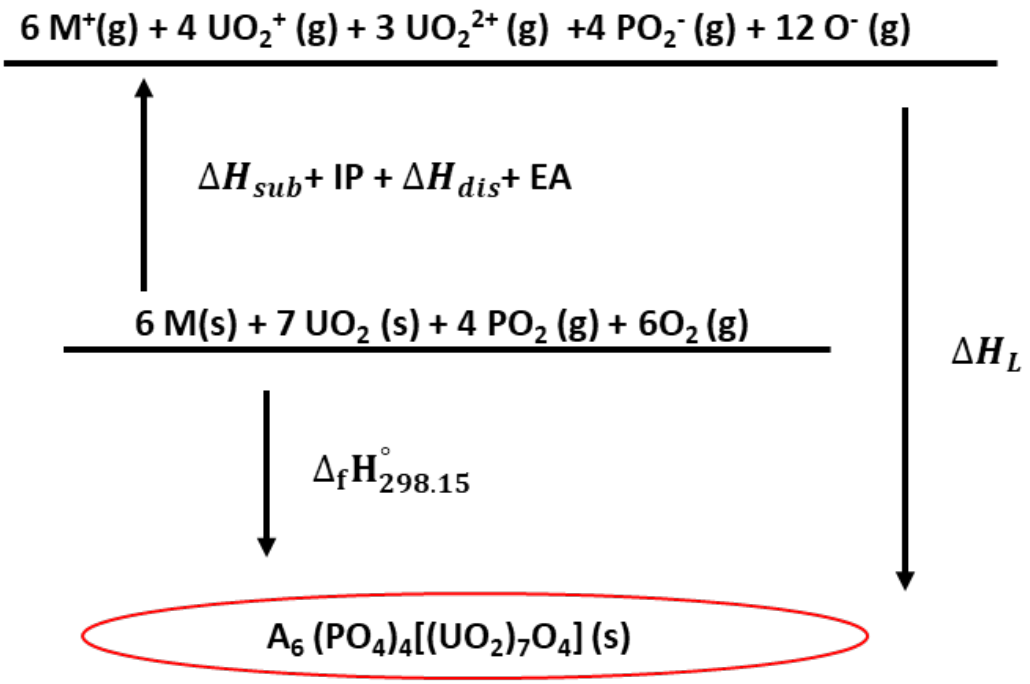


**Figure 4.8:** Born-Haber cycle used to calculate the formation enthalpy **4.1** and **4.2**.

The VBT calculated Gibbs energy of the title compounds are of -9306 kJ/mol and -9062 kJ/mol, for the Rb and Cs phases, respectively indicating the structures are very stable. This supports the experimental observation that the title compounds can be synthesized over a wide range of temperatures (775-925 °C) and reagent-to-flux ratios. The results were also compared to the Gibbs energy values for the $A_4[(UO_2)_3O_2(PO_4)_2]$ family

(average energy of -6665 kJ/mol),[19] and showed that the CCI structure is significantly more favorable.

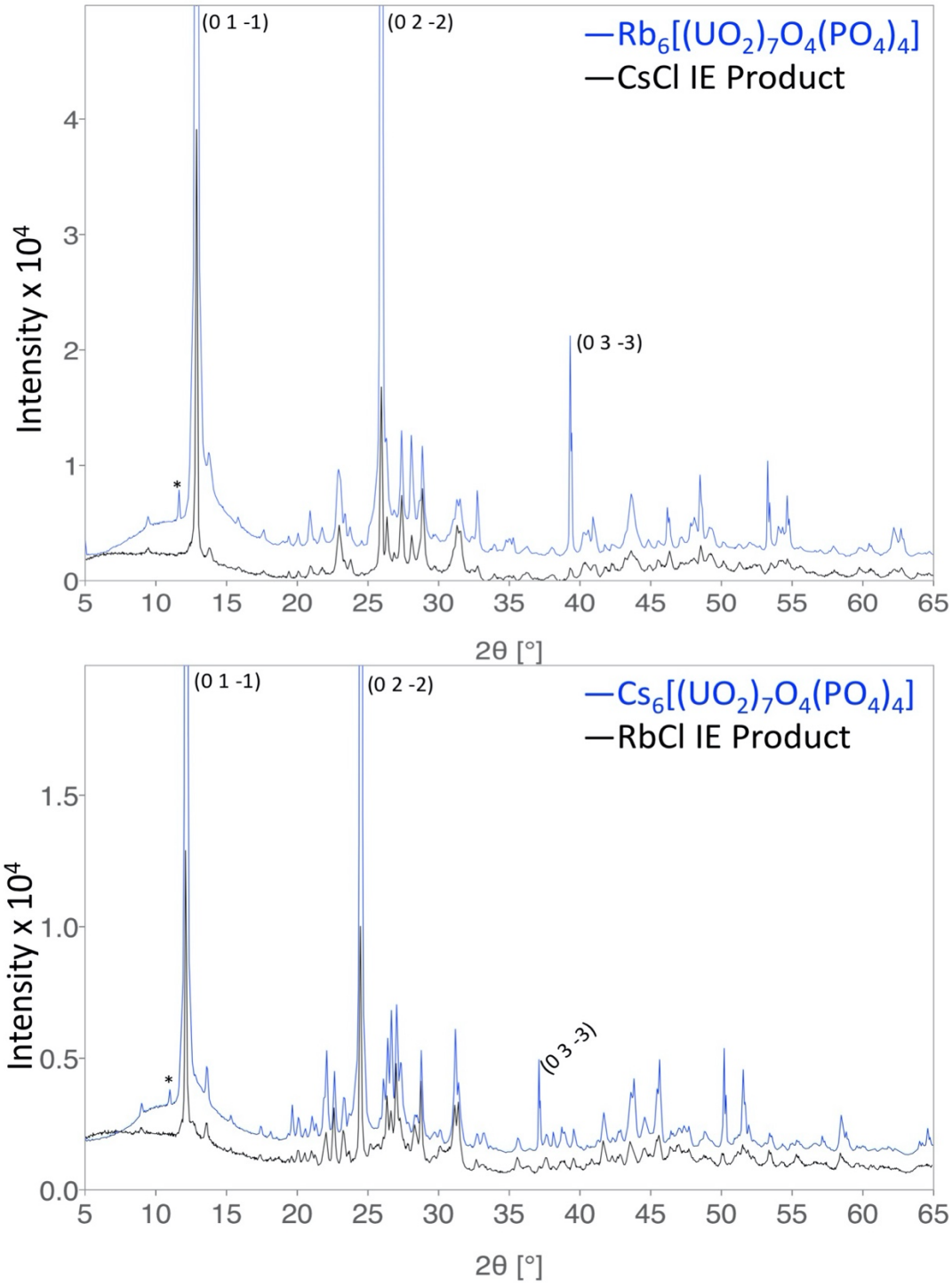


**Figure 4.9:** PXRD patterns of ion exchange products. Asterisk (*) denotes a weak $K_\beta$ peak.

**Table 4.4**: Results from Volume Based Thermodynamic Approach

| A | $V_m$ ($A^3$) | $S$ (J/mol/K) | $U_{pot}$ (kJ/mol) | $\Delta_f H^\circ_{298.15}$ (kJ/mol) | $\Delta_f G^\circ_{298.15}$ (kJ/mol) |
|---|---|---|---|---|---|
| Rb | 868.7 | 1109 | 24147 | -10027 | -9306 |
| Cs | 917.7 | 1171 | 23710 | -9779 | -9062 |

Ion exchange experiments were performed on ground samples of both the Cs and Rb analogs to determine if the Cs and Rb cations could be replaced by Rb and Cs, respectively. The Cs and Rb analogs were soaked in aqueous 7 m RbCl and 11 m CsCl, respectively, for 8 days without stirring in an oil bath set to 90 ºC. Partial ion exchange was successful and confirmed by examining PXRD and EDS results. PXRD (. 4.9) confirmed that the layers remain intact during the ion exchange process and EDS confirms the presence of the second cation in the structure. The ion exchange was more extensive in the Cs phase than in the Rb phase, resulting in approximate ratios of 2:1 Rb:Cs for $Rb_6[(UO_2)_7O_4(PO_4)_4]$ soaked in CsCl, and 1:1 for $Cs_6[(UO_2)_7O_4(PO_4)_4]$ soaked in RbCl. These results suggest that the Rb is able to diffuse more quickly into the Cs phase, which has a larger interlayer gallery, then the reverse process, which would require the Cs cations to push the layers apart in order to interdiffuse.

In summary, we have synthesized and characterized two unique layered uranyl phosphates, $A_6[(UO_2)_7O_4(PO_4)_4]$ (A = Cs, Rb), that feature a CCI not previously observed in uranyl chemistry. The two phosphates were synthesized via molten flux growth methods and feature strong luminescence. The luminescence of these CCI containing compounds is noticeably more intense than that of the structurally related layered uranyl phosphate, $K_4[(UO_2)_3O_2(PO_4)_2]$, which is also based on the phosphuranylite topology, but has no CCI.

Basic ion exchange experiments demonstrated that the alkali metal cations can be partially exchanged by other monovalent cations.

**Acknowledgements.** Research was conducted by the Center for Hierarchical Wasteform Materials (CHWM), an Energy Frontier Research Center (EFRC). Research was supported by the U.S. Department of Energy, Office of Basic Energy Sciences, Division of Materials Sciences and Engineering under Award DE-SC0016574. C. Juillerat is additionally supported by an NSF IGERT Graduate Fellowship under grant number 1250052.

**References:**

(1) Burns, P. C., A new uranyl phosphate chain in the structure of parsonsite, *Am. Mineral.* **2000**, *85*, 801-805.

(2) Ling, J.; Wu, S.; Chen, F.; Simonetti, A.; Shafer, J. T.; Albrecht-Schmitt, T. E., Does Iodate Incorporate into Layered Uranyl Phosphates Under Hydrothermal Conditions, *Inorg. Chem.* **2009**, *48*, 10995-11001.

(3) Wu, S.; Kowalski, P. M.; Yu, N.; Malcherek, T.; Depmeier, W.; Bosbach, D.; Wang, S.; Suleimanov, E. V.; Albrecht-Schmitt, T. E.; Alekseev, E. V., Highly Distorted Uranyl Ion Coordination and One/Two-Dimensional Structural Relationship in the $Ba_2[UO_2(TO_4)_2]$ (T = P, As) System: An Experimental and Computational Study, *Inorg. Chem.* **2014**, *53*, 7650-7660.

(4) Yagoubi, S.; Renard, C.; Abraham, F.; Obbade, S., Molten salt flux synthesis and crystal structure of a new open-framework uranyl phosphate $Cs_3(UO_2)_2(PO_4)O_2$: Spectroscopic characterization and cationic mobility studies, *J. Solid State Chem.* **2013**, *200*, 13-21.

(5) Dolgopolova, E. A.; Ejebavwo, O. A.; Martin, C. R.; Smith, M. D.; Setyawan, W.; Karakalos, S. G.; Henager, C. H.; zur Loye, H.-C.; Shustova, N. B., Multidaceted modularity: A key for stepwise building of hierarchical complexity in actinide metal-oraganic frameworks, *J. Am. Chem. Soc.* **2017**, *139*, 16852-16861.

(6) Lussier, A. J.; Lopez, R. A. K.; Burns, P. C., A revised and expanded structure hierarchy of natural and synthetic hexavalent uranium compounds, *Can. Mineral.* **2016**, *54*, 177-283.; Burns, P. C., $U^{6+}$ minerals and inorganic compounds: insights into an expanded structural hierarchy of crystal structures, *Can. Mineral.* **2005**, *43*, 1839-1894.

(7) Krot, N. N.; Grigoriev, M. S., Cation-cation interaction in crystalline actinide compounds, *Russian Chemical Reviews* **2004**, *73*, 89-100.

(8) Serezhkin, V. N.; Sidorenko, G. V.; Pushkin, D. V.; Serezhkina, L. B., Cation-cation Interactions between uranyl(VI) ions, *Radiochemistry* **2014**, *56*, 115-133.

(9) Read, C. M.; Yeon, J.; Smith, M. D.; zur Loye, H.-C., Crystal growth, structural characterization, cation–cation interaction classification, and optical properties of uranium (vi) containing oxychlorides, $A_4U_5O_{16}Cl_2$ (A= K, Rb), $Cs_5U_7O_{22}Cl_3$, and $AUO_3Cl$ (A=Rb, Cs), *CrystEngComm* **2014**, *16*, 7259.

(10) Bugaris, D. E.; zur Loye, H.-C., Materials discovery by flux crystal growth: Quartenary and higher oxides, *Angew. Chem. Int. Ed.* **2012**, *51*, 3780-3811.

(11) Bruker. *APEX3, SAINT+, and SADABS*; Bruker AXS Inc.: Madison, Wisconsin, USA, 2015;

(12) Sheldrick, G. M., SHELXT - Integrated space-group and crystal-structure determination, *Acta Cryst.* **2015**, *A71*, 3-8.

(13) Sheldrick, G. M., Crystal structure refinement with SHELXL, *Acta Cryst.* **2015**, *C71*, 3-8.

(14) Dolomanov, O. V.; Bourhis, L. J.; Gildea, R. J.; Howard, J. A. K.; Pushman, H., OLEX2: a complete structure solution, *J. Appl. Crystallogr.* **2009**, *42*, 339-341.

(15) Fortier, S.; Hayton, T. W., Oxo ligand functionalization in the uranyl ion ($UO_2^{2+}$), *Coord. Chem. Rev.* **2010**, *254*, 197-214.

(16) Wiebe, C. R.; Gourrier, A.; Langet, T.; Britten, J. F.; Greedan, J. E., Synthesis, Structure, and Magnetic Behavior of $La_5Re_3MnO_{16}$: A New Perovskite-like Material, *J. Solid State Chem.* **2000**, *151*, 31-39.

(17) Brown, I. D.; Altermatt, D., Bond-valence parameters obtained from a systematic analyses of the inorganic cyrstal structure database, *Acta Cryst.* **1985**, *B41*, 244-247.

(18) Burns, P. C.; Ewing, R. C.; Hawthorne, F. C., The crystal chemistry of hexavalent uranium: polyhedron geometries, bond-valence parameters, and polymerization of polyhedra, *Can. Miner.* **1997**, *35*, 1551-1570.

(19) Kubelka, P.; Munk, F. Z., Ein Beitrag Zur Optik Der Farbanstriche, *Z. Techn. Phys.* **1931**, *12*, 593-601.

(20) Juillerat, C. A.; Moore, E. E.; Kocevski, V.; Besmann, T. M.; zur Loye, H.-C., A Family of Layered Phosphates Crystallizing in a Rare Geometrical Isomer of the Phosphuranylite Topology: Synthesis, Characterization, and Computational Modeling of $A_4[(UO_2)_3O_2(PO_4)_2]$ (A = alkali metals) Exhibiting Intra-layer Ion Exchange, *Inorg. Chem.* **2018**, *57,* 4726-4738.

# Chapter 5

## Observation of the Same New Sheet Topology in Both the Layered Uranyl Oxide-Phosphate $Cs_{11}[(UO_2)_{12}(PO_4)_3O_{13}]$ and the Layered Uranyl Oxyfluoride-Phosphate $Rb_{11}[UO_2)_{12}(PO_4)_3O_{12}F_2]$ Prepared by Flux Crystal Growth[1]

[1]Reproduced with permission from Juillerat, C. A.; Kocevski, V.; Besmann, T.; zur Loye, H.-C. *Frontiers in Chemistry* **2019**, *7*, 583.

**Abstract:** Single crystals of four new layered uranyl phosphates, including three oxyfluoride-phosphates, were synthesized by molten flux methods using alkali chloride melts, and their structures were determined by single-crystal X-ray diffraction. $Cs_{11}[(UO_2)_{12}(PO_4)_3O_{13}]$ (**5.1**) and $Rb_{11}[UO_2)_{12}(PO_4)_3O_{12}F_2]$ (**5.2**) contain uranyl phosphate layers exhibiting a new sheet topology that can be related to that of β-$U_3O_8$, while $Cs_{4.4}K_{0.6}[(UO_2)_6O_4F(PO_4)_4(UO_2)]$ (**5.3**) and $Rb_{4.4}K_{0.6}[(UO_2)_6O_4F(PO_4)_4(UO_2)]$ (**5.4**) contain layers of a known isomer of the prominent phosphuranylite topology. The location of the fluorine in structures **5.2**-**5.4** is discussed using bond valence sums. First principles calculations were used to explore why a pure oxide structure is obtained for the Cs containing phase (**5.1**) and in contrast an oxyfluoride phase for the Rb containing phase (**5.2**). Ion exchange experiments were performed on **5.1** and **5.2** and demonstrate the ability of these structures to exchange approximately half of the parent alkali cation with a target alkali cation in an aqueous concentrated salt solution. Optical measurements were performed on **5.1** and **5.2** and the UV-vis and fluorescence spectra show features characteristic of the $UO_2^{2+}$ uranyl group.

**Introduction.** Nuclear power has been well established for several decades and, nonetheless, studies continue to develop a deeper understanding of the nuclear fuel cycle, including exploring improved methods of both long-term and short-term waste storage,[1] and continuing to investigate the processes of radionuclide leaching into surrounding ecosystems. For these reasons, it is advantageous to further expand our understanding of uranium coordination chemistry, specifically in extended structures, as this can give us insights in understanding intermediate phases in the nuclear waste cycle, identifying

potential structures useful in nuclear waste processing or storage, and possible pathways within the environment for the migration of $U^{6+}$ and other actinides.

Nature often gives a good indication of what chemical compounds can be made synthetically. For example, uranium containing minerals present a few prominent sheet anion topologies that can be observed both in minerals and synthetic compounds. In Burns' most recent review of hexavalent uranium compounds, autunite, phosphuranylite, and uranophane are significant minerals classes with 40 proposed autunite minerals, 16 phosphuranylite, and 10 uranophane minerals.[2] Phosphuranylite and autunite minerals are the primary classes of phosphorus containing minerals, as phosphorus bearing uranium minerals make up nearly a quarter of all identified uranium minerals. The uranophane topology is specifically prominent among silicates, but as in the phosphuranylite topology the tetrahedrally coordinated Si or P sites can be replaced by other tetrahedrally—or even trigonal pyramidal or trigonal planar—coordinating elements. These sheet anion-topologies common among minerals have also been observed in numerous synthetic compounds including 38 belonging to the autunite, 18 belonging to the uranophane, and 16 belonging to the phosphuranylite classes. [2–5]

While nature certainly gives a good indication of what we might be able to synthesize in the laboratory, many additional sheet topologies outside of those found in minerals are also reported (62 reported in Burns 2016). All of the discussed sheet topologies so far have been for uranium oxide compounds and one way to expand the number of known sheet topologies, and thus our understanding of uranium chemistry, is to partially exchange oxygen within these sheets with other anions such as a halides or sulfides, although in this paper we will only discuss halides. While one may expect to make

radically different sheet structures using $Cl^-$ due to the commonly terminal nature and large size of this anion, causing it to stick out of the plane of the sheet, as seen in $K_4U_5O_{16}Cl_2$ and $Cs_5U_7O_{22}Cl_3$,[6] the inclusion of $F^-$ could lead to new sheet structures or to those already observed in oxides. This arises partially due to the similarity in size of O and F, and examples can be seen in the existence of both rare earth oxides and oxyfluorides that adopt the prominent apatite structure.[7, 8] In rare earth silicates, the coordination of the rare earth to F limits the available connectivity to the silicate tetrahedra, as $SiO_3F$ tetrahedra are unreported in crystalline structures.[9, 10] Although $PO_3F$ tetrahedra exist, i.e., $Sr(PO_3F)$, they have yet to be reported in uranium extended structures, although it is unclear whether this is due to chemical principles or whether the proper conditions for this structure motif have yet to be explored.

Herein we present the synthesis and structural characterization of two examples of uranium oxyfluorides that adopt the phosphuranylite topology, $Cs_{4.4}K_{0.6}[(UO_2)_6O_4F(PO_4)_4(UO_2)]$ (**5.3**) and $Rb_{4.4}K_{0.6}[(UO_2)_6O_4F(PO_4)_4(UO_2)]$ (**5.4**), and a new sheet anion topology that is observed for both a pure oxide, $Cs_{11}[(UO_2)_{12}(PO_4)_3O_{13}]$ (**5.1**), and an oxyfluoride, $Rb_{11}[UO_2)_{12}(PO_4)_3O_{12}F_2]$ (**5.2**).

**Experimental:**

**Synthesis.** Compounds **5.1**-**5.4** were synthesized via molten flux methods using alkali chloride fluxes.[11, 12] For all reactions $UF_4$ (International Bio-Analytical Industries, powder, ACS grade) was used as the uranium starting material, $AlPO_4$ (Alfa Aesar, powder, 99.99%) was used as the phosphate source, and an alkali halide, CsCl (Alfa Aesar, powder, 99.99%), KCl (Mallinckrodt Chemicals, powder, 99.6%), or RbCl (Alfa Aesar, powder, 99.8%), or a mix thereof was used as a flux. ***Caution!*** *Although the uranium*

*precursor used contained depleted uranium, standard safety measures for handling radioactive substances must be followed.* Generally, all solid reactants were loaded into either an alumina or platinum crucible and heated to 875 °C in 1.5 hours, held at this temperature for 12 hours, then cooled at 6 °C/h to 550 °C or 450 °C depending on the melting point of the flux. After slow cooling, the furnace was shut off and allowed to rapidly cool to room temperature before sonicating the reaction mixtures in water to remove the flux and isolate the crystalline products by vacuum filtration.

$Cs_{11}[(UO_2)_{12}(PO_4)_3O_{13}]$ (**5.1**) was synthesized by loading 1 mmol $UF_4$, 0.25 mmol $AlPO_4$ and 20 mmol of CsCl in a platinum crucible with a loose-fitting platinum lid and was slow cooled to 550 °C. The reaction produced red tablets (Figure 5.1) in a nearly quantitative yield with no identifiable by-products. $Rb_{11}[UO_2)_{12}(PO_4)_3O_{12}F_2]$ (**5.2**) was obtained by loading 0.5 mmol $UF_4$, 0.125 mmol $AlPO_4$ and 20 mmol of RbCl into a small alumina crucible in a concrete holder with a larger inverted crucible covering it. This mixture was heated as mentioned above and slow cooled to 550 °C and produced similar looking orange-red tablets as in **5.1** in a nearly quantitative yield with no identifiable byproducts.

$Cs_{4.4}K_{0.6}[(UO_2)_6O_4F(PO_4)_4(UO_2)]$ (**5.3**) and $Rb_{4.4}K_{0.6}[(UO_2)_6O_4F(PO_4)_4(UO_2)]$ (**5.4**) were obtained from reactions of 0.5 mmol $UF_4$, 0.2 mmol $AlPO_4$, and 5 mmol CsCl or RbCl and 5 mmol KCl loaded into an alumina crucible covered with an alumina plate held in place by rubber cement. These were heated and slow cooled to 450 °C and produced a yellow crystalline product identified as a mixture of the newly reported F containing phases and either $Cs_xK_{4-x}[(UO_2)_3(PO_4)_2O_2]$ or $Rb_{1.4}K_{2.6}[(UO_2)_3(PO_4)_2O_2]$ that are visibly indistinguishable. The purity and identity of the products were determined by powder X-

ray diffraction (PXRD) using a Bruker D2 Phaser equipped with a LYNXEYE silicon strip detector using a Cu Kα (λ = 1.54056 Å) source.

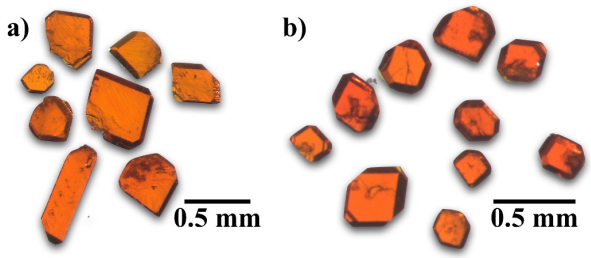


**Figure 5.1:** Optical images of single crystals of 5.1 and 5.2. a) $Cs_{11}[(UO_2)_{12}(PO_4)_3O_{13}]$ (**5.1**) and b) $Rb_{11}[UO_2)_{12}(PO_4)_3O_{12}F_2]$ (**5.2**).

**Structure.** The reported structure solutions were obtained from single crystal X-ray diffraction (SXRD) data collected on a Bruker D8 QUEST diffractometer equipped with an Incoatec IμS 3.0 microfocus radiation source (Mo Kα, λ = 0.71073 Å) and a PHOTON II area detector. The reduction absorption correction was applied to the raw data using SAINT+ and SADABS within the APEX3 software. [13] The SHELXL suite was used within the OLEX2 GUI to solve the structure using SHELXT and refine the solution using SHELXL.[14, 15] The TWINROTMAP functionality in PLATON was used to check for missed symmetry elements and twin laws, where **5.3** and **5.4** were both refined as two component inversion twins with a significant volume fraction of 0.414(6) for **5.3** and a minor twin component of 0.084(8) in **5.4**.[16] Full crystallographic information can be found in Table 5.1.

In all structures the refinement of the U sites is straightforward, while in all structures there is disorder among the alkali cation sites, and in structures **5.1** and **5.2** there

**Table 5.1:** Crystallographic details of structures 5.1-5.4.

| formula | $Cs_{11}[(UO_2)_{12}(PO_4)_3O_{13}]$ **5.1** | $Rb_{11}[UO_2)_{12}(PO_4)_3O_{12}F_2]$ **5.2** | $Cs_{4.4}K_{0.6}[(UO_2)_6O_4F(PO_4)_4(UO_2)]$ **5.3** | $Rb_{4.4}K_{0.6}[(UO_2)_6O_4F(PO_4)_4(UO_2)]$ **5.4** |
|---|---|---|---|---|
| S. G. | *Pnma* | *Pnma* | *Fdd2* | *Fdd2* |
| a, Å | 14.9561(3) | 14.1258(3) | 25.8529(6) | 25.6593(5) |
| b. Å | 17.9663(4) | 18.0121(4) | 28.9285(6) | 27.5792(5) |
| c, Å | 20.8520(4) | 20.6241(4) | 9.2321(2) | 9.2591(2) |
| V, $Å^3$ | 5603.1(2) | 5247.40(19) | 6904.6(3) | 6552.3(2) |
| Crystal size ($mm^3$) | 0.01 x 0.05 x 0.06 | 0.01 x 0.05 x 0.06 | 0.01 x 0.04 x 0.06 | 0.01 x 0.02 x 0.05 |
| Temperature (K) | 300 | 301 | 300 | 300 |
| Density (g $cm^{-3}$) | 6.158 | 5.944 | 5.671 | 5.549 |
| $\theta$ range (deg) | 2.381-36.355 | 2.445-36.353 | 2.446-36.355 | 2.452-36.343 |
| $\mu$ ($mm^{-1}$) | 41.774 | 47.232 | 37.649 | 41.374 |
| Collected reflections | 234955 | 190443 | 177628 | 168495 |
| Unique reflections | 13924 | 13063 | 8388 | 7945 |
| $R_{int}$ | 0.0485 | 0.0467 | 0.0401 | 0.0171 |
| *h* | *-24 ≤ h ≤ 24* | *-23 ≤ h ≤ 23* | *-43 ≤ h ≤ 43* | *-42 ≤ h ≤ 42* |
| *k* | *-29 ≤ k ≤ 29* | *-30 ≤ k ≤ 30* | *-48 ≤ k ≤ 48* | *-45 ≤ k ≤ 45* |
| *l* | *-34 ≤ l ≤ 34* | *-34 ≤ l ≤ 34* | *-15 ≤ l ≤ 15* | *-15 ≤ l ≤ 15* |
| $\Delta\rho_{max}$ (e $Å^{-3}$) | 3.422 | 3.155 | 2.072 | 1.773 |
| $\Delta\rho_{min}$ (e $Å^{-3}$) | -5.467 | -3.117 | -2.471 | -2.325 |
| *GoF* | 1.111 | 1.128 | 1.141 | 1.081 |
| Extinction coefficient | 0.000066(2) | 0.000011(2) | -- | -- |
| $R_1(F)$ for $F_0^2>2\sigma(F_0^2)$[a] | 0.0262 | 0.0278 | 0.0191 | 0.0179 |
| $R_w(F_0^2)$[b] | 0.0473 | 0.0551 | 0.0379 | 0.0402 |

[a] $R_1 = \Sigma\big||F_0| - |F_c|\big|/\Sigma|F_0|$. [b] $wR_2 = [\Sigma w\left(F_0^2 - F_c^2\right)^2/\Sigma w\left(F_0^2\right)^2]^{1/2}$; $P = (F_0^2 + 2F_c^2)/3$; $w = 1/\left[\sigma^2\left(F_0^2\right) + (0.038P)^2 + 58.7789P\right]$ for **5.1**, $w = 1/\left[\sigma^2\left(F_0^2\right) + (0.0117P)^2 + 51.4853P\right]$ for **5.2**, $w = 1/\left[\sigma^2\left(F_0^2\right) + (0.0032P)^2 + 174.9170P\right]$ for **5.3**, and $w = 1/\left[\sigma^2\left(F_0^2\right) + (0.0146P)^2 + 96.7826P\right]$ for **5.4**.

is disorder in one of the phosphate tetrahedra. Generally, the disorder in the alkali sites was treated by freely refining the sites as Cs or Rb as appropriate, and if less than one, then it was assumed that either the sites is shared by a smaller alkali cation, $K^+$ in **5.3** and **5.4**, or a disordered site across multiple positions. The presence of significant nearby electron density peaks suggests a disordered site, while the absence of these suggests sharing of the site between Cs/K or Rb/K. Mixed sites, and multiple disordered sites were constrained to occupancies of one using free variables or SUMP commands in cases of more complicated disorder, and the use of ISOR and EADP commands were implemented to constrain thermal parameters.

In structures **5.1** and **5.2** there is severe disorder in the Cs/Rb alkali cations that reside between the uranium phosphate sheets. In **5.1**, Cs1 is split across three sites, Cs1A, Cs1B, and Cs1C with occupancies of 0.528(10), 0.274(14), 0.196(17), respectively, where the sum of the three is constrained to 1 using a SUMP command. Cs2A/2B and Cs4A/4B are constrained to an occupancy of 1 using a free variable resulting in occupancies of 0.63(2)/0.37(2), and 0.50(4)/0.50(4), respectively. A SUMP command was necessary for constraining sites Cs7A and Cs7B, as Cs7B is projected through a mirror plane, and therefore the sum of Cs7A and two Cs7B were constrained to one. Additionally, an ISOR restraint was used on Cs1B and Cs1C to enforce reasonable thermal displacement parameters. The Rb cations in **5.2** were handled in a similar manner, where Rb1A/1B, Rb3A/3B, Rb4A/4B were constrained using free variables that resulted in occupancies of 0.913(3)/0.087(3), 0.83(3)/0.17(3), and 0.921(4)/0.079(4), respectively, and sites Rb7A, Rb7B, and Rb7C were constrained using a SUMP command resulting in occupancies of 0.043(3), 0.187(13), and 0.0969(19), respectively.

Similar methods were used in the refinement of **5.3** and **5.4**; however, these structures contain two different alkali species. In both structures the A1 site is shared by both Cs (or Rb) and K. This was determined by freely refining the sites as Cs (or Rb) and the absence of additional q-peaks and an occupancy level significantly less than one suggests the site is best modeled as a mixture of Cs/K or Rb/K. In **5.3** the Cs1/K1 occupancies are 0.389(5)/0.611(5) and in **5.4** the Rb1/K1 occupancies are similar at 0.413(11)/0.587(11). In both structures there is disorder on the A3 site, split across two sites, A3A and A3B, with occupancies of 0.837(2) and 0.163(2) for Cs3A/Cs3B in **5.3** and 0.700(2) and 0.300(2) for Rb3A/Rb3B in **5.4**.

In structures **5.1** and **5.2** the P3 site is half occupied because it is disordered across a mirror plane and the two disordered sites are too close to both be fully occupied sites. This is also true for O23, O27, O28 which are coordinated to P3 and O29 coordinated to P1 in **5.1**, and O28A and F28B in **5.2**. Labeling all sites within the coordination sphere of the U sites as O in structures **5.2**-**5.4**, does not result in charge balance, as there is an excess of negative charge. This could not be resolved by reasonable models of the alkali cation disorder and this observation, along with the identification of F in all three structures by EDS in both powdered and singly crystalline forms, confirms the presence of F. While the fluorine site could be easily located in structure **5.2** by using bond valence sums (BVS) and knowledge of U coordination chemistry (discussed in structure description), it was not easily identified in **5.3** and **5.4**. In **5.3** and **5.4** the O3 site was fixed as a half occupied O/F shared site to maintain charge balance in the crystallographic solution, and this arbitrary assignment will be discussed in later sections. EDS was used to verify the presence of F in **5.2**-**5.4** and all other elements present in each single crystal used for structure determination

as well as in bulk powder samples of **5.1** and **5.2.** Data were collected on a TESCAN Vega-3 SBU equipped with an EDS detector.

**Optical Spectroscopy.** UV-vis and fluorescence measurements were performed on bulk powder samples of **5.1** and **5.2** using a PerkinElmer Lambda 35 UV-vis scanning spectrophotometer equipped with an integrating sphere and a PerkinElmer LS55 Luminescence spectrometer. The UV-vis diffuse reflectance data were internally converted using the Kulbelka-Munk equation and then normalized.[17] Fluorescence excitation spectra were collected at emission wavelengths of 574 nm and 564 nm for **5.1** and **5.2**, respectively, and emission spectra were collected at an excitation wavelength of 437 nm for both **5.1** and **5.2**.

**Ion Exchange.** Ion exchange experiments were performed on powder and single crystalline samples of $Cs_{11}[(UO_2)_{12}(PO_4)_3O_{13}]$ (**5.1**) and $Rb_{11}[UO_2)_{12}(PO_4)_3O_{12}F_2]$ (**5.2**) where 20 mg of sample was soaked in ~4 mL of concentrated salt solution in a drying oven set to 90 °C for 3 days. The Rb analog, **5.2**, was soaked in 11 m CsCl solutions while the Cs analog, **5.1**, was soaked in 7 m RbCl or 4 m KCl solutions. Products were examined by EDS and PXRD as described above.

**First Principles Calculations.** We used first-principles calculations using the density functional theory (DFT) code VASP (Vienna Ab-initio Simulation Package)[18, 19] employing the projector augmented wave (PAW) method[20, 21] and generalized gradient approximation of Perdew, Burke and Ernzerhof (PBE)[22] to model the systems. These were spin-polarized calculations, using a plane wave basis set with an energy cut-off of 520 eV to expand the electronic wave functions, and $10^{-6}$ eV energy convergence criteria. A 2×2×2 **k**-point mesh was used for sampling the Brillouin zone. The ground state geometries at 0

K were obtained by relaxing the cell volume, atomic positions, and cell symmetry until the maximum forces on each atom were less than 0.01 eV/Å. To better represent the correlated nature of the U *f*-electrons, we employed the DFT+*U* method,[23, 24] with a $\boldsymbol{U_{eff}}$ for the U atoms of 4.0 eV ($\boldsymbol{U_{eff} = U - J}$, with $U = 4.0$ eV, and $J = 0.0$ eV). The $\boldsymbol{U_{eff}}$ value was chosen to be close to that obtained from related experimental results for $UO_2$. [25, 26] The valence electron configurations were [U] $6s^2 6p^6 5f^3 6d^1 7s^2$, [Cs] $5s^2 5p^6 6s^1$, [P] $3s^2 3p^3$, [O] $2s^2 2p^4$, and [F] $2s^2 2p^5$, respectively.

We used the experimentally generated CIF files for the $Rb_{11}(UO_2)_{12}(PO_4)_3O_{12}F_2$ and $Cs_{11}(UO_2)_{12}(PO_4)_3O_{13}$ compounds as starting structures in our DFT calculations. As mentioned previously, the alkali atom sites were freely refined, yielding a multiple alkali atom sites with different occupancies. To model the alkali atom partial occupancies, we would need to generate a very large supercell, which would be prohibitively costly to run DFT calculations. Therefore, when generating the structures for the DFT calculations, we took the weighted average of the neighboring alkali atoms as the alkali atom position. Also, we made sure that the generated structures have the same symmetry as the experimentally synthesized compounds.

In an effort to understand why Rb forms an oxyfluoride while Cs only an oxide, we also considered the two opposite cases, $Rb_{11}(UO_2)_{12}(PO_4)_3O_{13}$ and $Cs_{11}(UO_2)_{12}(PO_4)_3O_{13}F_2$. Because the oxide and oxyfluoride compounds have different composition, we cannot directly compare their calculated total energies, i.e., thermodynamic stability. Therefore, we need to investigate their relative stability by analyzing the reaction enthalpies, $\boldsymbol{\Delta_r H}$, considering the two reactions:

$$\mathbf{12UF_4 + 3AlPO_4 + 11RbCl + \frac{37}{2}O_2 \longrightarrow Rb_{11}(UO_2)_{12}(PO_4)_3O_{12}F_2 + 3AlF_3 + \frac{37}{2}F_2 + \frac{11}{2}Cl_2} \qquad \mathbf{(1)}$$

$$12UF_4 + 3AlPO_4 + 11CsCl + \frac{37}{2}O_2 \longrightarrow Cs_{11}(UO_2)_{12}(PO_4)_3O_{13} + 3AlF_3 + \frac{39}{2}F_2 + \frac{11}{2}Cl_2 \quad (2)$$

The $\Delta_r H$, values were calculated using:

$$\Delta_r H = \sum_{i=\text{products}} c_i \Delta_f H(i) - \sum_{j=\text{reactants}} c_j \Delta_f H(j), \quad (3)$$

where $\Delta_f H$ are the formation energies per formula unit of the products, *i*, and reactants, *j*, and the sum is over all products and reactants. $c_i$ and $c_j$ are the stoichiometric coefficients of the products and reactants, respectively. For each of the reactants and products we calculated their $\Delta_f H$ using the same VASP calculations input parameters listed above.

DFT gives only the reaction enthalpy at 0 K, and to include the temperature effect on the reactions, we calculate the finite temperature quasi-Gibbs formation energies, $\Delta_f g$,using the equation:

$$\Delta_f g = \Delta_f H - TS_{\text{conf}}. \quad (4)$$

$S_{\text{conf}}$ is the configurational entropy, defined as:

$$S_{\text{conf}} = k_b \sum_i x_i \ln(x_i) \quad (5)$$

where $k_b$ is the Boltzmann constant, $x_i$ is the mole fraction of the constituent *i*, and the sum is over each constituent *i* in the compound. Note that in our calculations we do not consider the vibrational contribution to the entropy because due to their very large size, calculating this term for the title compounds is outside the current capabilities of DFT, and hence the term quasi-Gibbs energy. In the case of the gases $O_2$, $F_2$, and $Cl_2$, we use tabulated values for the standard entropies. [27]

**Results and Discussion:**

**Synthesis.** There have been numerous reported uranium phosphate containing structures prepared by similar synthetic methods using $UF_4$, $AlPO_4$, and alkali chloride fluxes, predominantly loaded into alumina crucibles and heated at a temperature of 875

°C.[3, 4, 28, 29] $Cs_{11}[(UO_2)_{12}(PO_4)_3O_{13}]$ (**5.1**) and $Rb_{11}[UO_2)_{12}(PO_4)_3O_{12}F_2]$ (**5.2**) were first discovered as the minor product, previously unidentified red tablets, in the synthesis of $Cs_6[(UO_2)_7O_4(PO_4)_4]$ and $Rb_6[(UO_2)_7O_4(PO_4)_4]$, respectively.[28] The optimization of the Cs containing analog lead to the use of platinum crucibles, and was successful, but when using analogous synthetic techniques for the Rb analog, only simple rubidium oxides, such as $Rb_2U_2O_7$, were obtained in platinum crucibles. The use of alumina crucibles for the synthesis of $Rb_{11}[UO_2)_{12}(PO_4)_3O_{12}F_2]$ (**5.2**) proved necessary, although the reason is not well understood. Structures **5.3** and **5.4**, related to the phosphuranylite topology, were discovered when trying to optimize synthetic conditions for $Cs_{1.4}K_{2.6}[(UO_2)_3O_2(PO_4)_2]$, $Cs_{1.7}K_{4.3}[(UO_2)_5O_5(PO_4)_2]$, $Rb_{1.4}K_{2.6}[(UO_2)_3O_2(PO_4)_2]$ and $Rb_{1.6}K_{4.4}[(UO_2)_5O_5(PO_4)_2]$. The synthesis of these phases is described and discussed in a recent publication which concluded that higher flux to reactant ratios (40 mmol flux to 0.5 mmol $UF_4$) favored the formation of the phases $Cs_{1.4}K_{2.6}[(UO_2)_3O_2(PO_4)_2]$ and $Rb_{1.4}K_{2.6}[(UO_2)_3O_2(PO_4)_2]$, while 20 mmol of flux and 0.5 mmol $UF_4$ lead to synthesis of $Cs_{1.4}K_{2.6}[(UO_2)_3O_2(PO_4)_2]$ and $Cs_{1.7}K_{4.3}[(UO_2)_5O_5(PO_4)_2]$ or $Rb_{1.4}K_{2.6}[(UO_2)_3O_2(PO_4)_2]$ and $Rb_{1.6}K_{4.4}[(UO_2)_5O_5(PO_4)_2]$, which could not be successfully separated.[4] The title phases, $Cs_{4.4}K_{0.6}[(UO_2)_6O_4F(PO_4)_4(UO_2)]$ (**5.3**) and $Rb_{4.4}K_{0.6}[(UO_2)_6O_4F(PO_4)_4(UO_2)]$ (**5.4**), were obtained simultaneously with $Cs_{1.4}K_{2.6}[(UO_2)_3O_2(PO_4)_2]$ and $Rb_{1.4}K_{2.6}[(UO_2)_3O_2(PO_4)_2]$ by further reducing the flux to reactants ratio to 10 mmol and 5mmol of flux with 0.5 mmol $UF_4$; unfortunately, the title compounds could not be separated manually from $Cs_{1.4}K_{2.6}[(UO_2)_3O_2(PO_4)_2]$ and $Rb_{1.4}K_{2.6}[(UO_2)_3O_2(PO_4)_2]$, as all crystallize as yellow plates.

$Cs_{4.4}K_{0.6}[(UO_2)_6O_4F(PO_4)_4(UO_2)]$ (**5.3**) and $Rb_{4.4}K_{0.6}[(UO_2)_6O_4F(PO_4)_4(UO_2)]$ (**5.4**) contain relatively small amounts of potassium, and attempts were made to synthesize potassium-free Cs and Rb analogs of this uranyl oxyfluoride based on the phosphuranylite sheet topology; however, none were successful as pure CsCl or RbCl fluxes lead to the synthesis of **5.1**, **5.2**, $Cs_6[(UO_2)_7O_4(PO_4)_4]$, $Rb_6[(UO_2)_7O_4(PO_4)_4]$, $Cs_3[Al_2O(PO_4)_3][(UO_2)_3O_2]$, $Rb_3[Al_2O(PO_4)_3][(UO_2)_3O_2]$, or a mixture of these products.

**Structure.** $Cs_{11}[(UO_2)_{12}(PO_4)_3O_{13}]$ (**5.1**) and $Rb_{11}[UO_2)_{12}(PO_4)_3O_{12}F_2]$ (**5.2**) crystallize in the orthorhombic space group *Pnma* with lattice parameters $a$ = 14.9561(3), $b$ = 17.9663(4), $c$ = 20.8520(4), and $a$ = 14.1258(3), $b$ = 18.0121(4), $c$ = 20.6241(4), respectively. To our knowledge, the sheet topology present in both structures is unreported in the literature and can be deconstructed into units of the β-$U_3O_8$ topology as shown in Figure 5.2a. The β-$U_3O_8$ topology can be deconstructed into $U_3O_{16}$ and $U_2O_{14}$ units, where the $U_3O_{16}$ unit is a square bipyramid, edge-sharing with two pentagonal bipyramids on either side, and the $U_2O_{14}$ unit is two corner-sharing pentagonal bipyramids. These two units alternate to form the β-$U_3O_8$ topology as shown in Figure 5.2a. Structure **5.1** is also built-up of alternating $U_3O_{16}$ and $U_2O_{14}$ units and **5.2** contains the $U_3O_{16}$, $U_2O_{14}$, and $U_2O_{13}F$ units where the pentagonal bipyramids corner share through the F; however, every third $U_3O_{16}$ unit is missing in both structures (Figure 5.2b).

Between the group of four pentagonal bipyramids (two edge sharing $U_2O_{14}$ or $U_2O_{13}F$ units) is a disordered phosphate tetrahedra with two possible orientations as shown in Figure 5.3. Additional phosphate tetrahedra edge share with the $U_2O_{14}$/$U_2O_{13}F$ units that are located between two $U_3O_{16}$ units and corner share to the adjacent group of four pentagonal bipyramids. The disorder in the phosphate tetrahedron, P3 in both structures

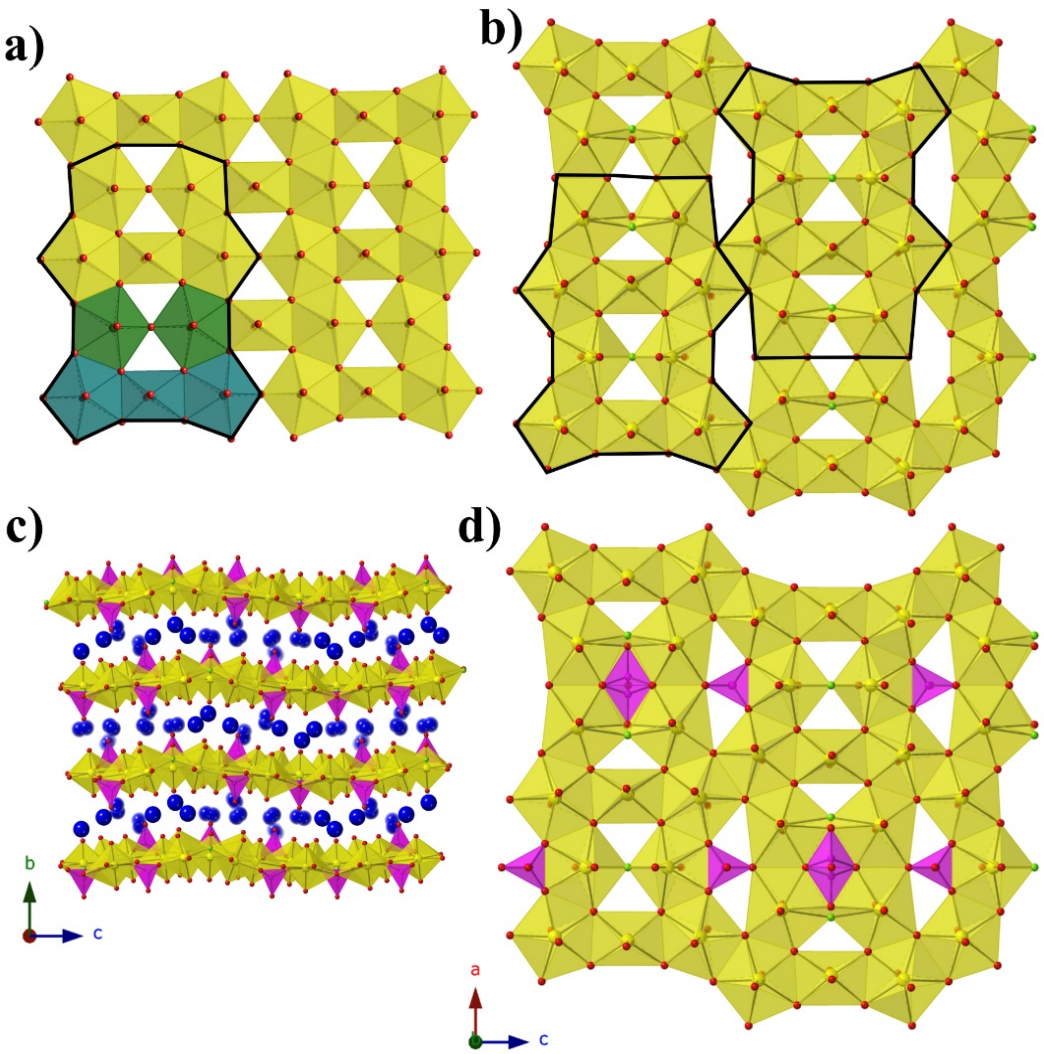


**Figure 5.2**: Sheet topology of 5.1 and 5.2. a) β-$U_3O_8$ topology with building unit outlined in black and $U_3O_{16}$ and $U_2O_{14}$ units shown in blue and green, respectively, b) Topology of **5.1** and **5.2** with building unit boldened, and phosphate tetrahedra omitted. c) View of **5.1** in the *a* direction. d) The sheets found in **5.2**. Uranium, phosphorus, oxygen, and alkali cations are shown in yellow, magenta, red, and blue, respectively.

**5.1** and **5.2**, is slightly different between the two structures as shown in Figure 5.3. In Figure 5.3a, depicting $Rb_{11}[UO_2)_{12}(PO_4)_3O_{12}F_2]$ (**5.2**), the phosphate tetrahedron is half occupied and accompanied by a split oxygen/fluorine site whose occupancies sum to 1. Therefore, either the phosphate tetrahedron points up or down (with respect to the plane of the sheet), where the oxygen site corresponds to the orientation of the phosphate

tetrahedron, and the fluorine site corresponds to the absence of the phosphate tetrahedron. This is supported by the P3-O28A and P3-F28B bond distances which are 1.555(8) and 2.170(8) Å, respectively where the P-F bond is much too long for the tetrahedral coordination environment of $P^{5+}$. Tables of bond valences and bond distances for U and P for all structures are collected in Tables 5.2-5.5 in the supporting information section.

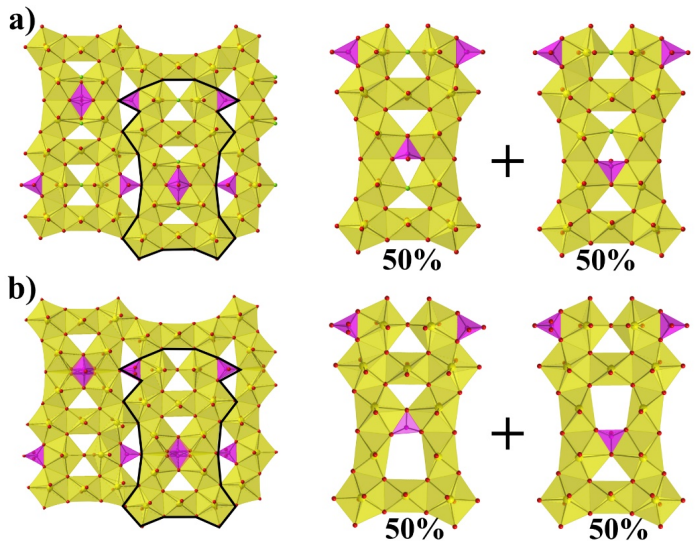


**Figure 5.3:** Sheets in 5.1 and 5.2. a) $Rb_{11}[UO_2)_{12}(PO_4)_3O_{12}F_2]$ (**5.2**) b) $Cs_{11}[(UO_2)_{12}(PO_4)_3O_{13}]$ (**5.1**)

The disorder in the P3 tetrahedron in the Cs analog, structure **5.1**, is similar by virtue of the phosphate tetrahedron pointing up or down within the plane of the sheet; however, the electron density near the O28 site freely refines to a half occupied oxygen site (rather than unity as in **5.2**), and therefore in the absence of the phosphate tetrahedron there are two square bipyramids (Figure 5.3b) as opposed to two corner-sharing pentagonal bipyramids as in **5.2.** The bond valence sums of U6 and U7, the corner-sharing pentagonal bipyramids in **5.2** and the two square bipyramids created by the absence of P3 in **5.1**, are slightly lower at values of 5.749 and 5.767, respectively, for **5.1**, as compared to 5.844 and

5.833, respectively for **5.2**; however, all values are within the accepted range for $U^{6+}$ (~5.6-6.1).[30] Tables of bond valences and bond distances for U and P for all structures are located in the supporting information as Tables 5.2-5.5.

**Table 5.2:** Bond valence sums and bond distances for $Cs_{11}[(UO_2)_{12}(PO_4)_3O_{13}]$ (5.1).

| Interaction | Distance | Interaction | Distance | Interaction | Distance |
|---|---|---|---|---|---|
| U1 – O1 | 1.833(5) | U4-O4 | 2.221(3) | U6-O12 | 2.180(3) |
| U1 – O2 | 1.822(5) | U4-O9 | 2.222(3) | U6-O19 | 2.141(3) |
| U1 – O3 x 2 | 2.541(3) | U4-O14 | 2.253(3) | U6-O20 | 1.825(3) |
| U1 – O4 x 2 | 2.296(3) | U4-O15 | 1.840(4) | U6-O21 | 1.825(4) |
| U1 – O5 | 2.103(5) | U4-O16 | 1.823(4) | U6-O22 | 2.482(2) |
| **BVS U1** | **6.007** | U4-O19 | 2.275(3) | U6-O23 x 0.5 | 2.276(5) |
| U2-O6 | 1.820(5) | **BVS U4** | **5.820** | U6-O23 x 0.5 | 2.697(5) |
| U2-O7 | 1.816(6) | U5-O3 | 2.380(3) | U6-O28 x 0.5 | 2.738(6) |
| U2-O8 x 2 | 2.579(3) | U5-O4 | 2.263(3) | **BVS U6** | **5.749** |
| U2-O9 x 2 | 2.281(3) | U5-O12 | 2.319(3) | U7-O13 | 2.191(3) |
| U2-F5 | 2.127(5) | U5-O13 | 2.327(3) | U7-O14 | 2.143(4) |
| **BVS U2** | **5.873** | U5-O17 | 1.817(3) | U7-O24 | 1.819(4) |
| U3-O8 | 2.382(3) | U5-O18 | 1.821(3) | U7-O25 | 1.816(4) |
| U3-O9 | 2.281(3) | U5-O19 | 2.461(3) | U7-O26 | 2.462(2) |
| U3-O10 | 1.811(5) | **BVS U5** | **5.962** | U7-O27 x 0.5 | 2.294(6) |
| U3-O11 | 1.805(4) | P1-O3 x 2 | 1.527(4) | U7-O27 x 0.5 | 2.756(6) |
| U3-O12 | 2.335(3) | P1-O26 | 1.556(5) | U7-O28 x 0.5 | 2.730(6) |
| U3-O13 | 2.310(3) | P1-O29 | 1.512(8) | **BVS U7** | **5.767** |
| U3-O14 | 2.488(4) | **BVS P1** | **5.058** | P3-O23 | 1.559(6) |
| **BVS U3** | **5.981** | P2-O8 x 2 | 1.536(4) | P3-O27 | 1.544(6) |
| | | P2-O22 | 1.565(4) | P3-O28 | 1.559(6) |
| | | P2-O30 | 1.481(6) | P3-O31 | 1.496(6) |
| | | **BVS P2** | **5.086** | **BVS P3** | 4.944 |

**Table 5.3:** Bond valence sums and bond distances for $Rb_{11}[UO_2)_{12}(PO_4)_3O_{12}F_2]$ (5.2).

| Interaction | Distance | Interaction | Distance | Interaction | Distance |
|---|---|---|---|---|---|
| U1 – O1 | 1.830(6) | U4-O4 | 2.255(3) | U6-O12 | 2.229(3) |
| U1 – O2 | 1.812(6) | U4-O9 | 2.244(3) | U6-O19 | 2.156(3) |
| U1 – O3 x 2 | 2.451(4) | U4-O14 | 2.225(3) | U6-O20 | 1.812(4) |
| U1 – O4 x 2 | 2.222(3) | U4-O15 | 1.837(4) | U6-O21 | 1.812(4) |
| U1 – F5 | 2.245(5) | U4-O16 | 1.821(4) | U6-O22 | 2.557(3) |
| **BVS U1** | **6.095** | U4-O19 | 2.240(3) | U6-O23 | 2.446(2) |
| U2-O6 | 1.822(6) | U4-F28B x 0.5 | 2.931(8) | U6-O28A x 0.5 | 2.569(8) |
| U2-O7 | 1.804(6) | **BVS U4** | **5.935** | U6-F28B x 0.5 | 2.554(7) |
| U2-O8 x 2 | 2.491(4) | U5-O3 | 2.371(4) | **BVS U6** | **5.844** |
| U2-O9 x 2 | 2.228(4) | U5-O4 | 2.327(3) | U7-O13 | 2.244(3) |
| U2-F5 | 2.276(5) | U5-O12 | 2.333(3) | U7-O14 | 2.165(4) |
| **BVS U2** | **5.939** | U5-O13 | 2.289(3) | U7-O24 | 1.802(4) |
| U3-O8 | 2.393(4) | U5-O17 | 1.812(4) | U7-O25 | 1.810(4) |
| U3-O9 | 2.341(4) | U5-O18 | 1.817(4) | U7-O26 | 2.536(3) |
| U3-O10 | 1.821(4) | U5-O19 | 2.329(3) | U7-O27 | 2.460(3) |
| U3-O11 | 1.812(4) | **BVS U5** | **6.080** | U7-O28A x 0.5 | 2.614(7) |
| U3-O12 | 2.301(3) | P1-O3 x 2 | 1.521(4) | U7-F28B x 0.5 | 2.558(7) |
| U3-O13 | 2.320(4) | P1-O26 | 1.521(6) | **BVS U7** | **5.833** |
| U3-O14 | 2.343(4) | P1-O29 | 1.492(10) | P3-O23 | 1.534(5) |
| **BVS U3** | **6.015** | **BVS P1** | **5.256** | P3-O27 | 1.525(6) |
| | | P2-O8 x 2 | 1.552(4) | P3-O28A | 1.555(8) |
| | | P2-O22 | 1.565(5) | P3-O31 | 1.515(6) |
| | | P2-O30 | 1.474(7) | **BVS P3** | **5.034** |
| | | **BVS P2** | **5.007** | | |

**Table 5.4:** BVSs and bond distances for $Cs_{4.4}K_{0.6}[(UO_2)_6O_4F(PO_4)_4(UO_2)]$ (5.3)..

| Interaction | Distance | Interaction | Distance | Interaction | Distance |
|---|---|---|---|---|---|
| U1 – O1 | 1.795(5) | U2 – O3 | 2.298(5) | U3 – O3 | 2.353(5) |
| U1 – O2 | 1.801(5) | U2 – O4 | 2.404(5) | U3 – O6 | 2.280(5) |
| U1 – O3 | 2.231(5) | U2 – O5 | 2.390(5) | U3 – O7 | 2.351(5) |
| U1 – O4 | 2.611(6) | U2 – O6 | 2.333(4) | U3 – O8 | 2.295(6) |
| U1 – O5 | 2.602(6) | U2 – O9 | 1.785(5) | U3 – O12 | 1.794(6) |
| U1 – O6 | 2.245(4) | U2 – O10 | 1.780(5) | U3 – O13 | 1.783(5) |
| U1 – O7 | 2.534(5) | U2 – O11 | 2.351(5) | U3 – O14 | 2.355(5) |
| U1 – O8 | 2.728(7) | **U2 BVS** | **6.145** | **BVS U3** | **6.261** |
| **U1 BVS** | **6.003** | P1 – O7 | 1.540(5) | P2 – O4 | 1.541(5) |
| U4 – O15 | 1.774(9) | P1 – O8 | 1.531(6) | P2 – O5 | 1.537(6) |
| U4 – O16 | 1.755(10) | P1 – O11 | 1.520(5) | P2 – O14 | 1.514(5) |
| U4 – O17 x 2 | 2.278(7) | P1 – O17 | 1.517(6) | P2 – O18 | 1.512(6) |
| U4 – O18 x 2 | 2.293(6) | **BVS P1** | **5.103** | **BVS P2** | **5.119** |
| **BVS U4** | **6.020** | | | | |

**Table 5.5:** BVSs and bond distances for $Rb_{4.4}K_{0.6}[(UO_2)_6O_4F(PO_4)_4(UO_2)]$ (5.4).

| Interaction | Distance | Interaction | Distance | Interaction | Distance |
|---|---|---|---|---|---|
| U1 – O1 | 1.804(5) | U2 – O3 | 2.329(4) | U3 – O3 | 2.405(4) |
| U1 – O2 | 1.795(5) | U2 – O4 | 2.443(4) | U3 – O6 | 2.247(4) |
| U1 – O3 | 2.279(4) | U2 – O5 | 2.419(5) | U3 – O7 | 2.356(4) |
| U1 – O4 | 2.585(5) | U2 – O6 | 2.300(4) | U3 – O8 | 2.268(5) |
| U1 – O5 | 2.569(5) | U2 – O9 | 1.789(5) | U3 – O12 | 1.792(5) |
| U1 – O6 | 2.202(4) | U2 – O10 | 1.773(5) | U3 – O13 | 1.796(5) |
| U1 – O7 | 2.507(5) | U2 – O11 | 2.357(5) | U3 – O14 | 2.369(5) |
| U1 – O8 | 2.877(8) | **U2 BVS** | **6.086** | **BVS U3** | **6.228** |
| **U1 BVS** | **5.984** | P1 – O7 | 1.547(4) | P2 – O4 | 1.549(4) |
| U4 – O15 | 1.771(9) | P1 – O8 | 1.517(6) | P2 – O5 | 1.540(5) |
| U4 – O16 | 1.740(9) | P1 – O11 | 1.519(5) | P2 – O14 | 1.514(5) |
| U4 – O17 x 2 | 2.265(6) | P1 – O17 | 1.514(6) | P2 – O18 | 1.523(6) |
| U4 – O18 x 2 | 2.294(6) | **BVS P1** | **5.143** | **BVS P2** | **5.043** |
| **BVS U4** | **6.112** | | | | |

While EDS identifies the presence (or absence) of fluorine in structures **5.1** and **5.2**, it does not identify the positions of the fluorine sites within structure **5.2**. In order to locate the F sites in **5.2** we calculated BVS for all possible F sites, which includes all oxygen sites coordinated to the uranium sites except for the axial uranyl oxygens, as F on a uranyl oxygen site would be extremely unexpected given the bond order of the ~1.8 Å U-O 'yl' bond (3) and multiple bonds are not possible for F. All of the uranyl U-O bond lengths in **5.2** are between 1.802(4)-1.830(6) Å and show no significant deviation from the expected ~1.8 Å bond length. Bond valence sums of the remaining O atoms are between 1.82 and 2.30 using $r_o$ = 2.051 and $B$ = 0.519 for U-O, [30] $r_o$ = 1.617 and $B$ = 0.370 for P-O, [31] and $r_o$ = 2.081 and $B$ = 0.515 for Rb-O,[31] except for 'O5' and 'O28B' which have low values of 1.42 and 1.28, and which are significantly lower than the expected value of 2. If $r_o$ = 1.98 and $B$ = 0.40 for U-F bonds, [32] these bond valence sums come out to 1.02 and 0.94, respectively, and match well with the expected value of 1 for F; therefore, these sites have been identified as F5 and F28B and are necessary for achieving charge balance in the

structure. For comparison, the bond valence sums for O5 and O28 sites in structure **5.1**, that contains no fluorine, are 1.86 and 1.90, respectively, and therefore these results also support our decision to assign the fluorine sites in **5.2** as F5 and F28B.

$Cs_{4.4}K_{0.6}[(UO_2)_6O_4F(PO_4)_4(UO_2)]$ (**5.3**) and $Rb_{4.4}K_{0.6}[(UO_2)_6O_4F(PO_4)_4(UO_2)]$ (**5.4**) also contain small amounts of fluorine as identified by EDS and by the need for charge balance in the structures. Similar methods as described above were used to identify the fluorine sites(s), again excluding uranyl oxygen sites as possibilities; however, the results are less definitive than the bond valence sums of **5.2**. In **5.3** all O bond valence sums are between 1.92 and 2.22, none of which signal good candidates for fluorine doping, and similarly in **5.4**, the O BVS are between 1.78 and 2.25. This suggests that there is no preferred site for F and for this reason we have arbitrarily set the occupancy of O3 to be half occupied by both F and O, as this site has the lowest BVS in both structures **5.3** and **5.4**, and the rarity of $PO_3F$ tetrahedra leaves O3 and O6 as the most plausible options. $[(UO_2)_5(HPO_4)_3(PO_4)F_4](H_9C_{10}N_2)_3$ synthesized hydrothermally using $PF_6^-$ as the $F^-$ source also contains phosphuranylite related layers and fluorine is present on sites similar to the ones found in **5.3** and **5.4**.[33]

The $Cs_{4.4}K_{0.6}[(UO_2)_6O_4F(PO_4)_4(UO_2)]$ (**5.3**) and $Rb_{4.4}K_{0.6}[(UO_2)_6O_4F(PO_4)_4(UO_2)]$ (**5.4**) structures are similar to the phosphuranylite mineral, $KCa(H_3O)_3[(UO_2)_6O_4(PO_4)_4(UO_2)(H_2O)_8]$,[34] as they contain the same phosphuranylite-type layers constructed of chains of alternating $UO_8$ and $U_2O_{12}$ units connected to adjacent chains through corner- and edge- sharing phosphate tetrahedra (Figure 5.4a). There is also an additional uranium site, square bipyramid, corner sharing with four phosphate tetrahedra to link adjacent sheets, as there is in phosphuranylite (Figure 5.4b). The alkali sites fill the

voids between the uranyl phosphate layers. Several recent papers have further characterized phosphuranylite type layers by the direction in which the phosphate tetrahedra point (up or down orthogonal to the plane of the sheet) and there are seven known isomers.[3, 4, 35] Both structures **5.3** and **5.4** are the uudduuO isomer, observed in the mineral phurcalite,[36] while phosphuranylite is the uudduuS isomer. In addition to the presence of fluorine in the uranyl phosphate sheets, the stacking of the uranyl phosphate sheets in **5.3** and **5.4** is also different from those observed in other phosphuranylite based structures. In phosphuranylite and recently reported phosphuranylite type structures, the chains of $UO_8$ and $U_2O_{12}$ units in adjacent sheets run parallel to each other, while in **5.3** and **5.4** there are two orientations of these chains that alternate between layers, where the torsion angle between chains in two adjacent layers is 37.8°. This is illustrated in Figure 5.4c where parallel layers are shown in yellow, and the layer between these is shown in orange.

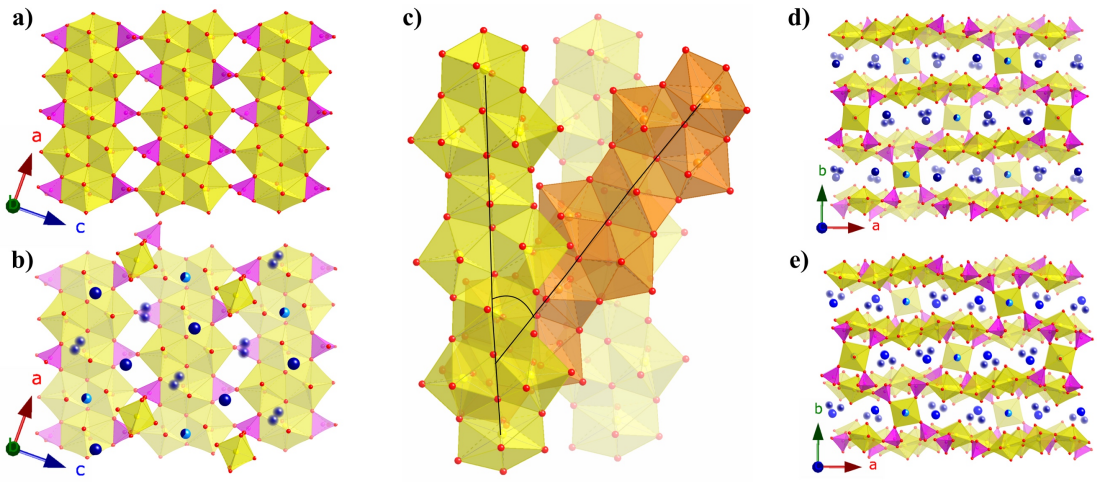


**Figure 5.4:** Structure of 5.3 and 5.4. a) The phosphuranylite layers of **5.3** and **5.4** b) The phosphuranylite layers plus the square bipyramid uranyl sites and alkali cations. c) The 37.8° torsion angle between chains in adjacent layers. d) View of **5.3** e) and **5.4** in the *c* Alkali cations are shown in blues, where blurred spheres are partially occupied sites, and half light/dark blue spheres are shared sites.

**First-Principles Calculations.** As was mentioned previously, Cs prefers to form the oxide structure, while Rb prefers the oxyfluoride structure, and to understand the cause of this different behavior, we studied their reaction enthalpies using DFT. Shown in Table 5.6 are the calculated $\boldsymbol{\Delta_r H}$ values which indicate reactions (1) and (2) are thermodynamically unfavorable, i.e., their $\boldsymbol{\Delta_r H}$ values are positive. Also, the [A, $O_{12}F_2$] compounds have more negative $\boldsymbol{\Delta_r H}$ compared to the respective [A, $O_{13}$] compound, indicating that forming the [A, $O_{12}F_2$] is preferred over the [A, $O_{13}$]. Experimental results confirm that this is the case for the Rb containing compound, it disagrees for that containing Cs. This discrepancy between experiment and calculations may come from the fact that the calculations are performed at 0 K, and thus, finite temperature enthalpy values could provide a different conclusion.

**Table 5.6:** Reaction enthalpies ($\Delta_r H$) and $\Delta\Delta_r H$ of **5.1**, **5.2**, and related phases.

| $A_{11}$ | [A, $O_{12}F_2$] | [A, $O_{13}$] | $\boldsymbol{\Delta\Delta_r H}$ ([A, $O_{13}$] – [A, $O_{12}F_2$]) (kJ/mol/atom) |
|---|---|---|---|
| Rb | 47.02 | 53.90 | 6.88 |
| Cs | 47.14 | 51.23 | 4.09 |

To consider the temperature effect, we calculated the $\Delta_f \boldsymbol{g}$ using Eq. (4), and substituted them in Eq. (3) to obtain the quasi-Gibbs reaction energies, $\Delta_r \boldsymbol{g}$. Shown in Figure 5.5 is the calculated $\Delta_r \boldsymbol{g}$ as a function of the temperature. With increasing temperature the $\Delta_r \boldsymbol{g}$ becomes more negative, eventually becoming < 0 at $T$ > 2200 K, implying that above that temperature the reactions are thermodynamically favorable. It is also important to note that the $\Delta_r \boldsymbol{g}$ of the [Cs, $O_{13}$] compound becomes more negative than the $\Delta_r \boldsymbol{g}$ of the [Cs, $O_{12}F_2$] compound for $T$ > 1900 K, the temperature at which a phase change occurs. Moreover, above the temperature at which the $\Delta_r \boldsymbol{g}$ becomes negative, the

[Cs, $O_{13}$] $\Delta_r g$ is more negative compared to the [Cs, $O_{12}F_2$] $\Delta_r g$, indicating that above 2200 K the formation of [Cs, $O_{13}$] is thermodynamically preferred over the formation of [Cs, $O_{12}F_2$]. The results suggest that the formation of the oxide is driven by the entropy, and that at high enough temperatures, above 2925 K from our calculations, the [Rb, $O_{13}$] can also be formed over the [Rb, $O_{12}F_2$]. Also, note that the difference between the phase change temperatures of the Cs and Rb compounds is 1025 K, which is big enough so that a phase change is observed in one case but not the other. However, the calculated reaction temperature, ~2200 K is much higher than the experimental one, 1148 K. The difference arises from the absence of the other entropic contributions in our calculations, except for the gases. Because of the large size of the systems we are not able to calculate the phonon spectra, whereas introducing the vibrational contribution might lower the calculated reaction temperature to better match the experimental results.

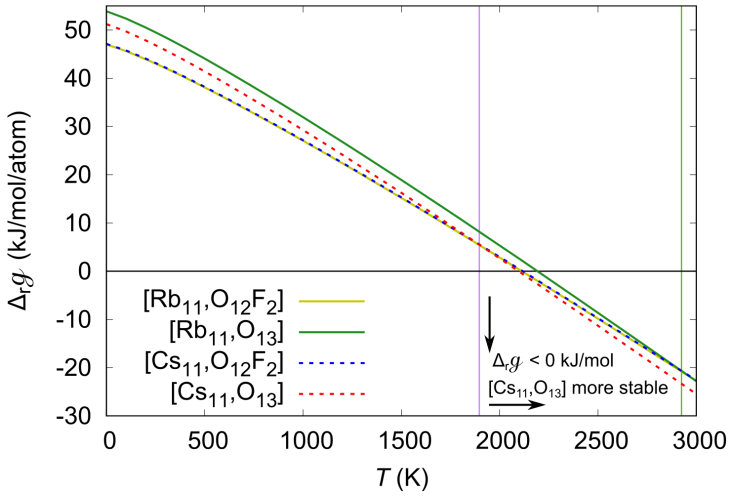


**Figure 5.5:** Quasi-Gibbs reaction energies ($\Delta_r g$) of 5.1, 5.2, and related phases. The purple and green vertical lines respectively show the temperature at which the [Cs, $O_{13}$] and [Rb, $O_{13}$] become more stable than the [Cs, $O_{12}F_2$] and [Rb, $O_{12}F_2$].

**Ion exchange.** The ion exchange products of **5.1** soaked in RbCl and KCl and **5.2** soaked in CsCl show small changes in the PXRD patterns shown in Figures 5.6 and 5.7, indicating the layered structures are maintained throughout the ion exchange process. EDS was used to qualitatively analyze the alkali contents of each sample before and after ion exchange. The results showed that after 3 days of soaking in concentrated salt solution approximately half of the alkali species are exchanged. In the exchange of Cs in **5.1** for Rb and K, the approximate contents of the post ion-exchange products are 5.3 Cs, 5.7 Rb, and 5.4 Cs, 5.6 K, respectively. While in the exchange of Rb for Cs in **5.2**, results in 6.3 Rb, 4.7 Cs.

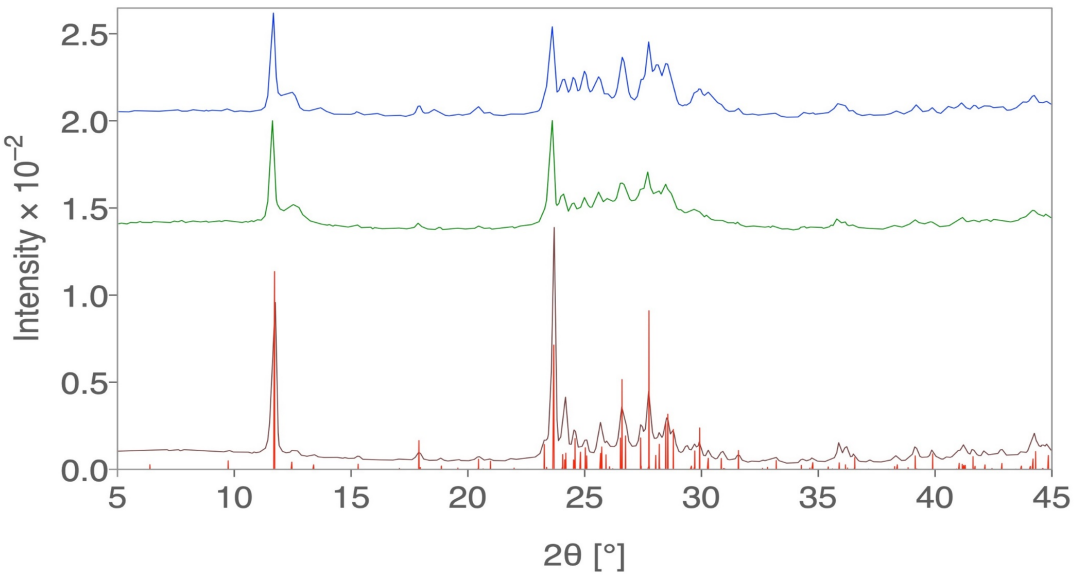


**Figure 5.6**: PXRD patterns for 5.1 and the resulting powder ion exchange products. The pattern of phase pure **5.1** is shown in black, the calculated pattern from the cif file is in red, the ion exchange product from soaking **5.1** in RbCl is shown in green, and the ion exchange product from soaking **5.1** in KCl is shown in blue.

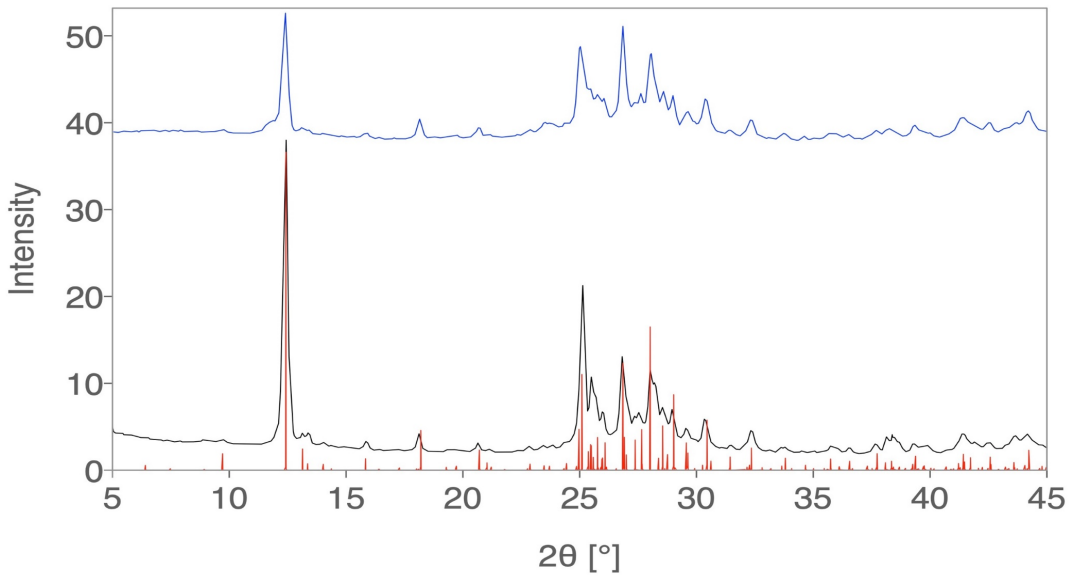


**Figure 5.7:** PXRD patterns for 5.2 and the resulting powder ion exchange product. The pattern of phase pure **5.2** is shown in black, the calculated pattern from the cif file is in red, and the ion exchange product from soaking **5.2** in CsCl is shown in blue.

**Optical Properties**. The UV-vis absorption spectra (Figure 5.8) and fluorescence emission spectra (Figure 5.9) of $Cs_{11}[(UO_2)_{12}(PO_4)_3O_{13}]$ (**5.1**) and $Rb_{11}[UO_2)_{12}(PO_4)_3O_{12}F_2]$ (**5.2**) are typical of $U^{6+}$ species in uranium oxide extended structures. Both **5.1** and **5.2** absorb broadly from 200 to 575 nm and can be classified as semiconductors. A careful look at the DFT calculated density of states (Figure 5.10) showed that these compounds are actually Mott insulators. The ligand to metal charge transfer transitions are at 377 and 379 nm, respectively and the transitions from the $UO_2^{2+}$ core are at 473 and 463 nm, respectively. The maximum fluorescence emission occurs at an excitation wavelength of 437 nm where the emission peak is centered on 574 and 564 nm, respectively for **5.1** and **5.2**.

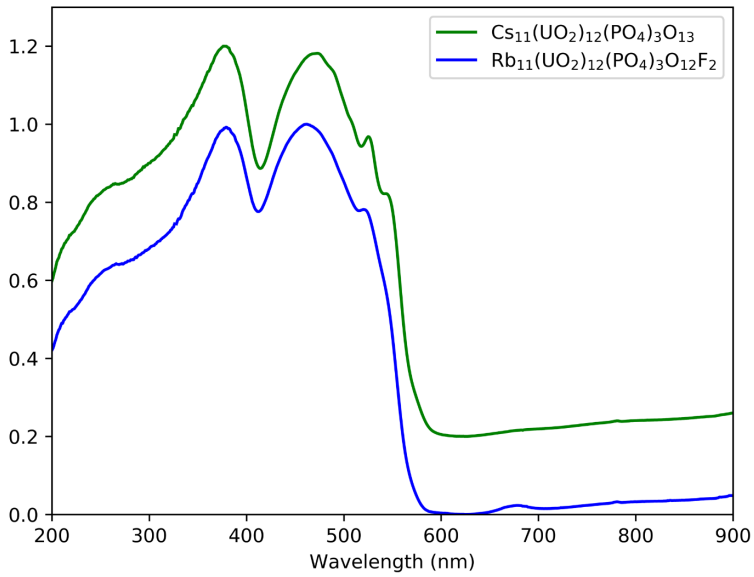


**Figure 5.8:** The UV-vis optical absorption spectra of **5.1** and **5.2**.

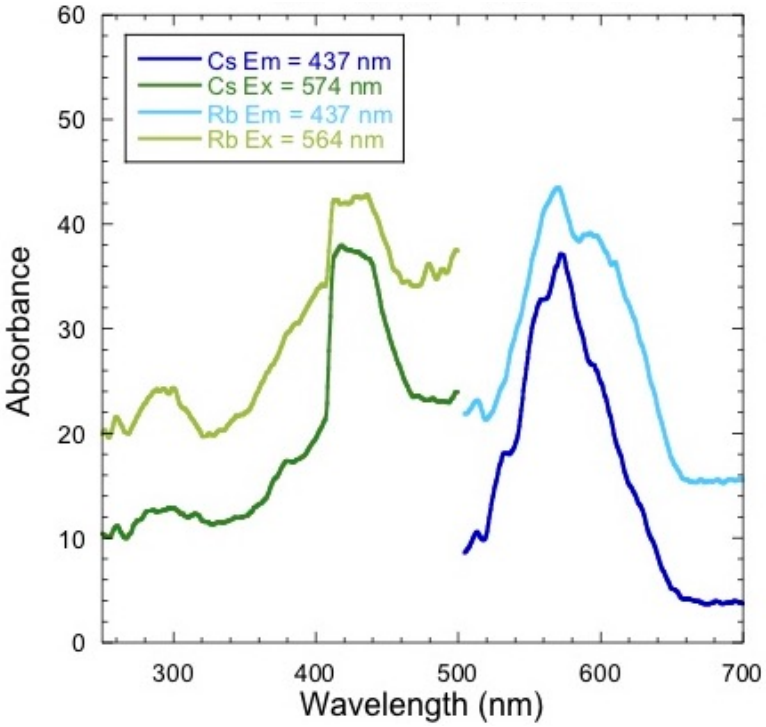


**Figure 5.9:** The fluorescence spectra of 5.1 and 5.2.

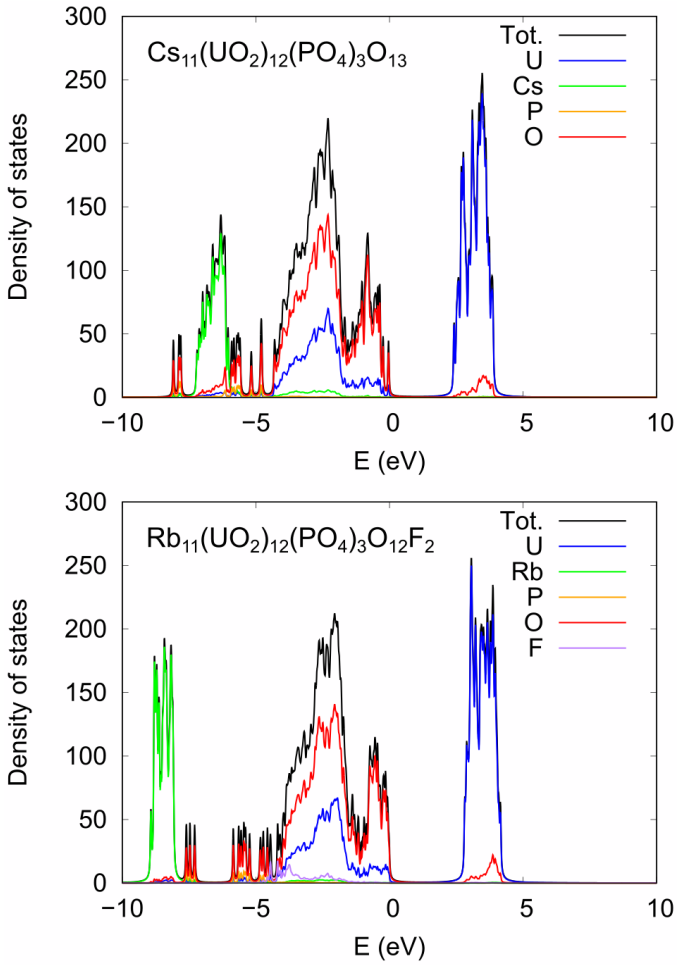


**Figure 5.10:** Density of states (DOS) and atom resolved projected DOS (PDOS) of the 5.1 and 5.2

**Conclusions.** Three new uranyl phosphate oxyfluorides, and one uranyl phosphate, have been synthesized by molten flux methods using alumina crucible reaction vessels and alkali chloride fluxes. Their structures were determined by SXRD and the presence of fluorine was confirmed by qualitative EDS. The location of the fluorine sites was deduced using bond valence sums, although they were inconclusive for determining the location of F in **5.3** and **5.4**. Structures **5.1** and **5.2** were further characterized by PXRD, DFT calculations, ion-exchange experiments, and optical spectroscopy. The DFT calculations support the observation of the Rb, oxyfluoride structures (**5.2**) in contrast to the pure Cs,

oxide structure of (**5.1**), indicating that the formation of pure oxide structure may be driven by entropy, and it might be obtained for both Rb and Cs, given high enough temperatures. The temperature difference in the temperatures at which the pure oxide structures can be obtained is 1025 K between the Rb and Cs, which hints at the reason why we see an oxyfluoride in the Rb containing (**5.2**) and the pure oxide in the Cs (**5.1**) containing phases. Structures **5.1** and **5.2** are capable of alkali ion exchange, where approximately half of the alkali cations in the parent structure can be replaced by a target alkali species in concentrated salt solutions, although the Cs containing structure, **5.1**, undergoes more extensive ion exchange than the Rb analog, **5.2**, perhaps due to the larger interlayer spacing in **5.1**. Alkali chloride fluxes continue to be a viable synthetic technique for crystallizing new uranium phosphate structures containing new structure types and further exploration should continue, in addition to expanding to alkaline fluxes in order to incorporate divalent cations and hopefully obtain new novel structure types.

**Acknowledgements.** Research was conducted by the Center for Hierarchical Wasteform Materials (CHWM), an Energy Frontier Research Center (EFRC). Research was supported by the U.S. Department of Energy, Office of Basic Energy Sciences, Division of Materials Sciences and Engineering under Award DE-SC0016574. C. Juillerat is additionally supported by an NSF IGERT Graduate Fellowship under grant number 1250052. V. Kocevski and T. M. Besmann acknowledge the use of computational resources provided by the National Energy Research Scientific Computing Center (NERSC) and the HPC cluster Hyperion, supported by The Division of Information Technology at University of South Carolina.

**References:**


(1) zur Loye, H.-C.; Besmann, T.; Amoroso, J.; Brinkman, K.; Grandjean, A.; Henager, C. H.; Hu, S.; Misture, S. T.; Phillpot, S.; Shustova, N. B.; Wang, H.; Koch, R. J.; Gregory Morrison; Dolgopolova, E., Hierarchical Materials as Tailored Nuclear Waste Forms: A Perspective, *Chem. Mater.* **2018**, *30*, 4475-4488.

(2) Lussier, A. J.; Lopez, R. A. K.; Burns, P. C., A revised and expanded structure hierarchy of natural and synthetic hexavalent uranium compounds, *Can. Mineral.* **2016**, *54*, 177-283.

(3) Juillerat, C. A.; zur Loye, H.-C., Crystal Growth and Structure Characterization of Three Layered Uranyl Phosphates and Their Relation to the Phosphuranylite Family, *Cryst. Growth Des.* **2019**, *19*, 1183-1189.

(4) Juillerat, C. A.; Moore, E. E.; Kocevski, V.; Besmann, T. M.; zur Loye, H.-C., A Family of Layered Phosphates Crystallizing in a Rare Geometrical Isomer of the Phosphuranylite Topology: Synthesis, Characterization, and Computational Modeling of $A_4[(UO_2)_3O_2(PO_4)_2]$ (A = alkali metals) Exhibiting Intra-layer Ion Exchange, *Inorg. Chem.* **2018**, *57*, 4726-4738.

(5) Wang, Y.; Duan, T.; Weng, Z.; Ling, J.; Yin, X.; Chen, L.; Sheng, D.; Diwu, J.; Chai, Z.; Liu, N.; Wang, S., Mild Periodic Acid Flux and Hydrothermal Methods for the Synthesis of Crystalline f-Element-Bearing Iodate Compounds., *Inorg. Chem.* **2017 Nov 06**, *56*, 13041-13050.

(6) Read, C. M.; Yeon, J.; Smith, M. D.; zur Loye, H.-C., Crystal growth, structural characterization, cation–cation interaction classification, and optical properties of uranium (vi) containing oxychlorides, $A_4U_5O_{16}Cl_2$ (A= K, Rb), $Cs_5U_7O_{22}Cl_3$, and $AUO_3Cl$ (A=Rb, Cs), *CrystEngComm* **2014**, *16*, 7259.

(7) Latshaw, A. M.; Smith, M. D.; zur Loye, H.-C., Crystal growth and structure of three new neodymium containing silicates: $Na_{0.5}0Nd_{4.50}(SiO_4)_3O$, $Na_{0.63}Nd_{4.37}(SiO_4)_3O_{0.74}F_{0.26}$ and $Na_{4.74}Nd_{4.26}(O_{0.52}F_{0.48})[SiO_4]_4$, *Solid State Sci.* **2014**, *35*, 28-32.

(8) Latshaw, A. M.; Wilkins, B. O.; Hughey, K. D.; Yeon, J.; Williams, D. E.; Tran, T. T.; Halasyamani, P. S.; zur Loye, H.-C., $A_5RE_4X[TO_4]_4$ crystal growth and photoluminescence. Fluoride flux synthesis of sodium and potassium rare earth silicate oxyfluorides, *CrystEngComm* **2015**, *17*, 4654-4661.

(9) Morrison, G.; Smith, M. D.; zur Loye, H.-C., Understanding the Formation of Salt-Inclusion Phases: An Enhanced Flux Growth Method for the Targeted Synthesis of Salt-Inclusion Cesium Halide Uranyl Silicates, *J. Am. Chem. Soc.* **2016**, *138*, 7121-7129.

(10) Leinenweber, K.; Johnson Hennifer, E.; Groy Thomas, L., *Am. Mineral.* **2005**, *90*, 115.

(11) Bugaris, D. E.; zur Loye, H.-C., Materials discovery by flux crystal growth: Quartenary and higher oxides, *Angew. Chem. Int. Ed.* **2012**, *51*, 3780-3811.

(12) Juillerat, C. A.; Klepov, V. V.; Morrison, G.; Pace, K. A.; zur Loye, H.-C., Flux Crystal Growth: A Versatile Technique to Reveal the Crystal Chemistry of Complex Uranium Oxides, *Dalton Trans.* **2019**, *48*, 3162-3181.

(13) Bruker. *APEX3, SAINT+, and SADABS.* Bruker AXS Inc.: Madison, Wisconsin, USA, 2015;

(14) Sheldrick, G. M., Crystal structure refinement with SHELXL, *Acta Cryst.* **2015**, *C71*, 3-8.

(15) Sheldrick, G. M., SHELXT - Integrated space-group and crystal-structure determination, *Acta Cryst.* **2015**, *A71*, 3-8.

(16) Spek, A. L., Structure validation in chemical crystallography, *Acta Cryst.* **2009**, *D65*, 148-155.

(17) Kubelka, P.; Munk, F. Z., Ein Beitrag Zur Optik Der Farbanstriche, *Z. Techn. Phys.* **1931**, *12*, 593-601.

(18) Kresse, G.; Furthmuller, J., Efficient iterative schemes for \sl ab-initio total-energy calculations using a plane-wave basis set, *Phys. Rev. B* **1996**, *54*, 11169-11186.

(19) Kresse, G.; Furthmuller, J., Efficiency of ab-initio total energy calculations for metals and semiconductors using a plane-wave basis set, *Comput. Mater. Sci.* **1996**, *6*, 15-50.

(20) Blöchl, P. E., Projector augmented-wave method, *Phys. Rev. B* **1994**, *50*, 17953-17979.

(21) Kresse, G.; Joubert, D., From ultrasoft pseudopotentials to the projector augmented-wave method, *Phys. Rev. B* **1999**, *59*, 1758-1775.

(22) Perdew, J. P.; Burke, K.; Ernzerhof, M., Generalized Gradient Approximation Made Simple, *Phys. Rev. Lett.* **1996**, *77*, 3865-3868.

(23) Anismov, V. I.; Solovyev, I. V.; Korotin, M. A.; Czyzyk, M. T.; Sawatzky, G. A., Density-functional theory and NiO photoemission spectra, *Phys. Rev. B* **1993**, *48*, 16929-16934.

(24) Liechtenstein, A. I.; Anisimov, V. I.; Zaanen, J., Density-functional theory and strong interactions: Orbital ordering in Mott-Hubbard insulators, *Phys. Rev. B* **1995 Aug**, *52*, R5467-R5470.

(25) Schoenes, J., Recent specroscopic studies of $UO_2$, *J. Chem. Soc., Faraday Trans. 2* **1987**, *83*, 1205-1213.

(26) Kotani, A.; Takao, Y., Systematic Analysis of Core Photoemission Spectra for Actinide Di-Oxides and Rare-Earth Sesqui-Oxides, *Prog. Theor. Phys. Suppl.* **1992**, *108*, 117-131.

(27) Jr., M. W. C., NIST-JANAF thermochemical tables fourth edition part I, Al-Co, *J. Phys. Chem. Ref. Data, Monogr.* **1998**, *9*, 811, 1099, 1745.

(28) Juillerat, C. A.; Moore, E. E.; Besmann, T. B.; zur Loye, H.-C., Observation of an Unusual Uranyl Cation-Cation Interaction in the Strongly Fluorescent Layered Uranyl Phosphates $Rb_6[(UO_2)_7O_4(PO_4)_4]$ and $Cs_6[(UO_2)_7O_4(PO_4)_4]$, *Inorg. Chem.* **2018**, *57*, 3675-3678.

(29) Juillerat, C. A.; Klepov, V. V.; Alekseev, E. V.; zur Loye, H.-C., Overstepping Löwenstein's Rule – a Route to Unique Aluminophosphate Frameworks with 3D Salt-Inclusion and Ion Exchange Properties, *Inorg. Chem.* **2019**, *58*, 724-736.

(30) Burns, P. C.; Ewing, R. C.; Hawthorne, F. C., The crystal chemistry of hexavalent uranium: polyhedron geometries, bond-valence parameters, and polymerization of polyhedra, *Can. Mineral.* **1997**, *35*, 1551-1570.

(31) Brown, I. D.; Altermatt, D., Bond-valence parameters obtained from a systematic analyses of the inorganic cyrstal structure database, *Acta Cryst.* **1985**, *B41*, 244-247.

(32) Zachariasen, W. H., Bond lengths in oxygen and halogen compounds of d and f elements, *J. Less-Common Met.* **1978**, *62*, 1-7.

(33) Nicholas P. Deifel, K. T. H., Christopher L. Cahill., $PF_6^-$ hydrolysis as a route to unique uranium phosphate materials, *Chem. Commun.* **2008**, 6037-6039.

(34) Demartin, F.; Diella, V.; Donzelli, S.; Gramaccioli, C. M.; Pilati, T., The importance of accurate crystal structure determination of uranium minerals. I. Phosphuranylite $KCa(H_3O)_3(UO_2)_7(PO_4)_4O_4[8H_2O]$, *Acta Cryst.* **1991**, *B47*, 439-446.

(35) Locock, A. J.; Burns, P. C., The crystal structure of bergenite, a new geometrical isomer of the phosphuranylite group, *Can. Mineral.* **2003**, *41*, 91-101.

(36) Atencio, D.; Neumann, R.; Silva, A. J. G. C.; Mascarenhas, Y. P., Phurcalite from Perus, Sao Paulo, Brazil, and redetermination of its crystal structure, *Can. Mineral.* **1991**, *29*, 95-105.

# Chapter 6

## Overstepping Löwenstein's Rule – a Route to Unique Aluminophosphate Frameworks with 3D Salt-Inclusion and Ion Exchange Properties[1]

[1]Reproduced from Juillerat, C. A.; Klepov, V. V.; Alekseev, E. V.; zur Loye, H.-C. *Inorg. Chem.* **2019,** *58*, 724-736. © 2019 American Chemical Society

**Abstract:** The synthesis of four non-Löwenstein uranyl aluminophosphates, $[Cs_{13}Cl_5][(UO_2)_3Al_2O(PO_4)_6]$, $Rb_7[Al_2O(PO_4)_3][(UO_2)_6O_4(PO_4)_2]$, $Cs_3[Al_2O(PO_4)_3][(UO_2)_3O_2]$, $Rb_3[Al_2O(PO_4)_3][(UO_2)_3O_2]$, the first uranyl phosphate salt-inclusion material $[Cs_4Cs_4Cl][(UO_2)_4(PO_4)_5]$ and a related structure $Cs_4[UO_2Al_2(PO_4)_4]$, all prepared by molten flux methods, is reported. All compounds are discussed from the point of view of their structural features favoring in some cases ion exchange properties. Löwenstein's rule, well known in the realm of zeolites, aluminosilicate and aluminophosphate minerals, describes the tendency of tetrahedra (Al, P, Si, Ge) linked by an oxygen bridge to be of two different elements resulting in the avoidance of Al-O-Al bonds. Zeolites and related aluminosilicate/aluminophosphate minerals are traditionally formed under relatively mild temperatures, where zeolites are synthesized using the hydrothermal synthetic technique. Few exceptions to Löwenstein's rule are known among aluminophosphates, and four of the five exceptions are synthesized under either high temperature or high pressure methods. For that reason, the high temperature flux synthesis of four new non-Löwenstein uranyl aluminophosphates realizes a unique synthetic approach to forming the new pyroaluminate based building block, $[Al_2O(PO_4)_6]^{14-}$, that can be easily obtained and employed for the construction of new porous structures.

**Introduction.** Although alternative energy sources have been extensively studied over the past decades in order to meet ever growing energy demands of industry and attain a sustainable energy cycle, nuclear power remains one of the most important and promising power suppliers and will retain this significant role in the future, especially in light of the development of new generations of breeder reactors, such as the thorium molten salt reactor.[1] The nuclear fuel cycle is a well-studied process; however, its final steps,

specifically the separation and disposal of spent nuclear fuel, including control to prevent the migration of radionuclides in the environment, have not yet achieved full implementation. The solution of this problem is still to be found and therefore actinide chemistry attracts significant interest from this applied point of view. Many known classes of inorganic materials have been proposed as matrices for the components of the spent nuclear fuel, particularly mineral-based ones. No universal storage material has been found so far, however, and the important task to develop and evaluate new candidates as host matrices remains.[2]

One of the relatively new classes of materials proposed for radionuclide storage are salt inclusion materials (SIMs), which consist of a covalent metal oxyanion framework containing voids filled by ionic salt lattices. We are particularly interested in three dimensional porous SIMs that are prospective new hosts for the safe, long-term storage of the most abundant radioisotopes found in nuclear waste such as $^{137}Cs$, $^{90}Sr$, $^{129}I$, Pu, and U, which pose significant environmental threats due to their mobility. Salt inclusion materials have the potential to sequester multiple radionuclides due to the presence of both a metal oxyanion framework that can incorporate actinide species, and the salt inclusion that can contain ionic radionuclides.[3] Such porous frameworks also offer additional flexibility by being good candidates for post synthetic modification via ion exchange.

This approach has already been validated by the synthesis of multiple Cs and U containing silicate and germanate SIMs including: $[Cs_3F][(UO_2)(Si_4O_{10})]$, $[Cs_2Cs_5F][[(UO_2)_3(T_2O_7)_2]$ (T = Si, Ge), $[Cs_9Cs_6Cl][(UO_2)_7(Si_6O_{17})_2(Si_4O_{12})]$, $[Cs_2Cs_5F][(UO_2)_2(Si_6O_{17})]$,[4] $[K_3Cs_4F][(UO_2)_3(Si_2O_7)_2]$,[5] $[Cs_6A_2Cl_2][(UO_2)_3(Ge_2O_7)_2]$ (A=Ag, K), and $[Cs_6Cs_{0.71}Cl_{0.71}][(UO_2)_3O_3(Ge_2O_7)]$.[6] In order to achieve better

performance of SIMs for ion exchange and improve their host properties, we aim to expand the library of uranium salt inclusion materials by introducing new framework building blocks, such as borate, molybdate, vanadate, phosphate, and aluminate oxyanions. Several phosphate SIMs are already known, although none contain actinide species, and include $[BaCl][CuPO_4]$,[7] $[Na_2Cs_2Cl_2][Cu_3(P_2O_7)_2]$, $[K_2Cs_3Cl_3][Cu_3(P_2O_7)_2]$, $[Cs_8Cl_6][Cu_7(P_2O_7)_4]$, $[Cs_5Cl_3][Cu_5(P_2O_7)]$,[8] $[CsCl][Na_2Mn_3(P_2O_7)_2]$, $[RbCl][Na_2Mn_3(P_2O_7)_2]$, $[CsCl][Na_2Fe_3(P_2O_7)_2]$, $[RbCl][Na_2Fe_3(P_2O_7)_2]$, $[CsK_2Cl][Fe_3(P_2O_7)_2]$, and $[CsK_2Cl_2][Mn_3(P_2O_7)]$.[9] To date there have not been any reported aluminophosphate SIMs, although aluminophosphate frameworks are numerous.[10–12] Herein we report the first uranium containing phosphate SIM, $[Cs_4Cs_4Cl][(UO_2)_4(PO_4)_5]$ (**6.1**), a layered uranyl aluminophosphate, $Cs_4[UO_2Al_2(PO_4)_4]$ (**6.2**), the first uranium aluminophosphate SIM with 3D salt inclusion component, $[Cs_{13}Cl_5][(UO_2)_3Al_2O(PO_4)_6]$ (**6.3**), and three new uranyl aluminophosphates with 3D frameworks, $Rb_7[Al_2O(PO_4)_3][(UO_2)_6O_4(PO_4)_2]$ (**6.4**), $Cs_3[Al_2O(PO_4)_3][(UO_2)_3O_2]$ (**6.5**), and $Rb_3[Al_2O(PO_4)_3][(UO_2)_3O_2]$ (**6.6**).

Aluminophosphates **6.3**-**6.6** reported in this paper contain $[Al_2O(PO_4)_6]^{14-}$ building blocks that consist of pyroaluminate groups where each $AlO_4$ tetrahedron corner shares with one $AlO_4$ and three $PO_4$ tetrahedra (Figure 6.1). The presence of the Al-O-Al bond among the phosphate tetrahedra breaks Löwenstein's rule, which states that aluminum silicate and aluminum phosphate structures will avoid the formation of Al-O-Al bonds in preference to each aluminate tetrahedron coordinating to four silicate (or phosphate) tetrahedra and vice versa.[13] Löwenstein's rule was developed to explain the non-random substitution of Al in silicate minerals, and also describes trends in synthetic aluminosilicate and aluminophosphate zeolites. In the case of both minerals and zeolites, the synthesis

usually takes place in hydrothermal conditions, with relatively mild temperatures of ~100-200 °C for zeolite synthesis.[14] Theoretical calculations have predicted that the formation of Al-O-Al linkages is energetically unfavorable, but that this could be overcome by excess thermal energy present in high temperature methods of synthesis.[10–12, 15] To date only five aluminophosphate exceptions to Löwenstein's rule have been reported and include ultramarine,[16] $MAlPO_5$ (M = Mg, Fe),[17, 18] $Cs_2Al_2P_2O_9$,[12] and $Li_6Na_3Sr_{14}Al_{11}P_{22}O_{90}$.[15] The latter four compositions were synthesized under high temperature or high pressure conditions, where $MAlPO_5$ was synthesized at 500 °C and 2000 bar and $Cs_2Al_2P_2O_9$ and $Li_6Na_3Sr_{14}Al_{11}P_{22}O_{90}$ were synthesized using molten flux methods with maximum temperatures of 800 °C and 950 °C, respectively. We synthesized structures **6.3**-**6.6** in high temperature molten fluxes, and they do not abide by Löwenstein's rule, further supporting that the excess thermal energy at high temperatures can lead to Al-O-Al linkages.

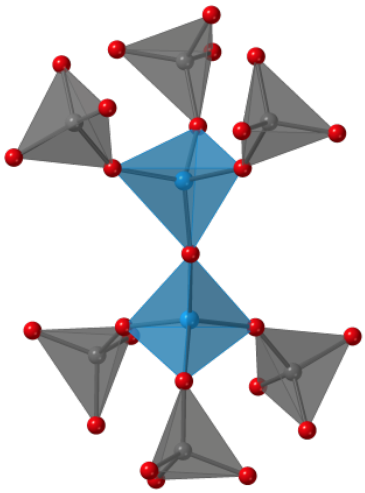

**Figure 6.1:** The $[Al_2O(PO_4)_6]^{14-}$ building block. The pyroaluminate group is blue, phosphate tetrahedra are gray, and oxygen atoms are red.

In addition to the scarcity of non-Löwenstein aluminophosphates, compounds that simultaneously contain uranium, aluminum, and phosphorus are rare and all twelve reported species to date, only seven of which have known crystal structures, are minerals. The known minerals are all layered and built of autinite-type sheets (e.g. sabugalite), phosphuranylite sheets (alutiphite), or novel sheets (kamitugaite).[19–24] Of the seven known crystal structures, only phuralumite, upalite, kamitugaite, and furongite contain Al-O-P linkages and all abide by Löwenstein's rule.

**Experimental:**

**Synthesis.** $UO_2(CH_3CO_2)_2 \cdot 2H_2O$ (International Bio-Analytical Industries, powder, ACS grade), $UF_4$ (International Bio-Analytical Industries, powder, ACS grade), $AlPO_4$ (Alfa Aesar, powder, 99.99%), $(NH_4)_2HPO_4$ (VWR, ACS grade), CsCl (Alfa Aesar, powder, 99%), and RbCl (Alfa Aesar, powder, 99.8%) were used as received. ***Caution!*** *Although the uranium precursors used contained depleted uranium, standard safety measures for handling radioactive substances must be followed.*

$[Cs_4Cs_4Cl][(UO_2)_4(PO_4)_5]$ (**6.1**) was obtained by a reaction between 0.100 g of $UO_2(CH_3CO_2)_2 \cdot 2H_2O$ and 0.0623 g of $(NH_4)_2HPO_4$, molar ratio 1:2, in the presence of 2.60 g of CsCl flux in a platinum crucible. The reaction was carried out at 700 °C for 5 h and then cooled to 620 °C in 7 h. After the reaction cooled to room temperature by switching off the furnace, the flux was dissolved in distilled water and the resulting product was filtered and washed with distilled water and acetone. The product was found to consist of phase pure needle-like yellow crystals with the yield of 26% based on U.

$Cs_4[UO_2(AlP_2O_8)_2]$ (**6.2**) and $[Cs_{13}Cl_5][(UO_2)_3Al_2O(PO_4)_6]$ (**6.3**) can be obtained in a reaction of 0.050 g of uranyl acetate $UO_2(CH_3CO_2)_2 \cdot 2H_2O$, 0.0156 g of diammonium hydrophosphate $(NH_4)_2HPO_4$, and 0.0144 g of aluminum phosphate $AlPO_4$ (molar ratio

1:1:1) in 0.80 g of CsCl flux in a platinum crucible. The crucible was placed into a programmable furnace, ramped up to 700 °C, held at this temperature for 7 hours, and then cooled to 620 °C within another 7 hours. The furnace was shut down and let to cool down to room temperature. The crystals of both phases have a block-like morphology, which makes their manual separation unfeasible. However, large crystals of $[Cs_{13}Cl_5][(UO_2)_3Al_2O(PO_4)_6]$ in the shape of a hexagonal prism can be obtained as a major phase in a reaction of $UO_2(CH_3CO_2)_2 \cdot 2H_2O$ (0.050 g, 0.12 mmol) and $(NH_4)_2HPO_4$ (0.0467 g, 0.35 mmol) in $Al_2O_3$ crucible in the presence of 2.00 g of CsCl as a flux. After fast ramping up to 750 °C, the reaction dwelled for 12 h and then cooled to 540 °C with a rate of 6 °C/h. Upon reaching this temperature, the furnace was shut off and cooled to room temperature. The product was washed with distilled water to dissolve flux and the resulting mixture of both phases was filtered, washed with acetone and dried in air.

Phase pure sample of $Cs_4[UO_2(AlP_2O_8)_2]$ can be obtained by a reaction of 0.100 g of $UO_2(CH_3CO_2)_2 \cdot 2H_2O$ and 0.1868 g of $(NH_4)_2HPO_4$ in a 1:6 molar ratio in the presence of 0.50 g of CsCl flux in an alumina crucible. The reaction was ramped up to 770 °C, held at this temperature for 20 h, and then cooled down to 590 °C in 30 h. After that, the furnace was switched off and cooled to room temperature. The product was separated from the flux by dissolving the flux in distilled water, filtered and washed with acetone. The resulting plate- and block-shaped crystals are $Cs_4[UO_2(AlP_2O_8)_2]$, which was confirmed by PXRD. As the final product contains aluminum, the only possible source of which is the reaction vessel, it appears that CsCl flux dissolves the walls of the alumina crucible, providing the reaction mixture with aluminum. The yield of the product is 72% based on uranium.

In order to obtain a phase pure sample of $[Cs_{13}Cl_5][(UO_2)_3Al_2O(PO_4)_6]$, we performed a solid state reaction between $UO_2(CH_3CO_2)\cdot 2H_2O$, CsCl, $AlPO_4$, $(NH_4)_2HPO_4$, and $CsNO_3$ in the molar ratio 3:5:2:4:8 corresponding to the composition of the targeted compound. A sample containing 0.4240 g (1 mmol) of $UO_2(CH_3CO_2)\cdot 2H_2O$ and the respective amounts of the other reagents were finely ground and heated to 400 °C in a quartz tube to decompose initial reagents. After the mixture was thoroughly ground a second time, it was transferred into platinum crucible and held at 520 °C for 24 h. The purity of the sample was confirmed by PXRD (Figure 6.2).

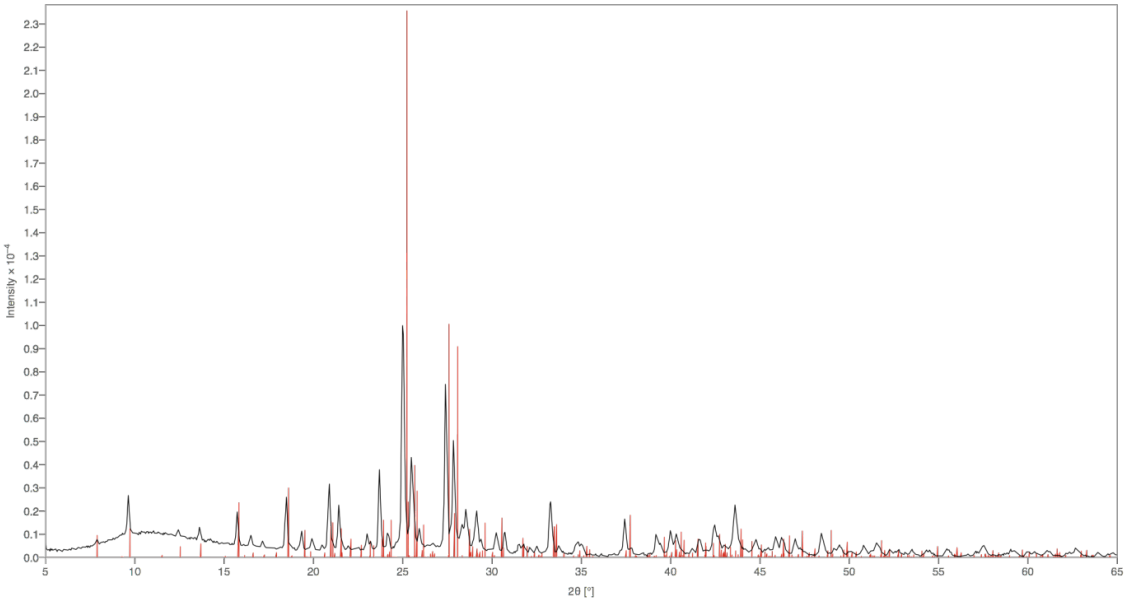


**Figure 6.2**: PXRD pattern of $[Cs_{13}Cl_5][(UO_2)_3Al_2O_7(PO_3)_6]$ (6.3) obtained by a solid state reaction.

$Rb_7[Al_2O(PO_4)_3][(UO_2)_6O_4(PO_4)_2]$ (**6.4**), $Cs_3[Al_2O(PO_4)_3][(UO_2)_3O_2]$ (**6.5**), and $Rb_3[Al_2O(PO_4)_3][(UO_2)_3O_2]$ (**6.6**) were synthesized by molten flux methods[25] using alkali chloride fluxes and alumina reaction vessels. For the Rb containing materials, 0.5 mmol of $UF_4$, 0.33 mmol of $AlPO_4$, and 20 mmol of RbCl flux were loaded into 5 mL alumina

crucibles measuring 2.6 mm high and 1.8 mm in diameter. For $Cs_3[Al_2O(PO_4)_3][(UO_2)_3O_2]$, stoichiometric ratios of U and P were used and 0.5 mmol of $UF_4$, 0.5 mmol of $AlPO_4$, and 10 mmol of CsCl flux were loaded into the same alumina crucibles. A larger inverted alumina crucible was placed over the reaction vessels in a ceramic holder in order to minimize flux volatility issues. All reactions were heated to the target temperature in 1.5 h, held for 12 h, and slow cooled to the desired temperature at 6 °C/h. $Rb_3[Al_2O(PO_4)_3][(UO_2)_3O_2]$ and $Cs_3[Al_2O(PO_4)_3][(UO_2)_3O_2]$ were heated to 775 °C and cooled to 550 °C, while $Rb_7[Al_2O(PO_4)_3][(UO_2)_6O_4(PO_4)_2]$ was heated to 875 °C and cooled to 400 °C. After reactions cooled to the desired temperatures, the furnace was shut off and allowed to reach room temperature before sonicating the reaction vessels in water to dissolve the flux and filter out the crystalline products. All reactions produced yellow rectangular blocks in good yield (>80%) along with minor impurities and were hand-picked to obtain pure samples for optical characterization and ion exchange experiments.

**Ion exchange.** Single crystal to single crystal ion exchange reactions were performed on structures $Cs_3[Al_2O(PO_4)_3][(UO_2)_3O_2]$ (**6.5**), and $Rb_3[Al_2O(PO_4)_3][(UO_2)_3O_2]$ (**6**) by loading 20 mg of single crystals into a 1 dram vial and adding 4 mL of aqueous 4 molal KCl and 6 molal NaCl solutions to crystals of **6.5** and **6.6**, respectively. The 1 dram vials were heated to 90 °C in a mineral oil bath and maintained at this temperature for five days. Afterwards, the crystals were thoroughly rinsed and examined by SXRD and the resulting ion exchange products of **6.5** and **6.6** are $Cs_{2.5}K_{0.5}[Al_2O(PO_4)_3][(UO_2)_3O_2]\cdot 2H_2O$ (**6.7**) and $Na_{2.5}Rb_{0.5}[Al_2O(PO_4)_3][(UO_2)_3O_2]\cdot 2.6H_2O$ (**6.8**), respectively. The details on how these formulas were determined will be discussed in subsequent sections. Bulk ion exchange reactions were also performed on

$Rb_3[Al_2O(PO_4)_3][(UO_2)_3O_2]$ (**6.6**) by using a 30 mg sample of finely ground crystals and soaking it in 6 molal NaCl; PXRD was performed before and after the ion exchange experiment. EDS was used to investigate ratios of the desired alkali metals in both single crystal and powder ion exchange products. A control experiment was performed by soaking a 20 mg powder sample of **6.6** in deionized water for five days at 90 ºC.

**Thermogravimetric Analysis (TGA).** The water content of the bulk ion exchange product of $Rb_3[Al_2O(PO_4)_3][(UO_2)_3O_2]$ (**6.6**) soaked in NaCl solution was investigated using TGA. The data were collected using an SDT Q600 DTA/TGA and the sample was heated in an alumina crucible at a rate of 10 ºC/min from room temperature to 500 ºC under a 100 mL/min nitrogen flow and then allowed to cool to room temperature in air.

**Energy Dispersive Spectroscopy (EDS).** EDS was performed on single crystals of all reported structures and ion exchange products directly affixed to an SEM stub by carbon tape to verify elements present in the samples. Data were collected using a Tescan Vega-3 SEM equipped with a Thermo EDS attachment.

**Optical Measurements.** UV-vis and fluorescence measurements were performed on pure phase samples of **6.1**-**6.6** using a PerkinElmer Lambda 35 UV/vis scanning spectrometer equipped with an integrating sphere and a PerkinElmer LS55 luminescence spectrometer, respectively. UV-vis diffuse reflectance data were internally converted to absorbance using the Kubelka-Munk equation.[26]

**Powder X-ray Diffraction.** A Bruker D2 Phaser equipped with a LYNXEYE silicon strip detector or a Rigaku Ultima IV diffractometer equipped with a DTex detector, which both use Cu K$\alpha$ ($\lambda$ = 1.54056 Å) sources, was used to collect PXRD data. PXRD

patterns were used for product identification and to verify phase purity of samples of compounds **6.1**-**6.6** used for optical measurements.

**Single Crystal X-ray Diffraction.** Single-crystal X-ray diffraction data were collected at 300(2) K on a Bruker D8 QUEST diffractometer equipped with an Incoatec IμS 3.0 microfocus radiation source (MoKα, λ = 0.71073 Å) and a PHOTON II area detector. The crystals were mounted on a microloop with immersion oil. For **6.4**-**6.8** the blocks were cleaved into thin plates and cut to an appropriate size. The programs SAINT+ and SADABS within the APEX 3 software were used to reduce and correct the raw data for absorption effects.[27] The SHELX suite was used within the Olex2 GUI to solve and refine the structure, specifically the SHELXT solution program was used.[28–30] Crystallographic data for all compounds are listed in Table 6.1. The programs ADDSYM and TwinRotMat within PLATON were used to check for missed symmetry elements and minor twin components.[31]

Preliminary unit cell determination for the rod- and needle-like crystals of $[Cs_4Cs_4Cl][(UO_2)_4(PO_4)_5]$ (**6.1**) revealed a body-centered orthorhombic unit cell with lattice parameters $a$ = 9.60, $b$ = 14.18, and $c$ = 25.62 Å. Absorption correction using SADABS program in the orthorhombic crystal system results in $R_{int}$ value of 8.35%, which is slightly higher than expected 4-6% usual for uranium phosphate compounds.[32] Attempts to solve the structure in the orthorhombic unit cell were not successful and did not result in a physically reasonable structural model. Diffraction data were reintegrated using the same lattice parameters with $\beta \approx 90°$ in the monoclinic crystal system. After reintegration $R_{int}$ value decreased to 4.82%, and an initial solution was successfully found in the space group $I2/a$. Despite an overall improvement of the model as compared to the solution in

the orthorhombic unit cell, it still contained high residual electron density peaks and severely distorted $PO_4$ groups, along with high $R_1$ value of ~16%. The model was significantly improved by a twin law (-1 0 0 0 -1 0 0 0 1), which was found by the TwinRotMat program implemented in the PLATON software and corresponds to pseudo-merohedral twinning. The final structure model was refined to $R_1$ = 1.70% in the standard *C*2/*c* setting of the monoclinic space group *I*2/*a*, with (1 0 2 0 -1 0 0 0 -1) twin law.

During initial unit cell determination for the crystals of $[Cs_{13}Cl_5][(UO_2)_3Al_2O(PO_4)_6]$ (**6.3**), a hexagonal unit cell with parameters $a = b = 25.91$, $c = 18.21$ Å was found. Full data integration in this unit cell resulted in unreasonably high $R_{int}$ value; therefore, suggesting that twinning was present. An orthorhombic unit cell with parameters $a = 22.39$, $b = 18.17$, and $c = 12.92$ Å was found using CELL_NOW program along with two other twin components with the same unit cell parameters, which both related to the major component by 120° rotation around the *b* axis.[33] The data were integrated in this unit cell, and a twin law (-0.5 0 1.5 0 1 0 -0.5 0 -0.5) was found using the TwinRotMat program.[31] In order to improve the quality of the final model it was refined as a 3-component twin using the TWIN and BASF instructions. Although the resulting $R_1$ value equal to 6.87% is rather large, the model contained physically reasonable interatomic distances and atomic thermal parameters.

$Rb_7[Al_2O(PO_4)_3][(UO_2)_6O_4(PO_4)_2]$ (**6.4**) crystallizes in the centrosymmetric triclinic space group, $P\bar{1}$, with unit cell parameters of $a = 7.0308(2)$ Å, $b = 14.2573(4)$ Å, $c = 19.7866(5)$ Å, $\alpha = 86.3690(1)$, $\beta = 80.3080(10)°$, and $\gamma = 89.6560(10)°$. The asymmetric unit is large with six uranium sites, 11 rubidium, six phosphorus, four aluminum, and 39 oxygen sites, where all atoms lie on general positions. There is disorder

present in both the aluminophosphate sheet as well as the rubidium cations. All uranium and oxygen sites, as well as the P1, P2, P3, P4, and P5 sites are all free of disorder. The P5A, P5B, Al1A, Al1B, Al2A, Al2B, Rb7A, and Rb7B sites are all 50% occupied, as the pairs (ex. P5A, P5B) are too close to be simultaneously present, and this can be explained by two different possible orientations of the aluminophosphate sheet which will be elaborated on in the discussion section. Rb4, Rb5, and Rb6, freely refine to an occupancy of 1, while the remaining rubidium sites are only partially occupied. The Rb1A, Rb1B, Rb2A, Rb2B, Rb3A, Rb3B pairs were constrained to have a total occupancy of 1, as they all the sites have occupancies less than one and the distances between the two sites in each pair is less than 2.6 Å.

Structures **6.5** and **6.6** crystallize in the orthorhombic space group *Cmce* and have asymmetric units containing two U sites, one Al site, two P sites, 13 O sites, and three disordered cation sites. The three-dimensional uranyl aluminophosphate framework is nearly identical in **6.5** and **6.6** and U2, O3, O7, O8, O9, are characterized by Wyckoff symbol 8*f* with *m* symmetry, P1 and O13 have 2-fold rotational site symmetry with either Wyckoff symbol 8*d* or 8*e*, and all other framework atoms lie on general positions. In **6.5**, Cs1A, Cs2A, and Cs3A are assigned to Wyckoff symbols 8*f*, 8*d*, and 8*e,* respectively, while Rb3A is the only cation site in **6.6** that lies on a special position, in this case 8*e*. All metal atoms in the framework were individually allowed to freely refine and showed no significant deviation from full occupancies of 1. In both structures there is minor disorder in the cation sites that is easily resolved by splitting the site, and/or using SUMP commands to enforce charge balance.

Structures **6.7** and **6.8** are post single crystal to single crystal ion exchange samples and suffer from poor data quality due to the loss of crystal quality during the ion exchange process. The solutions for **6.7** and **6.8** are approximate, but nevertheless confirm the framework survives during the ion exchange process. In **6.8**, the only deviation from the parent framework is the disorder of O13, which is the bridging Al-O-Al oxygen. It is clear that the electron density between the Al atoms is present, however suggests disorder that could not be accurately resolved considering the low crystal quality. The cation sites in **6.7** and **6.8** are heavily disordered, and the model of this disorder is also approximate and supports results of alkali ratios obtained by EDS and thermogravimetric analysis data indicating the presence of water in the channels after aqueous ion exchange. Obviously, the combination of the poor crystal quality of the ion exchanged products and the presence of heavy elements U and Cs or Rb prevents the location of the hydrogen atoms and is of little importance to this study.

In structure **6.7**, the Cs3, Cs2, and Cs1 sites freely refine to approximately 1, 0.5, and 0.8. The half occupancy of Cs2 is chemically reasonable, considering the Cs2-Cs2 distance is 2.430(3) Å, and would be too close for two adjacent fully occupied cation sites. By letting all of these sites freely refine, there are 2.7 Cs per formula unit, which does not charge balance the framework. By modeling Cs1 as partially occupied by both K and Cs, it satisfies charge balance, and freely refines to 0.401(7) K and 0.599(7) Cs. An additional smaller electron density peak remained, and was too small to be a potassium site, and the modeling of it as an alkali site would not allow for charge balance, so it was modeled as a water molecule and the WA1 oxygen freely refines to 1. This model of the disorder within the channels results in 2.6 Cs, 0.4 K, and 2 $H_2O$ per formula unit.

**Table 6.1:** Crystallographic information for structures 6.1-6.8

| Formula | $[Cs_4Cs_4Cl][(UO_2)_4(PO_4)_5]$ | $Cs_4[UO_2Al_2(PO_4)_4]$ | $[Cs_{13}Cl_5][(UO_2)_3Al_2O(PO_4)_6]$ | $Rb_7[Al_2O(PO_4)_3][(UO_2)_6O_4(PO_4)_2]$ |
|---|---|---|---|---|
| Number | **6.1** | **6.2** | **6.3** | **6.4** |
| S. G. | *C2/c* | $P\bar{1}$ | *Pnma* | $P\bar{1}$ |
| a, Å | 27.3192(10) | 10.8280(4) | 22.385(2) | 7.0308(2) |
| b. Å | 14.1800(5) | 10.8502(4) | 18.172(2) | 14.2573(4) |
| c, Å | 9.5900(4) | 13.1692(5) | 12.916(2) | 19.7866(5) |
| $\alpha$, ° | 90 | 84.0600(10) | 90 | 86.3690(10) |
| $\beta$, ° | 110.4000(14) | 81.3360(10) | 90 | 80.3080(10) |
| $\gamma$, ° | 90 | 88.6820(10) | 90 | 89.6560(10) |
| V, $Å^3$ | 3482.0(2) | 1521.29(10) | 5254.0(12) | 1951.16(9) |

**Table 6.1 cont.:** Crystallographic information for structures 6.1-6.8

| Formula | $[Cs_4Cs_4Cl][(UO_2)_4(PO_4)_5]$ | $Cs_4[UO_2Al_2(PO_4)_4]$ | $[Cs_{13}Cl_5][(UO_2)_3Al_2O(PO_4)_6]$ | $Rb_7[Al_2O(PO_4)_3][(UO_2)_6O_4(PO_4)_2]$ |
|---|---|---|---|---|
| Number | **6.1** | **6.2** | **6.3** | **6.4** |
| Crystal size ($mm^3$) | 0.08 × 0.02 × 0.02 | 0.16 × 0.04 × 0.03 | 0.10 × 0.08 × 0.06 | 0.04 × 0.01 × 0.01 |
| Temp. (K) | 300(2) | 300(2) | 300(2) | 300(2) |
| Density ($gcm^{-3}$) | 5.062 | 4.046 | 4.241 | 4.812 |
| $\theta$ range (deg) | 2.266-28.999 | 2.280-27.499 | 2.408-27.500 | 2.460-26.390 |
| $\mu$ ($mm^{-1}$) | 27.188 | 15.560 | 18.649 | 33.848 |
| Collected reflections | 100735 | 30513 | 116182 | 197851 |
| Unique reflections | 4613 | 6960 | 116182* | 18961 |
| $R_{int}$ | 0.0389 | 0.0270 | 0.0669 | 0.0540 |
| $h$ | $-37 \le h \le 37$ | $-14 \le h \le 14$ | $-29 \le h \le 29$ | $-11 \le h \le 11$ |
| $k$ | $-19 \le k \le 19$ | $-14 \le k \le 14$ | $-23 \le k \le 23$ | $-23 \le k \le 23$ |
| $l$ | $-13 \le l \le 13$ | $-17 \le l \le 17$ | $-16 \le l \le 16$ | $-32 \le l \le 33$ |
| $\Delta\rho_{max}$ (e $Å^{-3}$) | 1.289 | 3.025 | 4.472 | 4.342 |
| $\Delta\rho_{min}$ (e $Å^{-3}$) | -1.782 | -1.676 | -3.705 | -4.461 |
| *GoF* | 1.051 | 1.055 | 1.119 | 1.040 |
| $R_1(F)$ for $F_0^2 > 2\sigma(F_0^2)^a$ | 0.0170 | 0.0294 | 0.0687 | 0.0418 |
| $R_w(F_0^2)^b$ | 0.0507 | 0.0822 | 0.1961 | 0.0841 |

*reflections were not merged because of twinning; [a] $R_1 = \Sigma||F_0| - |F_c||/\Sigma|F_0|$. [b] $wR_2 = [\Sigma w(F_0^2 - F_c^2)^2/\Sigma w(F_0^2)^2]^{1/2}$; $P = (F_0^2 + 2F_c^2)/3$; $w = 1/[\sigma^2(F_0^2) + (0.155P)^2 + 45.3606P]$ for **6.1**, $w = 1/[\sigma^2(F_0^2) + (0.195P)^2 + 76.9419P]$ for **6.2**, $w = 1/[\sigma^2(F_0^2) + (0.0524P)^2 + 380.5913P]$ for **6.3**, $w = 1/[\sigma^2(F_0^2) + (0.0097P)^2 + 35.5190P]$ for **6.4**, and $w = 1/[\sigma^2(F_0^2) + (0.0151P)^2 + 387.4263P]$ for **6.5**..

**Table 6.1 cont.:** Crystallographic information for structures 6.1-6.8

| Formula | $[Al_2O(PO_4)_3][(UO_2)_3O_2]^{3-}$ | | | |
|---|---|---|---|---|
| | $Cs_3$ | $Rb_3$ | $Cs_{2.5}K_{0.5}$ x $2H_2O$ | $Na_{2.5}Rb_{0.5}$ x 2.6 $H_2O$ |
| Number | **6.5** | **6.6** | **6.7** | **6.8** |
| S. G. | *Cmce* | *Cmce* | *Cmce* | *Cmce* |
| a, Å | 21.9898(10) | 21.9016(8) | 21.8703(4) | 21.7761(6) |
| b. Å | 14.7796(6) | 14.4801(6) | 14.9507(4) | 14.5323(4) |
| c, Å | 13.9792(6) | 13.9796(7) | 14.0742(3) | 14.0322(4) |
| $\alpha$, ° | 90 | 90 | 90 | 90 |
| $\beta$, ° | 90 | 90 | 90 | 90 |
| $\gamma$, ° | 90 | 90 | 90 | 90 |
| V, $Å^3$ | 4543.2(3) | 4433.5(3) | 4601.93(18) | 4440.6(2) |
| Crystal size ($mm^3$) | 0.05 × 0.04 × 0.02 | 0.04 × 0.02 × 0.01 | 0.04 × 0.04 × 0.01 | 0.04 × 0.04 × 0.01 |
| Temp. (K) | 300(2) | 300(2) | 300(2) | 300(2) |
| Density ($gcm^{-3}$) | 4.666 | 4.355 | 4.590 | 3.999 |
| $\theta$ range (deg) | 2.209-36.342 | 2.228-36.313 | 2.195-25.242 | 2.224-36.350 |
| $\mu$ ($mm^{-1}$) | 26.450 | 28.794 | 25.571 | 23.306 |
| Collected reflections | 228284 | 223235 | 228853 | 221394 |
| Unique reflections | 5626 | 5486 | 5691 | 5512 |
| $R_{int}$ | 0.0446 | 0.0597 | 0.0464 | 0.0559 |
| $h$ | $-36 \le h \le 36$ | $-36 \le h \le 36$ | $-36 \le h \le 36$ | $-36 \le h \le 36$ |
| $k$ | $-24 \le k \le 24$ | $-23 \le k \le 24$ | $-24 \le k \le 24$ | $-24 \le k \le 24$ |
| $l$ | $-23 \le l \le 23$ | $-23 \le l \le 23$ | $-23 \le l \le 23$ | $-23 \le l \le 23$ |
| $\Delta\rho_{max}$ (e $Å^{-3}$) | 2.481 | 5.754 | 5.621 | 10.800 |
| $\Delta\rho_{min}$ (e $Å^{-3}$) | -1.544 | -4.012 | -3.334 | -7.192 |
| *GoF* | 1.146 | 1.143 | 1.268 | 1.134 |
| $R_1(F)$ for $F_0^2 > 2\sigma(F_0^2)^a$ | 0.0165 | 0.0263 | 0.0472 | 0.0582 |
| $R_w(F_0^2)^b$ | 0.0387 | 0.0643 | 0.1135 | 0.1686 |

In structure **6.8,** there are four sites total in the channel, and none of the sites in the channels could be refined as a fully occupied Rb, as none had sufficient electron density. The Rb1/Na1 site was too large to be a fully occupied Na site and is modeled as a mixture of Na and Rb with occupancies of 0.528(11) and 0.472(11), respectively. All other sites in the channel had electron densities smaller than Na. The WA1 site was of sufficient electron density to be modeled as a fully occupied oxygen atom, of a water molecule, and the Na2/WA2 site was modeled as mixture of Na and a water molecule with occupancies of 0.43(8) and 0.57(8), respectively. The remaining site, Na3, freely refines to an occupancy of 0.799 and was fixed to an occupancy of 0.785 in order to satisfy charge balance. This solution to the disorder in the channels results in 2.5 Na, 0.5 Rb, and 2.6 $H_2O$ per formula unit.

**Results and Discussion:**

**Synthesis.** Two different uranium sources were used in the syntheses, $UO_2(CH_3CO_2)_2 \cdot 2H_2O$ and $UF_4$ for **6.1**-**6.3** and **6.4**-**6.6**, respectively. The main difference in the uranium sources is the oxidation state of uranium which is +6 in $UO_2(CH_3CO_2)_2 \cdot 2H_2O$ and +4 in $UF_4$. Under the reaction conditions used, U(IV) oxidizes to U(VI).Additional reactions of **6.4**-**6.6** were carried out using $UO_2(CH_3CO_2)_2 \cdot 2H_2O$, as compared to $UF_4$ to compare the impact of the uranium source on the reaction product, and the same target products were identified by powder diffraction; however, the product was a polycrystalline powder rather than single crystals produced when a $UF_4$ source is used. No additional experiments were carried out and it is possible that further synthetic modifications could be made to result in single crystals using $UO_2(CH_3CO_2)_2 \cdot 2H_2O$ as the uranium source.

Although compounds **6.2** and **6.3** can be obtained in the presence of $AlPO_4$, better yield, size, and quality of the crystals can be achieved when using CsCl flux in an alumina crucible without any additional source of aluminum. This suggests that the CsCl flux is highly reactive towards the walls of the crucible, which are thought to be inert, although there are reported instances of a flux attacking alumina crucible.[34] As a result of these competing processes, the flux slowly dissolves the walls of the crucible, gradually increasing the concentration of aluminum in the system. Gradual and slow variation of one of the parameters in a chemical system, i.e. concentration of the reagents, temperature, etc., is almost always an important condition for obtaining large crystals of good quality. Indeed, the use of $AlPO_4$ in a platinum crucible allowed us to obtain small crystals of **6.2** and **6.3**, which is likely due to the readily soluble $AlPO_4$ oversaturating the melt with respect to aluminum.

Both salt-inclusion compounds **6.1** and **6,3** can be obtained under similar reaction conditions in an alumina crucible. Given their formulae, $[Cs_4Cs_4Cl][(UO_2)_4(PO_4)_5]$ (**6.1**) $[Cs_{13}Cl_5][(UO_2)_3Al_2O(PO_4)_6]$ (**6,3**), the CsCl to $UO_2^{2+}$ molar ratios in the compositions equal 1:4 and 5:3, respectively. This allowed us to hypothesize that introducing more CsCl flux into a reaction mixture would favor **6.3** over **6.1**. In addition, increasing the CsCl flux also introduces more aluminum into the system by increasing the dissolution of the reaction vessel, which also favors the formation of **6.3**. Therefore, although it is intuitively clear an excess of flux would help to the formation of a salt-inclusion phase with higher salt lattice content, it is uncertain which process is more important, because both of them favor the same product.

From our experience, it is unlikely for a salt-inclusion material to be obtained by a solid state reaction, and their preparation is generally favored by an excess of the flux. Therefore, it is quite unusual that compound **6.3**, having a strong excess of CsCl in its composition, can readily be prepared via a solid state reaction. This observation may serve as an indication of its stability and can be explained by the fact that all of the cesium atoms in the structure belong to the salt-inclusion component.

**Ion exchange.** Post-ion exchange single crystals were used to determine the crystal structures of **6.7** and **6.8** and revealed the perseverance of the uranyl aluminophosphate framework, while the sites of the species in the channels and the electron densities of those sites were different from the parent structures. As expected, the crystal quality of **6.7** and **6.8** was worse than the original samples of **6.5** and **6.6** due to the dynamic nature of the ion exchange process. For $Rb_3[Al_2O(PO_4)_3][(UO_2)_3O_2]$ (**6.6**) soaked in NaCl, EDS of the single crystal used for structure determination and the bulk powder sample revealed Na:Rb ratios of 10.5:1 and 2.4:1, respectively. The TGA curve of the powder ion exchange product shown in Figure 6.3 shows a 4.4% weight loss around 100 °C and a gradual 2.2% weight loss from 100-300 °C, where the first loss likely corresponds to surface waters, and the second corresponds to the loss of water molecules from the channels. This was compared to the TGA curve of pristine **6.6** (Figure 6.3) prior to ion exchange showing a 3.6% weight loss around 100 °C before and plateaus at 120 °C, further suggesting that the gradual weight loss between 100-300 °C in the post ion exchange curve is due to waters within the channels of the ion exchange product. The presence of water in the pores of the ion exchange product could be a result of the size difference between Rb and Na. The results from EDS and TGA confirm the successful exchange of Rb for Na and the inclusion of

water in the pores and were used to guide the solution of the crystal structure to arrive at the approximate formula, $Na_{2.5}Rb_{0.5}[Al_2O(PO_4)_3][(UO_2)_3O_2]\cdot 2.6H_2O$ (**6.8**). A PXRD pattern of **6.8** demonstrates good agreement with the cif; however, there are additional unidentified peaks in the pattern shown in Figure 6.4. It is possible that during the ion exchange process the sample begins to partially decompose into other products that could not be identified. These diffraction peaks were not present in the control experiment where **6.6** was heated in only deionized water. It is, therefore, possible that the extremly saturated salt solutions (the solutions used approach the maximum solubilities in water at room temperature) create an excesively harsh environment that causes some sample decomposition. The loss in crystallinity can also be seen in the PXRD pattern, as the $K\alpha_1/K\alpha_2$ splitting observed in the pre ion exchange pattern (Figure 6.5) is no longer present.

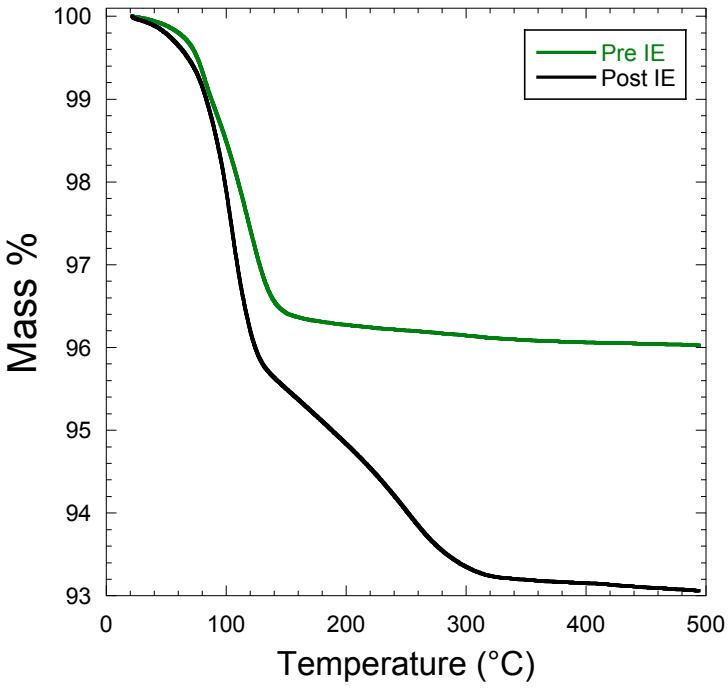


**Figure 6.3:** TGA analysis on powder samples of 6.6 before and after ion exchange with NaCl.

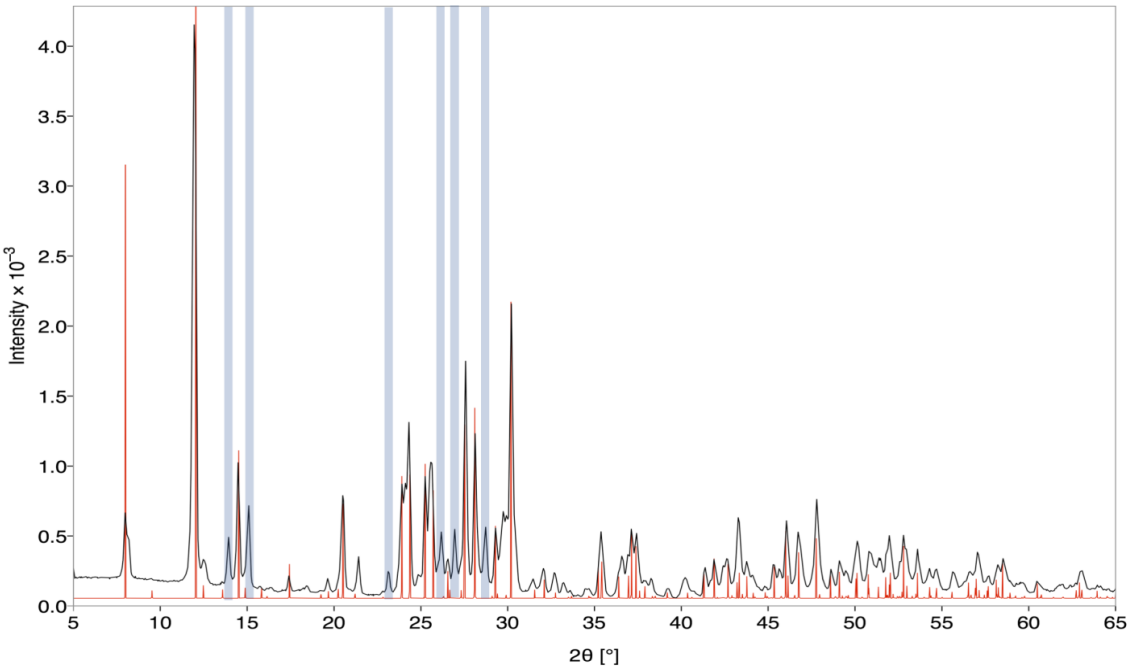


**Figure 6.4:** PXRD pattern of the bulk ion exchange product of 6.6 soaked in NaCl. The calculated pattern from the cif is overlaid in red. Peaks not belonging to the ion exchange product are highlighted in blue.

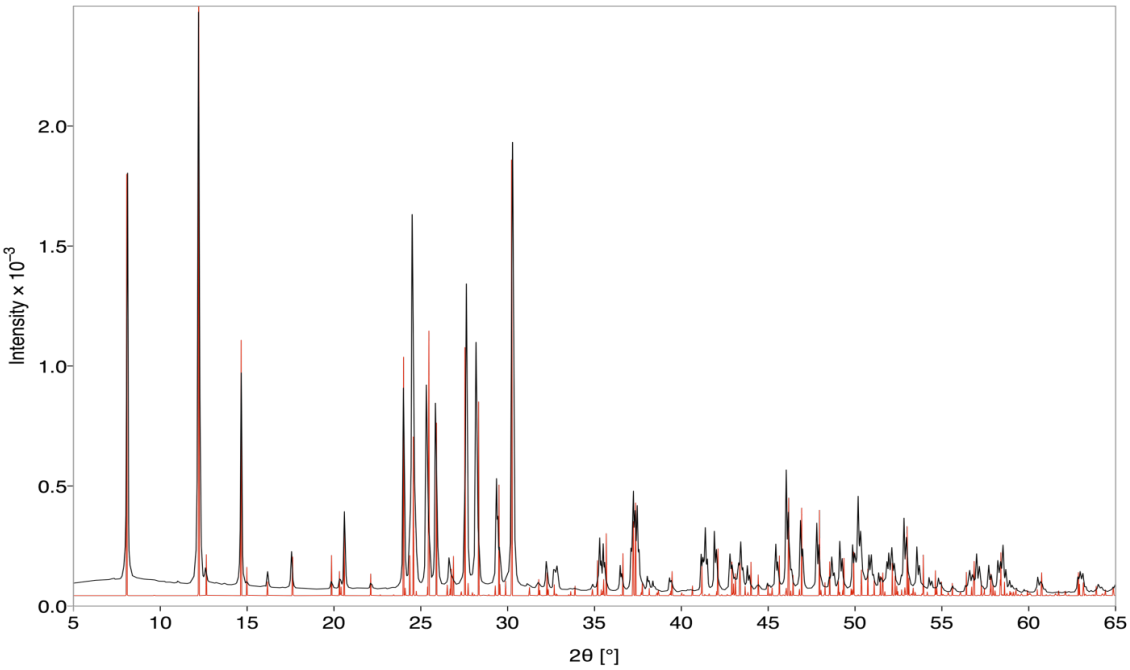


**Figure 6.5:** PXRD pattern of 6.6. The calculated pattern from the cif is overlaid in red.

The EDS results for the single crystal of **6.7** yielded an approximate ratio of Cs:K of 3:1 confirming the incorporation of K into the structures. The composition of **6.7** based on the single crystal diffraction data was determined to be $Cs_{2.5}K_{0.5}[Al_2O(PO_4)_3][(UO_2)_3O_2]\cdot 2H_2O$. The incorporation of sodium into the rubidium parent structure was more complete than the potassium into the cesium parent structure, a result that is likely due to the larger size of the cesium cation as compared to rubidium, which would hinder the removal of cesium from the pores. Similar trends in ion exchange have been recently observed in two families of layered uranyl phosphates.[35, 36]

**Structure.** $[Cs_4Cs_4Cl][(UO_2)_4(PO_4)_5]$ (**6.1**) consists of a $[(UO_2)_4(PO_4)_5]^{7-}$ uranyl phosphate framework with large channels running along the *c* axis that are filled with salt inclusion and Cs atoms. The uranyl phosphate framework is built of $UO_2O_5$ pentagonal bipyramids and $PO_4$ tetrahedra. The uranium coordination polyhedra contain two shorter and five longer bonds, 1.792(5)–1.799(5) and 2.270(4)–2.585(5) Å, corresponding to the uranyl and equatorial coordination bonds, respectively. Both crystallographically unique uranyl groups play the role of a tetracoordinate node, whereas one phosphate group is connected to four uranium atoms sharing each of its four vertices with uranium polyhedra ($Q^4$ coordination type),[37, 38] and the other two are coordinated via one vertex- and two edge-sharing, corresponding to $T^{12}$ coordination type. This coordination mode is accompanied by markedly different P–O bond distances with terminal and bridging O atoms, 1.475(6)–1.498(6) and 1.526(5)–1.566(5) Å, respectively.

The salt inclusion part of the structure consists of edge-sharing $ClCs_6$ anion-centered coordination polyhedra in the shape of an octahedron with Cs–Cl bonds varying from 3.2536(5) to 3.4845(5) Å. The edge-sharing octahedra form chains propagating along

the *c* axis. The salt inclusion chains occupy the central, larger part of the channels in the uranyl phosphate framework, whereas the non-salt inclusion cesium atoms, i.e. cesium atoms that are not connected directly to the chlorine atoms, are located in the windows between the channels. Some cesium atoms also reside inside the framework pores (Figure 6.6).

In order to illustrate better the topology of the uranyl phosphate framework it was simplified using a standard procedure[39] by which the cesium cations and the salt inclusion part were both removed, and the phosphate groups were contracted to their mass center, only retaining their connectivity to the uranium atoms through the oxygen bridges. This process reveals a three-periodic net consisting of 3- and 4-coordinate nodes. This net can also be derived from a square planar **sql** topology in several steps. In the first step, which is shown to the left in Figure 6.6, some of the 4-coordinated nodes are removed to obtain larger edge-sharing 8-membered rings. It is worth pointing out that at this point there are 2-coordinated nodes that do not contribute to the layer topology; however, they are important for the connectivity in the other dimension. The layer then is corrugated to bring the 2-coordinated nodes above and below the layers. Finally, the layers are connected into a 3-periodic net by sharing the 2-coordinated nodes, changing the coordination of the latter to 4. The underlying net contains large 24-member rings, which correspond to the channels accommodating the salt inclusion part, whereas the 8-membered rings are occupied by cesium atoms and play role of windows between the channels.

$Cs_4[UO_2Al_2(PO_4)_4]$ (**6.2**) crystallizes in the triclinic space group $P\bar{1}$ and exhibits a layered structure where the cesium cations reside between the layers. The main anionic unit of the structure is the $[Al_2(PO_4)_4]^{6-}$ chain (Figure 6.7). In accordance with

Löwenstein's rule, each aluminum cation is connected to four different phosphate groups,[13] and there are two types of the phosphate groups: those that connect three aluminum cations and therefore provide connectivity within the chains, and those that decorate the chains and attach them to the uranyl groups, thereby connecting the chains into layers parallel to the (111) plane. The negatively charged layers are connected through electrostatic interactions via the cesium atoms residing between the layers.

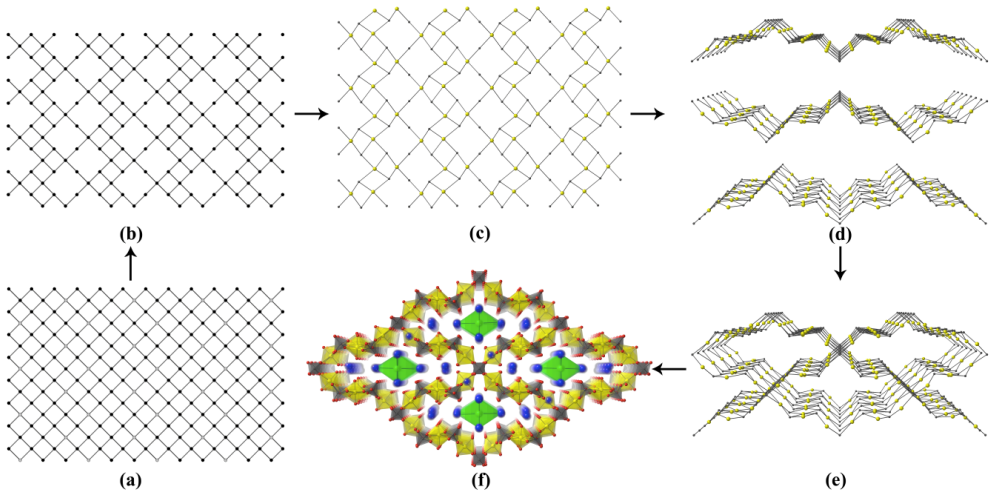


**Figure 6.6:** Structure of 6.1: (a) **sql** layer topology; and (b and c) a related net obtained by partial removal of the 4-coordainated nodes. (d and e) The interconnection of pseudolayers, resulting in (f). Uranium is shown in yellow, phosphorous in gray, chlorine in green, cesium in blue.

Two crystallographically unique uranium atoms in **6.2** form coordination polyhedra in the shape of a tetragonal and pentagonal bipyramid for U1 and U2, respectively. U1 is located at an inversion center and forms two short uranyl bonds with d(U=O) = 1.792(5) Å and four longer equatorial bonds, d(U–O) = 2.243(6) and 2.264(5) Å. The other uranium atom U2 occupies a general position and forms two nearly symmetric uranyl bonds with lengths of 1.793(5) and 1.795(5) Å. There is an uneven length distribution among the five equatorial bonds, four of them fall into a narrow range of 2.266(5)–2.355(5) Å, whereas

the fifth one, which involves a bridging oxygen atom, is elongated to 2.650(5) Å. Despite this difference, the volumes of the Voronoi polyhedra of these two uranium sites are quite similar, 9.20 and 9.24 $Å^3$, respectively, agreeing well with the average of 9.3(4) $Å^3$ for uranium(VI) in an oxygen environment.[40] Bond valence sums of 5.99 and 6.01 are consistent with the formal oxidation state of +6 for uranium.

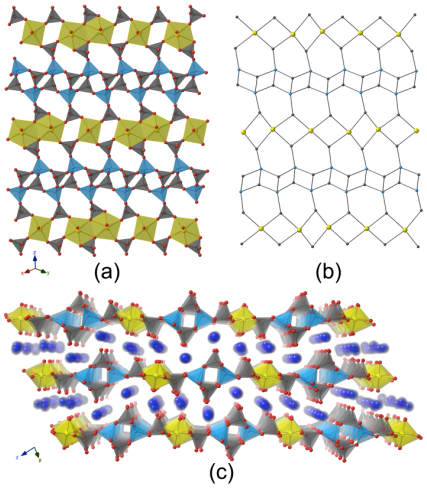


**Figure 6.7:** Structure of 6.2**.** (a) A $[UO_2Al_2(PO_4)_4]^{4-}$ layer (b) its topology, and (c) a perspective view of the structure.

Both aluminum and phosphorus atoms adopt a tetrahedral coordination environment. The aluminum atoms are almost uniformly surrounded by the O atoms with Al–O bond lengths ranging from 1.726(6) to 1.749(6) Å. Each phosphate tetrahedron, on the other hand, contains three longer bonds with bridging O atoms, d(P–O) = 1.529(6)–1.564(5) Å, and one short bond with a terminal O atom, d(P=O) = 1.470(6)–1.489(6) Å.

$[Cs_{13}Cl_5][(UO_2)_3Al_2O(PO_4)_6]$ (**6.3**) can be described as consisting of a negatively charged uranyl aluminophosphate open framework $[(UO_2)_3Al_2O(PO_4)_6]^{8-}$ containing an extended system of intersecting channels that are occupied by the salt-inclusion (Figure

6.8). The salt-inclusion is defined here as chlorine atoms and only those cesium atoms that are directly connected to them. Given this definition, all the cesium atoms in this compound are part of the $[Cs_{13}Cl_5]^{8+}$ salt-inclusion. The anionic framework and the cationionic salt inclusion are electrostatically connected via ionic bonds between the cesium atoms of the salt-inclusion and the oxygen atoms of the uranyl aluminophosphate framework.

The uranyl aluminophosphate framework consists of uranyl, $UO_2^{2+}$, and aluminophosphate, $[Al_2O(PO_4)_6]^{14-}$ groups that function as inorganic linkers between the metal centers (Figure 6.8a and b). In contradiction to Löwenstein's rule of "aluminum avoidance",[13] the aluminum atoms share a bridging oxygen atom to form an Al-O-Al fragment. Each uranyl cation coordinates four oxygen atoms from two different $[Al_2O(PO_4)_6]^{14-}$ aluminophosphate groups, forming a coordination polyhedron in the shape of a distorted octahedron. The aluminophosphate groups act as dodecadentate ligands towards uranium atoms, and symmetrically bind three uranium atoms at both ends of the $[(PO_4)_3AlOAl(PO_4)_3]^{14-}$ group. In a simplified net representation of the framework (Figure 6.5c), both the $UO_2^{2+}$ metal centers play the role of two-coordinated nodes, whereas the aluminophosphate groups function as six-coordinated nodes. Since the two-coordinated nodes do not change the connectivity of a net the uranyl groups they, consequenlty, serve as a metal linker between the aluminophosphate groups, which in turn determines the topology of the net. The resulting uninodal net was assigned to the **acs** topology by the TOPOS software (Figure 6.5c).[41–43] It is noteworthy that the highest possible symmetry of the net is $P6_3/mmc$. Considering that the heavier atoms of the framework, U and P, follow the hexagonal symmetry, this agrees well with the observed orthorhombic-hexagonal twinning of the crystals of this compound.

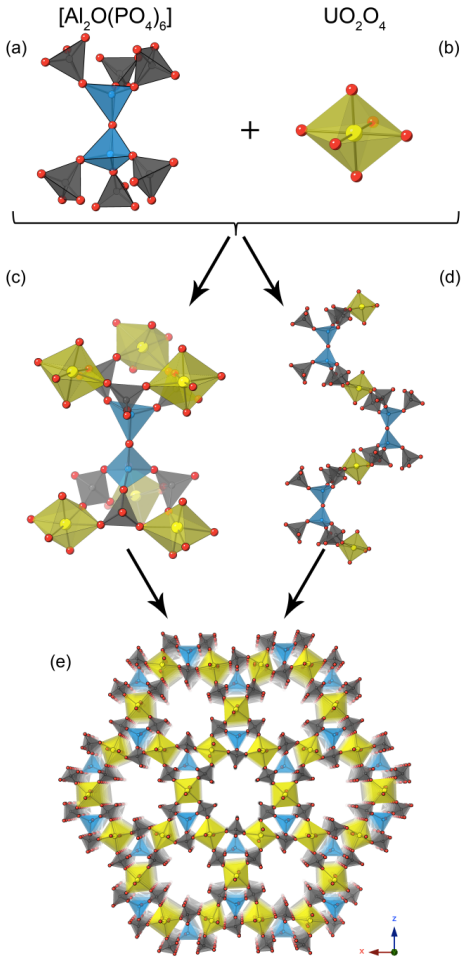


**Figure 6.8.** The framework structure of 6.3. (a and b) The main structural units, $[Al_2O(PO_4)_6]$ and $UO_2O_4$ and (c and d) their connection to each other resulting in (e).

The $[Cs_{13}Cl_5]^{8+}$ salt-inclusion of $[Cs_{13}Cl_5][(UO_2)_3Al_2O(PO_4)_6]$ consists of face- and edge-sharing cesium chloride polyhedra. There are five unique chlorine sites, each occupying a special position with either $C_s$ or $C_i$ site-symmetry. While most other salt-inclusion materials contain halide sites within an octahedral environment, the $[Cs_{13}Cl_5]^{8+}$ salt inclusion exhibits a wider set of chloride environments, including monocapped and bicapped trigonal prisms, and octahedra. The salt inclusion part of the structure fills the voids within the uranyl aluminophosphate framework and forms a 3D entity of face- and

edge-sharing chlorine coordination polyhedra. Each void, as well as the channels betweenthe voids, in the uranyl aluminophosphate framework are filled with the salt inclusion component, which is connected throughout the framework in all three dimensions. The topology of the salt inclusion part is therefore assumed to be dual to the framework topology. Indeed, according to the RCSR database, the dual net for **acs** topology is graphite **gra**, which can also be obtained by abstracting the salt inclusion component from the aluminophosphate framework and its simplification by considering the chlorine atoms as nodes connected through bridging cesium atoms. The interweaving of both the framework and the salt-inclusion nets is shown in Figure 6.9e.

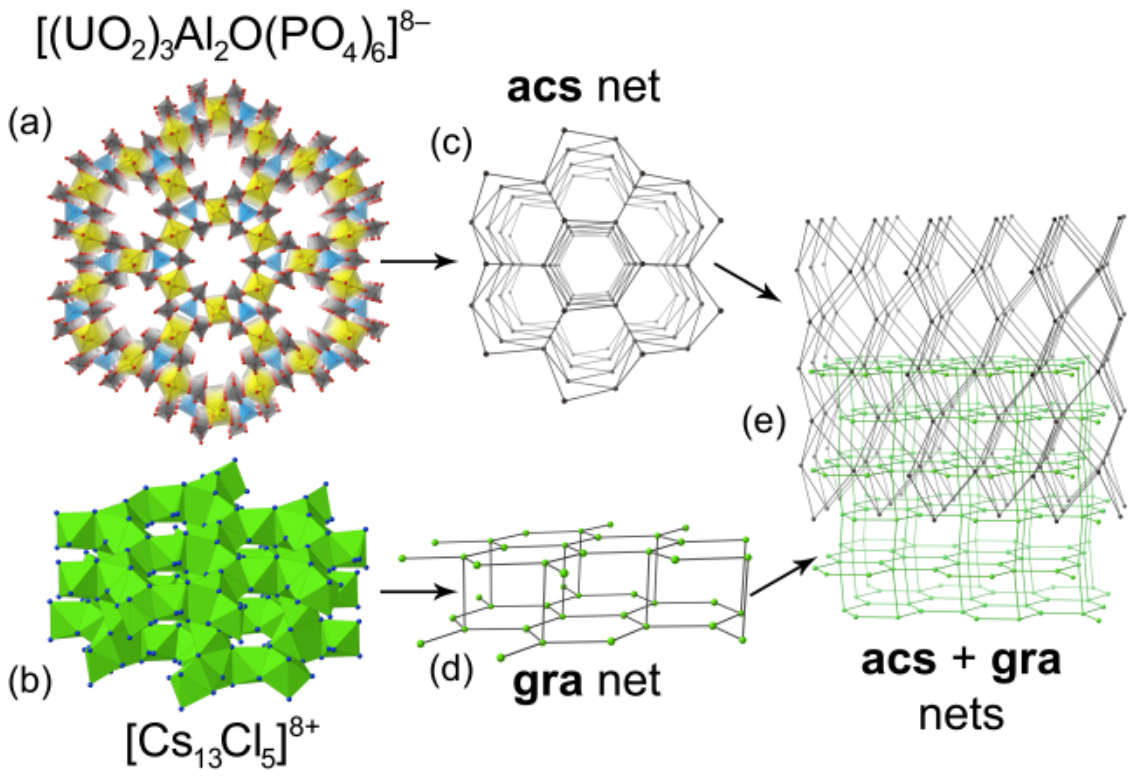


**Figure 6.9:** Topologies of the framework and salt inclusion 6.3. (a) and (b) represent a view of the framework and the salt inclusion. (c) and (d) show their respective **acs** and **gra** simplified nets.[43] (e) shows the arrangement of the uranyl framework and the salt inclusion component with the dual **acs** and **gra** topologies.

$Rb_7[Al_2O(PO_4)_3][(UO_2)_6O_4(PO_4)_2]$ (**6.4**), $Cs_3[Al_2O(PO_4)_3][(UO_2)_3O_2]$ (**6.5**), and $Rb_3[Al_2O(PO_4)_3][(UO_2)_3O_2]$ (**6.6**) are constructed of chains of alternating uranyl hexagonal bipyramids and $U_2O_{12}$ pentagonal bipyramid dimers, as found in the predominant phosphuranylite topology, and $[Al_2O(PO_4)_6]^{14-}$ buliding blocks. The uranium, aluminum, and phosphorus atoms adopt typical coordination environments and bond distances of pentagonal and hexagonal bipyramids, $AlO_4$ tetrahedra, and $PO_4$ tetrahedra, respectively. In the three structures, the uranyl bonds range between 1.796(3) and 1.823(5) Å, while the equitorial bonds are considerably longer at 2.221(3)-2.703(6) Å. The equitorial bonds of the 7-coordinate pentagonal bipyramids have shorter bond distances between 2.261(2)-2.422(5) Å, while the 8-coordinate hexagonal bipyramids have two shorter bonds with the oxygen shared between two pentagonal and one hexagonal bipyramid at distances of 2.221(3)-2.256(4) Å and four longer bonds between 2.482(5) and 2.703(6) Å. The Al-O and P-O bond distances average at the expected values of 1.7 and 1.5 Å.

In $Cs_3[Al_2O(PO_4)_3][(UO_2)_3O_2]$ (**6.5**) and $Rb_3[Al_2O(PO_4)_3][(UO_2)_3O_2]$ (**6.6**) the aluminum and phosphate tetrahedra within the $[Al_2O(PO_4)_6]^{14-}$ building blocks corner share to form a 2D network (Figure 6.10c), or pillars when rotated by 90 °, that connect to the uranyl chains by edge-sharing through the phosphate tetrahedra. Each uranyl chain edge shares with two aluminophosphate pillars, so that each uranyl chain is separated from the next by one of these aluminophosphate pillars. This structure can also be described as uranyl phosphate sheets linked to adjacent sheets by the pyroaluminate groups, creating intersecting channels in the *a* and *c* directions. The cesium or rubidium cations lie in these channels, where one is located in the plane of the aluminophosphate sheet between

phosphate tetrahedra, and the remaining cations are locted between the chains of uranyl polyhedra.

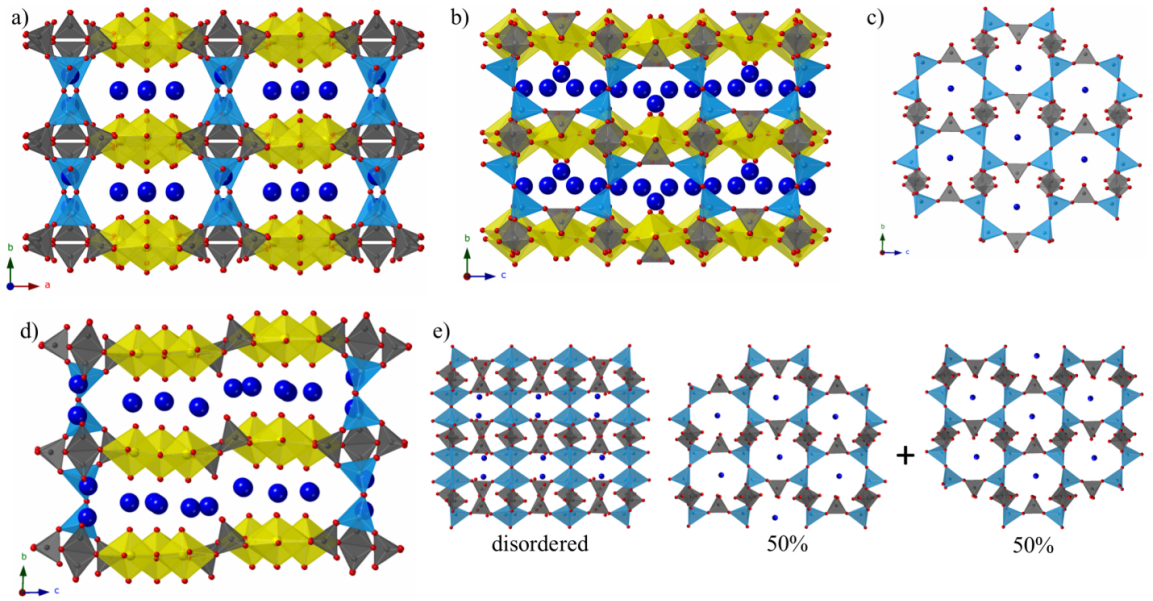


**Figure 6.10:** Structure of 6.4-6.6. a) **6.5** and **6.6** along the *c* direction. b) **6.5** and **6.6** along the *a* direction. c) Isolated aluminophosphate sheet in **6.5** and **6.6**. d) **6.4** along the *a* direction. e) The disordered aluminophosphate sheet in **6.4**.

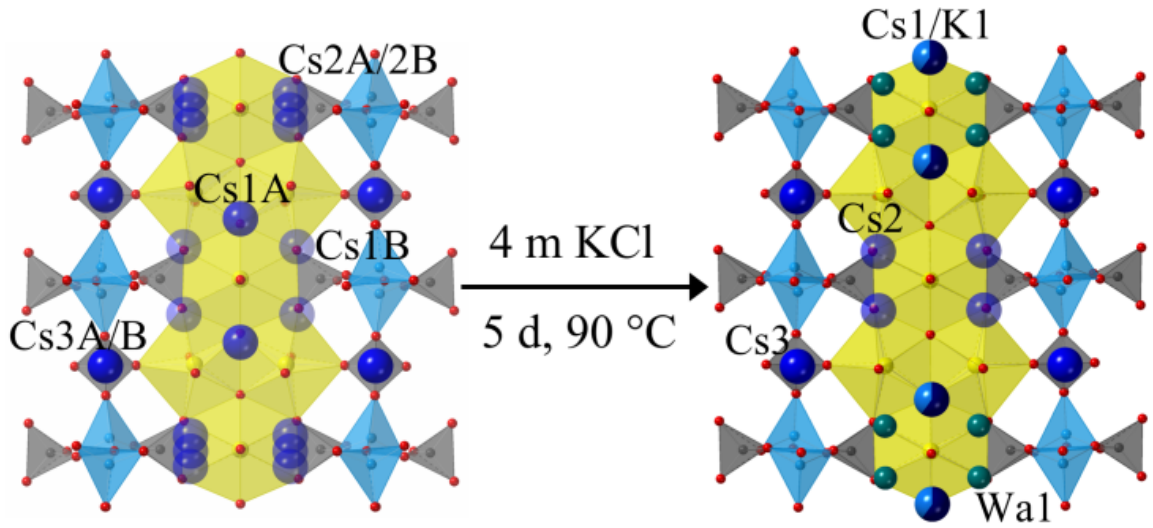


**Figure 6.11:** Comparison of the alkali metal sites in the parent structure 5 and in the ion exchange product 7. Cs atoms are dark blue and the transparency of the spheres approximately represents the occupancies. O atoms of water are teal and the shared Cs1/K1 site is dark blue and light blue.

$Rb_7[Al_2O(PO_4)_3][(UO_2)_6O_4(PO_4)_2]$ (**6.4**) while constructed of the same building blocks, contains one fewer aluminophosphate pillar than **6.5** and **6.6**. Instead of each uranyl chain being separated from the next by a pillar, two uranyl chains are connected by edge- and corner-sharing through phosphate tetrahedra, like sheets of the phosphuranylite topology, and every pair of uranyl chains is separated from the next pair by an aluminophosphate pillar. The aluminophosphate network is disordered, there are two possible orientations of the network, as shown in Figure 6.10e.

Structures $Cs_{2.5}K_{0.5}[Al_2O(PO_4)_3][(UO_2)_3O_2]\cdot 2H_2O$ **(6.7)** and $Na_{2.5}Rb_{0.5}[Al_2O(PO_4)_3][(UO_2)_3O_2]\cdot 2.6\ H_2O$ **(6.8)** are ion exchange products obtained by soaking $Cs_3[Al_2O(PO_4)_3][(UO_2)_3O_2]$ (**6.5**), and $Rb_3[Al_2O(PO_4)_3][(UO_2)_3O_2]$ (**6.6**) in KCl and NaCl, respectively. The framework is unaltered during the ion exchange process with the exception of the appearance of a minor disorder in the Al-O-Al bridging oxygen in **6.8**, but not in **6.7** (Figure 6.12). In both ion exchange experiments the sites of the cations and water molecules are changed (Figure 6.11, Figure 6.12). The species in the channels tend to lie above the vertices of the uranyl polyhedra, as these sites are larger than those directly above the uranyl oxygens that align in adjacent chains and protrude into the channels. In the parent structures **6.5** and **6.6**, the cations lie in approximately the same positions with additional disorder in the Cs2A/2B sites not seen in **6.5**. In ion exchange product **6.8**, the Rb3 site, which lies between phosphate tetrahedra in the plane of the aluminophosphate network is not present, rather there are additional sodium sites that lie above the uranyl polyhedra as compared to the parent structure. The absence of this cation site may explain the observation of the disorder in the Al-O-Al bridging oxygen in **6.8.**

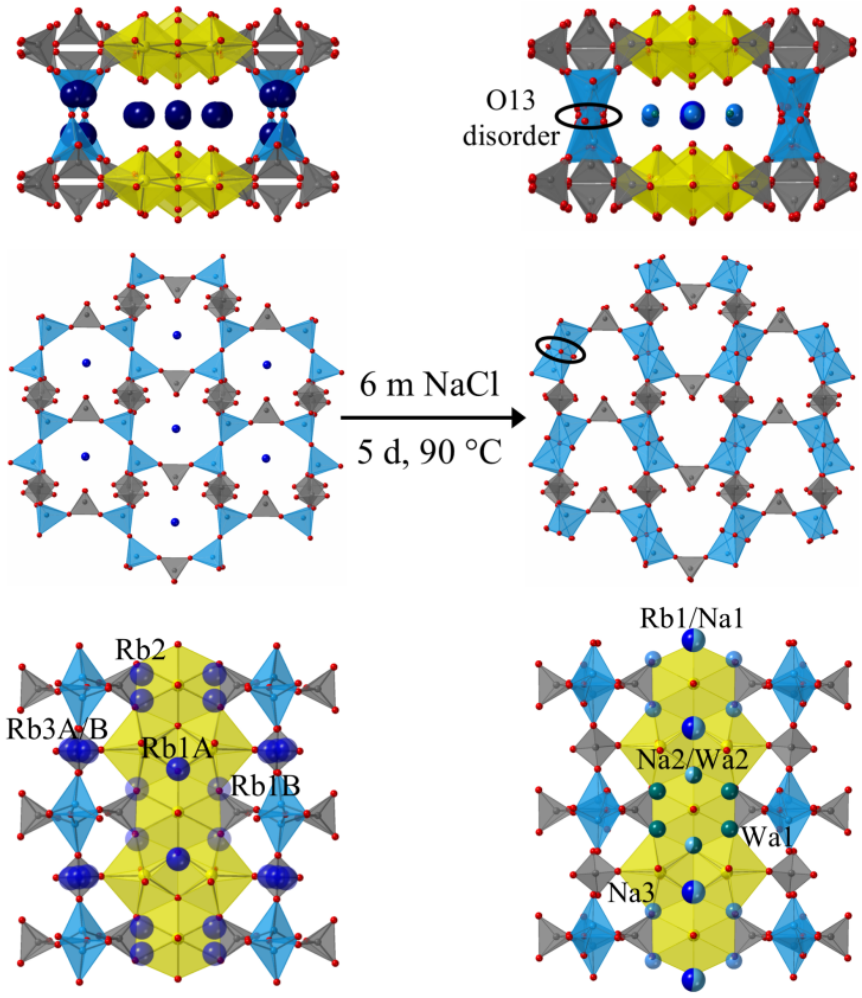


**Figure 6.12:** Comparison of 6.6 and ion exchange product 6.8. On the left is **6.6** and the NaCl ion exchange product, **6.8**, on the right highlighting the O13 disorder in the framework and the change in alkali sites. Rubidium cations are in dark blue the degree of transparency of the spheres approximatly represents the occupancies. Sodium sites are in a lighter shade of blue and oxygen sites that belong to water molecules are in teal.

**Structure building.** The primary goal of this study was to investigate the possibility of introducing a salt inclusion component into a uranyl phosphate framework and compare them to the silicate uranyl SIM materials in order to probe possible routes towards advanced SIMs with expanded ion exchange properties. The underlying idea behind replacing the silicate units with the phosphate building blocks to obtain new SIMs

was that the charge of the $PO_4^{3-}$ phosphate group is less than that of the silicate group $SiO_4^{4-}$ and, therefore, a uranyl phosphate framework in general is more likely to have a lower charge per volume unit, allowing it to accommodate more halide atoms and increasing the fraction of the salt inclusion component in the structure. This assumption is valid only if the condensation of the silicate units is ruled out, and only uranyl orthosilicate frameworks are considered. This, however, is rather rare because silicate groups tend to form condensed building units that result in a significantly reduced charge per silicon atom, whereas phosphate anions have significantly less tendency towards condensation. The first uranyl phosphate SIM, $[Cs_4Cs_4Cl][(UO_2)_4(PO_4)_5]$ (**6.1**), reported herein indeed consists of isolated phosphate groups, and other numerous attempts to obtain a phosphate SIM with condensed phosphate units, i.e. pyrophosphate or triphosphate, were unsuccessful.

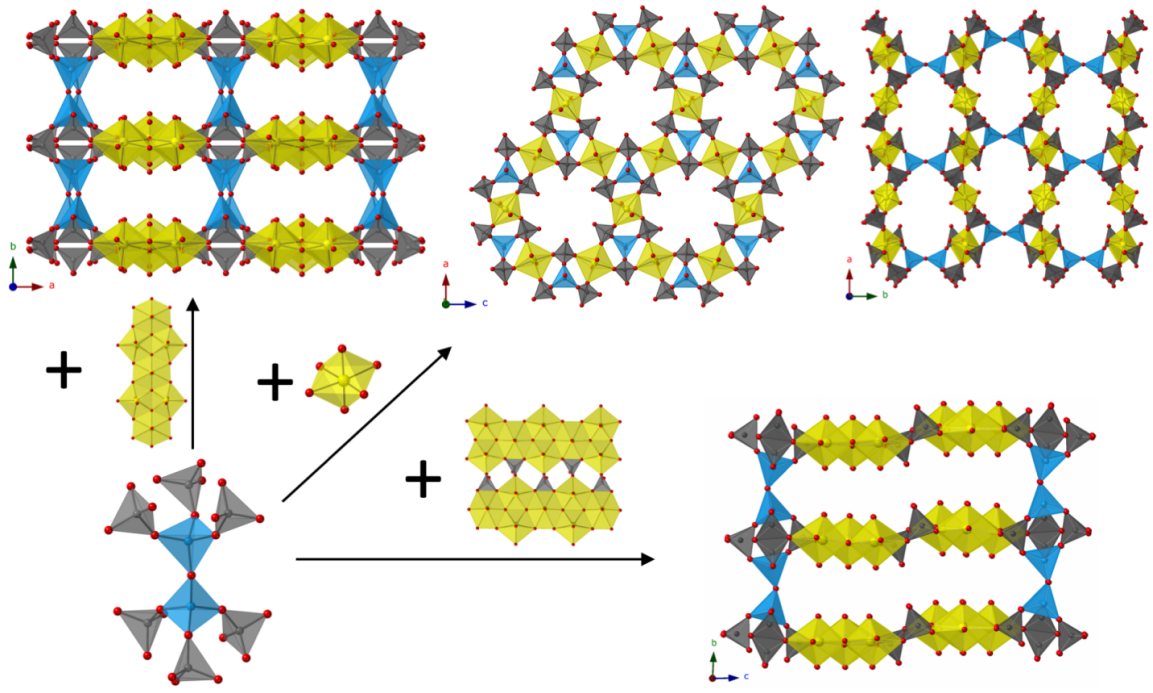

**Figure 6.13:** Construction of 6.3-6.5 from the aluminophosphate building block. When combined with different uranyl building blocks, chains, isolated polyhedra, and sheets, create structures **6.5** (top left), **6.3** (top right), and **6.4** (bottom right).

In order to improve the chances of obtaining a more complex building units with a lower charge and to obtain a SIM with larger salt inclusion fraction, an approach that has proven effective in zeolite chemistry, namely the use of aluminum together with phosphorus to create extended building units and frameworks, was employed. Using this approach a unique aluminophosphate buliding block, $[Al_2O(PO_4)_6]^{14-}$, was obtained that can be combined with different uranyl building blocks, such as isolated polyhedra, chains, or sheets, to result in the complex three dimensional frameworks of $[Cs_{13}Cl_5][(UO_2)_3Al_2O(PO_4)_6]$, $A_3[Al_2O(PO_4)_3][(UO_2)_3O_2]$ (A=Cs, Rb), and $Rb_7[Al_2O(PO_4)_3][(UO_2)_6O_4(PO_4)_2]$, respectively (Figure 6.13). Each of these structures can also be described as consisting of uranyl phosphate sheets that are linked together by the pyroaluminate group. This new building block can conceivably be used to assemble many more new structures by combining it with other transition metal building blocks including uranium.

This novel aluminophosphate building unit enabled us to build the first, to the best of our knowledge, SIM with a 3-dimentional salt-inclusion part, $[Cs_{13}Cl_5][(UO_2)_3Al_2O(PO_4)_6]$. (Figure 6.14). The extended salt inclusion component was a promising candidate for ion exchange and, in fact, multiple ion exchange experiments showed that both powder and single crystals of this compound undergo ion exchange even at room temperature. In most cases, 2-day room temperature ion exchange experiments went to completion resulting in an almost complete replacement of the salt inclusion (both Cs and Cl atoms) with the aliovalent cations from an ion exchange solution, i.e. $SrCl_2$, RbCl, KCl, NaCl, $Mn(CH_3CO_2)_2$, and $Eu(NO_3)_3$. A significant drawback of this rapid ion exchange is, unfortunately, a complete loss or significant deterioration of the crystallinity

in both single crystals and powder samples. Although EDS experiments show the presence of Al, U, P in the samples after ion exchange, powder X-ray diffraction patterns cannot be associated with the initial structures, meaning that the uranyl aluminophosphate framework either undergoes a significant change or decomposition.

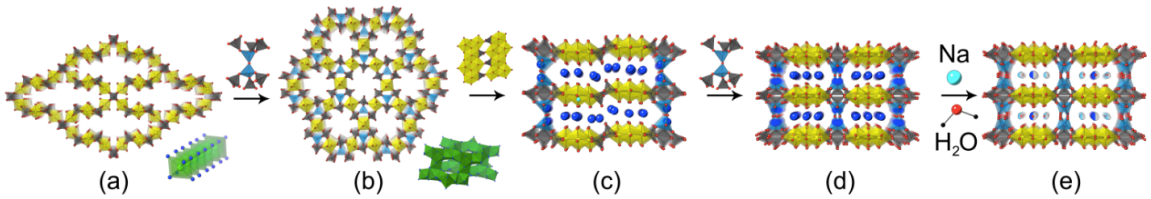


**Figure 6.14:** Structural evolution of 6.1-6.8. (a) Framework consisting of $UO_2^{2+}$ and $PO_4^{3-}$ groups along with salt inclusion component in $[Cs_4Cs_4Cl][(UO_2)_4(PO_4)_5]$, (b) replacement of the $PO_4$ units by complex $[Al_2O(PO_4)_6]$ building units, resulting in a framework accommodating 3-dimensiaonal salt inclusion part, (c) replacement of the $UO_2^{2+}$ units by phosphuranylite layers with (d) further incorporation of $[Al_2O(PO_4)_6]^{14-}$ building units to create (e) a rigid framework capable of single crystal to single crystal ion exchange.

In order to create a framework that is more resistant to deformation during ion exchange, a more rigid uranyl-bearing can be used. Phosphuranylite layers readily form in the flux reaction conditions and therefore can be used for the uranyl unit replacement, and after some synthetic conditions optimization, this unit was introduced into the final structure. The resulting two frameworks, $A_3[Al_2O(PO_4)_3][(UO_2)_3O_2]$ (A=Cs, Rb) and $Rb_7[Al_2O(PO_4)_3][(UO_2)_6O_4(PO_4)_2]$, showed significantly increased resilience of the framework although the ion exchange process proceeds more slowly in these two compounds and requires elevated temperatures of 90°C. Given the very promising results of these early steps, this new building unit, $[Al_2O(PO_4)_6]^{14-}$ in combination with other uranyl containing building blocks, has the potential to open up a new field of synthetic uranyl aluminophosphates.

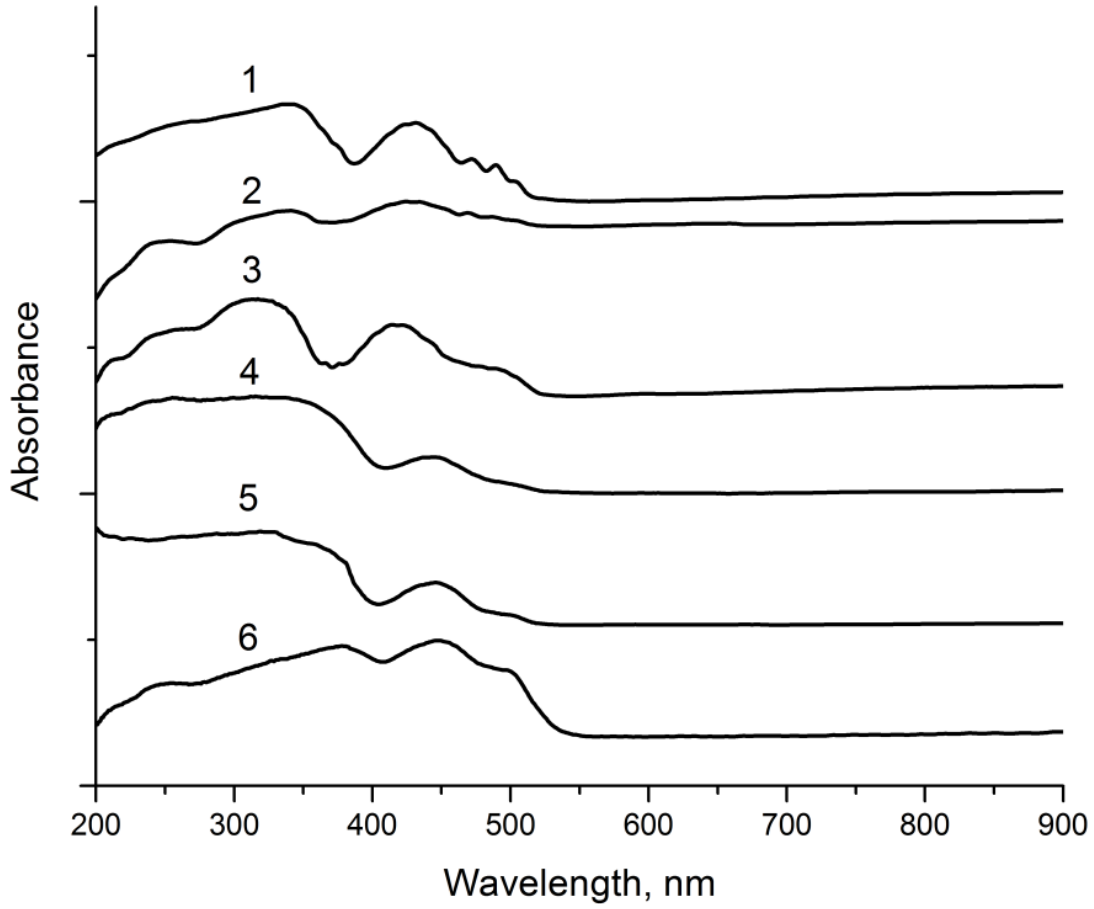


**Figure 6.15:** UV-vis spectra of compounds 6.1-6.6.

**Optical Properties.** UV-vis measurements of compounds **6.1**-**6.6** are included in the supporting information, Figure 6.15, and are typical of uranyl species with broad absorbance over 200-525 nm classifying these materials as semi-conductors. Fluorescence spectra (Figure 6.16) of **6.1**-**6.6** show typical yellow-green luminescence of uranyl-containing materials with emission speaks between 500-650 nm. The most intense emission peaks that occur between 525-550 nm can be assigned to electronic emission from the lowest vibrational level of the first excited state to the lowest vibrational level of the ground state, while the smaller peaks surrounding the main emission originate from different vibrational levels of the same electronic emission.

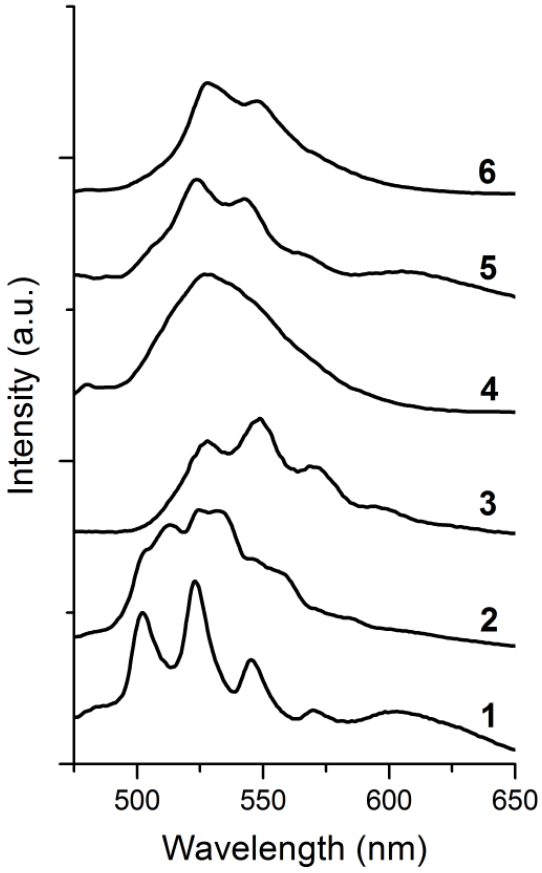


**Figure 6.16:** Emission fluorescence spectra of 6.1–6.6. Excited at 439, 439, 426, 377, 445, and 379 nm, respectively.

**Conclusion.** The synthesis of first uranyl phosphate and aluminophosphate salt inclusion materials (SIMs), non-Löwenstein aluminophosphates with ion exchange properties are reported, namely $[Cs_4Cs_4Cl][(UO_2)_4(PO_4)_5]$ (**6.1**), $Cs_4[UO_2Al_2(PO_4)_4]$ (**6.2**), $[Cs_{13}Cl_5][(UO_2)_3Al_2O(PO_4)_6]$ (**6.3**), $Rb_7[Al_2O(PO_4)_3][(UO_2)_6O_4(PO_4)_2]$ (**6.4**), $Cs_3[Al_2O(PO_4)_3][(UO_2)_3O_2]$ (**6.5**), and $Rb_3[Al_2O(PO_4)_3][(UO_2)_3O_2]$ (**6.6**). **6.1** and **6.3** are salt inclusion materials which are sought after for their potential applications in nuclear waste storage and structures **6.3**-**6.6** are non-Löwenstein aluminophosphates that feature a unique building block, $[Al_2O(PO_4)_6]^{14-}$, with Al-O-Al linkages. The formation of Al-O-Al linkages in the prescense of phosphorus seems to be favorable by high temperature methods

considering the reports on the non-Löwenstein aluminophosphates in this work, and those reported by Hesse, Huang, and Yao.[12, 15, 17, 18] Löwenstein's rule, which is a general rule based on the Pauling's rules, was developed to explain the distribution of aluminum in silicate and phosphate minerals and, in particular, was easily adapted to zeolite materials, albeit not limited to them, synthesized by hydrothermal methods. The absence of Al-O-Al linkages in zeolites and minerals, and the presence of Al-O-Al linkages in materials synthesized at high temperatures suggests that Löwenstein's rule can be overcome given enough thermal energy. The high temperature molten flux method seems to be a viable route to synthesis new structures, specifically salt inclusion phases, that feature unique building blocks.

Characterizing the ion exchange properties of these new uranium containing materials is important for nuclear waste storage applications. The Cs and Rb containing structures of $A_3[Al_2O(PO_4)_3][(UO_2)_3O_2]$ readily ion exchange in aqueous solutions of KCl and NaCl, respectively. While the concentrations used are likely much greater than necessary for potential applications, the ability of the framework to release Cs in favor of K is unfavorable for long term waste storage, but could be useful in waste processing. The framework appears to be thermally stable up to 500 °C, suggesting that uranium aluminophosphate materials are good waste form candidates when considering thermal stability.

**Acknowledgements.** C. Juillerat and V. Klepov contributed equally to this manuscript. The authors declare no competing financial interest. This work was supported as part of the Center for Hierarchical Waste Form Materials, an Energy Frontier Research Center funded by the U.S. Department of Energy, Office of Science, Basic Energy Sciences

under Award No. DE-SC0016574. C. Juillerat is additionally supported by an NSF IGERT Graduate Fellowship under grant number 1250052.

**References:**

(1) Nuttin, A.; Heuer, D.; Billebaud, A.; Brissot, R.; Brun, C. L.; Liatard, E.; Loiseaux, J.-M.; Mathieu, L.; Meplan, O.; Merle-Lucotte, E.; Nifenecker, H.; Perdu, F.; David, S., Potential of thorium molten salt reactorsdetailed calculations and concept evolution with a view to large scale energy production, *Prog. Nucl. Energy* **2005**, *46*, 77-99.

(2) Dacheuz, N.; Clavier, N.; Wallez, G.; Brandel, V.; Emery, J.; Quarton, M.; Genet, M., Characterization of the thorium phosphate-hydrogenphosphate hydrate (TPHPH) and study of its transformation into the thorium phosphate-diphosphate (β-TPD), *Mater. Res. Bull.* **2005**, *40*, 2225-2242.

(3) zur Loye, H.-C.; Besmann, T.; Amoroso, J.; Brinkman, K.; Grandjean, A.; Henager, C. H.; Hu, S.; Misture, S. T.; Phillpot, S.; Shustova, N. B.; Wang, H.; Koch, R. J.; Gregory Morrison; Dolgopolova, E., Hierarchical Materials as Tailored Nuclear Watse Forms: A Perspective, *Chem. Mater.* **2018**, *30*, 4475-4488.

(4) Morrison, G.; Smith, M. D.; zur Loye, H.-C., Understanding the Formation of Salt-Inclusion Phases: An Enhanced Flux Growth Method for the Targeted Synthesis of Salt-Inclusion Cesium Halide Uranyl Silicates, *J. Am. Chem. Soc.* **2016**, *138*, 7121-7129.

(5) Lee, C. S.; Wang, S. L.; Chen, Y. H.; Lii, K. H., Flux synthesis of salt-inclusion uranyl silicates:$[K_3Cs_4F][(UO_2)_3(Si_2O_7)_2]$ and $[NaRb_6F][(UO_2)_3(Si_2O_7)_2]$, *Inorg. Chem.* **2009**, *48*, 8357-8361.

(6) Juillerat, C. A.; Moore, E. E.; Besmann, T. M.; zur Loye, H.-C., Versatile Uranyl Germanate Framework Hosting Twelve Different Alkali Halide 1D Salt Inclusions, *Inorg. Chem.* **2018**, *57, 11606-11615.*

(7) Etheredge, K. M. S.; Hwu, S.-J., A Novel Honeycomb-like Copper(II) Phosphate Framework, [BaCl][CuPO4], *Inorg. Chem.* **1995**, *34*, 3123-3125.

(8) Hwu, S. J. *A New Class of Hybrid Materials via Salt-inclusion Synthesis.* John Wiley & Sons: 2006;

(9) Gao, J.; Li, J.; Sulejmanovic, D.; Hwu, S.-J., $M_3(P_2O_7)^{22-}$Type Open Frameworks Featuring $[M_2O_8]$ and $[M_3O_{12}]$ Multinuclear Transition-Metal Oxide Units.

Serendipitous Synthesis of Six Polymorphic Salt-Inclusion Magnetic Solids: $Na_2M_3(P_2O_7)_2 \cdot ACl$ (M = Mn, Fe; A = Rb, Cs) and $K_2M_3(P_2O_7)_2 \cdot CsCl$ (M = Fe, Mn), *Inorg. Chem.* **2015**, *54*, 1136-1144.

(10) Jihong Yu, R. X., Insight into the construction of open-framework aluminophosphates, *Chem. Soc. Rev.* **2006**, *35*, 593-604.

(11) Oliver, S.; Kuperman, A.; Ozin, G. A., A New Model for Alumiophosphate Formation: Transformation of a Linear Chain Aluminophosphate to Chain, Layer, and Framework Structures, *Angew. Chem.* **1998**, *37*, 46-62.

(12) Shiou-Jyh Hwu; Huang, Q., $Cs_2Al_2P_2O_9$: an exception to Lowenstein's rule. Synthesis and characterizatino of a novel layered aluminophosphte containing linear Al-O-Al linkages, *Chem. Commun.* **1999**, 2343-2344.

(13) Löwenstein, W., The distribution of aluminum in the tetrahedra of silicates and aluminates, *Am. Mineral.* **1954**, *39*, 92-96.

(14) Cundy, C. S.; Cox, P. A., The Hydrothermal Synthesis of Zeolites: History and Development from the Earliest Days to the Present Time, *Chemical Reviews* **2003**, 663-702.

(15) Yao, X.-N.; Chen, Y.-G.; Guo, Y.; Jia, Y.-J.; Jiang, X.-X.; Zhang, X.-M., $L1_6Na_3Sr_{14}Al_{11}P_{22}O_{90}$: an oxo-centered $Al_3$ cluster based phosphate constructed from two types of (3,6)-connected kgd layers, *Dalton Trans.* **2018**, *47*, 298.

(16) Tarling, S. E.; Barnes, P.; Klinowski, J., The Structure and Si,Al Distribution of the Ultramarines, *Acta Cryst.* **1988**, *B44*, 128-135.

(17) Hesse, K.-F.; Cemic, L., Crystal structure of $FeAlPO_5$, *Z. Kristallogr.* **1994**, *209*, 346.

(18) Hesse, K.-F.; Cemis, L., Crystal structure of $MgAlPO_5$, *Z. Kristallogr.* **1994**, *209*, 660.

(19) Locock, A. J.; Kinman, W. S.; Burns, P. C., The sructure and composition of uranospathite, $Al_{1-x}[]_x[(UO_2)(PO_4)]_2(H_2O)_{20+3x}F_{1-3x}$, $0 < x < 0.33$, a non-centrosymmetric fluorine-bearing mineral of the autuinte group, and of a related synthetic lower hydrate, $Al_{0.67}[]_{0.33}[(UO_2)(PO_4)]_2(H_2O)_{15.5}$, *Can. Mineral.* **2005**, *43*, 989-1003.

(20) Plasil, J., A novel sheet topology in the structure of kamitugaite, $PbAl[(UO_2)_5(PO_4)_{2.38}(AsO_4)_{0.062}O_2(OH)_2](H_2O)_{11.5}$, *J. Geosci.* **2017**, *62*, 253-260.

(21) Piret, P.; Declercq, J.-P.; Wauters-Stoop, D., Structure of threadgoldite, *Acta Cryst.* **1979**, *B35*, 3017.

(22) Piret, P.; Piret-Meunier, J.; Declercq, J.-P., Structure of Phurmalite, *Acta Cryst.* **1979**, *B35*, 1880-1882.

(23) Piret, P.; Deliens, M., Uranyl and aluminum phosphates from Kobokobo. IX. Althupite, $AlTh(UO_2)[(UO_2)_3O(O_H)(PO_4)_2]_2(OH)_3.15H_2O$, a new mineral. Properties and crystal structure, *Bull. Mineral.* **1987**, *110*, 65-72.

(24) Dal Bo, F.; Hatert, F.; Philippo, S., A new uranyl phosphate sheet in the crystal structure of furongite, *Eur. J. Mineral.* **2017**, *29*, 517-527.

(25) Bugaris, D. E.; zur Loye, H.-C., Materials discovery by flux crystal growth: Quartenary and higher oxides, *Angew. Chem. Int. Ed.* **2012**, *51*, 3780-3811.

(26) Kubelka, P.; Munk, F. Z., Ein Beitrag Zur Optik Der Farbanstriche, *Z. Techn. Phys.* **1931**, *12*, 593-601.

(27) Bruker. *APEX3, SAINT+, and SADABS.* Bruker AXS Inc.: Madison, Wisconsin, USA, 2015;

(28) Sheldrick, G. M., Crystal structure refinement with SHELXL, *Acta Cryst.* **2015**, *C71*, 3-8.

(29) Sheldrick, G. M., SHELXT - Integrated space-group and crystal-structure determination, *Acta Cryst.* **2015**, *A71*, 3-8.

(30) Dolomanov, O. V.; Bourhis, L. J.; Gildea, R. J.; Howard, J. A. K.; Pushman, H., OLEX2: a complete structure solution, *J. Appl. Crystallogr.* **2009**, *42*, 339-341.

(31) Spek, A. L., Structure validation in chemical crystallography, *Acta Cryst.* **2009**, *D65*, 148-155.

(32) Villa, E. M.; Alekseev, E. V.; Depmeier, W.; Albrecht-Schmitt, T. E., Syntheses, structures, and comparisons of thallium uranium phosphites, mixed phosphate-phosphites, and phosphate, *Cryst. Growth Des.* **2013**, *13*, 1721-1729.

(33) Sheldrick, G. M. *CELL_NOW.* Version 2008/4; Georg-August-Universität Göttingen: Göttingen, Germany,

(34) Yang, L.; Pisoni, A.; Magrez, A.; Katryck, S.; Arakcheeva, A.; Piazza, B. D.; Prsa, K.; Jacimovic, J.; Akrap, A.; Teyssier, J.; Forro, L.; Ronnow, H. M., Crystal Structure, Transport, and Magnetic Properties of an $Ir^{6+}$ Compound $Ba_8Al_2IrO_{14}$, *Inorg. Chem.* **2015**, *54*, 4371-4376.

(35) Juillerat, C. A.; Moore, E. E.; Besmann, T. B.; zur Loye, H.-C., Observation of an Unusual Uranyl Cation-Cation Interaction in the Strongly Fluorescent Layered

Uranyl Phosphates $Rb_6[(UO_2)_7O_4(PO_4)_4]$ and $Cs_6[(UO_2)_7O_4(PO_4)_4]$, *Inorg. Chem.* **2018**, *57*, 3675-3678.

(36) Juillerat, C. A.; Moore, E. E.; Kocevski, V.; Besmann, T. M.; zur Loye, H.-C., A Family of Layered Phosphates Crystallizing in a Rare Geometrical Isomer of the Phosphuranylite Topology: Synthesis, Characterization, and Computational Modeling of $A_4[(UO_2)_3O_2(PO_4)_2]$ (A = alkali metals) Exhibiting Intra-layer Ion Exchange, *Inorg. Chem.* **2018**, *57*, 4726-4738.

(37) Serezhkin, V. N.; Vologzhanina, A. V.; Serezhkina, L. B.; Smirnova, E. S.; Grachova, E. V.; Ostrova, P. V.; Antipin, M. Y., Crystallochemical formula as a tool for describing metal–ligand complexes – a pyridine-2,6-dicarb-oxylate example, *Acta Cryst.* **2009**, *B65*, 45-53.

(38) Vologzhanina, A. V.; Serezhkina, L. B.; Neklyudova, N. A.; Serezhkin, V. N., Synthesis and characterisation of a trinuclear uranyl complex: Crystal structure of $(CN_3H_6)_5[(UO_2)_3O(OH)_2(CH_3COO)(C_2O_4)_3]$, *Inorg. Chim. Acta* **2009**, *362*, 4921-4925.

(39) Blatov, V. A.; Shevchenko, A. P.; Proserpio, D. M., Applied Topological Analysis of Crystal Structures with the Program Package ToposPro, *Cryst. Growth Des.* **2014**, *14*, 3576-3586.

(40) Serezhkin, V. N., Structural Chemistry of Inorganic Actinide Compounds, **2007**, 31-65.

(41) Blatov, V. A.; Shevchenko, A. P.; Serezhkin, V. N., TOPOS3.2: a new version of the program package for multipurpose crystal-chemical analysis, *J. Appl. Crystallogr.* **2000**, *33*, 1193.

(42) Blatov, V. A., Multipurpose Crystallochemical Analysis with the Program Package TOPOS., *IUCr CompComm Newslett.* **2006**, *7*, 4.

(43) O'Keeffe, M.; Peskov, M. A.; Ramsden, S. J.; Yaghi, O. M., The Reticular Chemistry Structure Resource (RCSR) Database of, and Symbols for, Crystal Nets, *Acc. Chem. Res.* **2008**, *41*, 1782-1789.

# Chapter 7

# $Cs_2(UO_2)Al_2O_5$: An Unprecedented Uranium Aluminate Discovered Serendipitously by Molten Flux Methods[1]

[1]Reproduce with permission from Juillerat, C. A.; Kocevski, V.; Besmann, T.; zur Loye, H.-C. *Inorg. Chem.* **2019**, *58*, 4099-4102. © 2019 American Chemical Society

**Abstract:** The flux synthesis, solid state synthesis, and characterization of a new aluminate, $Cs_2(UO_2)Al_2O_5$, are reported. $Cs_2(UO_2)Al_2O_5$ crystallizes in the tetragonal space group $I4_1/amd$ with lattice parameters $a$ = 7.3254(2) and $c$ = 30.9849(7) and is constructed from edge-sharing chains of $UO_7$ pentagonal bipyramids that are connected to $[Al_2O_5]^{4-}$ two-dimensional sheets. The cesium cations, which are heavily disordered, occupy small channels in the $a$ and $b$ directions in the framework structure. The optical properties and ion exchange behaviors are reported along with DFT calculations that support the observed results of the ion exchange experiments.

The crystal chemistry of uranium continues to expand as nuclear energy and nuclear waste storage receive ongoing attention in the scientific community. The number of reported inorganic extended structures containing uranium has steadily grown from 180 well-refined published uranium(VI) containing structures in 1996, to 368 in 2005, and to 727 in 2016. Much of this data was summarized in the expansive hexavalent uranium structural reviews by Burns et al.[1–3] In addition, uranium (IV) structures, while quite plentiful, are not nearly as widely reported as U(VI) structures. The recent expansion in our understanding of uranium crystal chemistry is mainly credited to exploratory crystal growth,[4] which utilizes different combinations of reagents to incorporate the desired elements into the single crystal products. This approach has resulted in a plethora of new, targeted structure types with new compositions as well as, at times, serendipitous results.

While uranium phosphates, arsenates, and silicates are well established classes of materials and flux growth of these materials is a well-established process, uranium germanates, by contrast, have only recently come into play as the number of flux grown uranium germanates increased from a single reported crystal structure in 2013 to 20 in

2018. Phosphate, arsenate, silicate, and germanate $TO_4^{n-}$ units all commonly adopt tetrahedral coordination environments and have functioned as building blocks in compositionally diverse extended uranium structures; consequently, we decided to pursue other $TO_4^{n-}$ tetrahedral building blocks to achieve similar structures, specifically aluminum as $AlO_4^{5-}$. Aluminum commonly adopts a tetrahedral coordination environment when found in combination with highly electropositive cations and is well known in the realm of zeolites and silicate minerals, where it substitutes on silicon sites.[5] A simple ICSD search of U, Al, and O containing compounds yields 25 structures consisting of 18 minerals, one synthetic perovskite, one novel aluminoborate prepared by high temperature - high pressure methods,[6] and five flux grown uranium aluminophosphates recently published by our group.[7] Additionally, the synthesis of uranyl aluminate nanoparticles has also been reported. [8] Herein, we report a novel cesium uranium aluminate, the first uranium extended structure to contain solely aluminate tetrahedra as the secondary building unit.

Crystals of $Cs_2(UO_2)Al_2O_5$ (**7.1**) were initially obtained serendipitously from a flux reaction using 0.5 mmol $UF_4$ (International Bio-Analytical Industries, powder, ACS grade), 0.33 mmol $LaPO_4$ (Alfa Aesar, powder, 99.99%), 11 mmol of CsCl (Alfa Aesar, powder, 99.99%), and 9 mmol of CsF (Alfa Aesar, 99% ) loaded into a silver tube covered loosely with a silver cap and held upright in the furnace with an alumina crucible. The mixture was heated to 875 °C in 1.5 hours, held for 12 hours, and slow cooled to 400 °C at 6 °C/h. It appeared that the flux was not contained in the silver tube and reacted with the alumina crucible producing yellow crystals of the title compound on the rim of the alumina crucible (Figure 1). The reaction vessels were sonicated in water following removal from the furnace in order to loosen the crystals from the surface of the vessels by dissolving any

remaining flux. All attempts to duplicate these conditions were unsuccessful, and these crystals could not be resynthesized using flux methods alone.

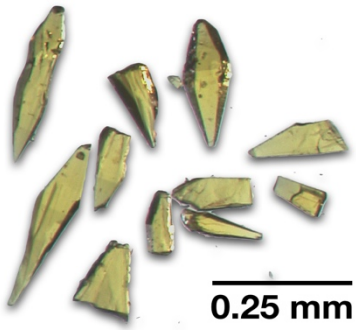


**Figure 7.1:** Single crystals of $Cs_2(UO_2)Al_2O_5$.

The structure and composition of $Cs_2(UO_2)Al_2O_5$ were determined by single crystal X-ray diffraction and this information was used to successfully synthesize the title compound by traditional solid state methods. Combining 0.5 mmol $UO_2(NO_3)_2$•6 $H_2O$ (International Bio-Analytical Industries, powder), 1 mmol $Al_2O_3$ (Alfa Aesar, powder, 99.9%), and 1 mmol of $CsNO_3$ (Alfa Aesar, powder, 99.8%) into an alumina crucible and heating the mixture with intermittent grindings to 900 °C for 250 h, 950 °C for 48 h, 1000 °C for 96 h and finally 1050 °C for 48 h resulted in the product phase. Between 900-1000 °C the target phase $Cs_2(UO_2)Al_2O_5$ forms together with $Cs_2U_2O_7$ (yellow), and at 1050 °C the target phase is present together with $Cs_4U_5O_{17}$ (orange). This mixture of $Cs_4U_5O_{17}$ and $Cs_2(UO_2)Al_2O_5$ was loaded into a platinum crucible with 9 mmol CsF and 11 mmol CsCl and heated under the same conditions as the original flux reaction. These reaction conditions promoted the recrystallization of $Cs_4U_5O_{17}$ and $Cs_2(UO_2)Al_2O_5$ as orange plates and yellow crystals, respectively, that could be manually separated to obtain a relatively pure sample of $Cs_2(UO_2)Al_2O_5$. Powdered and single crystalline products were identified

by powder X-ray diffraction (PXRD) using a Bruker D2 Phaser equipped with an LXYENE silicon strip detector and a Cu Kα source (Figure 7.2).

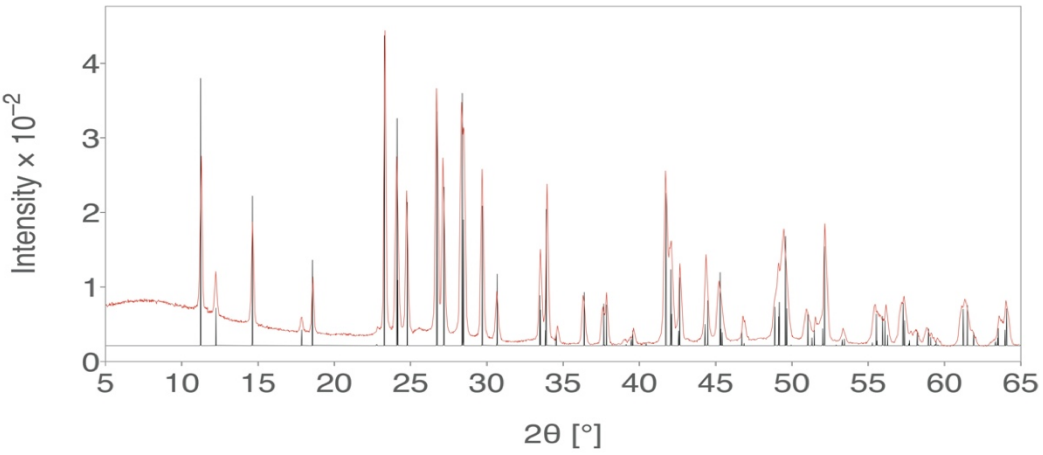


**Figure 7.2:** PXRD pattern of $Cs_2(UO_2)Al_2O_5$. Experimental pattern is red and the calculated pattern from the cif is in black.

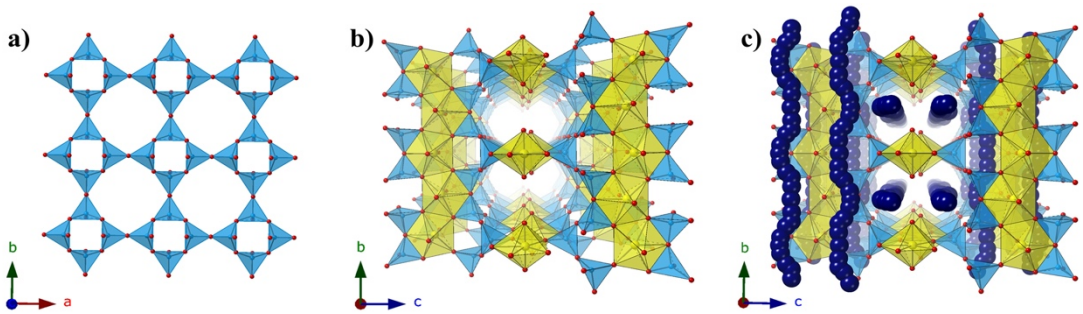


**Figure 7.3:** Structure of $Cs_2(UO_2)Al_2O_5$. a) 2D aluminate sheet constructed of vierer and achter rings. b) Aluminate sheets connected by edge sharing chains of $UO_7$ polyhedra. c) $Cs_2(UO_2)Al_2O_5$ shown with all sites. Uranyl polyhedra are yellow, aluminate tetrahedra blue, cesium cations in dark blue, and oxygen atoms in red.

Single crystal X-ray diffraction data were collected on a yellow plate crystal cut from the larger polyhedral crystals of $Cs_2(UO_2)Al_2O_5$ using a Bruker D8 Quest single-crystal X-ray diffractometer equipped with a Mo Kα microfocus source (λ = 0.71073 Å). The structure of the single crystal was determined by reducing the data and applying an

absorption correction using the SAINT+ and SADABS programs within APEX 3,[9] solving using the SHELXT solution method, and refining the solution using SHELXL within the Olex 2 GUI. [10–12] Full crystallographic data can be found in Table 7.1 along with bond distances and bond valence sums in Table 7.2. The refinement of the U, Al, and O sites was straightforward, while the refinement of the Cs sites was difficult due to the extreme disorder of the cations in the channels of the structures. Partially occupied Cs sites were added by freely refining significant electron density peaks near the largest Cs sites, Cs1 and Cs4, until the summed occupancies of these sites approached charge balance, 2 Cs per formula unit. At this point the occupancies of the sites were fixed as is, refined anisotropically, and an ISOR command was implemented to restrain the thermal parameters on the Cs sites, and then the occupancies of individual sites were manually and slowly increased to achieve charge balance. This was done manually instead of using a constraint such as the SUMP command, due to the instability of the refinement when this constraint is applied. The final occupancies of Cs1-Cs7 are 0.32, 0.16, 0.04, 0.33, 0.15, 0.05, and 0.025, respectively.

As a result of the extreme disorder in the Cs cations, diffuse scattering was visible in the diffraction frames of the single-crystal diffraction data (Figure 4). The final solution has an $R_1$ value of 1.69% and maximum/minimum electron density peaks of 0.9 and -1, indicating the model of the Cs disorder matches well with the collected data; however, the positions and occupancies of the seven partially occupied cesium sites should be considered approximate. The elements in the structure solution were confirmed qualitatively by energy-dispersive spectroscopy (EDS) using a TESCAN Vega-3 SBU scanning electron microscope equipped with an EDS detector.

**Table 7.1:** Full crystallographic data for $Cs_2UO_2Al_2O_5$.

| | $Cs_2UO_2Al_2O_5$ |
|---|---|
| S. G. | *$I4_1/amd$* |
| a, Å | 7.3254(2) |
| c, Å | 30.9849(7) |
| V, Å$^3$ | 1662.70(10) |
| Crystal size (mm$^3$) | 0.01 x 0.04 x 0.05 |
| Temperature (K) | 300 |
| Density (g cm$^{-3}$) | 5.352 |
| $\theta$ range (deg) | 3.410-36.318 |
| $\mu$ (mm$^{-1}$) | 28.361 |
| Collected reflections | 32561 |
| Unique reflections | 1130 |
| $R_{int}$ | 0.0267 |
| *h* | *-12 ≤ h ≤ 12* |
| *k* | *-12 ≤ k ≤ 12* |
| *l* | *-51 ≤ l ≤ 51* |
| $\Delta\rho_{max}$ (e Å$^{-3}$) | 0.936 |
| $\Delta\rho_{min}$ (e Å$^{-3}$) | -1.047 |
| *GoF* | 1.319 |
| Extinction coefficient | 0.00082(6) |
| $R_1(F)$ *for* $F_0^2 > 2\sigma(F_0^2)$[a] | 0.0169 |
| $R_w(F_0^2)$[b] | 0.0464 |

[a] $R_1 = \Sigma\big||F_0| - |F_c|\big|/\Sigma|F_0|$. [b] $wR_2 = [\Sigma w\left(F_0^2 - F_c^2\right)^2/\Sigma w\left(F_0^2\right)^2]^{1/2}$;
$P = (F_0^2 + 2F_c^2)/3$; $w = 1/\left[\sigma^2\left(F_0^2\right) + (0.0113P)^2 + 18.7509P\right]$.

**Table 7.2:** Bond valence sums and bond distances for $Cs_2UO_2Al_2O_5$

| Interaction | Distance | Interaction | Distance |
|---|---|---|---|
| U1 – O1 x 2 | 1.842(3) | Al1-O2 | 1.773(3) |
| U1 – O2 x 2 | 2.353(3) | Al1-O3 x 2 | 1.7263(16) |
| U1 – O2 | 2.231(3) | Al1 – O4 | 1.7489(13) |
| U1 – O2 | 2.230(3) | **BVS Al1** | **3.079** |
| U1 – O4 | 2.521(5) | | |
| **BVS U1** | **5.929** | | |

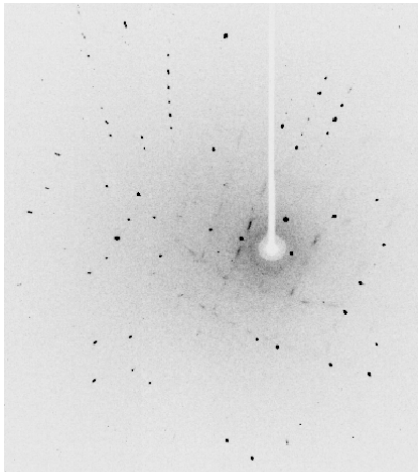

**Figure 7.4:** Diffuse scattering of 7.1. A diffraction frame from the SXRD data of 7.1 showing the diffuse scattering in the h k 0 plane corresponding to the Cs disorder in the *ab* plane.

$Cs_2(UO_2)Al_2O_5$ crystallizes in the tetragonal space group $I4_1/amd$ with lattice parameters $a$ = 7.3254(2) and $c$ = 30.9849(7) where all sites lie on special positions. U1, O4, and Cs4 lie on Wyckoff site 8e with *2mm.* symmetry and O3 lies on Wyckoff site 16g with *..2* symmetry, while all others lie on 16h with *.m.* symmetry. The structure of $Cs_2(UO_2)Al_2O_5$ consists of parallel 2D $[Al_2O_5]^{4-}$ sheets in the *bc* plane (Figure 3a) connected by chains of edge-sharing $UO_7$ square bipyramids. The 2D $[Al_2O_5]^{4-}$ sheets contains four membered (vierer) and 8 membered (achter) rings where vierer rings are linked to form a layer through corner sharing so that only achter rings are formed between them. This aluminate sheet topology is similar to that of the silicate sheets found in $K_2[(UO_2)Si_4O_{10}]$ $Na_2(UO_2)(Si_4O_{10})$, $KNa_3[(UO_2)_2(Si_4O_{10})_2]$, and $Na_4[(UO_2)_2(Si_4O_{10})_2]$ where the 2D nets are identical, however the direction in which the tetrahedra point are different for all three structures.[13–16] This sheet topology is also observed in several aluminosilicate and silicate minerals such as paracelsian, feldspars, harmotome, philipsite,

merlinoite, gismondine, garronite, apophyllite, in addition to many other synthetic materials.[17] Liebau explicitly lists the 29 different isomers of this simple topology that differ only by the direction that the tetrahedra point (up or down), of which only five have been observed to date. The title compound is, to our knowledge, the first example of no. 18.[17] Figure 7.3b shows the connection of the aluminate sheets through edge-sharing on two sides of the equatorial planes of the pentagonal bipyramids, where the $UO_7$ chains alternate between the *a* and *b* directions between each aluminate sheet. The cesium atoms lie within the channels created by the gaps between parallel $UO_7$ chains.

As part of our interest in nuclear waste forms, first principle calculations were used to determine whether aqueous $Cs^+$ ion exchange with $K^+$ is energetically favorable. First-principles calculations on the basis of density functional theory (DFT) were performed using the Vienna Ab-initio Simulation Package (VASP) pseudopotential code,[18, 19] with the projector augmented plane wave (PAW) method [20, 21] and the Perdew-Burke-Ernzerhof (PBE) generalized-gradient approximation.[22] The energy cutoff for the plane wave basis expansion was set to 520 eV, using 5×5×1 **k**-mesh, and convergence criteria for the total energies and the ionic forces set to $10^{-6}$ eV and $10^{-3}$ eV/Å, respectively. Spin-polarized calculations were performed, employing the DFT+*U* method,[23, 24] with $U = 4.0$ eV, and $J = 0.0$ eV. The *U*-value was chosen to be close to that obtained from relating experimental results for $UO_2$. [25, 26] We used 96 atom cells, where the Cs atoms were placed on the average position of the partially occupied Cs sites, resulting in a structure with the same symmetry as the experimentally synthesized compound. Every cell was fully relaxed, i.e., cell volume, cell shape and ionic positions. From the DFT+*U* calculated total energies we

calculated the energies for exchanging ion A with ion B (A = $Cs^+$, B = $K^+$), $\Delta E_{ie}$, using the equation:

$$\Delta \boldsymbol{E_{ie}} = \boldsymbol{E^B_{tot}} - \boldsymbol{E^A_{tot}} + \boldsymbol{N\mu^A} - \boldsymbol{N\mu^B} \quad \textbf{(1)}$$

where $\boldsymbol{E^A_{tot}}$ and $\boldsymbol{E^B_{tot}}$ are the total energy of the system containing ion A and B, respectively, $\boldsymbol{\mu^A}$ and $\boldsymbol{\mu^B}$ are the chemical potential of the ion A and B, respectively, and *N* is the total number of ions being exchanged, in our case 16. For comparison purposes, we used the chemical potential of the ions in vacuum and in water. The chemical potential for the ions in vacuum is the DFT calculated total energy of a single ion in vacuum, while for calculating the chemical potential for ions in water we used the method proposed by Persson et. al. [27] (see Table 7.3 for details on the used chemical potentials). The calculated $\Delta E_{ie}$ are negative, -4.2484 eV in vacuum and -1.1235 eV in water, indicating a strong driving force towards exchanging $Cs^+$ ions with $K^+$.

**Table 7.3:** Chemical potential, in eV, of the ions, in vacuum and in water.

| Ion | $\mu^{ion}$ (vacuum) | $\mu^{ion}$ (water) |
|---|---|---|
| $K^+$ | 4.3233 | -2.7623 |
| $Cs^+$ | 3.8455 | -2.8495 |

**Table 7.4:** Crystallographic data from DFT+*U* relaxed structures.

| | $Cs_2UO_2Al_2O_5$ | $K_2UO_2Al_2O_5$ |
|---|---|---|
| S.G. | *$I4_1/amd$* | *$I4_1/amd$* |
| a, Å | 7.3885 | 7.2187 |
| c, Å | 31.0919 | 30.7763 |
| V, $Å^3$ | 1697.2869 | 1603.7561 |

Ion exchange experiments were performed both on single crystal and ground crystalline samples by soaking 20 mg samples in 4 molal KCl for 3 days at 90 °C without

stirring. A control experiment was performed by soaking $Cs_2(UO_2)Al_2O_5$ in water at 90 °C for four days. After the experiments, the single crystals were no longer single crystalline but rather had transformed into a polycrystalline powder. The control experiment showed no significant change in the PXRD pattern indicating the stability of $Cs_2(UO_2)Al_2O_5$ in water over the short period of four days. The powder ion exchange product was analyzed by EDS and PXRD methods described previously and support near complete exchange of Cs for K. A calculated pattern for the K bearing ion exchange product was obtained by replacing the Cs sites with K and refining the lattice parameters in Jade 9 which resulted in lattice parameters $a$ = 7.2165(7) and $c$ = 30.323(7).[28] The DFT+$U$ calculations well reproduce the change in lattice parameter when Cs is completely exchanged by K (see Table 4). The experimental and calculated patterns are shown in Figure 5 and demonstrate a good fit. There are unidentified peaks at approximately 13° and 26° $2\theta$ that were not present in the PXRD pre-ion exchange and are possibly a result of some decomposition. Our experimental results support the DFT calculations that predicted the exchange of $Cs^+$ to $K^+$ is energetically favorable.

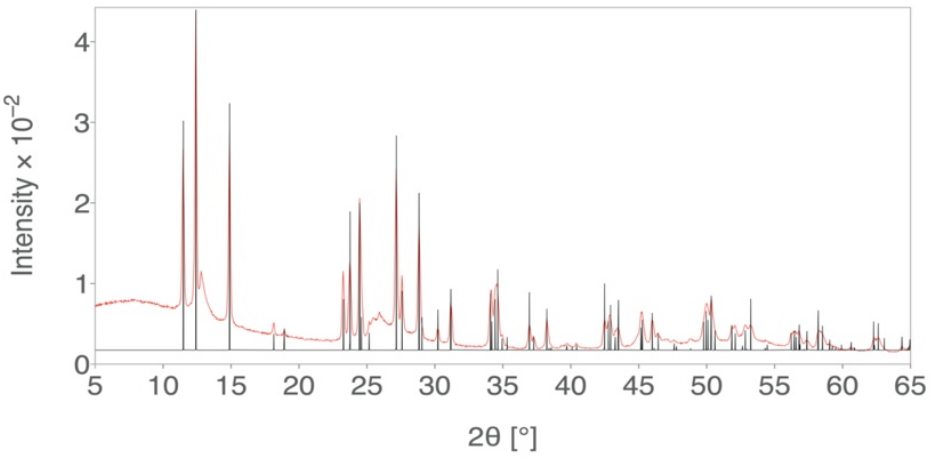


**Figure 7.5:** PXRD pattern of the K ion exchange product. The calculated pattern is in black.

Optical measurements on $Cs_2(UO_2)Al_2O_5$ were performed using a PerkinElmer Lambda 35 UV-vis spectrometer equipped with an integrating sphere and a PerkinElmer LS55 luminescence spectrometer. The UV-vis diffuse-reflectance data were collected over 200-900 nm and converted internally using the Kubelka-Munk equation.[29] $Cs_2(UO_2)Al_2O_5$ absorbs broadly from 200-530 nm, classifying the title compound as a semiconductor, with the charge transfer band centered at 354 nm and the $UO_2^{2+}$ transitions at 435 and 446 nm with a shoulder at 505 nm (Figure 7.7a). The DFT+*U* calculations show that the title compound is specifically a charge-transfer insulator (see Figure 7.6), where the states at the top of the valence band are mainly from O atoms, while the states at the bottom of the conduction band are from U atoms. This is unlike $UO_2$ and the previously studied uranyl phosphates,[30] with slightly larger band gap of 423 nm. Replacing P with the less electronegative element, Al, makes the $Cs_2(UO_2)Al_2O_5$ system more ionic, pushing the O states to higher energies, consequently the states at the top of the valence band are exclusively from the O atoms . The maximum fluorescence emission occurs when exciting at 408 nm, and the maximum peak of the emission spectrum is at 573 nm with a smaller peak at 530 nm, which is typical of $UO_2^{2+}$ fluorescence (Figure 7.7b). While the fluorescence emission spectra is typical of solid state $UO_2^{2+}$ species, the UV-vis diffuse reflectance data are unusual in the fact that the vibronically coupled transitions of the $UO_2^{2+}$ are significantly narrower than in spectra of other recently reported solid state $UO_2^{2+}$ species.[7, 31–35]

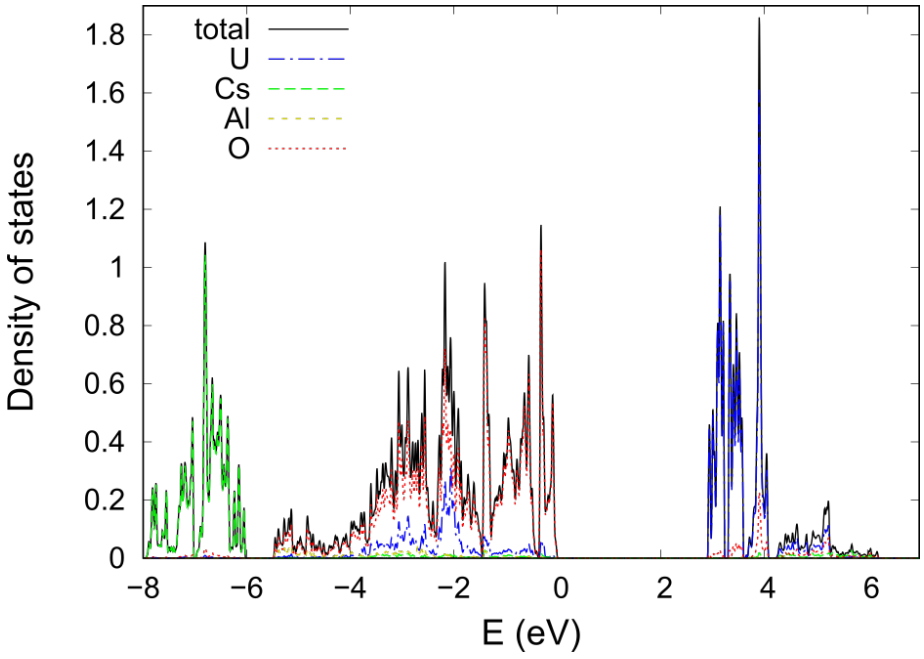


**Figure 7.6:** Total and partial density of states (DOS) of $Cs_2UO_2Al_2O_5$

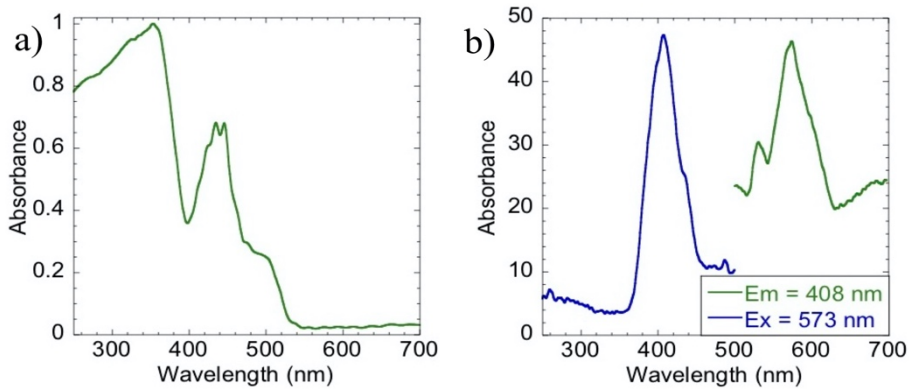


**Figure 7.7:** a) Normalized UV-vis spectra and b) fluorescence spectra of $Cs_2(UO_2)Al_2O_5$.

In summary, the first uranium material solely containing aluminum tetrahedra as the secondary building unit was discovered serendipitously by molten flux methods and synthesized by combined solid state and flux methods. The structure was characterized by SXRD, PXRD, EDS, optical spectroscopy, and modeled by DFT calculations to determine

the feasibility of the exchange of $Cs^+$ cations for $K^+$ in water. The ion exchange reaction was shown to be favorable by DFT+*U* calculations, which was supported by our analysis of the ion exchange product that was confirmed to have exchanged essentially all $Cs^+$ for $K^+$ and to have a similar powder pattern that can be indexed with unit cell parameters similar to those of the parent phase. This work demonstrates the ability to form uranium aluminates by molten flux methods, although the exact reaction conditions that produced this phase are poorly understood and should be the subject of future investigations in order to expand this new class of uranium aluminate materials.

**Acknowledgements.** Research was conducted by the Center for Hierarchical Wasteform Materials (CHWM), an Energy Frontier Research Center (EFRC). Research was supported by the U.S. Department of Energy, Office of Basic Energy Sciences, Division of Materials Sciences and Engineering under Award DE-SC0016574. C. Juillerat is additionally supported by an NSF IGERT Graduate Fellowship under grant number 1250052.

**References:**

(1) Lussier, A. J.; Lopez, R. A. K.; Burns, P. C., A revised and expanded structure hierarchy of natural and synthetic hexavalent uranium compounds, *Can. Mineral.* **2016**, *54*, 177-283.

(2) Burns, P. C., $U^{6+}$ minerals and inorganic compounds: insights into an expanded structural hierarchy of crystal structures, *Can. Mineral.* **2005**, *43*, 1839-1894.

(3) Burns, P. C.; Ewing, R. C.; Hawthorne, F. C., The crystal chemistry of hexavalent uranium: polyhedron geometries, bond-valence parameters, and polymerization of polyhedra, *Can. Mineral.* **1997**, *35*, 1551-1570.

(4) Juillerat, C. A.; Klepov, V. V.; Morrison, G.; Pace, K. A.; zur Loye, H.-C., Flux Crystal Growth: A Versatile Technique to Reveal the Crystal Chemistry of Complex Uranium Oxides, *Dalton Trans.* **2019**, *48*, 3162-3181.

(5) Santamaría-Pérez, D.; Vegas, A., The Zintl-Klemm concept applied to cations in oxides. I. The structures of ternary aluminates., *Acta Cryst.* **2003**, *B59*, 305-323.

(6) Wu, S.; Beermann, O.; Wang, S.; Holzheid, A.; Depmeier, W.; Malcherek, T.; Modolo, G.; Alekseev, E. V.; Albrecht-Schmitt, T. E., Synthesis of Uranium Materials under Extreme Conditions: $UO_2[B_3Al_4O_{11}(OH)]$, a Complex 3D Aluminoborate, *Chemistry—A European journal* **2012**, *18*, 4166-4169.

(7) Juillerat, C. A.; Klepov, V. V.; Alekseev, E. V.; zur Loye, H.-C., Overstepping Löwenstein's Rule – a Route to Unique Aluminophosphate Frameworks with 3D Salt-Inclusion and Ion Exchange Properties, *Inorg. Chem.* **2019**, *58*, 724-736.

(8) Chave, T.; Nikitenko, S. I.; Scheinost, A. C.; Berthon, C.; Arab-Chapelet, B.; Moisy, P., First synthesis of uranyl aluminate nanoparticles., *Inorg. Chem.* **2010**, *49*, 6381-6383.

(9) Bruker. *APEX3, SAINT+, and SADABS.* Bruker AXS Inc.: Madison, Wisconsin, USA, 2015;

(10) Sheldrick, G. M., Crystal structure refinement with SHELXL, *Acta Cryst.* **2015**, *C71*, 3-8.

(11) Sheldrick, G. M., SHELXT - Integrated space-group and crystal-structure determination, *Acta Cryst.* **2015**, *A71*, 3-8.

(12) Dolomanov, O. V.; Bourhis, L. J.; Gildea, R. J.; Howard, J. A. K.; Pushmann, H., OLEX2: a complete structure solution, refinement and analysis program, *J. Appl. Crystallogr.* **2009**, *42*, 339-341.

(13) Liu, H.-K.; Peng, C.-C.; Chang, W.-J.; Lii, K.-H., Tubular Chains, Single Layers, and Multiple Chains in Uranyl Silicates: $A_2[(UO_2)Si_4O_{10}]$ (A = Na, K, Rb, Cs), *Cryst. Growth Des.* **2016**, *16*, 5268-5272.

(14) Wang, X.; Huang, J.; Liu, L.; Jacobson, A. J., The novel open-framework uranium silicates $Na_2(UO_2)(Si_4O_{10})\cdot 2.1H_2O$ (USH-1) and $RbNa(UO_2)(Si_2O_6)\cdot H_2O$ (USH-3), *J. Mater. Chem.* **2002**, *12*, 406-410.

(15) Burns, P. C.; Olson, R. A.; Finch, R. J.; Hanchar, J. M., $KNa_3(UO_2)_2(Si4O_{10})_2(H_2O)_4$, a new compound formed during vapor hydration of an actinide-bearing borosilicate waste glass, *J. Nucl. Mater.* **2000**, *278*, 290-300.

(16) Li, Y.; Burns, P. C., The structures of two sodium uranyl compounds relevant to nuclear waste disposal, *J. Nucl. Mater.* **2001**, *299*, 219=236.

(17) Liebau, F. *Structural Chemistry of Silicates: Structure, Bonding, and Classification.* Springer-Verlag: Berlin, 1985;

(18) Kresse, G.; Furthmuller, J., Efficient iterative schemes for ab-initio total-energy calculations using a plane-wave basis set, *Phys. Rev. B* **1996**, *54*, 11169-11186.

(19) Kresse, G.; Furthmuller, J., Efficiency of ab-initio total energy calculations for metals and semiconductors using a plane-wave basis set, *Comput. Mater. Sci.* **1996**, *6*, 15-50.

(20) Blöchl, P. E., Projector augmented-wave method, *Phys. Rev. B* **1994**, *50*, 17953-17979.

(21) Kresse, G.; Joubert, D., From ultrasoft pseudopotentials to the projector augmented-wave method, *Phys. Rev. B* **1999**, *59*, 1758-1775.

(22) Perdew, J. P.; Burke, K.; Ernzerhof, M., Generalized Gradient Approximation Made Simple, *Phys. Rev. Lett.* **1996**, *77*, 3865-3868.

(23) Anisimov, V. I.; Solovyev, I. V.; Korotin, M. A.; Czyzyk, M. T.; Sawatzky, G. A., Density-functional theory and NiO photoemission spectra, *Phys. Rev. B* **1993 Dec**, *48*, 16929-16934.

(24) Liechtenstein, A. I.; Anisimov, V. I.; Zaanen, J., Density-functional theory and strong interactions: Orbital ordering in Mott-Hubbard insulators, *Phys. Rev. B* **1995 Aug**, *52*, R5467-R5470.

(25) Schoenes, J., Recent specroscopic studies of $UO_2$, *J. Chem. Soc., Faraday Trans. 2* **1987**, *83*, 1205-1213.

(26) Kotani, A.; Takao, Y., Systematic Analysis of Core Photoemission Spectra for Actinide Di-Oxides and Rare-Earth Sesqui-Oxides, *Prog. Theor. Phys. Suppl.* **1992**, *108*, 117-131.

(27) Persson, K. A.; Waldswick, B.; Lazic, P.; Cedar, G., Prediction of solid-aqueous equilibria: Scheme to combine first-principles calculations of solids with experimental aqueous states, *Phys. Rev. B* **2012**, *85*, 235438-235449.

(28) *Jade*, version 9.6.0; PXRD analysis software; Materials Data, Inc.: Livermore, CA 2014

(29) Kubelka, P.; Munk, F. Z., Ein Beitrag Zur Optik Der Farbanstriche, *Z. Techn. Phys.* **1931**, *12*, 593-601.

(30) Kocevski, V.; Juillerat, C. A.; Moore, E. E.; zur Loye, H.-C.; Besmann, T., Understanding the polymorphism of $A_4[(UO_2)_3(PO_4)_2O_3]$ (A=alkali metals) uranyl phosphate framework structures, *Cryst. Growth Des.* **2019**, *19*, 966-975.

(31) Juillerat, C. A.; Moore, E. E.; Morrison, G.; Smith, M. D.; Besmann, T. M.; zur Loye, H.-C., Versatile Uranyl Germanate Framework Hosting Twelve Different Alkali Halide 1D Salt Inclusions, *Inorg. Chem.* **2018**, *57*, 11606-11615.

(32) Juillerat, C. A.; Moore, E. E.; Besmann, T. B.; zur Loye, H.-C., Observation of an Unusual Uranyl Cation-Cation Interaction in the Strongly Fluorescent Layered Uranyl Phosphates $Rb_6[(UO_2)_7O_4(PO_4)_4]$ and $Cs_6[(UO_2)_7O_4(PO_4)_4]$, *Inorg. Chem.* **2018**, *57*, 3675-3678.

(33) Juillerat, C. A.; Moore, E. E.; Kocevski, V.; Besmann, T.; zur Loye, H.-C., A Family of Layered Phosphates Crystallizing in a Rare Geometrical Isomer of the Phosphuranylite Topology: Synthesis, Characterization, and Computational Modeling of A, *Inorg. Chem.* **2018**, *57*, 4726-4738.

(34) Morrison, G.; Smith, M. D.; Tran, T. T.; Halasyamani, S.; zur Loye, H.-C., Synthesis and structure of the new pentary uranium(VI) silicate, $K_4CaUSi_4O_{14}$, a member of a structural family related to frenoite, *CrystEngComm* **2015**, *17*, 4218-4224.

(35) Read, C. M.; Yeon, J.; Smith, M. D.; zur Loye, H.-C., Crystal growth, structural characterization, cation–cation interaction classification, and optical properties of uranium (vi) containing oxychlorides, $A_4U_5O_{16}Cl_2$ (A= K, Rb), $Cs_5U_7O_{22}Cl_3$, and $AUO_3Cl$ (A=Rb, Cs), *CrystEngComm* **2014**, *16*, 7259.

# Chapter 8

## Targeted Crystal Growth of Uranium Gallates Via the Systematic Exploration of the $UF_4$-$GaPO_4$-ACl (A = Cs, Rb) Phase Space[1]

[1]Reproduced from Juillerat, C. A.; Klepov, V. V. ; Smith, M. D.; zur Loye, H.-C. Targeted Crystal Growth of Uranium Gallates Via the Systematic Exploration of the $UF_4$-$GaPO_4$-ACl (A = Cs, Rb) Phase Space, *CrystEngComm*, **2020**, *Accepted.* with permission from the Royal Society of Chemistry.

**Abstract:** The molten flux synthesis of a uranium gallophosphate and a uranium gallate, $Cs_4[UO_2Ga_2(PO_4)_4]$ (**8.1**) and $Cs_2UO_2Ga_2O_5$ (**8.2**), and four uranium phosphates, $[Rb_2Rb_{3.93}Cl_{0.93}][(UO_2)_5(PO_4)_5]$ (**8.3**), $Rb_{11}[(UO_2)_8(PO_4)_9]$ (**8.4**), $Rb_{7.6}[(UO_2)_8O_{8.6}F_{0.4}(PO_4)_2]$ (**8.5**), and $Rb_6[(UO_2)_5O_2(PO_4)_4]$ (**6**) is reported. A systematic exploration of the $UF_4$-$GaPO_4$-ACl (A = Cs, Rb) phase space resulted in the synthesis of targeted $Cs_4[UO_2Ga_2(PO_4)_4]$ (**8.1**) and $Cs_2UO_2Ga_2O_5$ (**2**), which are gallium analogs to the previously reported aluminates, $Cs_4[UO_2Al_2(PO_4)_4]$ and $Cs_2UO_2Al_2O_5$ (**8.2**). The exploration of this phase space simultaneously led to the synthesis and characterization of four new uranium phosphate phases. $Rb_2Rb_{3.93}Cl_{0.93}][(UO_2)_5(PO_4)_5]$ (**8.3**), a salt inclusion material, and $Rb_{11}[(UO_2)_8(PO_4)_9]$ (**8.4**) both of which have complex 3D, porous, framework structures, and $Rb_{7.6}[(UO_2)_8O_{8.6}F_{0.4}(PO_4)_2]$ (**8.5**) and $Rb_6[(UO_2)_5O_2(PO_4)_4]$ (**8.6**) both of which are layered structures related to the $U_3O_8$ topology. Fluorescence spectroscopy data is reported for all compositions and is found to be typical for uranyl compounds.

**Introduction.** According to the periodic law, the elements in the same groups have similar properties and reactivities and, consequently, can be found to form analogous compounds. Specifically, in solid state chemistry, there are several well-known pairs of main group elements that form many analogous compounds, such as Si and Ge, P and As, and Al and Ga. Some well-known structure types that accommodate these pairs interchangeably are Si and Ge wadeites,[1–6] P and As apatites,[7–9] and Al and Ga corundum structures.[10] Among these pairs, Al and Ga are most similar in size with tetrahedra crystal radii of 0.53 and 0.61 Å when compared to Si and Ge, whose tetrahedral crystal radii are 0.40 and 0.53 Å, to P and As, whose tetrahedral crystal radii are 0.31 and 0.475 Å. In

addition, both Al and Ga adopt trigonal pyramidal and octahedral coordination environments with crystal radii of 0.62 and 0.69 Å, and 0.675 and 0.76 Å for each element and coordination geometry, respectively, and are thus significantly closer in size to each other than are other main group element pairs.[11] Due to the chemical similarity of these elements, once a compound containing one of them has been synthesized, one can expect that the analog will adopt the same structure, which, however, is not always the case, and sometimes even a subtle size change (and respective change in the lattice energy) can result in a completely different structure.[12] The structure types that are sensitive to the size changes can even be used for element separations,[13] fostering studies on isostructural series.

Recently, our group has published several uranium and aluminum containing oxides with complex, unique structure types and because of the similarity of Al and Ga in oxide structures,[14, 15] in addition to the lack of uranium and gallium containing phases (only two reported in the ICSD),[16] we sought to prepare the Ga analogs of these aluminum based structures. In order to target these Ga analogs, we used the same synthetic approach as was used for the aluminum phases and systematically explored the phase space in close proximity to the successful conditions for the Al containing phases. The Al structures were synthesized via molten flux crystal growth methods[17, 18] and, as in most synthetic techniques, there is a continuum of experimental conditions that control and influence the products obtained in addition to their quality and yield. In this study, we identified the crucible size/shape, crucible material, $UF_4$/$GaPO_4$ reagent ratio, amount of flux, identity of the flux, and dwell temperature, and found them all strongly to influence the formation the

desired products. There are a number of other variables such as dwell time, slow cooling rate, atmosphere, uranium source, gallium source, etc., that were also considered.

Not unexpectedly, in the process of exploring the $UF_4$-$GaPO_4$-ACl (A = Cs, Rb) phase space, we came across several new structure types in addition to two of the desired uranium and gallium containing phases we targeted. We explored a significant fraction of the phase space targeting the desired phases, and while these experiments certainly are not exhaustive and leave several variables to be explored further, they embody a representative cross section of phase space. Herein, we present the two uranium-gallium analogs, $Cs_4[UO_2Ga_2(PO_4)_4]$ (**8.1**) and $Cs_2UO_2Ga_2O_5$ (**8.2**), in addition to the compilation of uranium phosphate structures obtained in the same phase space: $[Rb_2Rb_{3.93}Cl_{0.93}][(UO_2)_5(PO_4)_5]$ (**8.3**), $Rb_{11}[(UO_2)_8(PO_4)_9]$ (**8.4**), $Rb_{7.6}[(UO_2)_8O_{8.6}F_{0.4}(PO_4)_2]$ (**8.5**), and $Rb_6[(UO_2)_5O_2(PO_4)_4]$ (**8.6**).

**Experimental:**

**Synthesis.** For the synthesis of all of the reported structures, molten flux methods using alkali chloride or alkali fluoride fluxes were used.[17, 18] $UF_4$ (International Bio-Analytical Industries, powder, ACS grade), $UO_2(CH_3CO_2)_2{\cdot}2H_2O$ (International Bio-Analytical Industries, powder, ACS grade), $(NH_4)_2HPO_4$ (VWR, ACS grade), CsCl (VWR, ultra pure), CsF (Alfa Aesar, 99% ), RbCl (BTC, 99.0%) were all used as received. $GaPO_4$ is not available commercially and was therefore synthesized by us using a 1:2 mol mixture of $Ga_2O_3$ (Alfa Aesar, 99.999%) and $(NH_4)_2HPO_4$ that was intimately ground in a mortar and pestle before heating the mixture at 1000 °C for 40 hours. The resulting $GaPO_4$ was determined to be a mixture of two polymorphs and contained a small $Ga_2O_3$ impurity and was used, as is, in the following reactions. ***Caution!*** *Although the uranium precursors used*

*contained depleted uranium, standard safety measures for handling radioactive substances must be followed.*

$Cs_4[UO_2Ga_2(PO_4)_4]$ (**8.1**). Synthesis methods are based on those used to synthesize $Cs_4[UO_2Al_2(PO_4)_4]$.[14] Single crystals of **8.1** were obtained by reacting 0.5 mmol of $UF_4$, 1 mmol $GaPO_4$, 1 mmol $(NH_4)_2HPO_4$, and 20 mmol CsCl in a 17 mL Pt crucible, open to atmosphere, (28.5 mm ID x 27 mm tall) and heating the mixture at 700 °C for 12 h and slow cooling to 600 °C at 6 °C/h. Crystals were isolated from the reaction vessel by sonicating the reaction in water to dissolve the flux, followed by vacuum filtration—the same method was used for all syntheses reported. Small, pale yellow needle shaped crystals (Figure 8.1) were obtained in good yield alongside other minor impurity phases. Solid state reactions were also carried out by intimately grinding 1 mmol of $UO_2(CH_3CO_2)_2•2H_2O$, 2mmol $GaPO_4$, 2 mmol $(NH_4)_2HPO_4$, and 4 mmol of $CsNO_3$ and pressing a pellet and heating at 575 °C for 66 h, and 700, 800, and 900 °C for 12 h. In between changes in temperature, the pellets were intermittently ground and pressed into pellets before heating at a high temperature. While $Cs_4[(UO_2Ga_2(PO_4)_4]$ (**8.1**) was obtained, the simultaneous formation of a significant quantify of an impurity phase could not be avoided; unfortunately, this impurity phase could not be identified (Figure 8.2).

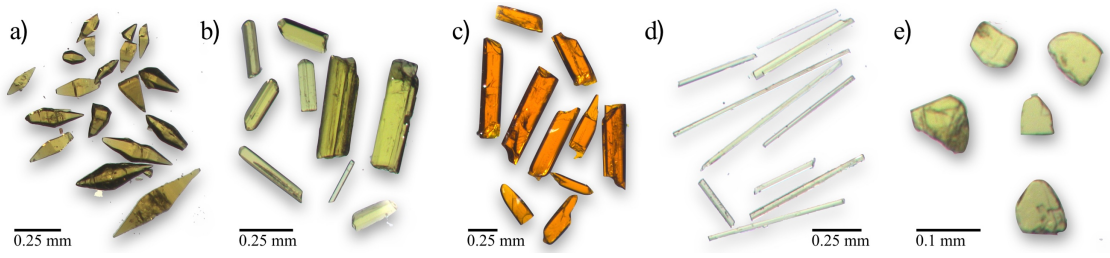


**Figure 8.1**: Optical images of single crystals of a) $Cs_2UO_2Ga_2O_5$ (**8.2**) b) $[Rb_2Rb_{3.93}Cl_{0.93}][(UO_2)_5(PO_4)_5]$ (**8.3**) c) $Rb_{7.6}[(UO_2)_8O_{8.6}F_{0.4}(PO_4)_2]$ (**8.5**), d) $Rb_{11}[(UO_2)_8(PO_4)_9]$ (**8.4**), and e) $Rb_6[(UO_2)_5O_2(PO_4)_4]$ (**8.6**).

$Cs_2UO_2Ga_2O_5$ (**8.2**). Yellow, kite-shaped single crystals of **8.2** were grown by loading 0.5 mmol $UF_4$, 0.5 mmol $Ga_2O_3$, 11 mmol of CsCl, and 9 mmol of CsF in a 17 mL Pt crucible (28.5 mm ID x 27 mm tall) and heating at 875 °C for 12h before slow cooling to 450 °C at 6 °C/h. $Cs_4U_5O_{17}$ was simultaneously obtained as orange rods that grew on the walls of the crucibles, while the yellow crystals of **8.2** were found at the bottom of the crucible.

Crystals of $[Rb_2Rb_{3.93}Cl_{0.93}][(UO_2)_5(PO_4)_5]$ (**8.3**) and $Rb_6[(UO_2)_5O_2(PO_4)_4]$ (**8.6**) were obtained by loading 0.5 mmol $UF_4$, 0.5 mmol $GaPO_4$, and 20 mmol RbCl in an open fused silica tube (14 mm ID x ~26 mm tall) and covered with a silica cap (17 mm ID x ~20 mm tall). The reactions were heated to 875 °C and held there for 12 h before slow cooling to 550 °C at 6 °C/h. Both **8.3** and **8.6** are yellow crystals, where **8.3** is the more predominant product that crystallizes as rods/needles, while **8.6** crystallizes as plates.

$Rb_{11}[(UO_2)_8(PO_4)_9]$ (**8.4**) was obtained from a reaction of 0.5 mmol of $UF_4$, 1 mmol $GaPO_4$, and 20 mmol of RbCl loaded into a 5 mL Pt crucible (15 mm ID x 26 mm tall) and heated at 875 °C for 12 h before slow cooling to 550 °C at 6 °C/h. The single crystals are pale-yellow in color and are long needles, a side product that is deeper yellow in color as well as more rod like was also obtained and was identified as $Rb_9U_5P_6O_{34.5}$; however, the crystal quality was very poor and the SXRD structure cannot be reported with confidence.

Single crystals of $Rb_{7.6}[(UO_2)_8O_{8.6}F_{0.4}(PO_4)_2]$ (**8.5**) were obtained in a reaction of 0.5 mmol $UF_4$, 0.33 mmol of $GaPO_4$, and 20 mmol of RbCl in a 5 mL alumina crucible (16 mm ID x 26 mm tall) with a larger 17 mL alumina crucible (23.5 mm ID x 41.5 mm tall) inverted overtop. The reaction was heated at 775 °C for 12 h and slow cooled to 650 °C at 6 °C/h. This synthesis produced a least 5 different phases either yellow or orange in color

and varying in crystal morphology. $Rb_6[(UO_2)_5O_5(PO_4)_2]$, $Rb_7[Al_2O(PO_4)_3][(UO_2)_6O_4(PO_4)_2]$, $Rb_3[Al_2O(PO_4)_3][(UO_2)_3O_2]$, were among those identified. Crystals of **8.5** form as orange rectangular prisms (Figure 8.1).

**PXRD.** A Bruker D2 Phaser equipped with a LYNXEYE silicon strip detector with a Cu K$\alpha$ ($\lambda$ = 1.54056 Å) source was used to collect PXRD data. PXRD patterns were used for product identification.

**Single Crystal X-ray Diffraction.** Except for **8.1**, the structures of each of the reported compounds were determined by single crystal X-ray diffraction (SXRD) using data collected on a Bruker D8 QUEST diffractometer with an PHOTON II area detector and a microfocus source (Mo K$\alpha$ radiation, $\lambda$ = 0.71073 Å) or a Bruker D8 QUEST diffractometer equipped with a PHOTON 100 CMOS area detector and a microfocus source (Mo K$\alpha$ radiation, $\lambda$ = 0.71073 Å). The raw data were reduced and corrected for absorption effects using SAINT+ and SADABS programs within APEX 3.[19] The SHELXT solution program employing intrinsic phasing was used to obtain an initial structure that was refined using the SHELXL refinement program.[20] Both SHELXT and SHELXL were used within the Olex2 GUI.[21, 22] Full crystallographic details can be found in Table 8.1. Elemental compositions of the compounds were confirmed qualitatively by EDS using a TESCAN Vega-3 SBU equipped with an EDS detector.

Attempts were made to collect high quality SXRD data on compound **8.1**; however, due to multiple twinning and generally insufficient crystal quality, a publishable structure solution could not be obtained. The unit cell data obtained from single crystals is reported in Table 8.1 and the PXRD pattern of the product obtained by solid state synthesis with calculated pattern using the cif of $Cs_4[UO_2Al_2(PO_4)_4]$ and changing the unit cell contents

**Table 8.1**: Full crystallographic data for compounds **8.1-8.6**.

| Formula | $Cs_4[UO_2Ga_2(PO_4)_4]$ | $Cs_2UO_2Ga_2O_5$ | $[Rb_{5.93}Cl_{0.93}][(UO_2)_5(PO_4)_5]$ | $Rb_{11}[(UO_2)_8(PO_4)_9]$ | $Rb_{7.6}[(UO_2)_8O_{8.6}F_{0.4}(PO_4)_2]$ | $Rb_6[(UO_2)_5O_2(PO_4)_4]$ |
|---|---|---|---|---|---|---|
| Number | **8.1** | **8.2** | **8.3** | **8.4** | **8.5** | **8.6** |
| S. G. | -- | *I*4/*amd* | $P\bar{1}$ | $P4_2/mbc$ | $P2_1/n$ | $P\bar{1}$ |
| a, Å | 10.837(1) | 7.41690(10) | 9.548(4) | 25.7697(6) | 9.5935(5) | 7.3052(8) |
| b. Å | 10.857(1) | 7.41690(10) | 13.488(5) | 25.7697(6) | 13.7652(8) | 9.0828(10) |
| c, Å | 13.018(1) | 31.9700(7) | 14.898(6) | 9.3962(2) | 13.2983(8) | 11.7254(13) |
| $\alpha$, ° | 80.564(4) | 90 | 64.755(16) | 90 | 90 | 75.857(4) |
| $\beta$, ° | 82.786(4) | 90 | 72.369(16) | 90 | 101.343(2) | 72.834(4) |
| $\gamma$, ° | 87.026(4) | 90 | 89.511(16) | 90 | 90 | 86.974(4) |
| V, Å$^3$ | 1498.1(2) | 1758.68(6) | 1637.7(11) | 6239.8(3) | 1721.82(17) | 720.65(14) |

[a] $R_1 = \Sigma||F_0| - |F_c||/\Sigma|F_0|$. [b] $wR_2 = [\Sigma w(F_0^2 - F_c^2)^2/\Sigma w(F_0^2)^2]^{1/2}$

**Table 8.1**: Full crystallographic data for compounds **8.1-8.6**.

| Formula | $Cs_4[UO_2Ga_2(PO_4)_4]$ | $Cs_2UO_2Ga_2O_5$ | $[Rb_{5.93}Cl_{0.93}][(UO_2)_5(PO_4)_5]$ | $Rb_{11}[(UO_2)_8(PO_4)_9]$ | $Rb_{7.6}[(UO_2)_8O_{8.6}F_{0.4}(PO_4)_2]$ | $Rb_6[(UO_2)_5O_2(PO_4)_4]$ |
|---|---|---|---|---|---|---|
| Number | **8.1** | **8.2** | **8.3** | **8.4** | **8.5** | **8.6** |
| Crystal size ($mm^3$) | -- | 0.02 x 0.04 x 0.06 | 0.02 x 0.03 x 0.04 | 0.02 x 0.02 x 0.1 | 0.01 x 0.02 x 0.03 | 0.04 x 0.12 0.16 |
| temp. (K) | -- | 302 | 301 | 301 | 303 | 301 |
| density ($g\ cm^{-3}$) | -- | 5.708 | 4.796 | 4.212 | 6.066 | 5.242 |
| $\theta$ range (deg) | -- | 2.548–36.353 | 2.260–28.437 | 2.499–27.500 | 2.151–27.492 | 2.313–37.883 |
| $\mu$ ($mm^{-1}$) | -- | 32.620 | 33.813 | 29.564 | 48.351 | 38.389 |
| collected reflec. | -- | 61580 | 74700 | 100392 | 109936 | 52660 |
| unique reflections | -- | 1204 | 8125 | 3807 | 3952 | 7778 |
| $R_{int}$ | -- | 0.0352 | 0.0882 | 0.0452 | 0.0674 | 0.0499 |
| $h$ | -- | $-12 \le h \le 12$ | $-12 \le h \le 12$ | $-33 \le h \le 33$ | $-12 \le h \le 12$ | $-12 \le h \le 12$ |
| $k$ | -- | $-12 \le k \le 11$ | $-18 \le k \le 16$ | $-33 \le k \le 32$ | $-17 \le k \le 17$ | $-15 \le k \le 15$ |
| $l$ | -- | $-53 \le l \le 53$ | $-19 \le l \le 19$ | $-12 \le l \le 12$ | $-17 \le l \le 17$ | $-20 \le l \le 20$ |
| $\Delta\rho_{max}$ (e $Å^{-3}$) | -- | 1.481 | 2.772 | 2.126 | 2.573 | 2.800 |
| $\Delta\rho_{min}$ (e $Å^{-3}$) | -- | -1.450 | -3.161 | -1.686 | -2.114 | -2.897 |
| *GoF* | -- | 1.326 | 1.098 | 1.326 | 1.362 | 1.056 |
| $R_1(F)$ for $F_0^2 > 2\sigma(F_0^2)$[a] | -- | 0.0210 | 0.0482 | 0.0350 | 0.0405 | 0.0282 |
| $R_w(F_0^2)$[b] | -- | 0.0498 | 0.0960 | 0.0910 | 0.0865 | 0.0728 |

[a] $R_1 = \Sigma||F_0| - |F_c||/\Sigma|F_0|$. [b] $wR_2 = [\Sigma w(F_0^2 - F_c^2)^2/\Sigma w(F_0^2)^2]^{1/2}$

from Al to Ga and unit cell parameters produces a nice fit (Figure 7.2) and confirms that the Ga analog has been obtained.

For $Cs_2UO_2Ga_2O_5$ (**8.2**), the refinement of the U, Ga, and O sites was straightforward, while the refinement of the Cs sites was difficult due to the extreme disorder of the cations in the channels of the structures, similar to what was observed in the Al analog. Partially occupied Cs sites were added by freely refining significant electron density peaks near the largest Cs sites, Cs1 and Cs2, until the summed occupancies of these sites approached charge balance, 2 Cs per formula unit. At this point the occupancies of the sites were fixed, refined anisotropically, and an ISOR command was implemented on Cs2 to restrain the thermal parameters on the Cs sites, and then the occupancies of individual sites were manually and slowly increased to achieve charge balance. This was done manually instead of using a constraint such as the SUMP command, due to the instability of the refinement when this constraint is applied. The final occupancies of Cs1-Cs7 are 0.6338, 0.13, 0.0445, 0.052, 0.0408, 0.10, and 0.05, respectively.

For $[Rb_2Rb_{3.93}Cl_{0.93}][(UO_2)_5(PO_4)_5]$ (**8.3**), difficulty was encountered in finding a crystal of suitable diffraction quality for structure determination. Several crystals and cleaved crystal fragments were screened for quality and most exhibited problematic, twinned diffraction patterns consisting of very closely run-together spots, also having poorly shaped, asymmetric Bragg peak profiles with long tails. Three datasets were collected on small cleaved fragments, and the best is reported here. The compound crystallizes in the triclinic system. The space group $P\bar{1}$ (No. 2) was confirmed by structure solution. The asymmetric unit consists of five uranium atoms, six rubidium atoms, five phosphorus atoms, one chloride atom, one mixed and partially occupied Rb/Cl site and

thirty unique oxygen atoms. All atoms are located on positions of general crystallographic symmetry (site 2*b*). Several displayed poorly shaped displacement ellipsoids arising from the moderate crystallinity or from crystallographic disorder.

Uranium atoms U1-U4 refine normally. U5 is disordered over three closely separated sites. Refinement of the U5 site as a single position resulted in an elongated displacement ellipsoid, two large satellite electron density peaks (9.4 and 3.2 e-/Å$^3$) at *ca.* 0.8 Å from the position, and an $R_1$ value > 9%. A disordered, 3-part U5 site better accounted for the observed electron density and reduced the $R_1$ value to 4.82%. The three components were restrained to sum to one uranium per site and refined to U5(A/B/C) = 0.730(3)/0.190(3)/0.080(3). This results in distorted coordination environments for U5B and U5C (Figure 8.5e) and very short and long equatorial bond distances. It is possible that the O atoms coordinated to these U sites are also disordered to create more reasonable coordination environments, but due to the small scattering factors and low occupancy of the O, this disorder could not be modeled. The uranyl oxygen, however, was able to be modeled as a split site. Oxygen O28, as a U5 uranyl unit oxygen atom, is disordered over two sites A/B. Occupancies of the two sites were tied to the U5A (O28A) and U5(B/C) (O28B) occupancies, thereby corresponding to two typical, nearly linear $UO_2$ groups (with O29).

Disorder or partial occupancy was also observed for rubidium sites Rb3 - Rb6. Only Rb1 and Rb2 refined to full occupancy and without the appearance of large nearby residual density. Rb3 and Rb4 are each disordered over two sites with occupancies Rb3(A/B) = 0.69(8)/0.31(8) and Rb4A/B = 0.65(2)/0.35(2) (both constrained to sum to one). Rb5 refines to a partial occupancy value of 0.844(7). There were no residual peaks close to Rb5

suggesting a split site. Rb6 was modeled with three independent sites distributed roughly linearly, with occupancies Rb6(A/B/C) = 0.770(3)/0.111(3)/0.119(3). The unique chlorine atom Cl1 is disordered across an inversion center and was refined as half-occupied. Another site near the Rb6 disorder assembly was modeled as a mixed and split Rb/Cl site, Rb7A/Cl2A. This site refined to a partial occupancy value significantly less than one even if modeled as 100% Cl and was further split into two discrete electron density maxima. Several disorder models for this site were refined, but only the reported model resulted in an essentially electroneutral composition. Distances to surrounding atoms are reasonable for both Rb and Cl. Occupancies refined to Rb7A = 0.082(6) and Cl2A = 0.45(2). The $U_{ij}$ values of oxygen O16 were restrained to adopt a spherical shape to prevent an oblate ellipsoid. All atoms were refined with anisotropic displacement parameters except for minor disorder components B and C of site Rb6 and the Rb7A/Cl2A site (isotropic).

The structure solution of $Rb_{11}[(UO_2)_8(PO_4)_9]$ (**8.4**) is highly disordered and the structural significance of the disorder will be discussed in the structure description section, vide infra, while the crystallographic approach to modeling the disorder is discussed in this section. $Rb_{11}[(UO_2)_8(PO_4)_9]$ (**8.4**) crystallizes in the tetragonal space group $P4_2/mbc$ and the asymmetric unit contains four uranium atoms, six rubidium atoms, three phosphorus atoms, and 17 unique oxygen atoms. A large number of sites, namely U1-3, Rb1, Rb3, Rb4B, Rb6, O1. O2. O7, O13, and O14 lie on Wyckoff site 8*h* with ..*m* symmetry, Rb2, Rb5A, Rb5c lie on Wyckoff site 8*g* with ..2 symmetry, P1 is assigned to Wyckoff site 4*d* with 2.22 symmetry, and all other sites lie on general positions.

U4, along with its uranyl oxygens O17 and O18, are disordered across a mirror plane and were assigned an occupancy of 0.5. The equatorial oxygens bonded to U4,

O4A/B and O5A/B are also disordered over two positions each and were assigned occupancies of 0.5 to match the U4 disorder. P3A/P3B are coordinated to O4A/B and O5/B such that the phosphate tetrahedron has two possible orientations, each half occupied to match the U4 disorder, and are coordinated to O6A/B and O3. The disorder of the P2A/B, coordinates to oxygens O9-O12, sites also represent two possible orientations for the phosphate tetrahedron (A and B) which were allowed to freely refine while constrained to a summed occupancy of 1 and result in 0.51/0.49 for part A and B, respectively. P1, coordinated to O15A/B, is also disordered over two orientations with occupancies of 0.5.

Additionally, the Rb cations are heavily disordered where there are three positions for Rb4 and four for Rb5 and Rb1-3 and Rb6 are fully occupied. Rb4A/B represents a disordered, half occupied Rb site where Rb4A is disordered over a mirror plane and the three resulting positions were constrained to a sum of 0.5 using a SUMP command resulting in occupancies of 0.2166 and 0.067, respectively for Rb4A and Rb4B. Similarly, a SUMP command was used for Rb5A/B/C (occupancies 0.475/0.1763/0.172) where Rb5B is disordered over a two-fold rotation axis and the Rb5 sites are constrained to an occupancy of 1. All atoms were refined anisotropically, although ISOR commands were used to constrain the thermal ellipsoids of Rb4A/B, O9A, O11A, and O12A.

$Rb_{7.6}[(UO_2)_8O_{8.6}F_{0.4}(PO_4)_2]$ (**8.5**) crystallizes in the monoclinic space group $P2_1/c$ and the asymmetric unit contains four uranium atoms, five rubidium atoms, one phosphorus atom, and 17 oxygen atoms. All atoms are located in positions of general crystallographic symmetry (4*e*) except for Rb1, which is located on an inversion center with Wyckoff site label 2*a*. Rb1 and 2 are fully occupied, while Rb3 and Rb4 are disordered and Rb5 is partially occupied. Rb3A/B and Rb4A/B were constrained to sum to an

occupancy of one and refine to 0.79/0.21 and 0.66/0.34, respectively. Rb5 when freely refined resulted in a partial occupancy of 0.30. With this partially occupied Rb site, the structure formula does not charge balance if all anion sites are modeled as oxygen; however, the O4 site freely refined to an occupancy of ~1.15 suggesting that it is a shared site of oxygen and fluorine. Since the scattering factors of O and F are very similar, they are often difficult to distinguish based on X-ray diffraction data so the O4/F4 occupancies were set to 0.80/0.20 to achieve charge balance. There is minor disorder in the uranium sheets, where O11 is disordered over an inversion center and set to an occupancy of 0.5. U4A/B, coordinated to O11, is disordered over two sites, and the occupancies were set to 0.5 which maintains regular coordination environments for the U4A/B where U4A adopts a square bipyramidal coordination and U4B adopts a pentagonal coordination environment. The disorder is further discussed in the structure description section. All atoms were refined anisotropically.

The refinement of $Rb_6[(UO_2)_5O_2(PO_4)_4]$ (**8.6**) was straightforward and the compound crystallizes in the triclinic space group $P\bar{1}$ (No. 2) and was confirmed by structure solution. The asymmetric unit consists of three uranium atoms, three rubidium atoms, two P atoms and 14 unique oxygen atoms. All atoms are all located on positions of general crystallographic symmetry (site 2*i*), except for U3, which is located on an inversion center (site 1*d*). All atoms were refined with anisotropic displacement parameters.

**Optical Spectroscopy.** Fluorescence emission spectra (400-650 nm) were collected for single crystals of **8.1**-**8.6** using a free space coupled 375 nm laser and Horiba iHr320 spectrometer equipped Olympus BX53 microscope.

**Results and Discussion:**

**Synthesis.** The recent success of obtaining uranium aluminophosphates and uranium aluminates by molten flux methods prompted a more expansive exploration of the $UF_4$, $GaPO_4$, and ACl (A = Rb, Cs) phase space with the goal of obtaining Ga analogs of the recently obtained Al containing structures: $Cs_2UO_2Al_2O_5$, $Cs_4[(UO_2Al_2(PO_4)_4]$, $[Cs_{13}Cl_5][(UO_2)_3Al_2O(PO_4)_6]$, $A_3[Al_2O(PO_4)_3][(UO_2)_3O_2]$ (A = Cs, Rb), and $Rb_7[Al_2O(PO_4)_3][(UO_2)_6O_4(PO_4)_2]$.[14, 15] While several of these compounds could be obtained using uranyl nitrate ($U^{6+}$) because the $U^{4+}$ (from $UF_4$) readily oxidizes in oxygen-rich atmosphere at high temperatures to $U^{6+}$, which is found in all compositions, the use of $UF_4$ produced larger crystals of higher quality; therefore, we have continued to use $UF_4$. In several publications by Juillerat et al. the crucible size and shape was found to be essential in obtaining certain products.[23–26] In order to specifically target the Ga analogs of the recently published U and aluminum containing materials, reaction vessels of the same size were used as in the Al synthesis. Visual summaries of the phase space explored in this work are given in Tables 8.2-8.4.

Initially, reactions were performed in 5 mL alumina vessels, which were used in the synthesis of the Al structures, as in the reported synthesis of **8.5**; however, the chloride flux dissolved small amounts of the alumina crucible (no visible damage) and led to Al containing products. In order to avoid alumina incorporation, reaction vessels of the same size but different material were sought out. Fused silica reaction vessels were made from tubing to match the size of the alumina crucible and lead to the formation of **8.3** and **8.6** and reactions in this phase space are summarized in Table 8.2. It was verified that the reactions reported for the synthesis of $Rb_3[Al_2O(PO_4)_3][(UO_2)_3O_2]$ could be successfully

carried out in the fused silica tubes. To further study the impact of crucible size and crucible material, 5 mL Pt crucibles were used in this study. $Rb_3[Al_2O(PO_4)_3][(UO_2)_3O_2]$ could also be obtained in the 5 mL Pt vessels. The use of these crucibles led to the synthesis of **8.4** and **8.5**. The phase space of the RbCl and CsCl fluxes in Pt crucibles is summarized in Tables 8.3 and 8.4.[25, 27, 28] Interestingly, using the same reactant loading for the synthesis of **8.3** and **8.6** $UF_4/GaPO_4$ 1:1, but using Pt crucibles, led to a different product, $Rb_9U_5P_6O_{34.5}$, the complete structure of which cannot be reported due to insufficient crystal quality. However, **8.6** could be obtained in the 5 mL Pt crucibles at 775 °C and a 1.5:1 ratio of $UF_4/GaPO_4$. It seems that although Pt and Si did not participate in the reaction, the material of the crucible, in addition to the size/shape, played a role in the synthesis, possibly due to the difference in nucleation sites in the crucibles of different materials.

**Table 8.2**: Phase space summary of $UF_4$-$GaPO_4$-RbCl in 5mL fused silica crucibles.

| mmols of RbCl | 1.5:1 | 1:1 |
|---|---|---|
| | | **---875** ---775 |
| 20 | ? poor xtals | **$[Rb_{5.93}Cl_{0.93}][(UO_2)_5(PO_4)_5]$‡ + ?**<br>$[Rb_{5.93}Cl_{0.93}][(UO_2)_5(PO_4)_5]$‡ + ? |
| 10 | **$Rb_6[(UO_2)_5O_2(PO_4)_4]$‡** | **$Rb_{11}U_{12}P_3O_{48}F_2$[23]**<br>$[Rb_{5.93}Cl_{0.93}][(UO_2)_5(PO_4)_5]$‡ |

Molar ratio of $UF_4$:$GaPO_4$

NOTE: The lack of more than one phase listed does not imply a phase pure product, but rather that only the major phase is reported. In many cases small impurities could not be identified.
‡Structures from this work

$Cs_4[UO_2Ga_2(PO_4)_4]$ (**8.1**) can also be synthesized using $UO_2(CH_3CO_2)_2$•$2H_2O$ (instead of $UF_4$), similar to the synthesis of the Al analog,[14] and using only $GaPO_4$ for the Ga and phosphate source. Additionally, **8.1** can be synthesized in the smaller 5 mL Pt

crucibles at 775 °C and 875 °C at a ratio of 1:2 $UF_4$:$GaPO_4$. At lower ratios, $Cs_2(UO_2)_2(PO_4)_2$,[29] $[Cs_4Cs_4Cl][(UO_2)_4(PO_4)_5]$,[14] or $Cs_6[(UO_2)_7O_4(PO_4)_4]$[30] are obtained.

**Table 8.3**: Phase space summary of $UF_4$-$GaPO_4$-RbCl in 5mL Pt crucibles.

| mmols of RbCl | 1.5:1 | 1:1 | 1:2 |
|---|---|---|---|
| | | | **---875** ---775 |
| 20 | **$Rb_{11}[(UO_2)_8(PO_4)_9]$**‡<br>$Rb_6[(UO_2)O_5(PO_4)_2]$[25] +<br>$Rb_4[(UO_2)_3O_2(PO_4)_2]$[25,27] +<br>$Rb_9U_5P_6O_{34.5}$* | **$Rb_9U_5P_6O_{34.5}$*** | **$Rb_9U_5P_6O_{34.5}$* +<br>$GaPO_4$ + $Ga_2O_3$**<br>$Rb_9U_5P_6O_{34.5}$* |
| 10 | **$Rb_6[(UO_2)_5O_2(PO_4)_4]$[25] +<br>$Rb_6[(UO_2)_5O_5(PO_4)_2]$** ‡+<br>**$Rb_9U_5P_6O_{34.5}$***<br>$Rb_4U_5O_{17}$[28] +<br>$Rb_9U_5P_6O_{34.5}$* | **$Rb_9U_5P_6O_{34.5}$*** | **$Rb_9U_5P_6O_{34.5}$***<br>**$GaPO_4$ + $Ga_2O_3$**<br>$Rb_{11}[(UO_2)_8(PO_4)_9]$‡<br>+ $Rb_9U_5P_6O_{34.5}$* |

Molar ratio of $UF_4$:$GaPO_4$

NOTE: The lack of more than one phase listed does not imply a phase pure product, but rather that only the major phase is reported. In many cases small impurities could not be identified

*Crystal quality poor with extensive disorder, $a$ = 13.7939(7) Å, $c$ = 9.5213(6) Å, α= β = γ = 90°, $R_1$ = 0.0886

‡Structures from this work,

[25,27]Analogous to other layered phosphuranylite structures in ref. 21, 22, expected corrugation based on $Rb_6[(UO_2)O_5(PO_4)_2]$, poor crystal quality, $a$ = 6.9127(6) Å, $b$ = 7.0226(7) Å, $c$ = 16.9750(15) Å, α = 89.981(4), β = 89.989(4), γ = 89.595(4), $R_1$ = 0.01443

In the publication reporting $Cs_2UO_2Al_2O_5$,[15] crystals were obtained serendipitously; however, attempts to reproduce crystal growth were unsuccessful. In this work, we report the flux synthesis of $Cs_2UO_2Ga_2O_5$ using $UF_4$, $Ga_2O_3$, and CsCl flux in 17 mL Pt crucibles. Since the synthesis was successful for the gallium analog, adapting the same crystal growth conditions, specifically using 17 mL Pt crucibles, but substituting $Al_2O_3$ for $Ga_2O_3$, we were able to reproducibly grow crystals of $Cs_2UO_2Al_2O_5$; crystal quality, however, was poor. The original publication reporting $Cs_2UO_2Al_2O_5$, described the many variables that were changed in attempts to obtain crystals; however, the size of the reaction vessel was not one of them. Interestingly, it appears that the size of the reaction

vessel is an essential variable that was overlooked in previous studies. Additionally, it was reported that $Cs_2UO_2Al_2O_5$ could not be obtained using silver tubes, and similarly, $Cs_2UO_2Ga_2O_5$ could not be obtained in silver tubes either.

**Table 8.4**: Phase space summary of $UF_4$-$GaPO_4$-CsCl in 5mL Pt crucibles.

| mmols of CsCl | 1.5:1 | 1:1 | 1:2 |
|---|---|---|---|
| | | | **---875** ---775 |
| 20 | **$Cs_6[(UO_2)_7O_4(PO_4)_4]$[30]** | **$[Cs_4Cs_4Cl][(UO_2)_4(PO_4)_5]$[14]** | **$Cs_4[(UO_2Ga_2(PO_4)_4]$‡** |
| | $Cs_6[(UO_2)_7O_4(PO_4)_4]$[30] | $Cs_2(UO_2)_2(PO_4)_2$[29] | $Cs_4[(UO_2Ga_2(PO_4)_4]$ ‡ |
| 10 | **$Cs_6[(UO_2)_7O_4(PO_4)_4]$[30]** | **??** | **$Cs_4[(UO_2Ga_2(PO_4)_4]$ ‡ + $[Cs_4Cs_4Cl]$ $[(UO_2)_4(PO_4)_5]$[14]** |
| | $Cs_6[(UO_2)_7O_4(PO_4)_4]$[30] | $Cs_2(UO_2)_2(PO_4)_2$[29] | $Cs_2(UO_2)_2(PO_4)_2$[29] |

Molar ratio of $UF_4$:$GaPO_4$

NOTE: The lack of more than one phase listed does not imply a phase pure product, but rather that only the major phase is reported. In many cases small impurities could not be identified
‡Structures from this work,
?? Single crystals were not of sufficient quality to determine a reliable unit cell or unit cell contents

**Structure.** $Cs_4[UO_2Ga_2(PO_4)_4]$ (**8.1**) and $Cs_2UO_2Ga_2O_5$ (**8.2**) are analogous to $Cs_4[UO_2Al_2(PO_4)_4]$ and $Cs_2UO_2Al_2O_5$, which are discussed in an earlier publications.[14,15] The single crystals of **8.1** suffered from extreme twinning and low crystal quality; however, the phase could be identified by the single crystal unit cell parameters and by comparing the calculated Ga powder diffraction pattern (using the atomic coordinates of $Cs_4[UO_2Al_2(PO_4)_4]$ and replacing Al sites with Ga and adjusting lattice parameters to match SXRD data) with measured powder diffraction data (Figure 8.2). The structure of **8.1** is shown in Figure 8.3 and contains uranium gallophosphate layers (Figure 8.3b) where $[Ga_2(PO_4)_4]^{6-}$ layers are connected through uranyl square bipyramids and dimers of uranyl pentagonal bipyramids.

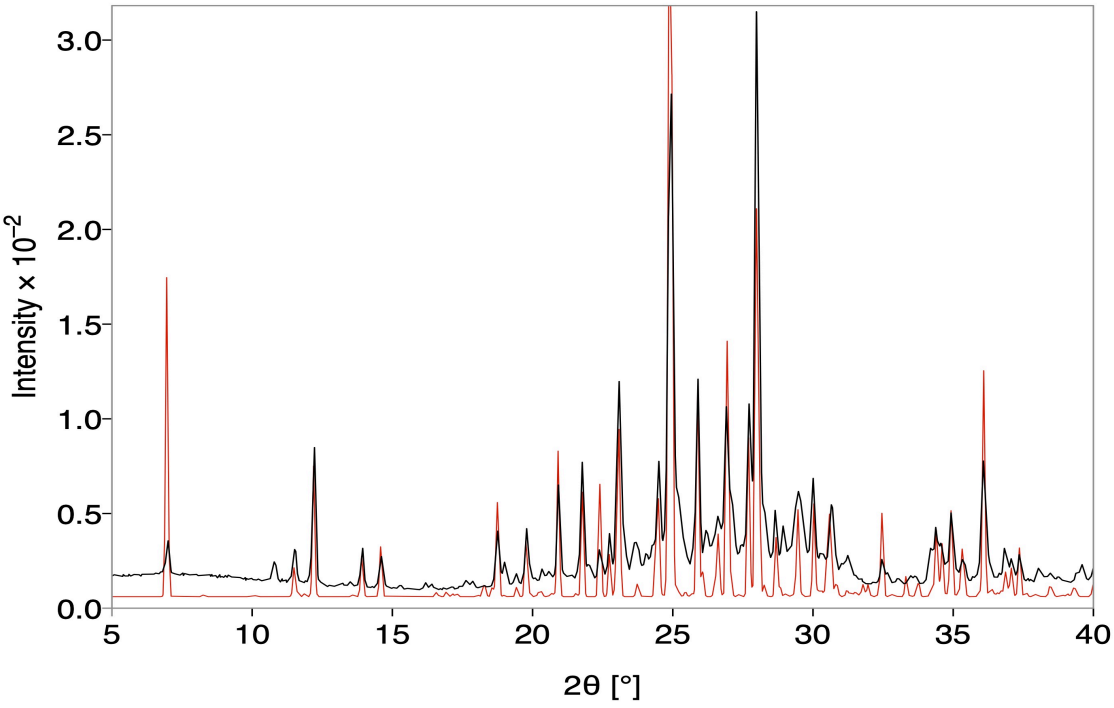


**Figure 8.2**: Powder X-ray diffraction data of **8.1**. The experimentally collected pattern is in black and the red is the calculated pattern from the cif of $Cs_4[UO_2Al_2(PO_4)_4]$ with Al sites replaced with Ga and unit cell parameters from the SXRD data.

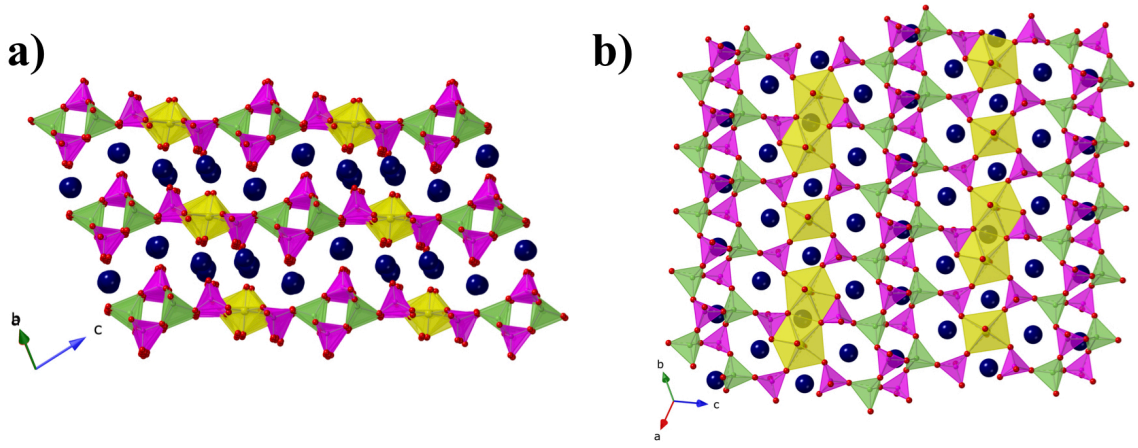


**Figure 8.3**: The layered structure of $Cs_4[UO_2Al_2(PO_4)_4]$. For all figures, alkali cations are blue, uranium polyhedra are yellow, phosphate tetrahedra are magenta, gallate tetrahedra are green, and oxygen atoms are red.

The structure of **8.2** is shown in Figure 8.4 and is constructed of 2D gallate sheets constructed of vierer and achter rings and edge sharing chains of $UO_7$ polyhedra. All of the gallate sheets are parallel to the *ab* plane, while the $UO_7$ chains alternate between the *a* and *b* directions between each gallate sheet. As expected, the Ga-O bonds are longer than the Al-O bonds in the Al analog. For comparison, the Ga-O bonds in **8.2** are 1.806(2), 1.8229(13), 1.849(4) Å, while the Al-O bond distances are 1.7263(16), 1.773(3), and 1.7489(13) Å (bond distances and bond valence sums for all structures are in Tables 8.5-8.9). In both structures the tetrahedra are slightly distorted with the smallest angle being 95.159 ° in the Al and 91.022 ° in the Ga structure. Between the Ga and Al analogs, there is no significant change in the equatorial U-O bond lengths with average bond lengths of 2.34 Å and 2.33 Å in the Al and Ga structures, respectively; therefore, the longer Ga-O bond lengths lead to a larger distortion in the tetrahedron. As in the Al structure, the Cs cations are heavily disordered throughout the channels created by the parallel $UO_7$ chains.

U, Ga, O containing structures are limited to a handful of compositions in the ICSD database, namely $Cs[UO_2Ga(PO_4)_2]$ and $Cs_4[(UO_2)_2(GaOH_2)(PO_4)_4]\bullet H_2O$ which were synthesized by mild hydrothermal methods.[16] Both structures are constructed of uranyl pentagonal bipyramid dimers, phosphate tetrahedra, gallate tetrahedra, and $Cs_4[(UO_2)_2(GaOH_2)(PO_4)_4]\bullet H_2O$ additionally contains gallium octahedra.

**Table 8.5**: BVS and bond distances for $Cs_2UO_2Ga_2O_5$ (**8.2**).

| Interaction | Distance | Interaction | Distance |
|---|---|---|---|
| U1 – O1 x 2 | 1.849(4) | Ga2 – O2 | 1.849(4) |
| U1 – O2 x 4 | 2.401(4) | Ga2 – O3 x2 | 1.806(2) |
| U1 – O4 | 2.425(6) | Ga2 – O4 | 1.8229(13) |
| **BVS U1** | **5.926** | **BVS Ga2** | **3.132** |

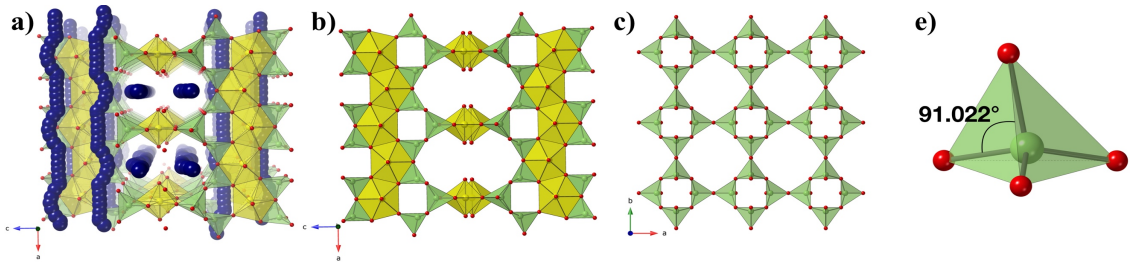


**Figure 8.4**: The structure of $Cs_2UO_2Ga_2O_5$ (**8.2**), a) a perspective view, b) framework with Rb cations removed, c) the 2D gallate sheets, and d) the distorted tetrahedral coordination of Ga1.

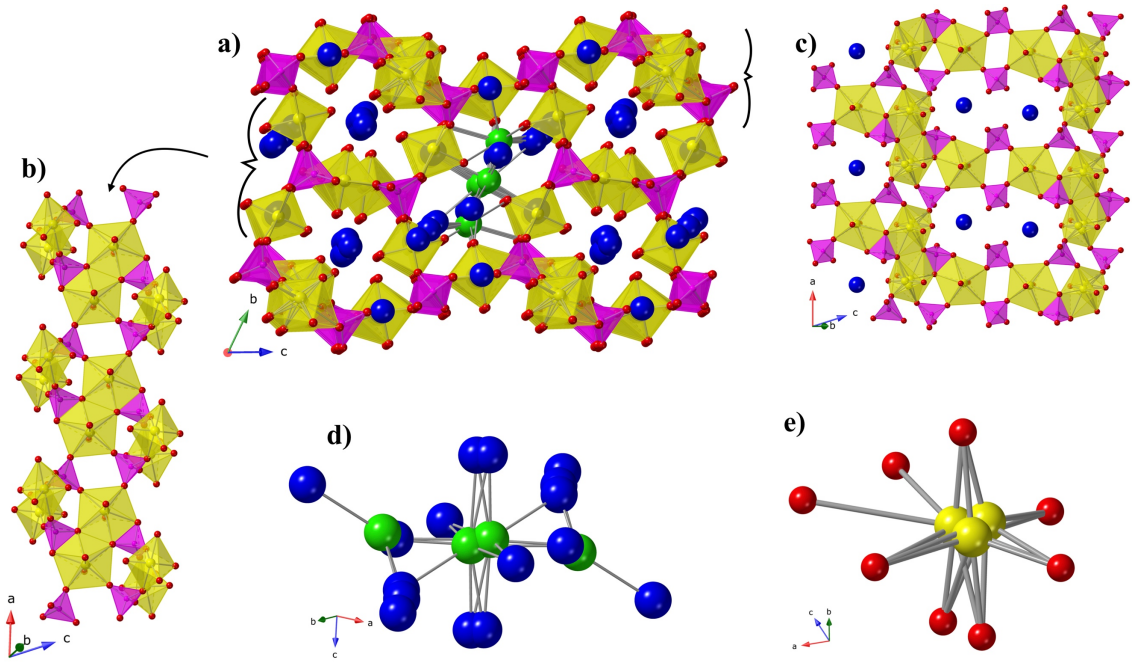


**Figure 8.5:** The structure of $[Rb_2Rb_{3.93}Cl_{0.93}][(UO_2)_5(PO_4)_5]$ (**8.3**). a) the framework and all ions, b) the $[(UO_2)_3(PO_4)_2]$ chains, c) the $[(UO_2)_2(PO_4)_3]^{5-}$ sheets, d) the $[Rb_{3.93}Cl_{0.93}]^{3+}$ salt inclusion, and e) the disordered U5A/B/C site.

$[Rb_2Rb_{3.93}Cl_{0.93}][(UO_2)_5(PO_4)_5]$ (**8.3**) is a uranyl phosphate salt inclusion material (SIM), where the salt inclusion and non-salt inclusion ions are in the first set of brackets, and the framework is in the second set of brackets. Many uranyl silicate and germanate SIMs have been recently reported,[31–35] and while there are several transition metal phosphate SIMs,[36–40] only two other uranyl phosphate SIMs have been reported thus far.[14]

**Table 8.6**: BVS and bond distances for $[Rb_{5.93}Cl_{0.93}][(UO_2)_5(PO_4)_5]$(**8.3**).

| Interaction | Distance | Interaction | Distance | Interaction | Distance |
|---|---|---|---|---|---|
| U1 – O9 | 2.428(9) | U2 – O12 | 2.241(12) | U3 – O1 | 2.443(15) |
| U1 – O10 | 2.492(9) | U2 – O15 | 2.257(12) | U3 – O4 | 2.672(13) |
| U1 – O10 | 2.384(9) | U2 – O18 | 2.263(11) | U3 – O5 | 2.294(11) |
| U1 – O14 | 2.248(10) | U2 – O19 | 2.210(11) | U3 – O20 | 2.270(10) |
| U1 – O16 | 2.244(10) | U2 – O23 | 1.803(11) | U3 – O25 | 1.781(11) |
| U1 – O21 | 1.774(10) | U2 – O24 | 1.778(12) | U3 – O30 | 1.782(11) |
| U1 – O22 | 1.786(10) | **BVS U2** | **6.07** | **BVS U3** | **6.07** |
| **BVS U1** | **6.18** | U5B – O2 | 2.255(16) | U5C – O2 | 2.671(18) |
| U5A – O2 | 2.440(14) | U5B – O2 | 3.03(3) | U5C – O2 | 3.17(3) |
| U5A – O2 | 2.641(18) | U5B – O4 | 3.00(4) | U5C – O4 | 2.800(19) |
| U5A – O4 | 2.425(14) | U5B – O6 | 2.489(13) | U5C – O6 | 2.096(17) |
| U5A – O6 | 2.296(12) | U5B – O8 | 1.784(14) | U5C – O8 | 1.835(17) |
| U5A – O8 | 2.308(13) | U5B – O28B | 1.75(4) | U5C – O28B | 1.96(4) |
| U5A – O28A | 1.803(14) | U5B – O29 | 1.808(12) | U5B – O29 | 1.654(14) |
| U5A – O29 | 1.738(10) | **BVS U5B** | **6.49** | **BVS U5C** | **6.43** |
| **BVS U5A** | **5.95** | P1 – O1 | 1.530(16) | P2 – O5 | 1.511(11) |
| U4 – O3 | 2.297(11) | P1 – O2 | 1.436(13) | P2 – O6 | 1.521(13) |
| U4 – O7 | 2.245(12) | P1 – O3 | 1.486(11) | P2 – O7 | 1.486(14) |
| U4 – O11 | 2.257(10) | P1 – O4 | 1.600(14) | P2 – O8 | 1.529(14) |
| U4 – O13 | 2.291(10) | **BVS P1** | **5.37** | **BVS P2** | **5.26** |
| U4 – O26 | 1.809(11) | P4 – O10 | 1.547(11) | P5 – O17 | 1.527(11) |
| U4 – O27 | 1.690(12) | P4 – O14 | 1.508(10) | P5 – O18 | 1.505(11) |
| **BVS U4** | **6.071** | P4 – O15 | 1.515(12) | P5 – O19 | 1.522(11) |
| P3 – O9 | 1.532(8) | P4 – O16 | 1.515(10) | P5 – O20 | 1.527(10) |
| P3 – O10 | 1.547(10) | **BVS P4** | **5.19** | **BVS P5** | **5.20** |
| P3 – O11 | 1.504(11) | | | | |
| P3 – O12 | 1.514(12) | | | | |
| **BVS P3** | **5.15** | | | | |

The framework consists of $PO_4$ tetrahedra, $UO_6$, and $UO_7$ polyhedra and contains two different types of channels, one channel houses the non-salt inclusion Rb cations, and the other hosts the $Rb_{3.93}Cl_{0.93}^{3+}$ salt inclusion. The structure can be broken down into uranium phosphate sheets, Figure 8.5c, that are connected to other sheets by the chains in Figure 8.5b. The $[(UO_2)_2(PO_4)_3]^{5-}$ sheets contain chains of edge sharing dimers of uranyl pentagonal bipyramids that edge share to two phosphate tetrahedra and that are connected

to other dimers through corner sharing phosphate tetrahedra. The edge sharing phosphate tetrahedra also edge shares with a $UO_2$ polyhedron. These chains and additional $UO_7$ polyhedra create 12 membered (U-P) rings that create pores orthogonal to the channels in the *a* direction. The $[(UO_2)_2(PO_4)_3]^{5-}$ sheets are connected to the $[(UO_2)_3(PO_4)_2]$ chains, which are the same as those in the sheets, through the $UO_6$ polyhedra. The complex, disordered 1D salt inclusion is shown in Figure 8.5d, and roughly consists of two isolated Cl atoms, one coordinated to 4-7 Rb cations and the other coordinated to 4 O and 1-2 Rb.

The structure of $Rb_{11}[(UO_2)_8(PO_4)_9]$ (**8.4**) is a 3D channel structure with three unique channels and is built of phosphate tetrahedra and $UO_7$ pentagonal bipyramids (Figure 8.6). It can be deconstructed into large channels, pinwheels, and chains. The $[(UO_2)_2(PO_4)_4]^{8-}$ channels (two per formula unit) are shown in Figure 8.6d and consist of pairs of uranyl pentagonal bipyramids bridged together through edge sharing of two phosphate tetrahedra. The edge sharing $PO_4$ groups connected to these $UO_7$ polyhedra are disordered, where the purple and magenta colored tetrahedra represent two possible orientations. The idealized structure would have one edge sharing phosphate per $UO_7$ polyhedra and all of these tetrahedra would point in the same direction down the *c* axis. These $[(UO_2)_2(PO_4)_4]^{8-}$ units, similar to those seen in the $[(UO_2)_2(PO_4)_3]^{5-}$ sheets found in **8.3** (Figure 8.6c), connect to others that are approximately orthogonal to create the channels that house the Rb cations. These channels are quite large with a distance of 9.442 Å between two O8 atoms across the channels.

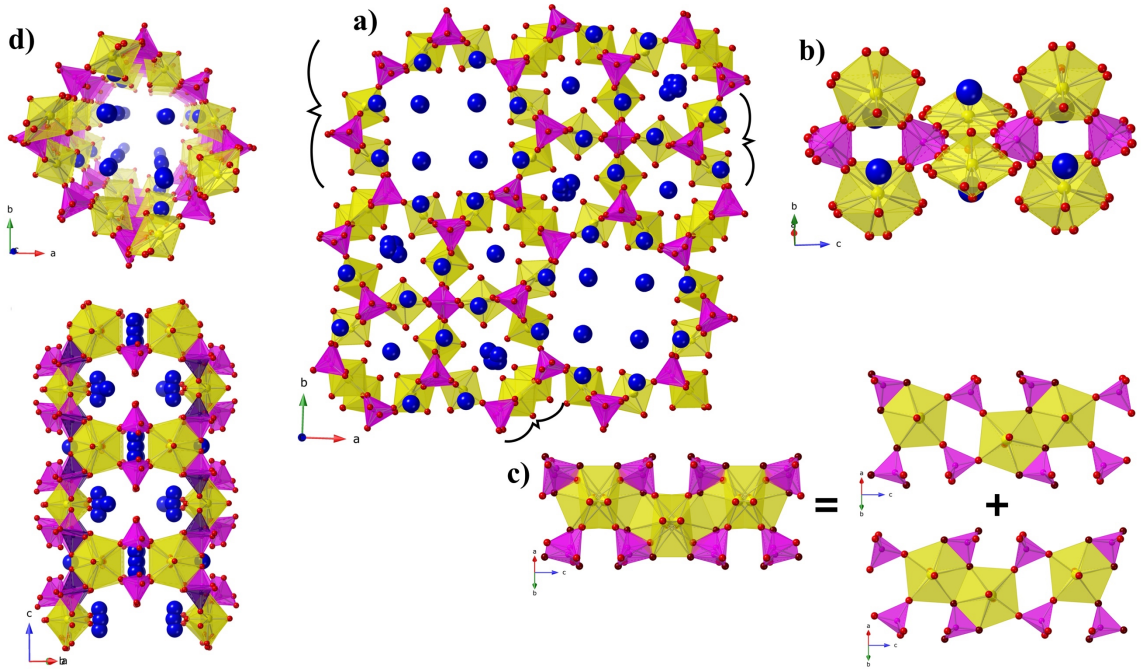


**Figure 8.6:** The structure of $Rb_{11}[(UO_2)_8(PO_4)_9]$ (**8.4**). a) the overall structure, b) the $[(UO_2)_2(PO_4)]^+$ pinwheels, d) the disordered chains of $(UO_2)_2^{4+}$ dimers, and d) the $[(UO_2)_2(PO_4)_4]^{8-}$ channels.

**Table 8.7**: BVS and bond distances for $Rb_{11}[(UO_2)_8(PO_4)_9]$ (**8.4**).

| Interaction | Distance | Interaction | Distance | Interaction | Distance |
|---|---|---|---|---|---|
| U1 – O1 | 1.810(10) | U2 – O6A | 2.23(3) | U3 – O10B | 2.483(12) |
| U1 – O2 | 1.787(10) | U2 – O6B | 2.39(3) | U3 – O12A | 2.34(3) |
| U1 – O3 x 2 | 2.270(8) | U2 – O7 | 1.766(10) | U3 – O12B | 2.41(3) |
| U1 – O10A | 2.413(13) | U2 – O8 | 1.822(14) | U3 – O13 | 1.778(10) |
| U1 – O11A | 2.43(2) | U2 – O9A | 2.22(2) | U3 – O14 | 1.780(10) |
| U1 – O11B | 2.323(19) | U2 – O9B | 2.532(18) | U3 – O15A | 2.26(3) |
| **BVS U1** | **6.14** | U2 – O10B | 2.490(11) | U3 – O15B | 2.28(3) |
| U4 – O4A | 2.506(19) | **BVS U2** | **6.06** | **BVS U4** | **6.20** |
| U4 – O4A | 2.359(17) | P1(A) – O15A x 4 | 1.52(3) | P1(B) – O15B x 4 | 1.56(3) |
| U4 – O4B | 2.25(2) | **BVS P1(A)** | **5.20** | **BVS P1(B)** | **4.67** |
| U4 – O5A | 2.385(14) | P2A – O9A | 1.49(2) | P2B – O9B | 1.515(17) |
| U4 – O5B | 2.246(14) | P2A – O10A | 1.556(15) | P2B – O10B | 1.579(13) |
| U4 – O16 | 1.804(12) | P2A – O11A | 1.49(2) | P2B – O11B | 1.47(2) |
| U4 – O17 | 1.807(15) | P2A – O12A | 1.55(3) | P2B – O12B | 1.50(3) |
| **BVS U4** | **6.07** | **BVS P2A** | **5.20** | **BVS P2B** | **5.29** |
| | | P3A – O3 | 1.487(16) | P3B – O3 | 1.533(16) |
| | | P3A – O4A | 1.565(18) | P3B – O4B | 1.505(19) |
| | | P3A – O5A | 1.536(18) | P3B – O5B | 1.511(19) |
| | | P3A – O6A | 1.48(3) | P3B – O6B | 1.55(3) |
| | | **BVS P3A** | **5.36** | **BVS P3B** | **5.14** |

The channels are directly connected through corner sharing tetrahedra to the $[(UO_2)_2(PO_4)]^+$ pinwheels shown in Figure 8.6b. There are two possible orientations of the phosphate tetrahedra in this unit with two possible equatorial oxygen positions for each U atom. The last building unit for structure **8.4** is the $(UO_2)_2^{4+}$ dimers of uranyl pentagonal bipyramids (Figure 8.6c) that coordinate to phosphate tetrahedra in the $[(UO_2)_2(PO_4)_4]^{8-}$ channels. The chains created by the $(UO_2)_2^{4+}$ dimers and the phosphate tetrahedra from the $[(UO_2)_2(PO_4)_4]^{8-}$ channels are disordered over two possible orientations as shown in Figure 8.6c. The $(UO_2)_2^{4+}$ dimers connect diagonally adjacent $[(UO_2)_2(PO_4)_4]^{8-}$ channels and between $(UO_2)_2^{4+}$ dimers and pinwheels are small pores which house additional Rb cations.

Both structures $Rb_{7.6}[(UO_2)_8O_{8.6}F_{0.4}(PO_4)_2]$ (**8.5**) and $Rb_6[(UO_2)_5O_2(PO_4)_4]$ (**8.6**) are uranyl phosphate layered structures that house Rb cations between layers and are related to the $U_3O_8$ topologies. Building units of the α- and β-$U_3O_8$ topologies are shown in Figure 8.7e and 8.7f, respectively and are constructed of two chains of edge-sharing pentagonal bipyramids that mirror each other and are connected through additional edge-sharing $UO_7$ or $UO_6$ polyhedra in the α- and β- topologies, respectively. Figure 8.7c shows the disordered $U_3O_8$ based building units in **8.5** and Figure 8.7d shows the idealized unit where one of the U sites that connects the two chains is a square bipyramid and the other is a pentagonal bipyramid, which can be described as a combination of the α- and β-$U_3O_8$ topologies. The bridging U atom is disordered over two sites, where one corresponds to the square and the other to the pentagonal coordination environment. These $U_3O_8$ building units are combined into a sheet where adjacent units are rotated 90° and phosphate tetrahedra occupy the small trapezoidal gaps in the sheets. These sheets are then stacked with Rb cations residing between the layers.

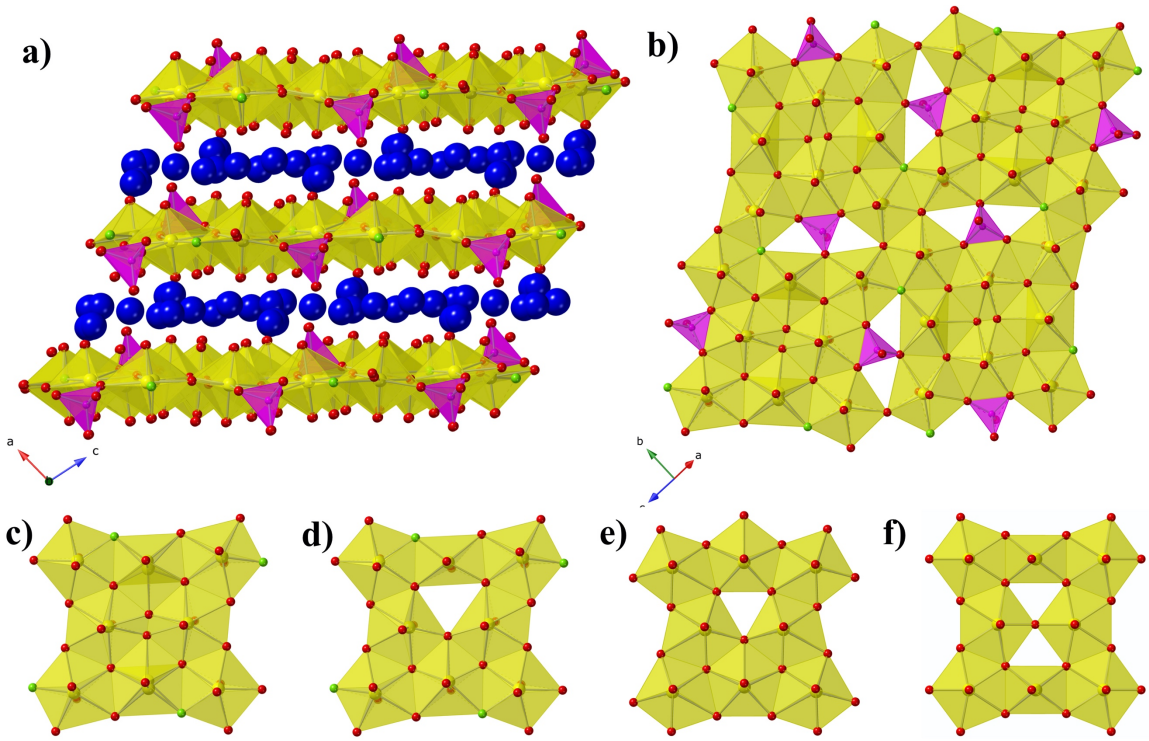


**Figure 8.7**: The layered structure of $Rb_{7.6}[(UO_2)_8O_{8.6}F_{0.4}(PO_4)_2]$ (**8.5**). a) sheets and Rb cation layers, b) the uranyl phosphate sheets, c) disordered $U_3O_8$ like, d) idealized $U_3O_8$ like, e) α-$U_3O_8$ building, and e) β-$U_3O_8$ building units.

**Table 8.8**: BVS and bond distances for $Rb_{7.6}[(UO_2)_8O_{8.6}F_{0.4}(PO_4)_2]$(**8.5**).

| Interaction | Distance | Interaction | Distance | Interaction | Distance |
|---|---|---|---|---|---|
| U1 – O1 | 1.811(11) | U4A – O4/F4 | 2.177(10) | U4B – O4/F4 | **2.464(10)** |
| U1 – O2 | 1.817(11) | U4A – O8 | 2.343(13) | U4B – O8 | 2.133(15) |
| U1 – O3 | 2.328(10) | U4A – O11 | 2.890(19) | U4B – O11 | 2.484(19) |
| U1 – O3 | 2.293(10) | U4A – O14 | 2.297(11) | U4B – O14 | 2.547(11) |
| U1 – O4/F4 | 2.354(10) | U4A – O15 | 1.796(13) | U4B – O15 | 1.820(13) |
| U1 – O12 | 2.342(10) | U4A – O16 | 1.837(13) | U4B – O16 | **1.818(13)** |
| U1 – O17 | 2.343(12) | U4A – O17 | 2.246(12) | U4B – O17 | 2.061(12) |
| **BVS U1** | **6.07** | **BVS U4A** | 6.01 | **BVS U4B** | **6.20** |
| U2 – O7 | 2.612(14) | U3 – O3 | 2.294(10) | P1 – O7 | 1.572(14) |
| U2 – O8 | 2.228(11) | U3 – O4/F4 | 2.221(9) | P1 – O12 | **1.543(11)** |
| U2 – O9 | 1.824(12) | U3 – O5 | 1.800(11) | P1 – O13 | 1.497(17) |
| U2 – O10 | 1.833(11) | U3 – O6 | 1.799(11) | P1 – O14 | 1.567(10) |
| U2 – O11 | 2.31(2)/2.13(2) | U3 – O7 | 2.481(13) | **BVS P1** | 4.87 |
| U2 – O12 | 2.435(11) | U3 – O8 | 2.381(13) | | |
| U2 – O17 | 2.207(11) | U3 – O14 | 2.547(11) | | |
| **BVS U2** | **6.07** | **BVS U3** | 5.94 | | |

In other uranyl phosphate oxyfluoride structures,[23] bond valences sums of the anion sites have been useful in identifying the fluorine site, since X-ray diffraction is not always sufficient in determining the location. The bond valence sums[41, 42] for the non-uranyl oxygens range between 1.841 and 2.214 which are in good agreement with the expected value of 2 and do not give any insight as to the location of the fluorine site. The O4 site, which freely refined to an occupancy of ~1.15 in the SXRD structure solution had a bond valence sum value of 1.90. It is important to note that since the occupancy of this site is expected to be 0.80/0.2 O/F based on charge balance, it is not surprising that the small amount of fluorine does not noticeably impact BVS values. In the fluorine doped phosphuranylite composition the half-occupied fluorine site could not be supported by BVS.[23]

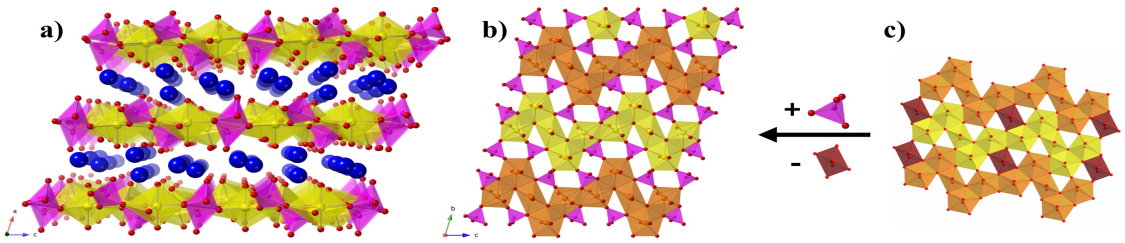


**Figure 8.8**: The layered structure of $Rb_6[(UO_2)_5O_2(PO_4)_4]$ (**8.6**). a) uranyl phosphate sheets and layers of Rb cations, b) the sheet topology of **8.6**, and c) the sheet topology of β-$U_3O_8$ and its relation to **8.6**. Uranium polyhedra are yellow, orange, or red for clarity.

Figure 8c shows the β-$U_3O_8$ sheets where the chains in $Rb_6[(UO_2)_5O_2(PO_4)_4]$ (**8.6**) are colored in orange and yellow, and the red uranium polyhedra are the sites removed to obtain the sheet topology in structure **8.6**. By removing the red uranium polyhedra, separating the yellow and orange chains, and adding phosphate tetrahedra between chains one can obtain the topology of **8.6** in Figure 8.8b, which has been previously observed in the As analog synthesized under high-temperature high-pressure methods.[43] These uranyl

phosphate sheets stack perpendicular to the *b* direction and the Rb cations reside between the layers.

**Table 8.9**: BVS and bond distances for $Rb_6[(UO_2)_5O_2(PO_4)_4$ (**8.6**).

| Interaction | Distance | Interaction | Distance | Interaction | Distance |
|---|---|---|---|---|---|
| U1 – O1 | 2.308(3) | U2 – O2 | 2.326(3) | U3 – O7 x 2 | 2.414(3) |
| U1 – O3 | 2.398(3) | U2 – O2 | 2.517(3) | U3 – O11 x 2 | 1.813(4) |
| U1 – O5 | 2.292(3) | U2 – O3 | 2.423(3) | U3 – O12 x 2 | 2.199(3) |
| U1 – O6 | 2.451(3) | U2 – O6 | 2.277(3) | **BVS U3** | **5.661** |
| U1 – O12 | 2.318(3) | U2 – O9 | 1.802(3) | P1 – O1 | 1.526(3) |
| U1 – O13 | 1.795(3) | U2 – O10 | 1.804(4) | P1 – O2 | 1.576(3) |
| U1 – O14 | 1.812(3) | U2 – O12 | 2.248(3) | P1 – O3 | 1.565(3) |
| **BVS U1** | **6.033** | **BVS U2** | **6.041** | P1 – O4 | 1.488(4) |
| | | | | **BVS P1** | **4.964** |

Several of the structures in this paper, such as **8.2**, **8.3**, and **8.4**, are highly disordered by crystallographic standards, and in order to attempt to quantify the resulting complexity of these structures we have we performed calculations for the total information content of the crystal structures in ToposPro. [44] The procedure as described by Krivovichev was followed and involves calculating the total information of a crystal structure, $I_{G,total}$ (bits/unit-cell) for both the published structure solutions and the idealized solutions where the disorder is removed.[45] For structures where symmetry elements had to be removed in order to simplify the disorder, the total information of the published structure and idealized structure are reported for the lower symmetry space group (Table 8.10). Structures **8.2** and **8.6** are categorized as intermediate structures, while **8.3** and **8.4** are complex and **8.4** is very complex. By looking at the ratio of $I_{G,total}$ (disordered)/ $I_{G,total}$ (ideal), the complexity of **8.2**, **8.3**, and **8.5** is only mildly increased with the disorder, while the complexity of **8.4** is nearly doubled as a result of the disorder (ratio of 1.74).[46]

**Table 8.10**: Total information content for structures **8.2-8.6** (left) and classification (right).[44]

| Structure | | $I_{G,total}$ (bits/ u.c.) | S. G. |
|---|---|---|---|
| $Cs_2UO_2Ga_2O_5$ (**8.2**) | Ideal | 152 | *I*4/*amd* |
| | Disordered | 242 | |
| $[Rb_2Rb_{3.93}Cl_{0.93}][(UO_2)_5(PO_4)_5]$ (**8.3**) | Ideal | 530 | $P\bar{1}$ |
| | Disordered | 644 | |
| $Rb_{11}[(UO_2)_8(PO_4)_9]$ (**8.4**) | Ideal | 1854 | *Pbam* |
| | Disordered | 3234 | |
| $Rb_{7.6}[(UO_2)_8O_{8.6}F_{0.4}(PO_4)_2]$ (**8.5**) | Ideal | 536 | $P2_1$ |
| | Disordered | 650 | |
| $Rb_6[(UO_2)_5O_2(PO_4)_4]$ (**8.6**) | | 191 | $P\bar{1}$ |

| Category | $I_{G,total}$ (bits/ u.c.) |
|---|---|
| Very simple | < 20 |
| Simple | 20-100 |
| Intermediate | 100-500 |
| Complex | 500-1000 |
| Very complex | >1000 |

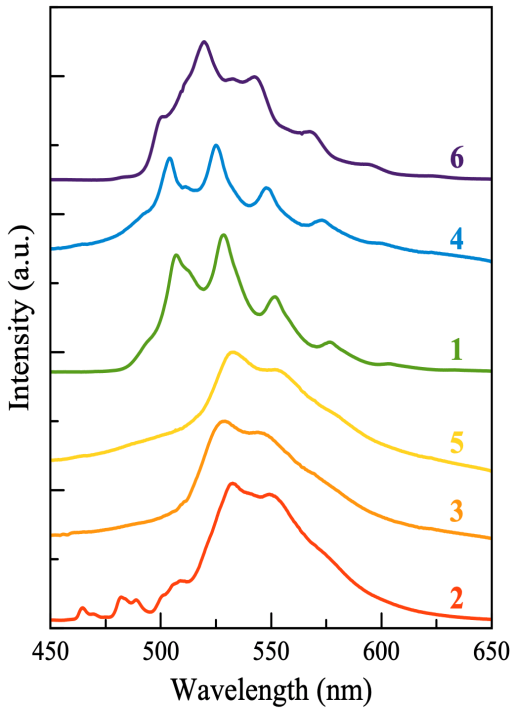


**Figure 8.9:** The fluorescence emission spectra of structures **8.1-8.6.**

**Optical Properties.** Fluorescence emission peaks for structures **8.1-8.6** lie in the green-yellow region of the visible spectrum which is typical for the uranyl cation (Figure 8.9). The most intense peaks for structures **8.1-8.6** are 528, 533, 529, 524, 533, and 520 nm, respectively and result from the electronic emission from the lowest vibrational level

of the first excited state to the lowest vibrational level of the ground state. Smaller peaks around the most intense peak arise from different vibrational levels of the same electronic emission.[47] In the spectra for **8.1**, **8.4**, and **8.6** these vibronic features with defined peak spacing are observed, while in **8.2**, **8.3**, and **8.5** they are not. One explanation is based on the observation that the strength of the uranyl bond affects the spacing between the vibronic features and that stronger bonding decreases the splitting of the emission peaks.[48] To investigate, the average uranyl bond lengths were calculated for structures **8.2**-**8.5** and are 1.848, 1.775, 1.794, 1.815, and 1.807 Å, respectively. While **8.2** and **8.5** have the longest uranyl bonds and fit this previous observation and have essentially no splitting and **8.1** and **8.4** have shorter uranyl bond lengths and observable splitting, the shortest bond length, 1.775 Å in **8.3** does not. In previous fluorescence studies, data collected at lower temperatures has been found to significantly increase the resolution of the different vibrational peaks and could help explain the poor peak splitting in **8.3**.[47]

**Conclusion.** The targeted crystal growth of gallium analogs to the recently published uranium aluminates led to the discovery of a new uranium gallophosphate and a uranium gallate, analogous to previously reported aluminates, in addition to four new uranium phosphates that were obtained within the same phase space. Both the material and the size/shape of the reaction vessels proved crucial in the isolation of these products, which is somewhat unexpected considering that many publications reporting flux crystal growth neglect to report the size of the crucible used. The phase space explored was not exhaustive, and was explored within reason to target the specific Ga analogs to uranium aluminates and it cannot be concluded whether the Ga analogs of $[Cs_{13}Cl_5][(UO_2)_3Al_2O(PO_4)_6]$, $A_3[Al_2O(PO_4)_3][(UO_2)_3O_2]$ (A = Cs, Rb), and

$Rb_7[Al_2O(PO_4)_3][(UO_2)_6O_4(PO_4)_2]$ could not be obtained due to the stability of the other uranium phosphates synthesized from these reactions, or the inability for Ga to replace Al in these structures. While compound **8.1** could be identified by the powder diffraction and unit cell data, the crystals were not of sufficient quality to obtain a publishable crystal structure, and perhaps different crystal growth methods are necessary to elucidate its structure. Fluorescence spectra for all 6 compositions were obtained and featured typical green-yellow luminescence of the uranyl species.

**Acknowledgements.** Research was conducted by the Center for Hierarchical Wasteform Materials (CHWM), an Energy Frontier Research Center (EFRC). Research was supported by the U.S. Department of Energy, Office of Basic Energy Sciences, Division of Materials Sciences and Engineering under Award DE-SC0016574.

**References:**

(1) Henshaw, D. E., The structure of wadeite, *Mineralogical Magazine and Journal of the Mineralogical Society* **1955**, *30*, 585-595.

(2) Choisnet, J.; Deschanvres, A.; Raveau, B., Evolution structurale de nouveaux germanates et silicates de type wadeite et de structure apparentee, *J. Solid State Chem.* **1973**, *7*, 408-417.

(3) Fleet, M. E.; Muthupari, S., Structure of $A_2Ge_4O_9$-Type Sodium Tetragermanate ($Na_2Ge_4O_9$) and Comparison with Other Alkali Germanate and Silicate Mixed Tetrahedral–Octahedral Framework Structures, *J. Solid State Chem.* **1998**, *140*, 175-181.

(4) Redhammer, G. J.; Tippelt, G., The tetragermanates A2Ge4O9 (A= Na, K and Rb), *Acta Crystallographica Section C: Crystal Structure Communications* **2013**, *69*, 995-1001.

(5) Morrison, G.; Wilkins, B. O.; Spagnuolo, N. R.; Smith, M. D.; zur Loye, H.-C., Rare earth silicates and germanates crystallizing in the wadeite and related structure types, *J. Solid State Chem.* **2019**, *269*, 51-55.

(6) Morrison, G.; Kocevski, V.; Misture, S. T.; Spagnuolo, N. R.; Hines, A. T.; Besmann, T.; zur Loye, H.-C., Superwadeites: Elucidation of a Structural Family Related to the Wadeite Structure and Prediction of $Cs_2Ge_5O_{11}$, *Cryst. Growth Des.* **2019**, *19*, 5477-5482.

(7) Pasero, M.; Kampf, A. R.; Ferraris, C.; Pekov, I. V.; Rakovan, J.; White, T. J., Nomenclature of the apatite supergroup minerals, *Eur. J. Mineral.* **2010**, *22*, 163-179.

(8) White, T., Apatite - An Adaptive Framework Structure, *Reviews in Mineralogy and Geochemistry* **2005**, *57*, 307-401.

(9) Grisafe, D. A.; Hummel, F. A., Pentavalent ion substitutions in the apatite structure Part A. Crystal chemistry, *J. Solid State Chem.* **1970**, *2*, 160-166.

(10) Shaw, D. M., The geochemistry of gallium, indium, thallium—a review, *Physics and Chemistry of the Earth* **1957**, *2*, 164-211.

(11) Shannon, R. D., Revised effective ionic radii and systematic studies of interatomic distances in halides and chalcogenides, *Acta Cryst.* **1976**, *A32*, 751-767.

(12) Yu, N.; Klepov, V. V.; Modolo, G.; Bosbach, D.; Suleimanov, E. V.; Gesing, T. M.; Robben, L.; Alekseev, E. V., Morphotropy and Temperature-Driven Polymorphism in A2Th (AsO4) 2 (A= Li, Na, K, Rb, Cs) Series, *Inorg. Chem.* **2014**, *53*, 11231-11241.

(13) Yin, X.; Wang, Y.; Bai, X.; Wang, Y.; Chen, L.; Xiao, C.; Diwu, J.; Du, S.; Chai, Z.; Albrecht-Schmitt, T. E., Rare earth separations by selective borate crystallization, *Nature communications* **2017**, *8*, 1-8.

(14) Juillerat, C. A.; Klepov, V. V.; Alekseev, E. V.; zur Loye, H.-C., Overstepping Löwenstein's Rule – a Route to Unique Aluminophosphate Frameworks with 3D Salt-Inclusion and Ion Exchange Properties, *Inorg. Chem.* **2019**, *58*, 724-736.

(15) Juillerat, C. A.; Kocevski, V.; Besmann, T.; zur Loye, H.-C., Discovery of $Cs_2(UO_2)Al_2O_5$ by Molten Flux Methods: A Uranium Aluminate Containing Solely Aluminate Tetrahedra as the Secondary Building Unit, *Inorg. Chem.* **2019**, *58*, 4099-4102.

(16) Shvareva, T. Y.; Sullens, T. A.; Shehee, T. C.; Albrecht-Schmitt, T. E., Syntheses, structures, and ion-exchange properties of the three-dimensional framework uranyl gallium phosphates, $Cs_4[(UO_2)_2(GaOH)_2(PO_4)_4]\cdot H_2O$ and $Cs[UO_2Ga(PO_4)_2]$, *Inorg. Chem.* **2005**, *44*, 300-305.

(17) Bugaris, D. E.; zur Loye, H.-C., Materials discovery by flux crystal growth: Quartenary and higher oxides, *Angew. Chem. Int. Ed.* **2012**, *51*, 3780-3811.

(18) Juillerat, C. A.; Klepov, V. V.; Morrison, G.; Pace, K. A.; zur Loye, H.-C., Flux Crystal Growth: A Versatile Technique to Reveal the Crystal Chemistry of Complex Uranium Oxides, *Dalton Trans.* **2019**, *48*, 3162-3181.

(19) Bruker. *APEX3, SAINT+, TWINABS, and SADABS.* Bruker AXS Inc.: Madison, Wisconsin, USA, 2015;

(20) Sheldrick, G. M., Crystal structure refinement with SHELXL, *Acta Cryst.* **2015**, *C71*, 3-8.

(21) Sheldrick, G. M., SHELXT - Integrated space-group and crystal-structure determination, *Acta Cryst.* **2015**, *A71*, 3-8.

(22) Dolomanov, O. V.; Bourhis, L. J.; Gildea, R. J.; Howard, J. A. K.; Pushmann, H., OLEX2: a complete structure solution, refinement and analysis program, *J. Appl. Crystallogr.* **2009**, *42*, 339-341.

(23) Juillerat, C. A.; Kocevski, V.; Besmann, T.; zur Loye, H.-C., Observation of the Same New Sheet Topology in Both the Layered Uranyl Oxide-Phosphate $Cs_{11}[(UO_2)_{12}(PO_4)_3O_{13}]$ and the Layered Uranyl Oxyfluoride-Phosphate $Rb_{11}[UO_2)_{12}(PO_4)_3O_{12}F_2]$ Prepared by Flux Crystal Growth, *Frontiers in Chemistry* **2019**, *7*, 583.

(24) Juillerat, C. A.; Kocevski, V.; Karakalos, S.; Morrison, G.; Misture, S.; Besmann, T.; zur Loye, H.-C., Flux Crystal Growth of U(V) containing oxyfluoride perovskites, *Inorganic Chemsitry Frontiers* **2019**, *6*, 3202-3214.

(25) Juillerat, C. A.; zur Loye, H.-C., Crystal Growth and Structure Characterization of Three Layered Uranyl Phosphates and Their Relation to the Phosphuranylite Family, *Cryst. Growth Des.* **2019**, *19*, 1183-1189.

(26) Juillerat, C. A.; Kocevski, V.; Klepov, V. V.; Amoroso, J. W.; Besmann, T. M.; zur Loye, H.-C., Structure and Stability of Alkali Gallates Structurally Reminiscent of Hollandite, *J. Am. Ceram. submitted*.

(27) Juillerat, C. A.; Moore, E. E.; Kocevski, V.; Besmann, T. M.; zur Loye, H.-C., A Family of Layered Phosphates Crystallizing in a Rare Geometrical Isomer of the Phosphuranylite Topology: Synthesis, Characterization, and Computational Modeling of $A_4[(UO_2)_3O_2(PO_4)_2]$ (A = alkali metals) Exhibiting Intra-layer Ion Exchange, *Inorg. Chem.* **2018**, *57*, 4726-4738.

(28) Saad, S.; Obbade, S.; Renard, C.; Abraham, F., Synthesis, crystal structure, infrared and electrical conductivity of the layered rubidium uranate $Rb_4U_5O_{17}$, *J. Alloys Compd.* **2007**, *474*, 68-72.

(29) Ling, J.; Wu, S.; Chen, F.; Simonetti, A.; Shafer, J. T.; Albrecht-Schmitt, T. E., Does Iodate Incorporate into Layered Uranyl Phosphates Under Hydrothermal Conditions?, *Inorg. Chem.* **2009**, *48*, 10995-11001.

(30) Juillerat, C. A.; Moore, E. E.; Besmann, T. B.; zur Loye, H.-C., Observation of an Unusual Uranyl Cation-Cation Interaction in the Strongly Fluorescent Layered Uranyl Phosphates $Rb_6[(UO_2)_7O_4(PO_4)_4]$ and $Cs_6[(UO_2)_7O_4(PO_4)_4]$, *Inorg. Chem.* **2018**, *57*, 3675-3678.

(31) Chang, Y.-C.; Chang, W.-J.; Boudin, S.; Lii, K.-H., High-Temperature, High-Pressure Hydrothermal Synthesis and Characterization of a Salt-Inclusion Mixed-Valence Uranium(V,VI) Silicate: $[Na_9F_2][(U^VO_2)(U^{VI}O_2)_2(Si_2O_7)_2]$, *Inorg. Chem.* **2013**, *52*, 7230-7235.

(32) Juillerat, C. A.; Moore, E. E.; Morrison, G.; Smith, M. D.; Besmann, T. M.; zur Loye, H.-C., Versatile Uranyl Germanate Framework Hosting Twelve Different Alkali Halide 1D Salt Inclusions, *Inorg. Chem.* **2018**, *57*, 11606-11615.

(33) Lee, C. S.; Wang, S. L.; Chen, Y. H.; Lii, K. H., Flux synthesis of salt-inclusion uranyl silicates: $[K_3Cs_4F][(UO_2)_3(Si_2O_7)_2]$ and $[NaRb_6F][(UO_2)_3(Si_2O_7)_2]$, *Inorg. Chem.* **2009**, *48*, 8357-8361.

(34) Morrison, G.; Smith, M. D.; zur Loye, H.-C., Understanding the Formation of Salt-Inclusion Phases: An Enhanced Flux Growth Method for the Targeted Synthesis of Salt-Inclusion Cesium Halide Uranyl Silicates, *J. Am. Chem. Soc.* **2016**, *138*, 7121-7129.

(35) Li, H.; Langer, E. M.; Kegler, P.; Modolo, G.; Alekseev, E. V., Formation of Open Framework Uranium Germanates: The Influence of Mixed Molten Flux and Charge Density Dependence in U-Silicate and U-Germanate Families, *Inorg. Chem.* **2018**, *57*, 11201-11216.

(36) Gao, J.; Li, J.; Sulejmanovic, D.; Hwu, S.-J., $M_3(P_2O_7)^{22-}$-Type Open Frameworks Featuring $[M_2O_8]$ and $[M_3O_{12}]$ Multinuclear Transition-Metal Oxide Units. Serendipitous Synthesis of Six Polymorphic Salt-Inclusion Magnetic Solids: $Na_2M_3(P_2O_7)_2 \cdot ACl$ (M = Mn, Fe; A = Rb, Cs) and $K_2M_3(P_2O_7)_2 \cdot CsCl$ (M = Fe, Mn), *Inorg. Chem.* **2015**, *54*, 1136-1144.

(37) Huang, Q.; Hwu, S. J., The fascinating noncentrosymmetric copper (II) phosphates synthesized via CsCl salt-inclusion, *Inorg. Chem.* **2003**, *42*, 655-657.

(38) Hwu, S. J. *A New Class of Hybrid Materials via Salt-inclusion Synthesis.* John Wiley & Sons: 2006; pp 239-250.

(39) West, J. P.; Hwu, S. J., Noncentrosymmetric salt inclusion oxides: Role of salt lattices and counter ions in bulk polarity, *J. Solid State Chem.* **2012**, *195*, 101-107.

(40) Winiarski, M. J.; Tran, T. T.; Chamorro, J. R.; McQueen, T. M., $(CsX)Cu_5O_2(PO_4)_2$ (X = Cl, Br, I): A Family of $Cu^{2+}$ S = 1/2 Compounds with Capped Kagomé Networks COmposed of $OCu_4$ Units, *Inorg. Chem.* **2019**, *58*, 4328-4336.

(41) Burns, P. C.; Ewing, R. C.; Hawthorne, F. C., The crystal chemistry of hexavalent uranium: polyhedron geometries, bond-valence parameters, and polymerization of polyhedra, *Can. Mineral.* **1997**, *35*, 1551-1570.

(42) Brown, I. D.; Altermatt, D., Bond-valence parameters obtained from a systematic analyses of the inorganic cyrstal structure database, *Acta Cryst.* **1985**, *B41*, 244-247.

(43) Liu, H. K.; Ramachandran, E.; Chen, Y. H.; Chang, W. J.; Lii, K. H., High-Temperature, High-Pressure Hydrothermal Synthesis, Characterization, and Structural Relationships of Layered Uranyl Arsenates, *Inorg. Chem.* **2014**, *53*, 9065-9072.

(44) Blatov, V. A.; Shevchenko, A. P.; Proserpio, D. M., Applied Topological Analysis of Crystal Structures with the Program Package ToposPro, *Cryst. Growth Des.* **2014**, *14*, 3576-3586.

(45) Krivovichev, S. V., Which inorganic structures are the most complex?, *Angewandte Chemie International Edition* **2014**, *53*, 654-661.

(46) Carone, D.; Klepov, V. V.; Smith, M. D.; zur Loye, H.-C., Flux Crystal Growth of Lanthanide Tungsten Oxychlorides, $La_{8.64}W_6O_{30.45}Cl$, $Ce_{8.64}W_{5.74}O_{30}Cl$, and $Ln_{8.33}W_6O_{30}Cl$ (Ln = Pr, Nd): Structural Stability in the Presence of Extreme Cation and Anion Disorder., *Inorg. Chem.* **2019**, *58*, 16831-16837.

(47) Wang, Z.; Zachara, J. M.; Gassman, P. L.; Liu, C.;, O. Qafoku; Yantasee, W.; Catalano, J. G., Fluorescence spectroscopy of U(VI)-silicates and U(VI)-contaminated Hanford sediment, *Geochim. Cosmochim. Acta* **2005**, *69*, 1391-1403.

(48) Morrison, G.; Tran, T. T.; Halasyamani, P. S.; zur Loye, H.-C., $K_8(K_5F)U_6Si_8O_{40}$: An Intergrowth Uranyl Silicate, *Inorg. Chem.* **2016**, *55*, 3215-3217.

# Chapter 9

# Structure and Stability of Alkali Gallates Structurally Reminiscent of Hollandite[1]

[1]Juillerat, C. A.; Kocevski, V.; Klepov, V. V.; Amoroso, J. W.; Besmann, T. M.; zur Loye, H.-C. Structure and Stability of Alkali Gallates Structurally Reminiscent of Hollandite. *Journal of the American Ceramic Society*, **2020**, DOI: 10.1111/jace.17327.

**Abstract:** Single crystals of $CsGa_7O_{11}$, $RbGa_7O_{11}$, and $RbGa_4In_5O_{14}$ were grown from alkali halide melts and their structures were characterized by single crystal and powder X-ray diffraction. $CsGa_7O_{11}$ and $RbGa_7O_{11}$ adopt the same structure type, reminiscent of the hollandite structure type, as it contains nearly rectangular channels made up of two dimers of edge sharing $GaO_6$ octahedra, and two corner sharing octahedron/tetrahedron pairs. The structure of $RbGa_4In_5O_{14}$ is more complex and is comprised of indium octahedra, gallium trigonal bipyramids, and gallium tetrahedra, and contains similar sized tunnels as $CsGa_7O_{11}$ and $RbGa_7O_{11}$. $CsGa_7O_{11}$ and $RbGa_4In_5O_{14}$ were further characterized by TGA, ion exchange experiments, and DFT studies revealing that both structures are thermodynamically stable up to 850 °C; however, $CsGa_7O_{11}$ decomposes to $GaO(OH)•xH_2O$ when heated in warm aqueous solutions. $CsGa_7O_{11}$ undergoes ion exchange in both an aqueous solution of RbCl and a $RbNO_3$ melt, as predicted by DFT studies, where the ion exchange is more extensive in the $RbNO_3$ melt.

**Introduction.** The US development of nuclear weapons and nuclear energy has created, and will continue to create, a significant quantity of radioactive waste that requires durable, effective, and efficient waste forms in order to safely sequester radionuclides from the biosphere.[1] While developed waste forms have been largely successful, there remains an interest in discovering novel materials for some of the more problematic components, and for finding means for increasing the efficiency of processing and increasing waste loading. Furthermore, on the way to finding new waste form materials, we can broaden our chemical understanding that will aid in the discovery, development, and design of future materials for a variety of waste disposal related applications.[2, 3]

Crystalline ceramic waste forms, particularly SYNROC[4] and titanate/alumina based ceramics, have received a lot of attention due to their ability to incorporate a broad spectrum of chemical species within available lattice sites, potentially higher waste loadings, and resistance to hydrothermal leaching.[5–7] Among the ceramic materials studied are hollandite-type structures, generally $A_xM_8O_{16}$. These are composed of dimers of $MO_6$ octahedra that build edge sharing chains resulting in channels that host +1 and +2 cations depending on the charge of the octahedral metal(s) (Figure 9.1). The titanium based hollandite, $A_x(Ti^{4+}, M)_8O_{16}$, is an example of a ceramic that has been studied as a waste form due to its favorable leach resistance and ability to immobilize Cs at crystalline lattice sites. [8] Herein we report the synthesis, crystal structure, and characterization of the three new crystalline ceramics, $CsGa_7O_{11}$ (**9.1**), $RbGa_7O_{11}$ (**9.2**), and $RbGa_4In_5O_{14}$ (**9.3**) that adopt structure types reminiscent of the hollandite structure.

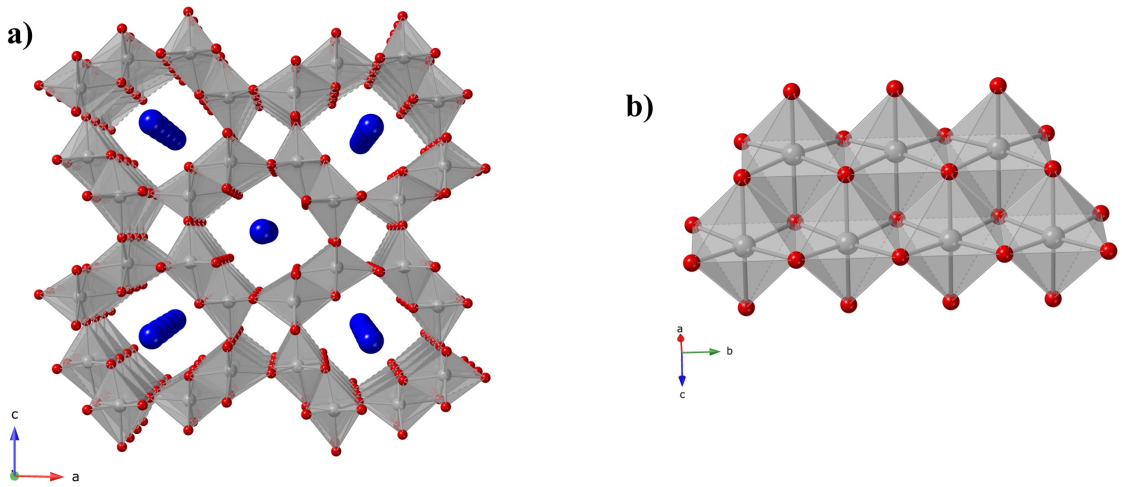


**Figure 9.1:** The hollandite structure type, $A_xM_8O_{16}$, where the M sites are shown in gray, the A sites in blue, and oxygen atoms in red.

**Experimental:**

**Synthesis.** Gallium oxide (Alfa Aesar, 99.999%), gallium nitrate (Beantown Chemical 99.9%), indium oxide (Alfa Aesar, 99.9%), cesium chloride (VWR, ultra pure),

cesium nitrate (Alfa Aesar, 99.8%), and rubidium chloride (BTC, 99.0%) were all used as received. $CsGa_7O_{11}$ and $RbGa_7O_{11}$ were prepared by molten flux methods[9] using 0.5 mmol of $Ga_2O_3$, 10 mmol of the alkali chloride, and 10 mmol of the alkali fluoride loaded into 15 mL platinum crucibles and heated to 875 °C for 12h followed by slow cooling to 450 °C at 6 °C/h, after which the oven was shut off. The products were isolated from the flux by sonicating the crucibles in deionized water to dissolve the flux and then separated from the solution by vacuum filtration. $RbGa_4In_5O_{14}$ was prepared in a similar manner using 0.25 mmol $In_2O_3$ and 0.25 mmol $Ga_2O_3$; however, 14 mL Ag crucibles were used instead. In all cases, ~60 mg of product could be isolated as clumps of very thin, clear, colorless needles.

Solid state synthesis reactions were attempted for all phases using the appropriate metal oxides and alkali nitrates but only solution assisted solid state reactions using 3.5 mmol (1.4625g) of $GaNO_3 \cdot 9H_2O$ and 0.6 mmol (0.11694g) of $CsNO_3$ were successful for synthesizing bulk $CsGa_7O_{11}$. The nitrates were weighed and combined with enough water (~5ml) to dissolve the nitrates in a PTFE cup, and then the PTFE cup was mildly heated and stirred on a hot plate to evaporate the liquid. Subsequently, the powder was ground in a mortar and pestle, transferred to an alumina crucible, and heated at 900 °C for a total of 60 h with two intermittent grindings performed to obtain a phase pure product by PXRD (Figure 9.10).

**PXRD.** Powder X-ray diffraction (PXRD) data were collected on all compounds using a Bruker D2 Phaser equipped with an LYNXEYE silicon strip detector and a Cu Kα source to identify and to evaluate the phase purity of the samples.

**SXRD.** The structure of each compound was determined by single crystal X-ray diffraction data collected on a Bruker D8 Quest single crystal X-ray diffractometer equipped with a Mo Kα microfocus source. The data were reduced and corrected for sample absorption using the SAINT+ and SADABS programs within the APEX 3 software.[10] The SHELX software suite was used within the Olex 2 GUI to solve and refine the structures.[11–13] The intrinsic phasing solution method, SHELXT, and the least squares refinement method, SHELXL were used.

**Table 9.1**: Full crystallographic data for compounds **9.1-9.3**.

| formula | $CsGa_7O_{11}$ **9.1** | $RbGa_7O_{11}$ **9.2** | $RbGa_4In_5O_{14}$ **9.3** |
|---|---|---|---|
| S. G. | *P2/m* | *P2/m* | *P2/m* |
| a, Å | 8.2821(3) | 8.3224(3) | 8.9859(9) |
| b. Å | 3.03840(10) | 3.03160(10) | 3.1867(3) |
| c, Å | 9.5817(3) | 9.4566(3) | 10.7911(12) |
| ß, ° | 113.9510(10) | 114.5860(10) | 95.524(4) |
| V, $Å^3$ | 220.355(13) | 216.960(13) | 307.57(5) |
| Crystal size ($mm^3$) | 0.01 x 0.02 x 0.07 | 0.01 x 0.01 x 0.08 | 0.01 x 0.02 x 0.07 |
| Temperature (K) | 304 | 301 | 303 |
| Density (g $cm^{-3}$) | 6.006 | 5.736 | 6.276 |
| $\theta$ range (deg) | 2.691 – 28.960 | 2.691 – 32.300 | 2.820 – 33.141 |
| $\mu$ ($mm^{-1}$) | 25.204 | 27.036 | 21.818 |
| Collected reflections | 1156 | 12560 | 12362 |
| Unique reflections | 684 | 858 | 1347 |
| $R_{int}$ | 0.0107 | 0.0232 | 0.0210 |
| $h$ | $-11 \le h \le 10$ | $-11 \le h \le 12$ | $-13 \le h \le 13$ |
| $k$ | $-4 \le k \le 4$ | $-4 \le k \le 4$ | $-4 \le k \le 4$ |
| $l$ | $0 \le l \le 13$ | $-14 \le l \le 13$ | $-16 \le l \le 16$ |
| $\Delta\rho_{max}$ (e $Å^{-3}$) | 1.391 | 0.760 | 2.417 |
| $\Delta\rho_{min}$ (e $Å^{-3}$) | -1.888 | -1.190 | -2.103 |
| *GoF* | 1.093 | 1.252 | 1.110 |
| Extinction coefficient | 0.0059(17) | 0.0082(10) | -- |
| $R_1(F)$ *for* $F_0^2>2\sigma(F_0^2)$[a] | 0.0287 | 0.0204 | 0.0276 |
| $R_w(F_0^2)$[b] | 0.0832 | 0.0443 | 0.0636 |

[a] $R_1 = \Sigma||F_0| - |F_c||/\Sigma|F_0|$. [b] $wR_2 = [\Sigma w(F_0^2 - F_c^2)^2/\Sigma w(F_0^2)^2]^{1/2}$; $P = (F_0^2 + 2F_c^2)/3$; $w = 1/[\sigma^2(F_0^2) + (0.0344P)^2 4.1783P]$ for **9.1**, $w = 1/[\sigma^2(F_0^2) + +1.2583P]$ for **9.2**, and $w = 1/[\sigma^2(F_0^2) + 5.9597P]$ for **9.3**.

The structure refinement for each material was fairly straight forward, where the occupancies of the In, Ga, and O sites did not deviate from unity when freely refined, and **9.2** and **9.3** were free from twinning. No $CsGa_7O_{11}$ crystals free of twinning could be found, and for that reason TWINABS was used for the absorption correction. In all three structures the alkali cations are mildly disordered as described below.[10] Unit cell parameters and refinement details for each compound are listed in Table 9.1.

$CsGa_7O_{11}$ and $RbGa_7O_{11}$ are analogous to one another and crystallized in the monoclinic space group *P*2/*m* with lattice parameters $a$ = 8.2821(3) Å, $b$ = 3.03840(10) Å, $c$ = 9.5817(3) Å, ß = 113.9510(10)°, and $a$ = 8.3224(3) Å, $b$ = 3.03160(10) Å, $c$ = 9.4566(3) Å, ß = 114.5860(10)°, respectively. In both structures, three of the Ga and five of the O sites have *m* symmetry while the remaining Ga and O site have 2/*m* symmetry. The modeled disorder of the alkali cations is slightly different between the Cs and Rb analogs. In the Cs structure Cs1 has an occupancy of 0.25 with 2 symmetry and Cs2 has an occupancy of 0.5 with 2/*m* symmetry creating three possible positions for the Cs atoms. In the Rb structure a SUMP command was used to constrain the total occupancy of the neighboring Rb sites to 1, this results in Rb1 with *m* symmetry and an occupancy of 0.3963, and Rb2 with 2 symmetry and an occupancy of 0.1036, for a total of four possible Rb positions.

$RbGa_4In_5O_{14}$ also crystallizes in the monoclinic space group *P*2/*m* with similar lattice parameters of $a$ = 8.9859(9) Å, $b$ = 3.1867(3) Å, $c$ = 10.7911(12) Å, and ß = 95.524(4). All atomic sites observe *m* symmetry except for In1 which has 2/*m* symmetry. All In, Ga, and O sites have occupancies of one, where the Rb1 site is disordered over a mirror plane and is half occupied.

**TGA.** Thermogravimetric analysis (TGA) was performed on $CsGa_7O_{11}$ and $RbGa_4In_5O_{14}$ in order to investigate their thermal stabilities. Data were collected on 10 mg samples heated to 850 °C at a rate of 10 °C/min in a nitrogen atmosphere using an SDT Q600 (TA instruments). The samples were analyzed by PXRD after TGA to confirm the persistence of the structures.

**Ion Exchange.** Ion exchange experiments using aqueous alkali chloride solutions and molten alkali nitrates were performed on samples of $CsGa_7O_{11}$ and $RbGa_4In_5O_{14}$. For aqueous ion exchange experiments approximately 4 mL of a concentrated salt solution of either 4 molal KCl, 7 molal RbCl, or 11 molal CsCl was added to 40 mg of starting material in glass vials with screw top lids. The vials were heated in a drying oven at 90 °C for 60-72 h without stirring the mixture. Control experiments were performed by adding 40 mg of starting material to 4 mL of deionized water and heating the sample under the same conditions to evaluate the stability in water. Because $CsGa_7O_{11}$ was found to decompose in water at 90 °C, and the deionized water contains dissolved $CO_2$ creating a mild acidic environment, 40 mg of $CsGa_7O_{11}$ was treated with 4 mL of a solution of 0.01M HCl with a pH of 2 and a potassium buffer solution with a pH of 10 (Fisher Chemical).

For molten nitrate ion exchange experiments, the starting material and alkali nitrate were added in a 1:10 mass ratio with 50-100 mg starting material to a 2 mL alumina crucible covered with a fused silica cap and heated at 450 °C for 12 or 48h. For both aqueous and molten nitrate ion exchange reactions, the products were washed with water three times followed by an acetone rinse before drying and examining by PXRD and ICP-MS to determine structure persistence and elemental ratios.

**ICP-MS.** The alkali content of ion exchange products was quantified using inductively coupled plasma mass spectrometry (ICP-MS). For each sample, approximately 5 mg of powdered sample was digested in 4 mL aqua regia at 180 °C overnight. A Finnigan ELEMENT XR double focusing magnetic sector field inductively coupled plasma-mass spectrometer (SF-ICP-MS) was used for the analysis with Rh as internal standards. A 0.2 ml/min Micromist U-series nebulizer (GE, Australia), quartz torch, and injector (Thermo Fisher Scientific, USA) were used for sample introduction. Cs concentration in acidified leachate solutions was measured directly, or after dilution if necessary, using ICP-MS (Agilent). Standards were intermittently measured to ensure the performance of the instruments over the course of the analyses.

**Chemical Durability.** Controlled aqueous leach tests following the guidelines in ASTM aqueous leach testing (e.g. ASTM 1285) were used to evaluate the chemical durability of $CsGa_7O_{11}$. However, the as-synthesized material (solid state reaction) was not subjected to any additional preparation steps (e.g,. washing and sieving) nor was its surface area measured. The test procedure maintained constant sample mass to leachate volumes in order to facilitate comparison among samples within this study.

Leach testing was conducted in duplicate at 30˚C and at pH values of approximately 2, 7 and 10 using hydrochloric acid-potassium chloride solution, phosphate buffered saline (PBS) solution, and sodium carbonate-bicarbonate solution, respectively. An additional single sample was prepared using de-ionized water. Approximately 0.05g of sample was combined with ~15 mL of buffer solution in sealed stainless steel pressure vessels. Approximately 0.5 mL of leachate solution from each vessel was sub-sampled and added to ~5.5 mL of 0.4 M $HNO_3$ after 2, 4, 6, 24, 48, and 168 hour durations. Following each

sub-sample, an amount of the respective leachate or buffer solution needed to replenish leachate volume lost was added back to each vessel and re-sealed before the subsequent sampling. The acidified leachates were stored in a refrigerator prior to measuring Cs concentration with ICP-MS. One blank was prepared alongside the samples with DI water and for each pH and measured at 24, 48, and 168 hours. The pH was measured at the start and conclusion of the test. The amount of Cs released from the sample was calculated as a fraction of the amount of Cs in the sample for each measurement duration. The initial Cs concentration was based on stoichiometry, but because the Cs concentration in the sample changed with time, all subsequent Cs concentrations in the samples were adjusted according to the total amount of Cs released at the end of the previous time duration.

**Table 9.2**: Measured pH of leachate solutions before and after leach testing.

| | Leach solutions before testing | | pH of Replicate leach solutions after leach testing | | | | | | | | | | |
|---|---|---|---|---|---|---|---|---|---|---|---|---|---|
| | Ionic Strength (M) | pH | 1 | 2 | blank | 1 | 2 | blank | 1 | 2 | blank | 1 | blank |
| KCl/HCl Buffer | 0.12 | 2.3 | 2.7 | 2.6 | 2.3 | | | | | | | | |
| $NaHCO_3/Na_2CO_3$ Buffer | 0.15 | 10 | | | | 9.9 | 9.9 | 10 | | | | | |
| Phosphate Buffered Saline | 0.21 | 7.2 | | | | | | | 7.2 | 7.2 | 7.1 | | |
| DI $H_2O$ | n/a | n/a | | | | | | | | | | 7.4 | 6.4 |

**DFT.** We performed DFT calculations using the Vienna Ab-initio Package (VASP) code,[14, 15] with the generalized gradient approximation of Perdew, Burke and Ernzerhof (PBE)[16] exchange-correlation potential, and using the projector augmented wave (PAW) method.[17, 18] To model the partial occupancy of the Rb atoms in $RbGa_7O_{11}$ and $RbGa_4In_5O_{14}$, we used a 1×2×1 supercell with 38 atoms, placing the Rb atoms in the two opposite Rb positions. with atomic coordinates (-0.427, 0.5, -0.49196) and (-0.5, 0.295, -0.5). To see if the CsGa7O11 and RbGa7O11 compounds are thermodynamically stable,

we compared their formation energy with Cs-Ge-O and Rb-Ge-O convex hulls, respectively, reported in the Open Quantum Materials Database (OQMD).[19, 20] When the formation energy of the $CsGa_7O_{11}$ and $RbGa_7O_{11}$ compounds is more negative than their respective convex hull, i.e., the formation energy is below the convex hull, this indicates that there is a driving force for forming these compounds, and the compounds are thermodynamically stable. Contrarily, if the formation energy is above the convex hull (more positive), the compounds are considered to be thermodynamically unstable. We used the OQMD calculational values and configuration: 520 eV cut-off energy for the plane wave basis set, $10^{-4}$ eV energy convergence criterion, 7×8×6 **k**-point mesh. We also studied Cs exchange with alkali ion A (A = Rb or K) in a nitrate melt, i.e., using $KNO_3$, $RbNO_3$ and $CsNO_3$ as references, by calculating the ion exchange energy, $\Delta E_{ie}$, using:

$$\Delta E_{ie} = [\Delta H(AGa_7O_{11}) + \Delta H(CsNO_3) - \Delta H(CsGa_7O_{11}) - \Delta H(ANO_3)]/N_{tot} \quad (1)$$

where $\Delta H(AGa_7O_{11})$, $\Delta H(CsGa_7O_{11})$, $\Delta H(CsNO_3)$, and $\Delta H(ANO_3)$ are the formation enthalpies per formula unit of $AGa_7O_{11}$, $CsGa_7O_{11}$, $CsNO_3$ and $ANO_3$ (A = Rb, Cs), respectively, and $N_{tot}$ is the total number of atoms in the reaction, in this case 28. The $\Delta E_{ie}$ for Rb exchange with alkali ion A ( A = K or Cs) in $RbGa_4In_5O_{14}$ was also calculated using Eq. (1), by replacing $\Delta H(AGa_7O_{11})$ with $\Delta H(AGa_4In_5O_{14})$, and $N_{tot}$ = 29. The formation enthalpies used in the calculation of $\Delta E_{ie}$ were obtained by relaxing the structures using stricter energy and force convergence criteria of $10^{-6}$ eV and $10^{-2}$ eV/Å, respectively. In the case of $RbGa_4In_5O_{14}$, we used 6×8×5 and 8×5×5 **k**-point meshes for $AGa_4In_5O_{14}$ and $ANO_3$ (A = K, Rb, Cs), respectively. All structures were fully relaxed by allowing for the volume, cell shape and atomic positions to change during the process.

**Results and Discussion:**

**Synthesis.** Recent publications by our group have detailed that reaction vessel size, in addition to the vessel material, significantly influences the products that are obtained in a reaction. [21–23] While the reaction vessel material has always been regarded as important in the solid state community, as elements from the reaction vessel have been known to incorporate into the final product under certain reaction conditions, reaction vessel size is not always reported especially for alumina and metal crucibles, as vessel shape is not typically assumed to affect product formation. $CsGa_7O_{11}$ and $RbGa_7O_{11}$ can be synthesized using either a Ag or Pt crucible, both of which have similar volumes of 14 and 15 mL, respectively, but whose surface area to volume ratios are significantly different due to the large taper on the Ag crucible. Both compounds, $CsGa_7O_{11}$ and $RbGa_7O_{11}$ are also thermodynamically stable at 0 K, being 50 and 33 meV/atom below their respective OQMD convex hulls. Silver tubes measuring 5.7 cm tall and 1.2 cm in diameter were also used for the synthesis of $CsGa_7O_{11}$ and $RbGa_7O_{11}$ but resulted in water soluble products that were not further investigated. $RbGa_4In_5O_{14}$ could only be produced in the 14 mL Ag crucibles and it is unclear whether the crucible shape or the potential nucleation sites play a more important role in the crystallization of the product. Flux reactions of the alkali and Al analogs of $CsGa_7O_{11}$ and $RbGa_7O_{11}$, in addition to the K and Na analogs, were attempted, but none were successful and resulted in $Al_2O_3$, $Ga_2O_3$ or impure β-alumina type phases. Additionally, we attempted to substitute the octahedrally coordinated Ga in $CsGa_7O_{11}$ and $RbGa_7O_{11}$ with In to obtain $AGa_2In_5O_{11}$, but these reactions inevitably resulted in $RbGa_4In_5O_{14}$. $RbGa_4In_5O_{14}$ is also thermodynamically stable, 6 meV/atom below the Rb-Ga-In-O OQMD convex hull.

Traditional solid state reactions were attempted by pressing pellets of stochiometric amounts of $Ga_2O_3$ and $CsNO_3$ (in 10% excess) and heating at temperatures of 600, 700, 800, 900, 1000, and 1200 °C in order to obtain $CsGa_7O_{11}$; however, in all cases $Ga_2O_3$ persists and does not react to produce the desired product. We also evaluated the enthalpy of the used solid state reaction using DFT, and the reaction enthalpy is very positive, 0.167 eV/atom, which explains why the reaction was unsuccessful in producing $CsGa_7O_{11}$. Alternatively, we dissolved the cesium and gallium nitrates in water and stirred while heating on a hot plate, and after all water was evaporated, reground the white powder before heating in an alumina crucible at 700, 800, and 900 °C. An amorphous phase is obtained at 700 and 800 °C and $CsGa_7O_{11}$ begins to form at 800 °C and can be easily obtained in pure form after heating at 900 °C for 60 h with intermittent grindings. Due to the success of the solution assisted solid state reaction we attempted similar reactions for $RbGa_7O_{11}$, $RbGa_4In_5O_{14}$, and their potential analogs with Cs, K, Na, Al, In; however, none resulted in phase pure products. In reactions targeting $RbGa_7O_{11}$, the rubidium gallate analog, the ß-alumina structure, $AGa_{11}O_{17}$, was always obtained with no evidence of $RbGa_7O_{11}$ and further attempts to increase the amount of excess rubidium to encourage the $RbGa_7O_{11}$ phase were also unsuccessful. For $RbGa_4In_5O_{14}$, mixtures of $RbGa_4In_5O_{14}$ and an $In_2O_3$ structure type were obtained between 800 °C and 950 °C, where reactions below these temperatures yielded only the $In_2O_3$ type phase and the amount of $RbGa_4In_5O_{14}$ decreases as temperatures increases.

**Structure.** Structures **9.1** and **9.2,** $AGa_7O_{11}$ (A = Rb, Cs), are analogous and are tunnel structures consisting of $GaO_6$ octahedra, $GaO_4$ tetrahedra, and disordered alkali cations within the small tunnels (Figure 9.2a). Each tunnel is approximately rectangular

where two opposite sides are formed by two edge sharing $GaO_6$ octahedra and the other pair of opposite sides are constructed of a corner sharing $GaO_6$ octahedron and $GaO_4$ tetrahedron. This is similar to the hollandite structure type, where all four sides of the approximately square tunnels are created by dimers of edge-sharing octahedra.

To reveal topological relations between the frameworks in the structures of $CsGa_7O_{11}$ and hollandite, we performed a topological analysis of their underlying nets. The standard simplification procedure,[24–26] which offers a convenient way to compare

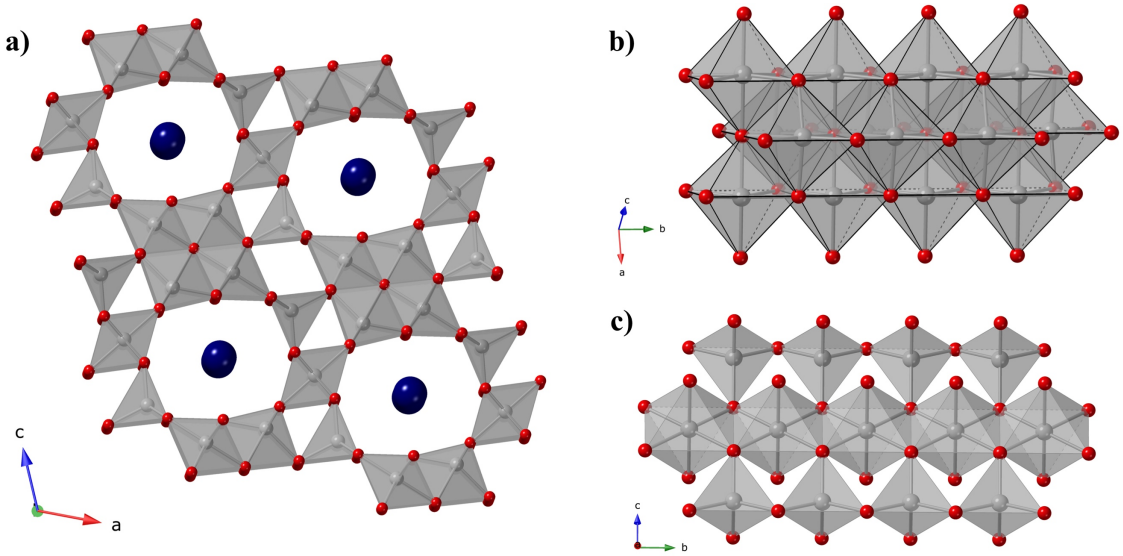


**Figure 9.2:** Structure of **9.1** and **9.2** $AGa_7O_{11}$ (A = Rb, Cs). a) View of the *ac* plane. b) chains of $Ga_4O_9$ in the *b* direction. c) Edge sharing chains of $GaO_6$ octahedra connected to corner-sharing chains of $GaO_4$ tetrahedra through corner sharing.

topologies by reducing the structure to only framework forming cations and connectivity between them, was carried out by excluding the alkali metal cations from the structures and replacing the gallate units with their centers of gravity. The edges in the underlying net correspond to the connectivity between the gallate units that was present in the initial structure (Figure 9.3). $CsGa_7O_{11}$ has a more complex underlying net as compared to hollandites, although there is a similarity between them. The relation between the

underlying nets can be shown by removing edges from the $CsGa_7O_{11}$ net and connecting nodes as shown in Figure 9.3. Given the close relation between the two structures, one can expect that other complex topologies can be derived from the parent hollandite net.

For comparison, the oxygen-oxygen distances across the tunnels are given for hollandite, **9.1**, **9.2**, and **9.3** as shown in Figure 9.4. In $AGa_7O_{11}$ the tunnels stack in the *c* direction and two of the tunnel sides of dimers of edge-sharing octahedra edge share to form infinite chains of $Ga_4O_9$ in the *b* direction where each octahedron shares six of its 12

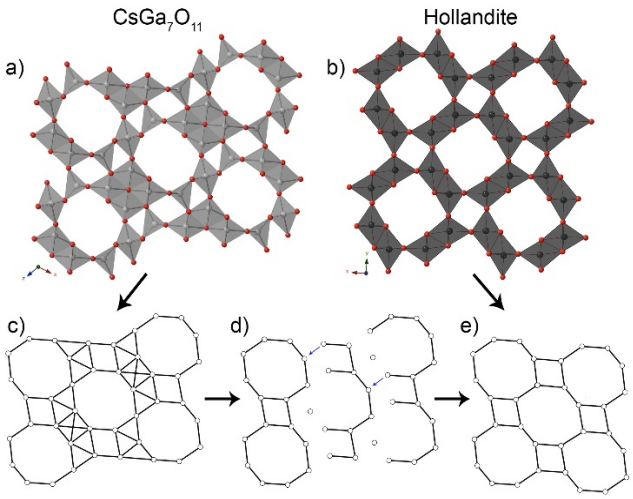


**Figure 9.3**. (a and b) frameworks of the $CsGa_7O_{11}$ and hollandite structure types. (c, d, and e) show their underlying nets and relations between them.

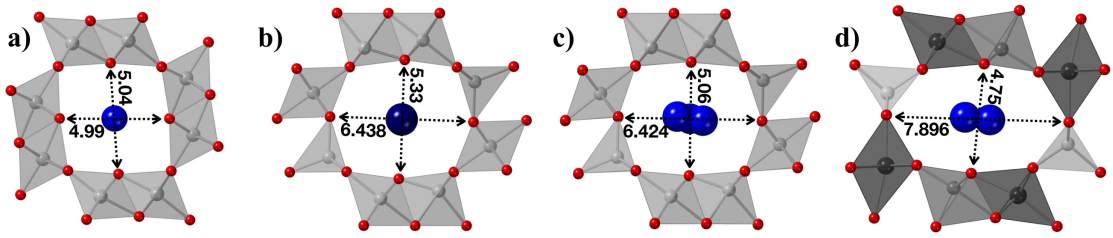


**Figure 9.4:** Tunnel dimensions in Å of a) hollandite, b) $CsGa_7O_{11}$, c) $RbGa_7O_{11}$, and d) $RbGa_4In_5O_{14}$.

edges with adjacent octahedra (Figure 9.2b). These chains consist of two crystallographically unique gallium octahedra where one is significantly distorted with two long bonds of length 2.4192 or 2.3634 Å and O-Ga-O bond angles of 145.2° or 149.9°, respectively for **9.1** and **9.2**, likely to minimize electrostatic repulsions of the Ga atoms (Figure 9.5a). Metal oxygen bond lengths for all compounds can be found in Table 9.3. Adjacent channels in the *a* direction share the $GaO_6$ octahedron that corner shares with the $GaO_4$ tetrahedra to comprise the other pair of tunnel sides. These octahedra edge share to form chains in the *b* direction and the tetrahedra corner share to form chains in the same direction (Figure 9.2c).

**Table 9.3**: M-O bond distances in structures **9.1-9.3**.

| $CsGa_7O_{11}$ (**9.1**) | | $RbGa_7O_{11}$ (**9.2**) | | $RbGa_4In_5O_{14}$ (**9.3**) | |
|---|---|---|---|---|---|
| Interaction | Distance (Å) | Interaction | Distance (Å) | Interaction | Distance (Å) |
| Ga1-O1 x 2 | 2.081(3) | Ga1-O1 x 2 | 2.0669(18) | In1-O1 x 4 | 2.151(3) |
| Ga1-O4 x 2 | 1.938(3) | Ga1-O4 x 2 | 1.9471(17) | In2-O2 x 2 | 2.292(4) |
| Ga1-O5 | 1.931(5) | Ga1-O5 | 1.935(3) | In2-O1 | 2.146(4) |
| Ga1-O6 | 1.957(8) | Ga1-O6 | 1.9980(4) | In2-O3 x 2 | 2.101(3) |
| Ga2-O1 | 1.880(5) | Ga2-O1 | 1.873(3) | In2-O4 | 2.244(4) |
| Ga2-O2 | 1.809(5) | Ga2-O2 | 1.804(3) | In2-O5 x 2 | 2.087(3) |
| Ga2-O5 x 2 | 1.836(3) | Ga2-O5 x 2 | 1.8323(15) | In3-O1 | 2.302(4) |
| Ga3-O1 | 1.986(5) | Ga3-O1 | 1.996(3) | In3-O2 x 2 | 2.201(3) |
| Ga3-O3 x 2 | 1.867(3) | Ga3-O3 x 2 | 1.8618(16) | In3-O6 | 2.193(4) |
| Ga3-O4 | 1.878(6) | Ga3-O4 | 1.9994(17) | In3-O7 x 2 | 2.075(3) |
| Ga3-O6 x 2 | 2.4192(7) | Ga3-O6 x 2 | 2.3634(3) | Ga1-O2 | 1.865(4) |
| Ga4-O2 x 4 | 2.006(3) | Ga4-O2 x 4 | 1.9994(17) | Ga1-O5 | 1.820(5) |
| Ga4-O3 x 2 | 1.995(5) | Ga4-O3 x 2 | 1.982(3) | Ga1-O6 x 2 | 1.852(2) |
| | | | | Ga2-O3 x 2 | 2.217(5) |
| | | | | Ga2-O4 x 2 | 1.871(2) |
| | | | | Ga2-O7 | 1.874(5) |

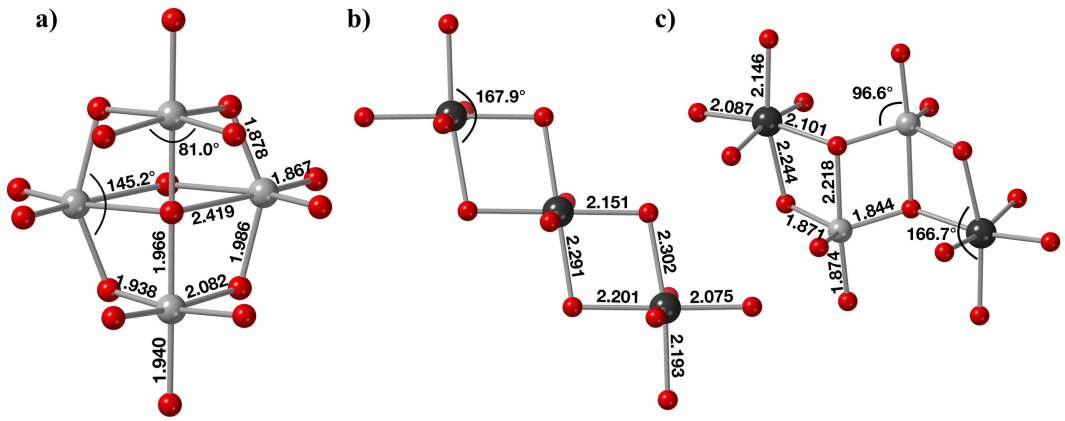


**Figure 9.5:** Selected Metal coordination environments in $CsGa_7O_{11}$ (a) and $RbGa_4In_5O_{14}$ (b, c).

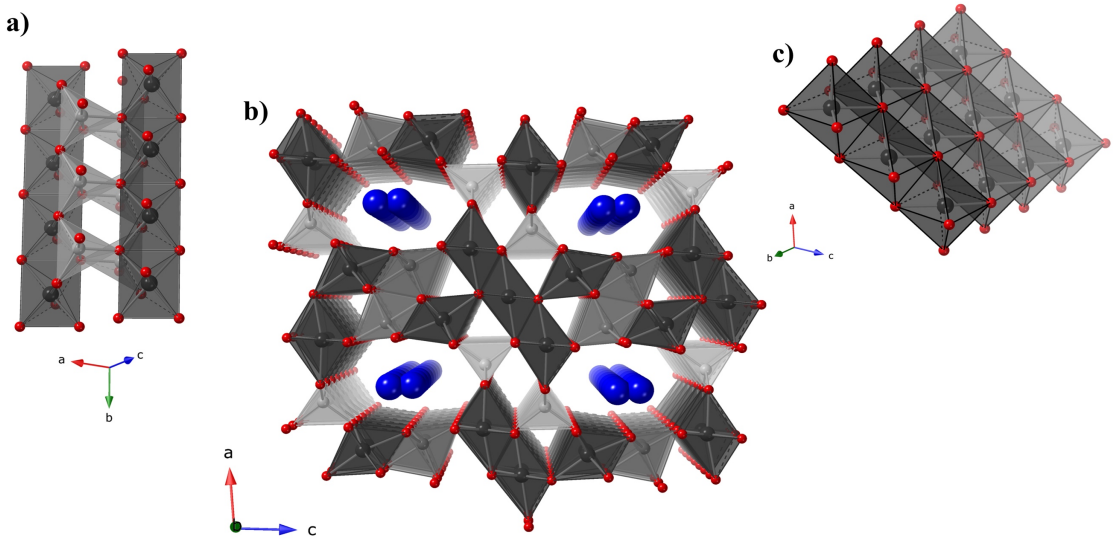


**Figure 9.6:** Structure of $RbGa_4In_5O_{14}$ with In octahedra shown in black, Ga trigonal bipyramids in dark grey, and tetrahedral Ga in light gray. a) $Ga_2O_8$ dimers sandwiched by chains of edge sharing $InO_6$ octahedra. b) View of the *ac* plane. c) $Ga_3O_8$ chains in the *b* direction.

$RbGa_4In_5O_{14}$ is comprised of $InO_6$ octahedra, $GaO_5$ trigonal bipyramids, and $GaO_4$ tetrahedra and has similarly sized tunnels as the $AGa_7O_{11}$ structure (Figure 9.4). One of the pairs of opposing tunnel sides are comprised of an edge sharing $InO_6$ octahedron and a

$GaO_5$ trigonal bipyramid and the other pair of sides are comprised of a corner sharing $InO_6$ octahedron and a $GaO_4$ tetrahedron. Adjacent tunnels stack in the *a* direction where the $GaO_5$ trigonal bipyramids edge share and form chains of corner sharing $Ga_2O_8$ dimers that are sandwiched by chains of edge sharing $InO_6$ octahedra (Figure 9.6a). Both the $InO_6$ and $GaO_5$ units in Figure 9.6a are distorted and a closer look at their coordination is given in Figure 9.5c showing a long Ga-O bond distance of 2.218 Å, a non-planar Ga coordination with an axial O-Ga-equatorial O bond angle of 96.6°, and a compressed axial O-In-axial O bond angle of 166.7°. The indium octahedra of the other sides of the tunnels corner share with two gallium tetrahedra, one gallium trigonal bipyramid, and another indium octahedron. There is one indium site that does not frame the channel, and instead fills the void between two of the indium octahedra that make up the corner sharing sides of two diagonally adjacent channels. This forms $Ga_3O_8$ chains in the *b* direction that contain slightly distorted octahedra as depicted in Figure 9.4b.

**TGA.** Both $CsGa_7O_{11}$ and $RbGa_4In_5O_{14}$ are thermodynamically stable in a nitrogen atmosphere up to 850 °C with less than 1.5 % weight loss that occurred at temperatures less than 200 °C and which is attributed to surface water.

**Ion Exchange.** The control experiments revealed that $CsGa_7O_{11}$ decomposed to GaO(OH), identified by PXRD, when treated in an aqueous environment at 90 °C for 60 hours. However, the structure persists in water, mildly acidic, and basic environments (pH of 2 and 10) at room temperature for at least 7 days and is thermodynamically stable to 850 °C; it appears that the combination of heat and an aqueous environment causes the decomposition. The same decomposition product, GaO(OH), is also obtained when $CsGa_7O_{11}$ is soaked in KCl and NaCl; however, in RbCl the structure ion exchanges to a

final Cs/Rb ratio of 0.78/0.22 as determined by ICP-MS (see Figure 9.7). Ion exchange reactions in molten $RbNO_3$ and $KNO_3$ were also attempted. The overnight (~16h) molten $RbNO_3$ ion exchange results in a final Cs/Rb ratio of 0.38/0.62 and the 48 h ion exchange reactions had final ratios of Cs/Rb 0.20/0.80, which are both more extensive than the aqueous ion exchange perhaps due to the excess thermal energy. The DFT calculations indicate that there is a thermodynamic force for exchanging Cs with Rb in $AGa_7O_{11}$, with an ion exchange energy of -13 meV/atom. While ion exchange was not successful in aqueous KCl, the treatment of $CsGa_7O_{11}$ in molten $KNO_3$ for 48 hours resulted in a Cs/K ratio of 0.12/0.88. This is substantiated by the DFT calculated ion exchange energy of -23 meV/atom, indicating a thermodynamic force for exchanging Cs with K. The PXRD patterns are shown in Figure 9.8-9.9 and support the ICP-MS results with subtle changes in d-spacing and peak intensities due to ion exchange.

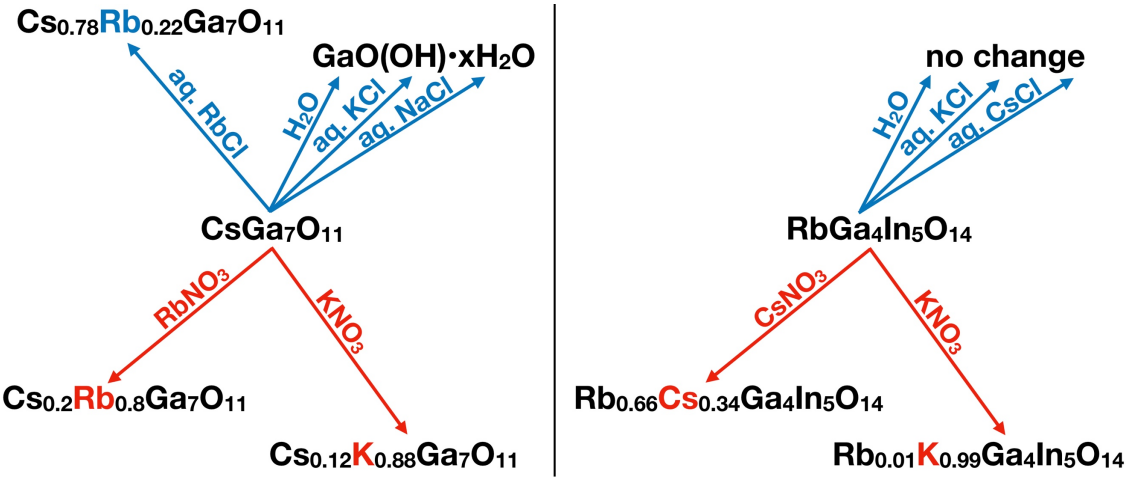


**Figure 9.7**: Visual summary of ion exchange reactions. Aqueous ion exchange reactions (blue arrows) were carried out at 90 °C for 60-72 h and molten nitrate reactions (red arrows) were carried out at 450 °C for 48 h.

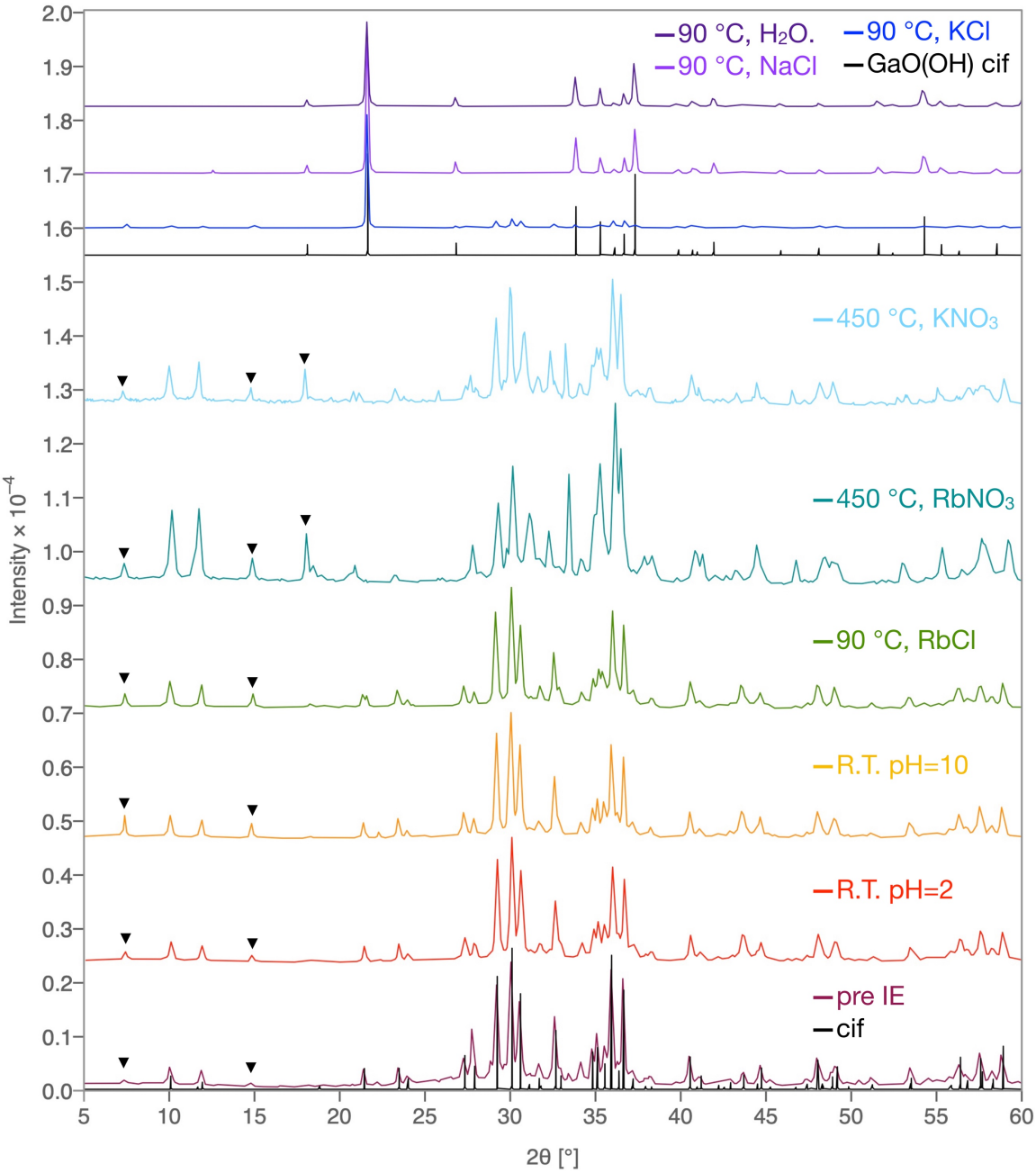


**Figure 9.8**: PXRD patterns of $CsGa_7O_{11}$ ion exchange (IE) reactions. Peaks belonging to the $AGa_{11}O_{17}$ impurity are marked with inverted triangles. (RT = room temperature)

$RbGa_4In_5O_{14}$ is stable in water at 90 °C with no observable change in the PXRD pattern for at least a week (Figure 9.9). PXRD patterns of $RbGa_4In_5O_{14}$ before and after aqueous CsCl and KCl ion exchange reactions are near identical to the parent structure and suggest that no significant aqueous ion exchange takes place under these mild conditions.

The PXRD patterns of $RbGa_4In_5O_{14}$ before and after treatment with molten $CsNO_3$ and $KNO_3$ show subtle changes in d-spacing and peak intensity and the ICP-MS results show ratios of Rb/Cs and Rb/K to be 0.66/0.34 and 0.01/0.99, respectively. The K ion exchange goes to near completion, while less than half of the Rb ions could be exchanged for Cs, which could be attributed to the much larger size of Cs that plays a role in the kinetics of the ion exchange reaction. DFT supports the experimental observation, showing that there is a -5 meV/atom ion exchange energy for exchanging Rb with K. On the other hand, the energy for exchanging Rb with Cs is 18 meV/atom, indicating that this is an endothermic process requiring energy input, which can explain the observed partial ion exchange.

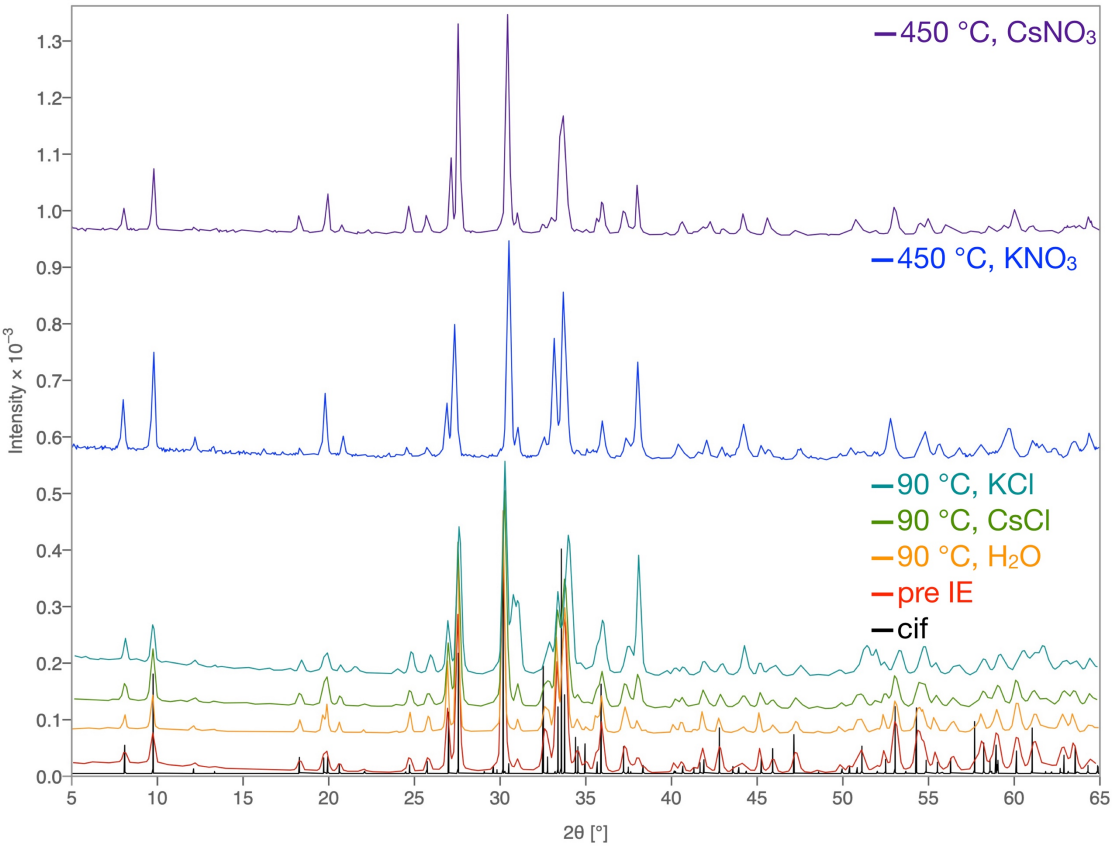


**Figure 9.9**: PXRD patterns of $RbGa_4In_5O_{14}$ ion exchange (IE) reactions.

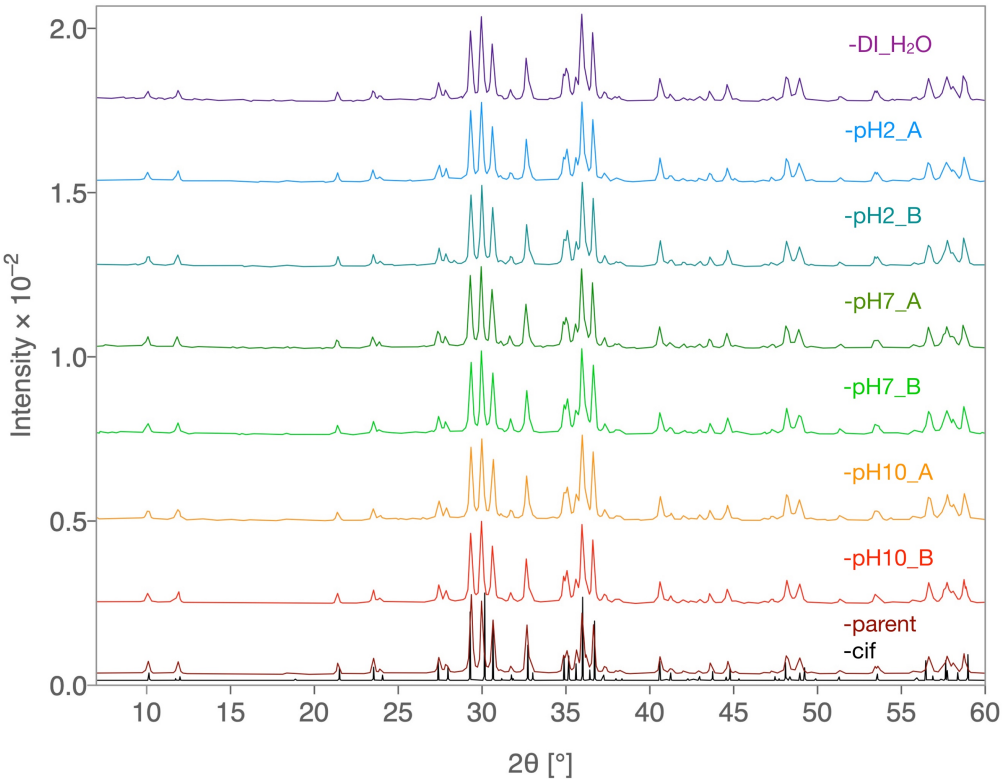


**Figure 9.10**: PXRD patterns of $CsGa_7O_{11}$ before and after leach experiments.

**Chemical Durability.** The fractional Cs release from $CsGa_7O_{11}$ is shown in Figure 9.11 as a ratio of Cs concentration in the leachate to Cs concentration in the sample. In all instances, the control blanks leached Cs below the detection limit. It is apparent that the behavior of Cs release under basic and acidic conditions was different compared to a neutral pH. In both pH2 and pH10 buffer solutions, relatively greater amounts of Cs were released compared to a neutral pH and the Cs release did not appear to reach steady state after 7 days, although the release rate decreased over time. While the leach results indicate approximately 9 % and 25 % of the Cs mass was removed from $CsGa_7O_{11}$ at pH2 and pH10, respectively, PXRD of the material post leaching revealed no decomposition products or measurable structural changes. In the previously discussed ion exchange experiments, $CsGa_7O_{11}$ was also observed to persist if placed in pH2 or pH10 solutions

with little to no decomposition as measured by PXRD (Figure 9.10). EDS of the dried leachate after 168 h revealed Ga present. It was not possible to quantify a representative Ga/Cs ratio owing to the non-uniform elemental distribution in the dried leachate, but gross estimates did not suggest congruent dissolution. It is possible that the $CsGa_7O_{11}$ is slightly soluble in pH2 and pH10 solutions or ion-exchange may occur between these solutions and the $CsGa_7O_{11}$ phase.

The leaching behavior of $CsGa_7O_{11}$ is markedly different in pH 7 buffer and DI water solutions. In both solutions, a significant amount of Cs initially went into solution, but then decreased over time to an apparent steady state within 24 hours. PXRD of the material post leaching revealed no decomposition products or measurable structural changes. This result is in contrast to the ion exchange experiments, wherein $CsGa_7O_{11}$ decomposed into GaO(OH) when placed in DI water at 90°C for 60 hours as measured by PXRD. It is possible that elevated temperatures are needed to dissolve $CsGa_7O_{11}$ but, ion-exchange reactions may also help explain the behavior. The estimated alkali concentration in the ion exchange solutions was ~200x that of the buffer solutions used in the leach studies and that difference in chemical gradient may also have affected the ability of the $CsGa_7O_{11}$ to exchange Na for Cs while maintaining structural stability. The initially high (see Figure 9.11) Cs release at <2 hours, and the subsequent *decrease* in Cs release to a steady state may also suggest complex reactions taking place. It would appear that the samples exposed to pH 7 buffer and DI water took up Cs after an initial Cs loss, which might be explained by ion-exchange reactions or possibly re-precipitated phase evolution. Although no decomposition products or precipitate phases were identified post leaching, their concentrations in the neutral pH tests may not have been significant to definitively

identify. It is also apparent that the initial Cs concentration, while observed in the pH 7 buffered solution, was significantly less pronounced than in the DI water. This strongly suggests a link between ion-exchange equilibrium between the sample and the solution.

Taken together, the results suggest temperature and pH have a significant effect on the stability of $CsGa_7O_{11}$, but that complex ion exchange reactions may also occur with $CsGa_7O_{11}$ in aqueous environments, affecting its stability. Additional characterization and more controlled experiments to quantify parameters such as surface area, corrosion depth, and higher resolution chemical analyses are needed to elucidate the behavior of $CsGa_7O_{11}$ in aqueous environments further.

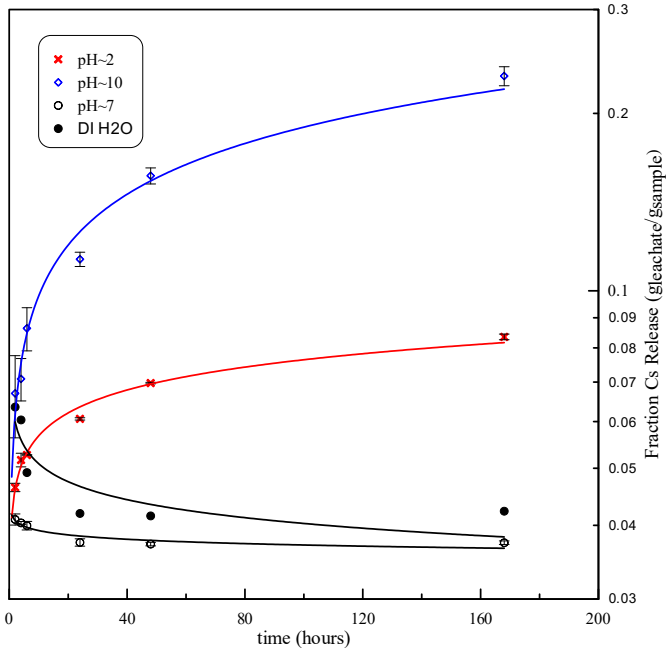


**Figure 9.11:** The calculated fractional release of Cs as a function of time from $CsGa_7O_{11}$ exposed to different aqueous solutions at 30 °C. Error bars represent the spread between the duplicate measurements as calculated according to the standard error.

**Conclusion.** Two new tunnel structure types, $AGa_7O_{11}$ (A = Cs, Rb) and $RbGa_4In_5O_{14}$, have been synthesized and characterized by X-ray diffraction, ICP-MS, thermal analysis, ion exchange experiments, DFT calculations, and aqueous leach studies. The structures consist of tunnels constructed from Ga/In octahedra similar to the hollandite phase with the alkali cations housed within these tunnels. Due to the relevance of hollandite as a waste form material, specifically for the sequestration of Cs, we have further characterized these structures and determined that although both are thermally stable up to 850 °C, $CsGa_7O_{11}$ exhibits complex Cs leaching behavior in aqueous environments. Preliminary results indicate mild temperatures decompose $CsGa_7O_{11}$ in water, but leach studies in buffered pH solutions suggest more complex ion-exchange behavior at room temperature. As such, further study of the behavior of $CsGa_7O_{11}$ in aqueous environments may be of interest for its ability to capture and release alkali ions via controlled solution chemistry. Alternatively, the $RbGa_4In_5O_{14}$ structure type showed no significant changes in aqueous environments and showed no signs of ion exchange, as predicted by DFT calculations, which is promising and may be beneficial to study further. While the Cs analog of $RbGa_4In_5O_{14}$ could not be obtained by flux or solid state methods, the ability to exchange Rb for Cs in a molten nitrate salt could lead to a Cs-pure analog under appropriate heating and process time conditions. Further studies of Cs containing $RbGa_4In_5O_{14}$ in aqueous environments should also be conducted in order to further characterize this structure type as a potential waste form material for Cs sequestration.

**Acknowledgements.** Research was conducted by the Center for Hierarchical Wasteform Materials (CHWM), an Energy Frontier Research Center (EFRC). Research was supported by the U.S. Department of Energy, Office of Basic Energy Sciences,

Division of Materials Sciences and Engineering under Award DE-SC0016574. V. Kocevski and T. M. Besmann acknowledge the use of computational resources provided by the National Energy Research Scientific Computing Center (NERSC) and the HPC cluster Hyperion, supported by The Division of Information Technology at University of South Carolina. Work conducted at Savannah River National Laboratory was supported by the U.S. Department of Energy under contract DE-AC09-08SR22470.

**References:**

(1) zur Loye, H.-C.; Besmann, T.; Amoroso, J.; Brinkman, K.; Grandjean, A.; Henager, C. H.; Hu, S.; Misture, S. T.; Phillpot, S.; Shustova, N. B.; Wang, H.; Koch, R. J.; Gregory Morrison; Dolgopolova, E., Hierarchical Materials as Tailored Nuclear Waste Forms: A Perspective, *Chem. Mater.* **2018**, *30*, 4475-4488.

(2) Council, N. R. *Waste Forms Technology and Performance: Final Report.* National Academies Press: Washington, DC, 2011;

(3) Crum, J. V.; Turo, L.; Riley, B.; Tang, M.; Kossoy, A., Multi-Phase Glass-Ceramics as a Waste Form for Combined Fission Products: Alkalis, Alkaline Earths, Lanthanides, and Transition Metals, *J. Am. Ceram. Soc.* **2012**, *95*, 1297-1303.

(4) Vance, E. R.; Chavara, D. T.; Gregg, D. J., Synroc development—Past and present applications, *MRS Energy & Sustainability* **2017**, *4*,

(5) Ringwood, A. E.; Kesson, S. E.; Ware, N. G.; Hibberson, W. O.; Major, A., The SYNROC process: A geochemical approach to nuclear waste immobilization, *Geochemical Journal* **1979**, *13*, 141-165.

(6) Ringwood, A. E.; Kesson, S. E.; Ware, N. G.; Hibberson, W.; Major, A., Immobilisation of high level nuclear reactor wastes in SYNROC, *Nature* **1979**, *278*, 219-223.

(7) Amoroso, J.; Marra, J. C.; Tang, M.; Lin, Y.; Chen, F.; Su, D.; Brinkman, K. S., Melt processed multiphase ceramic waste forms for nuclear waste immobilization, *J. Nucl. Mater.* **2014**, *454*, 12-21.

(8) Utlak, S. A.; Besmann, T. M.; Brinkman, K. S.; Amoroso, J. W., Thermodynamic assessment of the hollandite high-level radioactive waste form, *J. Am. Ceram. Soc.* **2019**, *102*, 6284-6297.

(9) Bugaris, D. E.; zur Loye, H.-C., Materials discovery by flux crystal growth: Quartenary and higher oxides, *Angew. Chem. Int. Ed.* **2012**, *51*, 3780-3811.

(10) Bruker. *APEX3, SAINT+, TWINABS, and SADABS.* Bruker AXS Inc.: Madison, Wisconsin, USA, 2015;

(11) Sheldrick, G. M., Crystal structure refinement with SHELXL, *Acta Cryst.* **2015**, *C71*, 3-8.

(12) Sheldrick, G. M., SHELXT - Integrated space-group and crystal-structure determination, *Acta Cryst.* **2015**, *A71*, 3-8.

(13) Dolomanov, O. V.; Bourhis, L. J.; Gildea, R. J.; Howard, J. A. K.; Pushmann, H., OLEX2: a complete structure solution, refinement and analysis program, *J. Appl. Crystallogr.* **2009**, *42*, 339-341.

(14) Kresse, G.; Furthmuller, J., Efficient iterative schemes for ab-initio total-energy calculations using a plane-wave basis set, *Phys. Rev. B* **1996**, *54*, 11169-11186.

(15) Kresse, G.; Furthmuller, J., Efficiency of ab-initio total energy calculations for metals and semiconductors using a plane-wave basis set, *Comput. Mater. Sci.* **1996**, *6*, 15-50.

(16) Perdew, J. P.; Burke, K.; Ernzerhof, M., Generalized Gradient Approximation Made Simple, *Phys. Rev. Lett.* **1996**, *77*, 3865-3868.

(17) Blöchl, P. E., Projector augmented-wave method, *Phys. Rev. B* **1994**, *50*, 17953-17979.

(18) Kresse, G.; Joubert, D., From ultrasoft pseudopotentials to the projector augmented-wave method, *Phys. Rev. B* **1999**, *59*, 1758-1775.

(19) Saal, J. E.; Kirklin, S.; Aykol, M.; Meredig, B.; Wolverton, C., Materials design and discovery with high-throughput density functional theory: the open quantum materials database (OQMD), *Jom* **2013**, *65*, 1501-1509.

(20) Kirklin, S.; Saal, J. E.; Meredig, B.; Thompson, A.; Doak, J. W.; Aykol, M.; Rühl, S.; Wolverton, C., The Open Quantum Materials Database (OQMD): assessing the accuracy of DFT formation energies, *npj Computational Materials* **2015**, *1*, 15010.

(21) Juillerat, C. A.; Kocevski, V.; Besmann, T.; zur Loye, H.-C., Observation of the Same New Sheet Topology in Both the Layered Uranyl Oxide-Phosphate $Cs_{11}[(UO_2)_{12}(PO_4)_3O_{13}]$ and the Layered Uranyl Oxyfluoride-Phosphate

$Rb_{11}[UO_2)_{12}(PO_4)_3O_{12}F_2]$ Prepared by Flux Crystal Growth, *Frontiers in Chemistry* **2019**, *7*, 583.

(22) Juillerat, C. A.; Kocevski, V.; Karakalos, S.; Morrison, G.; Misture, S.; Besmann, T.; zur Loye, H.-C., Flux Crystal Growth of U(V) containing oxyfluoride perovskites, *Inorganic Chemsitry Frontiers* **2019**, *6*, 3202-3214.

(23) Juillerat, C. A.; zur Loye, H.-C., Crystal Growth and Structure Characterization of Three Layered Uranyl Phosphates and Their Relation to the Phosphuranylite Family, *Cryst. Growth Des.* **2019**, *19*, 1183-1189.

(24) Blatov, V. A.; Shevchenko, A. P.; Serezhkin, V. N., TOPOS3.2: a new version of the program package for multipurpose crystal-chemical analysis, *J. Appl. Crystallogr.* **2000**, *33*, 1193.

(25) Baburin, I. A.; Blatov, V. A.; Carlucci, L.; Ciani, G.; Proserpio, D. M., Interpenetrating metal-organic and inorganic 3D networks: a computer-aided systemative investigation. Part II [1]. Analysis of the Inoganic Crystal Structure Database (ICSD), *J. Solid State Chem.* **2005**, *178*, 2452-2474.

(26) Blatov, V. A.; Shevchenko, A. P.; Proserpio, D. M., Applied Topological Analysis of Crystal Structures with the Program Package ToposPro, *Cryst. Growth Des.* **2014**, *14*, 3576-3586.

# Chapter 10

## Flux Crystal Growth of Uranium(V) Containing Oxyfluoride Perovskites[1]

[1]Reproduced from Juillerat, C. A.; Kocevski, V.; Karakalos, S.; Morrison, G.; Patil, D.; Misture, S.; Besmann, T.; zur Loye, H.-C. *Inorg. Chem. Front.,* **2019**, *6*, 3202-3214 with permission from the Chinese Chemical Society, Peking University and the Royal Society of Chemistry.

**Abstract:** The novel phases $Rb_4NaU_3O_{12-x}F_x$ (**10.1**), $K_4NaU_3O_{12-x}F_x$ (**10.2**), and $Rb_{2.1}K_{1.9}KU_3O_{12-x}F_x$ (**10.3**) were synthesized by molten flux methods using mixed alkali fluoride melts. The oxyfluorides crystallize in the cubic space group *Im-3m* with *a* lattice parameters of 8.7472(2) Å, 8.6264(2) Å, and 8.8390(3) Å, respectively. All three structures crystallize in a cubic perovskite structure, $ABO_3$ ($A_4BB'_3O_{12}$), where the A site is fully occupied by an alkali cation, and the B site is shared by the remaining smaller alkali cation and uranium in an ordered fashion such that the alkali cation on the B site is surrounded by square uranyl bipyramids. The structures were characterized by single crystal X-ray diffraction, energy dispersive spectroscopy, X-ray absorption near edge structure spectroscopy, X-ray photoelectron spectroscopy, magnetic susceptibility measurements, DFT calculations, thermogravimetric analysis, and UV-vis spectroscopy, all of which support the presence of U(V) in the three new materials.

**Introduction**. The exploration of uranium crystal chemistry continues as nuclear technologies continue to receive attention in order to improve the nuclear fuel cycle, develop environmental remediation projects, and establish waste-forms to effectively immobilize waste radioisotopes and prevent migration of radionuclides in the environment.[1] The recent review on the flux crystal growth of uranium oxides emphasizes the contributions of the flux crystal growth technique in expanding the number of known uranium extended structures, and thus our understanding of uranium crystal chemistry. In particular, it brings attention to the abundance of U(VI) containing compounds, the readily achievable incorporation of U(IV) by using reducing reaction conditions, and the sparse examples of U(V) containing structures grown by flux methods. Specifically, out of the 180 structures in the review, 22 contain U(IV), only two contain solely U(V), and two

contain mixed U(V/VI).[2] Uranium (V) chemistry is still relatively undeveloped, as reaction conditions that are conducive to incorporating this species into extended structures remain poorly understood; however, recent publications highlight the use of hydrothermal methods as an effective approach to target U(V) containing structures.[3, 4] Given these realities, it was a welcome surprise that we were able to grow three new uranium (V) containing structures from molten alkali fluoride fluxes using $UF_4$ as the uranium precursor in vessels open to the atmosphere. In our experience, starting with $UF_4$ in similar reaction conditions open to air has led to the complete oxidation of U(IV) to U(VI), resulting in U(VI) containing oxide structures.[5–12] One thus speculates if the presence of fluorine in these perovskite oxyfluorides can play a role in stabilizing the 5+ oxidation state of uranium.

The three reported U(V) containing structures, $Rb_4NaU_3O_{12-x}F_x$ (**10.1**), $K_4NaU_3O_{12-x}F_x$ (**10.2**), and $Rb_{2.1}K_{1.9}KU_3O_{12-x}F_x$ (**10.3**) adopt a cubic quadruple perovskite structure of the type $A_4BB'_3O_{12}$. In general, the highly adaptable $ABO_3$ perovskite structure consists of corner sharing $BO_6$ octahedra that create a central cavity in which the large A cation is located in a 12-fold coordination environment.[13] The perovskite structure readily accommodates a wide range of elements, including mixed site occupancies, and almost any property can be found for some perovskite composition, including a broad range of magnetic behaviors, such as ferro- and antiferromagnetism as well as, sometimes, superconductivity.

The perovskite family is versatile and contains numerous structural variants beyond the simple $ABO_3$ composition and even beyond the more complex quadruple perovskite structure $A_4BB'_3O_{12}$ mentioned above. [14] Specifically, the $ABO_3$ perovskite can be

expanded into a double perovskite, where a third site is introduced, either as an A' or B' site, $A_2BB'O_6$, and this double perovskite structure, like the $ABO_3$ structure, can exhibit numerous structural distortions depending on the sizes of the A and B cations. More complex hexagonal/trigonal structures, such as the triple perovskite $A_3BB'_2O_9$[15] and quadruple perovskite $A_4BB'_3O_{12}$,[16] as well as an extensive family of 2H-perovskite related structures, $A_{3n+3m}A'_nB_{3m+n}O_{9m+6n}$ are all known for a wide variety of compositions and exhibit unique structural variations.[17]

The simple $A_2BB'O_6$ double perovskite's B and B' (or A and A') sites can be ordered in three distinct ways, rock-salt ($Ba_2LnUO_6$),[18] columnar ($NdSrMn^{3+}Mn^{4+}O_6$), or layered ($La_2CuSnO_6$).[19] If the ratio of B to B' is not 1:1 as in the example of the double perovskite, but rather 3:1, the perovskite family can be extended into either trigonal/hexagonal or cubic quadruple perovskites with the general formula $A_4BB'_3O_{12}$; the latter case being observed in the family of cubic structures reported in this paper. As one may imagine the cubic quadruple perovskite structure can also display ordering schemes similar to the double perovskite, although there are more possibilities and they are not as simple to describe as in the case of the double perovskites, and thus are beyond the scope of this paper.[20–22]

In addition to perovskites being a rewarding structural family to investigate for magnetic properties, modeling the magnetism arising from the unpaired electron in U(V)-containing perovskite structures is simplified in standard theoretical treatments due to the absence of 5f-5f electron repulsion effects that are of the same magnitude as spin-orbit coupling energies. Although studies on magnetic properties of U(V) oxides are few due to the small number of reported U(V) containing materials, there are in fact a small number

reported for U(V) perovskites, namely the simple ternary $AUO_3$ (A = Na, K, Rb) family, and complex rare earth uranium oxides, e.g., $Ba_2LnUO_6$ (Ln = La, Nd, Sm).[3, 4, 18, 23–27] $KU^VO_3$ and $RbU^VO_3$ crystallize in the cubic perovskite structure while $NaU^VO_3$ crystallizes in a distorted orthorhombic structure type due to the smaller size of the sodium ion. In contrast, $Ba_2LnUO_6$ crystallizes in the double perovskite structure with rock salt type ordering of the Ln and U containing octahedra. The three compositions reported herein should be considered cubic quadruple perovskites with complex ordering of the Na (or K) and U containing octahedra, and partial substitution of oxygen by fluorine. Herein the synthesis, crystal structure and physical property measurements for these three compositions are presented.

**Experimental:**

**Synthesis.** $UF_4$ (International Bio-Analytical Industries, powder, ACS grade), $AlPO_4$ (Alfa Aesar, powder, 99.99%), RbF (Strem Chemicals, powder, 99.8%), KF (Alfa Aesar, 99%), and NaF (Alfa Aesar, powder, 99%) were used as received. ***Caution!*** *Although the uranium precursor used contained depleted uranium, standard safety measures for handling radioactive substances must be followed.*

The title compounds were synthesized by molten flux methods using a mixed alkali fluoride flux. For each reaction, 0.5 mmol $UF_4$, 0.2 mmol $AlPO_4$, and a 20 mmol mixture of RbF/NaF (0.65/0.35), RbF/KF (0.6/0.4), or KF/NaF (0.6/0.4) were loaded into platinum crucibles covered with lids and heated to 875 °C in 1.5 h, held for 12 h, and cooled to 600 °C at 6 °C/h. The bright red cubic crystals (Figure 10.1) were obtained in good yield (>80% based on uranium) and were separated from the flux by sonicating in water to dissolve the salt and isolated by vacuum filtration. Crystals were hand-picked to separate them from a

small amount of an unidentified, poorly crystalline colorless product to obtain a phase pure sample.

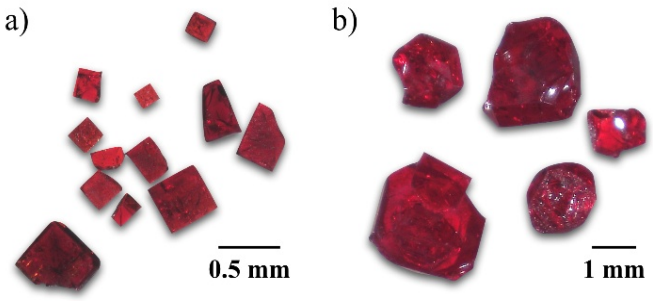


**Figure 10.1:** Single of crystals of a) 10.2 and b) 10.1.

Powder diffraction data were collected on a Bruker D2 Phaser equipped with an LYNXEYE silicon strip detector and a Cu K$\alpha$ source to confirm the phase purity of the ground crystalline samples. EDS was used to verify the elemental compositions of the title compounds both on single crystals used for structure solution and bulk powders. EDS data were collected on a TESCAN Vega-3 SBU equipped with an EDS detector.

**X-ray Absorption Near Edge Spectroscopy (XANES).** XANES data were collected on the title samples $Rb_4NaU_3O_{12-x}F_x$ (**10.1**), $K_4NaU_3O_{12-x}F_x$ (**10.2**), and $Rb_{2.1}K_{1.9}KU_3O_{12-x}F_x$ (**10.3**) in addition to $NaU^{V}O_3$, $U^{IV}O_2$, and $Sr_3U^{VI}O_6$, which were used as standards for the various uranium oxidation states. Samples for measurement were ~4 mg thin powder compacts in a double containment cell, with Kapton tape serving as the primary containment with a polymer bag as a second enclosure. The measurements were made at Beamline 10BM A, B at the Advanced Photon Source (APS) at Argonne National Laboratory in transmission mode near the uranium $L_3$-edge (17.1663 keV) with a yttrium foil K-edge (17.0384 keV) filter and a beam spot size of 2000 μm. Nine scans were

collected for each sample, with the data sets averaged and normalized using ATHENA software.[28]

**X-ray photoelectron spectroscopy** (**XPS**). X-ray photoelectron spectroscopy measurements were performed on powdered samples using a Kratos AXIS Ultra DLD XPS system with a hemispherical energy analyzer and a monochromatic Al Kα source operated at 15 keV and 150 W. The X-rays were incident at an angle of 45° with respect to the surface normal. Analysis was performed at a pressure below $1x10^{-9}$ mbar. High resolution core level spectra were measured with a pass energy of 40 eV. The XPS experiments were performed while using an electron gun directed on the sample for charge neutralization. Measurements were performed on both the as-prepared sample and after ion sputtering performed by accelerating $Ar^+$ ions (4 kV, 15 mA emission) towards the surface, as utilized in XPS analysis of other U(V) perovskites.[29]

**SXRD.** The structure of each compound was determined by single-crystal X-ray diffraction (SXRD) using a Bruker D8 Quest single crystal X-ray diffractometer equipped with a Mo Kα microfocus source (λ = 0.71073 Å). The programs SAINT+ and SADABS within the APEX 3 software were used to perform the absorption correction. [30] The structure was solved using an intrinsic phasing solution method, SHELXT, and SHELXL was used to perform least-square refinements. [31, 32] Both SHELXT and SHEXL were used within the Olex 2 GUI. [33] Full sets of crystallographic values are listed in Table 10.1. Structure solutions for all three compounds were straightforward as they all crystallize in the cubic *Im-3m* space group and the asymmetric unit contains five unique sites in the analogous structures, U1, A1, A2, O1, and O2/F2 which occupy special positions and are assigned to Wyckoff sites 6b, 8c, 2a, 12d, and 12e, respectively. Note that for the

$A_4BB'_3O_{12}$ structure type, A corresponds to the A1 site, B corresponds to the A2 site, and B' corresponds to the U1 site. The A1 sites are occupied by Rb, K, and mixed Rb/K and A2 sites are occupied by Na, Na, and K in structures **10.1**, **10.2**, and **10.3** respectively. All metal sites show no deviation from full occupancy when allowed to vary in refinements, except for the A1 site in **10.3**, which refines as 1.6 when modeled as a K and 0.73 when modeled as a Rb site, therefore it is best modeled as a mixture of the two, and freely refines to 47% K and 53% Rb. Assignment of the O1 and O2 sites as 100% occupied in all structures leads to a formula of $A_4NaU_3O_{12}$ and, in the highest oxidation state of U(VI),

**Table 10.1:** Crystallographic information for structures **10.1-10.3**.

| Compound | $Rb_4NaU_3O_{12-x}F_x$ **10.1** | $K_4NaU_3O_{12-x}F_x$ **10.2** | $Rb_{2.1}K_{1.9}KU_3O_{12-x}F_x$ **10.3** |
|---|---|---|---|
| Space group | *Im-3m* | *Im-3m* | *Im-3m* |
| $a$ (Å) | 8.7472(3) | 8.6264(2) | 8.8390(3) |
| $V$ (Å$^3$) | 669.28(7) | 641.93(3) | 690.57(7) |
| Crystal size (mm$^3$) | 0.02 x 0.04 x 0.08 | 0.02 x 0.02 x 0.02 | 0.02 x 0.02 x 0.02 |
| Temperature (K) | 302.01 | 296.5 | 302.01 |
| Density (g cm$^{-3}$) | 6.366 | 5.678 | 5.777 |
| $\theta$ range (deg) | 3.294-36.265 | 3.340-36.247 | 3.259-36.219 |
| $\mu$ (mm$^{-1}$) | 50.766 | 39.157 | 43.294 |
| Collected reflections | 2831 | 2752 | 2941 |
| Unique reflections | 191 | 188 | 198 |
| $R_{int}$ | 0.0313 | 0.0258 | 0.0252 |
| $h$ | $-14 < h < 11$ | $-6 < h < 14$ | $-14 < h < 13$ |
| $k$ | $-10 < k < 14$ | $-10 < k < 10$ | $-8 < k < 14$ |
| $l$ | $-9 < l < 14$ | $-11 < l < 14$ | $-11 < l < 14$ |
| $\Delta\rho_{max}$ (e Å$^{-3}$) | 0.919 | 0.550 | 0.487 |
| $\Delta\rho_{min}$ (e Å$^{-3}$) | -0.819 | -1.067 | -0.627 |
| *GoF* | 1.092 | 1.150 | 1.146 |
| Extinction coefficient | 0.00172(10) | -- | 0.00132(9) |
| $R_1(F)$ for $F_0^2 > 2\sigma(F_0^2)$[a] | 0.0081 | 0.0086 | 0.0109 |
| $R_w(F_0^2)$[b] | 0.0231 | 0.0216 | 0.0228 |

[a] $R_1 = \Sigma||F_0| - |F_c||/\Sigma|F_0|$. [b] $wR_2 = [\Sigma w(F_0^2 - F_c^2)^2/\Sigma w(F_0^2)^2]^{1/2}$; $P = (F_0^2 + 2F_c^2)/3$; $w = 1/[\sigma^2(F_0^2) + (0.0128P)^2 + 1.0000P]$ for $Rb_4NaU_3O_{12-x}F_x$, $w = 1/[\sigma^2(F_0^2) + (0.0111P)^2 + 0.8022P]$ for $K_4NaU_3O_{12-x}F_x$, and $w = 1/[\sigma^2(F_0^2) + (0.0126P)^2]$ for $Rb_{2.1}K_{1.9}KU_3O_{12-x}F_x$.

this formula does not charge balance having one residual negative charge. The X-ray scattering factors for fluorine and oxygen are negligibly different, and X-ray diffraction data is not sufficient for determining the ratio of oxygen to fluorine on the O2 sites. Fluorine was positively identified by EDS and XPS and the O2 site was fixed to F and O occupancies of 16.7% and 83.3%, respectively. No fluorine was modeled on the uranyl oxygen O1 site, as it is unlikely fluorine would form these stronger 'yl' bonds. The set occupancies of O and F on the O2 site slightly effect the free refinement of the Rb/K A2 site in structure **10.3** and introduce an uncertainty of 3%. While we choose to report the structures in this paper as $Rb_4NaU_3O_{12-x}F_x$ ($1 \leq x \leq 4$) due to the uncertainty in the fluorine content, the crystallographic files reflect compositions of $A_5U_3O_{11}F$ as the XANES results suggest the samples are predominantly U(VI).

**Magnetic properties.** Magnetic measurements were performed using a Quantum Design MPMS 3 SQUID magnetometer. Both field cooled (fc) and zero field cooled (zfc) measurements were performed over the temperature range of 2 K to 400 K under an applied magnetic field of 0.1 T. Magnetization measurements were also collected at 2 K, 50 K, and 300K by sweeping the applied magnetic fields between -5 and 5 T. Measurements were performed on both polycrystalline powders obtained by grinding single crystal products, and on samples consisting of many single crystals. The raw data were corrected for radial offset and shape effects following the method described by Morrison and zur Loye.[34]

**Optical properties.** UV-vis diffuse reflectance measurements were made on powdered samples of all three compositions using a PerkinElmer Lambda 35 UV-vis scanning spectrophotometer equipped with an integrating sphere. The diffuse reflectance

data were internally converted to absorbance using the Kubelka-Munk equation and normalized.[35]

**Thermal properties.** Thermogravimetric analysis (TGA) was performed on $Rb_4NaU_3O_{12-x}F_x$ using an SDT Q600 (TA instruments), to determine thermal stability in atmospheres of 4% $H_2$ in Ar and air. The samples were loaded in alumina crucibles and heated to 800 °C under 4% $H_2$ and to 1000 °C in air at a rate of 10 °C/min. An additional experiment was run to further examine weight changes due to oxidation or reduction, where the sample was heated under $N_2$ to 600 °C at 10 °C/min and allowed to stabilize at this temperature for 10 minutes before switching to 4% $H_2$ for 30 mins, and then to $N_2$ for 5 mins, then to air for 30 mins, followed by $N_2$ for 5 mins, and finally back to 4% $H_2$ for 30 mins. All samples were analyzed by PXRD after TGA.

**First-principles calculations.** Density functional theory (DFT) calculations were performed using the VASP (Vienna Ab-initio Simulation Package) pseudopotential code,[36, 37] using the projector augmented waves (PAW) method[38, 39] and generalized gradient approximation (GGA) of the exchange-correlation potential in the PBE form.[40] Spin-polarized calculations were performed, with 520 eV cut-off energy for the plane waves, and $10^{-6}$ eV energy convergence criterion. A 4×4×4 **k**-point mesh and 0.005 eV/Å force convergence criterion were used for the calculations. The ground state geometries at 0 K were obtained by relaxing the cell volume and atomic positions, while keeping the cubic cell shape. Considering the correlated nature of the uranium 5-*f* electrons, the DFT+*U* method[41] was employed with $U$ = 4.0 eV and J = 0.0 eV. To model the O sites partially occupied with F atoms (12d Wycoff position), super quasi-random structures (SQS) were generated with the compositions $K_4NaU_3O_9F_3$, $Rb_2K_3U_3O_9F_3$, $Rb_4NaU_3O_9F_3$, $K_4NaU_3O_8F_4$,

$Rb_2K_3U_3O_8F_4$, and $Rb_4NaU_3O_8F_4$ using the mcsqs code provided by the Alloy Theoretic Automated Toolkit (ATAT) toolkit.[42–45] The chosen compositions are used to study the oxidation of U(V) and its effect on the magnetic properties of the compounds, providing insight into the U(V) chemistry in oxyfluorides. The generated SQS have U atoms with only one, two and three F atoms as first nearest neighbors (FNN).

**Results and Discussion:**

**Synthesis.** As observed in previously reported flux crystal growth experiments,[9, 46] the reaction vessel plays an important role in the successful formation of the target products. $Rb_4NaU_3O_{12-x}F_x$ was initially synthesized using the same reagent amounts and RbF/NaF flux described in the experimental section contained in silver tubes measuring 5.7 cm tall by 1.2 cm in diameter and welded shut on one end, and covered loosely with a silver cap. The reaction resulted in a yield greater than 80% based on uranium; however, when this reaction was repeated using the KF/NaF flux, the desired $K_4NaU_3O_{12-x}F_x$ phase was not obtained, but rather a mixture of simple potassium uranates was isolated. Performing this reaction in a platinum crucible instead of a silver tube resulted in the desired product. The reason the potassium sodium product preferentially forms in platinum crucibles, but not in silver tubes, unlike the rubidium sodium composition which forms in either, is not apparent.

The addition of $AlPO_4$, despite the fact the product contains neither Al or P, proved necessary for good yield of the product, and some cases the formation of the product. In silver tube reactions without the $AlPO_4$, the rubidium sodium composition does not form at all, and in the platinum reaction vessel the yield is decreased to less than 50% and is accompanied by an amorphous orange-yellow powder. When using the KF/NaF flux in a

platinum crucible, the $K_4NaU_3O_{12-x}F_x$ phase forms without the addition of $AlPO_4$, but the yield is also significantly lower, and the products consist of approximately half of the target product and approximately half poorly crystalline yellow plates that could not be identified. The synthesis of the Rb/K phase was only attempted in a platinum crucible using a RbF/KF flux and, in the absence of $AlPO_4$, results in only an amorphous product. However, in the presence of $AlPO_4$ it forms the desired product along with another unidentified phase that crystallizes as red-orange plates that turn yellow after sonication in water.

The synthesis of $K_4NaU_3O_{12-x}F_x$ was attempted by traditional solid state routes in reaction vessels open to air using stochiometric amounts of $UF_4$, $U_3O_8$, $KNO_3$, and $NaNO_3$; both compositions of x = 1 (all $U^{6+}$) and x = 4 (all $U^{5+}$) were attempted. Stochiometric mixtures of neither the x = 1 or x = 4 lead to a phase pure product. Regardless of the length of time or the temperature, the target phase was always accompanied by formation of $KUO_3F$ and/or $K_2U_2O_7$. It is interesting to note that solid state reactions using only $U_3O_8$, $UF_4$, or $(UO_2)(NO_3)_2•6H_2O$ resulted in predominantly $K_2U_2O_7$ formation, whereas reactions with $UF_4$ and $U_3O_8$ produced a cubic perovskite phase with lattice parameters matching the desired composition. Using an excess of NaF to avoid the competitive formation of $K_2U_2O_7$ over the target phase, $K_4NaU_3O_{12-x}F_x$, was also unsuccessful in producing phase pure $K_4NaU_3O_{12-x}F_x$. Mixed fluxes of CsF/NaF and CsF/KF were also tried in platinum crucibles in the presence of the $AlPO_4$ that had proved essential for the synthesis of the three title compounds, but the Cs containing analog could not be obtained, and instead the reaction resulted in $K_2U_2O_7$ and $Na_2U_2O_7$ as the major products.

**Structure.** Compounds $Rb_4NaU_3O_{12-x}F_x$ (**10.1**), $K_4NaU_3O_{12-x}F_x$ (**10.2**), and $Rb_{2.1}K_{1.9}KU_3O_{12-x}F_x$ (**10.3**) all adopt the cubic quadruple perovskite structure $A_4BB'_3O_{12}$,

where Rb, K, and Rb/K occupy the A site for compounds **10.1**, **10.2**, and **10.3**, respectively and Na (or K in the case of **10.3**) and U occupy the B and B' sites, respectively (Figure 10.2c). The fact that the cubic structure is observed for all three compositions can be explained by calculating the Goldschmidt tolerance factor *t*, for these compositions. Using a weighted average for the ionic radius of the B site, *t* values of 1.00, 0.974, and 0.948 are obtained for **10.1**, **10.2**, and **10.3** respectively. These *t* factors are typical for cubic perovskites and, hence, it is expected that all three compositions crystallize in a cubic rather than in a distorted structure. In order to illustrate the ordering of the B and B' cation sites in the cubic quadruple perovskite structure, a cubic perovskite, i.e., $KUO_3$ is shown in Figure 10.2a, while a cubic rocksalt ordered double perovskite, $A_2BB'O_6$ is shown in Figure 10.2b and the cubic quadruple perovskite structure of $Rb_4NaU_3O_{12-x}F_x$, is shown in Figure 10.2c. In **10.1-10.3,** each B' (Na or K) octahedron is surrounded by six uranium polyhedra, and the square uranium bipyramids corner share to form infinite chains in all three crystallographic directions. This structure is similar to other uranium perovskites such as $K_4CaU^{VI}_3O_{12}$, $K_4SrU^{VI}_3O_{12}$, $BaK_4U^{VI}_3O_{12}$, and $K_9U^{VI}_6O_{22.5}$, which are all based on the same type of B and B' site ordering, and all crystallize in the cubic space group, *Im*-3*m*.[47–49] The uranium polyhedra exhibit a uranyl coordination environment with two short axial bonds of 1.903(3), 1.904(4), and 1.856(3) Å for **10.1**, **10.2**, and **10.3**, respectively and equatorial U-O bond lengths of 2.18680(8) Å, 2.15660(5) Å, and 2.20975(8) Å, respectively. While a uranyl coordination environment for U(V) species has not been observed in the handful of U(V) perovskites that have been well characterized, $AUO_3$ (A = Na, K, Rb) and $Ba_2LnU^vO_6$ (Ln = La, Nd, Sm),[18, 23] uranyl coordination for U(V) species is often observed in other uranium extended structures. In the U(V) perovskites the U-O

bonds lengths are between 2.124 Å and 2.33 Å. In general, the observed uranyl bonds for the title compounds are long for U(VI), where 1.8 Å is average and the values of 1.9 Å fit well into the range of observed uranyl oxygen bond lengths for U(V), ~1.9-2.1 Å.[39] However, it is not unusual to observe long uranyl bonds for U(VI) species in perovskites that range from 1.737 Å to 1.966 Å and the equatorial U-O bonds range from 2.083 Å to 2.464 Å.[47, 48, 50–54] The coordination environments of the U atoms in the title compounds do not give any insight as to the oxidation state of the U species.

Bond valence sums (BVS) were determined for structures **10.1**-**10.3** using values of 2.074 and 0.554 for $r_0$ and $B$, respectively for U-O bonds and values of 1.966 and 0.37 for $r_0$ and $B$, respectively for U-F bonds.[55, 56] The bond valence sums were calculated using 11 oxygen and 1 fluorine per formula unit, to ensure that each U atom has two axial oxygens, and four equatorial anion sites that are 16.7% fluorine and 83.3% oxygen. This resulted in BVS values of 5.81, 5.99, and 5.92 for **10.1**, **10.2**, and **10.3**. The BVSs reasonably agree with the expected value of 6 for $U^{VI}$ in these structures. It is important to note, however, that the BVSs are greatly dependent on the amount O and F on the O2 site and, as the amount of F increases, the BVS approach values closer to 5, thus BVS gives no insight into the oxidation state of U without knowing the quantitative ratio of F/O. We have used the values of 1/6 F and 5/6 O since XANES suggests U(VI) is predominant in these structures.

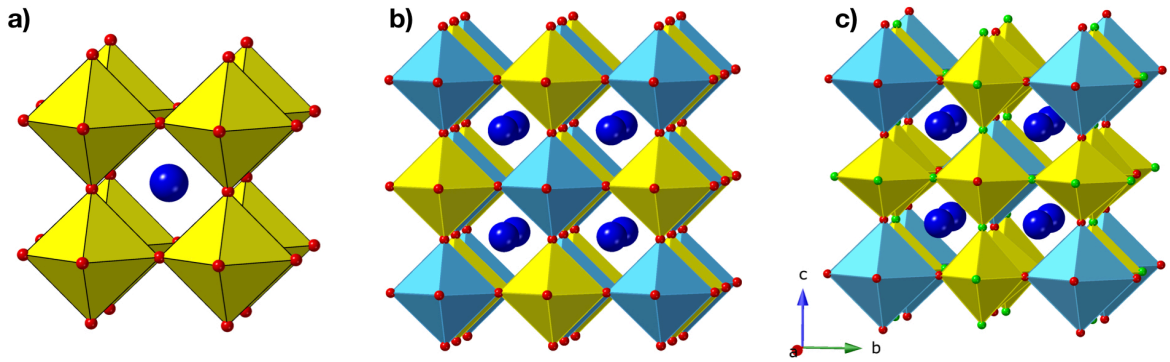


**Figure 10.2**: Structure of 10.1 and its relation to the perovskite family. a) Cubic perovskite structure of $KUO_3$ b) cubic rock-salt ordered double perovskite, $A_2BB'O_6$, and c) cubic quadruple perovskite structure of $Rb_4NaU_3O_{12-x}F_x$ (**1**) where uranium polyhedra (B') are yellow, sodium octahedra (B) are light blue, rubidium atoms (A) are dark blue, oxygen atoms are red, and the mixed oxygen/fluorine sites are in green.

**XANES.** XANES is a useful technique to determine oxidation states because as the formal oxidation state, and thus the binding energy for exciting a core photoelectron increases, the transition energy shifts to higher energy. However, due to the fact the kinetic energy of the photoelectron is small in the XANES region, it is very sensitive to the chemical environment. Ideally, standards would have U atoms in similar coordination environments—square bipyramids with shorter axial bonds and coordinate equatorially to four anions, where the anions are a mix of oxygen and fluorine. This is not possible to achieve given the limited library of known U(V) containing compounds, specifically in the $UO_2^+$ environment as U(V) is not ubiquitously found in the uranyl coordination, unlike U(VI), and the additional requirement of containing U-F bonds cannot be satisfied. $NaUO_3$ and $Sr_3UO_6$ standards were used for U(V) and U(VI), respectively, where U in these perovskite type structures adopts an octahedral coordination environment with bond distances of 2.142-2.151 Å and 2.061-2.098 Å, for $NaUO_3$ and $Sr_3UO_6$, respectively. Additionally, $UO_2$ was used as a U(VI) reference. The energies of the $L_3$ edge for all

samples lie in the narrow region of 17173-17181 eV, where the standards progressively shift upfield as the U oxidation state increases (Figure 10.3b). The edge energies for compounds **10.1**-**10.3** lie between the reference samples $NaUO_3$ and $Sr_3UO_6$ where **10.1** and **10.2** are more upfield than **10.3** which features a different peak shape, perhaps due to the shorter axial bonds in **10.3** (1.856 Å) as compared to **10.1** and **10.2** (1.903 Å). For all three structures, the XANES results suggest the presence of both U(V) and U(VI), although the ratio of U(V)/U(VI) remains undetermined, due to the lack of proper U oxyfluoride reference materials. Few studies have been published on the effect of F substitution in uranium oxides on the shift in XANES edge transition energy; however, the work by Allen et al. shows that structures contain F have slightly lower transition energies than pure U(VI) oxides.[57–59] This could suggest that the F containing perovskites in this study contain more U(VI) than suggested by the comparison of the samples to the $NaUO_3$ and $Sr_3UO_6$ standards.

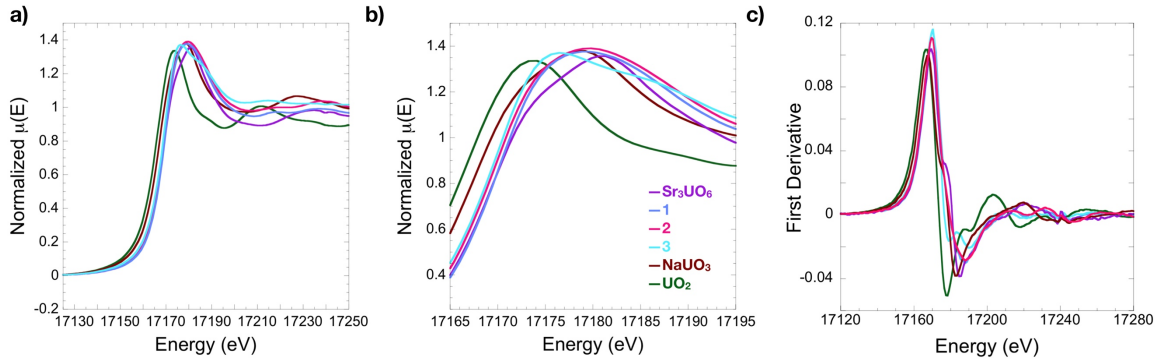


**Figure 10.3:** XANES spectra of 10.1-10.3. a) Normalized XANES spectra b) closer view of peaks in normalized XANES spectra and c) derivative normalized XANES spectra of $Rb_4NaU_3O_{12-x}F_x$ (**1**), $K_4NaU_3O_{12-x}F_x$ (**2**), and $Rb_{2.1}K_{1.9}KU_3O_{12-x}F_x$ (**3**) compared to reference samples of $UO_2$, $NaUO_3$, and $Sr_3UO_6$. The legend in b) applies to all three plots.

**XPS.** X-ray photoelectron spectroscopy measurements were performed on the as-prepared samples. Figure 10.4 shows the U 4f peaks of the corresponding materials after peak deconvolution, which indicated the presence of two U oxidation states. The presence of U(V) in the XPS spectra, indicates that after synthesis, at least part of the U in the material is in the U(V) oxidation state and in all cases U(V) was measured to be ~10% of the total amount of U (Table 10.2). Taking into account that the XPS analysis depth is ~10nm and that ambient oxidation towards U(VI) takes place at the outermost atomic layers, the U(V) content in the bulk of the materials can be higher than the 10% measured by XPS on the surface of the sample. The quantification of the XPS spectra (Table 10.3), confirmed the presence of fluorine in the structure, although the presence of adventitious carbon changed the expected surface atomic ratio.

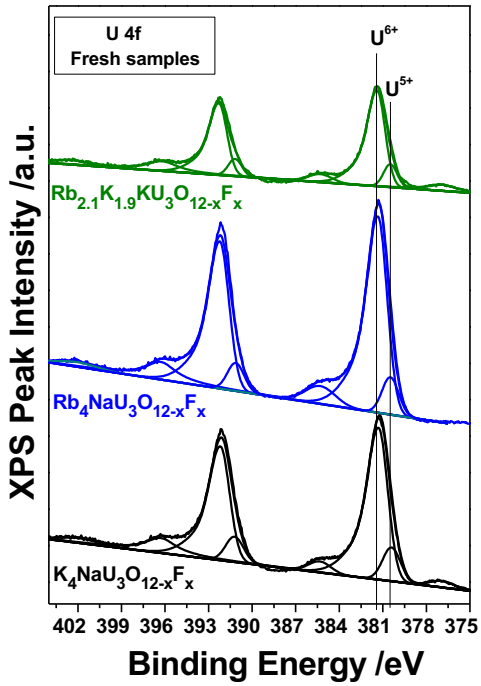


**Figure 10.4:** XPS spectra of 10.1-10.3 measured after synthesis with no further treatment.

**Table 10.2:** The % ratio of U oxidation states recorded by XPS for 10.1-10.

| Compound | $K_4NaU_3O_{12-x}F_x$ | $Rb_4NaU_3O_{12-x}F_x$ | $Rb_{2.1}K_{1.9}KU_3O_{12-x}F_x$ |
|---|---|---|---|
| $U^{6+}$ (%) | 88.5 | 90.6 | 89.1 |
| $U^{5+}$ (%) | 11.5 | 9.4 | 10.9 |

**Table 10.3:** Surface atomic ratios determined by XPS before and after sputtering

| **$K_4NaU_3O_{12-x}F_x$** | Fresh | | | | | | Sputtering | | | | | |
|---|---|---|---|---|---|---|---|---|---|---|---|---|
| | C | K | U | O | F | Na | C | K | U | O | F | Na |
| Mass Conc. % | 28.4 | 11.0 | 35.4 | 22.3 | 1.7 | 1.2 | 30.3 | 10.1 | 36.1 | 20.3 | 1.9 | 1.3 |
| Atomic Conc. % | 54.6 | 6.5 | 3.4 | 32.2 | 2.1 | 1.2 | 57.9 | 5.9 | 3.5 | 29.1 | 2.3 | 1.3 |
| **$Rb_4NaU_3O_{12-x}F_x$** | Fresh | | | | | | Sputtering | | | | | |
| | Rb | C | U | O | F | Na | Rb | C | U | O | F | Na |
| Mass Conc. % | 25.1 | 17.2 | 35.0 | 19.6 | 1.9 | 1.2 | 23.2 | 16.4 | 38.8 | 18.0 | 2.3 | 1.3 |
| Atomic Conc. % | 9.1 | 44.0 | 4.6 | 37.7 | 3.0 | 1.6 | 8.8 | 44.0 | 5.3 | 36.2 | 3.9 | 1.8 |
| **$Rb_2K_2KU_3O_{12-x}F_x$** | Fresh | | | | | | Sputtering | | | | | |
| | Rb | C | K | U | O | F | Rb | C | K | U | O | F |
| Mass Conc. % | 10.6 | 38.5 | 8.2 | 20.8 | 20.9 | 1.0 | 11.1 | 40.7 | 6.6 | 24.3 | 16.1 | 1.2 |
| Atomic Conc. % | 2.5 | 64.3 | 4.2 | 1.8 | 26.2 | 1.0 | 2.7 | 69.7 | 3.5 | 2.1 | 20.7 | 1.3 |

XPS studies on the U(V) perovskites, $NaUO_3$ and $KUO_3$, demonstrated that the satellite 4f peaks of U(V) could not be observed on as-prepared samples of $NaUO_3$ and $KUO_3$ due to surface oxidation; however, short Ar sputtering times (20-30 sec) could remove the top most layer to reveal these satellite peaks which are considered "fingerprints" of a single U(V) chemical state.[4, 29] The etching time was critical, as too short a time did not completely remove the surface oxidation, while sputtering times of upwards of 60 sec reduced U(V) to U(IV). This study is highly relevant to the XPS study on U(V) containing perovskites, as similar methods were used with 30 sec of in-situ $Ar^+$ sputtering to remove contamination on the topmost atomic layer on the sample, including oxidation of the uranium, due to the exposure of the sample to the atmosphere. After sputtering, the four peak sequence named 1, 1', 2, 2' characteristic of a single U(V) chemical state was observed and is shown in Figure 10.5. The fact that the XANES data,

which is a method that measures the response of the bulk sample, supports a predominantly U(VI) state, while the XPS after Ar sputtering suggest an entirely U(V) state could suggest that even the short 30 sec sputtering time was sufficient to reduce the U(VI) in the samples. Nevertheless, the presence of U(V) in the XPS spectra prior to sputtering confirm that a fraction of the U in the title materials is in the U(V) state. Further XPS experiments are needed on a variety of U(VI), U(V)/U(VI), and U(V) samples whose oxidation states can be confirmed be complimentary methods in order to explore the effects of Ar sputtering on the oxidation state of uranium.

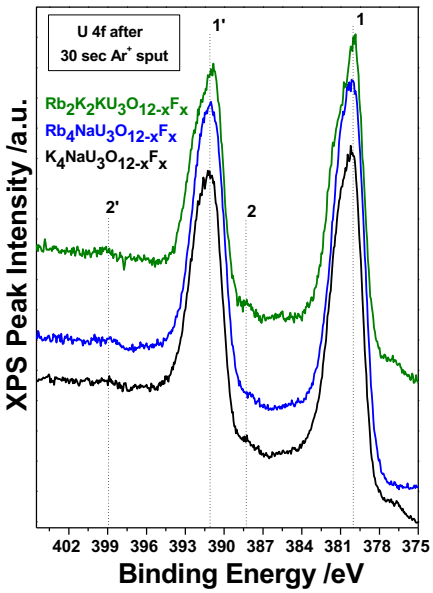


**Figure 10.5:** XPS spectra of **10.1-10.3** after 30 seconds of Ar sputtering.

**Magnetic properties.** Uranium V magnetism is not well understood despite the fact that it has only a single 5f electron, eliminating electronic 5f-5f repulsion interactions and simplifying experimental analysis. Many studies on U(V) structures yield moments much lower than the calculated 2.54 $\mu_B$ and often the experimental magnetism does not

follow the Curie-Weiss law even at high temperatures, making the calculation of the moment more difficult.[18, 23, 27] The simple alkali perovskites, $KUO_3$ and $RbUO_3$, have been the subject of several magnetic studies reporting low moments of 0.2-0.66 $\mu_B$ determined using a modified Curie-Weiss law with a temperature independent susceptibility term.[23, 25–27, 60] Similarly, the magnetism of $Ba_2LnU^{V}O_6$ (Ln = La, Nd, Sm) , which adopts a double perovskite structure, although monoclinically distorted, was reported to have a moment of 0.4 $\mu_B$ for the La composition, where a temperature independent susceptibility term was necessary to fit the data.[18] Besides the difference in cubic versus monoclinic symmetry in the $KUO_3$ and $Ba_2LaU^{V}O_6$ structures, the ordering of the uranium polyhedra is important to consider. In the cubic perovskite, $KUO_3$, U fully occupies the B site and therefore there are U-O-U linkages; however, in the double perovskite structure of $Ba_2LaU^{V}O_6$, the La and U sites order in a rock-salt fashion and all uranium polyhedra are isolated from each other. The magnetic data for both of these compositions represent an important comparison for title compounds, in which the uranium polyhedra form infinite chains; however, the ordered Na polyhedra set this structure apart from the simpler $KUO_3$ structure. Magnetic data for all three title compounds were collected on both powdered and single crystalline samples from 2 to 400 K in an applied field of 0.1 T and were found to exhibit low moments and non-Curie Weiss behavior even at high temperatures; however, the measurements of the magnitude of the moments was not repeatable on multiple samples of the same composition, and therefore a reliable moment for the $U^{5+}$ ions could not be determined. Similar measurements performed on $NaUO_3$ found that the raw moment of the title compounds is an order of magnitude smaller than $NaUO_3$, which agrees well with the ~10% U(V) estimated by XPS experiments. Differences between powder and single crystal

samples were investigated for potential effects of surface oxidation; however, even measurements on separate single crystal samples produced magnetic moments of differing magnitudes. The inconsistency among multiple data sets for the same composition could not be attributed to impurities, as none were detected by powder diffraction (Figure 10.6), and may be attributed to inconsistent amounts of U(V) in the perovskite samples, as none of the methods used have been able to conclusively quantify the amount of U(VI) and U(V) in the title compounds. However, the presence of a small magnetic moment and non-Curie Weiss behavior is consistent with the presence of U(V) in the title compounds, especially, when compared to the reported magnetic data of $KUO_3$, $RbUO_3$, and $Ba_2LnU^{V}O_6$ (Ln = La, Nd, Sm). The magnetic susceptibility for $K_4NaU_3O_{12-x}F_x$ is shown in Figure 10.7.

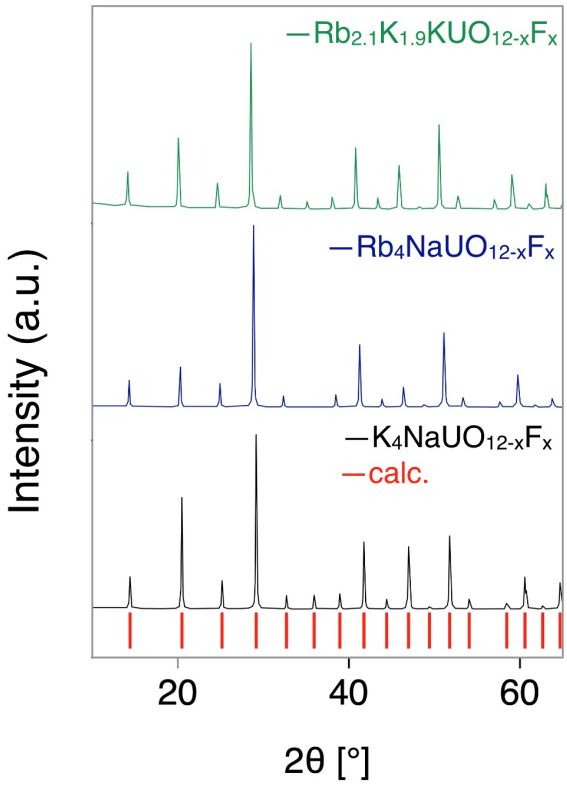


**Figure 10.6:** PXRD of **10.1-10.3.**

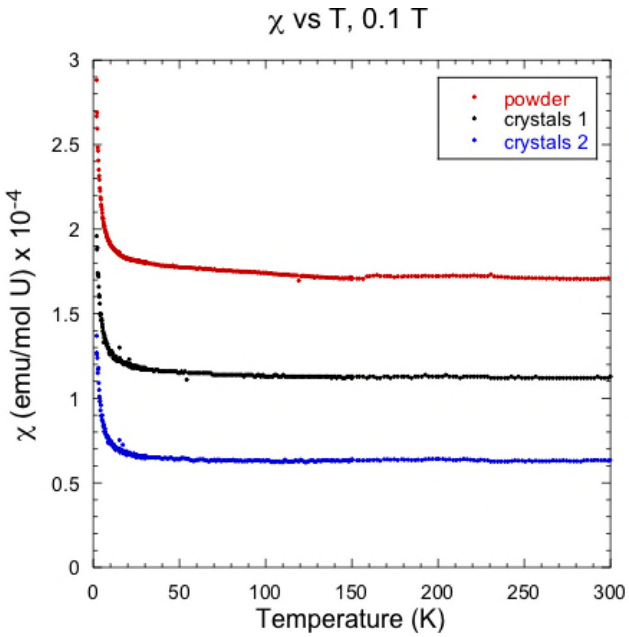


**Figure 10.7:** χ vs T plot of three different samples of **10.2.**

**First-Principles Calculations.** To better understand the influence of U-f interactions on magnetic behavior of the title compounds, their density of states (DOS) were calculated, see Figure 10.8. From the DOS it is evident that the states at the top of the valence band and bottom of the conduction band come from the U atoms, indicating that these compounds are Mott insulators, just like $UO_2$. In the DFT calculations, the super quasi-random structures (SQSs) relaxed to states with 0 $\mu_B$ net magnetic moment, which agrees with the experimentally observed paramagnetic state of the title compounds. The DFT calculated band gaps of the $Rb_2K_2KU_3O_9F_3$, $Rb_4NaKU_3O_9F_3$ and $K_4NaU_3O_9F_3$ compounds are 2.866, 2.225 and 2.773 eV, respectively. Beside the apparent larger band gaps, the calculated and experimentally observed adsorption indexes show a similar shape with two distinct peaks, a large peak at lower energies and a smaller peak at higher energies.

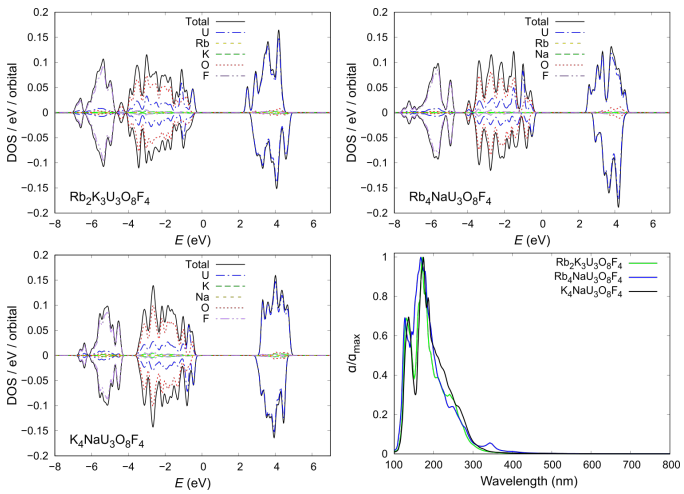


**Figure 10.8:** Density of states (DOS) of 10.1-10.3.

To better understand the low magnetic moments observed in the SQUID data and the possible effects of surface oxidation on bulk magnetic measurements, the magnetic moments of the U atoms were estimated in the $A_5U_3O_8F_4$ and $A_5U_3O_9F_3$ SQSs. They were estimated by integrating the spin-up and spin-down DOS up to the Fermi level. In the $A_5U_3O_8F_4$ SQSs all U atoms have $|1|\ \mu_B$ magnetic moment indicating that the U atoms have 1 unpaired electron, and hence are in the +5 oxidation states. However, two U atoms have -1 $\mu_B$ magnetic moment, while the other four U atoms have +1 $\mu_B$ magnetic moment, giving rise to a total of +2 $\mu_B$ of the SQSs of $A_5U_3O_8F_4$. On the other hand, the calculations show that the average oxidation state of the U atoms in the $A_5U_3O_9F_3$ SQSs is 5.33, where two of the U atoms do not have a magnetic moment, indicating that these U atoms are in the +6 oxidation state. The other four U atoms have +1 $\mu_B$ and -1 $\mu_B$ magnetic moment, implying that these U atoms have 1 unpaired electron and, hence, are in the +5 oxidation state. The magnetic moment of these four U atoms cancel each other to give the 0 $\mu_B$ net magnetic moment of the SQSs. A closer look at the F atom coordination around the U atoms showed that U atoms with one, two and three F atoms FNN have 0, +1 and -1 $\mu_B$ magnetic moments,

respectively. This is illustrated in Figure 10.7, where the DOS of U with 1 F atom as a FNN are almost equal, while the spin-up and spin-down DOS are more dominant for the U with 2 and 3 F atoms as FNNs, respectively. While with the SQSs only a small portion is sampled of an otherwise complex structure of the title compounds, the results reinforce the fact that the random distribution of F atoms in the studied composition can yield a paramagnetic phase. Furthermore, the random distribution of the F atoms provides another reason for the varying paramagnetic SQUID data, although without experimental means of obtaining quantitative U(V)/U(VI) ratios it is impossible to identify the causes of the inconsistencies in the SQUID data.

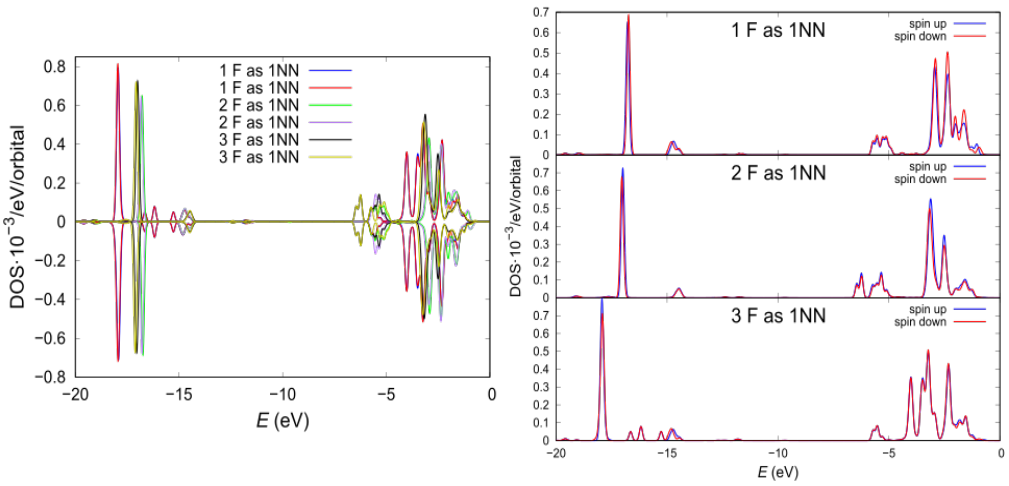


**Figure 10.9:** Effect of F atoms as FNN in projected density of states (pDOS). Left: The pDOS of the two U atoms in $Rb_2K_2KU_3O_9F_3$ with 1, 2 and 3 F atoms as first nearest neighbor (FNN). Right: Comparison between the spin-up and spin-down pDOS of the U atoms with 1, 2 and 3 F atoms as FNN.

**Thermal properties.** Thermogravimetric analysis revealed that under a reducing atmosphere, $Rb_4NaU_3O_{12-x}F_x$ decomposes to $RbUO_3$ at 708 °C while it remains stable up to 1000 °C in air. Switching between these two atmospheres at a constant temperature of 600 °C results in mass changes of less than 0.3 wt % and cannot be attributed to either the

complete oxidation of $U^{5+}$ to $U^{6+}$ or the complete reduction of $U^{6+}$ to $U^{5+}$ or $U^{5+}$ to $U^{4+}$, as the weight change due to these processes is expected to be 1.9 wt %. Because XANES and XPS suggest predominantly $U^{6+}$ with small amounts of $U^{5+}$ and XPS showed that Ar sputtering easily reduces the $U^{6+}$ in these samples to entirely $U^{5+}$, it would be reasonable to expect that under these conditions that the sample would show a larger weight change due to the reduction of $U^{6+}$ to $U^{5+}$.

**Optical properties.** UV-vis diffuse reflectance data of the three title compounds display two broad bands centered at 430 nm and 540 nm (Figure 10.10). Reported U(VI) diffuse reflectance spectra[5–8, 61–63] contain two broad bands centered around ~350 nm and ~450 nm where the first feature arises from the equatorial ligand to metal charge transfer, and the second feature arises from the vibronically coupled transitions of the $UO_2^{2+}$ core.[3, 64] There are fewer examples of U(V) diffuse reflectance spectra in extended structures;[3, 4, 64] however, in those that are reported the U(V) charge transfer band is centered around 550 nm, as compared to a U(VI) charge transfer band of ~350 nm. By comparison, the spectra for **1-3** with bands centered at 430 nm and 540 nm are unusual for U(VI) species and could support the presence of U(V).

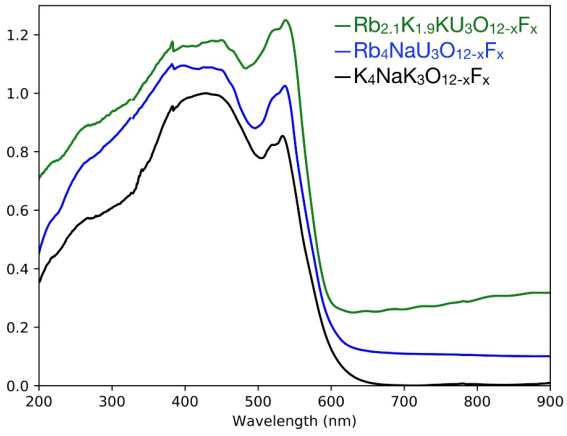


**Figure 10.10:** UV-vis spectra of **10.1-10.1.1**

**Conclusions.** A series of U(V) containing oxyfluorides crystallizing in the perovskite structure, $Rb_4NaU_3O_{12-x}F_x$ (**10.1**), $K_4NaU_3O_{12-x}F_x$ (**10.2**), and $Rb_{2.1}K_{1.9}KU_3O_{12-x}F_x$ (**10.3**) were characterized by SXRD, PXRD, EDS, XANES, XPS, magnetic measurements, DFT calculations, TGA, and UV-vis diffuse reflectance spectroscopy. The structural characterization reveals square uranyl bipyramidal coordination environments. EDS and XPS both confirm the presence of fluorine, although neither provides a quantitative assessment of the fluorine content within the structure and there are no satisfactory methods to experimentally determine the F/O ratio or to investigate the F/O ordering. XANES data suggest the compounds are predominantly U(VI), while XPS, UV-vis, and magnetic data suggest small amounts of U(V) are present in the structure, although none of these methods have led to the quantification of the amounts of U(V) or U(VI). XPS estimates about 10% of U(V); however, the tendency for surface oxidation in U(V) species could lead to an underestimation of the content. PXRD confirms the phase purity of all samples. Magnetic measurements on multiple samples of all three compounds, powder and single crystalline, produced inconsistent small magnetic moments, but consistently showed non-Curie Weiss behavior, the presence of which supports the detection of small amounts of U(V) in all three materials. The DFT calculations reveal the importance of the F/O ordering in the $A_5U_3O_9F_3$ perovskite structure, where one, two, or three fluorine FNNs lead to magnetic moments of 0, 1, and -1 μB for the U atom in question, and thus the F/O ordering will have significant and possibly inconsistent effects (if there is only local rather than global ordering) on the average magnetic moment of the bulk material. The absence of the U(VI) charge transfer band at 350 nm in the UV-vis spectroscopy, and the appearance of bands centered on 430 nm and 540 nm is unusual for U(VI) species and can

support the presence of U(V). The difficulty of quantifying the amounts of U(VI) and U(V) in this structure illustrate the need for the development of new methods to do so, but also the need to further characterize U(V) and U(V)/U(VI) structures for comparison. The knowledge and understanding of U(V) containing structures in aspects of the synthesis, structural, magnetic, and optical characterization will continue to develop as new structures are synthesized and thoroughly characterized; a process in which this family of U(V) perovskites aids and enhances our understanding.

**Acknowledgements.** Research was conducted by the Center for Hierarchical Wasteform Materials (CHWM), an Energy Frontier Research Center (EFRC). Research was supported by the U.S. Department of Energy, Office of Basic Energy Sciences, Division of Materials Sciences and Engineering under Award DE-SC0016574. C. Juillerat is additionally supported by an NSF IGERT Graduate Fellowship under grant number 1250052. V. Kocevski and T. Besmann acknowledge the use computational resources provided by the National Energy Research Scientific Computing Center (NERSC) and the HPC cluster Hyperion, supported by The Division of Information Technology at University of South Carolina. XANES data collected on Beamline 10-BM-B at the Advanced Light Source, a U.S. Department of Energy (DOE) Office of Science User Facility operated for the DOE Office of Science by Argonne National Laboratory under Contract No. DE-AC02-06CH11357, and is directed by MRCAT and supported by the Department of Energy and the MRCAT member institutions.

**References:**


(1) zur Loye, H.-C.; Besmann, T.; Amoroso, J.; Brinkman, K.; Grandjean, A.; Henager, C. H.; Hu, S.; Misture, S. T.; Phillpot, S.; Shustova, N. B.; Wang, H.; Koch, R. J.; Gregory Morrison; Dolgopolova, E., Hierarchical Materials as Tailored Nuclear Waste Forms: A Perspective, *Chem. Mater.* **2018**, *30*, 4475-4488.

(2) Juillerat, C. A.; Klepov, V. V.; Morrison, G.; Pace, K. A.; zur Loye, H.-C., Flux Crystal Growth: A Versatile Technique to Reveal the Crystal Chemistry of Complex Uranium Oxides, *Dalton Trans.* **2019**, *48*, 3162-3181.

(3) Pace, K. A., Klepov, V. V., Morrison, G., zur Loye, H.-C., "Moderate Supercritical Synthesis as a Facile Route to Mixed-Valent Uranium (IV/V) and (V/VI) Silicates", *Chem. Commun.*, **2018**, *54*, 13794-13797.

(4) Pace, K. A.; Kocevski, V.; Karakalos, S. G.; Morrison, G.; Besmann, T.; zur Loye, H.-C., $Na_2(UO_2)(BO_3)$: An All-Uranium(V) Borate Synthesized under Mild Hydrothermal Conditions, *Inorg. Chem.* **2018**, *57*, 4244-4247.

(5) Juillerat, C. A.; Moore, E. E.; Besmann, T. B.; zur Loye, H.-C., Observation of an Unusual Uranyl Cation-Cation Interaction in the Strongly Fluorescent Layered Uranyl Phosphates $Rb_6[(UO_2)_7O_4(PO_4)_4]$ and $Cs_6[(UO_2)_7O_4(PO_4)_4]$, *Inorg. Chem.* **2018**, *57*, 3675-3678.

(6) Juillerat, C. A.; Moore, E. E.; Morrison, G.; Smith, M. D.; Besmann, T. M.; zur Loye, H.-C., Versatile Uranyl Germanate Framework Hosting Twelve Different Alkali Halide 1D Salt Inclusions, *Inorg. Chem.* **2018**, *57*, 11606-11615.

(7) Juillerat, C. A.; Klepov, V. V.; Alekseev, E. V.; zur Loye, H.-C., Overstepping Löwenstein's Rule – a Route to Unique Aluminophosphate Frameworks with 3D Salt-Inclusion and Ion Exchange Properties, *Inorg. Chem.* **2019**, *58*, 724-736.

(8) Juillerat, C. A.; Moore, E. E.; Kocevski, V.; Besmann, T. M.; zur Loye, H.-C., A Family of Layered Phosphates Crystallizing in a Rare Geometrical Isomer of the Phosphuranylite Topology: Synthesis, Characterization, and Computational Modeling of $A_4[(UO_2)_3O_2(PO_4)_2]$ (A = alkali metals) Exhibiting Intra-layer Ion Exchange, *Inorg. Chem.* **2018**, *57*, 4726-4738.

(9) Juillerat, C. A.; zur Loye, H.-C., Crystal Growth and Structure Characterization of Three Layered Uranyl Phosphates and Their Relation to the Phosphuranylite Family, *Cryst. Growth Des.* **2019**, *19*, 1183-1189.

(10) Kocevski, V.; Juillerat, C. A.; Moore, E. E.; zur Loye, H.-C.; Besmann, T., Understanding the polymorphism of $A_4[(UO_2)_3(PO_4)_2O_3]$ (A=alkali metals) uranyl phosphate framework structures, *Cryst. Growth Des.* **2019**, *19*, 966-975.

(11) Morrison, G.; Smith, M. D.; zur Loye, H.-C., Understanding the Formation of Salt-Inclusion Phases: An Enhanced Flux Growth Method for the Targeted Synthesis of Salt-Inclusion Cesium Halide Uranyl Silicates, *J. Am. Chem. Soc.* **2016**, *138*, 7121-7129.

(12) Morrison, G.; Smith, M. D.; zur Loye, H.-C., Flux versus Hydrothermal Growth: Polymorphism of $A_2(UO_2)Si_2O_6$ (A = Rb, Cs), *Inorg. Chem.* **2017**, *56*, 1053-1056.

(13) Giaquinta, D. M.; zur Loye, H.-C., Structural predictions in the $ABO_3$ phase diagram, *Chem. Mater.* **1994**, *6*, 365-372.

(14) Stitzer, K. E., Darriet, J., zur Loye, H.-C., "Advances in the Synthesis and Structure Description of 2H-Hexagonal Perovskite Related Oxides", DOI:10.1016/S1359-0286(01)00032-8. *Curr. Opin. Solid State Mater. Sci.*, **2001**, *5*, 535-544.

(15) Stitzer, K.; Smith, M. D.; Gemmill, W. R.; zur Loye, H.-C., Novel mixed-valent (V/VI) triple perovskite ruthenates: Observation of a complex low-temperature structural and magnetic transition, *J. Am. Chem. Soc.* **2002**, *124*, 13877-13885.

(16) Ferreira, T.; Heald, S. M.; Smith, M. D.; zur Loye, H.-C., Unusual Coexistence of Nickel(II) and Nickel(IV) in the Quadruple Perovskite $Ba_4Ni_2Ir_2O_{12}$ Containing $Ir_2NiO_{12}$ Mixed-Metal-Cation Trimers, *Inorg. Chem.* **2018**, *57*, 2973-2976.

(17) zur Loye, H.-C.; Zhao, Q.; Bugaris, D. E.; Chance, W. M., 2 H-perovskite related oxides: Synthesis, structures, and predictions, *CrystEngComm* **2012**, *14*, 23-39.

(18) Phatak, R.; Yadav, A. K.; Pathak, N.; Prajapat, C. L.; Kasar, U. M.; Singh, M. R.; Jha, S. N.; Bhattacharyya, D.; Das, A.; Sali, S. K., Pentavalent uranium complex oxides: A case study on double perovskites $Ba_2REU^{5+}O_6$ (RE = La, Nd, Sm), *J. Alloys Compd.* **2017**, *708*, 1168-1177.

(19) King, G.; Woodward, P. M., Cation ordering in perovskites, *J. Mater. Chem.* **2010**, *20*, 5785.

(20) Belik, A. A.; Khalyavin, D. D.; Zhang, L.; Matsushita, Y.; Katsuya, Y.; Tanaka, M.; Johnson, R. D.; Yamaura, K., Intrinsic Triple Order in A-site Columnar-Ordered Quadruple Perovskites: Proof of Concept, *ChemPhysChem* **2018**, *19*, 2449-2452.

(21) Belik, A. A.; Matsushita, Y.; Kumagai, Y.; Katsuya, Y.; Tanaka, M.; Stefanovich, S. Y.; Lazoryak, B. I.; Oba, F.; Yamaura, K., Complex Structural Behavior of $BiMn_7O_{12}$ Quadruple Perovskite, *Inorg. Chem.* **2017**, *56*, 12272-12281.

(22) Yin, Y. Y.; Liu, M.; Dai, J. H.; Wang, X.; Zhou, L.; Cao, H.; dela Cruz, C.; Chen, C. T.; Xu, Y.; Shen, X.; Yu, R.; Alonso, J. A.; Muñoz, A.; Yang, Y. F.; Jin, C.; Hu, Z.; Long, Y., $LaMn_3Ni_2Mn_2O_{12}$: An A- and B-Site Ordered Quadruple Perovskite with A-Site Tuning Orthogonal Spin Ordering, *Chem. Mater.* **2016**, *28*, 8988-8996.

(23) Van den Berghe, S.; Leenaers, A.; Ritter, C., Antiferromagnetism in MUO3 (M = Na, K, Rb) studied by neuron diffraction, *J. Solid State Chem.* **2004**, *177*, 2231-2236.

(24) Lin, C.; Chen, C.-S.; Shiryaev, A. A.; Zubavichus, Y. V.; Lii, K.-H., $K_3(U_3O_6)(Si_2O_7)$ and $Rb_3(U_3O_6)(Ge_2O_7)$: a pentavalent-uranium silicate and germanate, *Inorg. Chem.* **2008**, *47*, 4445-4447.

(25) König, E.; Rudowicz, C.; Desai, V. P.; Kanellakopulos, B., Low-temperature magnetism of some alkali metal uranates(V) and alkaline earth neptunates(IV). Examples for ferrimagnetism in mixed actinide oxides, *The Journal of Chemical Physics* **1983**, *78*, 5764-5771.

(26) Hinatsu, Y., Magnetic Susceptibility an Electron Paramagnetic Resonance Study of $KUO_3$ with cubic perovskite structure, *J. Solid State Chem.* **1994**, *1120*, 118-123.

(27) Hinatsu, Y.; Shimojo, Y.; Morri, Y., Magnetic and neutron diffraction studies on potassium uranate $KUO_3$, *J. Alloys Compd.* **1998**, *270*, 127-131.

(28) Ravel, B.; Newville, M., ATHENA, ARTEMIS, HEPHAESTUS: data analysis for X-ray absorption spectroscopy using IFEFFIT, *J. Synchrotron Rad.* **2005**, *12*, 537-541.

(29) Liu, J.-H.; Van den Berghe, S.; Konstantinovíc., XPS spectra of the $U^{5+}$ compounds $KUO_3$, $NaUO_3$ and $Ba_2U_2O_7$, *J. Solid State Chem.* **2009**, *182*, 1105-1108.

(30) Bruker. *APEX3, SAINT+, and SADABS.* Bruker AXS Inc.: Madison, Wisconsin, USA, 2015;

(31) Sheldrick, G. M., Crystal structure refinement with SHELXL, *Acta Cryst.* **2015**, *C71*, 3-8.

(32) Sheldrick, G. M., SHELXT - Integrated space-group and crystal-structure determination, *Acta Cryst.* **2015**, *A71*, 3-8.

(33) Dolomanov, O. V.; Bourhis, L. J.; Gildea, R. J.; Howard, J. A. K.; Pushmann, H., OLEX2: a complete structure solution, refinement and analysis program, *J. Appl. Crystallogr.* **2009**, *42*, 339-341.

(34) Morrison, G.; zur Loye, H.-C., Simple correction for the sample shape and radial offset effects on SQUID magnetometers: Magnetic measurements on $Ln_2O_3$ (Ln=Gd, Dy, Er) standards, *J. Solid State Chem.* **2015**, *221*, 334-337.

(35) Kubelka, P.; Munk, F. Z., Ein Beitrag Zur Optik Der Farbanstriche, *Z. Techn. Phys.* **1931**, *12*, 593-601.

(36) Kresse, G.; Furthmuller, J., Efficient iterative schemes for ab-initio total-energy calculations using a plane-wave basis set, *Phys. Rev. B* **1996**, *54*, 11169-11186.

(37) Kresse, G.; Furthmuller, J., Efficiency of ab-initio total energy calculations for metals and semiconductors using a plane-wave basis set, *Comput. Mater. Sci.* **1996**, *6*, 15-50.

(38) Blöchl, P. E., Projector augmented-wave method, *Phys. Rev. B* **1994**, *50*, 17953-17979.

(39) Kresse, G.; Joubert, D., From ultrasoft pseudopotentials to the projector augmented-wave method, *Phys. Rev. B* **1999**, *59*, 1758-1775.

(40) Perdew, J. P.; Burke, K.; Ernzerhof, M., Generalized Gradient Approximation Made Simple, *Phys. Rev. Lett.* **1996**, *77*, 3865-3868.

(41) Dudarev, S. L.; Botton, G. D.; Savrasov, S. Y.; Humphreys, C. J.; Sutton, A. P., Electron-energy-loss spectra and the structural stability of nickel oxide: An LSDA+U study, *Phys. Rev. B* **1998**, *57*, 1505-1509.

(42) Walle, A., Multicomponent multisublattice alloys, nonconfigurational entropy and other additions to the Alloy Theoretic Automated Toolkit, *Calphad* **2009**, *33*, 266-278.

(43) Walle, A.; Ceder, G., Automating first-principles phase diagram calculations, *J. Phase Equilib.* **2002**, *23*, 521-538.

(44) Walle, A.; ASta, M.; Ceder, G., The alloy theoretic automated toolkit: A user guide, *CALPHAD: Comput. Coupling Phase Diagrams Thermochem.* **2002**, *26*, 539-553.

(45) Walle, A.; Asta, M., Self-driven lattice-model Monte Carlo simulations of alloy thermodynamic properties and phase diagrams., *Modell. Simul. Mater. Sci. Eng* **2002**, *10*, 521-538.

(46) Morrison, G.; zur Loye, H.-C., Flux Growth of $[NaK_6F][(UO_2)_3(Si_2O_7)_2]$ and $[KK_6Cl][(UO_2)_3(Si_2O_7)_2]$: The Effect of Surface Area to Volume Ratios on Reaction Products, *Cryst. Growth Des.* **2016**, *16*, 1294-1299.

(47) Read, C. M.; Bugaris, D. E.; zur Loye, H.-C., Single crystal growth and structural characterization of four complex uranium oxides: $CaUO_4$, β-$Ca_3UO_6$, $K_4CaU_3O_{12}$, and $K_4SrU_3O_{12}$, *Solid State Sci.* **2013**, *17*, 40-45.

(48) Roof, I. P.; Smith, M. D.; zur Loye, H.-C., Crystal growth of uranium-containing complex oxides: $Ba_2Na_{0.83}U_{1.17}O_6$, $BaK_4U_3O_{12}$ and $Na_3Ca_{1.5}UO_6$, *Solid State Sci.* **2010**, *12*, 1941-1947.

(49) Saine, M. C.; Gasperin, M.; Jove, J.; Cousson, A., Relation entre la structure cristalline d'un uranate de potassium $K_9U_6O_{22.5}$ et les spectres mössbauer ($^{237}Np$) des phases apparentées de neptunium, *J. Less-Common Met.* **1987**, *132*, 141-148.

(50) Read, C. M.; Smith, M. D.; zur Loye, H.-C., Single Crystal Growth and Structural Characterization of a Novel Mixed-Valent Ternary Uranium Oxide, $K_8U_7O_{24}$, *J Chem Crystallogr* **2014**, *44*, 604-608.

(51) Chernorukov, N. G.; Knyazev, A. V.; Dashkina, Z. S., Synthesis, structures, and physicochemical properties of $Sr_2A^{II}UO_6$($A^{II}$ = Mg, Ca, Sr, Ba, Mn, Fe, Co, Ni, Zn, and Cd) compounds, *Russian Journal of Inorganic Chemistry* **2010**, *55*, 904-912.

(52) Groen, W. A.; Ijdo, D. J. W., The monoclinic perovskites $Sr_2CaUO_6$ and $Ba_2SrUO_6$. A Rietveld refinement of neutron powder diffraction data, *Acta Cryst.* **1987**, *C43*, 1033-1036.

(53) Pinacca, R.; Viola, M. C.; Pedregosa, J. C.; Muñoz, A.; Alonso, J. A.; Martínez, J. L.; Carbonio, R. E., Crystal and magnetic structure of the double perovskite $Sr_2CoUO_6$: a neutron diffraction study, *Dalton Trans.* **2005**, 447-451.

(54) Pinacca, R. M.; Viola, M. C.; Pedregosa, J. C.; Martínez-Lope, M. J.; Carbonio, R. E.; Alonso, J. A., Preparation, crystal structure and magnetic behavior of new double perovskites Sr2B′ UO6 with B′= Mn, Fe, Ni, Zn, *J. Solid State Chem.* **2007**, *180*, 1582-1589.

(55) Burns, P. C.; Ewing, R. C.; Hawthorne, F. C., The crystal chemistry of hexavalent uranium: polyhedron geometries, bond-valence parameters, and polymerization of polyhedra, *Can. Mineral.* **1997**, *35*, 1551-1570.

(56) Brese, N. E.; O'Keeffe, M., Bond-Valence Parameters for Solids, *Acta Cryst.* **1991**, *B47*, 192-197.

(57) Allen, S.; Barlow, S.; Halasyamani, P. S.; Mosselmans, J. F. W.; O'Hare, D.; Walker, S. M.; Walton, R. I., Hydrothermal Synthesis of $(C_6N_2H_{14})_2(U^{VI}_2U^{IV}O_4F_{12})$, a Mixed-Valent One-Dimensional Uranium Oxyfluoride, *Inorg. Chem.* **2000**, *39*, 3791-3798.

(58) Kosog, B.; La Pierre, H. S.; Denecke, M. A.; Heinemann, F. W.; Meyer, K., Oxidation state delineation via U $L_{III}$-edge XANES in a series of isostructural uranium coordination complexes., *Inorg. Chem.* **2012**, *51*, 7940-7944.

(59) Sanyal, K.; Khooha, A.; Das, G.; Tiwari, M. K.; Misra, N. L., Direct Determination of Oxidation States of Uranium in Mixed-Valent Uranium Oxides Using Total Reflection X-ray Fluorescence X-ray Absorption Near-Edge Spectroscopy., *Anal. Chem.* **2017**, *89*, 871-876.

(60) Kanellakopulos, B.; Henrich, E.; Keller, C.; Baumgärtner, F.; König, E.; Desai, V. P., Optical spectra and magnetism between 4.2 and 300 K for some alkali metal and

alkaline earth metal uranates(V), neptunates(VI), and a plutonate(VII), *Chem. Phys.* **1980**, *53*, 197-213.

(61) Morrison, G.; Smith, M. D.; Tran, T. T.; Halasyamani, S.; zur Loye, H.-C., Synthesis and structure of the new pentary uranium(VI) silicate, $K_4CaUSi_4O_{14}$, a member of a structural family related to frenoite, *CrystEngComm* **2015**, *17*, 4218-4224.

(62) Read, C. M.; Yeon, J.; Smith, M. D.; zur Loye, H.-C., Crystal growth, structural characterization, cation–cation interaction classification, and optical properties of uranium (vi) containing oxychlorides, $A_4U_5O_{16}Cl_2$ (A= K, Rb), $Cs_5U_7O_{22}Cl_3$, and $AUO_3Cl$ (A=Rb, Cs), *CrystEngComm* **2014**, *16*, 7259-7267.

(63) Juillerat, C. A.; Kocevski, V.; Besmann, T.; zur Loye, H.-C., Observation of the Same New Sheet Topology in Both the Layered Uranyl Oxide-Phosphate $Cs_{11}[(UO_2)_{12}(PO_4)_3O_{13}]$ and the Layered Uranyl Oxyfluoride-Phosphate $Rb_{11}[UO_2)_{12}(PO_4)_3O_{12}F_2]$ Prepared by Flux Crystal Growth, *Frontiers in Chemistry*, **2019**, *7*, 583.

(64) Stritzinger, J. T.; Alekseev, E. V.; Polinski, M. J.; Cross, J. N.; Eaton, T. M.; Albrecht-Schmitt, T. E. L. M. C. T., Further Evidence for the Stabilization of U(V) within a tetraoxo Core, *Inorg. Chem.* **2014**, *53*, 5294-5299.

# Chapter 11

## Fluorination and Reduction of $CaCrO_3$ by Topochemical Methods[1]

[1] Reproduced from Juillerat, C. A.; Tsujimoto, Y.; Chikamatsu, A.; Masubuchi, Y.; Hasegawa, T.; Yamaura, K. *Dalton Trans.* **2020**, *49*, 1997-2001 with permission from the Royal Society of Chemistry.

**Abstract:** Topochemical reactions between $CaCrO_3$ and polyvinylidene difluoride yield the new fluorinated phase $CaCrO_{2.5}F_{0.5}$, which was characterized by powder synchrotron X-ray diffraction, X-ray photoemission spectroscopy, and magnetic susceptibility measurements. The reaction proceeds via reduced oxide intermediates, $CaCrO_{2.67}$ and $CaCrO_{2.5}$, in which $CrO_6$ octahedral and $CrO_4$ tetrahedral layers are stacked in a different manner along the *c* axis of $CaCrO_3$. These two intermediate phases can be selectively synthesized by the carbothermal reduction with g-$C_3N_4$. Both $CaCrO_3$ and $CaCrO_{2.5}F_{0.5}$ adopt the same orthorhombic space group, *Pbnm*; however, the fluorinated phase has decreased Cr-O-Cr bond angles as compared to the parent compound in both the *ab* plane and along the *c*-direction, which indicates an increased orthorhombic distortion due to the fluorination. While the oxygen vacancies are ordered in both intermediate phases, $CaCrO_{2.67}$ and $CaCrO_{2.5}$, a site preference for fluorine in the oxyfluoride phase cannot be confirmed. $CaCrO_3$ and $CaCrO_{2.5}F_{0.5}$ undergo antiferromagnetic phase transitions involving spin canting, where the fluorination causes the transition temperature to increase from 90 K to 110 K, as a result of the competition between the increased octahedral tilting and the enhancement of superexchange interactions involving $Cr^{3+}$ ions in the $CaCrO_{2.5}F_{0.5}$ structure.

**Introduction.** Recently, the development of topochemical techniques have allowed for the facile synthesis of phases with new anion lattices or metal coordination geometries in oxides, the synthesis of which has been central in solid state chemistry, as it expands our knowledge of structure property relationships.[1] A number of oxygen deficient or oxyfluoride phases have been obtained by treating oxides normally obtained easily by solid state reactions with either a reducing or fluorinating agent.[2, 3] Topochemical reduction

using an alkali/alkaline hydride yields novel oxyhydrides and oxygen-vacancy ordered compounds. For example, $LaSr_3NiRuO_4H_4$ with metal hydride sheets and $AFeO_2$ ($A$ = Ca, Sr, Ba) with square-planar oxides [4] are obtained from the corresponding oxide phases.[5–7] Low-temperature fluorination reactions using fluorine gas, fluoropolymer or a binary metal fluoride also allow for unique anion-lattice modification via the substitution of fluorine for oxygen and/or fluorine insertion,[8] as exemplified by the synthesis of superconducting $Sr_2CuO_2F_{2+\square}$ from $Sr_2CuO_3$. [9]

Applying these topochemical methods to materials obtained from high-pressure synthesis, a 'hard-soft' synthetic approach, is under explored and can lead to the exploration of metal coordination environments that aren't readily accessible at ambient pressures. For example, it is well known the tetravalent chromium cation strongly favors tetrahedral coordination over octahedral coordination and the ionic radius is too small to be incorporated into perovskite structures, although these observations are not without exceptions.[10] Previously, alkaline chromium oxide perovskites such as $ACrO_3$ ($A$ = Ca, Sr) have been stabilized under high pressures,[11, 12] and Arevalo-Lopez and Attfield *et al*. have discovered new oxygen-vacancy ordered phases $CaCrO_{3-x}$ ($x$ = 0.33, 0.4, 0.5)[13, 14] and $SrCrO_{3-y}$ ($y$ = 0.2, 0.25), [15] which were synthesized by reduction of $ACrO_3$ ($A$ = Ca, Sr) with hydrogen gas. $CaCrO_{2.5}$ was found to adopt the brownmillerite structure. These oxygen deficient layers depend on the A site cations: vacancies in $CaCrO_{3-x}$ are formed in the (001) plane of the cubic perovskite structure, but vacancies in $SrCrO_{3-y}$ are formed in the (111) plane (Figure 11.1).

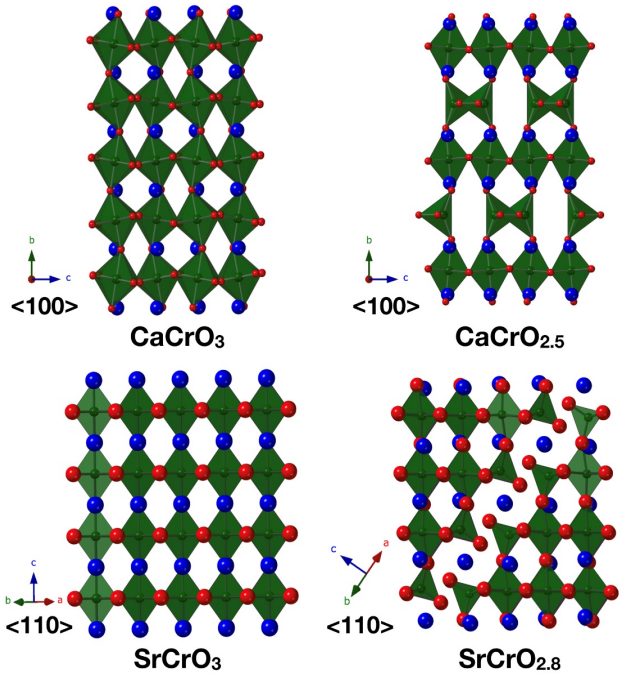


**Figure 11.1:** Structures of $A$CrO$_3$ ($A$ = Ca, Sr) and their reduced products obtained by reductive reactions carried out with g-C$_3$N$_4$. CaCrO$_{2.5}$ adopts the brownmillerite structure. Chromium octahedra are shown in green, oxygen atoms in red, and $A$ atoms in blue.

Very recently, our research group reported the topochemical fluorination of SrCrO$_3$ with polyvinylidene difluoride (PVDF), which involved the formation of SrCrO$_{2.8}$ as an intermediate oxide.[16] The layers of tetrahedrally coordinated $Cr^{4+}$ in SrCrO$_{2.8}$ create a pathway for the subsequent fluorine insertion, and the resulting oxyfluoride phase was the cubic SrCrO$_{2.8}$F$_{0.2}$ with fluoride ions randomly distributed in the structure. Furthermore, SrCrO$_{2.8}$ could be isolated for the first time by topochemical reduction with g-C$_3$N$_4$.[16] It should be noted that the degree of fluorination in SrCrO$_3$ seems to be restricted by the amount of the oxygen deficiencies in the intermediate phase. Thus, to gain deeper understanding of the fluorination mechanism for SrCrO$_3$, it is useful to perform chemical

substitution in the parent materials and explore the different types of oxygen deficient phases obtained by reduction.

In this study, we report the fluorination and reduction of $CaCrO_3$ with PVDF and g-$C_3N_4$, which revealed stepwise fluorination processes similar to that for $SrCrO_3$ but different pathways for oxygen removal and fluorine insertion as well as higher degree of fluorination.

**Experimental:**

**Synthesis.** $CaCrO_3$ powder was obtained using a multi-anvil high-pressure method previously reported by Weiher *et al*.[11] $CaCO_3$ was heated over night at 1000 °C in air to obtain CaO, which was combined stoichiometrically with $CrO_2$ (Aldrich) in an Ar filled glovebox and loaded into a Pt capsule. The Pt capsule was loaded into a high-pressure cell and heated at 900 °C under a pressure of 5 GPa for 1 h before quenching to room temperature by turning off the heat before releasing the pressure. The black polycrystalline product, $CaCrO_3$, contained a $CaCr_2O_4$ impurity (13 wt.%) and was fluorinated using PVDF (Aldrich) in molar ratios of 0.1 to 0.5 (PVDF/$CaCrO_3$). PVDF and $CaCrO_3$ were mixed, pelletized, and sealed in a glass tube under vacuum before heating at temperatures of 350, 370, and 400 °C. $CaCrO_3$ was also reduced using g-$C_3N_4$ (synthesized in house) in ratios of 0.25 ($C_3N_4$/$CaCrO_3$) following a similar procedure.

**Structure.** The structures of the resulting powders were analyzed by Rietveld refinement using synchrotron X-ray powder diffraction (SXRD) data collected at room temperature using one-dimensional X-ray detectors installed on BL15XU, NIMS beamline at SPring-8 in Japan. The synchrotron radiation X-rays were monochromatized to the wavelength of 0.65298 Å. The samples were loaded in glass capillaries and inner diameter

of 0.1mm, and the diffraction data were recorded in 0.003° increments over the range of 4 ≤ $2\theta$ ≤ 60°. Structure refinements were performed using the Rietveld method with the program RIETAN-FP.[17] X-ray Photoemission spectroscopy (XPS) measurements were performed by using Mg *K*α X-ray source (JEOL JPS-9010MC). The Fermi level was calibrated using the C1s signal.

**Results and Discussion:**

**Synthesis.** For both post-synthetic fluorination and reductive reactions, a temperature of 400 °C produced better results, although the reactions can be carried out at 350 and 370 °C but the reactions did not reach completion at these temperatures. The reactions of $CaCrO_3$ with PVDF at different ratios show a stepwise fluorination of $CaCrO_3$, where $CaCrO_3$ is first reduced to $CaCrO_{2.67}$ and $CaCrO_{2.5}$, before the fluorinated phase forms (see Figure 11.2). At ratios of 0.1 and 0.2 (PVDF/$CaCrO_3$) $CaCrO_{2.67}$ and $CaCrO_{2.5}$ are formed, and these phases disappear as the fluorinated phase, $CaCrO_{3-x}F_x$, begins to form at a ratio of 0.3 (PVDF/$CaCrO_3$). These behaviors suggest that fluorine is inserted into the tetrahedral layers of $CaCrO_{2.5}$. The fluorinated phase obtained at 0.5 (PVDF/$CaCrO_3$) can be assigned to an orthorhombic cell with $a$ = 5.34098(9) Å, $b$ = 5.40324(9) Å, and $c$ = 7.53180(10) Å. Low-temperature reduction using g-$C_3N_4$ was also examined on $CaCrO_3$, which resulted in the successful isolation of $CaCrO_{2.5}$ and $CaCrO_{2.67}$ under controlled reaction temperatures, although a few uncharacterized peaks, which disappear at higher temperatures, were detected in $CaCrO_{2.67}$ as indicated in the right panel of Fig. 2. We notice that both the fluorination and reduction of $CaCrO_3$ causes peak broadening, which is probably due to a reduced crystallinity through the topochemical reactions.

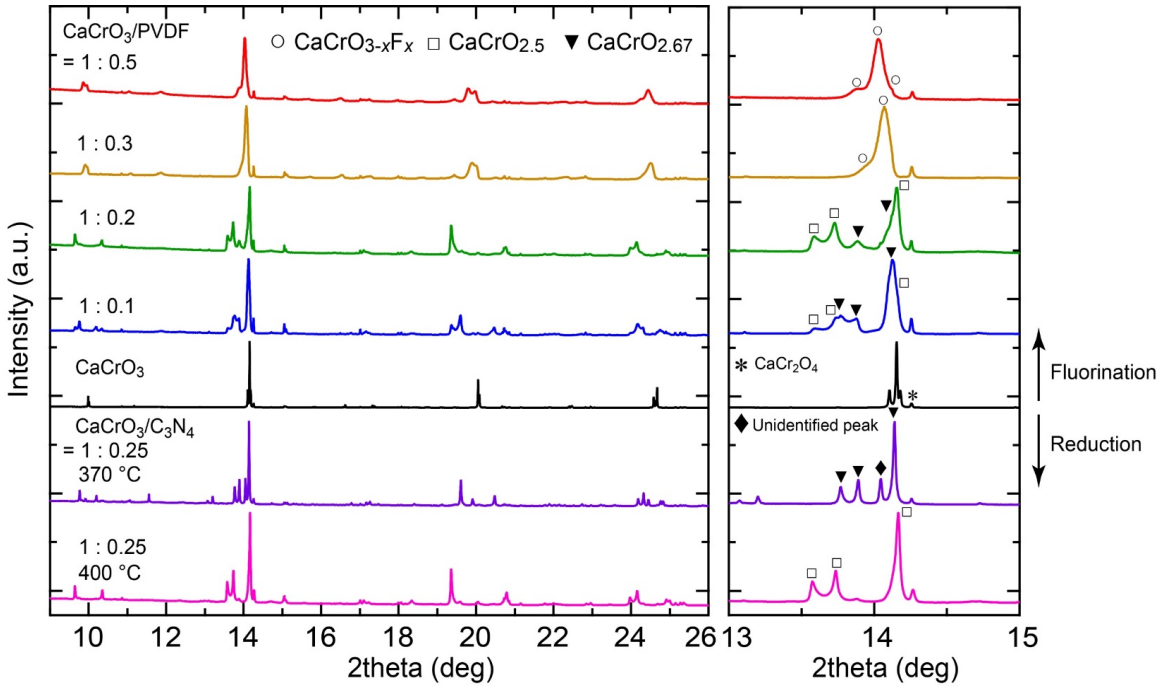


**Figure 11.2**: SXRD patterns of the products of $CaCrO_3$ and PVDF or g-$C_3N_4$. $CaCrO_3$ is fluorinated via two oxygen deficient phases, i.e. $CaCrO_{2.67}$ and $CaCrO_{2.5}$. These reduced phases can be isolated by controlling the reaction temperature with g-$C_3N_4$.

**Structure.** Figure 11.3 shows the result of Rietveld refinement against the PXRD data collected from the product obtained by the reaction of $CaCrO_3$ with PVDF at 400 °C. Even after the fluorination reaction, the structure retained the orthorhombic space group *Pbnm*, but the lattice constants increased by 0.98, 1.60, and 0.60% along *a*, *b*, and *c* directions, respectively. The variation in volume ($\Delta V/V$) is 3.2%, which is larger than the volume change between $SrCrO_3$ and $SrCrO_{2.8}F_{0.2}$ (2.5%) but smaller than that between $SrFeO_3$ and $SrFeO_2F$ (8.2%).[15, 16] No additional peaks associated with O/F anion ordering were detected. For structural refinement of the oxyfluoride phase, the crystal structure of $CaCrO_3$ was used as a starting model. No attempt was made to distinguish oxide and fluoride ions because of their similar X-ray scattering factors. $CaCr_2O_4$ and $CaF_2$ were also added to the refinement as secondary phases. The refinement readily converged well to $R_{wp}$

= 2.01% and $R_B$ = 3.73 %. No anion-site deficiencies were found within the error margin, indicating that the oxygen vacant sites in $CaCrO_{2.5}$ were completely filled with fluoride ions. Thus, the expected chemical composition is $CaCrO_{2.5}F_{0.5}$, implying higher degree of fluorination than that for $SrCrO_3$.[16] Rietveld refinements were performed on PXRD data collected on the parent structure, $CaCrO_3$, and the reduced structure, $CaCrO_{2.5}$, and are shown in Figures 11.4 and 11.5, although there are no new results considering both structures have previously been thoroughly characterized.[14,11,18] The refined atomic coordinates for $CaCrO_{2.5}F_{0.5}$, $CaCrO_3$, and $CaCrO_{2.5}$ are shown in Tables 11.1-3.

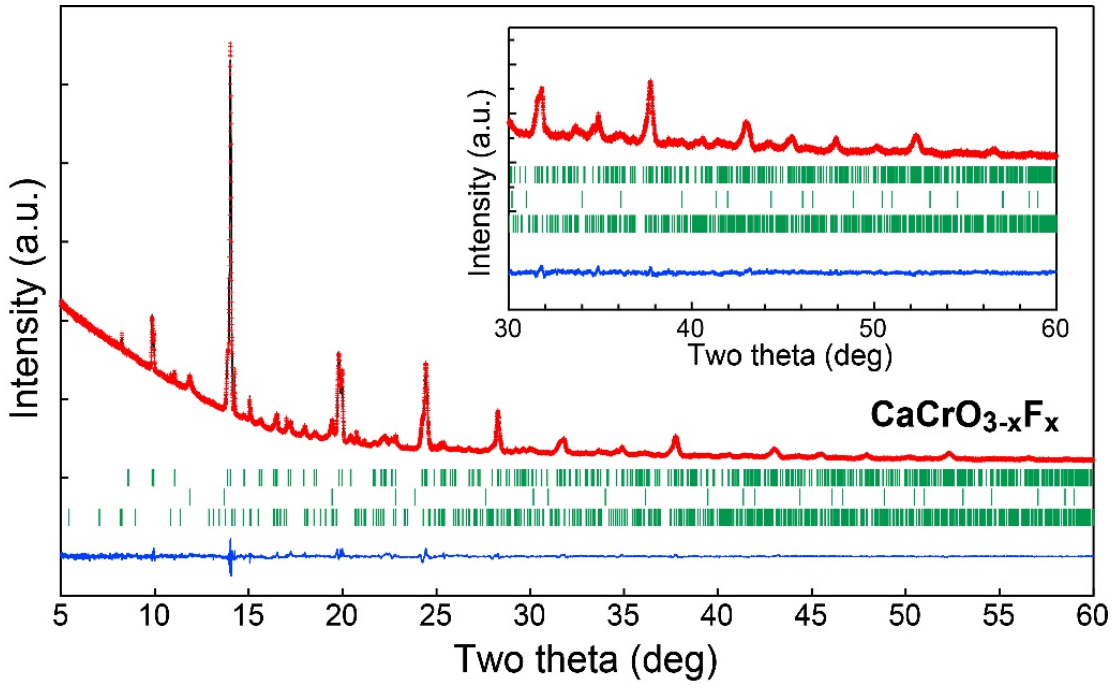


**Figure 11.3**: Rietveld refinement against PXRD data of fluorinated $CaCrO_3$. The observed (red crosses), calculated (black solid line), and difference (blue solid line) plots are shown. The vertical lines represent the fluorinated phase (81%), $CaF_2$ (12%), and $CaCr_2O_4$ (7%) from top to bottom.

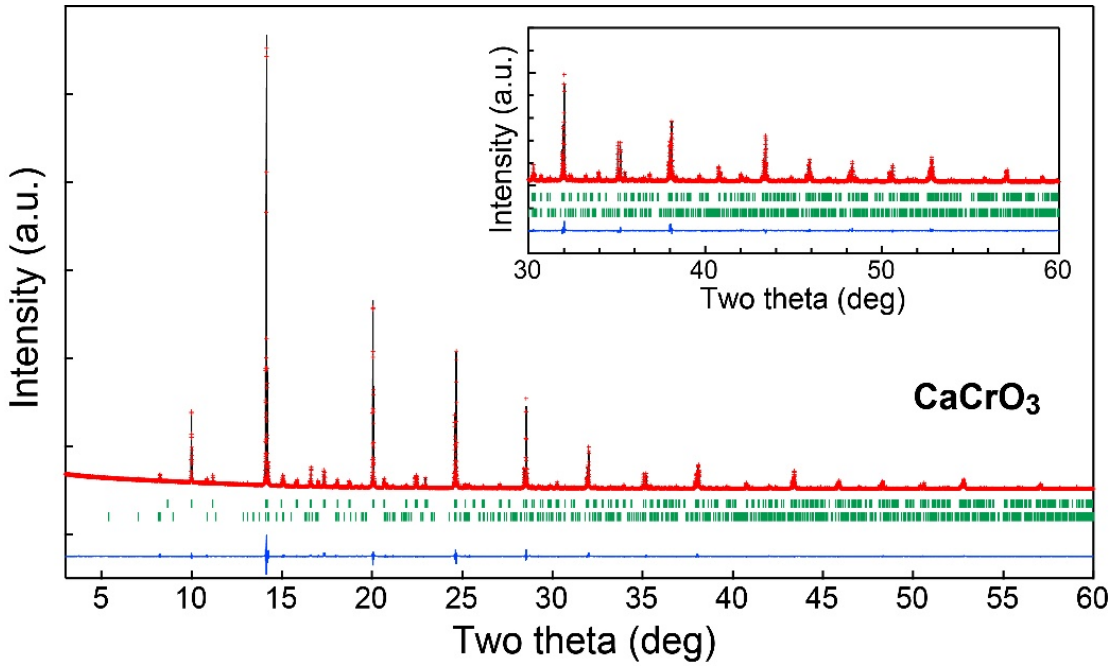


**Figure 11.4:** Rietveld refinement against PXRD data of $CaCrO_3$. The observed (red crosses), calculated (black solid line), and difference (blue solid line) plots are shown. The vertical lines represent $CaCrO_3$ (87%) and $CaCr_2O_4$ (13%) from top to bottom. The inset shows an enlarged plot in a high 2**θ** region.

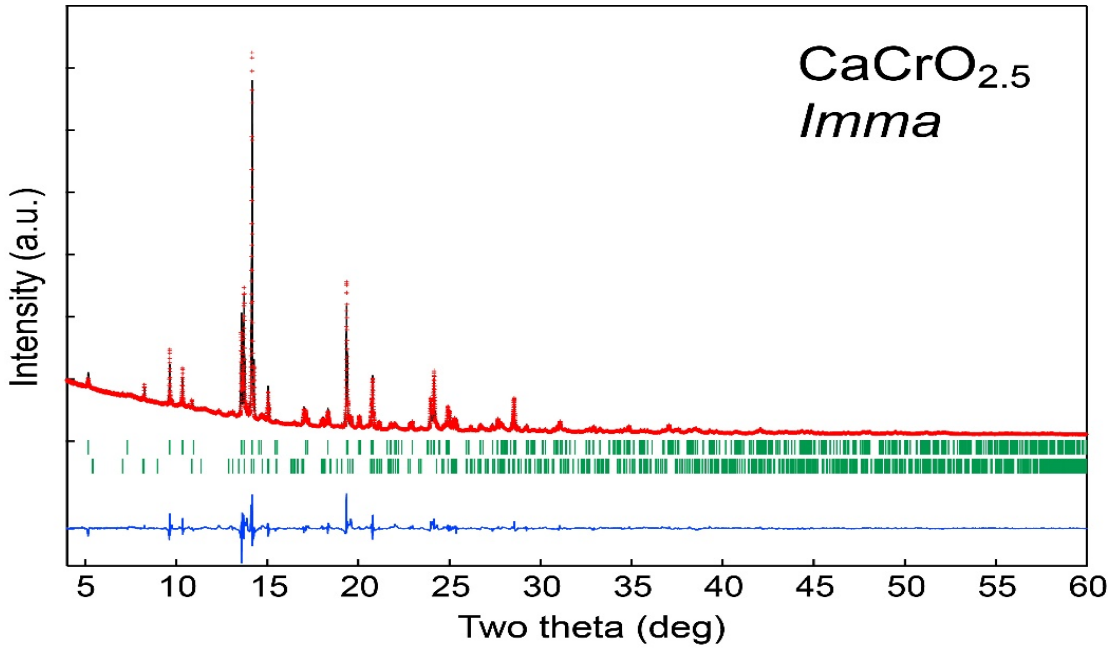


**Figure 11.5:** Rietveld refinement against PXRD data of $CaCrO_{2.5}$. The observed (red crosses), calculated (black solid line), and difference (blue solid line) plots are shown. The vertical lines represent $CaCrO_{2.5}$ (86%) and $CaCr_2O_4$ (14%) from top to bottom.

**Table 11.1:** Crystallographic parameters of fluorinated $CaCrO_3$ refined from room temperature synchrotron X-ray powder diffraction data.

| atom | site | *x* | *y* | *z* | *g* | $B_{iso}$/ Å$^2$ |
|---|---|---|---|---|---|---|
| Ca | 4c | 0.0068(4) | 0.0411(1) | 1/4 | 1 | 0.347(14) |
| Cr | 4b | 1/2 | 0 | 0 | 1 | 0.559(11) |
| *X*1 | 8d | 0.7096(6) | 0.2949(5) | 0.0294(4) | 1 | 0.25(3) |
| *X*2 | 4c | 0.0825(8) | 0.4857(6) | 1/4 | 1 | 0.25 |

Space group *Pbnm* (No. 62): *a* =5.34098(9) Å, *b* = 5.40324(9) Å, *c* = 7.53180(10) Å. *R* indices are $R_{wp}$ = 2.01%, $R_B$ = 3.73%, and $R_F$ = 2.40%. No deficiencies were found at all site occupancies (*g*). All of the anion sites (*X*) were assumed to be O. $B_{iso}$ values for *X*1 and *X*2 sites were constrained to the same.

**Table 11.2:** Crystallographic parameters of $CaCrO_3$ refined from room temperature synchrotron X-ray powder diffraction data.

| atom | site | *x* | *y* | *z* | *g* | $B_{iso}$/ Å$^2$ |
|---|---|---|---|---|---|---|
| Ca | 4c | –0047(2) | 0.03029(8) | 1/4 | 1 | 0.511(7) |
| Cr | 4b | 1/2 | 0 | 0 | 1 | 0.235(6) |
| O1 | 8d | 0.7132(2) | 0.2863(2) | 0.0331(2) | 1 | 0.31(2) |
| O2 | 4c | 0.0611(3) | 0.4896(3) | 1/4 | 1 | 0.38(3) |

Space group *Pbnm* (No. 62): *a* = 5.28912(1) Å, *b* =5.31796(1) Å, *c* = 7.48677(1) Å. *R*

**Table 11.3:** Crystallographic parameters of $CaCrO_{2.5}$ refined from room temperature synchrotron X-ray powder diffraction data.

| atom | site | *x* | *y* | *z* | *g* | $B_{iso}$/ Å$^2$ |
|---|---|---|---|---|---|---|
| Ca | 8h | 0 | 0.61380(15) | 0.4980(7) | 1 | 1.19(5) |
| Cr1 | 4a | 0 | 0 | 0 | 1 | 0.59(5) |
| Cr2 | 8i | 0.4273(4) | 1/4 | 0.5114(8) | 0.5 | 0.17(7) |
| O1 | 8g | 1/4 | 0.0065(7) | 1/4 | 1 | 0.94(9) |
| O2 | 8h | 0 | 0.1399(3) | 0.0608(9) | 1 | 0.94 |
| O3 | 8i | 0.197(2) | 1/4 | 0.673(2) | 0.5 | 0.94 |

Space group *Imma* (No. 74): *a* = 5.52141(6) Å, *b* =14.48419(13) Å, *c* = 5.46196(5) Å. *R* indices are $R_{wp}$ = 6.20%, $R_B$ = 9.83%, and $R_F$ = 6.93%. All site occupancies were fixed to unity or half. $B_{iso}$ values for O1, O2, and O3 sites were constrained to the same value.

**Table 11.4:** Bond Valence Sums for different anion ordering models.

| Structure | Ca | *Cr* | *X1* | *X2* |
|---|---|---|---|---|
| $CaCrO_3$ | 2.28 | 3.98 | 2.08 | 2.11 |
| Expected values | 2 | 3.5 | 2 | 2 |
| $CaCrO_{2.5}F_{0.5}$ (Full anion disorder) | 2.15 | 3.34 | 1.8 | 1.88 |
| Expected values | 2 | 3.5 | 1.83 | 1.83 |
| $CaCrO_{2.5}F_{0.5}$ (Occupation of X1 by fluorine) | 2.14 | 3.34 | 1.75 | 1.98 |
| Expected values | 2 | 3.5 | 1.75 | 2 |
| $CaCrO_{2.5}F_{0.5}$ (Occupation of X2 by fluorine) | 1.89 | 3.34 | 1.68 | 1.89 |
| Expected values | 2 | 3.5 | 1.5 | 2 |

We investigated the change in oxidation state of the chromium ions due to the fluorination of $CaCrO_3$ by XPS measurements. Figure 11.6 shows the Cr 2*p* spectra collected from $CaCrO_3$ and its fluorinated phase. The Cr $2p^{3/2}$ spectrum of $CaCrO_3$ is decomposed into three components which could be assigned as $Cr^{3+}$, $Cr^{4+}$, and $Cr^{6+}$ with binding energies of 576.38, 578.96, and 582.35 eV, respectively.[19] The trivalent and tetravalent chromium should be derived from $CaCr_2O_4$ and $CaCrO_3$, respectively. The atomic ratio of $Cr^{3+}$ to $Cr^{4+}$ estimated from the spectral area is 0.15:0.80, which agrees well with that obtained from the Rietveld analysis (0.17:0.83). The $Cr^{6+}$ species, which were not detected by the SXRD pattern, should be attributed to surface defects. For the oxyfluoride phase, the Cr $2p^{3/2}$ spectrum can be decomposed into $Cr^{3+}$ and $Cr^{4+}$ species in an atomic ratio of 0.40:0.60. The increase in the $Cr^{3+}$ component is consistent with O-to-F substitution in $CaCrO_3$. However, the atomic ratio of $Cr^{3+}$ to $Cr^{4+}$ determined by XPS (0.40:0.60) deviates from that estimated from the PXRD analysis (0.50:0.50) assuming the oxyfluoride phase as $CaCrO_{2.5}F_{0.5}$. This discrepancy is likely due to the low signal-to-noise ratio caused by residual C-F species from the fluorinating agent, as seen from the wide-scan spectra in Figure 11.7.

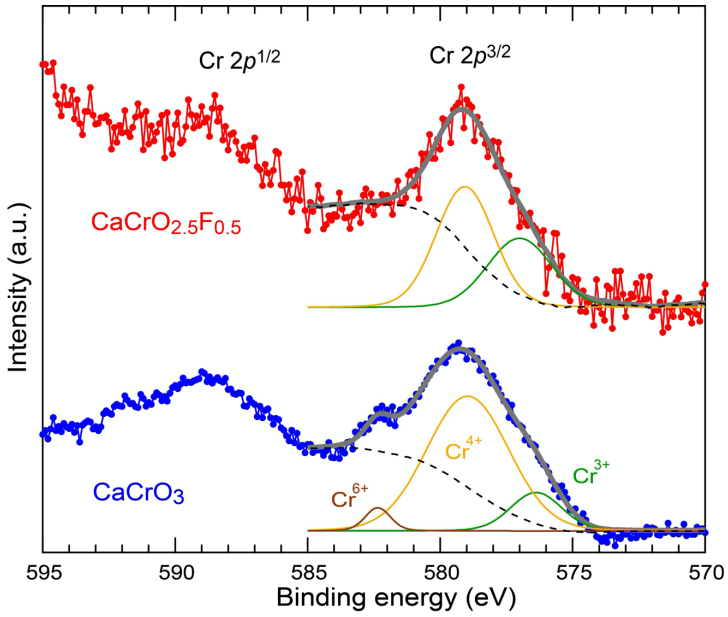


**Figure 11.6:** Cr 2*p* core level XPS spectra of $CaCrO_3$ and its fluorinated phase. The bold grey and dashed black lines represent the fitting curves and the Shirley background, respectively. The green, orange, and brown solid lines correspond to $Cr^{3+}$, $Cr^{4+}$ and $Cr^{6+}$ components.

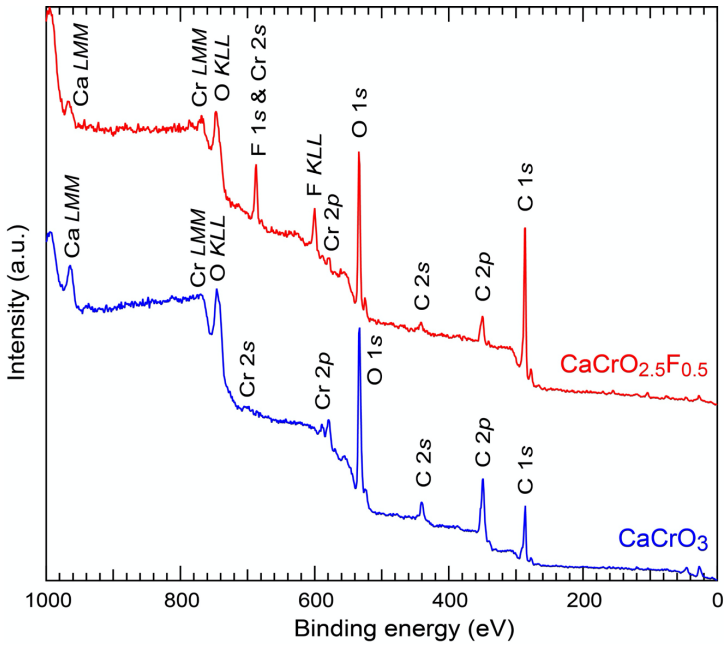


**Figure 11.7:** Wide scan XPS spectra of $CaCrO_3$ and its fluorinated phase.

The structure of $CaCrO_3$ is well studied and adopts the $ABO_3$ perovskite structure with an orthorhombic distortion due to the small size of the $Ca^{2+}$ ion,[18, 20] as compared to the cubic $SrCrO_3$, and crystallizes in the *Pbnm* space group with lattice parameters $a$ = 5.28912(1) Å, $b$ = 5.31796(1) Å, and $c$ = 7.48677(1) Å. The oxygen vacancies are ordered in $CaCrO_{2.5}$ and $CaCrO_{2.67}$, creating layers of Cr octahedra and tetrahedra (Figure 11.8). In $CaCrO_{2.67}$, the tetrahedral layer occurs every third layer, while in $CaCrO_{2.5}$, which adopts the brownmillerite structure, it occurs every other layer. The relationship of the octahedral layers to the tetrahedral layers can be understood as the removal of every other infinite chain of oxygen atoms as illustrated in Figure 11.8. This reduces the coordination of Cr from 6 to 4, and as a result the Cr-O-Cr bond which is nearly linear in the octahedral layers contracts to form the approximately 109° bond angle found in tetrahedral coordination environments.

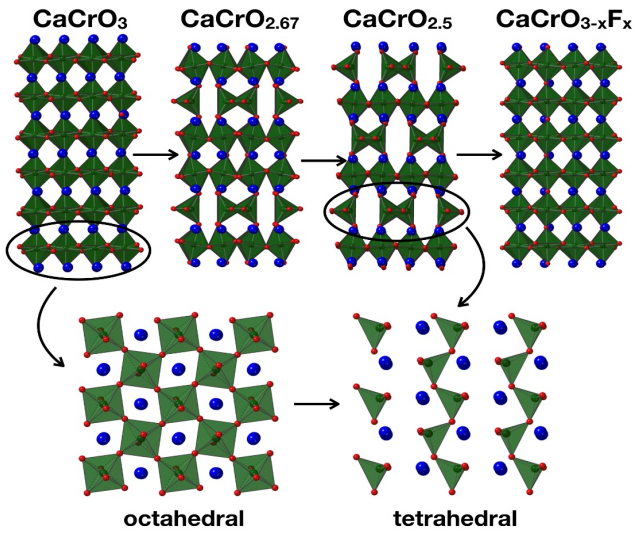


**Figure 11.8:** Structures of $CaCrO_3$, $CaCrO_{2.5}$, $CaCrO_{2.67}$, and $CaCrO_{3-x}F_x$ showing the sequences of octahedral and tetrahedral layers as a result of oxygen vacancies where chromium octahedra are shown in green, oxygen atoms in red, and calcium atoms in blue.

Rietveld refinement against the SXRD data of $CaCrO_{2.5}F_{0.5}$ revealed all of the anion sites in the $ABO_3$ structure were fully occupied upon fluorination and $CaCrO_{2.5}F_{0.5}$ adopted the same space group of the parent compound. The structure symmetry allows anions to occupy two unique sites, namely the sites on the *ab* plane (*X*1) and along the *c* axis (*X*2). Thus, the existence of a selective fluorine distribution over the anion sites cannot be ruled out. To examine the possible anion ordering of O/F ions, bond-valence-sum (BVS) calculations were carried out on the assumption of three types of fluorine distribution, namely, on *X*1, *X*2, or both sites. The BVS values for all atoms are summarized in Table 11.4. Unfortunately, we could not conclude any types of anion ordering: the BVS values for *X*1 and *X*2 sites as well as Ca and Cr sites were consistent with the assumed fluorine distribution patterns.

Figure 11.9 shows a comparison between the refined crystal structures of $CaCrO_3$ and $CaCrO_{2.5}F_{0.5}$. Hereafter, the full anion disordered model is employed to discuss the structure and properties of the oxyfluoride phase, since no selective fluorine distribution was observed. All the Cr-F/O bond lengths are increased from 1.9002(4), 1.911(1), and 1.912(1) Å to 1.935(1), 1.960(4), and 1.919(4) Å (see Figure 11.9). These behaviors are consistent with the increased $Cr^{3+}/Cr^{4+}$ via the substitution of fluorine for oxygen. The oxyfluoride structure also contains tightened Cr-O/F-Cr bond angles of 156.6(2) and 153.3(3)° as compared to 157.70(8) and 160.13(13)° in the parent structure. A higher degree of the octahedral tilting in the fluorinated perovskite can be accounted for by considering Goldschmidt's tolerance factor (*t*), which is expressed as $t = (r_A+r_X)/\sqrt{2}(r_B+r_X)$.[21, 22] The $r_A$, $r_B$, and $r_X$ are the Shannon's ionic radii of *A*-site cation, *B*-site cation, and *X*-site anion.[22] The calculated *t* factor of $CaCrO_{2.5}F_{0.5}$ is 0.979, lower than

more ideal value of $CaCrO_3$ ($t$ = 0.994). Although no examples of $B$-O-$B$ bond angle compression upon fluorinating could be found for chromium oxides, $LaSrCoFeO_5F$ contains tightened (Co/Fe)-(O/F)-(Co/Fe) bond angles as compared to the oxygen-stoichiometric oxide $LaSrCoFeO_6$, both of which adopt the trigonal space group $R$-3$c$. [23] $La_{0.5}Sr_{0.5}FeO_{2.5}F_{0.5}$, which crystallizes in the lower symmetry *Pnma* as compared to the oxide which adopts the $R$-3$c$ space group, also exhibits similar changes in local coordination around the metal center where the Fe-O-Fe bond angles contract from 167.0(3) to 163. 39(11) and 159.68(13) and the Fe-O bond distances increase from 1.9567(6) to 1.996(4), 1.9996(6), and 1.986(4), upon fluorination. [24]

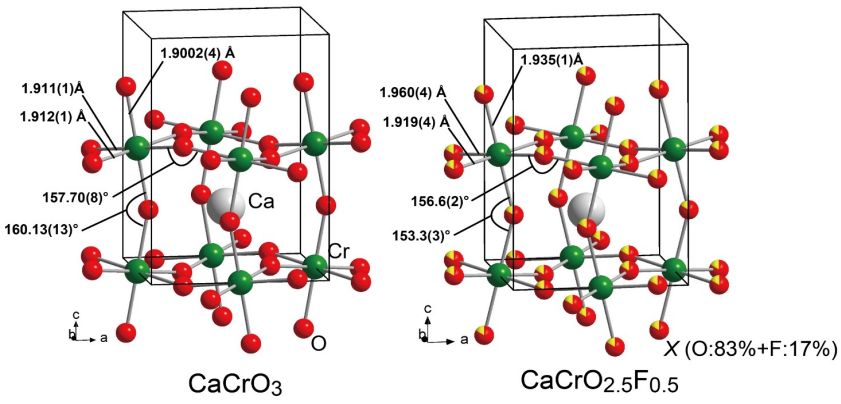


**Figure 11.9**: Chromium coordination environments in $CaCrO_3$ and $CaCrO_{3-x}F_x$ where the Cr atoms are shown in green, oxygen atoms in red, and the calcium atoms in white.

**Reaction pathway.** $CaCrO_3$ exhibited stepwise fluorination processes as observed in $SrCrO_3$.[16] However, the important differences between the fluorination mechanisms of $CaCrO_3$ and $SrCrO_3$ are as follows, (1) the degree of fluorination for $CaCrO_3$ is higher than that for $SrCrO_3$, (2) the formation of two intermediate oxide phases of $x$ = 0.33 and 0.5 are involved, and (3) the plane where oxygen removal and fluorine insertion occurs is (001)

for $CaCrO_3$ but (111) for $SrCrO_3$. It is apparent that the larger amount of fluorine atoms inserted into $CaCrO_3$ is attributable not only to its deoxidation capacity but also the reducing power of PVDF. Indeed, the first reduced phase $CaCrO_{2.67}$ is subsequently reduced to $CaCrO_{2.5}$ prior to the fluorination, whereas for the fluorination of $SrCrO_3$ the first reduced phase $SrCrO_{2.8}$ is not further reduced to $SrCrO_{2.75}$ but directly fluorinated to $SrCrO_{2.8}F_{0.2}$. The pathway of the oxygen removal and fluorine insertion for $CaCrO_3$, which is different from those for $SrCrO_3$, also play an important role in the formation of the highly fluorinated phase $CaCrO_{2.5}F_{0.5}$. The fluorine insertion mechanism remains an open question. If fluorine atoms simply occupy the oxygen vacant sites, a partial O/F order on the *X*1 sites is realized. In contrast, fluorine insertion involving migration of apical oxygen, which was observed for layered perovskite compounds,[9, 25] would result in a partial anion order on the *X*2 sites or the full anion disorder. Mitra et al. investigated the oxygen diffusion pathways in brownmillerite $SrCoO_{2.5}$ by first-principle calculations, and found that the one-dimensional-ordered oxygen vacant channels in the $CoO_4$ tetrahedral layers provide the easiest diffusion pathway compared with the directions perpendicular to the vacant channels.[25] Based on this study, it is likely that fluorine also migrates and resides in the $CrO_4$ tetrahedral layers. Similar to the observed O/F disorder in $SrCrO_{2.8}F_{0.2}$, the oxygen-deficiency ordered structures do not influence the fluorine sites, perhaps due to the transformation of the Cr coordination from tetrahedron to octahedron which causes the rearrangement of the fluorine atom positions. Similar fluorine migration during fluorination reaction is observed in related perovskite compounds.[9, 26, 27]

**Magnetism.** Figure 11.10 shows the temperature dependence of the magnetic susceptibility $\chi$ (= $M/H$) of $CaCrO_3$, $CaCrO_{2.5}$, and $CaCrO_{2.5}F_{0.5}$, measured under zero-

field-cooled (ZFC) and field-cooled (FC) conditions in the temperature range between 5 and 300 K. Anomalies in the magnetic susceptibility of the samples, or the inverse (Figure 11.11), from the magnetic impurity, $CaCr_2O_4$, with features at 100 K and 21 K,[28] were not observed indicating that $CaCr_2O_4$ did not significantly impact the susceptibility data. The $\chi(T)$ of $CaCrO_3$ exhibited a sudden increase at $T_N = 90$ K followed by a divergence between ZFC and FC data. These behaviors can be accounted for by a canted antiferromagnetism.[18] The weak temperature dependence above $T_N$, which does not obey the Curie-Weiss law, is consistent with the metallic state unambiguously characterized by spectroscopic techniques.[20, 29] For $CaCrO_{2.5}$, a small cusp associated with an antiferromagnetic ordering was observed at around 240 K in the ZFC data. The $T_N$ value is close to that determined by the neutron diffraction analysis in Attfield *et al.*.[14] The small anomaly in the susceptibility at $T_N$ is probably due to the decrease in crystallinity during the reductive reaction. In contrast to $CaCrO_{2.5}$, the $\chi(T)$ of $CaCrO_{2.5}F_{0.5}$ is similar to that of $CaCrO_3$: an antiferromagnetic phase transition involving spin canting was observed at 110 K. The moderate increase in $\chi(T)$ below $T_N$ suggests decreased spin canting angles between Cr ions. It should be noted the high temperature data above $T_N$ cannot be described again by the Curie-Weiss law, although it is somewhat more dependent on temperature than that of $CaCrO_3$. In fact, the Curie-Weiss fit gave the Curie constant $C = 4.17(1)$ (emu K)/mol, which is unphysically large compared to the value expected from localized magnetic moments of Cr(III) with $S = 3/2$ and Cr(IV) with $S = 1$. This behavior suggests that the oxyfluoride has a metallic state like $CaCrO_3$ or insulating state located near the border between metallic and insulating phases. Unfortunately, even the cold-pressed sample after fluorination was so fragile that electrical measurements could not be performed. In light of

the fact that $CaCrO_3$ resides near the crossover regime from itinerant to localized electron system,[18] the O-to-F substitution involving a decrease in the Cr-O-Cr tilt angles and lowered *pd* hybridization via more electronegative fluoride would shift the chromium perovskite to an insulating phase. Similar enhanced Pauli paramagnetic behaviors are observed in early 3*d*-transition metal insulators such as $LaTiO_3$ and $LaVO_3$, [30, 31] which are assumed to be near the metal-insulator transition.

The impact of fluorination on the magnetism greatly differs between $CaCrO_3$ and $SrCrO_3$.[16] In $SrCrO_3$ showing a Pauli paramagnetic behavior, replacement of 6.7% of oxygen sites with fluorine induces an antiferromagnetic ordered state with $T_N$ = 230 K. In contrast, the fluorination of $CaCrO_3$ increased the magnetic ordering temperature by only 20 K despite the substitution of 16.7% oxygen for fluorine. The difference can be rationalized by considering variations in Cr–(O/F)–Cr bond angles and the oxidation number of Cr ions. In $SrCrO_{2.8}F_{0.2}$ with a cubic structure, the Cr–(O/F)–Cr bond angles are 180°, which maximizes the superexchange interactions between Cr ions. Moreover, the presence of $Cr^{3+}$ ions via the fluorination insertion contributes to the enhancement of magnetic interactions. As a result, the high Néel ordering temperature is obtained. In $CaCrO_{2.5}F_{0.5}$, however, Cr–(O/F)–Cr bond angles both along the *c* axis and on the *ab* plane become smaller via fluorination, which weakens the nearest neighbor interactions. Thus, the moderate increase in $T_N$ observed in $CaCrO_{2.5}F_{0.5}$ should result from a competition between the increased octahedral tilting and the enhancement of superexchange interactions involving $Cr^{3+}$ ions.

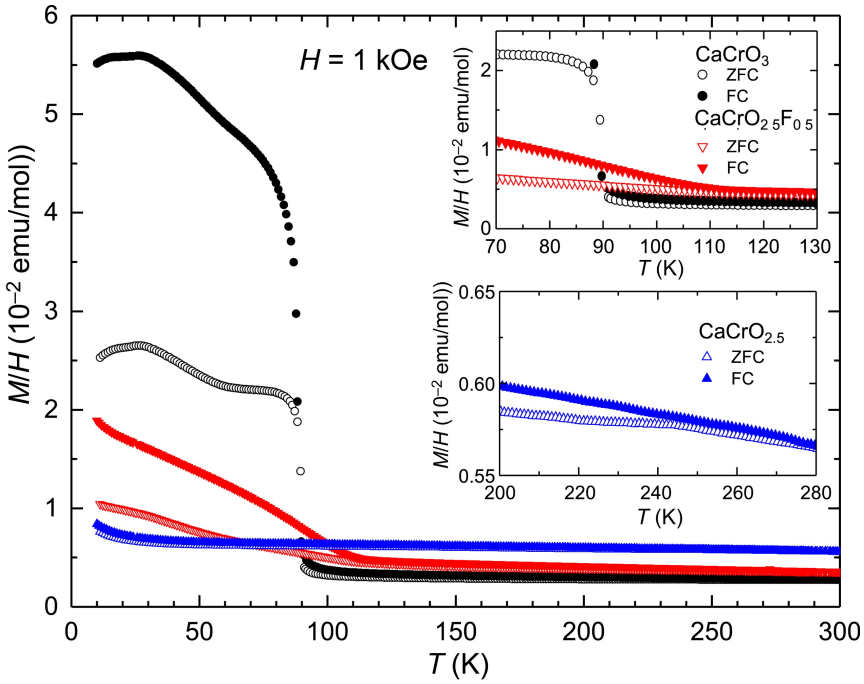


**Figure 11.10:** χ (*T*) plot of $CaCrO_3$, $CaCrO_{2.5}$, and $CaCrO_{2.5}F_{0.5}$, measured under zero field cooled and field cooled conditions.

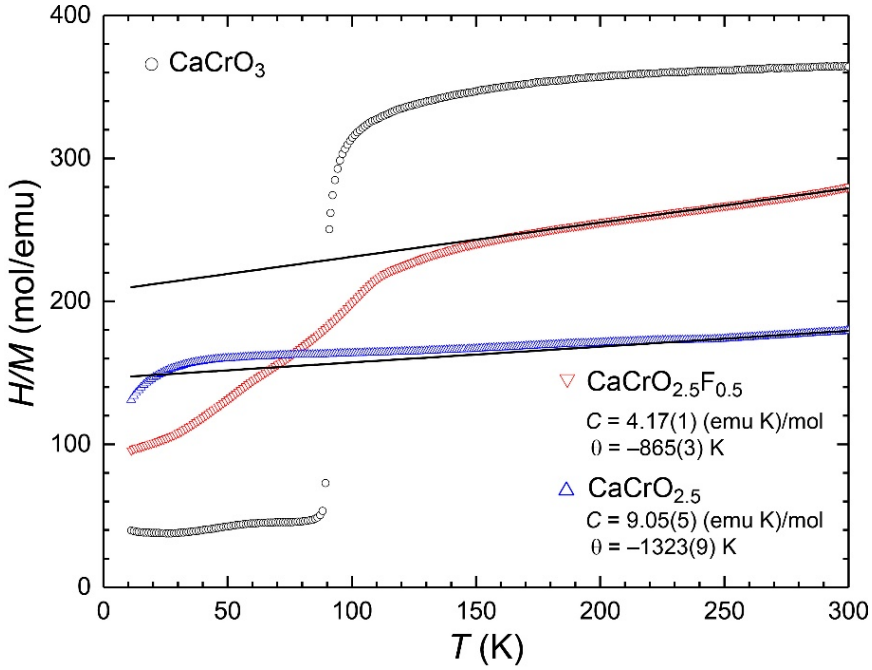


**Figure 11.11**: H/M plot of $CaCrO_3$, $CaCrO_{2.5}$, and $CaCrO_{2.5}F_{0.5}$.

**Conclusion.** In this study, the new fluorinated phase, $CaCrO_{2.5}F_{0.5}$, was isolated by reacting $CaCrO_3$ with PVDF at 400 °C. This reaction proceeds via reduced oxide intermediate phases $CaCrO_{2.67}$ and $CaCrO_{2.5}$, which can be obtained by reacting $CaCrO_3$ with g-$C_3N_4$. The degree of fluorination for $CaCrO_3$ is higher than that for $SrCrO_3$, which is attributed to the deoxidation capacity that is more easily maximized by PVDF. The structure of $CaCrO_{2.5}F_{0.5}$ was characterized by synchrotron powder diffraction and adopts the same structure as $CaCrO_3$ with slightly larger lattice parameters with no detectable O/F ordering. This structure is supported by the XPS results which reveal $Cr^{3+}/Cr^{4+}$ ratios close to the expected value of 0.5/0.5 for the proposed $CaCrO_{2.5}F_{0.5}$ structure based on full anion site occupancy. Magnetic measurements reveal that the fluorinated product has an increased spin-canted antimagnetic phase transition temperature as compared to $CaCrO_3$, which is due to the competition between the increased octahedral tilting and the enhancement of superexchange interactions involving $Cr^{3+}$ ions in the $CaCrO_{2.5}F_{0.5}$ structure.

**Acknowledgements.** This work was supported by the JSPS KAKENHI (Grant no. JP15H02024, JP16H06438, JP16H06441, JP19H02594, 19H04711, 16H06439, 16K21724), a research grant from Innovative Science and Technology Initiative for Security, ATLA, Japan. The SXRD experiments at SPring-8 were performed with the approval of JASRI (Proposal no. 2019A4501). C Juillerat was additionally supported by an NSF IGERT Graduate Fellowship under grant number 1250052 and by the U.S. Department of Energy, Office of Basic Energy Sciences, Division of Materials Sciences and Engineering under Award DE-SC0016574.

**References:**


(1) Kageyama, H.; Hayashi, K.; Maeda, K.; Attfield, J. P., Expanding frontiers in materials chemistry and physics with multiple anions, *Nature Communications* **2018**, *9*, 772.

(2) Hayward, M. A., Synthesis and Magnetism of Extended Solids Containing Transition-Metal Cations in Square-Planar, $MO_4$ Coordination Sites, *Inorg. Chem.* **2019**, *58*, 11961-11970.

(3) Tsujimoto, Y.; Yamaura, K.; Takayama-Muromachi, E., Oxyfluoride chemistry of layered perovskite compounds, *Applied Sciences* **2012**, *2*, 206-219.

(4) Jin, L.; Lane, M.; Zeng, D.; Kirschner, F. K. K.; Lang, F.; Manuel, P.; Blundell, S.; McGrady, J.; Hayward, M. A., $LaSr_3NiRuO_4H_4$: A 4d Transition-Metal Oxide–Hydride Containing Metal Hydride Sheets, *Angew. Chem.* **2018**, *57*, 5025-5028.

(5) Tsujimoto, Y.; Tassel, C.; Hayashi, N.; Watanabe, T.; Kageyama, H.; Yoshimura, K.; Takano, M.; Ceretti, M.; Ritter, C.; Paulus, W., Infinite-layer iron oxide with a square-planar coordination, *Nature* **2007**, *450*, 1062-1065.

(6) Tassel, C.; Pruneda, J. M.; Hayashi, N.; Watanabe, T.; Kitada, A.; Tsujimoto, Y.; Kageyama, H.; Yoshimura, K.; Takano, M.; Nishi, M.; Ohoyama, K.; Mizumaki, M.; Kawamura, N.; Íñigues, J.; Canadell, E., $CaFeO_2$: A New Type of Layered Structure with Iron in a Distorted Square Planar Coordination, *J. Am. Chem. Soc.* **2008**, *131*, 221-229.

(7) Yamamoto, T.; Kobayashi, Y.; Hayashi, N.; T, S.; Yamanaka, S.; Takano, M.; Ohoyama, K.; Shimakawa, Y.; Yoshimura, K.; Kageyama, H., $(Sr_{1-x}Ba_x)FeO_2$ ($0.4 \leq x \leq 1$): A New Oxygen-Deficient Perovskite Structure, *J. Am. Chem. Soc.* **2012**, *134*, 11444-11454.

(8) Clemens, O.; Slater, P. R., Topochemical modifications of mixed metal oxide compounds by low-temperature fluorination routes, *Reviews in Inorganic Chemistry* **2013**, *33*, 105-117.

(9) Ai-Mamouri, M.; Edwards, P. P.; Greaves, C.; Slaski, M., Synthesis and superconducting properties of the strontium copper oxy-fluoride $Sr_2CuO_2F_{2+\delta}$, *Nature* **1994**, *369*, 382-384.

(10) Zhang, R.; Read, G.; Lang, F.; Lancaster…, T., $La_2SrCrO_7F_2$: A Ruddlesden–Popper Oxyfluoride Containing Octahedrally Coordinated $Cr^{4+}$ Centers, *Inorg. Chem.* **2016**, *55*, 3169-3174.

(11) Weiher, J. F.; Chamberland, B. L.; Gillson, J. L., Magnetic and electrical transport properties of CaCrO3, *J. Solid State Chem.* **1971**, *3*, 529-532.

(12) Chamberland, B. L., Preparation and properties of $SrCrO_3$, *Solid State Commun.* **1967**, *5*, 663-666.

(13) Arevalo-Lopez, A. M.; Liang, B.; Senn, M. S.; Murray, C.; Tang, C.; Attfield, J. P., Hard–soft synthesis of a new series of vacancy-ordered perovskites, $CaCrO_{3-\partial}$, *J. Mater. Chem. C* **2014**, *2*, 9364-9367.

(14) Arevalo-Lopez, A. M.; Attfield, J. P., Crystal and magnetic structures of the brownmillerite $Ca_2Cr_2O_5$., *Dalton Trans.* **2015**, *44*, 10661-10664.

(15) Arévalo-López, A. M.; Rodgers, J. A.; Senn, M. S.; Sher, F.; Farnham, J.; Gibbs, W.; Attfield, J. P., "Hard-soft" synthesis of $SrCrO_{3-\delta}$ superstructure phases., *Angew Chem Int Ed Engl* **2012**, *51*, 10791-10794.

(16) Su, Y.; Tsujimoto, Y.; Fujii, K.; Masubuchi, Y.; Ohata, H.; Iwai, H.; Yashima, M.; Yamaura, K., Stepwise topochemical fluorination of $SrCrO_3$ perovskite a super-structured oxide, *Chem. Commun.* **2019**, *55*, 7239-7242.

(17) Izumi, F.; Momma, K., Three-dimensional visualization in powder diffraction, *Solid State Phenomena* **2007**, *130*, 15-20.

(18) Komarek, A. C.; Streltsov, S. V.; Isobe, M.; Möller, T.; Hoelzel, M.; Senyshyn, A.; Trots, D.; Fernández-Díaz, M. T.; Hansen, T.; Gotou, H.; Yagi, T.; Ueda, Y.; Anisimov, V. I.; Grüninger, M.; Khomskii, D. I.; Braden, M., $CaCrO_3$: An Anomalous Antiferromagnetic Metallic Oxide, *Phys. Rev. Lett.* **2008**, *101*, 167204.

(19) Sarma, D. D.; Maiti, K.; Vescovo, E.; Carbone, C.; Eberhardt, W.; Rader, O.; Gudat, W., Investigation of hole-doped insulating $La_{1-x}Sr_xCrO_3$ by soft-x-ray absorption spectroscopy, *Physical Review* **1996**, *53*, 13369.

(20) Komarek, A. C.; Möller, T.; Isobe, M.; Drees, Y.; Ulbrich, H.; Azuma, M.; Fernández-Díaz, M. T.; Senyshyn, A.; Hoelzel, M.; André, G.; Ueda, Y.; Grüninger, M.; Braden, M., Magnetic order, transport and infrared optical properties in the $ACrO_3$ system (A = Ca, Sr, and Pb), *Phys. Rev. B* **2011**, *84*, 125114.

(21) Goldschmidt, V. M., Crystal structure and chemical constitution, *Trans. Faraday Soc.* **1929**, *25*, 253-283.

(22) Shannon, R. D., Revised effective ionic radii and systematic studies of interatomic distances in halides and chalcogenides, *Acta Cryst.* **1976**, *A32*, 751-767.

(23) Shinawi, H. E.; Marco, J. F.; Berry, F. J.; Greaves, C., $LaSrCoFeO_5$, $LaSrCoFeO_5F$ and $LaSrCoFeO_{5.5}$: new La–Sr–Co–Fe perovskites, *J. Mater. Chem.* **2010**, *20*, 3253-3259.

(24) Clemens, O.; Kuhn, M.; Haberkorn, R., Synthesis and characterization of the $La_{1-x}Sr_xFeO_{3-\delta}$ system and the fluorinated phases $La_{1-x}Sr_xFeO_{3-x}F_x$, *J. Solid State Chem.* **2011**, *184*, 2870-2876.

(25) Mitra, C.; Meyer, T.; Lee, H. N.; Reboredo, F. A., Oxygen diffusion pathways in brownmillerite $SrCoO_{2.5}$: Influence of structure and chemical potential, *The Journal of chemical physics* **2014**, *141*, 084710.

(26) Tsujimoto, Y.; Yamaura, K.; Hayashi, N.; Kodama, K.; Igawa, N.; Matsushita, Y.; Katsuya, Y.; Shirako, Y.; Akaogi, M.; Takayama-Muromachi, E., Topotactic Synthesis and Crystal Structure of a Highly Fluorinated Ruddlesden–Popper-Type Iron Oxide, $Sr_3Fe_2O_{5+x}F_{2-x}$($x \approx 0.44$), *Chemistry of Materials* **2011**, *23*, 3652-3658.

(27) Blakely, C. K.; Davis, J. D.; Bruno, S. R.; Kraemer, S. K.; Zhu, M.; Ke, X.; Bi, W.; Alp, E. E.; Poltavets, V. V., Multistep synthesis of the $SrFeO_2F$ perovskite oxyfluoride via the $SrFeO_2$ infinite-layer intermediate, *Journal of Fluorine Chemistry* **2014**, *159*, 8-14.

(28) Damay, F.; Martin, C.; Hardy, V.; Maignan, A.; André, G.; Knight, K.; Giblin, S. R.; Chapon, L. C., Zigzag ladders with staggered magnetic chirality in the S=3/2 compound β-$CaCr_2O_4$, *Phys. Rev. B* **2010**, *81*, 214405.

(29) Bhobe, P. A.; Chainani, A.; Taguchi, M.; Eguchi, R.; Matsunami, M.; Ohtsuki, T.; Ishizaka, K.; Okawa, M.; Oura, M.; Senba, Y.; Ohashi, H.; Isobe, M.; Ueda, Y.; Shin, S., Electronic structure of an antiferromagnetic metal: $CaCrO_3$, *Phys. Rev. B* **2011**, *83*, 165132.

(30) Cheng, J. G.; Sui, Y.; Zhou, J. S.; Goodenough, J. B.; Su, W. H., Transition from Orbital Liquid to Jahn-Teller Insulator in Orthorhombic Perovskites $RTiO_3$, *Phys. Rev. Lett.* **2008**, *101*, 087205.

(31) Zhou, J. S.; Ren, Y.; Yan, J. Q.; Mitchell, J. F.; Goodenough, J. B., Frustrated Superexchange Interaction Versus Orbital Order in a $LaVO_3$ Crystal, *Phys. Rev. Lett.* **2008**, *100*, 046401.

# Chapter 12

# Conclusions and Future Directions

The objective of the dissertation research was to use exploratory crystal growth to discover and structurally characterize new uranium oxide single crystals obtained through molten flux synthetic methods. Specifically, 3D salt inclusion materials (SIMs) were sought out due to their promising characteristics for nuclear waste form advancement as discussed in the introduction. This dissertation contains the synthesis and structural characterization of 50 new crystal structures, demonstrating the importance and effectiveness of using molten flux synthetic methods for materials discovery. Included in the 50 new materials are 13 uranyl germanate SIMs, the first two examples of uranyl phosphate SIMs, and the first example of a uranyl aluminophosphate SIM, in addition to seven 3D uranyl structures, 21 uranyl layered structures, three $U^{5+}$ containing perovskites, and three alkali gallates.

The thirteen germanate SIMs (**1.1-1.13)** were synthesized using similar synthetic approaches as discussed for the previously reported uranium silicate SIMs,[1, 2] which consisted of heating $UF_4$, $GeO_2$ in an alkali halide flux contained in silver tubes at typically 875 °C. This resulted in 12 compositions that adopt framework structures containing pyrogermanate groups, analogous to pyrosilicate groups reported in silicate SIMs, as well as one entirely new framework type. When compared to the silicates, the germanates are more readily obtained at higher temperatures (875 °C compared to 800 °C) and their synthesis can be carried out using pure chloride fluxes, which were ineffective for the synthesis of silicates that require the use of mixed chloride-fluoride fluxes in order to dissolve the $SiO_2$ starting materials.

In an effort to expand the structural variety and known library of uranium containing SIMs, additional network forming oxyanions were explored for incorporation

into the frameworks. Initially, phosphates were targeted due to their presence in many naturally occurring uranium minerals, indicating the tendency of uranium phosphates to form. In order to investigate the synthesis of uranyl phosphates, a phosphate starting material had to be chosen and a number of potential candidates were explored, namely, $Na_3PO_4$, $(NH_4)_2HPO_4$, and $AlPO_4$. The use of $Na_3PO_4$ frequently led to water soluble products (undesirable for potential wasteform materials) and $(NH_4)_2HPO_4$ was found to be incompatible with silver tube crucibles, resulting in the loss of their structural integrity. For these reasons, $AlPO_4$ was used primarily for all phosphate reactions and was used in a variety of reaction vessels including silver tubes, 5 mL alumina crucibles, 5 mL platinum crucibles, and 14 mL platinum crucibles at temperatures between 700-900 °C. As discussed in several chapters, the crucible size and crucible material were identified as significant variables affecting the formation of certain products. The use of the $AlPO_4$ starting material resulted in the synthesis of 17 new layered uranyl phosphates (**2.1**-**2.8**, **3.1**-**3.3**, **4.1**-**4.2**, **5.1**-**5.4**), one 3D uranium phosphate (**B.1**), three 3D uranyl aluminophosphates (**6.4**-**6.6**), and surprisingly, three new uranium oxyfluoride perovskites (**10.1**-**10.3**).

While all of the germanate compounds obtained were 3D SIMs, the majority of the phosphate structures crystallized as 2D layered structures that are generally related to the phosphuranylite or $U_3O_8$ type topologies. This is perhaps due to the tendency of uranium polyhedra to coordinate through the equatorial plane, which arises from the strong uranyl bonds, in addition to the unfavourability of obtaining P-O-P linkages under these synthetic conditions, as evidenced in general by the fact that there are few examples of structures obtained under similar conditions containing these linkages.[3] In fact, none of the 29 phosphate containing compositions described in this dissertation contain P-O-P linkages.

Unexpectedly, we were able to incorporate $AlO_4^{5-}$ tetrahedra using the $AlPO_4$ precursor, and despite the high energy barrier to creating Al-O-Al linkages in the presence of P as discussed in chapter 6, these linkages formed under the reaction conditions used and resulted in novel 3D structures.

Inspired by the success in obtaining aluminophosphates, attempts were made to obtain gallophosphates, uranium aluminates, and uranium gallates, which ultimately lead to the synthesis of **7.1**, **8.1-8.2**, and **9.1-9.3**. Structures **7.1** and **8.2**, $CsUO_2T_2O_5$ (T= Al, Ga), demonstrate the ability for Al and Ga to create condensed, 3D structures through T-O-T linkages, similar to trends seen in the uranyl silicates and germanates. In order to achieve the synthesis of gallium containing phases, alumina reaction vessels were avoided due to the slight solubility of $Al_2O_3$ in chloride melts leading, almost inevitably, to the incorporation of Al in the products. Fused silica and platinum reaction vessels of approximately the same dimensions as the alumina crucibles employed in the synthesis of the aluminophosphates were used, in addition to substituting $GaPO_4$ for $AlPO_4$. Although only two uranyl gallophosphate (**8.1-8.2**) compounds were obtained, the use of $GaPO_4$ led to several new uranyl phosphate compounds (**8.3-8.6**).

The work presented in this dissertation suggests several promising avenues to be further explored: firstly, the expansion of the uranium aluminate and gallate families, as there are only a handful of examples of U, Al, and U, Ga containing compounds and secondly, further characterization of some of the materials presented in this work. The ability to form 3D networks through T-O-T linkages is advantageous for the targeted synthesis of potential nuclear waste form materials and warrants further exploration. This thesis research only targeted the synthesis of U, Al and U, Ga materials through the use of

alkali halide fluxes, but there are many other suitable fluxes that could be explored for the synthesis of these materials. Additionally, the Al and Ga building blocks can be combined with other successful network formers such as, but not limited to, Si and Ge to expand structural variety.

While this dissertation primarily reports the synthesis and structures of new materials, several of the structures are well suited for further modification through ion exchange, and characterization through leach and stability studies in order to explore their suitability for potential nuclear waste form applications. Preliminary aqueous ion exchange experiments were performed on the majority of the structures obtained as part of this research, using alkali halide salt solutions; however, the nature of these studies was qualitative and did not rigorously investigate the extent to which ion exchange takes place, the kinetics of the processes, or the selectivity of the processes. Additionally, alkali halide salt solutions were used to target the exchange of one alkali species for another, and further studies could explore the potential of exchanging one alkali species for other monovalent, divalent, neutral species, or various combinations thereof.

Compositions from this work that are most interesting or particularly well-suited for further characterization are $[Cs_{13}Cl_5][(UO_2)_3Al_2O(PO_4)_6]$ (**6.3**), $[Rb_{5.93}Cl_{0.93}][(UO_2)_5(PO_4)_5]$ (**8.3**), $Rb_{11}[(UO_2)_8(PO_4)_9]$ (**8.4**), and $RbGa_4In_5O_{14}$ (**9.3**). $[Cs_{13}Cl_5][(UO_2)_3Al_2O(PO_4)_6]$ (**6.3**) can be made in gram quantities by solid state methods making it a particularly promising candidate for further studies. While EDS indicated aqueous ion exchange takes place in **6.3**, significant structural changes occurred as well and have not yet been elucidated and are important for understanding the ion exchange process and stability of the structure. Structures **8.3** and **8.4** where synthetically difficult to

isolate, but the nature of the channeled structures, especially the large channels with diameters of 9.44 Å in **8.4**, call for further study. I-129, in particular, is one radionuclide of interest to contain within porous structures yet, so far, it has not been achieved for this class of materials, likely due to iodine's large size. For that reason, the extremely large channels in **8.4** are promising candidates to house iodine ions. Aqueous ion exchange experiments on $RbGa_4In_5O_{14}$ (**9.3**) showed no sign of alkali exchange, which is a particularly promising characteristic since this is usually correlated with leach resistance; however, **9.3** was found to ion exchange in molten nitrates. As a potential Cs wasteform, molten nitrate ion exchange could be used to obtain the composition '$CsGa_4In_5O_{14}$' which would be of particular interest for further stability, leach, and aqueous ion exchange studies.

In summary, the exploratory molten flux synthesis of uranium oxides is a very fruitful research area and has resulted in a wide variety of structures and compositions in part due to the coordination chemistry of the uranyl ion. This dissertation illustrates how molten flux synthesis of these classes of materials is particularly sensitive to the crucible surface area to volume ratio in addition to the crucible material, heating temperature, and reagent ratio. The exploratory synthesis of new materials requires close attention to these variables and small changes in any one of these variables can result in the synthesis of other new materials. While the phase spaces of $UF_4$-$GeO_2$-alkali halide flux and $UF_4$-$TPO_4$-ACl (T = Al, Ga; A= alkali metal) were thoroughly explored as part of this dissertation research, these are very narrow regions of phase space and leave large areas in which to continue the exploratory molten flux synthesis of complex uranium oxides.

**References:**


(1) Morrison, G.; Smith, M. D.; zur Loye, H.-C., Understanding the Formation of Salt-Inclusion Phases: An Enhanced Flux Growth Method for the Targeted Synthesis of Salt-Inclusion Cesium Halide Uranyl Silicates, *J. Am. Chem. Soc.* **2016**, *138*, 7121-7129.

(2) Morrison, G.; zur Loye, H.-C., Flux Growth of $[NaK_6F][(UO_2)_3(Si_2O_7)_2]$ and $[KK_6Cl][(UO_2)_3(Si_2O_7)_2]$: The Effect of Surface Area to Volume Ratios on Reaction Products, *Cryst. Growth Des.* **2016**, *16*, 1294-1299.

(3) Alekseev, E. V.; Krivovichev, S. V.; Depmeier, W.; Knorr, K., Complex topology of uranyl polyphosphate frameworks: crystal structures of α-, β-$K[(UO_2)(P_3O_9)]$ and $K[(UO_2)_2(P_3O_{10})]$, *Z. Anorg. Allg. Chem.* **2008**, *634*, 1527-1532.

# Appendix A

## Understanding the Stability of Salt-Inclusion Phases for Nuclear Waste-forms through Volume-based Thermodynamic[1]

[1]Reproduced with permission from Moore, E. E.; Kocevski, V.; Juillerat, C. A.; Morrison, G.; Zhao, M.; Brinkman, K.; zur Loye, H.-C.; Besmann, T. *Scientific Reports* **2018**, *8,* 15294.

**Abstract:** Formation enthalpies and Gibbs energies of actinide and rare-earth containing SIMs with silicate and germanate frameworks are reported. Volume-based thermodynamics (VBT) techniques complemented by density functional theory (DFT) were adapted and applied to these complex structures. VBT and DFT results were in closest agreement for the smaller framework silicate structure, whereas DFT in general predicts less negative enthalpies across all SIMs, regardless of framework type. Both methods predict the rare-earth silicates to be the most stable of the comparable structures calculated, with VBT results being in good agreement with the limited experimental values available from drop solution calorimetry.

**Introduction.** Nuclear waste sequestration, including legacy materials from weapons programs as well as spent fuel from research reactors and potential commercial fuel recycling remains an important contemporary issue. While many reprocessing techniques exist, and repository solutions have been proposed, there is still a large research focus on how to more effectively and efficiently immobilize certain problematic radionuclides, especially those which are easily volatilized or for which waste glass loading is limited. A novel approach to simultaneously capturing multiple nuclear waste products includes the use of hierarchical architectures of porous materials. The working definition of a hierarchical material is that of a structural motif contained within a larger structure or framework. A class of materials that exhibit this structural characteristic include salt inclusion materials (SIMs).

Salt-inclusion materials exhibit a hierarchical structure that consists of a covalent mixed-oxide framework which contains a void filled with simple ionic salts. While traditional SIMs are characterized by transition metal oxides interconnected with oxyanion

units of groups 14 and 15 elements such as Si, Ge, As, P[1–5] more recently, uranyl[6–9] and lanthanide[10] salt-inclusion phases are being explored for nuclear waste applications due to their porous or "stuffed" nature. The framework allows for structural variability forming uranyl-based silicate, germanate, vanadate, phosphate or borate networks with various 3-D void sizes, which are filled with ionic salts that preferentially contain radionuclides. The general description of uranyl SIMs is the structural formula $[A_mB_nX][(UO_2)_p(M_qO_r)_t]$, where $[(UO_2)_p(M_qO_r)_t]$ is the framework consisting of uranyl cations, $UO_2^{2+}$, and $M_qO_r$ units (M = network forming ion such as Si or Ge), $B_nX$ is the salt-inclusion, and A are non-salt-inclusion cations. To widen the class of materials, ion exchange in SIMs can be performed to include targeted isotopic compositions.

Preparation of the framework materials take size and charge variations into account during synthesis; however, little is known about their thermodynamic stability, including formation enthalpies or Gibbs energies. For known phases, calorimetric methods can provide a direct measure of the formation energy of the materials, however to date there is no published literature on the thermodynamic properties of SIMs. Predictive thermodynamics is an attractive technique as it can provide insight into the thermodynamic stability of novel new structures such as SIMs, as well as guide the synthesis of newly formulated materials. Volume-based thermodynamics (VBT) is a tool developed by Glasser et al.[11–13] which serves to estimate thermodynamic parameters of a class of newly synthesized or even hypothetical materials when experimental thermochemical data are lacking and other theoretical modeling and simulation techniques are uncertain and can be computationally prohibitive. In this work we aim to provide a library of Gibbs energy values for a set of systems that encompass a multitude of different structural frameworks

and potential salt inclusions to effectively inform the sequestration of radionuclides for waste management. To our knowledge this is the first attempt to apply VBT to complex hierarchical structures such as salt-inclusion materials.

**Methods:**

**Volume Based Thermodynamics (VBT).** The VBT method incorporates empirical relations to generate estimated quantities of the standard entropy ($\boldsymbol{S^{\circ}_{298.15}}$), enthalpy of formation ($\Delta_f \boldsymbol{H^{\circ}_{298.15}}$) and Gibbs energy of formation ($\Delta_f \boldsymbol{G^{\circ}_{298.15}}$). The method uses crystallographic information from X-ray diffraction or density measurements if the formula mass is known, to obtain the volume per formula unit ($\boldsymbol{V_m}$). In this work the formula unit volume is calculated by dividing the volume of the unit cell $\boldsymbol{V_{cell}}$ (from a crystallographic information file; CIF) by the number of formula units Z in the unit cell so that $\boldsymbol{V_m = V_{cell}/Z}$. This quantity is then used in conjunction with derived thermodynamic cycles to calculate the formation energetics, as presented in the schematic of Figure A.1.

The standard entropy is calculated with Eq. 1, where the fitted constants **k** (J/K/mol/nm$^3$) and **c** (J/mol/K) are applied with the formula unit volume, with the constants varying as to whether the system is organic (liquid or solid) or ionic (hydrous or anhydrous). In this case we take the constants as fitted for anhydrous ionic salts.[11]

$$\boldsymbol{S^{\circ}_{298.15} = k\, V_m + c} \qquad \textbf{(1)}$$

A lattice potential energy is required which is calculated from Eq. 2 and is indicative of the ability of an ionic solid to form from components in the gaseous state, where the ionic strength factor $\boldsymbol{I}$ $\left(\boldsymbol{I = {}^{1}/_{2}\ \sum_i n_i z_i^2}\right)$ is calculated from the constituents of the salt and the

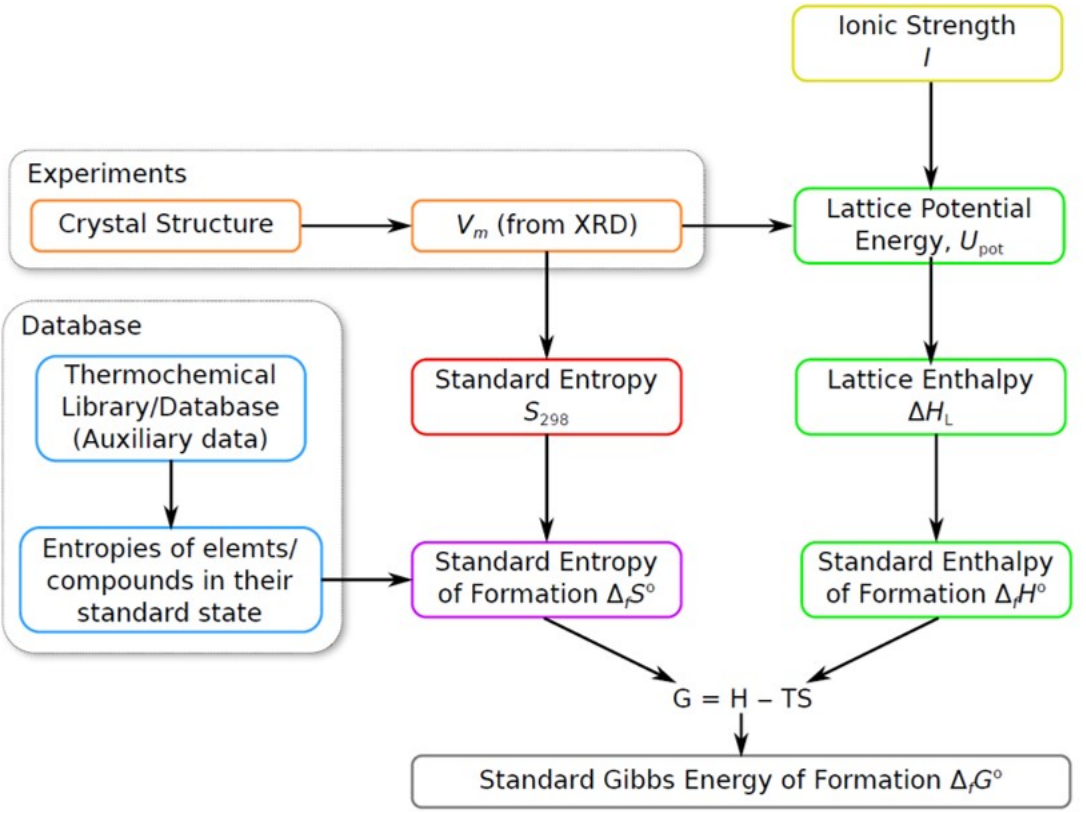


**Figure A.1:** Schematic for calculating thermodynamic values from VBT methods

salt-inclusion framework and their respective charges, with $n_i$ being the number of ion types, $z_i$ their respective charge; and $A$ the standard electrostatic Madelung constant (121.39 nm kJ/mol).[11, 12, 14]

$$U_{pot} = A\, I\, (2I/V_m)^{1/3} \quad (2)$$

The lattice energy is then converted into a useable enthalpic value by a multiplicative RT term that includes information on the ion types ($s_i$) and a constant ($c_i$) related to whether the ion types are monoatomic, polyatomic (linear or non-linear) as shown in Eq. 3, with $R$ being the ideal gas constant and $T$ the temperature in Kelvin.

$$\Delta H_L = U_{pot} + \sum_{i=1}^{n} s_i \left(\frac{c_i}{2} - 2\right) RT \quad (3)$$

**Table A.1:** Collection of auxiliary data for use in Born-Haber-Fajans cycle

| *Species* | $\Delta_f H_{gas}/\Delta H_{sub}$ *[kJ/mol]* | *IP [kJ/mol]* | *IP (2nd) [kJ/mol]* | *IP (3rd) [kJ/mol]* | $\Delta H_{dis}$ *[kJ/mol]* | *EA [kJ/mol]* | $S^{\circ}_{298.15}$ *[J/mol/K]* |
|---|---|---|---|---|---|---|---|
| $UO_2$ (s) | -462.[15] | 591.3[16] | 1380[17] | --- | --- | --- | 77.03[15] |
| Gd | 406.9[15] | 593.4[16] | 1166.5[16] | 1990.5[16] | --- | --- | 68.1[15] |
| Eu | 178.2[15] | 547.1[16] | 1084.6[16] | 2404.4[16] | --- | --- | 77.8[15] |
| $SiO_2$ (s) | -305.4[18] | --- | --- | --- | --- | -195.9[19] | 41.5[18] |
| $Si_2O_5^{2-}$ (g) | -1833.9[DFT] | --- | --- | --- | --- | --- | --- |
| $GeO_2$ (s) | -106.2[20] | --- | --- | --- | --- | -241.2[21] | 39.7[22, 23] |
| GeO (g) | -37.7[20] | --- | --- | --- | --- | -13.8[24] | --- |
| $Ge_2O_5^{2-}$ (g) | -1644.7[DFT] | --- | --- | --- | --- | --- | --- |
| $O_2$ (g) | 0 | --- | --- | --- | 493.6[23] | -42.5[18] | 205.2[18] |
| O (g) | 249.2[18] | --- | --- | --- | --- | -141.0[18] | 161.1[18] |
| Na (s) | 107.3[18] | 495.8[18] | --- | --- | --- | --- | 51.46[18] |
| K (s) | 89.0[18] | 418.8[18] | --- | --- | --- | --- | 65.67[18] |
| Rb (s) | 80.9[18] | 403.0[18] | --- | --- | --- | --- | 76.78[18] |
| Cs (s) | 76.5[18] | 375.7[18] | --- | --- | --- | --- | 85.15[18] |
| Ag (s) | 284.8[25] | 731.0[26] | --- | --- | 157.7[25] | --- | 42.48[25] |
| $F_2$ (g) | 0 | --- | --- | --- | 154.6[18] | -328.0[18] | 202.8[18] |
| $Cl_2$ (g) | 0 | --- | --- | --- | 239.2[18] | -349.0[18] | 223.1[18] |
| $Br_2$ (g) | 0 | --- | --- | --- | 190.2[18] | -324.7[18] | 152.2[18] |

The Born-Haber-Fajans cycle, which applies Hess' law is then used to calculate the standard enthalpy of formation in which the constituents of the salt-inclusion material are broken down into their gaseous ionic counterparts, where the salt inclusion components are broken down into their elemental state, and the framework consists of constituents in various oxide forms. Information regarding the gaseous components from the solid phase are obtained from auxiliary information in Table A.1 and include enthalpies of sublimation or dissociation, combined with ionization potentials (IP) or electron affinities (EA) for cationic and anionic species respectively, which are found in the literature.[27, 28] The summation of these energies in the gas state along with the lattice enthalpy (Eq. 4) results in a value for the standard enthalpy of formation. The latter value then allows for the

calculation of the Gibbs energy of formation by applying auxiliary information for the standard entropy to Eq. 1.

$$\Delta_f H^{\circ}_{298.15} = \Delta H_{sub} + IP + \Delta H_{dis} + EA + \Delta H_L \quad (4)$$

A mixing entropy accounts for the combining of the different components of the salt, where contributions of partially occupied and mixed salts are naturally greater than those with a single cation type. The relation is seen in Eq. 5, where $n$ is the total number of moles and $x_i$ is the mole fraction of each constituent.

$$S_{mix} = -nR \sum_i x_i ln(x_i) \quad (5)$$

**Table A.2:** List of SIMs treated using VBT, along with the crystallographic data to calculate the formula unit volume ($V_m$)

| Salt inclusion structure | $V_{cell}$ (Å$^3$) | Z | $V_m$ (Å$^3$) |
|---|---|---|---|
| $[Cs_3F][(UO_2)(Si_4O_{10})]$[9] | 1542.68 | 4 | 385.7 |
| $[Cs_9Cs_6Cl][(UO_2)_7(Si_6O_{17})_2(Si_4O_{12})]$[9] | 1890.08 | 1 | 1890.1 |
| $[NaK_6F][(UO_2)_3(Si_2O_7)_2]$[8] | 1139.71 | 2 | 569.9 |
| $[KK_6Cl][(UO_2)_3(Si_2O_7)_2]$[8] | 1184.82 | 2 | 592.4 |
| $[NaRb_6F][(UO_2)_3(Si_2O_7)_2]$[7] | 1187.73 | 2 | 593.9 |
| $[K_3Cs_4F][(UO_2)_3(Si_2O_7)_2]$[7] | 2451.13 | 4 | 612.8 |
| $[Cs_2Cs_5F][(UO_2)_3(Si_2O_7)_2]$[9] | 1382.41 | 2 | 691.2 |
| $[Cs_2Cs_5F][(UO_2)_2(Si_6O_{17})]$[9] | 1436.05 | 2 | 718.0 |
| $[Na_9F_2][(UO_2)(UO_2)_2(Si_2O_7)_2]$[5] | 516.53 | 1 | 516.5 |
| $[Cs_2Cs_5F][(UO_2)_3(Ge_2O_7)_2]$[29] | 1451.65 | 2 | 725.83 |
| $[Cs_6\ Ag_2Cl_2][(UO_2)_3(Ge_2O_7)_2]$[29] | 1450.41 | 2 | 725.21 |
| $[Cs_6\ Ag_{0.3}Na_{1.7}Cl_2][(UO_2)_3(Ge_2O_7)_2]$[29] | 1444.51 | 2 | 722.26 |
| $[Cs_6\ Ag_{0.4}Na_{1.6}Cl_2][(UO_2)_3(Ge_2O_7)_2]$[29] | 1445.17 | 2 | 722.59 |
| $[Cs_6K_2Cl_2][(UO_2)_3(Ge_2O_7)_2]$[29] | 1460.71 | 2 | 730.36 |
| $[Cs_6K_{1.9}Ag_{0.1}Cl_2][(UO_2)_3(Ge_2O_7)_2]$[29] | 1476.60 | 2 | 738.30 |
| $[KK_6Cl][(UO2)3(Ge_2O_7)_2]$[29] | 1257.44 | 2 | 628.72 |
| $[KK_6Br_{0.6}F_{0.4}][(UO_2)_3(Ge_2O_7)_2]$[29] | 1263.60 | 2 | 631.80 |
| $[Na_{0.9}Rb_{6.1}F][(UO_2)_3(Ge_2O_7)_2]$[29] | 1261.39 | 2 | 630.70 |
| $[K_{0.6}Na_{0.4}K_5CsCl_{0.5}F_{0.5}][(UO_2)_3(Ge_2O_7)_2]$[29] | 1258.66 | 2 | 629.33 |
| $[K_{0.8}Na_{0.2}K_{4.8}Cs_{1.2}Cl_{0.5}F_{0.5}][(UO_2)_3(Ge_2O_7)_2]$ | 1264.30 | 2 | 632.15 |
| $[KK_{1.8}Cs_{4.2}F][(UO_2)_3(Ge_2O_7)_2]$[29] | 2612.41 | 4 | 653.10 |
| $[Cs_6Cs_{0.71}Cl_{0.71}][(UO_2)_3(Ge_2O_7)O_3]$[29] | 1294.40 | 2 | 647.20 |
| $[K_2K_7F_2]\ [Eu_3Si_{12}O_{32}]$[10] | 888.39 | 1 | 888.39 |
| $[K_2K_7F_2][Gd_3Si_{12}O_{32}]$[10] | 888.87 | 1 | 888.87 |

The VBT approach was applied to three different classes of salt-inclusion frameworks: Uranyl silicates (9 compounds) uranyl germanates (13 compounds) and rare-earth silicates (2 compounds). The compositions were obtained from the literature or synthesized by the methods described in,[9, 29] and are listed in Table A.2 along with $V_m$ values derived from available crystallographic information.

**Density Functional Theory (DFT)**. The DFT calculations were performed using the code VASP, with the Perdew-Burke-Ernzerhof (PBE) generalized-gradient approximation,[30] employing the projector augmented plane wave (PAW) method.[31, 32] For calculating the enthalpies of formation of $Si_2O_5^{2-}$ and $Ge_2O_5^{2-}$ we considered the systems to be composed of a 2D sheet formed by two $SiO_4$ and $GeO_4$ tetrahedra, with three corner sharing O atoms and a -2*e* charge. Considering that the U atoms are surrounded by O atoms, we chose a value of $\boldsymbol{U_{eff}}$ = 4.0 eV, which is a $\boldsymbol{U_{eff}}$ value that is close to that obtained from experimental studies for $UO_2$[33, 34] and has been proven to well-reproduce the structural parameters and band gaps of for $UO_3$ polymorphs.[35–37] The calculations were performed using 12×12×1 *k*-point mesh, 520 eV cutoff energy for the planewave basis set, and $10^{-8}$ eV and 0.001 Å/eV energy and forces convergence criteria, respectively, allowing the systems to fully relax (volume, cell shape and ionic positions). [38, 39] For the SIMs the calculations utilized a 500 eV planewave energy cutoff, $10^{-6}$ energy convergence criteria, *k*-point mesh with 3000 KPPRA (k-point density per reciprocal atom), and fully relaxed systems.

**Thermochemical Cycles**. Each of the SIMs frameworks are broken down into individual constituents based on the available auxiliary information, where silicate and germanate oxide constituents are initially limited to $SiO_2$/$GeO_2$ and SiO/GeO components

with a single negative charge. To obtain a better representation of the silicate $SiO_4$, and germanate $GeO_4$ tetrahedra, which often arrange in $Si_4O_{10}$ and $Ge_4O_{10}$ columns, the components $Si_2O_5^{2-}(g)$ and $Ge_2O_5^{2-}$ are needed and thus density functional theory (DFT) calculations were performed to calculate the formation enthalpy of these constituents for which no information is available. The anion frameworks are charge-balanced by varying the oxidation state of uranium in the uranyl cations so that the overall salt-framework is neutral. An example of a balanced Born-Haber-Fajans cycle used to calculate the $\Delta_f H^{\circ}_{298.15}$ is depicted in Figure A.2. The remaining constituents that make up the various silicate, germanate and rare-earth framework cycles are reported in Table A.3, where the single-ion values that make up the salt-inclusions are directly taken from the auxiliary data table.

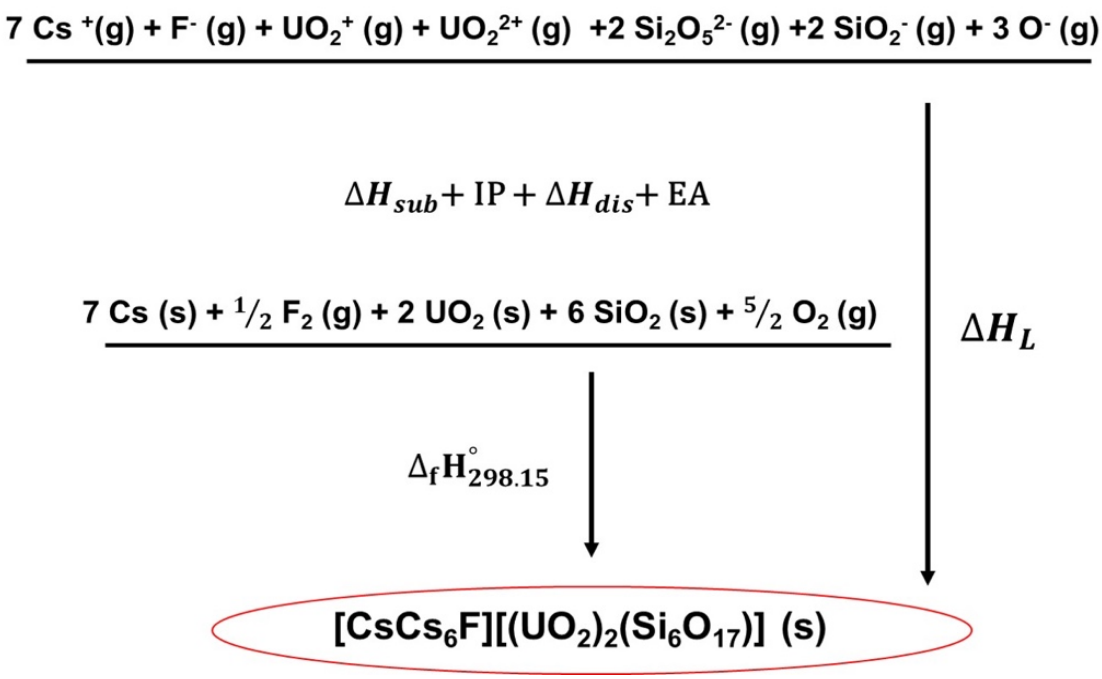


**Figure A.2:** Thermochemical cycle for a uranyl silicate salt inclusion.

**Table A.3:** Thermochemical cycles for SIMs framework components

| Framework Structure | Charge | Thermocycle components |
|---|---|---|
| $[(UO_2)(Si_4O_{10})]$ | 2- | $UO_2^{2+}$ (g) + 2 $Si_2O_5^{2-}$ (g) |
| $[(UO_2)_7(Si_6O_{17})_2(Si_4O_{12})]$ | 14- | 4 $UO_2^{+}$ (g) +3 $UO_2^{2+}$ (g) +6 $Si_2O_5^{2-}$ (g) +4 $SiO_2^{-}$ (g) + 8 $O^{-}$ (g) |
| $[(UO_2)_3(Si_2O_7)_2]$ | 6- | 3 $UO_2^{+}$ + $Si_2O_5^{2-}$ (g) +2 $SiO_2^{-}$ (g) + 5 $O^{-}$ (g) |
| $[(UO_2)_2(Si_6O_{17})]$ | 6- | $UO_2^{+}$ (g) + $UO_2^{2+}$ (g) +2 $Si_2O_5^{2-}$ (g) +2 $SiO_2^{-}$ (g) + 3 $O^{-}$ (g) |
| $[(UO_2)(UO_2)_2(Si_2O_7)_2]$ | 7- | 3 $UO_2^{+}$ (g) +4 $SiO_2^{-}$ (g) + 6 $O^{-}$ (g) |
| $[(UO_2)_3(Ge_2O_7)_2]$ | 6- | $UO_2^{2+}$ (g) + 2 $UO_2^{+}$ (g) + 4 $GeO_2^{-}$ (g) + 6$O^{-}$ (g) |
| $[(UO_2)_3\ O_3(Ge_2O_7)]$ | 6- | 3 $UO_2^{+}$ (g) + $GeO_2^{-}$(g) + $GeO^{-}$ (g) + 7 $O^{-}$ (g) |
| $[Ln_3Si_{12}O_{32}]$ (Ln= Eu or Gd) | 7- | 2 $Ln^{2+}$ (g) + $Ln^{3+}$ (g) +6 $Si_2O_5^{2-}$ (g) +2 $O^{-}$ (g) |

**Results and Discussion:**

The lattice potentials calculated using Eq. 2 are plotted as a function of the formula unit volume for the available SIMs in Figure A.3. The uranyl silicate materials include more versatile framework structures, where different charged frameworks and salts are considered. Both the lanthanoid (Ln) silicates and uranyl germanates (except for one structure) have the exact same framework composition. The increased variance of the salt inclusions, including their charge and composition, allows for a range of differently charged uranyl-silicate frameworks, which dictates the lattice stability, which is largely dependent on the ionic strength factor. Conversely, the germanate SIMs have identical frameworks for twelve of the thirteen structures. For both silicates and germanates with self-same frameworks, the lattice potential decreases with increasing $V_m$, as it is inversely proportional to its cube root of the value (see Eq. 2) and the ionic strength factor is less influential due to the similarity of the salt-inclusions. The $\Delta_f H^{\circ}_{298.15}$ are calculated using the auxiliary information in Table A.1 and are compared with experiment and values calculated by DFT in Table A.4. Only salt inclusions which did not have partial

occupancies were computed by DFT as the significantly larger unit cell required for considering partial occupancies made the calculations prohibitively computationally intensive. The $\Delta_f H^\circ_{298.15}$ value was also calculated with VBT using volumes derived from DFT relaxed structures, the energies are compared in Figure A.4. The VBT $\Delta_f H^\circ_{298.15}$ values plus the standard entropy calculated from Eq. 1 provide the Gibbs energy of formation, both of which are listed in Table A.4 and the latter depicted in Figure A.5. The energies include the mixing entropy of the salt-components as noted above and as was demonstrated in Juillerat et al.[40] for alkali metals.

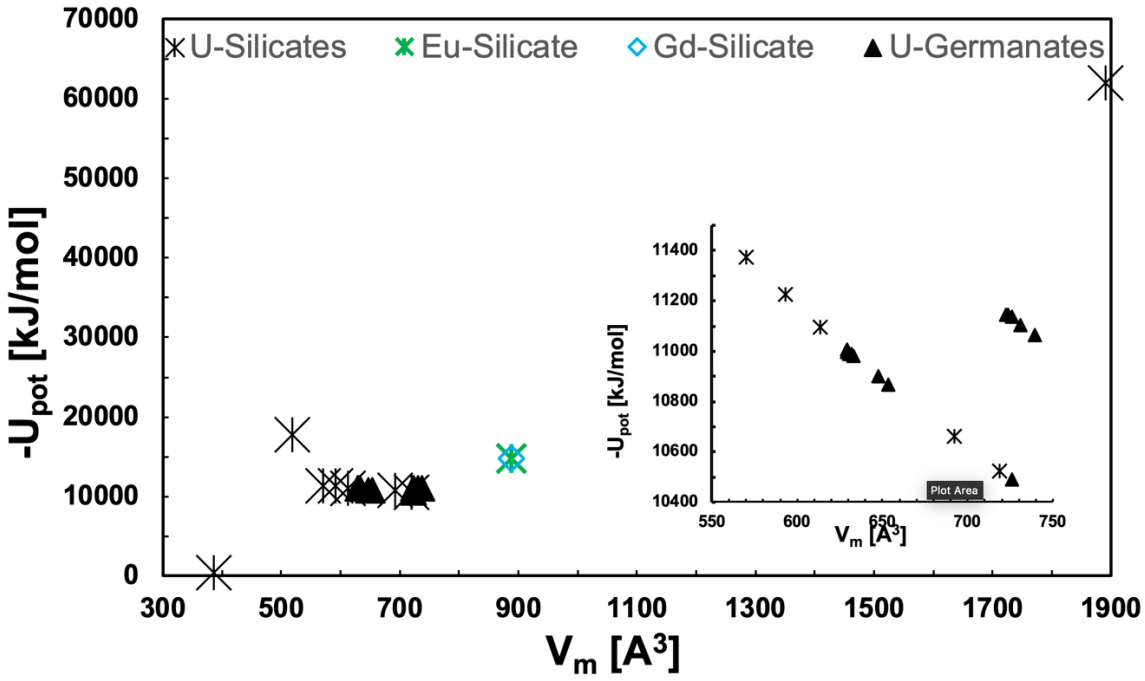


**Figure A.3:** Lattice potential energy ($U_{pot}$) as a function of $V_m$ for SIMs, the inset shows the Ge and Si frameworks with $V_m$ between 550-750 Å$^3$

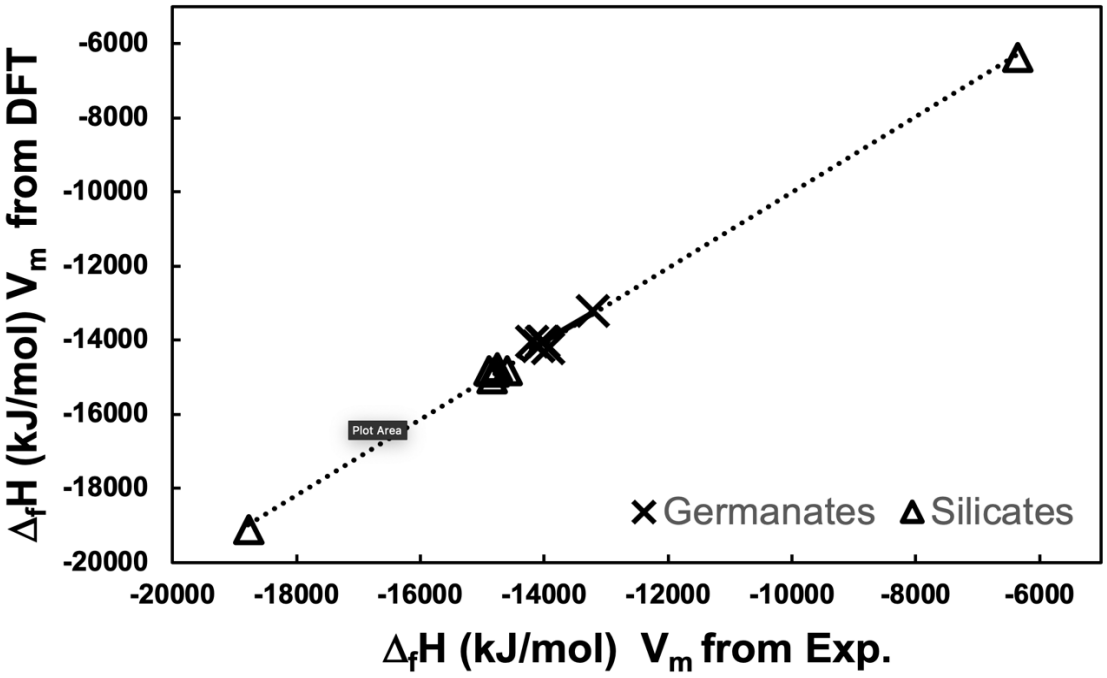


**Figure A.4:** VBT computed formation enthalpies using experimental and DFT calculated $V_m$.

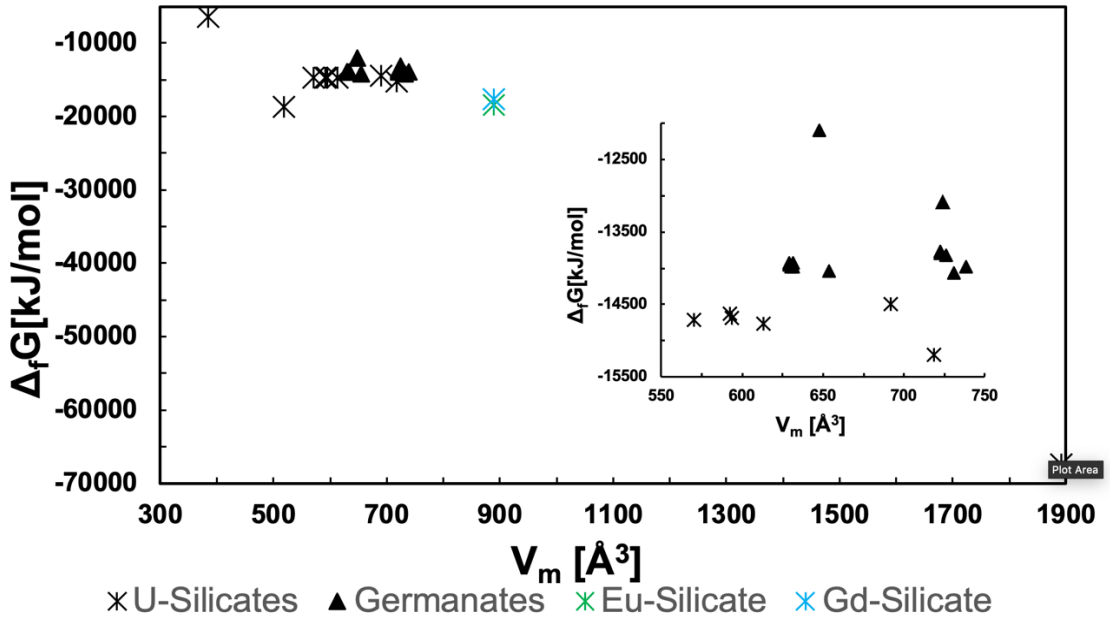


**Figure A.5:** Gibbs energy of formation as a function of $V_m$ for silicate and germanate SIMs. The inset shows the Ge and Si frameworks with $V_m$ between 550-750 Å$^3$.

**Table A.4:**Enthalpies of formation, Gibbs energies of formation, and standard entropies of SIMs from VBT compared with DFT and Experiment.

| Salt inclusion structure | $\Delta_f H^\circ_{298.15}$ (VBT) | $\Delta_f H^\circ_{0K}$ (kJ/mol) | $\Delta_f H^\circ_{298.15}$ (Exp) | $S_{298.15}$ (J/mol/K) | $\Delta_f G^\circ_{298.15}$ (kJ/mol) |
|---|---|---|---|---|---|
| $[Cs_3F][(UO_2)(Si_4O_{10})]$ | -6361 | -5719 | | 539.5 | -6344 |
| $[Cs_9Cs_6Cl][(UO_2)_7(Si_6O_{17})_2(Si_4O_{12})]$ | -67501 | | | 2585.5 | -67346 |
| $[NaK_6F][(UO_2)_3(Si_2O_7)_2]$ | -14833 | -9297 | | 790.0 | -14717 |
| $[KK_6Cl][(UO_2)_3(Si_2O_7)_2]$ | -14762 | -9214 | | 820.7 | -14644 |
| $[NaRb_6F][(UO_2)_3(Si_2O_7)_2]$ | -14821 | -9368 | | 822.7 | -14693 |
| $[K_3Cs_4F][(UO_2)_3(Si_2O_7)_2]$ | -14879 | -9254 | | 848.4 | -14757 |
| $[Cs_2Cs_5F][(UO_2)_3(Si_2O_7)_2]$ | -14609 | | | 955.0 | -14488 |
| $[Cs_2Cs_5F][(UO_2)_2(Si_6O_{17})]$ | -15262 | -9690 | | 991.5 | -15185 |
| $[Na_9F_2][(UO_2)(UO_2)_2(Si_2O_7)_2]$ | -18782 | -9930 | | 717.5 | -18616 |
| $[Cs_2Cs_5F][(UO_2)_3(Ge_2O_7)_2]$ * | -13931 | -7909 | | 1002.1 | -13826 |
| $[Cs_6\ Ag_2Cl_2][(UO_2)_3(Ge_2O_7)_2]$ * | -13202 | -7760 | | 1001.3 | -13084 |
| $[Cs_6\ Ag_{0.3}Na_{1.7}Cl_2][(UO_2)_3(Ge_2O_7)_2]$ * | -13919 | | | 997.3 | -13797 |
| $[Cs_6\ Ag_{0.4}Na_{1.6}Cl_2][(UO_2)_3(Ge_2O_7)_2]$ * | -13876 | | | 997.7 | -13755 |
| $[Cs_6K_2Cl_2][(UO_2)_3(Ge_2O_7)_2]$ * | -14192 | -8338 | | 1008.3 | -14063 |
| $[Cs_6K_{1.9}Ag_{0.1}Cl_2][(UO_2)_3(Ge_2O_7)_2]$* | -14101 | | | 1019.1 | -13977 |
| $[KK_6Cl][(UO2)_3(Ge_2O_7)_2]$ ¥ | -14035 | -7870 | | 870.1 | -13931 |
| $[KK_6Br_{0.6}F_{0.4}][(UO_2)_3(Ge_2O_7)_2]$ ¥ | -14017 | -7914 | | 874.2 | -13923 |
| $[Na_{0.9}Rb_{6.1}F][(UO_2)_3(Ge_2O_7)_2]$ ¥ | -14105 | -8012 | | 872.7 | -13992 |
| $[K_{0.6}Na_{0.4}K_5CsCl_{0.5}F_{0.5}][(UO_2)_3(Ge_2O_7)_2]$ ¥ | -14060 | | | 870.9 | -13965 |
| $[K_{0.8}Na_{0.2}K_{4.8}Cs_{1.2}Cl_{0.5}F_{0.5}][(UO_2)_3(Ge_2O_7)_2]$ | -14074 | | | 874.7 | -13977 |
| $[KK_{1.8}Cs_{4.2}F][(UO_2)_3(Ge_2O_7)_2]$ ¥ | -14151 | | | 903.2 | -14049 |
| $[Cs_6Cs_{0.71}Cl_{0.71}][(UO_2)_3(Ge_2O_7)O_3]$ § | -12202 | | | 895.2 | -12082 |
| $[K_2K_7F_2]$ $[Eu_3Si_{12}O_{32}]$ | -18594 | -16267 | | 1223.2 | -18436 |
| $[K_2K_7F_2][Gd_3Si_{12}O_{32}]$ | -17935 | -15978 | -17389[41] | 1223.9 | -17725 |

*monoclinic, ¥orthorhombic, §hexagonal (distinctions are made for germanates of equal charged frameworks)

The results in Table A.4 indicate relatively good agreement between DFT and VBT values for the formation enthalpy of $[Cs_3F][(UO_2)(Si_4O_{10})]$, whereas the formation enthalpies for the other uranyl-silicates derived using VBT are much more negative (more thermodynamically stable) than those calculated from DFT. However, both methods predict the following trend in framework energetics:

$$[(UO_2)(Si_4O_{10})]^{2-} < [(UO_2)_3(Si_2O_7)_2]^{6-} < [(UO_2)_2(Si_6O_{17})]^{6-} < [(UO_2)(UO_2)_2(Si_2O_7)_2]^{7-}$$

This indicates that for the silicates, the charge on the framework (which contributes to a higher ionic strength factor) and the overall size of the system (such as the total number of atoms per formula unit), influences the thermodynamic stability. More negatively charged frameworks that allow for larger salt inclusions have a more negative enthalpy of formation. With equivalently charged frameworks, the silicon-rich system is found to be more stable than its uranium-rich counterpart, according to both DFT and VBT. The VBT values for $[(UO_2)_3(Si_2O_7)_2]^{6-}$ and $[(UO_2)_2(Si_6O_{17})]^{6-}$ framework types with identical $Cs_2Cs_5F$ salt inclusion, imply that the silicon-rich composition is more thermodynamically stable (has a more negative formation enthalpy). While the increased negative value in formation enthalpy (+4.3 %) might be attributed to the increase in $V_m$ (+3.8%) for the silicon-rich framework, it seems more likely that the choice of constituents for the utilized thermodynamic cycle are more influential. In the case of the silicon rich $[(UO_2)_2(Si_6O_{17})]^{6-}$ framework the cycle includes the use of $UO_2^{2+}$, which has a greater impact on the formation energetics, since both the first and second ionization potentials are included. The silicon rich framework allows for a better representation of the structure by including both Si and U in their proper $Si^{4+}$ and $U^{6+}$ oxidation states respectively. This work attempts to use $U^{VI}$ ions in the thermodynamic cycles whenever possible as it is a more realistic description of

the system, since all frameworks but one contain this oxidation state of the uranyl cation. Nevertheless, given the limitations of the auxiliary information, $UO_2^{2+}$ is not always represented as such in the VBT cycles. As indicated in Table A.3, in order to properly charge-balance the system, only a singly charged uranyl cation ($UO_2^{+}$) is often used.

Equivalent frameworks in both composition and charge differ only in the salt-inclusion which dictates $V_m$, where the $Cs_2Cs_5F$ salt-inclusion results in a much larger $V_m$ (15.4%) compared to the other four $NaK_6F$, $KK_6Cl$, $Na_{0.9}Rb_{6.1}F$, $K_3Cs_4F$ salt compositions. The average framework $V_m$ was calculated as 508.0 ± 23.3 $Å^3$, where the thermochemical radii of the alkali metals and halides are used to compute the $V_m$ of the salt-inclusions. The volume of the salt is then subtracted from the overall formula unit volume of the five identical framework materials, which are then averaged. The larger formula unit volume of the pure cesium containing ($Cs_2Cs_5F$) SIM leads to a formation enthalpy that is less negative than its four counterparts; a similar trend was found in,[40] where larger alkali inclusions (and therefore $V_m$ values) resulted in less negative formation enthalpies. For the remaining SIMs of the $[(UO_2)_3(Si_2O_7)_2]^{6-}$ family, both DFT and VBT predict that the chlorine containing $KK_6Cl$ salt is the least stable structure and the $NaK_6F$ salt-inclusion is the second most stable structure. DFT predicts the $NaRb_6F$ to have the most negative formation enthalpy, whereas VBT predicts the mixed $K_3Cs_4F$ salt to be the most stable. A similar result was obtained for the mixed $KK_{1.8}Cs_{4.2}F$ salt in the monoclinic germanate framework presented below.

The uranyl germanate framework, $[(UO_2)_3(Ge_2O_7)_2]^{6-}$, is analogous to the silicate framework, $[(UO_2)_3(Si_2O_7)_2]^{6-}$, and twelve different salt inclusions have been incorporated into this framework producing structures in either the orthorhombic or monoclinic setting.

A lone hexagonal structure with a different framework, $[(UO_2)_3O_3(Ge_2O_7)]^{6-}$ has also been synthesized (the experimental results of all uranyl germanate SIMs are detailed in Juillerat et al. 2018).[29] The enthalpies of formation of the DFT and VBT values are listed in Table A.4 and overall are less negative than those for the silicates with a similar framework composition. DFT values predict the average formation enthalpies of the $[(UO_2)_3(Si_2O_7)_2]^{6-}$ silicates (-9365 kJ/mol) to be more negative by 16.1% than the $[(UO_2)_3(Ge_2O_7)_2]^{6-}$ germanates (-7967 kJ/mol), whereas VBT predicts a difference of 5.6% between the silicates (-14781 kJ/mol) and germanates (-13972 kJ/mol). Yet the effects of the choice of constituents for the thermochemical cycles, i.e., using $GeO^-/GeO_2^-$ and $SiO^-/SiO_2^-$ reveals that large discrepancies can arise. This highlights the importance and limitations of the auxiliary information when calculating the thermodynamic cycles, especially the need to charge balance the framework components.

VBT predicts the orthorhombic structures in general to be slightly more stable than monoclinic structures. This could in part be due to the symmetry of the structures (i.e., orthorhombic crystal systems have higher symmetry than monoclinic) or the difference in the salt-inclusions. All of the systems with monoclinic symmetry consist of dihalide salts (except for the $Cs_2Cs_5F$) and are cesium rich, whereas the orthorhombic structures generally incorporate less cesium and exclusively include only single halide salts. For the monoclinic structures calculated by DFT, the trends in relative stability are in agreement with the results from VBT, such that the silver containing structure is the least stable, followed by the pure cesium compound. As with the silicates, VBT predicts the K-Cs salt to be the most stable composition, where the salt-inclusion consists of $Cs_6K_2Cl_2$ in the monoclinic form and $KK_{1.8}Cs_{4.2}F$ in the orthorhombic form. DFT also predicts the

monoclinic $Cs_6K_2Cl_2$ salt-inclusion germanate structure to be the most stable. VBT suggests that the increase in silver content leads to less stable structures, as the formation energetics of silver ions is much larger than that of any of the alkali metals. For the orthorhombic structures calculated using both VBT and DFT (which include the following salt structures: $KK_6Cl$, $KK_6Br_{0.5}F_{0.5}$ and $Na_{0.9}Rb_{6.1}F$), the $Na_{0.9}Rb_{6.1}F$ structure was found to be most stable by both VBT and DFT, where DFT treated the salt-inclusion as fully occupied $Na_1Rb_6F$. The remaining two structures are comparable, differing only in the variation of the halide ($KK_6Cl$ vs $KK_6Br_{0.5}F_{0.5}$) with the mixed Br-F halide calculated to be more stable by DFT, which is the reverse for the VBT results, although both methods each predict very similar energies. Note that the DFT calculations for partial/mixed occupancies can be problematic as they demand significantly larger unit cells which are prohibitively computationally expensive, since both structure types include salts that have partial occupancies, only half of both the monoclinic and orthorhombic SIMs could be treated with DFT. The hexagonal structure with lower germanate content is predicted to have the least negative formation enthalpy of the germanate compounds, indicating that the uranium rich composition is significantly less stable than the other synthesized framework compositions. This is analogous to the uranyl silicate results, where Si-rich (or U-poor) frameworks are more stable than the uranium rich compositions for frameworks of identical charge.

With respect to the rare earth SIMs, experimental information regarding the formation enthalpies of one of the Ln-silicate structures, $[K_2K_7F_2][Gd_3Si_{12}O_{32}]$, is reported.[41] The VBT $\Delta_f H^{\circ}_{298.15}$ value from the elements for the SIM is in good agreement with that obtained by drop solution calorimetry (Table A.4). Both VBT and DFT predict

that the Eu-containing silicate is more stable than its Gd-analogue, however DFT under-predicts the values compared to experiment (for Gd-SIM) and VBT. For all of the SIMs considered here, VBT generally predicts more negative enthalpies of formation compared to DFT, however general trends are in agreement for the silicates, germanates and Ln-silicates.

Note that the formation enthalpies were calculated using $V_m$, from DFT relaxed structures, if experimental data on the crystal structure is lacking. A comparison in the results from using $V_m$, values from experimental and DFT computed structures for the uranyl silicate and germanate systems is found in Figure A.4. Overall, the volumes calculated with DFT lead to minor differences in the VBT computed energies, with a variation of no more than 2 percent. Most of the values computed with DFT-determined volumes are more negative (more stable) than those computed with experimental values for both silicates and germanate structures.

The formation enthalpies for DFT are calculated in vacuum at 0 K, however, to include temperature dependence and entropic contributions are out of the scope of this work as they are too computationally demanding and not every salt-inclusion can be treated since partial occupancies pose a problem when generating the structures. VBT does however, produce entropic values that allow calculating the Gibbs energy of formation of each of the respective compositions (Table A.4 and Figure A.5). The trends for the Gibbs energies remain consistent with those calculated for the formation enthalpies in that the silicates are found to be the more thermodynamically stable structures, except for one composition, which has a much smaller $V_m$ and salt-inclusion compared to the rest of the structures considered. Similarly, more negatively charged framework structures have

increased stability, where the impact of the overall charge of salt-inclusion influences this stability, i.e., more ions within the salt-inclusion increase the ionic strength factor, which contributes to the lattice potential used for these calculations.

**Conclusions.** In this work we compute relative stabilities of complex hierarchical structures for waste sequestration using computationally inexpensive techniques that rely on sound thermodynamic correlations. The enthalpies and Gibbs energies of formation of 24 SIMs were calculated using VBT methods and compared to the enthalpies of formation from DFT and experimental results when available. VBT and DFT results were in closest agreement for the smaller framework silicate structure, whereas DFT in general predicts less negative enthalpies across all SIMs, regardless of framework type. The uranyl-germanate structures were found to be slightly less thermodynamically stable than their silicate analogues. Both methods predict the Ln-silicates to be the most stable of the comparable structures calculated, with VBT results being in good agreement with an available experimental value from drop solution calorimetry. Additionally, DFT was used to calculate some of the framework components used in the thermochemical cycles for the volume-based methods. This allowed for a more physical representation of the structural units seen in experiment. As auxiliary information on $SiO/SiO_2$ and $GeO/GeO_2$ building blocks are limited to singly charged species, DFT aids in obtaining information on higher oxidation states, which are necessary to charge balance these complex systems. While certain thermochemical cycles yield VBT values in better agreement with DFT results, discrepancies still exist between the absolute values of both methods. Similarly, implementation of $\boldsymbol{U_{eff}}$ in DFT, as is standard for f-electron systems, leads to lower (more negative) formation energies, however this does not resolve the disparity as the values

calculated with $U_{eff}$= 4.0 eV are only about ~ 100 kJ/mol lower than those computed using $U_{eff}$= 0 eV. Improvements in the thermochemical cycles of VBT and manipulation of the $U_{eff}$ values might produce better agreement.

**Acknowledgements**. Research was conducted by the Center for Hierarchical Waste Form Materials (CHWM), an Energy Frontier Research Center (EFRC). Research was supported by the U.S. Department of Energy, Office of Basic Energy Sciences, Division of Materials Sciences and Engineering under Award DE-SC0016574.

**References:**

(1) Gao, J.; Li, J.; Sulejmanovic, D.; Hwu, S.-J., $M_3(P_2O_7)^{22-}$Type Open Frameworks Featuring $[M_2O_8]$ and $[M_3O_{12}]$ Multinuclear Transition-Metal Oxide Units. Serendipitous Synthesis of Six Polymorphic Salt-Inclusion Magnetic Solids: $Na_2M_3(P_2O_7)_2 \cdot ACl$ (M = Mn, Fe; A = Rb, Cs) and $K_2M_3(P_2O_7)_2 \cdot CsCl$ (M = Fe, Mn), *Inorg. Chem.* **2015**, *54*, 1136-1144.

(2) Huang, Q.; Hwu, S. J., The fascinating noncentrosymmetric copper (II) phosphates synthesized via CsCl salt-inclusion, *Inorg. Chem.* **2003**, *42*, 665-657.

(3) Mahjoor, P.; Latturner, S. E., Molten salt synthesis and structural characterization of novel salt-inclusion vanadium bronze $Cs_5FeV_5O_{13}Cl_6$, *Inorg. Chem.* **2010**, *49*, 4486-4490.

(4) Queen, W. L.; West, J. P.; Hwu, S. J.; VanDerveer, D. G.; Zarzyczny, M. C.; Pavlik, R. A., The Versatile Chemistry and Noncentrosymmetric Crystal Structures of Salt-Inclusion Vanadate Hybrids, *Angewandte Chemie International Edition* **2008**, *47*, 3791-3794.

(5) Sun, K.; Litvinchuk, A. P.; Tapp, J.; Moeller, A., Synthesis, crystal structures, magnetic properties, and lattice dynamics of $Ba_2XCu(OH)[V_2O_7]$ with X= Cl, Br, *J. Solid State Chem.* **2016**, *236*, 69-77.

(6) Chang, Y.-C.; Chang, W.-J.; Boudin, S.; Lii, K.-H., High-Temperature, High-Pressure Hydrothermal Synthesis and Characterization of a Salt-Inclusion Mixed-Valence Uranium(V,VI) Silicate: $[Na_9F_2][(U^VO_2)(U^{VI}O_2)_2(Si_2O_7)_2]$, *Inorg. Chem.* **2013**, *52*, 7230-7235.

(7) Lee, C. S.; Wang, S. L.; Chen, Y. H.; Lii, K. H., Flux synthesis of salt-inclusion uranyl silicates:$[K_3Cs_4F][(UO_2)_3(Si_2O_7)_2]$ and $[NaRb_6F][(UO_2)_3(Si_2O_7)_2]$, *Inorg. Chem.* **2009**, *48*, 8357-8361.

(8) Morrison, G.; zur Loye, H.-C., Flux Growth of $[NaK_6F][(UO_2)_3(Si_2O_7)_2]$ and $[KK_6Cl][(UO_2)_3(Si_2O_7)_2]$: The Effect of Surface Area to Volume Ratios on Reaction Products, *Cryst. Growth Des.* **2016**, *16*, 1294-1299.

(9) Morrison, G.; Smith, M. D.; zur Loye, H.-C., Understanding the Formation of Salt-Inclusion Phases: An Enhanced Flux Growth Method for the Targeted Synthesis of Salt-Inclusion Cesium Halide Uranyl Silicates, *J. Am. Chem. Soc.* **2016**, *138*, 7121-7129.

(10) Tang, M.-F.; Chiang, P.-Y.; Su, Y.-H.; Jung, Y.-C.; Hou, G.-Y.; Chang, B.-C.; Lii, K.-H., Flux synthesis, crystal structures, and luminescence properties of salt-inclusion lanthanide silicates: $[K_9F_2][Ln_3Si_{12}O_{32}]$(Ln= Sm, Eu, Gd), *Inorg. Chem.* **2008**, *47*, 8985-8989.

(11) Glasser, L.; Jenkins, H. D. B., Predictive thermodynamics for ionic solids and liquids, *Phys. Chem. Chem. Phys.* **2016**, *18*, 21226-22140.

(12) Glasser, L.; Jenkins, H. D. B., Volume-Based Thermodynamics: A prescription for its application and usage in approximating and predicting thermodynamic data, *J. Chem. Eng. Data.* **2011**, *56*, 874-880.

(13) Jenkins, H. D. B.;, H. K. R.; Passmore, J.; Glasser, L., Relationships amoung Ionic Lattice Energies, Molecular (formula Unit) Volumes and Thermochemical Radii., *Inorg. Chem.* **1999**, *38*, 3609-3620.

(14) Glasser, L.; Jenkins, H. D. B., Predictive thermodynamics for condensed phases, *Chem. Soc. Rev.* **2005**, *34*, 866-874.

(15) Konings, R. J. M.; Benes, O.; Kovacs, A.; Manara, D.; Sedmidubsky, D.; Gorokhov, L.; Iorish, V. S.; Yungman, V.; Shenyavskaya, E.; Osina, E., The thermodynami properties of f-elements and their compounds., *J. Phys. Chem. Ref. Data* **2014**, *43*, 0131101.

(16) Martin, W.; Zalubas, R.; Hagan, L., Atomic Energy Levels-The Rare Earth Elements, *Report NSRDS-NBS 60* **1978**,

(17) Infante, I.; Kovacs, A.; Macchia, G. L.; Shahi, A. R. M.; Gibson, J. K.; Gagliardi, L., Ionization energies for the actinide mono-and dioxides series, from Th to Cm: Theory versus experiment, *The Journal of Physical Chemistry A* **2010**, *114*, 6007-6015.

(18) Chase, M. W. J., NIST-JANAF thermochemical tables in NIST Standard Reference Database, *J. Phys. Chem. Ref. Data, Monogr.* **1998**, *9*, 429-1829.

(19) Brinkmann, N. R.; Tschumper, G. S.; Shaefer, H. F. I. I. I., Electron addinities of the oxides of aluminum, silicon, phosphorus, sulfur, and chlorine, *J. Chem. Phys.* **1999**, *110*, 6480-6245.

(20) Gurvich, L. V.; Veyts, I. *Thermodynamic Properties of Individual Substances, Elements C, Si, Ge, Sn, Pb, and their compounds.* CRC Press: 1990; pp 220-278.

(21) Bartmess, J. E., Negative Ion Energetics Data in, *NIST Chemistry WebBook, NIST Standard Reference Database Number 69,* National Institute of Standards and Technology, *https://doi.org/10.18434/T4D303.* February, 2018.

(22) Burgess, D. R., Thermochemical Data, *NIST Chemistry WebBook, NIST Standard Reference Database Number 69,* National Institute of Standards and Technology, *https://doi.org/10.18434/T4D303.* February, 2018.

(23) Cox, J. D.; Medvedev, V. A., CODATA Key Values for Thermodynamics, Hemisphere Publishing Corp, *http://www.science.uwaterloo.ca/~cchieh/cact/tools/thermodata.html.* 1984.

(24) Kalcher, J., Trend in ground and excited state electron affinities of group 14, 15, and 16, mixed diatomic anions: a computational study, *Phys. Chem. Chem. Phys.* **2002**, *4*, 3311-3317.

(25) Arblaster, J. W., Thermodynamic Properties of Silver, *J. Phase. Equilib. Diff.* **2015**, *36*, 573-591.

(26) Lias, S. G., Ion Energetics Data, *NIST Chemistry WebBook, NIST Standard Reference Database Number 69,* National Institute of Standards and Technology, *https://doi.org/10.18434/T4D303.* February, 2018.

(27) Smith, D. W., Ionic Hydration Enthalpies, *J. Chem. Educ.* **1977**, *54*, 540-542.

(28) Han, J.; Goncharov, V.; Kaledin, L. A.; Komissarov, A. V.; Heaven, M. C., Electronic spectroscopy and ionization potential of $UO_2$ in the gas phase, *J. Chem. Phys.* **2004**, *120*, 5155-5163.

(29) Juillerat, C. A.; Moore, E. E.; Morrison, G.; Smith, M. D.; Besmann, T. M.; zur Loye, H.-C., Versatile Uranyl Germanate Framework Hosting Twelve Different Alkali Halide 1D Salt Inclusions, *Inorg. Chem.* **2018**, *57*, 11606-11615.

(30) Perdew, J. P.; Burke, K.; Ernzerhof, M., Generalized Gradient Approximation Made Simple, *Phys. Rev. Lett.* **1996**, *77*, 3865-3868.

(31) Blöchl, P. E., Projector augmented-wave method, *Phys. Rev. B* **1994**, *50*, 17953-17979.

(32) Kresse, G.; Joubert, D., From ultrasoft pseudopotentials to the projector augmented-wave method, *Phys. Rev. B* **1999**, *59*, 1758-1775.

(33) Schoenes, J., Recent specroscopic studies of $UO_2$, *J. Chem. Soc., Faraday Trans. 2* **1987**, *83*, 1205-1213.

(34) Kotani, A.; Takao, Y., Systematic Analysis of Core Photoemission Spectra for Actinide Di-Oxides and Rare-Earth Sesqui-Oxides, *Prog. Theor. Phys. Suppl.* **1992**, *108*, 117-131.

(35) Brincat, N. A.; Parker, S. C.; Molinari, M.; Allen, G. C.; Storr, M. T., Ab Initio Investigation of the $UO_3$ Polymorphs: Structural Properties and Thermodynamic Stability, *Inorg. Chem.* **2014**, *53*, 12253-12264.

(36) Colmenero, F.; Bonales, L. J.; Cobos, J.; Timon, V., Density Functional Theory Study of the Thermodynamic and Rama Vibrational Properties of γ-$UO_3$ Polymorph, *J. Phys. Chem. C* **2017**, *121*, 14507-14516.

(37) Casillas-Trujillo, L.; Baldinozzi, G.; Patel, M. K.; Xu, H.; Sickafus, K. E., Comparison of bonding and charge denisty in δ-$UO_3$, γ-$UO_3$, and $La_6UO_12$, *Phys. Rev. Mat.* **2017**, *1*, 065404-065414.

(38) Kresse, G.; Furthmuller, J., Efficient iterative schemes for ab-initio total-energy calculations using a plane-wave basis set, *Phys. Rev. B* **1996**, *54*, 11169-11186.

(39) Kresse, G.; Furthmuller, J., Efficiency of ab-initio total energy calculations for metals and semiconductors using a plane-wave basis set, *Comput. Mater. Sci.* **1996**, *6*, 15-50.

(40) Juillerat, C. A.; Moore, E. E.; Kocevski, V.; Besmann, T. M.; zur Loye, H.-C., A Family of Layered Phosphates Crystallizing in a Rare Geometrical Isomer of the Phosphuranylite Topology: Synthesis, Characterization, and Computational Modeling of $A_4[(UO_2)_3O_2(PO_4)_2]$ (A = alkali metals) Exhibiting Intra-layer Ion Exchange, *Inorg. Chem.* **2018**, *57*, 4726-4738.

(41) Zhao, M.; Brinkman, K.; K., L.; Navrotsky, A.; Rock, P. A., High Temperature Oxide Melt Solution Calorimetry Measurements on Salt Inclusion Materials (SIMs), *Private Communication* **2017**,

# Appendix B

## Understanding the polymorphism of $A_4[(UO_2)_3(PO_4)_2O_2]$ (A=alkali metals) uranyl phosphate framework structure[1]

[1]Reproduced with permission from Kocevski, V.; Juillerat, C. A.; Moore, E. E.; zur Loye, H.-C.; Besmann, T. *Cryst. Growth Des.* **2019**, *19*, 966-975. © 2019 American Chemical Society

**Abstract:** In this study we combine experimental synthesis and density functional theory (DFT) calculations to gain an insight into the polymorphism of $A_4[(UO_2)_3(PO_4)_2O_2]$ (A = Na, K, Rb, Cs) uranyl phosphate structures. Single crystals of a new 3D uranyl phosphate, $Cs_4[(UO_2)_3(PO_4)_2O_2]$, were grown by molten flux methods using a CsCl flux. DFT calculations, using the DFT+*U* method, were carried out to study the difference between this new 3D uranyl phosphate and a family of recently described layered uranyl phosphates. Variation of the computed properties with changes in $\boldsymbol{U_{eff}}$-values are also studied. The DFT results agree with the experimental observations, showing that the Cs-containing 3D polymorph and the K-containing layered polymorphs are more stable than their respective layered and 3D polymorph. We show an increase in the difference between the total energies of the layered and 3D polymorphs, and an increase in the band gaps with increasing $\boldsymbol{U_{eff}}$-value. Volume based thermodynamic was also applied to calculate the total energies of the different polymorphs, showing consistently higher stability of the layered polymorphs compared to the 3D polymorphs. For each of the studied polymorphs we calculated the electronic, optical and bonding properties. We also show an anisotropy in the absorption indexes along the three crystallographic directions of the polymorphs, which is especially noticeable in the layered polymorphs. We attribute the difference in the density of states on the different coordination of the U atoms in the layered and 3D polymorphs. We attribute the preferred formation of the 3D Cs polymorph to the substantial increase in the U–A bond strength, which is more pronounced than the differences in the bond strength between structures for the other atomic pairs.

**Introduction.** Uranyl phosphates are important for applications in the field of nuclear waste sequestration, as well as for understanding actinide chemistry in general. In particular, when aided by the natural abundance of phosphate minerals, the study of uranyl phosphates is helping to develop an understanding of the mobility of uranium species in the environment, which can be applied towards environmental remediation and the separation, disposal, and the long-term storage of nuclear waste.[1] Particularly, mineral-based classes of inorganic materials have been proposed as matrices for various components of spent nuclear fuel; however, no universal storage material has been achieved and it remains important to develop and evaluate new candidates as host matrices.[2] While glasses and cements are widely accepted and already implemented on large scales, volatile and mobile species such as cesium, iodine, and technetium still present challenges in waste processing. Phosphates generally have low solubility, making them attractive to explore as potential nuclear waste storage materials; and moreover cesium uranyl phosphates are attractive because of their capability for sequestering hard to contain and mobile cesium.[3] Three-dimensional storage materials are of particular interest due to their potential to house ionic species in their pores and to undergo post synthetic ion-exchange.

Uranyl-based hierarchical nuclear waste forms are currently being explored,[2] as $UO_2^{2+}$ is an excellent building block for three-dimensional structures.[4] Uranyl phosphates make up a significant portion of known uranyl minerals and all 45 uranyl phosphate minerals reported are based on 2D sheets (layers), of corner and edge sharing uranyl polyhedra and phosphate tetrahedra.[1] The 2D characteristic of uranyl phosphates arises from the typical coordination chemistry of the uranyl cation, $UO_2^{2+}$, which has two short

axial bonds with average bond distances of ~1.80 Å that are typically non-bonding. The equatorial U–O bonds have bond distances ranging from 2.2 to 2.5 Å and typically connect adjacent uranyl groups, thereby naturally favoring a layered topology.[5, 6] Therefore, 3D structures are rather uncommon and can only form if either cation-cation interactions are present to connect adjacent layers, or if a functional group, such as a $PO_4^{3-}$ or $SiO_4^{4-}$ bridges uranyl groups within a sheet and connects to other uranyl sheets by bonding in a direction perpendicular to the sheet structure, as observed in the $Cs_4[(UO_2)_3(PO_4)_2O_2]$ compound reported in this paper. As 3D structures hold significant promise as waste form materials with an ability to engage in ion exchange for sequestering radionuclides, they are the subject of the current effort to understand the energetics of layered and 3D structures.

While 3D uranyl phosphates are significantly less common than layered materials, several are known, including but not limited to $Cs_4[(UO_2)_2(GaOH)_2(PO_4)_4]\cdot H_2O$, $Cs[UO_2Ga(PO_4)_2]$, [5] $Cs_2[(UO_2)_4[Co(H_2O)_2]_2(HPO_4)(PO_4)_4]$, $Cs_{3+x}[(UO_2)_3CuH_{4-x}(PO_4)_5]\cdot H_2O$, [7] $Cu_2UO_2(PO_4)_2$, [8] α-,β-$K[(UO_2)(P_3O_9)]$, $K[(UO_2)_2(P_3O_{10})]$, [9] $Li_2(UO_2)_3(PO_4)_2O$, [10] and $Cs_3(UO_2)_2(PO_4)O_2$.[11] The first five listed 3D uranyl phosphates were synthesized by mild-hydrothermal methods that have been extensively explored for the synthesis of new uranium phosphates, while the other 4 phosphates were prepared via less widely used solid state and molten flux methods.

Herein we report the synthesis and characterization of a new 3D uranyl phosphate, $Cs_4[(UO_2)_3(PO_4)_2O_2]$, grown as single crystals in a CsCl flux. This is in contrast to the solely K-containing phases which will form layered but not 3D structures. As noted above, the formation of a layered polymorph is expected from $UO_2^{2+}$ coordination chemistry, while obtaining the 3D polymorph requires more complex interaction between $UO_2^{2+}$ and

$PO_4^{3-}$. The question then arises, and which is addressed in this effort, why does the smaller K cation form a layered polymorph, while the larger Cs cation prefers to form a 3D polymorph? As an aside, it is also observed that the layered polymorphs, $A_4[(UO_2)_3(PO_4)_2O_2]$ (A=$Cs_{0.7}K_{3.3}$, $Rb_{1.4}K_{2.6}$, and $K_{2.9}Na_{0.9}Rb_{0.2}$) can be prepared, but not single alkali versions other than that for K. [12]

The current effort to understand why Cs-rich uranyl phosphate tends to form a 3D polymorph rather than the more typical layered polymorph, and why the K-rich uranyl phosphate does the opposite, explores the governing energetics using density functional theory (DFT) calculations and a technique termed volume-based thermodynamics (VBT). We compared computed structural parameters, bond distances, total energies, bond strength, and electronic and optical properties of the K and Cs containing polymorphs, as well as the Na and Rb analogues. To obtain the most accurate representation of the correlated electrons in these U- and O-containing systems, we used DFT with applied on-site Coulombic and exchange corrections, $U_{eff}$. To optimize the results, we studied the dependence of properties of the $A_4[(UO_2)_3(PO_4)_2O_2]$ polymorphs on $U_{eff}$-values. The results of VBT were contrasted with those of DFT+$U$ in evaluating relative stability of the studied polymorphs.

**Methods:**

**DFT.** The calculations were performed using the Vienna Ab initio Simulation Package (VASP) planewave code,[13, 14] with the Perdew-Burke-Ernzerhof (PBE) generalized-gradient approximation [15] and the projector augmented plane wave (PAW) method.[16, 17] We performed spin-polarized calculations, using 520 eV cut-off energy for the planewave basis set, **k**-point mesh of 6×2×6 and 4×5×4 for the layered and 3D polymorphs,

respectively. Energy and forces convergence criteria were chosen as $10^{-6}$ eV and 0.001 Å/eV, respectively. The volume, unit cell shape and ionic positions of each of the structures were fully relaxed. The valence electrons configuration for U, P, O, Na, K, Rb and Cs are [U] $6s^2 6p^6 5f^3 6d^1 7s^2$, [P] $3s^2 3p^3$, [O] $2s^2 2p^4$, [Na] $2p^6 3s^1$, [K] $3p^6 4s^1$, [Rb] $4s^2 4p^6 5s^1$, and [Cs] $5s^2 5p^6 6s^1$, respectively. The real, $\boldsymbol{\varepsilon_1(\omega)}$, and imaginary, $\boldsymbol{\varepsilon_2(\omega)}$, part of the dielectric function were determined from the frequency dependent dielectric response theory including local field effects in the random-phase-approximation. [18] The $\varepsilon_1(\omega)$ and $\boldsymbol{\varepsilon_2(\omega)}$ were used to calculate the absorption coefficient, $\boldsymbol{\alpha(\omega)}$, using:

$$\boldsymbol{\alpha(\omega) = \sqrt{2}\omega \left[ \frac{\sqrt{\varepsilon_1^2 + \varepsilon_2^2} - \varepsilon_1}{2} \right]^{\frac{1}{2}}}, \qquad \textbf{(1)}$$

where $\omega$ is the photon frequency. The static dielectric constant, $\boldsymbol{\varepsilon_c(\omega \rightarrow 0)}$, was estimated from the zero frequency limits $(\omega \rightarrow 0)$ of the real part of the dielectric function, $\boldsymbol{\varepsilon_1(\omega)}$. To obtain information on the bonding strength in the different polymorphs we performed crystal orbital Hamilton population (COHP) analysis using the code LOBSTER,[19–21] where the interatomic bond strength is directly proportional to the integral of the COHP curves (ICOHP) up to the Fermi level.

**DFT+*U*.** We used Dudarev's rotationally invariant approach to the DFT+*U*, [22] in which the total energy is expressed as:

$$\boldsymbol{E^{DFT+U} = E^{GGA} + \frac{U-J}{2} \sum_\sigma \left[ \left( \sum_m n^\sigma_{m,m} \right) - \left( \sum_{m,m'} n^\sigma_{m,m'} n^\sigma_{m',m} \right) \right]} \qquad \textbf{(2)}$$

where $\boldsymbol{n}$ is the occupational matrix of the 5*f* electrons, with $\boldsymbol{\sigma}$ indexing the spin and $\boldsymbol{m}$ representing the *f*-orbitals index (angular momentum quantum number). $\boldsymbol{U}$ and $\boldsymbol{J}$ are the onsite Coulomb parameter and the exchange parameter, respectively, with the spherically averaged effective interaction parameter, $\boldsymbol{U–J}$, referred to simply as effective $\boldsymbol{U}$, $\boldsymbol{U_{eff}}$. The

$U_{eff}$ in this study were chosen in three ways. Because in the studied structures, U atoms are bonded only to O atoms, we considered $U_{eff}$ = 3.96 eV ($U$ = 4.5 eV and $J$ = 0.54 eV) which is derived from spectroscopic measurements for $UO_2$ and used in DFT+$U$ studies of $UO_2$.[23, 24] To cover the large range of possible $U_{eff}$ values, we varied values from 0 (DFT) to 6 eV, with a step of 1.5 eV. Lastly, we derived a $U_{eff}$ = 4.29 utilizing the linear response approach proposed by Cococcioni et. al.,[25] using finite differences to obtain the elements of the response matrices, setting the $\alpha$ parameter to ±0.08 with a step of 0.02. We start the relaxation of the structures using $U_{eff}$ = 0 eV. To relax the structure at higher $U_{eff}$ we used the structures, and their respective charge densities and wavefunctions, relaxed at the lower $U_{eff}$; structures relaxed at $U_{eff}$ = 0 eV for relaxation at $U_{eff}$ = 1.5 eV, structures relaxed at $U_{eff}$ = 1.5 eV for relaxation at $U_{eff}$ = 3.0 eV and so on.

**VBT**. An alternate means for computing total energies of the polymorphs is VBT, which is dependent on the known formation energies for lower scale structural units together with experimentally derived crystallographic data, most notably the formula unit volume ($V_m$). It is also a substantially less computationally demanding way to calculate formation enthalpies and Gibbs energies of formation.[26, 27] VBT computational methods applied to layered polymorphs, specifically the phosphates, have been discussed in Juillerat et al., [12] where the formation energies of the uranyl-phosphate frameworks studied were found to be in good agreement with measured values of similar composition. The application to more complex 3D structures such as salt-inclusion materials (SIMs) is discussed in Moore et al. and are validated by experimental findings. [28]

In VBT the formation enthalpy is calculated from its lattice potential, $U_{pot}$, using the volume per formula unit, $V_m$, and the ionic strength factor for the structure, which is

converted to a useable enthalpic value, $\boldsymbol{H_L}$. The lattice enthalpy includes terms to describe the number of different ion types ($\boldsymbol{s_i}$) in the system and a constant ($\boldsymbol{c_i}$) related to whether these ions are monoatomic or polyatomic (linear or non-linear) as shown here:

$$\boldsymbol{H_L = U_{pot} + \sum_{i=1}^{n} s_i \left(\frac{c_i}{2} - 2\right) RT} \qquad \textbf{(3)}$$

where $\boldsymbol{R}$ is the ideal gas constant and $\boldsymbol{T}$ the thermodynamic temperature, in Kelvin.

Two distinct approaches for treating the uranyl phosphate polymorphs were used, differing with respect to how the ion types (notably the variable(s) $s_i$) are described. In the first approach, termed the 3D approach, the polymorphs are treated analogous to SIMs, in considering the framework as a single ion type, and the inclusion within the cavity/pore as a separate species or ion type. Ultimately there are only two entities to consider, i.e., the framework and the inclusion. In the second approach, termed the 2D approach, the polymorph uranyl, $UO_2^{2+}$, and phosphate, $PO_4^{3-}$, ions are considered as distinct building block units, with the cations in between the layers as individual ions. The formation enthalpies are then calculated using auxiliary information as described in Juillerat et al.[12] It is to be noted that the auxiliary information is limited to the formation of $PO_2^-$ ions, as energetics for the phosphate ion are lacking.

**Synthesis**. Single crystals of the $Cs_4[(UO_2)_3(PO_4)_2O_2]$ compound were synthesized by flux growth methods[29] using $UF_4$ (International Bio-Analytical Industries, powder, ACS grade), $AlPO_4$ (Alfa Aesar, powder, 99.99%), and CsCl (Alfa Aesar, powder, 99%) as received. *Caution! Although the uranium precursor used contained depleted uranium, standard safety measures for handling radioactive substances must be followed.* A ratio of 0.5:2:20 of U, P, and CsCl on a mmol scale was weighed out into a silver tube measuring 5.7 cm tall with a diameter of 1.2 mm. The silver tube was covered with a loose-fitting

silver cap and placed in a box furnace that was heated to 875 ºC in 1.5 hours, held for 12 h, and then slow cooled at a rate of 6 ºC/h to 400 ºC, at which temperature the furnace was shut off and the tube was allowed to cool to room temperature. The tube was then cut open and sonicated in water to aid in the dissolution of the CsCl flux. The bright orange polyhedral crystals of $Cs_4[(UO_2)_3(PO_4)_2O_2]$ were synthesized in a fair yield, with $AlPO_4$ and AgCl as the major byproducts, and an additional orange uranium containing impurity that will be reported on later.

**XRD.** A small fragment of an orange polyhedral crystal was cut to obtain a crystal of appropriate size for single crystal X-ray diffraction (SCXRD). The structure was determined by SCXRD data obtained using a Bruker D8 QUEST diffractometer with a microfocus source (Mo Kα radiation, λ = 0.71073 Å). The SAINT+ and SADABS programs within APEX 3 were used to reduce the raw data and correct for absorption effects. [30] SHELXT and SHELXL were used within the OLEX2 GUI to obtain an initial structure using intrinsic phasing and to refine the structure.[31–33] Full crystallographic data can be found in Table B.1. EDS data were used to confirm the presence of the elements in the structure using TESCAN Vega-3 SBU equipped with an EDS detector.

**Models.** As mentioned previously, our interest is in two $A_4[(UO_2)_3(PO_4)_2O_2]$ (A = Na, K, Rb, Cs) uranyl phosphate polymorphs, with layered and 3D structure, both having the $P2_1/c$ space group (ITC number 14), see Ref. 12 and Table B.1. The layered polymorphs have phospho-uranylite based layers comprised of chains of uranyl hexagonal and pentagonal bipyramids linked by phosphate tetrahedra, with the alkali atoms between these layers, see Figure B.1a and B.1b. The 3D polymorphs consist of square bipyramidal uranyl polyhedra that corner share to form trimers linked via corner-sharing phosphate tetrahedra

to create the 2D layers shown in Figure B.1d. These 2D sheets are connected to adjacent layers via uranyl polyhedra that bond approximately perpendicular to the 2D sheet, creating a 3D framework structure containing small channels in the *c*-direction as shown in Figure B.1c. Channels are also formed in the b-direction and are occupied by alkali atoms located between adjacent, non-bonding uranyl polyhedra.

**Table B.1:** Full crystallographic data for $Cs_4[(UO_2)_3(PO_4)_2O_2]$.

| Space group | $P2_1/n$ |
|---|---|
| $a$ (Å) | 10.8217(3) |
| $b$ (Å) | 8.2553(2) |
| $c$ (Å) | 11.7308(3) |
| $\alpha$ (deg) | 90 |
| $\beta$ (deg) | 113.3340(10) |
| $\gamma$ (deg) | 90 |
| $V$ (Å$^3$) | 962.27(4) |
| Crystal size (mm$^3$) | 0.08 x 0.07 x 0.06 |
| Temperature (K) | 302.71 |
| Density (g cm$^{-3}$) | 5.397 |
| $\theta$ range (deg) | 3.109-36.350 |
| $\mu$ (mm$^{-1}$) | 32.872 |
| Collected reflections | 86647 |
| Unique reflections | 4656 |
| $R_{int}$ | 0.0322 |
| $h$ | $-18 \leq h \leq 18$ |
| $k$ | $-13 \leq k \leq 13$ |
| $l$ | $-19 \leq l \leq 19$ |
| $\Delta\rho_{max}$ (e Å$^{-3}$) | 3.541 |
| $\Delta\rho_{min}$ (e Å$^{-3}$) | -2.616 |
| *GoF* | 1.166 |
| Extinction coefficient | 0.00266(7) |
| $R_1(F)$ for $F_0^2 > 2\sigma(F_0^2)$[a] | 0.0179 |
| $R_w(F_0^2)$[b] | 0.0401 |

[a] $R_1 = \Sigma\big||F_0| - |F_c|\big|/\Sigma|F_0|$. [b] $wR_2 = [\Sigma w\left(F_0^2 - F_c^2\right)^2 / \Sigma w\left(F_0^2\right)^2]^{1/2}$; $P = (F_0^2 + 2F_c^2)/3$; $w = 1/\left[\sigma^2\left(F_0^2\right) + (0.0089P)^2 + 4.2901P\right]$

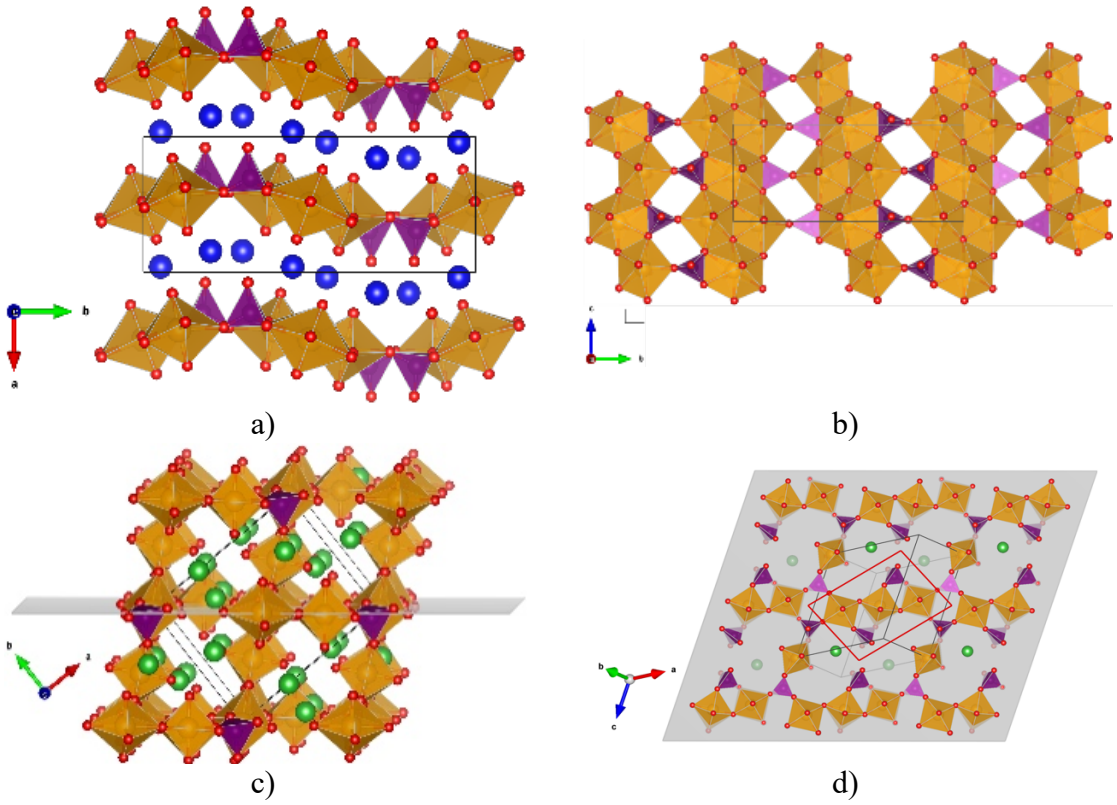


**Figure B.1:** Structures of the two polymorphs of $A_4[(UO_2)_3(PO_4)_2O_2]$. a) The A = K layered polymorph shown in the *c*-direction b) and the *a*-direction. c) The A = Cs 3D polymorph shown in the *c*-direction. d) Illustrates the uranyl phosphate 2D layer, with the structural unit shown as a red tetragonal structure. The U, P, O, K and Cs atoms are shown in orange, purple, red, blue and green, respectively.

Beside the noticeable difference in the structure and position of the alkali atoms, the two polymorphs also differ in the oxygen coordination around the U atoms. In the 3D structure the U atoms are surrounded by six O atoms forming a square bipyramid (Figure B.1d), whereas in the layered structure seven or eight O atoms form pentagonal or hexagonal bipyramids around the U atoms, respectively (Figure B.1b). Nevertheless, the U–O distances in the respective layered and 3D polymorphs are nearly identical, and the charge density is symmetrically distributed between the U and O atoms in both polymorphs. In addition, all of the studied systems relaxed to a non-magnetic state, in agreement with the observations.

**Results and Discussion:**

**Structural Parameters.** For each of the relaxed structures we calculated the volume (see Figure B.2) and structural parameters. In the case of the K and Cs polymorphs, the difference between the calculated and experimental lattice parameters increases with increasing $\boldsymbol{U}_{\mathbf{eff}}$ for both polymorphs. In the case of the K layered polymorph, the lattice parameter ***a*** is smaller than the measured and decreases with increasing $\boldsymbol{U}_{\mathbf{eff}}$, while the ***b*** and ***c*** lattice parameters are larger than the respective experimental values and increase with increasing $\boldsymbol{U}_{\mathbf{eff}}$. The lattice parameter dependence on the $\boldsymbol{U}_{\mathbf{eff}}$ in the Cs 3D polymorph is rather different, with the lattice parameter ***a*** increasing with increasing $\boldsymbol{U}_{\mathbf{eff}}$, approaching the measured value. The difference between the calculated and experimental values of the ***b*** and ***c*** lattice parameters increases with increasing $\boldsymbol{U}_{\mathbf{eff}}$, the parameters *b* and *c* increase and decrease in value, respectively. The β angle of the layered polymorphs is almost constant with varying $\boldsymbol{U}_{\mathbf{eff}}$ (standard deviation of 0.023° averaged over the 4 alkali-containing polymorphs), while in the 3D polymorph an increase in the β angle with increasing $\boldsymbol{U}_{\mathbf{eff}}$ is noticeable. Interestingly, the volume of each of the studied structures increases with increasing $\boldsymbol{U}_{\mathbf{eff}}$. In the case of the Cs 3D polymorph, the calculated volume is smaller than the experimental one, with their difference decreasing with increasing $\boldsymbol{U}_{\mathbf{eff}}$. On the other hand, the calculated volume of the K layered polymorph becomes larger than the experimental one at $\boldsymbol{U}_{\mathbf{eff}} \approx 2.55$ eV. Yet, despite the increasing difference between the calculated and experimental lattice parameters and β angle, the net effect yields decreasing differences between measured and computed volumes with increasing $\boldsymbol{U}_{\mathbf{eff}}$.

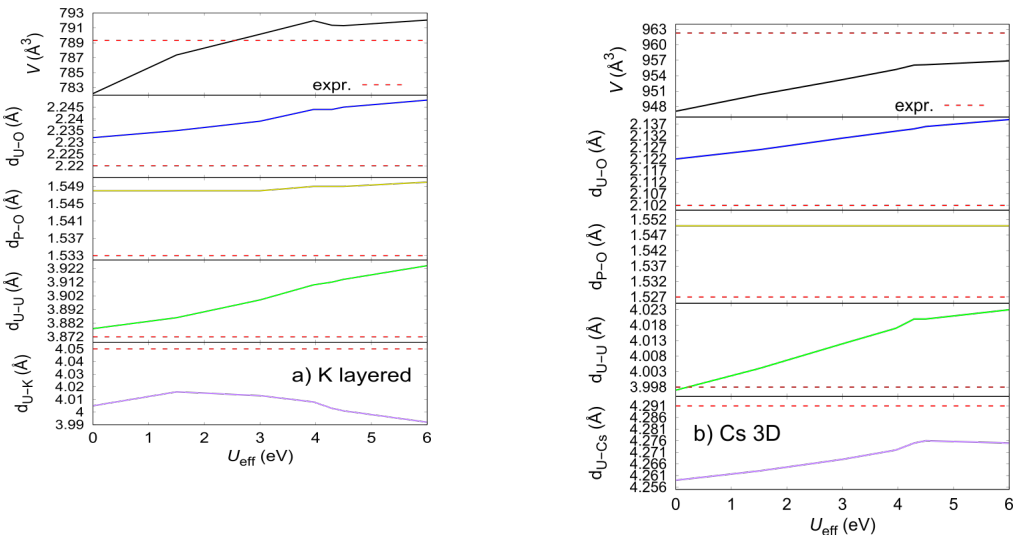


**Figure B.2.** Volume and bond distances of the layered and 3D polymorphs. (a) K layered polymorph, and (b) Cs 3D polymorph. The volume, average U–O, P–O, U–U and U–A (A = K, Cs) bond distances are shown in black, blue, yellow, green, and purple, respectively. Experimental values are shown as dashed red lines.

To understand polymorph formation via their bonding, it is important to the understand the relation between $\boldsymbol{U}_{\mathbf{eff}}$-values and bond distances. Shown in Figure B.2 are the calculated volume and the average U–O, P–O, U–U and U–A (A = K, Cs) bond distances as a function of the $\boldsymbol{U}_{\mathbf{eff}}$. We chose U–O, P–O, U–U and U–A bonds because, as we show later, their bond strengths are the largest, and hence any changes in the distance will have the largest influence on the total bond strength in the polymorphs. Evidently, calculated U–O, P–O, and U–U bond distances are overestimated, while U–A bond distances are underestimated. Note that bonds that include U atoms display a significant dependence on $\boldsymbol{U}_{\mathbf{eff}}$, which comes from the fact that we apply the $\boldsymbol{U}_{\mathbf{eff}}$-value only with respect to U. Also, the calculated bond distances agree best with experimental values at $\boldsymbol{U}_{\mathbf{eff}}$ = 0 eV, with exception of U–A. Considering all bond distances, dissimilar dependencies on $\boldsymbol{U}_{\mathbf{eff}}$ are seen for K layered and Cs 3D polymorphs. In the case of the K layered polymorph, agreement of calculated and experimental values is best for low $\boldsymbol{U}_{\mathbf{eff}}$

values, from 0 eV to 1.5 eV, with the average absolute error for both $\boldsymbol{U_{eff}}$ being 0.625 %. On the other hand, the bond distances in the Cs 3D polymorph are closest to experimental values for $\boldsymbol{U_{eff}}$ = 0 eV or large $\boldsymbol{U_{eff}}$-values of 4.5 eV and 6 eV. The average absolute error is lowest for $\boldsymbol{U_{eff}}$ = 0 eV, 1.171 %, with a very small increase in the average error with increasing $\boldsymbol{U_{eff}}$, with the average error for $\boldsymbol{U_{eff}}$ = 6 eV being 1.243 %. Implications of these results are that lower $\boldsymbol{U_{eff}}$-values may provide the best representation of bonding in these polymorphs.

**Stability of Polymorphs.** To understand the relative stabilities of layered and 3D polymorph structures at the studied compositions, we computed their total energies, defining the total energy difference as:

$$\boldsymbol{\Delta E = E_{3D} - E_{L}}. \quad \textbf{(4)}$$

Figure B.3 displays $\boldsymbol{\Delta E}$ as a function of the $U_{eff}$, indicating both, Na and K layered polymorphs have more positive values as compared to their respective 3D polymorph. This agrees with observations of a layered K polymorph synthesized preferentially.[12] In contrast, for Cs compounds the 3D polymorph is calculated to be more stable in agreement with the experimental observations. In addition, there is a clear difference in the stability of the Na, K and Cs polymorphs on the $\boldsymbol{U_{eff}}$, where their $\boldsymbol{\Delta E}$ is always above or below $\boldsymbol{\Delta E}$ = 0 kJ/mol, regardless of the used $\boldsymbol{U_{eff}}$. However, the situation with the Rb-containing polymorphs is very different, for $\boldsymbol{U}$ < 3.2 eV the $\boldsymbol{\Delta E}$ < 0 kJ/mol and for $\boldsymbol{U}$ > 3.2 eV the $\boldsymbol{\Delta E}$ > 0 kJ/mol. The total energies of the distinct polymorphs give information on their relative stability, and to understand if a polymorph can be formed information on the formation enthalpies of phases around the polymorph's composition is required. Although the layered Na polymorph has significantly lower energy than the 3D Na polymorph, and hence it is the

polymorph predicted to form, the result does not show if the synthesis is driven towards another, lower energy structure.

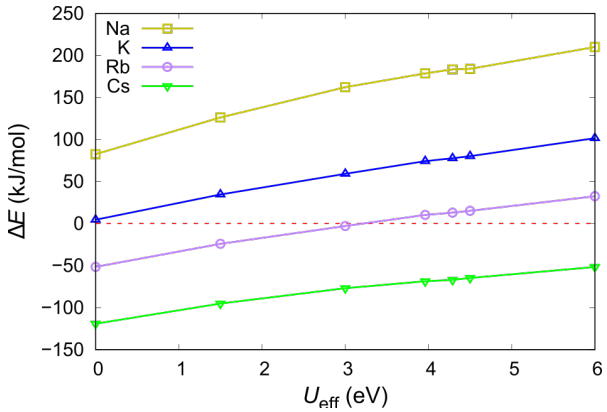


**Figure B.3.** Calculated total energy difference, between the 3D and layered polymorphs. Na (yellow), K (blue), Rb (purple) and Cs (green) uranyl phosphates. The dashed red line shows the position of $\Delta E$ = 0 kJ/mol.

While from Eq. (2), it is evident that the total energy of the system calculated using DFT+*U* depends on the $\boldsymbol{U_{eff}}$, why the total energy of the two polymorphs have slightly different dependencies on $\boldsymbol{U_{eff}}$ should be explained. To understand this, one needs to regard the structure of the two polymorphs, and specifically the U coordination. As mentioned previously, U atoms in the 3D polymorph have six O nearest neighbors, forming square bipyramids, while in the layered polymorph the U atoms have seven or eight O nearest neighbors forming pentagonal or hexagonal bipyramids. Because of the different U atom coordination in the two polymorphs, the occupational matrix, $\boldsymbol{n}$, of the U atoms in the lowest energy configuration will be different. The distinct matrices will have different influences on the second terms in Eq. (2), and hence, the total energies of the two polymorphs will depend differently on $\boldsymbol{U_{eff}}$.

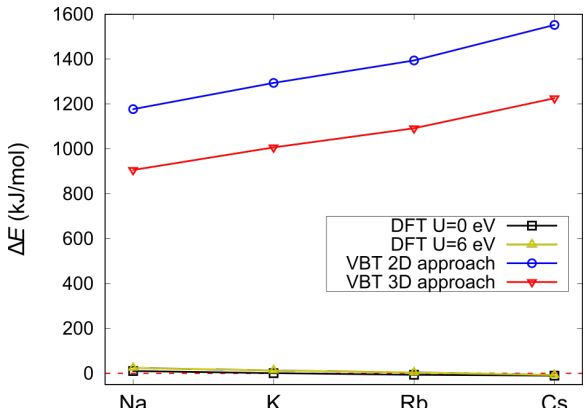


**Figure B.4.** Comparison of DFT- and VBT-derived $\Delta E$. The VBT values are calculated using two different approaches: 2D and 3D, shown in blue and red, respectively. The DFT $\boldsymbol{\Delta E}$ values are calculated using $\boldsymbol{U}_{\mathbf{eff}}$ = 0 eV and $\boldsymbol{U}_{\mathbf{eff}}$ = 6 eV, shown in black and yellow, respectively.

In addition to DFT, we also used VBT to calculate total energies using both the 2D and 3D approaches. Comparison between the DFT and VBT calculated $\boldsymbol{\Delta E}$ is shown in Figure B.4. Evidently, VBT always predicts layered polymorphs to be more stable than the 3D polymorphs, regardless of the used approach. This difference in calculated total energies derives from the different volumes of the layered and 3D polymorphs, with the layered polymorphs having smaller molar volumes, regardless of the alkali content (see Figure B.2). Considering the inverse relation between the $\boldsymbol{U}_{\mathbf{pot}}$ and $\boldsymbol{V}_{\mathbf{m}}$, and that both polymorphs have the same composition, a smaller volume yields a more negative $\boldsymbol{U}_{\mathbf{pot}}$ and hence, more negative total energy. Using the 3D approach, where the system is considered to house ions in a singular, rigid framework, the VBT computed $\Delta E$ values are smaller, and the computed total energies are also closer to the DFT calculated energies. The more rigid framework consideration for the 3D structures includes a lower ionic strength value when calculating the $\boldsymbol{U}_{\mathbf{pot}}$, leading to more positive lattice enthalpies, which dictates the decrease

in stability of the 3D polymorphs. Additionally, more information on the formation energetics of the individual ions within the framework could be useful to improve VBT methods, specifically the formation enthalpy of the $PO_4^{3-}$ (g) ion.

**Electronic Properties.** Expectedly, all of the studied systems are semiconductors with clearly defined band gaps, as seen in experiment[12] and as is common for oxide materials. For each of the studied systems we calculated the band gaps as the energy difference between the conduction band minimum (CBM) and valence band maximum (VBM). Shown in Figure B.5 are the band gaps of the layered and 3D polymorphs as a function of the $\boldsymbol{U}_{\mathbf{eff}}$. It is evident that the band gaps of the polymorphs with different alkali atoms are very similar. This is because the states at the CBM and VBM arise mainly from the U and O atoms (see Figure B.6a and b), with the alkali atoms having negligible contribution. Also, it is noticeable that the band gaps of the layered polymorphs are slightly lower compared to the band gaps of the 3D polymorphs. This is due to the different U coordination of the two polymorphs. Having 7 or 8 O atoms coordination of the U atoms will cause a slight decrease in the band gap of the layered polymorph, as compared to the 6 coordinate U atoms in the 3D polymorph, as in $U_3O_8$ and $UO_3$, with band gaps of 1.67 eV and 2.6 eV,[34] respectively. As expected from DFT+*U*, the band gaps increase with increasing $\boldsymbol{U}_{\mathbf{eff}}$. The best estimate for $\boldsymbol{U}_{\mathbf{eff}}$ that reproduces the experimentally observed band gap of the K layered polymorph is 1.5 eV.[12] Considering this, and the observation that lower $\boldsymbol{U}_{\mathbf{eff}}$ values provide a better estimate of the bond distances in the K layered polymorph, our calculations adopted $\boldsymbol{U}_{\mathbf{eff}}$ = 1.5 eV. The results for other values of $\boldsymbol{U}_{\mathbf{eff}}$ are given in the supporting information.

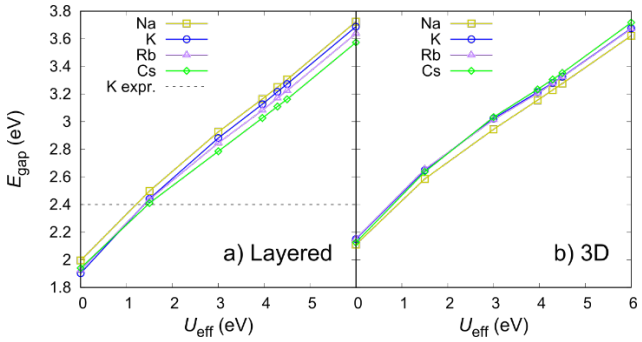


**Figure B.5.** Band gaps of a) layered, and b) 3D polymorphs. The band gaps of the Na, K, Rb, and Cs polymorphs are shown in yellow, blue, purple and green, respectively. The experimentally measured band gap of the layered K polymorph, taken from Ref.12, is shown as a dashed black line.

Information about the electronic structure of the studied polymorphs can be obtained from the density of states (DOS), shown in Figure B.6. There is a noticeable similarity between the DOS around the band gap, -5 to 5 eV region, for the same polymorph, regardless of alkali atom. This is due to the nature of the states around the gap, which almost exclusively come from the U and O atoms (see Figure B.7a and c). The Na polymorphs, however, have a somewhat noticeable difference, which can be attributed to the distortion of the structures by the comparatively much smaller Na atom. The largest difference in the DOS is evident above 5 eV, with a broad peak centered at 9 eV, and below -5 eV. With decreasing alkali atom size from Cs to Na, the intense peak below -5 eV is shifted towards lower energies and the peak centered at 9 eV becomes broader. The difference in the DOS peaks with changes in the alkali atom is a clear indication that alkali atoms contribute the most to the states in the energy regions, which is detailed in the next paragraph. Comparing the DOS of the layered and 3D polymorphs, the most notable difference is in the broadening of the valence bands. The valence bands of the 3D

polymorphs are narrower (within a smaller energy range) compared to the layered polymorphs, which can be related to the first nearest neighbor (1NN) distances in the polymorphs. The distribution of 1NN distances in the 3D polymorphs is smaller than in the layered polymorphs, allowing for more uniform hybridization between the NN atomic orbitals, and hence the formed molecular orbitals will be closer in energy, giving rise to bands in smaller energy ranges.

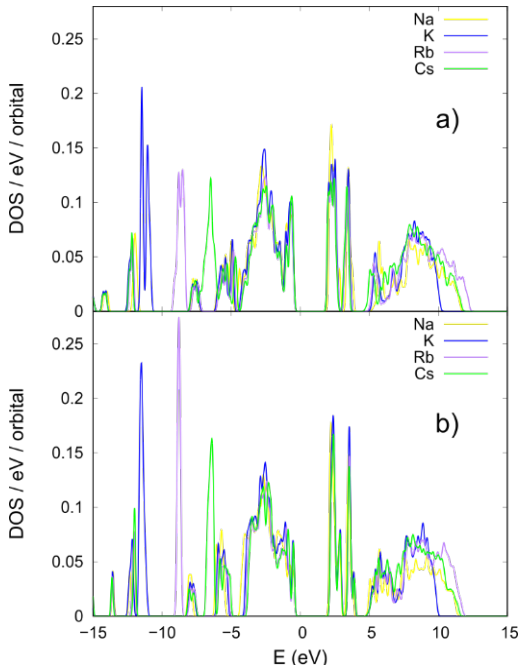


**Figure B.6.** Density of states (DOS) of a) layered polymorphs, and b) 3D polymorphs. The DOS of the Na, K, Rb, and Cs polymorphs are shown in yellow, blue, purple and green, respectively.

More detailed information on the difference between the electronic properties of the polymorphs can be obtained from the projected DOS (PDOS). Shown in Figure B.7 are the PDOS of the K layered and 3D polymorphs, calculated using $\boldsymbol{U}_{\mathbf{eff}}$ = 1.5 eV. The PDOS

of all of the studied polymorphs, calculated using each of the $\boldsymbol{U}_{\mathbf{eff}}$-values. Evidently, the states at the top of the VB come predominantly from the U and O atoms, whereas the states at the bottom of the CB come solely from the U atom. A closer look shows that the U 5-*f* states dominate near the band gap, as is the case for $UO_2$, indicating that this material is a Mott insulator. Moving further away from the gap to the either side; below -5 eV and above 5 eV, the contribution from the A (A = Na, K, Rb and Cs) and P atoms significantly increases, while the contribution from the U and O atoms decreases. For the same polymorph type (see Figure B.7a and c), a change in the alkali atom leads to small changes in the U, O and P atom PDOS. A noticeable difference in PDOS related to the nature of the A atom is observed, where the high intensity VB peak is shifted towards higher energy with increasing atomic number alkali metals from Na- to Cs-polymorphs (see Figure B.6). This VB peak shift comes from the increased energy of the states of the alkali atom with increasing size. A change in the electronic properties is reflected in increased localization of the conduction bands with increasing $\boldsymbol{U}_{\mathbf{eff}}$, in the region up to 8 eV, which is the reason for the increase in band gap. Despite the localization of the conduction bands, the change in $\boldsymbol{U}_{\mathbf{eff}}$ has a rather weak influence on the relative position of the PDOS peaks. Thus, the electronic properties of the different polymorphs are comparable for calculations performed with the same $\boldsymbol{U}_{\mathbf{eff}}$ value.

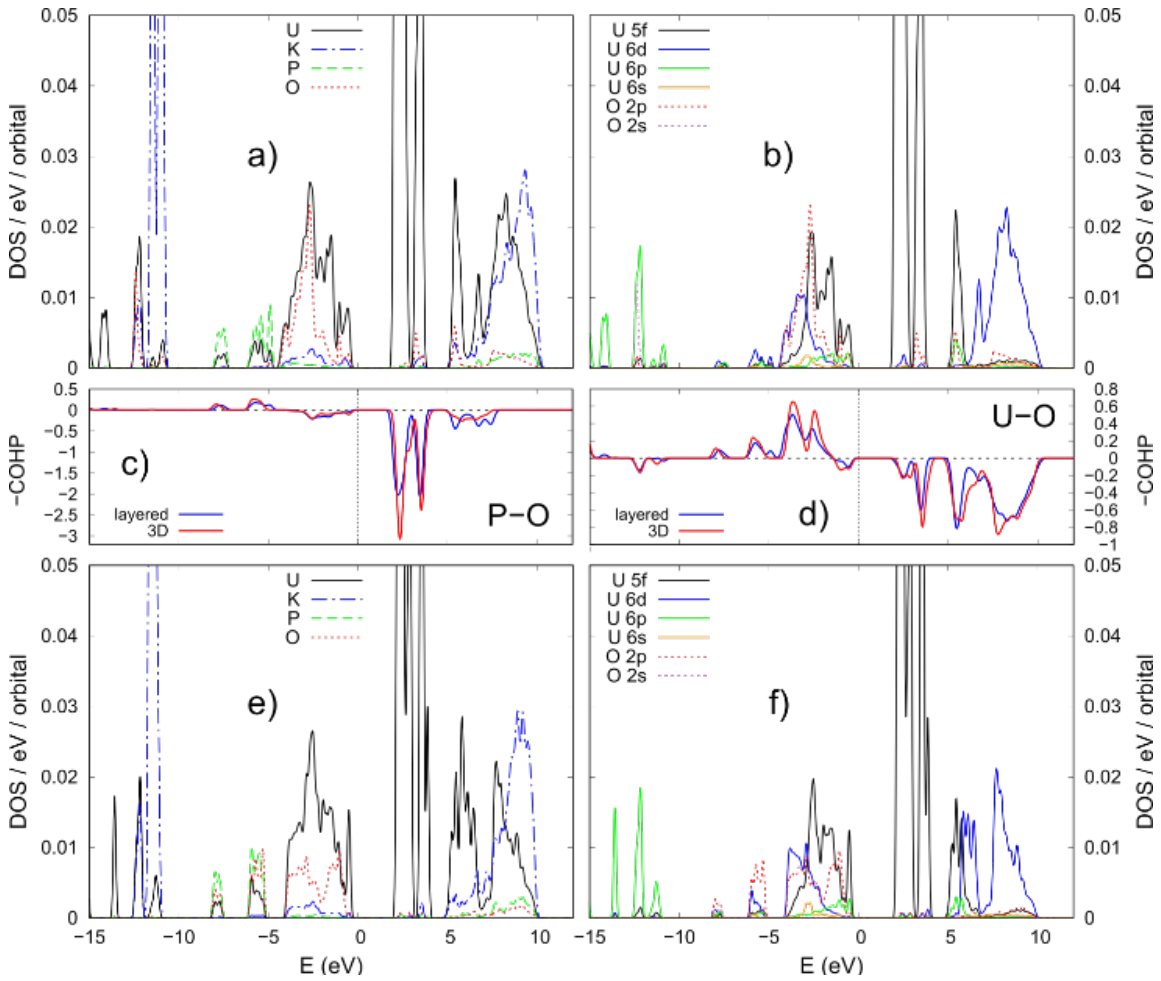


**Figure B.7.** Projected DOS (PDOS) of K containing polymorphs. a), b) layered polymorph; and e), f) 3D polymorph, calculated using $U_{eff}$ = 1.5 eV. The U, K, P and O PDOS are shown in black, blue, red and green, respectively. The U-5*f*, U-6*d*, U-6*p*, U-6*s*, O-2*p*, and O-2*s* PDOS are shown in black, blue, green, orange, red and a) and violet, respectively. –COHP diagrams of c) P–O and d) U–O 1NN bonds in the layered (blue) and 3D (red) K polymorphs.

There is a rather significant difference between the PDOS of the layered and 3D polymorphs (see Figure B.7b and f). The VBM of the 3D polymorph is entirely made up of U-5*f* states, except for some hybridization with O-2*p* and U-6*p*, which is not the case for the layered polymorph, where a moderate contribution from the O-2*p* and U-6*p* is evident. This difference in the VBM states is due to the distinct crystal field splitting of the U-*f* states coming from the differing coordination between the U atoms in the two polymorphs.

It is also noticeable that the U states of the layered polymorphs are broader than those of the 3D polymorph. The O-2*p* states in the 3D polymorph are shifted slightly below the VBM but are more intense and extend to lower energies (to -6 eV), as compared to the O-2*p* states of the layered polymorph. This causes an increased overlap between U and O-2*p* states, i.e., increased hybridization between the U and O-2*p* states, indicating stronger U–O interactions in the 3D polymorph. In addition, the PDOS peaks from the P atoms are at the same energy for both polymorphs (<-5 eV) which is expected from the clearly defined phosphate tetrahedra in the polymorphs. Because the VB O states of the 3D polymorph continue into energies below -5 eV, they overlap with the PDOS of P atoms. The larger overlap between the VB PDOS of P and O indicates a possible stronger P–O bonding in the 3D as compared to the layered polymorph. Besides the previously mentioned difference in the peak broadening, there is no significant difference between the PDOS of A atoms in the layered and 3D polymorph.

**Bonding Properties.** To further understand the preference for the formation of a particular polymorph, we analyzed the bond strength of 1NN atomic pairs in the structures. We performed COHP analysis as shown in Figure B.7c and d, where negative values indicate bonding, and positive values antibonding character. Note that following the convention we plotted the negative COHP (-COHP) diagrams as function of energy. Analogously to the DOS, the COHP of the 3D polymorph displays narrower bands. Also, bonding character in the COHP is observed in energy regions where overlap between the DOS of the two types of atoms in an atomic pair is present, note the position of the –COHP peaks in Figure B.7c and d. In addition to the bonding (antibonding) character for the

considered energy region, the integral of the COHP (ICOHP) gives information on the relative bonding strength between atoms of an atomic pair.

Therefore, to obtain information on the bonding strength, we calculated the average ICOHP per bond type, up to the Fermi level ($E_f$) for each of the 1NN bonds in the polymorphs. The ICOHP of both polymorphs, calculated using $U_{eff}$ = 1.5 eV, are shown in Figure B8a and b. From the results the U–O and P–O bond are the strongest, which is expected from the structure as the uranyl polyhedra and phosphate tetrahedra form the main structural framework. However, there is a difference in the ICOHP of the U–O and P–O in both polymorphs. In the layered polymorph the average U–O and P–O ICOHP are 2.62 and 3.12, respectively, while the average U–O and P–O ICOHP in the 3D polymorph are 3.09 and 3.19, respectively. The similarity in the ICOHP of the P–O, 3.12 in the layered and 3.19 in the 3D polymorph, comes from the uniform P tetrahedra, with similar P–O distances in both polymorphs. On the other hand, the U coordination, see Figure B.1, and U–O bond distances in both polymorphs are different, with the average U–O distances being shorter in the 3D polymorph. The shorter U–O distances will induce stronger bonding, and hence, increased ICOHP for the U–O bonds in the 3D polymorph. The U–U and U–A bonds are the next strongest, but still only a third of the U–O bond strength, with the A–A bond strength next, being ~20 % of the U–O bond strength. Lastly, the bond strength of the other five atomic pairs are each less than 5 % of the U–O bond strength. Note the change in alkali atomic radius causes an insignificant change in the X–O bond strength (X = U, A, P), while there is a significant change in the bond strength of the more distant atoms (second NN shell atoms). For example, both U–U and U–P bond strengths decrease, and the U–A and A–A bond strengths increase with increasing alkali atomic

radius size, which is inversely related to the change in alkali atoms. To accommodate the increasing alkali atomic radius, the 1NN U–U and U–P distance increases, decreasing the overlap between the U and P states, reducing the interaction. On the other hand, the U–A and A–A 1NN distance decreases with increasing alkali atomic radius, increasing the overlap between the U and A states, and thus increasing the bond strength.

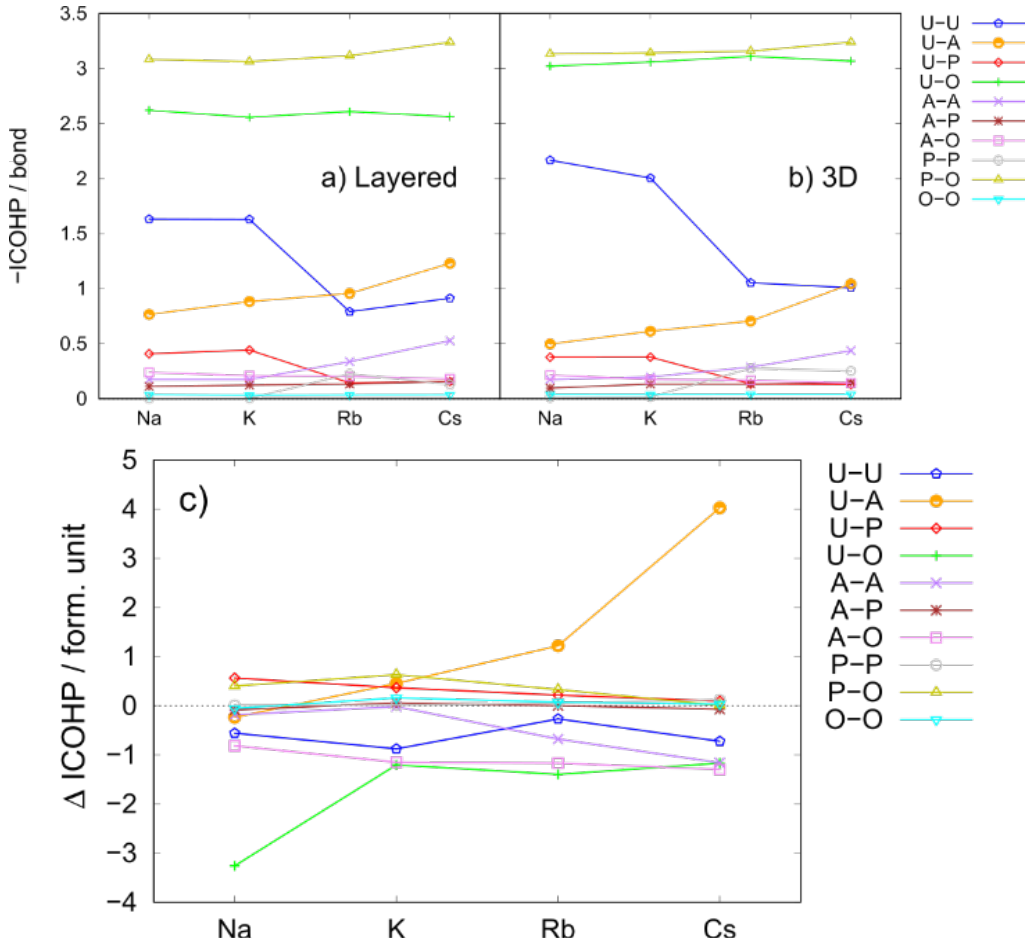


**Figure B.8.** ICOHP per 1NN bonds in the a) layered polymorphs and b) 3D polymorphs. c) Difference between the layered and 3D polymorphs ICOHP (ΔICOHP) per formula unit of the different 1NN bonds. Calculations utilized $U_{eff}$ = 1.5 eV.

To evaluate the influence of the polymorph structure on the bonding strength, we calculated the difference between the ICOHP of the layered and 3D polymorphs

(ΔICOHP), for each of the 1NN atomic pairs (see Figure B.8c). As the polymorphs have different structures with differing number of 1NN atoms, and the contribution to the total 1NN bond strength depends on the number of 1NN bonds, and it is most appropriate to compare the ICOHP per formula unit (Figure B.8c). Calculated ΔICOHP for all 1NN bonds and at each $\boldsymbol{U}_{\mathbf{eff}}$ illustrate that increasing the $\boldsymbol{U}_{\mathbf{eff}}$ has a weak influence on the ΔICOHP of the different polymorphs. From Figure B.8 it is evident that the U–A bond strength in the 3D polymorphs significantly increases with increasing alkali size. As discussed previously, this can be attributed to the smaller average U–A distance and larger overlap between the U and A states in the 3D polymorphs. The substantial increase in the U–A bond strength in the 3D Cs polymorph can be the main driving force for the formation of the 3D over the layered polymorph. On the other hand, U–O bonds in the layered polymorph are stronger compared to the 3D polymorph, with the difference being significantly larger for the Na polymorphs, while the difference in U–O bond strength in the other three polymorphs is very similar. A decrease in the A–A and U–P bond strengths with increasing alkali atomic radius in the 3D polymorph is also noted. Increasing alkali size has a rather weak influence on the ΔICOHP of the other five atomic pairs, with the ΔICOHP values varying ±0.5.

**Optical Properties.** We calculated the real, $\boldsymbol{\varepsilon_1}$, and imaginary, $\boldsymbol{\varepsilon_2}$, part of the dielectric function, for each of the studied polymorphs, from which the absorption indexes were evaluated using Eq. (1). Because of the monoclinic structure of the polymorphs, the dielectric tensor will not be symmetric and the dielectric functions, $\boldsymbol{\varepsilon_1}$ and $\boldsymbol{\varepsilon_2}$, will display anisotropic behavior, depending on which crystallographic direction is considered. For example, $\boldsymbol{\varepsilon_c(\omega \rightarrow 0)}$, calculated using $\boldsymbol{U}_{\mathbf{eff}}$ = 1.5 eV, in the [100], [010] and [001] crystallographic directions of the layered and 3D K polymorphs are 1.90, 2.12, 2.25 and

2.00, 1.97, 1.70, respectively. There is an evident decrease in the $\varepsilon_c$ with increasing $U_{eff}$, where the $\varepsilon_c$ in the three crystallographic directions of each of the studied polymorphs display converging trend towards each other with increasing $U_{eff}$. The increase in the band gap with increasing $U_{eff}$ (see Figure B.5), and the known decrease in $\varepsilon_1$, and hence $\varepsilon_c$ with increasing band gap in a semiconductor/insulator,[35] explains the decrease in the $\varepsilon_c$ with increasing $U_{eff}$.

Values of $\alpha(\omega)$ also depend on the crystallographic direction in the same manner as do $\varepsilon_1$ and $\varepsilon_2$. Shown in Figure B.9 are the calculated $\alpha(\omega)$ for each of the polymorphs, for $U_{eff}$ = 1.5 eV, as well as the $\alpha(\omega)$ in the three crystallographic directions [100], [010] and [001] of the K-containing polymorphs. It is evident that the fundamental absorption edge occurs at energies close to the polymorphs' respective band gaps, corresponding to the optical transitions between the VBM and CBM. It is also worth noting the similarity between the experimentally measured $\alpha(\omega)$ and the calculated $\alpha(\omega)$, especially the $\alpha(\omega)$ in the [010] and [001] crystallographic directions.[12]

Three dominant $\alpha(\omega)$ peaks are seen near 3.25, 4.8 and 6.25 eV (Figure B.9c and d). The first peak originates from the transition from the hybridized U-5*f*, U-6*p* and O-2*p* states to U-5*f* (see Figure B.7b and f). The second peak is generated also by transitions from the U-6*d* and U-7*s* states to U-5*f*. Contribution to the third peak come also from transitions from P-3*p* states to U-5*f* and O-2*p* states to alkali atom states. In addition, similarly to the DOS, the $\alpha(\omega)$ of the Na polymorphs have the most variation compared to the polymorphs containing the other three alkali metals, which have very similar $\alpha(\omega)$ in the three crystallographic directions (Figure B.9a and b). Considering the relation between

the DOS and $\boldsymbol{\alpha(\omega)}$, the dependence on the $\boldsymbol{U_{eff}}$, is seen to depend on the localization of the bands, with the increasing $\boldsymbol{U_{eff}}$ promoting sharper, more defined peaks in the $\boldsymbol{\alpha(\omega)}$.

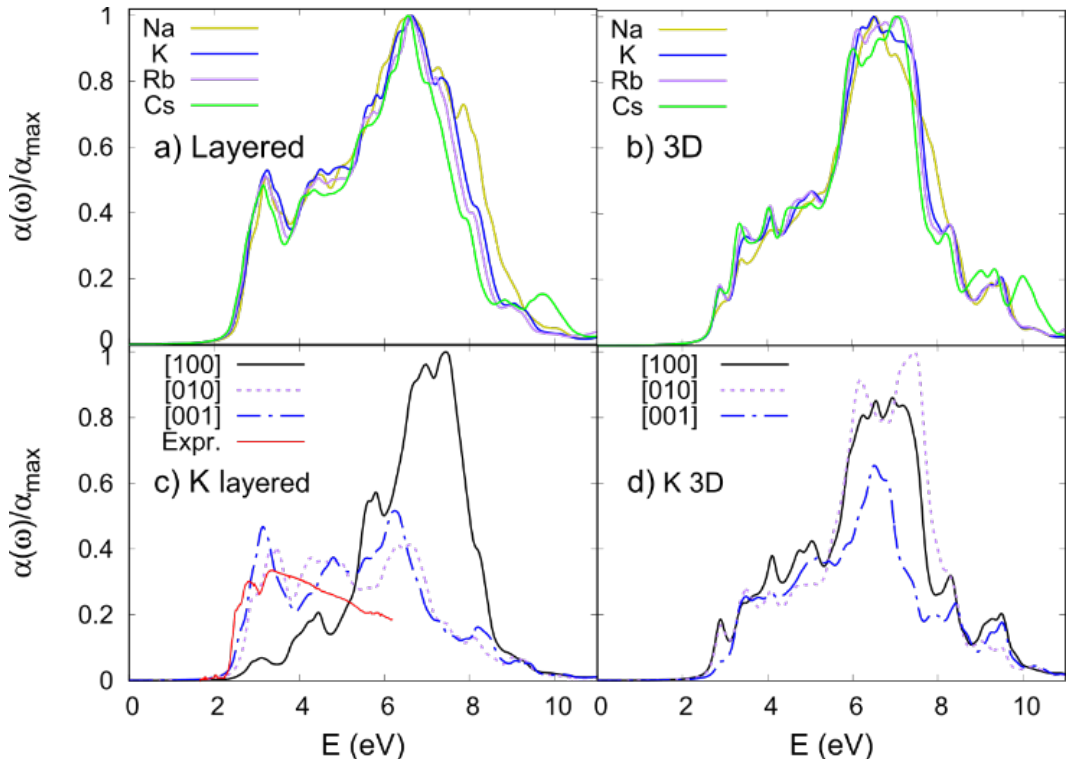


**Figure B.9:** Absorption indexes for: a) Layered polymorphs, and b) 3D polymorphs. The $\alpha$ in the three crystallographic directions are plotted for of c) layered and d) 3D K polymorphs. The $\boldsymbol{\alpha}$ of the Na, K, Rb, and Cs polymorphs are shown in yellow, blue, purple and green, respectively. The $\alpha$ in [100], [010] and [001] directions are shown in black, purple and blue lines, respectively. The experimentally measured $\boldsymbol{\alpha(\omega)}$ of the K layered polymorph, Ref. 12, is shown in red.

The $\boldsymbol{\alpha(\omega)}$ of the layered polymorphs in the [100] direction is significantly different than that in the other two directions due to its structure. Due to the presence of uranyl bipyramids in the layers which with the alkali metals run along the [010] and [001] directions, their $\boldsymbol{\alpha(\omega)}$ are broader and more intense at lower energies compared to $\boldsymbol{\alpha(\omega)}$ along the perpendicular [100]. In the case of the 3D polymorphs, on the other hand, the $\boldsymbol{\alpha(\omega)}$ in the three crystallographic directions are more similar and are comparable to $\boldsymbol{\alpha(\omega)}$

for the [100] direction in the layered polymorphs. This similarity derives from the channel-like structure of the 3D polymorphs, with an average contribution to the optical transition states from the uranyl octahedral, phosphate tetrahedra and the A–O interactions.

**Conclusion.** We have prepared $Cs_4[(UO_2)_3(PO_4)_2O_2]$ via high temperature flux growth methods and determined its single-crystal structure. We performed DFT, DFT+*U* and VBT calculations to determine relative layered versus 3D polymorph stability. DFT calculations showed the 3D Cs polymorph is energetically more stable than the layered polymorph. There is a trend, however, of increasing stability of the layered structures with decreasing alkali ion size, with the layered K and Na polymorphs being more stable. However, the energy difference between the layered and 3D polymorphs increases with increasing $\boldsymbol{U}_{\mathbf{eff}}$, giving rise to inconclusive results for Rb polymorphs. VBT calculations revealed 3D polymorphs to be less thermodynamically stable than those of the layered uranyl phosphate family, $A_4(PO_4)_2[(UO_2)_3O_2]$, regardless of the VBT method and formula unit volume used for calculating the total energies. This helps explain why layered structures are more abundant in uranyl phosphate chemistry, especially structures containing smaller alkali atoms.

The band gaps of the 3D polymorphs are slightly larger than the band gaps of the layered polymorphs, originating from the U coordination and its influence on the states around the band gap. Bands in the DOS of the layered polymorphs are broader than those of the 3D polymorph, which was attributed to the broader distribution of 1NN bond distances in the layered polymorph. We argued that the different distribution of the DOS will have a distinct influence on the bond strength in the polymorphs.

Significant anisotropy in the optical absorption along the three crystallographic directions is observed, arising from the distinct structures of the polymorphs. The similarities between the absorption index in the [010] and [001] directions of the layered polymorphs are due to the absorption in the uranyl phosphate layers. The similarities in the absorption index in the three crystallographic directions of the 3D polymorphs are related to their channel-like structure.

Using COHP analysis we show that the U–O and P–O are the strongest bonds in both polymorphs, followed by the U–U, U–A, and A–A, in descending bond strength order. In addition, we demonstrate that when considering the bond strength per formula unit, the U–A bonds are stronger in the 3D polymorphs, while the U–O bonds are stronger in the layered polymorphs. The preferred formation of the Cs 3D structure is attributed to the significant bond strength of U–A 1NN atomic pairs in the polymorph.

**Acknowledgment.** This work is supported by the U.S. Department of Energy, Office of Science, Basic Energy Sciences, under Award No. DE-SC0016575 (Center for Hierarchical Waste Form Materials). This research used computational resources provided by the National Energy Research Scientific Computing Center (NERSC) and the HPC cluster Hyperion, supported by The Division of Information Technology at University of South Carolina.

**References:**

(1) Burns, P. C., A new uranyl phosphate chain in the structure of parsonsite, *Am. Mineral.* **2000**, *85*, 801-805.

(2) zur Loye, H.-C.; Besmann, T.; Amoroso, J.; Brinkman, K.; Grandjean, A.; Henager, C. H.; Hu, S.; Misture, S. T.; Phillpot, S.; Shustova, N. B.; Wang, H.; Koch, R. J.;

Gregory Morrison; Dolgopolova, E., Hierarchical Materials as Tailored Nuclear Waste Forms: A Perspective, *Chem. Mater.* **2018**, *30*, 4475-4488.

(3) Villa, E. M.; Marr, C. J.; Jouffret, L. J.; Alekseev, E. V.; Depmeier, W.; Albrecht-Schmitt, T. E., Systematic evolution from uranyl(VI) phosphites to uranium(IV) phosphates., *Inorg. Chem.* **2012**, *51*, 6548-6558.

(4) Lussier, A. J.; Lopez, R. A. K.; Burns, P. C., A revised and expanded structure hierarchy of natural and synthetic hexavalent uranium compounds, *Can. Mineral.* **2016**, *54*, 177-283.

(5) Shvareva, T. Y.; Sullens, T. A.; Shehee, T. C.; Albrecht-Schmitt, T. E., Syntheses, structures, and ion-exchange properties of the three-dimensional framework uranyl gallium phosphates, $Cs_4[(UO_2)_2(GaOH)_2(PO_4)_4]\cdot H_2O$ and $Cs[UO_2Ga(PO_4)_2]$, *Inorg. Chem.* **2005**, *44*, 300-305.

(6) Burns, P. C.; Finch, R. *Uranium: Mineralogy, Geochemistry & the Environment (Reviews in Mineralogy & Geochemistry).* Mineralogical Society of America: 1999-10;

(7) Shvareva, T. Y.; Albrecht-Schmitt, T. E., General route to three-dimensional framework uranyl transition metal phosphates with atypical structural motifs: the case examples of $Cs_2\{(UO_2)_4[Co(H_2O)_2]_2(HPO_4)(PO_4)_4\}$ and $Cs_{3+x}[(UO_2)_3CuH_{4-x}(PO_4)_5]\cdot H_2O$., *Inorg. Chem.* **2006**, *45*, 1900-1902.

(8) Guesdon, A.; Chardon, J.; Provost, J.; Raveau, B., A copper uranyl monophosphate built up from $[CuO_2]_\infty$ Chains: $Cu_2UO_2(PO_4)_2$, *J. Solid State Chem.* **2002**, *165*, 89-93.

(9) Alekseev, E. V.; Krivovichev, S. V.; Depmeier, W.; Knorr, K., Complex topology of uranyl polyphosphate frameworks: crystal structures of α-, β-$K[(UO_2)(P_3O_9)]$ and $K[(UO_2)_2(P_3O_{10})]$, *Z. Anorg. Allg. Chem.* **2008**, *634*, 1527-1532.

(10) Renard, C.; Obbade, S.; Abraham, F., Channels occupancy and distortion in new lithium uranyl phosphates with three-dimensional open-frameworks, *J. Solid State Chem.* **2009**, *182*, 1377-1386.

(11) Yagoubi, S.; Renard, C.; Abraham, F.; Obbade, S., Molten salt flux synthesis and crystal structure of a new open-framework uranyl phosphate $Cs_3(UO_2)_2(PO_4)O_2$: Spectroscopic characterization and cationic mobility studies, *J. Solid State Chem.* **2013**, *200*, 13-21.

(12) Juillerat, C. A.; Moore, E. E.; Kocevski, V.; Besmann, T. M.; zur Loye, H.-C., A Family of Layered Phosphates Crystallizing in a Rare Geometrical Isomer of the Phosphuranylite Topology: Synthesis, Characterization, and Computational

Modeling of $A_4[(UO_2)_3O_2(PO_4)_2]$ (A = alkali metals) Exhibiting Intra-layer Ion Exchange, *Inorg. Chem.* **2018**, *57*, 4726-4738.

(13) Kresse, G.; Furthmuller, J., Efficient iterative schemes for ab-initio total-energy calculations using a plane-wave basis set, *Phys. Rev. B* **1996**, *54*, 11169-11186.

(14) Kresse, G.; Furthmuller, J., Efficiency of ab-initio total energy calculations for metals and semiconductors using a plane-wave basis set, *Comput. Mater. Sci.* **1996**, *6*, 15-50.

(15) Perdew, J. P.; Burke, K.; Ernzerhof, M., Generalized Gradient Approximation Made Simple, *Phys. Rev. Lett.* **1996**, *77*, 3865-3868.

(16) Blöchl, P. E., Projector augmented-wave method, *Phys. Rev. B* **1994**, *50*, 17953-17979.

(17) Kresse, G.; Joubert, D., From ultrasoft pseudopotentials to the projector augmented-wave method, *Phys. Rev. B* **1999**, *59*, 1758-1775.

(18) Hybertsen, M. S.; Louie, S. G., Electron correlation in semiconductors and insulators: Band gaps and quasiparticle energies, *Phys. Rev. B* **1986**, *34*, 5390.

(19) Dronskowski, R.; Blöchl, P. E., Crystal orbital Hamilton populations (COHP): energy-resolved visualization of chemical bonding in solids based on density-functional calculations, *The Journal of Physical Chemistry* **1993**, *97*, 8617-8624.

(20) Deringer, V. L.; Tchougréeff, A. L.; Dronskowski, R., Crystal orbital Hamilton population (COHP) analysis as projected from plane-wave basis sets, *The journal of physical chemistry A* **2011**, *115*, 5461-5466.

(21) Maintz, S.; Deringer, V. L.; Tchougréeff, A. L.; Dronskowski, R., Analytic projection from plane-wave and PAW wavefunctions and application to chemical-bonding analysis in solids, *J. Comput. Chem.* **2013**, *34*, 2557-2567.

(22) Dudarev, S. L.; Botton, G. D.; Savrasov, S. Y.; Humphreys, C. J.; Sutton, A. P., Electron-energy-loss spectra and the structural stability of nickel oxide: An LSDA+U study, *Phys. Rev. B* **1998**, *57*, 1505-1509.

(23) Schoenes, J., Recent specroscopic studies of $UO_2$, *J. Chem. Soc., Faraday Trans. 2* **1987**, *83*, 1205-1213.

(24) Kotani, A.; Takao, Y., Systematic Analysis of Core Photoemission Spectra for Actinide Di-Oxides and Rare-Earth Sesqui-Oxides, *Prog. Theor. Phys. Suppl.* **1992**, *108*, 117-131.

(25) Cococcioni, M.; De Gironcoli, S., Linear response approach to the calculation of the effective interaction parameters in the LDA+ U method, *Phys. Rev. B* **2005**, *71*, 035105.

(26) Glasser, L.; Jenkins, H. D. B., Volume-Based Thermodynamics: A prescription for its application and usage in approximating and predicting thermodynamic data, *J. Chem. Eng. Data.* **2011**, *56*, 874-880.

(27) Glasser, L.; Jenkins, H. D. B., Predictive thermodynamics for ionic solids and liquids, *Phys. Chem. Chem. Phys.* **2016**, *18*, 21226-22140.

(28) Moore, E. E.; Kocevski, V.; Juillerat, C. A.; Morrison, G.; Zhao, M.; Brinkman, K.; Loye, H.-C. Z.; Besmann, T., Understanding the Stability of Salt Inclusion Phases for Nuclear Waste-forms through Volume-based Thermodynamics, *Scientific Reports* **2018**, *8*, 15294.

(29) Bugaris, D. E.; Ibers, J. A., Syntheses and characterization of some solid-state actinide (Th, U, Np) compounds, *Dalton Trans.* **2010**, *39*, 5925-6128.

(30) Bruker. *APEX3, SAINT+, TWINABS, and SADABS.* Bruker AXS Inc.: Madison, Wisconsin, USA, 2015;

(31) Sheldrick, G. M., SHELXT - Integrated space-group and crystal-structure determination, *Acta Cryst.* **2015**, *A71*, 3-8.

(32) Sheldrick, G. M., Crystal structure refinement with SHELXL, *Acta Cryst.* **2015**, *C71*, 3-8.

(33) Dolomanov, O. V.; Bourhis, L. J.; Gildea, R. J.; Howard, J. A. K.; Pushmann, H., OLEX2: a complete structure solution, refinement and analysis program, *J. Appl. Crystallogr.* **2009**, *42*, 339-341.

(34) He, H.; Andersson, D. A.; Allred, D. D.; Rector, K. D., Determination of the insulation gap of uranium oxides by spectroscopic ellipsometry and density functional theory, *The Journal of Physical Chemistry C* **2013**, *117*, 16540-16551.

(35) Wooten, F. *Optical properties of solids.* Academic press: 2013.

Appendix C

Permission to Reproduce Published Materials

**American Chemical Society License: Thesis/Dissertation**

**Chapters 1-4, 6, 7 and Appendix B**

*American Chemical Society's Policy on Theses and Dissertations*

Permission is now automatically granted; please pay special attention to the implications paragraph below. The Copyright Subcommittee of the Joint Board/Council Committees on Publications approved the following:

Copyright permission for published and submitted material from theses and dissertations ACS extends blanket permission to students to include in their theses and dissertations their own articles, or portions thereof, that have been published in ACS journals or submitted to ACS journals for publication, provided that the ACS copyright credit line is noted on the appropriate page(s).

If your paper has already been published by ACS and you want to include the text or portions of the text in your thesis/dissertation, please print the ACS copyright credit line on the first page of your article: "Reproduced (or 'Reproduced in part') with permission from [FULL REFERENCE CITATION.] Copyright [YEAR] American Chemical Society." Include appropriate information.

**Frontiers Copyright Statement**

**Chapter 5**

*Licenses (Permissions) You Grant as an Author*

As an author or contributor you grant permission to others to reproduce your articles, including any graphics and third-party materials supplied by you, in accordance with the Frontiers Terms and Conditions.

When you submit an article to Frontiers, you grant to Frontiers and to the world at large a permanent, non-cancellable, free-of-charge, worldwide license (permission) to publish, display, store, copy and re-use that article – including any third-party materials – and to create derivative works from it.

In summary, the CC-BY license means that anyone may copy, re-publish and/or re-use your content, and create derivative works from it, for commercial or non-commercial purposes, without charge, but must clearly attribute the work to you and any co-authors, and they must cite Frontiers as the original publisher of that content.

**Royal Society of Chemistry License: Re-use permission requests**

**Introduction, Chapters 8, 10, and 11**

*Author reusing their own work published by the Royal Society of Chemistry*

You do not need to request permission to reuse your own figures, diagrams, etc., that were originally published in a Royal Society of Chemistry publication. However, permission should be requested for use of the whole article or chapter except if reusing it in a thesis. If you are including an article or book chapter published by us in your thesis please ensure that your co-authors are aware of this.

Reuse of material that was published originally by the Royal Society of Chemistry must be accompanied by the appropriate acknowledgement of the publication. The form of the acknowledgement is dependent on the journal in which it was published originally, as detailed in 'Acknowledgements'.

Standard acknowledgement statement (Chapter 7 and 11): Reproduced from Ref. XX with permission from the Royal Society of Chemistry.

Acknowledgement statement for Inorganic Chemistry Frontiers (Chapter 10): Reproduced from Ref. XX with permission from the Chinese Chemical Society (CCS), Peking University (PKU), and the Royal Society of Chemistry.

**Scientific Reports Editorial and Publishing Policies**

**Appendix A**

*License agreement and author copyright*

*Scientific Reports* does not require authors to assign copyright of their published original research papers to the journal. Articles are published under a CC BY license (Creative Commons Attribution 4.0 International License). The CC BY license allows for maximum dissemination and re-use of open access materials and is preferred by many research funding bodies. Under this license users are free to share (copy, distribute and transmit) and remix (adapt) the contribution including for commercial purposes, providing they attribute the contribution in the manner specified by the author or licensor.